Metal-Organic Frameworks For Adsorption Driven Energy Transformation –

From Fundamentals To Applications

Cover illustration: Water adsorbed in CAU-10(Al)-H (*artist's impression*)

Metal-Organic Frameworks For Adsorption Driven Energy Transformation –
From Fundamentals To Applications

Proefschrift

ter verkrijging van de graad van doctor

aan de Technische Universiteit Delft,

op gezag van de Rector Magnificus prof. ir. K.C.A.M. Luyben,

Voorzitter van het College voor Promoties,

in het openbaar te verdedigen op

vrijdag 22 mei 2015 om 12:30 uur

door

Martijn Ferdinand DE LANGE

Scheikundig ingenieur

geboren te Rotterdam, Nederland

Dit proefschrift is goedgekeurd door de promotoren:

Prof. dr. F. Kapteijn

Prof. dr. J. Gascon

Prof. dr. ir. T.J.H. Vlugt

Samenstelling promotiecommissie:

Rector Magnificus	Voorzitter
Prof. dr. F. Kapteijn	Technische Universiteit Delft, Promotor
Prof. dr. J. Gascon	Technische Universiteit Delft, Promotor
Prof. dr. ir. T.J.H. Vlugt	Technische Universiteit Delft, Promotor

Independent members:

Dr. S. Henninger	Fraunhofer Institute
Prof. dr. G. Maurin	Université Montpellier II
Prof. dr. R. Gläser	Universität Leipzig
Prof. dr. ir. A.I. Stankiewicz	3mE, Technische Universiteit Delft
Prof. dr. B. Dam	TNW, Technische Universiteit Delft, reservelid

Proefschrift, Technische Universiteit Delft

Met samenvatting in het Nederlands / Including summary in Dutch

ISBN: 978-94-6186-453-6

Cover design: Martijn F. de Lange

Printed by: Wohrmann Print Service B.V.

Nihil Ex Nihilo Fit

Contents

CHAPTER 1

METAL-ORGANIC FRAMEWORKS AND
HEAT PUMPS – AN INTRODUCTION

Global energy consumption shows a continuous rise, despite the increased tangibility of (anthropogenic) global climate change [1]. Households worldwide are responsible for about one third of the world energy consumption. This energy is mainly used for heating and cooling in residential areas [2]. The building sector accounted for 25% of the total global energy consumption in 2010, predominantly for space heating and hot water production, respectively 53% and 16% of this sector [3]. Furthermore, combined energy demands for heating, and especially cooling, are forecasted to increase significantly in the coming years, the magnitude of which depends on model assumptions used for the prediction [2]. The urgent need to address this situation has prompted international action from governments and industries. *E.g.*, the EU-28 countries have specified ambitious energy efficiency targets, as expressed in Directive 2012/27/EU [4], to reduce primary energy consumption by 20% in 2020. The Netherlands, specifically, has committed to reduce the total annual energy consumption to 2,183 PJ in 2020 [4, 5], a 38% reduction compared to 2010 [6]. Of the total energy consumption in this country, roughly 40% is spent on heating (38.4%) and cooling (2.4%) [6]. Especially, the energy demand for cooling in the Netherlands is forecasted to increase substantially in the coming years [6]. This clearly highlights the importance of mitigating primary energy requirements for heating and cooling as a tool to decrease fossil fuel consumption and associated CO_2 emissions.

To mitigate, (part of) these energetic expenses, one could opt for the utilization of solar energy for these purposes. However, the supply of solar energy and demand for heating are not always in phase [7]. When energy supply and heating demand are in phase, *e.g.* for air-conditioning, refrigeration and hot water production, thermally driven heat pumps can be employed, sustainably utilizing the available energy (*e.g.* solar or waste heat), a clear advantage over devices based on vapor compression [8], which use electrical energy. There are multiple possible working principles for heat pumps driven by thermal energy [9], *e.g.* chemical reactions [9, 10], absorption [9, 11] and adsorption [9, 12]. The main advantage of the adsorption driven heat pump, which is the topic of this thesis, is that low driving or regeneration temperatures (< 100 $^{\circ}$C) can be employed efficiently [9, 11, 13-15], which fits the available temperatures of the desired energy sources (solar, industrial waste heat). Further, environmentally benign working fluids (*e.g.* water) can be used. A drawback is that the performance of currently available devices is somewhat lower than of alternatives based on chemical reactions or absorption. Additionally, one could further use adsorption based open system air-conditioning by desiccation [14-17]. A great advantage is that water vapor can be

removed directly from the ambient air, whereas the closed devices require cooling down of the incoming air to temperatures below the dew point [18]. Often this means that the dried air has to be reheated, resulting in an energetically more expensive system. Additional advantages of desiccant air conditioning over vapor compression systems are the ability to use low-grade thermal energy (similar to adsorption driven heat pumps) and the working fluid (ambient water) is environmentally benign by default.

When energy supply and demand are out of phase, temporary energy storage is required. Among the different options, thermochemical storage is interesting, as it requires significantly less volume to store the same amount of energy [19, 20] compared to systems based on latent [21] or sensible energy [22]. Main alternatives for thermochemical storage primarily store and release energy based on either chemical reactions (*e.g.* hydration of inorganic salts) or adsorption.

Thermochemical energy storage and desiccant air conditioning are considered alternative applications for porous adsorbents in this thesis and are only concisely discussed in Chapter 4, the main focus of this thesis being on adsorption driven heat pumps. Devices based on this principle could use thermal energy to supply cooling and heating.

WORKING PRINCIPLES OF AN ADSORPTION DRIVEN HEAT PUMP

The working mechanism, in its simplest form, is shown in Fig. 1.1. An initially dry adsorbent is connected with a working fluid-filled evaporator (Fig. 1.1, left). During this process, heat is withdrawn from the surroundings by evaporation of the working fluid (Q_{ev}), due to the adsorption of the working fluid by the (porous) adsorbent. As adsorption is exothermic, heat will be released to the surroundings at an intermediate temperature (Q_{ads}). As the adsorbent will become saturated with working fluid, regeneration is required (Fig. 1.1, right). Energy is withdrawn from a relatively high temperature (Q_{des}) to desorb the working fluid, which is subsequently condensed, releasing heat at an intermediate temperature (Q_{con}). One can operate such an adsorption cycle as heat pump to produce heat at the intermediate temperature (Adsorption driven Heat Pump, AHP), using effectively Q_{con} and Q_{ads} or to produce cold at the lower temperature by making use of Q_{ev} (Adsorption Driven Chiller, ADC). A detailed thermodynamic description of such a cycle can be found in Chapter 4 of this thesis. In any case, the cycle requires thermal energy as input. The temperature of this input can be relatively low (below 100°C) [13, 14], making efficient use of industrial waste heat or solar energy.
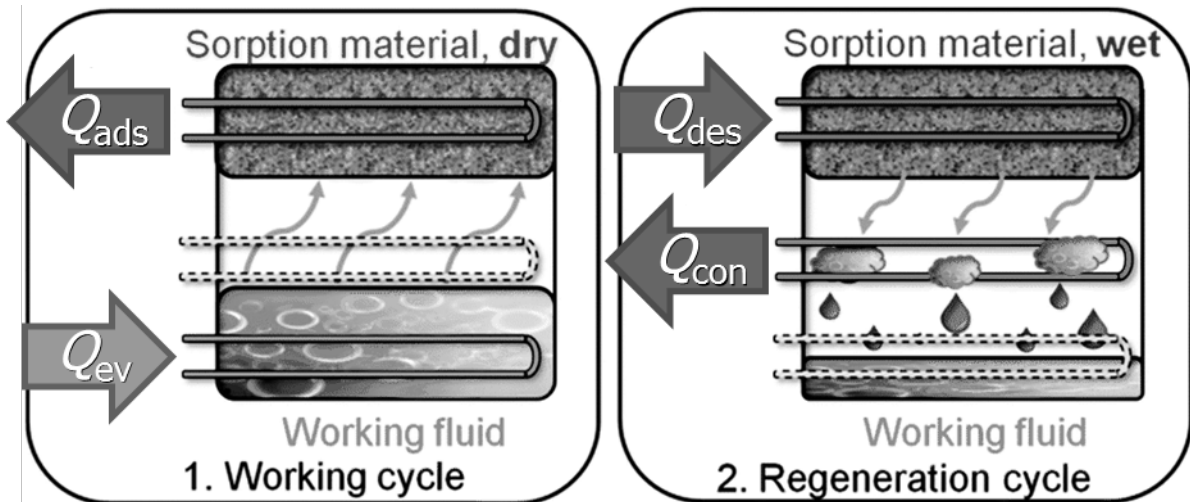
Figure 1.1: Principle of operation of an adsorption driven heat cycle with the adsorption stage (*left*) and the desorption stage (*right*). Reproduced with permission from Ref. [23].

HISTORICAL PERSPECTIVE ON AHP/ADC'S

Adsorption driven heat and cold allocation is not a novel technology. After the first quantitative work on adsorption by Scheele and Fontana [24] and the pioneering work of Michael Faraday, who demonstrated adsorptive based cooling in 1823 using an ammonia-silver chloride working pair [25, 26], and some early commercial products [27-29], the technology was swiftly replaced due to the development of more efficient vapor compression systems (based on chlorinated fluorocarbons, CFC's) [24, 26]. However, following the prohibition of commonly used fluids in vapor compression (CFCs) because of environmental concerns,[30, 31] and the aforementioned global energy consumption prognosis, research on adsorption driven heat pumps is again in full swing (timeline depicted in Fig. 1.2) [24, 32].
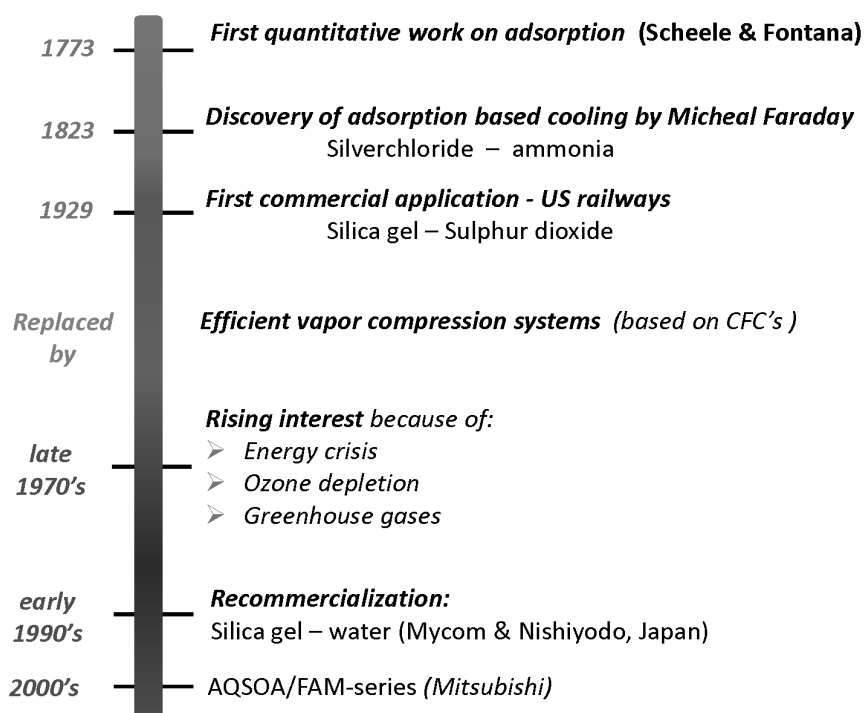
Figure 1.2: Historical timeline (brief) of adsorption driven heat pump and chiller research and commercialization.

ELIGIBLE WORKING FLUIDS

For application, the selected working fluid should have a high enthalpy of evaporation. Furthermore, the capacity of the adsorbent should be maximized, reason why the working fluid molecules are preferentially relatively small. In addition, the working fluid should be condensable under operating conditions. Obviously, selected working fluids should have no global warming or ozone depletion potential. It is therefore not surprising to say that commonly used working fluids for adsorption driven purposes are water, methanol and ammonia [24]. Because of its lower toxicity compared to methanol, ethanol is also used [12, 33-35]. As shown in Fig. 1.3, water has the highest enthalpy of evaporation and ammonia the lowest, making the latter thermodynamically less efficient [24]. However, the high vapor pressure of NH_3 ensures that mass transport limitations are eliminated in cycle times down to the order of minutes [24]. In addition, in AHP/ADCs no use can be made of copper-based parts when ammonia is used [24]. Water has a significantly lower vapor pressure (Fig. 1.3) and cannot be used for sub-zero temperatures, due to its relatively high triple point temperature (273.16 K). Methanol and ethanol both are somewhat intermediate in properties compared to water and ammonia.
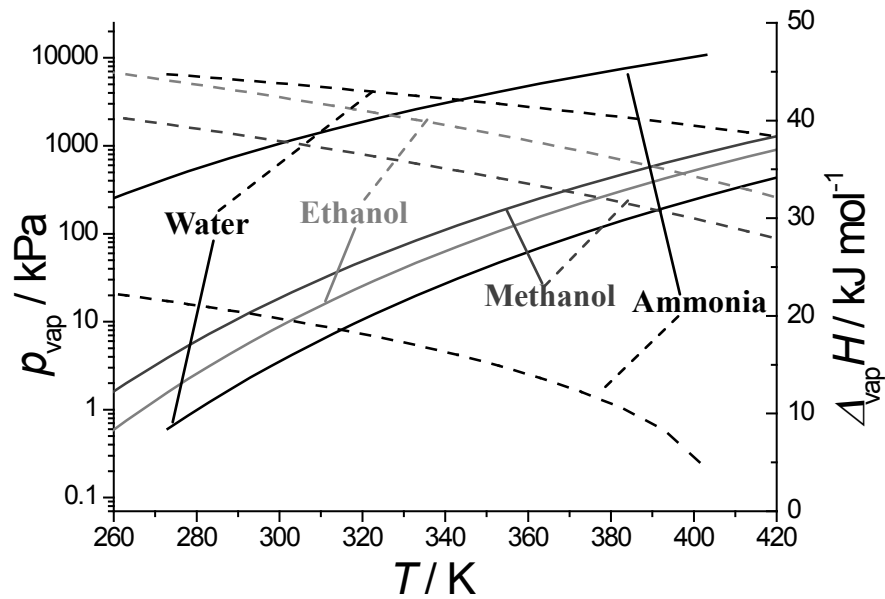
Figure 1.3: Vapor pressure (*solid lines*) and enthalpy of evaporation (*dashed lines*) as function of temperature, for water (*black*), methanol (*dark grey*), ethanol (*light grey*) and ammonia (*black*). Data from [36].

In this thesis, working fluids under consideration are water, methanol, ethanol and ammonia. Different adsorbents can be used in conjunction with these working fluids. Silica gels (water), zeolites (water) and activated carbons (methanol, ammonia) are popular in academia [24, 34, 37]. Commercially, water is dominantly used as working fluid in combination with silica gels or zeolites (*vide infra*).

DESIRED ADSORPTION BEHAVIOR

Regardless of the working pair, an adsorption isotherm with one single very steep uptake step at a low to intermediate relative pressure is preferred from an energetic perspective, as this will display the highest thermodynamic efficiency [38]. Also from a dynamic perspective, a stepwise isotherm is preferred [39, 40], as only a small change in relative sorbate pressure is needed for a large change in loading (working capacity), *i.e.* a large heat effect (see *e.g.* AQSOA-Z01, Fig. 1.4). Hysteresis during desorption is undesired, as this will increase the required desorption temperature. For realistic applications, the step in adsorption should be located at $p/p_o < 0.3$ [38] − 0.4 [41], here p_o represents the saturation pressure, for water (at room temperature), as for higher relative pressures the difference between the low (evaporator) temperature, T_{ev}, and intermediate (adsorption/condenser) temperature, T_{con},

becomes increasingly smaller. *E.g.,* for $0.3 < p/p_o < 0.45$, only $T_{ev} > 10 - 15$ ^oC and $T_{con} <$ 30 ^oC can be used, achieving only narrow operation window (often called 'temperature lift', see Chapter 4 for details) [38]. Furthermore the adsorption step should be preferentially located at $p/p_o > 0.05$[41] $- 0.1$[38] to ensure a sufficiently low desorption temperature. For methanol and ethanol the operating windows are similar to that of water, for ammonia this is shifted to higher relative pressures ($0.15 < p/p_o < 0.55$).

COMMERCIALLY APPLIED SORBENTS AND DEVICES

Nishiyodo [42] and Mycom pioneered the re-commercialization of adsorption driven devices, in both cases based on silica gel-water as working pair [32, 43]. Later, Sortech marketed silica-gel based sorption systems for cooling purposes [32]. Invensor has made commercial a coated zeolite-water based cooling system [32, 44]. Both Vaillant and Viesmann [45] have commercialized zeolite-water based heat pumps driven by the combustion of natural gas, which can in principle reduce the energy requirements of a conventional household boiler by up to 30% [32]. Commercially applied sorbents that perhaps show most advantageous adsorption isotherms, when contacted with water, are those of the FAM Z-series (Functional Adsorbent Material Zeolite). FAM Z05[46], and especially both Z01 [47] and Z02 [48] as commercialized by Mitsubishi Plastics, though referred to as the AQSOA^{tm} series [49], show very suitable adsorption characteristics. Adsorption isotherms of commercially used adsorbents are shown in Fig. 1.4.
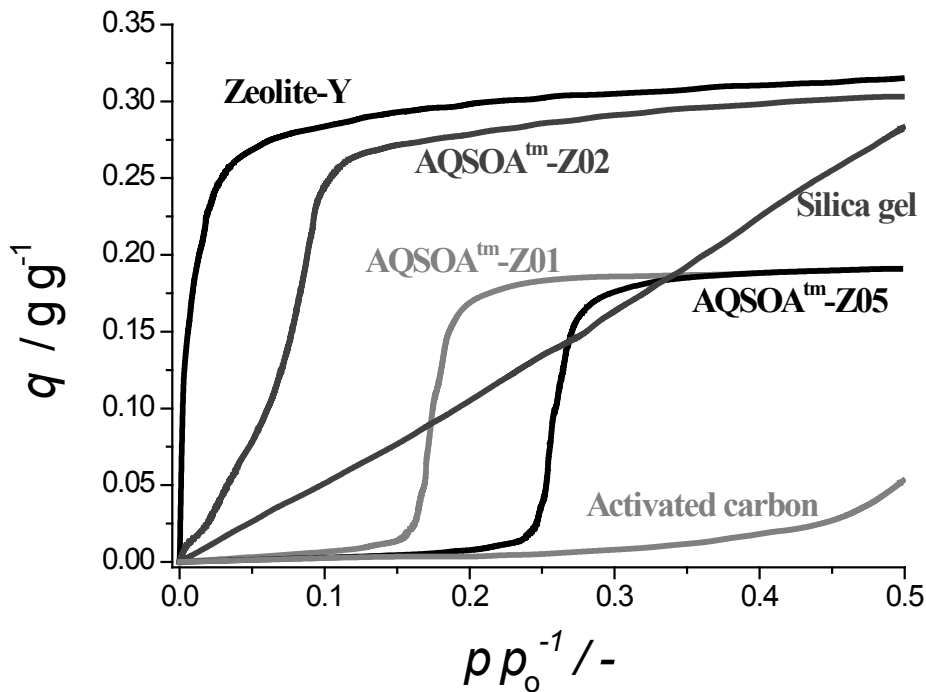
Figure 1.4: Water adsorption isotherms of commercially employed adsorbents. Here p_o represents the saturated vapor pressure (of water). Adapted from Ref. [49].

Zeolite Y has a very steep uptake at extremely low p/p_o, due to the strongly hydrophilic nature of high Al-containing zeolites. This in turn means that regeneration needs to be done at unfeasibly high desorption temperatures, a commonly reported drawback for application of these materials [38]. On the other hand, pure silica zeolites are too hydrophobic [38]. The adsorption behavior of silica gel is not desired, due to the clear absence of a stepwise uptake. The FAM/AQSOA^{tm} series show this stepwise uptake and especially Z01 and Z02 are employed in heat pumps (Z05 is used primarily for dehumidification) [49]. AQSOA-Z01 and Z05 are $AlPO_4$-5-based zeotypes with the AFI-structure (Z01 is partially iron-exchanged) [50], and AQSOA-Z02 is a SAPO-34 zeotype material with the CHA-structure [50]. In addition, these materials have been shown to exhibit high cyclic stability to ad- and desorption of water [51, 52]. The total uptake (capacity) of these materials however, is somewhat low.

From the above, it is clear that there is a large commercial interest in the development of new adsorption based devices, and that the market for such devices is expected to grow as performance improves [32]. Such a scenario could be realized by different approaches [32]. Increasing specific power input through enhanced mass and heat transport by *e.g.* the use of

adsorbent coatings [32, 53], or decrease the heat input by improved cycle design and/or heat integration are two approaches being explored for already defined working pairs [32, 54]. On the other hand, the development of novel working pairs can certainly improve performance [38, 55-58] by, *e.g.* decreasing the required desorption temperature [32].

THE PROMISE THAT METAL-ORGANIC FRAMEWORKS (MOFs) HOLD

In this thesis, the feasibility for application in adsorption driven heating and cooling of one specific emerging class of porous adsorbents: Metal-Organic Frameworks (MOFs) is explored and critically assessed. MOFs, comprising inorganic clusters connected by organic ligands in 1, 2 or 3 dimensions [59], display a rich variety of topologies. The combination of organic ligands and inorganic building blocks [60] makes up for an almost infinite number of different possible structures, of which currently more than 20.000 MOF structures are known [61], where seemingly the sky is the limit regarding porosity and surface area [62, 63]. In addition, the organic ligands can be decorated with functional moieties, by either pre- or post-synthesis methods, to tune material properties [64-68]. No wonder that MOFs have received attention for a plethora of applications, *e.g.* adsorption/separation [69-72], storage [73, 74] and catalysis [75-78]. From this large set of different MOF structures, it is very likely that MOFs can be selected, and further tuned if needed, to have outstanding adsorption characteristics for the application at hand. This in turn may lead to materials that will perform better than commercially used zeolites, activated carbons or silica gel, for the application at hand. Finding this out is, in short, the aim of this thesis.

OUTLINE OF THIS THESIS

Characterization is vital for proper assessment of (synthesized) MOFs and porous materials in general. Central in the palette of characterization tools and methods, especially for porous adsorbents under study in this thesis, is adsorptive characterization. Most commonly used probe molecule for this purpose is nitrogen, often measured at its normal boiling point (77 K). Because of the importance of this technique, its frequent utilization and often observed mistakes in the interpretation of measured isotherms in literature, a detailed uncertainty analysis of these measurements along with a critical assessment of the derived properties and uncertainties of this technique have been performed for a variety of porous adsorbents, including but not limited to MOFs. The results, described in Chapter 2 in great detail, lead to concrete guidelines to properly perform adsorption measurements and the interpretation thereof. These will be used in the remainder of this thesis wherever possible.

In Chapter 3, combining experimental vapor adsorption measurements and Monte Carlo simulations [79], the adsorption mechanism of water and methanol, commonly applied working fluids, in two prototypical mesoporous MOFs is unraveled. The MOFs chosen for this study are MIL-100(Cr) [80] and MIL-101(Cr) [81], two of the most famous MOF structures in the field, because of their high thermal stability and large specific surface area, amongst others. Especially simulating water adsorption in accordance with experimentally observed water is challenging. The insights obtained by these simulations in these particular structures leads to a better understanding of adsorption phenomena observed in other MOF structures as well.

In Chapter 4 a thorough and up-to-date review is presented, highlighting the potential of MOFs in adsorption driven allocation of heat and cold. The different adsorption mechanisms and interaction sites are defined (based in part on Chapter 3) firstly. Stability of MOFs towards the adsorbates of choice, with a clear focus on water, is discussed in detail as this is an issue for a significant amount of structures, and various strategies to enhance the stability of MOFs towards the (prolonged) exposure of water vapor are chronicled. With knowledge of the prior in hand, a comprehensive summary of adsorption behavior in MOFs is given for all four working fluids of choice (water, methanol, ethanol and ammonia). From this, a selection is made of promising working pairs (MOF-working fluid). These are then compared, based on energetic efficiency and working capacity, to state-of-the-art working pairs that are commercially available. Furthermore, the potential of MOFs is briefly assessed in the aforementioned alternative applications, *i.e.* thermochemical energy storage and desiccant air conditioning. Finally, a summary and a detail outlook are presented to direct further directions for research and development for MOFs in adsorption driven heat pumps and chillers.

For actual application, it is vital that mass and especially heat transfer are fast to ensure a high energy uptake or release in a short time. One elegant way of doing so is by coating a selected adsorbent materials on a thermally conductive interface. In Chapter 5, investigations have been made to select one from a set of aluminium-containing MOFs and to interface the selected MOF on both porous aluminium oxides and metallic aluminium substrates. CAU-10-H was selected because of its very suitable adsorption properties and is based on aluminium and isophthalic acid, precursors that are both produced on an industrial scale are thus abundantly available.

Because of the average quality of CAU-10-H coatings observed on metallic aluminium, in Chapter 5, a detailed study was performed to improve these coatings in Chapter 6. In addition to metallic aluminium substrates, aluminium supports with a porous anodized aluminium oxide layer were employed, in attempts to exploit further the impressive results observed for aluminium oxides in Chapter 5. In addition, based on experimental techniques, the adsorption mechanism of water in CAU-10-H is unraveled. Lastly, note that all chapters have been written as individual articles and can be read individually. This however makes that some overlap between these chapters may exist.

REFERENCES

[1]   M. Höök, X. Tang, Depletion of fossil fuels and anthropogenic climate change - a review, Energy Policy, 52 (2013) 797-809.

[2]   M. Isaac, D.P. van Vuuren, Modeling global residential sector energy demand for heating and air conditioning in the context of climate change, Energy Policy, 37 (2009) 507-521.

[3]   International Energy Agency, World energy outlook. 2011, 696. http://www.iea.org/publications/freepublications/publication/weo2011_web.pdf (accessed 17-01-2015).

[4]   Eurostat database for energy statistics. http://ec.europa.eu/eurostat/web/energy/publications (accessed 17-01-2015).

[5]   European Commission Energy, Projected primary energy consumption in 2020 (nl). http://ec.europa.eu/energy/efficiency/eed/reporting_en.htm (accessed 17-01-2015).

[6]   Agentschap NL, Warmte in Nederland, publ. Nr. 2necw1003. http://www.rvo.nl/sites/default/files/Warmte%20en%20Koude%20NL%202NECW1202%20jan13.pdf (accessed 17-01-2015).

[7]   P. Tatsidjodoung, N. Le Pierrès, L. Luo, A review of potential materials for thermal energy storage in building applications, Renewable and Sustainable Energy Reviews, 18 (2013) 327-349.

[8]   M.J. Moran, H.N. Shapiro, Fundamentals of engineering thermodynamics, 5th ed., Wiley, 2006.

[9]   W. Wongsuwan, S. Kumar, P. Neveu, F. Meunier, A review of chemical heat pump technology and applications, Applied Thermal Engineering, 21 (2001) 1489-1519.

[10]   M.I. Fadhel, K. Sopian, W.R.W. Daud, M.A. Alghoul, Review on advanced of solar assisted chemical heat pump dryer for agriculture produce, Renewable and Sustainable Energy Reviews, 15 (2011) 1152-1168.

[11]   W. Wu, X. Zhang, X. Li, W. Shi, B. Wang, Comparisons of different working pairs and cycles on the performance of absorption heat pump for heating and domestic hot water in cold regions, Applied Thermal Engineering, 48 (2012) 349-358.

[12]   N.C. Srivastava, I.W. Eames, A review of adsorbents and adsorbates in solid-vapour adsorption heat pump systems, Applied Thermal Engineering, 18 (1998) 707-714.

[13]   C.A. Balaras, G. Grossman, H.-M. Henning, C.A. Infante Ferreira, E. Podesser, L. Wang, E. Wiemken, Solar air conditioning in europe - an overview, Renewable and Sustainable Energy Reviews, 11 (2007) 299-314.

[14]   H.-M. Henning, Solar assisted air conditioning of buildings - an overview, Applied Thermal Engineering, 27 (2007) 1734-1749.

[15]   H.M. Henning, T. Erpenbeck, C. Hindenburg, I.S. Santamaria, The potential of solar energy use in desiccant cooling cycles, International Journal of Refrigeration, 24 (2001) 220-229.

[16]   G. Grossman, Solar-powered systems for cooling, dehumidification and air-conditioning, Solar Energy, 72 (2002) 53-62.

[17]   K. Daou, R.Z. Wang, Z.Z. Xia, Desiccant cooling air conditioning: A review, Renewable and Sustainable Energy Reviews, 10 (2006) 55-77.

[18]   X. Zheng, T. Ge, R. Wang, Recent progress on desiccant materials for solid desiccant cooling systems, Energy, 74 (2014) 280-294.

[19]   J. Hadorn, Advanced storage concepts for active solar energy - IEA SHC task 32 2003-2007, Eurosun - 1st international conference on solar heating, cooling and buildings. Lisbon2008.

[20]   N. Yu, R.Z. Wang, L.W. Wang, Sorption thermal storage for solar energy, Progress in Energy and Combustion Science, 39 (2013) 489-514.

[21]   A. Fernandez, M. Martínez, M. Segarra, I. Martorell, L. Cabeza, Selection of materials with potential in sensible thermal energy storage, Solar Energy Materials and Solar Cells, 94 (2010) 1723-1729.

[22]   A. Sharma, V. Tyagi, C. Chen, D. Buddhi, Review on thermal energy storage with phase change materials and applications, Renewable and Sustainable Energy Reviews, 13 (2009) 318-345.

[23]   F. Jeremias, V. Lozan, S.K. Henninger, C. Janiak, Programming MOFs for water sorption: Amino-functionalized MIL-125 and UiO-66 for heat transformation and heat storage applications, Dalton Transactions, 42 (2013) 15967-15973.

[24]   R. Critoph, Y. Zhong, Review of trends in solid sorption refrigeration and heat pumping technology, Proceedings of the Institution of Mechanical Engineers, Part E: Journal of Process Mechanical Engineering, 219 (2005) 285-300.

[25]   S.D. Waszkiewicz Adsorption refrigeration system using zeolite and methanol.Ph.D. Thesis, University of Bristol, 2003.

[26]   R.E. Critoph, Solid sorption cycles: A short history, International Journal of Refrigeration, 35 (2012) 490-493.

[27]   R. Plank, J. Kuprianoff, Die kleinkältemaschine, Springer-Verlag, 1948.

[28]   G. Hulse, Freight car refrigeration by an adsorption system employing silica gel, Refrigerating Engineer, 17 (1929) 41-54.

[29]   E. Miller, The development of silica gel refrigeration, The American Society of Refrigerating Engineers, 17 (1929) 103-108.

[30]   U.N.E.P., Handbook for the montreal protocol on substances that deplete the ozone layer, 7th ed.2006.

[31]   F. Meunier, Solid sorption: An alternative to CFCs, Heat Recovery Systems and CHP, 13 (1993) 289-295.

[32]   F. Meunier, Adsorption heat powered heat pumps, Applied Thermal Engineering, 61 (2013) 830-836.

[33]   M. Kanamori, M. Hiramatsu, K. Katsurayama, F. Watanabe, H. Matsuda, M. Hasatani, Production of cold heat energy by alcohol/activated carbon adsorption heat pump with a disk-module-type adsorber, Journal of Chemical Engineering of Japan, 30 (1997) 434-439.

[34]   H. Demir, M. Mobedi, S. Ülkü, A review on adsorption heat pump: Problems and solutions, Renewable and Sustainable Energy Reviews, 12 (2008) 2381-2403.

[35]   B. Saha, I. El-Sharkawy, A. Chakraborty, S. Koyama, Study on an activated carbon fiber–ethanol adsorption chiller: Part I–system description and modelling, International Journal of Refrigeration, 30 (2007) 86-95.

[36]   D.W. Green, R.H. Perry, Perry's chemical engineers' handbook, 8th ed., McGraw-Hill, 2008.

[37]   L.W. Wang, R.Z. Wang, R.G. Oliveira, A review on adsorption working pairs for refrigeration, Renewable and Sustainable Energy Reviews, 13 (2009) 518-534.

[38]   Y.I. Aristov, Challenging offers of material science for adsorption heat transformation: A review, Applied Thermal Engineering, 50 (2013) 1610-1618.

[39]   I.S. Glaznev, D.S. Ovoshchnikov, Y.I. Aristov, Kinetics of water adsorption/desorption under isobaric stages of adsorption heat transformers: The effect of isobar shape, International Journal of Heat and Mass Transfer, 52 (2009) 1774-1777.

[40]   B.N. Okunev, A.P. Gromov, Y.I. Aristov, Modelling of isobaric stages of adsorption cooling cycle: An optimal shape of adsorption isobar, Applied Thermal Engineering, 53 (2013) 89-95.

[41]   F. Jeremias, A. Khutia, S.K. Henninger, C. Janiak, MIL-100(Al, Fe) as water adsorbents for heat transformation purposes - a promising application, Journal of Materials Chemistry, 22 (2012) 10148-10151.

[42]   Y.M. Yonezawa, Masao; Oku, Kenzo; Nakano, Hiroki; Okumura, Shin-ichi; Yoshihara, Motoshi; Sakai, Akiyoshi; Morikawa, Atsushi Adsorption refrigeration system.United States Patent 4881376, 1989

[43]   R.Z. Wang, R.G. Oliveira, Adsorption refrigeration - an efficient way to make good use of waste heat and solar energy, Progress in Energy and Combustion Science, 32 (2006) 424-458.

[44]   Invensor. http://www.invensor.com/en/technology/cooling-system.htm (accessed 17-01-2015).

[45]   B. Dawoud, P. Hoefle, A. Bornmann, S. Chmielewski, C. Marburger Vacuum sorption apparatus.Unites States Patent 8544293, 2013

[46]   S. Shimooka, K. Oshima, H. Hidaka, T. Takewaki, H. Kakiuchi, A. Kodama, M. Kubota, H. Matsuda, The evaluation of direct cooling and heating desiccant device coated with FAM, Journal of Chemical Engineering of Japan, 40 (2007) 1330-1334.

[47]   H. Kakiuchi, S. Shimooka, M. Iwade, K. Oshima, M. Yamazaki, S. Terada, H. Watanabe, T. Takewaki, Novel water vapor adsorbent FAM-Z01 and its applicability to an adsorption heat pump, Kagaku Kogaku Ronbunshu, 31 (2005) 361-364.

[48]   H. Kakiuchi, S. Shimooka, M. Iwade, K. Oshima, M. Yamazaki, S. Terada, H. Watanabe, T. Takewaki, Water vapor adsorbent FAM-Z02 and its applicability to adsorption heat pump, Kagaku Kogaku Ronbunshu, 31 (2005) 273-277.

[49]   MITSUBISHI PLASTICS, Zeolitic water vapor adsorbent: AQSOA. http://www.aaasaveenergy.com/products/001/pdf/AQSOA_1210E.pdf (accessed 17-01-2015).

[50]   International Zeolite Association - database of zeolite structures. http://www.iza-structure.org/databases/ (accessed 17-01-2015).

[51]   S.K. Henninger, G. Munz, K.F. Ratzsch, P. Schossig, Cycle stability of sorption materials and composites for the use in heat pumps and cooling machines, Renewable Energy, 36 (2011) 3043-3049.

[52]   H. Chen, Q. Cui, J. Wu, Y. Zhu, Q. Li, K. Zheng, H. Yao, Hydrothermal stability of SAPO-34 for refrigeration and air conditioning applications, Materials Research Bulletin, 52 (2014) 82-88.

[53]   G. Restuccia, A. Freni, G. Maggio, A zeolite-coated bed for air conditioning adsorption systems: Parametric study of heat and mass transfer by dynamic simulation, Applied Thermal Engineering, 22 (2002) 619-630.

[54]   M. Pons, F. Poyelle, Adsorptive machines with advanced cycles for heat pumping or cooling applications: Cycles á adsorption pour pompes á chaleur ou machines frigor: Figues, International Journal of Refrigeration, 22 (1999) 27-37.

[55]   Y.I. Aristov, Novel materials for adsorptive heat pumping and storage: Screening and nanotailoring of sorption properties, Journal of Chemical Engineering of Japan, 40 (2007) 1242-1251.

[56]   Y. Aristov, New family of solid sorbents for adsorptive cooling: Material scientist approach, Journal of Engineering Thermophysics, 16 (2007) 63-72.

[57]   S.K. Henninger, F.P. Schmidt, H.M. Henning, Water adsorption characteristics of novel materials for heat transformation applications, Applied Thermal Engineering, 30 (2010) 1692-1702.

[58]   C. Janiak, S.K. Henninger, Porous coordination polymers as novel sorption materials for heat transformation processes, Chimia, 67 (2013) 419-424.

[59]   S. Kitagawa, R. Kitaura, S.-i. Noro, Functional porous coordination polymers, Angewandte Chemie International Edition, 43 (2004) 2334-2375.

[60]   D.J. Tranchemontagne, J.L. Mendoza-Cortes, M. O'Keeffe, O.M. Yaghi, Secondary building units, nets and bonding in the chemistry of Metal-Organic Frameworks, Chemical Society Reviews, 38 (2009) 1257-1283.

[61]   N.C. Burtch, H. Jasuja, K.S. Walton, Water stability and adsorption in Metal-Organic Frameworks, Chemical Reviews, 114 (2014) 10575-10612.

[62]   O.K. Farha, I. Eryazici, N.C. Jeong, B.G. Hauser, C.E. Wilmer, A.A. Sarjeant, R.Q. Snurr, S.T. Nguyen, A.O. Yazaydın, J.T. Hupp, Metal-Organic Framework materials with ultrahigh surface areas: Is the sky the limit?, Journal of the American Chemical Society, 134 (2012) 15016-15021.

[63]   H. Furukawa, N. Ko, Y.B. Go, N. Aratani, S.B. Choi, E. Choi, A.Ö. Yazaydin, R.Q. Snurr, M. O'Keeffe, J. Kim, O.M. Yaghi, Ultrahigh porosity in Metal-Organic frameworks, Science, 329 (2010) 424-428.

[64]   Q. Yang, A.D. Wiersum, P.L. Llewellyn, V. Guillerm, C. Serre, G. Maurin, Functionalizing porous zirconium terephthalate UiO-66(zr) for natural gas upgrading: A computational exploration, Chemical Communications, 47 (2011) 9603-9605.

[65]   G.E. Cmarik, M. Kim, S.M. Cohen, K.S. Walton, Tuning the adsorption properties of UiO-66 via ligand functionalization, Langmuir, 28 (2012) 15606-15613.

[66]   K.K. Tanabe, Z. Wang, S.M. Cohen, Systematic functionalization of a Metal-Organic Framework via a postsynthetic modification approach, Journal of the American Chemical Society, 130 (2008) 8508-8517.

[67]   M. Kim, J.F. Cahill, Y. Su, K.A. Prather, S.M. Cohen, Postsynthetic ligand exchange as a route to functionalization of 'inert' Metal-Organic Frameworks, Chemical Science, 3 (2012) 126-130.

[68]   M.G. Goesten, J. Juan-Alcañiz, E.V. Ramos-Fernandez, K.B. Sai Sankar Gupta, E. Stavitski, H. van Bekkum, J. Gascon, F. Kapteijn, Sulfation of Metal-Organic Frameworks: Opportunities for acid catalysis and proton conductivity, Journal of Catalysis, 281 (2011) 177-187.

[69]   C. Gücüyener, J. van den Bergh, J. Gascon, F. Kapteijn, Ethane/ethene separation turned on its head: Selective ethane adsorption on the Metal-organic Framework ZIF-7 through a gate-opening mechanism, Journal of the American Chemical Society, 132 (2010) 17704-17706.

[70]   J. van den Bergh, C. Gücüyener, E.A. Pidko, E.J. Hensen, J. Gascon, F. Kapteijn, Understanding the anomalous alkane selectivity of ZIF-7 in the separation of light alkane/alkene mixtures, Chemistry-a European Journal, 17 (2011) 8832-8840.

[71]   J.-R. Li, R.J. Kuppler, H.-C. Zhou, Selective gas adsorption and separation in Metal-Organic Frameworks, Chemical Society Reviews, 38 (2009) 1477-1504.

[72]   S. Couck, J.F.M. Denayer, G.V. Baron, T. Rémy, J. Gascon, F. Kapteijn, An amine-functionalized MIL-53 Metal-Organic Framework with large separation power for CO_2 and CH_4, Journal of the American Chemical Society, 131 (2009) 6326-6327.

[73]   L.J. Murray, M. Dinca, J.R. Long, Hydrogen storage in Metal-Organic Frameworks, Chemical Society Reviews, 38 (2009) 1294-1314.

[74]   H.J. Choi, M. Dinca, A. Dailly, J.R. Long, Hydrogen storage in water-stable Metal-Organic Frameworks incorporating 1,3- and 1,4-benzenedipyrazolate, Energy & Environmental Science, 3 (2010) 117-123.

[75]   J. Gascon, M.D. Hernández-Alonso, A.R. Almeida, G.P.M. van Klink, F. Kapteijn, G. Mul, Isoreticular MOFs as efficient photocatalysts with tunable band gap: An operando FTIR study of the photoinduced oxidation of propylene, ChemSusChem, 1 (2008) 981-983.

[76]   J. Gascon, U. Aktay, M.D. Hernandez-Alonso, G.P.M. van Klink, F. Kapteijn, Amino-based Metal-Organic Frameworks as stable, highly active basic catalysts, Journal of Catalysis, 261 (2009) 75-87.

[77]   S. Hasegawa, S. Horike, R. Matsuda, S. Furukawa, K. Mochizuki, Y. Kinoshita, S. Kitagawa, Three-dimensional porous coordination polymer functionalized with amide groups based on tridentate ligand: Selective sorption and catalysis, Journal of the American Chemical Society, 129 (2007) 2607-2614.

[78]   J. Lee, O.K. Farha, J. Roberts, K.A. Scheidt, S.T. Nguyen, J.T. Hupp, Metal-Organic Framework materials as catalysts, Chemical Society Reviews, 38 (2009) 1450-1459.

[79]   D. Dubbeldam, A. Torres-Knoop, K.S. Walton, On the inner workings of monte carlo codes, Molecular Simulation, 39 (2013) 1253-1292.

[80]   G. Férey, C. Serre, C. Mellot-Draznieks, F. Millange, S. Surblé, J. Dutour, I. Margiolaki, A hybrid solid with giant pores prepared by a combination of targeted chemistry, simulation, and powder diffraction, Angewandte Chemie International Edition, 43 (2004) 6296-6301.

[81]   G. Férey, C. Mellot-Draznieks, C. Serre, F. Millange, J. Dutour, S. Surblé, I. Margiolaki, A chromium terephthalate-based solid with unusually large pore volumes and surface area, Science, 309 (2005) 2040-2042.

CHAPTER 2

ADSORPTIVE CHARACTERIZATION OF POROUS SOLIDS

ABSTRACT:

Adsorptive characterization using nitrogen at 77 K is one of the most widely used techniques to assess textural properties of porous solids, such as pore volume, specific surface area and pore size distributions. Based on a thorough error analysis the influence of experimental uncertainties on the accuracy of volumetric nitrogen adsorption isotherms and derived properties using the most popular methods is analyzed in detail, comprising the pore volume and specific surface area determined using the method posed by Brunauer, Emmet and Teller (BET) and the pore size distribution according to the method developed by Barrett, Joyner and Halenda (BJH). Based on series of isotherms measurements with different sorbents (MOFs, zeolite, activated carbon and alumina) and on examples from literature (MIL-101), the extensive error analysis shows that these methods may yield highly inaccurate or even statistically irrelevant (BJH) results. To improve the meaningfulness of derived properties and to minimize statistical uncertainties, practical recommendations and guidelines are proposed for experimental operation variables and data analysis.

2.1. INTRODUCTION

Adsorptive characterization using probe gas molecules is one of the most widely used techniques to assess textural properties of porous solids [1]. The most commonly used adsorbate for this purpose is nitrogen, recommended by IUPAC for porous materials with a specific surface area, S, larger than 5 m^2 g^{-1} [2, 3]. From measuring adsorption of N_2 at its normal boiling point, information about the total pore volume, specific surface area and pore size distribution can be derived [4]. This characteristic information is vital for application of porous materials in heterogeneous catalysis and adsorptive separation or storage, amongst others. In spite of the importance of this technique, in general, little or no attention is paid to the accuracy and relevance of the obtained quantitative characteristics reported in literature.

In this work, uncertainties in nitrogen adsorption isotherms and derived textural properties using the most commonly applied protocols are thoroughly analyzed. An indication of the uncertainty in these quantities is a requirement to draw sound conclusions about material(s) under investigation (and to avoid possible 'statistical errors'). Furthermore, the results obtained with these methods are prone to misinterpretation. As it will be demonstrated, not adhering to underlying assumptions, definitions and guidelines, might lead to erroneous results and/or large uncertainties in obtained values ('human errors'). The detailed analysis is based on five notably different materials. Model adsorbents have deliberately not been chosen, but instead a selection of widely different porous materials often reported in literature is made.

Two materials selected are Metal-Organic Frameworks (MOFs), porous crystalline materials that have gained increasing interest in the past decade because of unprecedented topological richness and comprising large specific surface areas and pore volumes. The combination of organic and inorganic building blocks offers an almost infinite number of combinations, resulting in enormous variation in pore size, shape, and structure. These materials have found application in adsorptive separation [5-7], storage [8], encapsulation [9] and catalysis [10]. MIL-101(Cr) [11] is among the most famous structures. It contains both meso- and micropores and displays high stability and interesting properties [12-17]. Second MOF is the fully microporous UiO-66 [18], which also gained significant attention because of excellent (thermal) stability and interesting properties [19-22]. Sigma-1, a microporous zeolite and member of the DDR structural topology, known for its high separation performance in

membrane and adsorptive processes, incorporates aluminium into the framework, making the material also suitable for catalysis [23-25]. γ-Alumina is chosen as representative for mesoporous metal-oxide supports, which are used frequently in heterogeneous catalysis [26-28]. From the group of activated carbons, widely used for gas separation and storage [29, 30] and water purification [31], the commercially available Norit RB2, frequently also used as reference carbon material, is selected [32].

As the nitrogen adsorption isotherm forms the basis of the texture characterization, firstly the accuracy and reproducibility of the adsorption isotherm measurements on these materials is assessed. From these isotherms the pore volume is determined, simply derived from the amount of N_2 adsorbed inside the pores of the material, and assuming that the density therein is that of liquid nitrogen, as it is seen most often in literature [4].

The most popular method to determine the specific surface area of a porous solid, despite profound criticism on underlying assumptions [33], is the one put forward by Brunauer, Emmett and Teller in 1938 ('BET-method') [34], a multi-layer extension of Langmuir's monolayer description of adsorption [35]. Although the underlying assumptions of the BET-method suggest that this method cannot be used for microporous materials, Rouquerol *et al.* demonstrated its applicability, albeit that the physical meaning of the resulting surface area is weaker than for mesoporous materials [33]. Furthermore, Walton and Snurr have shown that BET areas determined for microporous MOFs can correspond well to geometrically accessible surface areas, as calculated by molecular simulations [36]. The method relies on curve-fitting the BET-equation on a specific part of the adsorption isotherm. The absolute value of the obtained surface area is, even for a material that behaves very much BET-like, dependent on which part of the isotherm is used [37]. It will be shown that for the materials under investigation the fitting strategy applied (number of data points, part of the isotherm and fitting method) strongly influences the value obtained for the BET area. Furthermore, not only the absolute value for BET area but also its uncertainty is investigated as function of fitting strategy.

The most commonly applied method to determine the pore size distribution for mesopore containing materials is the one developed by Barrett, Joyner and Halenda in 1951 ('BJH-method') [38]. This method is based on the Kelvin equation and modified to include multilayer adsorption. In this work it is investigated how the uncertainty in a measured isotherm propagates in the pore size distribution, something not published in prior literature.

Furthermore, despite the highly appreciated work of Groen *et al.* [39], the current literature is still plagued by erroneous conclusions drawn from BJH pore size distributions.

MIL-101(Cr) is one of the most reported Metal-Organic Frameworks in scientific literature. Because of the large availability of nitrogen derived material characterization data [11, 12, 40-66] this structure lends itself well to an analysis of the reported scatter in pore volume and BET surface area (Fig. 2.1).

As these parameters refer to the same material, a strong correlation between these quantities should be expected. The origin of the scatter will be illustrated, and based on the proposed guidelines it will be shown how standardization can improve the correlation between pore volume and BET surface area for the same material.

Throughout this work, it is tacitly assumed that during an adsorption measurement for each measured point adsorption equilibrium is reached or approached closely, so deviations from equilibrium are not addressed here. With this assumption and error propagation analysis the uncertainty in volumetric isotherm measurements and in the derived properties are estimated. Based on these findings, guidelines are proposed to improve the experimental operation and to assist in the determination of the adsorption isotherm, pore volume and BET area, in order to decrease their uncertainty and hopefully also the variation in absolute values reported for the same material in literature.
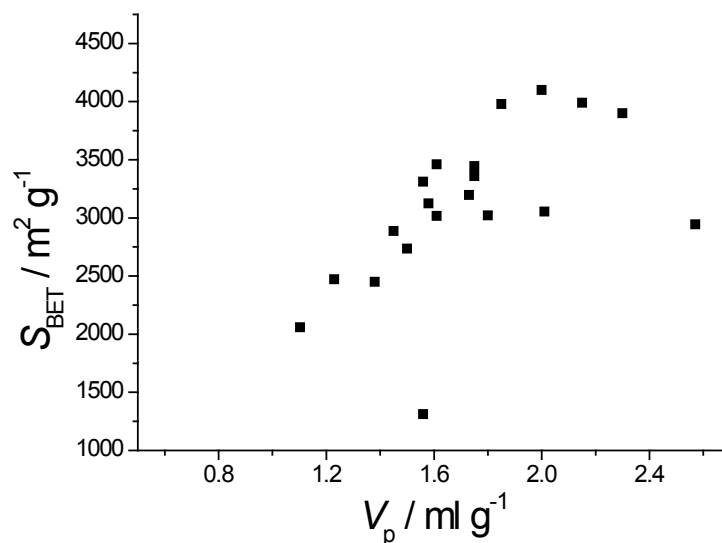
Figure 2.1: Reported values of BET surface area as function of reported pore volume for MIL-101(Cr), from various literature sources [11, 12, 40-66].

2.2. EXPERIMENTAL

2.1.1. SORBENTS – MATERIAL SYNTHESIS

All chemicals were obtained from Sigma-Aldrich and were used without further purification. MIL-101(Cr) was synthesized as previously reported in literature [11]. 1.63 g of chromium nitrate [$Cr(NO_3)_3 \cdot 9H_2O$, 97%], 0.70 g of terephthalic acid [C_6H_4-1,4-$(CO_2H_2)_2$, 97%], 0.20 g of hydrofluoric acid (HF, 40%) and 20 g of distilled water were added to a Teflon container that was inserted in a stainless steel autoclave. The autoclave was heated for 8 h at 493 K in an oven under static conditions. After synthesis, the solid product was filtered from the synthesis solution. The as-synthesized material was activated solvothermally using ethanol (EtOH, 95%) at 353 K for 24 h. The resulting solid was exchanged in a 1 M solution of ammonium fluoride (NH_4F) at 343 K for 24 h and was immediately filtered off and washed with hot water. MIL-101(Cr) was finally dried overnight at 433 K in air and stored under air atmosphere.

Synthesis of UiO-66 was carried out according to literature as well [18]. 0.053 g of zirconium chloride [$ZrCl_4$, 99%], 0.034 g terephthalic acid [C_6H_4-1,4-$(CO_2H_2)_2$, 97%] and 24.9 g N,N'-dimethylformamide (DMF) were added to a Teflon container, inserted in a stainless steel autoclave. The autoclave was heated at 393 K for 24 hours under static conditions. After

19

cooling in air to room temperature, the resulting solid was filtered, washed with DMF and dried at room temperature.

Synthesis of Sigma-1 was performed adapting the method patented by Stewart [67] with minor modifications, keeping the synthesis composition as adamantylamine (ADA): Na_2O: SiO_2 : Al_2O_3: H_2O = 20: 3: 60: 1: 2400 (Ex. 1 of patent). 5.39 g of Ludox HS-40 was added to vial A and was diluted with 20 g of deionized water. After 5 minutes of stirring, 3.62 g of ADA was added and the obtained solution further diluted using 19.4 g of deionized water. Finally, contents of vial A were stirred for over 15 min, until a homogenous solution was obtained. In vial B, firstly 0.2 g of $NaAlO_2$ was dissolved in 5.41 g of water. After obtaining a clear solution, 0.19 g of NaOH and 4 g of deionized water was added. After stirring vial B for 15 min, vial B is mixed over vial A and aging was continued for 30 minutes. The obtained solution was transferred to Teflon containers and synthesis was carried out at 453 K under autogenous pressure for 6 days under 200 rpm of rotational speed. Obtained powder was rinsed with water thoroughly and finally rinsed with ethanol to remove residual ADA. Calcination of the powder was carried out at 923 K for 7 h, with an initial heating rate of 2 K min^{-1}.

2.1.2. SORBENTS – COMMERCIAL SAMPLES

Activated carbon (Norit RB 2) and γ-alumina (CK-300), were both purchased from their respective suppliers, Cabot Norit and Akzo Nobel. A second sample of γ-alumina (000-3p, Akzo Nobel) was used to investigate the effect of sample cell volume on measurements (details in Section A.8, Appendix A), to which is referred as γ-alumina(2) if used.

2.1.3. INSTRUMENTATION AND MEASUREMENT PROCEDURE

Nitrogen physisorption measurements were performed at 77 K using a Quantachrome Autosorb-6B unit gas adsorption analyzer, using an equilibration time of 2 min, meaning that a data point is considered in equilibrium when the pressure varies less than 80 Pa in 2 minutes. All samples were pretreated ex-situ for at least 16 h under vacuum at 473 K, except for Sigma-1 (573 K instead), before adsorption measurements. Sample amounts used and sample cell volumes determined are given in Table A.1.

2.3. ADSORPTION DERIVED PROPERTIES

2.3.1. PORE VOLUME

One frequently derived property from a nitrogen adsorption isotherm is the total pore volume, V_p. Frequently it is assumed that at saturation the adsorbed nitrogen has the same density as in the liquid phase at the same temperature [4], which makes that the pore volume (V_p) can be calculated by making use of the Gurvich principle [68]:

$$V_p = q_{sat} \frac{\rho_{STP}^{vap}}{\rho_{nbp}^{liq}}$$

(2.1)

Herein, ρ is the density for the vapor phase (vap) at standard temperature and pressure (STP, 0 ^{o}C, 1 bar) and for the liquid phase (liq) at normal boiling point (nbp), and q_{sat} is the loading at saturation expressed in ml_{STP} g^{-1}. Note that the assumption of the adsorbed phase having liquid density is strictly never exactly true but more questionable for microporous materials [4]. Hence the obtained values for such materials should be interpreted with care. As it will be shown later, the choice of the exact loading of saturation is not always trivial. Generally it is recommended to calculate the pore volume at the plateau in adsorption, for type I (microporous) and type IV (mesoporous) materials (IUPAC classification [2, 3]) to avoid including inter-particle nitrogen condensation [4]. This means in practice that relative pressure should not be close to unity, $p/p_o \leq 0.9$ is used often in literature (p_o is the saturated vapor pressure of nitrogen at 77 K).

2.3.2. BET SURFACE AREA

Nitrogen physisorption is a key technique to obtain the specific surface area of a material. Most commonly, the theory developed by Brunauer, Emmet and Teller (BET) is used [34] for the isotherm data interpretation, though occasionally surface areas are calculated using the Langmuir isotherm [35]. Since the first publication of the BET equation, it has been the major tool to assess specific surface area, despite criticism towards its derivation and underlying assumptions [1], of which the more important ones are briefly addressed. Firstly, the adsorbent is assumed to have a homogeneous surface, onto which molecules adsorb in multiple layers. This is notably different to the method developed by Langmuir, which is limited to a single layer of adsorbate molecules on a surface [35]. Secondly, to the second

layer and onwards, molecules can be adsorbed before complete filling of the lower layers. There is an infinite amount of layers when p/p_o reaches unity. Thirdly, there are no lateral interactions between molecules located in the same layer, making the 'molar adsorption energy' within one layer constant. For the second and further layers the 'molar adsorption energy' is assumed to be equal (E_2), and differs from that for the first layer (E_1). These assumptions give rise to the well-known BET relation, that can be formulated as [34]:

$$q = q_m \left(\frac{C\left(\frac{p}{p_o}\right)}{\left\{1 - \frac{p}{p_o} + C\left(\frac{p}{p_o}\right)\right\} \cdot \left\{1 - \left(\frac{p}{p_o}\right)\right\}} \right) \tag{2.2}$$

Here q_m is the BET monolayer capacity and C the dimensionless BET parameter, calculated as the ratio between the adsorption constants of the first and second and further layers, often approximated by [37]:

$$C \approx \exp\left(\frac{E_1 - E_2}{RT}\right) \tag{2.3}$$

Note that negative values of C are physically meaningless. The specific surface area can be calculated after the monolayer capacity, q_m, has been determined, via [34]:

$$S_{BET} = \frac{q_m \rho_{STP}^{vap} N_A A_{CS}}{M_{N_2}} \tag{2.4}$$

Here ρ^{vap}_{STP} is the density of nitrogen vapor at standard temperature and pressure (STP), N_A is Avogadro's constant, M_{N2} is nitrogen's molar mass and A_{CS} is the cross-sectional area of a nitrogen molecule. The current standard value of the latter is 0.162 nm^2 [69], derived from the density of liquid nitrogen assuming a hexagonally closed packed system. Historically this value has varied between 0.13 and 0.20 nm^2 [70]. One could directly obtain both C and q_m from nonlinear fitting the BET equation to adsorption data directly. However, it is common practice to obtain these parameters from a linearized form of the BET equation:

$$\frac{\frac{p}{p_o}}{q\left(1 - \frac{p}{p_o}\right)} = \left(\frac{1}{Cq_m}\right) + \left(\frac{C-1}{Cq_m}\right) \cdot \left(\frac{p}{p_o}\right) = I + s\left(\frac{p}{p_o}\right) \tag{2.5}$$

The left-hand side of Eq. 2.5 is plotted versus relative pressure. The intercept (*I*) and slope (*s*) can be obtained using a simple linear least squares fitting routine. From these two parameters, the BET *C*-parameter and monolayer capacity, q_m, can be back-calculated via:

$$q_m = \left(\frac{1}{I+s} \right), \quad C = \left(\frac{I+s}{I} \right) \qquad (2.6)$$

As mentioned above, intercept *I* should have a positive value. Furthermore, the linearization does not hold for the entire pressure range. Originally, based on their own experimental results, Brunauer et al. indicated that Eq. 2.5 should only be applied for $0.05 < p/p_o < 0.35$, as outside these boundaries the left-hand side of Eq. 2.5 was found to strongly deviate from linearity [34]. No physical phenomena were mentioned as reason for these limitations. Later, IUPAC recommended the use of a slightly narrower pressure window, $0.05 < p/p_o < 0.30$ [2, 3]. The linear fitting method may be preferred over directly fitting *C* and q_m because of visual tractability and simplicity of fitting, not because of profound physical insights or statistical benefits. Regarding the latter, the error distribution is changed by linearization [71], similarly as in the determination of (bio)catalytic reaction kinetic parameters (Hougen-Watson, Lineweaver-Burk approach) [72-74].

The extent to which the BET parameters vary as function of the pressure range and the degrees of freedom used for fitting is calculated for the materials under investigation, including the variation of uncertainty in the BET parameter values.

2.3.3. BJH PORE SIZE DISTRIBUTION

The pore size distribution is calculated based on the method developed by Barrett, Joyner and Halenda (BJH) [38]. Herein it is assumed that the total amount adsorbed in a pore of a material is based upon two separate consequent contributions. Firstly, the pores contain a surface on which layers of adsorbate molecules can be formed, consistent of a certain thickness. The thickness of this layer on the pore surface increases with increasing p/p_o. Secondly, there is an inner capillary radius in this pore of which the volume is filled by condensation of the adsorbate and no longer by prolonged layer formation. For a given adsorbate species, the relative pressure at which this volume condensation occurs, is determined by the size of this capillary radius, and can be calculated with the Kelvin equation (r_K). The thickness of adsorbate molecules attached to a pore surface (*t*) was originally estimated for different relative pressures based on experiments by Shull [75] but can currently

23

be calculated with a variety of equations, including those of De Boer [76] and Harkins-Jura [77, 78]. Here the latter is applied, as it is used in the accompanying software of the adsorption equipment. For a given relative pressure thus, the volume of adsorbate present inside a porous material is the sum of (i) the amount of adsorbate present in all pores that are already fully filled via condensation, for which the pore radius must be smaller than or equal to the Kelvin radius for the given relative pressure ($r_i \leq r_K$ (p/p_o)), and (ii) the amount of adsorbate that is present in the layers of certain thickness on the walls of the pores for which the radius larger than the Kelvin radius ($r_i > r_K$ (p/p_o)). Summing up over all pore sizes present in the material, this can be written as:

$$q\left(\left.\frac{p}{p_o}\right|_k\right)\frac{\rho_{STP}^{vap}}{\rho_{nbp}^{liq}} = \sum_{i=1}^{k}\Delta V_{p,i}\left(r_i \leq r_K\left(\left.\frac{p}{p_o}\right|_k\right)\right) + \sum_{i=k+1}^{n}\Delta S_i t_i\left(r_i > r_K\left(\left.\frac{p}{p_o}\right|_k\right)\right) \qquad (2.7)$$

Here q is the amount adsorbed (in ml_{STP} g^{-1}) as function of relative pressure, $\Delta V_{p,i}$ are the incremental pore volumes that are already completely filled, associated with radii r_i, ΔS_i are the incremental pore surface areas that belong to pore radii ,r_i, that are not yet completely filled and only contain layers of adsorbate molecules, t_i the layer thicknesses thereof and r_K the Kelvin radius for a given relative pressure. Furthermore, the kth pore size is the largest pore filled completely via condensation (for given p/p_o) and the nth pore size is the largest present. As q is given in volume of N_2 vapor at standard temperature and pressure (STP), this requires conversion to liquid phase at measurement conditions, as has been done for the calculation of the total pore volume (Eq. 2.1). To be able to apply Eq. 2.7 to determine the pore size distribution, calculations should be started for a measured point at saturation (adsorption plateau in type IV isotherms) [2, 3] and an adjacent data point at lower relative pressure. It is thus tacitly assumed (see Eq. 2.7) that the difference in loading between these two points is only caused by depletion of the completely filled largest pore. Subsequently, from the difference in loading, one can determine the incremental pore volume (ΔV_p) for the largest pore in the adsorbent. The radius of this pore follows directly from the relative pressure, as it is the sum the thickness (t) and Kelvin radius (r_K). The difference in loading between the second and third point is not only assumed to originate from a smaller pore but also from the surface of the larger one, of which in the previous step the size was determined. Thus starting from saturation, the distribution of pore sizes can be recursively calculated following the desorption branch, for which it was derived. It is also feasible to apply this approach to the adsorption branch, although this is not advised based on the underlying

assumptions of the model. A frequently observed phenomenon for many desorption hysteresis branches is that they are not extended below a certain critical p/p_o [4]. This lower limit is only dependent on temperature and used adsorbate, and thus independent of the material under investigation. For nitrogen adsorption at 77 K, this limit is at $p/p_o = 0.42$ [4]. In general one should not make use of the isotherm below $p/p_o = 0.42$, when determining a BJH-pore size distribution [4]. This in turn means that the BJH-pore size distribution is limited to $D_p \geq 3.4$ nm and thus should strictly not be applied to the microporous region. In this work, the BJH pore size distribution was calculated as described in this section and subsequently the uncertainty in the pore size distribution was analyzed, details of which can be found in Section A.3.

2.3.4. UNCERTAINTY ANALYSIS

To assess the uncertainty in measured nitrogen adsorption isotherms, the theory of propagation of uncertainties is applied (see, *e.g.* J.R. Taylor [79]). For independent random errors, the variance can be formulated as:

$$\sigma_y^2 = \sum \left(\frac{\partial y}{\partial x_i} \right)^2 \sigma_{x_i}^2 \qquad (2.8)$$

Here y is a variable calculated from i measured variables x_i, and σ_y is the uncertainty in this variable y, clearly a function of the uncertainties in x_i, σ_{xi}. Applying Eq. 2.8 consecutively on all calculated variables, will ultimately lead to the variance in the adsorbed amount as a function of relative pressure (calculation details are given in Section A.2), from which the absolute uncertainty (square root of variance) and consequently the absolute confidence interval can be calculated. All confidence intervals in this work are calculated for a 95% confidence level.

Assuming no uncertainties in the determination of density, the variance in pore volume can be related directly to the variance in the measured isotherm (adsorbed amount) via:

$$\sigma_{V_p}^2 = \sigma_{q_{sat}}^2 \left(\frac{\rho_{STP}^{vap}}{\rho_{nbp}^{liq}} \right)^2 \qquad (2.9)$$

The variance in the adsorbed amount of nitrogen is also required to determine the uncertainty in the BJH-pore size distribution (details given in Section A.3). The uncertainty in BET

surface area is directly determined from the fitting procedure (Section A.4). The number of degrees of freedom used (*i.e.* the difference between the number of data points and the number of model parameters to be estimated) is important for the data fitting. Obviously, in order to have a meaningful fitting, one should, at least, have one degree of freedom ($N_{D.O.F.}$). As the BET-equation contains two parameters, either C and q_m or I and S, depending on the applied approach, at least three data points are needed for a fit. 95% Confidence intervals in measured temperatures (± 0.1 K), pressures (± 0.1% of measurement range), weighted amounts (± 0.1 mg) and manifold volume (± 5%), as reported by respective suppliers, are used in the error analysis.

2.4. RESULTS AND DISCUSSION

Firstly, the uncertainties that arise from performing N_2 adsorption measurements (at 77 K) are discussed and the optimal measurement conditions are determined (Section 2.4.1). This forms the basis for the determination in the uncertainty of determined pore volumes (Section 2.4.2). Afterwards the uncertainties and variance of the BET surface are elucidated (Section 2.4.3). As mentioned in the introduction, MIL-101 lends itself for a detailed case study to investigate how the specific surface area and pore volume are assessed (Section 2.4.4). The uncertainties and issues that may arise when using the BJH-pore size distribution are discussed (Section 2.4.5). Before stating briefly the conclusions of this work (Section 2.5), the recommendations for sound adsorption measurements and proper determination of derived properties are listed (Section 2.4.6). For clarity, a full list of symbols used is given in Appendix A.

2.4.1. UNCERTAINTY IN ADSORPTION MEASUREMENTS

To properly assess the uncertainties in variables derived from physisorption measurements, *e.g.* pore volume and surface area, nitrogen adsorption isotherms were determined in threefold by repeating the measurement with the same sample in the same sample holder and identical pre-treatment protocol, and subjected to a detailed error propagation analysis. Results are shown Fig. 2.2.

Uncertainties in relative pressure (*x*-axis) are insignificant, except for the lowest relative pressures, and therefore not depicted. Clearly for each material under investigation, the three isotherms and their confidence intervals are very similar, showing very good reproducibility of the measurement procedure. This reproducibility is also shown by the fact that for all

investigated materials none of the isotherms is outside of the confidence interval of the other two. A closer investigation of this confidence interval clearly shows the cumulative nature of the propagation of uncertainties, see Eq. A2.14. For each additional measured point, the interval widens slightly. At low relative pressures, the confidence intervals are insignificant. At relative pressures above 0.3, the growing confidence intervals become clearly visible and are the largest for the last point measured during desorption. The calculated absolute confidence interval is generally below ±10 ml$_{STP}$ g^{-1} for adsorption and below ±20 ml$_{STP}$ g^{-1} for desorption (Fig. A.1). A detailed analysis of the different contributions to the overall uncertainty shows that an increase in accuracy of the adsorbed amount can be realized by increasing the accuracy of the pressure sensor used, a more accurate calibration of the manifold volume (Section A.6) or by optimizing the ratio of manifold volume and sample volume. To determine this optimal ratio, the uncertainty in pore volume is determined as function of V_{man}/V_{cell} , using a representative Langmuir-Type isotherm (q_m = 500 ml$_{STP}$ g^{-1}, K = 10 bar^{-1}). Results, as depicted in Fig. 2.3, show that preferably V_{man}/V_{cell} is between 2 and 3 (see Section A.7 for calculation details). As pressure sensors often have an accuracy, which is a percentage of the full range, an increase in adsorption measurement accuracy might be best realized by using multiple pressure sensors with different pressure ranges, although it might be rather difficult to retrofit this in already existing adsorption equipment.
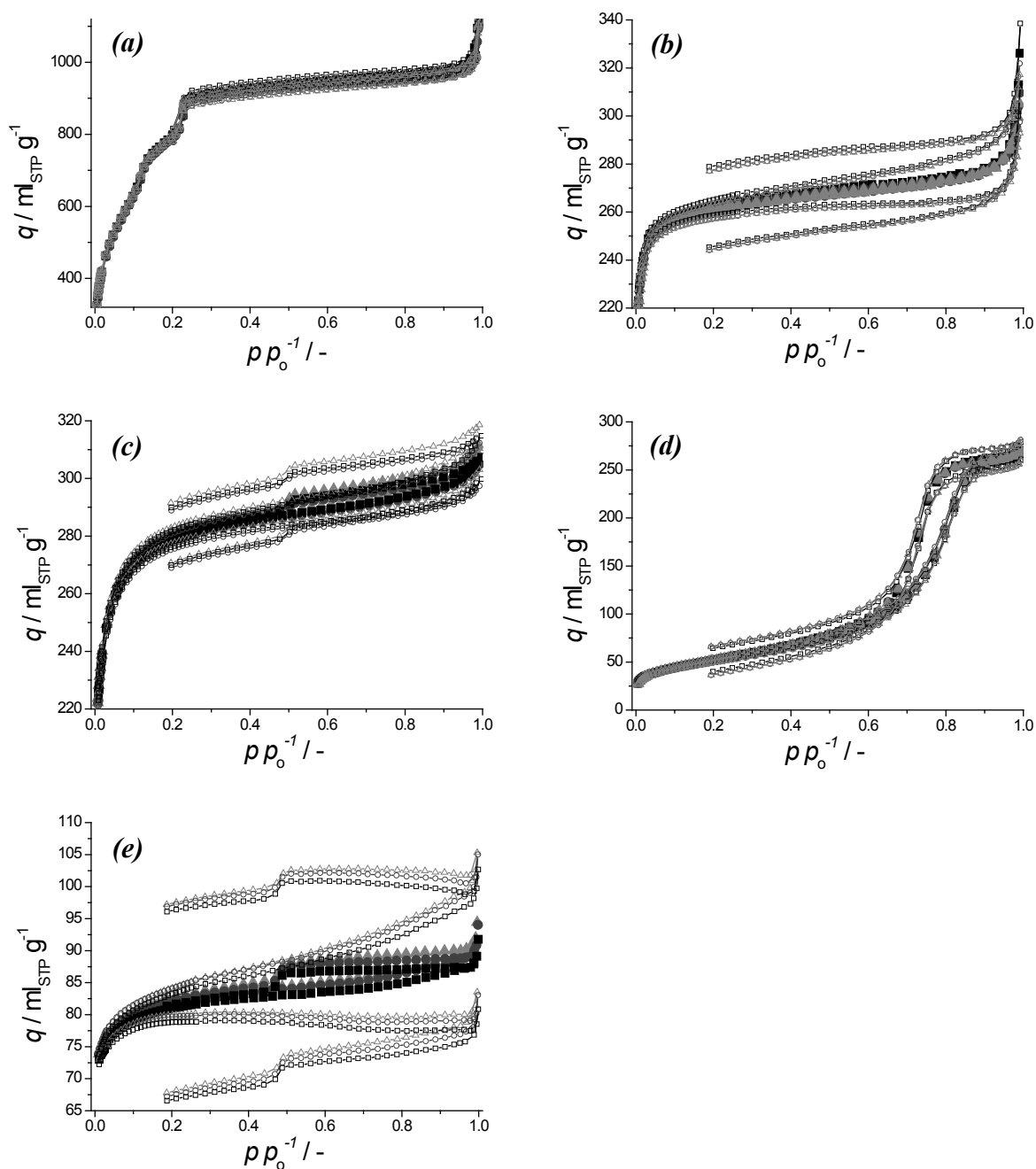
Figure 2.2: Repeated isotherm measurements and confidence intervals calculated using error propagation for MIL-101(Cr) (*a*), UiO-66 (*b*), Norit RB 2 (*c*), γ-alumina (*d*) and Sigma-1 (*e*). First (■), second (●) and third (▲) measurement (same sample and holder) depicted with closed symbols, confidence intervals given with lines and open symbols. Here p_o is the saturated vapor pressure of N_2 (at 77 K) and STP refers to standard pressure and temperature (0 ^{o}C and 1 bar).
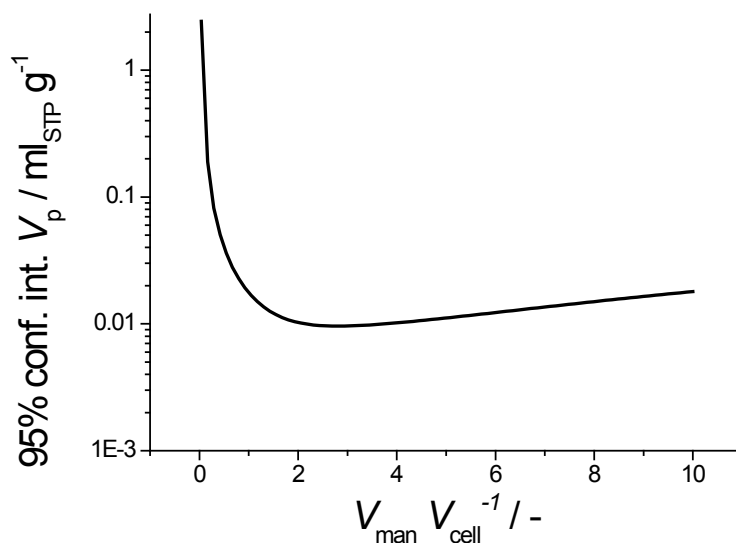
Figure 2.3: Simulated 95% confidence interval for the calculated pore volume at p/p_o = 0.9 as function of V_{man}/V_{cell} based on a Langmuir isotherm (q_m = 500 ml$_{STP}$ g^{-1}, K = 10 bar^{-1}) and a sample mass of 0.2 g. For calculation details, see Section A.7.

In the preceding discussion, sample mass and cell volume have been fixed purposely to investigate reproducibility of the measurement procedure. Separate efforts have been conducted to envisage the influence of these two variables experimentally, based on measurements on γ-alumina(2). Five cells with different cell volumes have been employed for measurements (cell 1 smallest, cell 5 largest) and the three measurements per cell progressively contain less sample mass (~0.15 g for 1st, ~0.09 for 2nd and ~ 0.05g for 3rd), all employing γ-alumina(2) (exact details are depicted in Section A.8). For cells 1, 3 and 5, measured isotherms and calculated confidence intervals are depicted in Fig. 2.4, left. Firstly, as was expected (Fig. A.5), decreasing sample mass and increasing cell volume both enlarge the confidence interval. More interestingly, an artificially increased desorption hysteresis can be observed when the cell volume is increased, becoming more noticeable for lower sample masses, as depicted in Fig. 2.4, right. For the smallest cell volume (cell 1, V_{cell} ~ 10 ml) under investigation, closure of the hysteresis loop at p/p_o ~ 0.42 (which is the closing limit for hysteresis loops for N$_2$ at 77 K [4])) can be observed, where for the largest cell (cell 5, V_{cell} ~ 35 ml) the hysteresis loop is not yet closed at p/p_o ~ 0.2, suggesting unphysical desorption behavior. For all measurements, the manifold volume (V_{man}) was 24.3 ml.

29
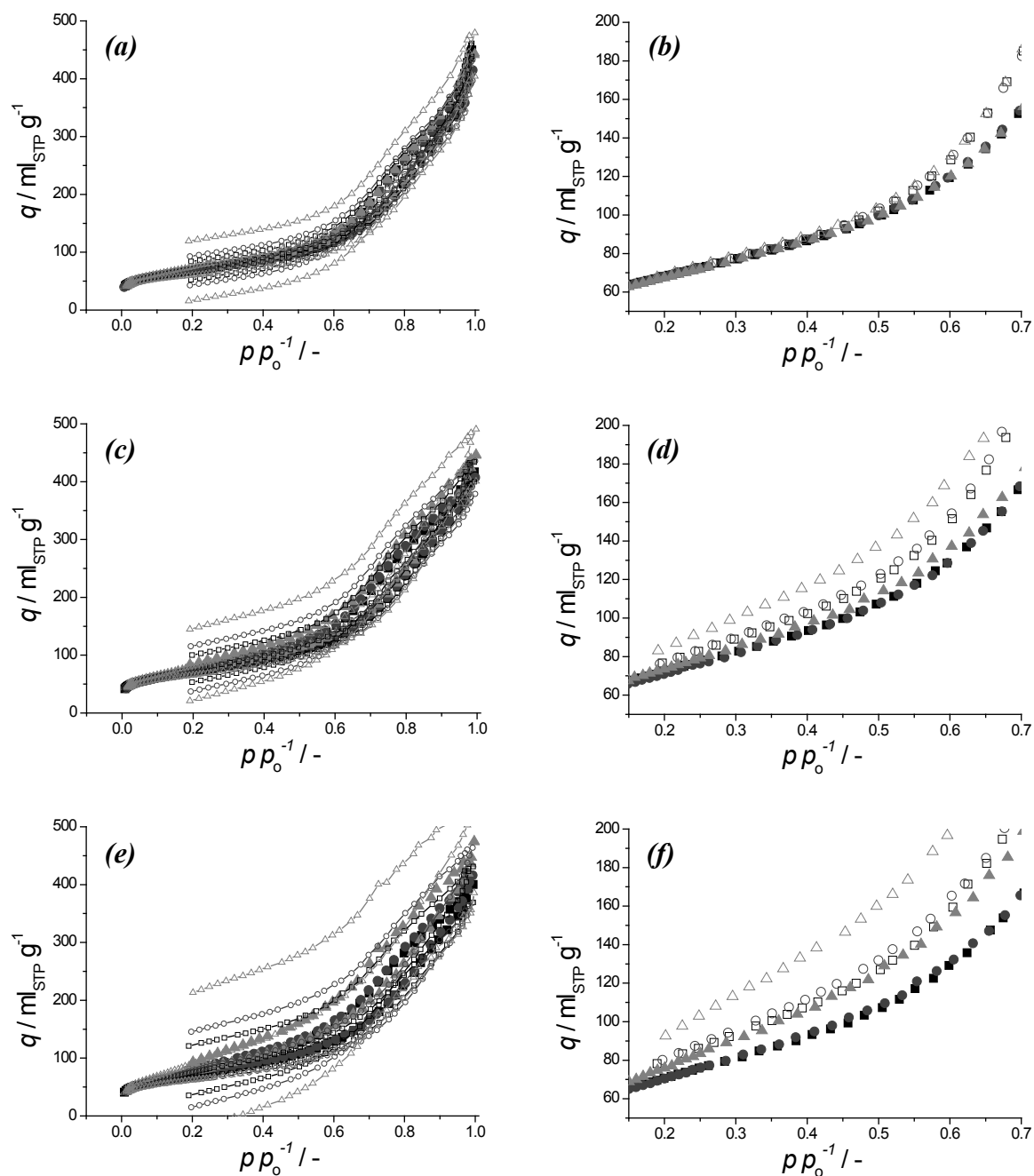
Figure 2.4: Repeated isotherms measurements for γ-alumina(2) and confidence intervals calculated using error propagation (*a, c, e*). First(■), second(●) and third(▲) measurement depicted with closed symbols, confidence intervals given with lines and open symbols. Zoom in on adsorption-desorption hysteresis of γ-alumina(2) (*b, d, f*). Adsorption of first (■), second (●) and third (▲) measurement depicted with closed symbols, desorption with open symbols. Confidence intervals omitted for clarity. Both for Cell 1 (*a, b*), Cell 3 (*c, d*) and Cell 5 (*e, f*). Exact measurement volumes and weights used can be found in Fig. A.7.

This effect can be easily rationalized. Increasing the sample cell, while keeping sample masses fixed, means that the gas-phase volume in contact with the sample increases, while the total amount that will be ad- or desorbed from the sample has not changed. This in turn means that the gas-phase pressure changes less for the same ad- and desorption steps if a larger cell is used. As the stabilization in gas-phase pressure is used as criterion for equilibration of each measured point by all volumetric adsorption equipment, using a larger sample cell volume can lead to satisfying the equilibration criterion further away from actual equilibrium, because of the inherent loss of sensitivity towards pressure variation when a larger cell is used (for the same sample mass). This effect is stronger for a lower sample mass as less molecules are transferred from or to the gas-phase, also leading to a smaller variation in pressure for the same material. The cumulative measurement times of the three measurements for cells 1 and 5 (Fig. A.8), reveal that a large discrepancy is created by the reduced sensitivity due to a larger cell volume and/or a decreased sample mass in the adsorption branch only at high relative pressure and becomes increasingly large at the first desorption points (measurement points where significant ad- or desorption occurs (Fig. 2.4) as at these points measurement time is significantly reduced for more pressure-insensitive measurement steps.

Importantly, the absolute volume of the sample cell thus determines whether an erroneous hysteresis between ad- and desorption occurs. Clearly, a small sample cell ($V_{cell} \sim 10$ ml) is desired. However, minimization of this cell is not unconstrained. Obviously, the cell should have a finite inner diameter to be able to load the actual sample. Furthermore, and less trivial, the cell length cannot be shortened, because of liquid nitrogen level control. Keeping the liquid nitrogen level constant is crucial, as minor deviations of this level have a significant influence on adsorption measurements, as has been shown by Pendleton and Badalyan [80]. As nitrogen is continuously evaporating, the liquid level is naturally decreasing over time. To counter this, the liquid nitrogen vessel is moved upwards with respect to the sample cell, making that the cell should be sufficiently long. Alternatively, a sleeve around the sample cell and capillary suction may keep the effective liquid nitrogen level around the cell constant. To obtain a smaller cell volume, it is recommended to insert a (glass) filler rod in the sample cell after loading the sample, as was used in this work.

Table 2.1: Estimated pore volume at $p/p_o = 0.9$ and its 95% confidence interval for the third isotherm measurement of each material.

Material	V_p / cm^3 g^{-1}	95% conf. int. / cm^3 g^{-1}
MIL-101(Cr)	1.51	± 0.017
UiO-66	0.43	± 0.016
Sigma-1	0.14	± 0.014
γ-alumina	0.40	± 0.011
Norit RB2	0.46	± 0.010

2.4.2. UNCERTAINTY IN PORE VOLUME

Using the measured adsorption isotherms and error analysis, one can directly determine the pore volume and its uncertainty. Results are given in Table 2.1 for the third measurement of each material.

The relative confidence interval in pore volume can be as large as ±10%, as is the case for Sigma-1. Both the absolute value of the pore volume and its uncertainty are very similar for the three measurements of the same sample, showing good reproducibility (Section A.14). Furthermore, values for the relative 95% confidence obtained here are very similar to those obtained by Pendleton and Badalyan for micropore volumes for a different set of materials, using either the α_s-plot method or the theory of volume filling, methods not discussed in this work [81, 82]. This indicates that the uncertainty in pore volume is not strongly dependent on the method used to determine it.

Note that, since the adsorption equipment used does not provide information about the exact dosing procedure during measurements, the results mentioned in preceding paragraph were obtained under the simplifying assumption that each measured data point requires only single dosage of nitrogen (Section A.2). Releasing this assumption, the uncertainty can become more than two times larger, as it is the case for MIL-101(Cr) (Section A.9), depending on how the number of doses required per measured point is estimated. The increased uncertainty is caused by the additional doses needed to encompass a given adsorbed amount and is a function of the total amount adsorbed by a material and of the shape of the nitrogen isotherm (Section A.9). According to our analysis, this increase in uncertainty is higher for microporous materials, because a significant fraction of total nitrogen loading is already adsorbed at the first measured point, *i.e.* at low pressure. This means that this point requires a significant number of doses, generating a large uncertainty therein. Obviously, this effect is

notably less important in mesoporous materials (containing hardly any micropores), as for these materials the number of doses at low pressures is lower (Section A.9).

To decrease the uncertainty in the pore volume, one could, for example, consider decreasing the number of measured points. However this would reduce the information obtained from the isotherm. One could calculate the pore volume at a lower relative pressure, but this is only possible if there is a distinct plateau in adsorption to avoid arriving at a too low value for the pore volume. *E.g.*, for MIL-101(Cr) the latter would be feasible. However, as apparent from the previous, two other parameters can be used to decrease the uncertainty in the measured isotherm and thus in the derived pore volume: the mass of the material under investigation and the volume of the sample cell used relative to that of the manifold. Varying both parameters for e.g. a Langmuir isotherm with $q_m = 500$ ml_{STP} g^{-1} and $K = 10$ bar^{-1}, has shown that V_{man}/V_{cell} should be between two and three (Fig. 2.3). A much larger or smaller cell volume will have a detrimental influence on the accuracy of the measurement and therefore on the pore volume (Section A.7). Furthermore, a sample mass below 0.05 g leads to a prohibitively high uncertainty. With increasing sample mass, the uncertainty is lowered, although this may result in much longer measurement times, and diffusion issues of heat and mass. A Langmuir isotherm was chosen to model adsorption behavior, because of the inability of the BET equation to describe saturation and thus a well-defined pore volume. Experimentally, these conclusions are confirmed. Increasing cell volume ($V_{man}/V_{cell} < 2$), and decreasing sample mass both show an increase in both confidence interval and variation in obtained pore volumes from different measurements (Section A.8).

Variation of both K and q_m, representing the difference in adsorptive properties of various materials, shows that the relative uncertainty in pore volume is especially high when both parameters are small, as in case of poorly adsorbing materials (see S.I. of [83]). Of course the concept of pore volume is ill-defined for poorly or non-adsorbing materials as these materials show little porosity. Nevertheless, the uncertainty in pore volume is directly proportional to the uncertainty in adsorbed amounts (at $p/p_o = 0.9$), see Eq. 2.9, and therefore the uncertainty in the measured adsorption isotherm is especially large for small values for K and q_m. With increasing K and q_m, this uncertainty is decreased (see S.I. of [83]). Because the uncertainty is a function of the total amount adsorbed ($q \cdot w_{sample}$) the sample mass should be adjusted in relation to these parameters. As an indication, the minimal sample mass required to obtain a pore volume with a relative confidence interval less than ±5% has been simulated as function of the Langmuir parameters (Fig. 2.5).
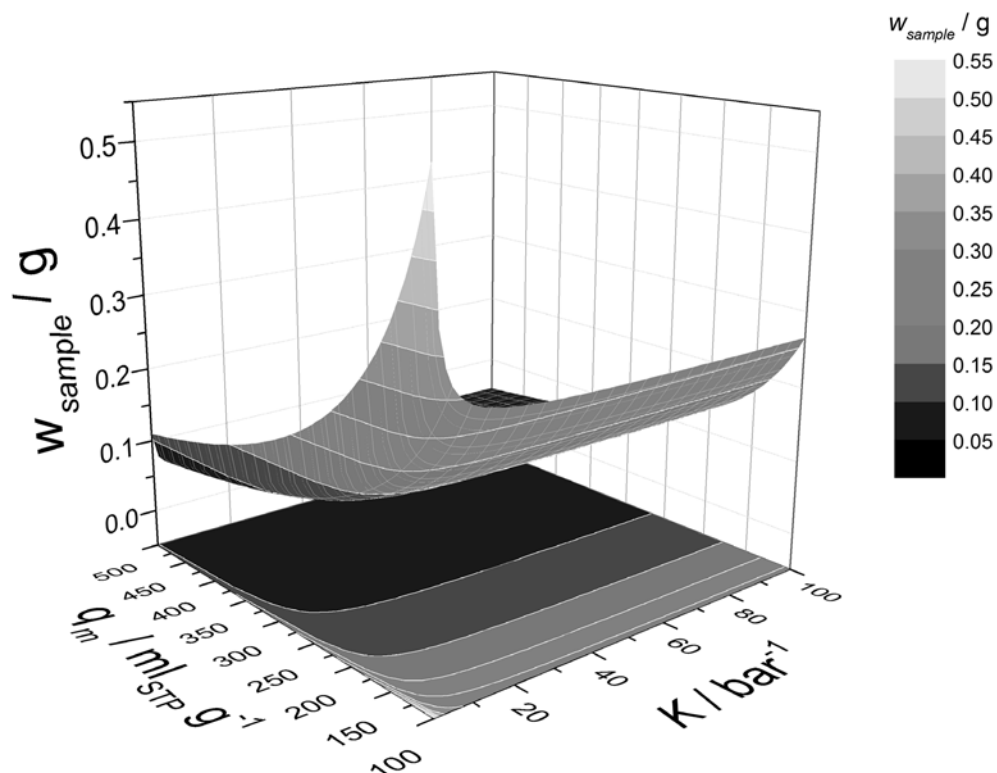
Figure 2.5: The required sample mass, depicted both on *z*-axis and in color-scale, to obtain a pore volume, calculated at $p/p_o = 0.9$, with a relative confidence interval of $\pm5\%$, as function of the Langmuir monolayer capacity, q_m, and equilibrium constant, K, when $V_{man}/V_{cell} = 2$. A two-dimensional projection is depicted in the *x-y* plane.

For poorly adsorbing materials, represented by very low q_m and K values, this is more than 0.5 gram. For reasonably adsorbing materials, represented by $K > 10$ bar^{-1} and $100 < q_m < 200$ ml$_{STP}$ g^{-1}, the required amount is 0.2-0.3 gram. For more strongly adsorbing materials, this can even become less than 0.1 gram. As it is not always possible to estimate *a priori* the amount adsorbed, the relative confidence interval in V_p as function of the total amount adsorbed ($q_{sat}\cdot w_{sample}$, see Fig. A.6) has been calculated. This is also useful as tool to estimate uncertainties of pore volumes reported in literature, provided the sample mass is reported as well, as is recommended by IUPAC [2, 3].

2.4.3. UNCERTAINTY AND VARIATION IN BET SURFACE AREA

The variation in BET parameter values, q_m and C, and uncertainty therein has been determined as a function of the used degrees of freedom and the applied pressure window for the five materials under investigation. Detailed results can be found in Figs. A.11, A.12 and S.I. of [83]. For comparison, the average 95% confidence interval is calculated for each number of degrees of freedom ($N_{D.O.F.}$) under consideration (Fig. 2.6). It is apparent that one degree of freedom yields an unsatisfactory confidence interval. Confidence intervals become acceptable from three degrees of freedom onwards, which is in line with the preference put forward by IUPAC to at least use five data points ($\equiv$ three degrees of freedom) [2, 3]. The uncertainty is especially high for MIL-101(Cr), attributed to the peculiar shape of its isotherm. The different inflections caused by filling the medium and large cavities, make the isotherm poorly represented by the BET equation. The uncertainty is especially high around these kinks for various degrees of freedom used in the fitting (Fig. A.11). Increasing the number of degrees of freedom will lower the uncertainty found, as the relative influence of these inflections will be suppressed. In case of UiO-66, Norit RB2 and Sigma-1 this is notably different. For these materials, the average uncertainty in the BET area is rather similar. This is in accordance with adsorption isotherms of these materials, which show similarity in adsorption curvature for $p/p_o < 0.30$. In all cases, a minimum in average uncertainty exists around seven degrees of freedom. This is attributed to the opposite effect of (i) the increase of degrees of freedom that will decrease the uncertainty in the fitted parameters (roughly proportionally with $N_{D.O.F.}^{-1}$ (see Eqs. A4.4 - A4.8) and (ii) the sum of squared residuals, SS_{RES}, which increases with each degree of freedom added.

As clearly visible in Fig. A.13, the linearized BET equation plots are not fully linear. For purely microporous UiO-66, Norit RB2 and Sigma-1 the restriction of non-negativity of the BET constant C is violated for $p/p_o > 0.04 - 0.07$, (Fig. A.14, S.I. of [83]). This fact limits the quantity of fits available for certain number of degrees of freedom. From Fig. 2.6, Fig. A.12 and S.I. of [83], it becomes apparent that the uncertainty in the BET surface area for fits adhering to $C > 0$ is smaller than for those where $C < 0$.

Finally, for γ-alumina, the average uncertainty decreases with the number of degrees of freedom and has the lowest average absolute uncertainty. This is attributed to the shape of the nitrogen adsorption isotherm which is, of these five materials, most in accordance with a BET-type isotherm, yielding the most linear BET plot (Fig. A.11).
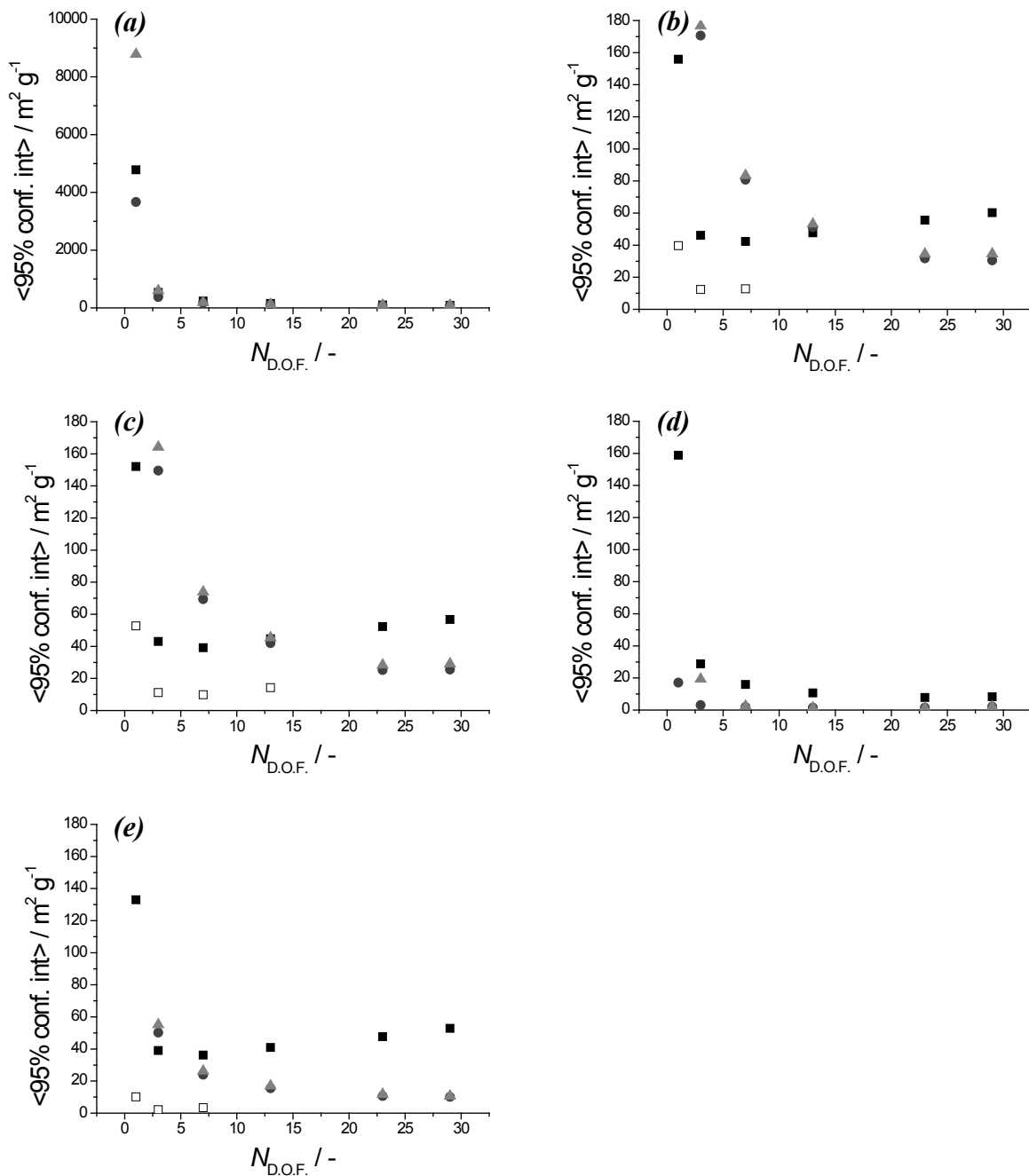
Figure 2.6: The average 95% confidence interval determined from fits varying the window of adjacent data points for the selected degree of freedom over the relative pressure range limited by the upper bound recommended by IUPAC ($0 \leq p/p_o \leq 0.3$) [2, 3], is depicted as function of the used degrees of freedom for MIL-101(Cr) (*a*), UiO-66 (*b*), Norit RB 2 (*c*), γ-alumina (*d*) and Sigma-1 (*e*). Results for the linear (■), direct (●) and weighted direct (▲) fitting methods. Closed symbols are based on full dataset, open symbols are obtained when the BET *C* parameter is constrained to positive values, only if the constraint excludes part(s) of the data set.

Table 2.2: Estimated BET surface area and both absolute and relative confidence interval, for the maximum degrees of freedom (for $0 \leq p/p_o \leq 0.3$) and for the additional restriction of non-negativity on the BET C parameter, for the third isotherm measurement of each material.

	max. $N_{D.O.F.}$ (=29)			Restriction of $C > 0$ [a]			
	S_{BET} / m^2 g^{-1}	95% Conf. Int.		S_{BET} / m^2 g^{-1}	95% Conf. Int.		$N_{D.O.F.}$ / -
Material		m^2 g^{-1}	%		m^2 g^{-1}	%	
MIL-101(Cr)	2810	± 88	± 3.1	←	←	←	29
UiO-66	860	± 60	± 7.0	1070	± 4.9	± 0.5	7
Sigma-1	270	± 53	± 20	321	± 2.3	± 0.7	7
γ-alumina	183	± 8.2	± 4.5	←	←	←	29
Norit RB2	930	± 57	± 6.1	1080	± 10	± 1.0	13

[a] For UiO-66, Sigma-1 and Norit RB2 in many fits, including those with the maximum degrees of freedom present in the isotherm data used for BET analysis, the C parameter obtained is negative, yielding unphysical results. Therefore, in this part of the Table for these materials the results are given obtained for the highest degrees of freedom, $N_{D.O.F.}$, that still yielded a positive C. If multiple fits were available with the same $N_{D.O.F.}$, the one with lowest uncertainty in the BET surface area was selected.

In Table 2.2 the BET surface areas found when using all degrees of freedom available in the dataset (for $p/p_o \leq 0.3$) for each of the materials, as well as the maximum degrees of freedom useable when also implementing the constraint of $C > 0$ are shown. Relative confidence intervals are below ±10%, except for Sigma-1 for which it is around ±20%.

The BET area is often used as quality indicator: comparison of samples of a given material, *e.g.* reported in literature, is expected to be conclusive. However, the variability in obtained BET surface areas for a given sample and chosen number of degrees of freedom might severely skew this comparison. Variability, in this work is defined as the ratio of minimum and maximum BET surface area determined from fits varying the window of adjacent data points of a selected degree of freedom over the relative pressure range limited by the upper bound recommended by IUPAC ($0.05 \leq p/p_o \leq 0.3$) [2, 3]. Clearly, from Fig. 2.7 can be seen that the variability can exceed a factor of four difference for low degrees of freedom (for MIL-101(Cr). Since it is not common practice to report the relative pressure range applied, in spite of the IUPAC recommendations [2, 3], nor the degrees of freedom used to determine the BET surface area, a comparison of literature results is not straightforward.
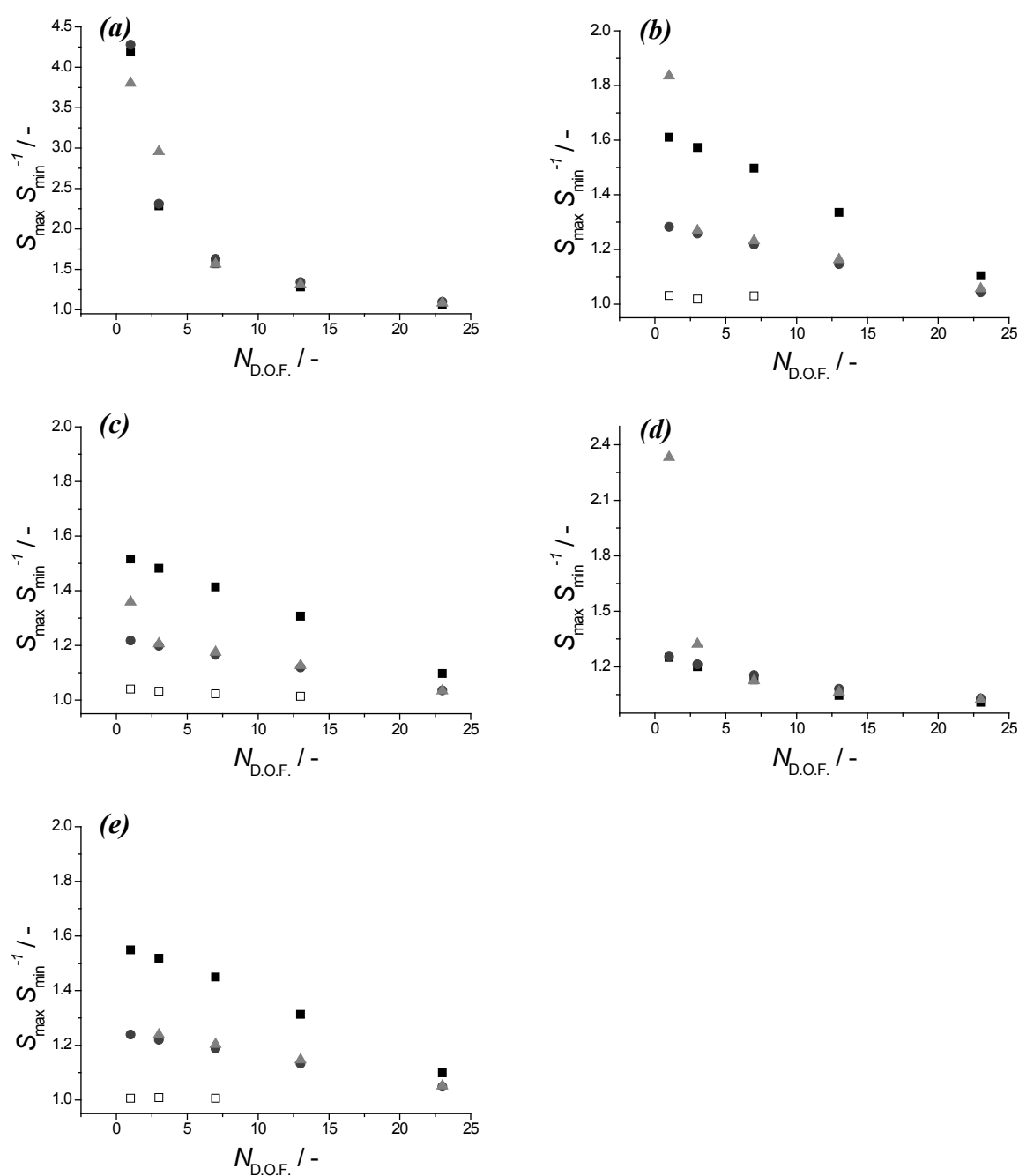
Figure 2.7: The ratio of minimum and maximum BET surface area determined from fits varying the window of adjacent data points of the selected degree of freedom over the relative pressure range limited by the upper bound recommended by IUPAC ($0 \leq p/p_o \leq 0.3$) [2, 3], is depicted as function of the used degrees of freedom for MIL-101(Cr) (*a*), UiO-66 (*b*), Norit RB 2 (*c*), γ-alumina (*d*) and Sigma-1 (*e*). Results for the linear (■), direct (●) and weighted direct (▲) fitting methods. Closed symbols are based on full dataset, open symbols are obtained when the BET *C* parameter is constrained to positive values, only if the constraint excludes part(s) of the data set.

Van Erp and Martens [37] proposed the direct fitting of the BET equation instead of linearizing the adsorption isotherm. The BET monolayer capacity, q_m, and dimensionless parameter, C, were obtained directly by non-linear estimation ('direct method'). Moreover, they also applied weights to each data point ('weighted direct method'), based on the relative vicinity of each point to nearest neighbors, effectively penalizing data points that are close to each other. This, according to the authors, to better balance the relative importance of monolayer and multilayer adsorption in the determination of the BET parameters. Indeed, when the unweighted direct method is applied to the materials under investigation, the variability in the absolute value of the BET surface area is lower (Fig. 2.7) than for the linear method. This is due to the fact that linearization puts significantly more emphasis on measured points at higher relative pressures (Section A.15) [37]. The weighted direct method performs similarly as the unweighted direct method, except for low degrees of freedom, where the performance of the weighted direct method is significantly worse (see Section A.16 for more detailed explanation). Using the nonlinear parameter estimation method, the uncertainty in surface area is obtained from the fit directly. Hence the unweighted nonlinear parameter estimation is preferred. Note, however, that when the fit is applied to a region in the isotherm which is near or at saturation it becomes insensitive to the BET C parameter, increasing strongly the uncertainty in the surface area (Fig. A.12 and S.I. of [83]) for $p/p_o >$ 0.04-0.07). Using the linear method one does not encounter problems with sensitivity of the parameters, but, this method suffers from statistical criticism (error distribution is changed), and might yield negative values for C. This calls for recommendations on the relative pressure range to be used to obtain BET surface areas not prone to a large variability, keeping the uncertainty as low as possible and avoiding physically unacceptable results. In order to formulate such recommendations, a distinction between micro- and mesoporous materials is made.

In case of *microporous materials*, when using the linear method, for $p/p_o >$ 0.04-0.07 the BET C parameter becomes negative while the direct method becomes invariant for the BET C parameter at higher relative pressures, increasing significantly the uncertainty in the BET surface area. In both cases thus, approaching saturation results in fitting problems. Therefore measured points that are close enough to saturation to contribute to a convex linearized BET curve should be excluded, as saturation is not properly described by the BET method. A simple mathematical routine using zero degrees of freedom is proposed to calculate the relative pressure for which C becomes negative, so where the linearized form of the BET

relation breaks down. Thus, for two data points and using the linear BET equation, the C parameter can be calculated:

$$y_i = \underbrace{\left(\frac{1}{Cq_m}\right)}_{I_i} + \underbrace{\left(\frac{C-1}{Cq_m}\right)}_{s_i} x_i \qquad (2.10)$$

Using two adjacent data points, one can extract intercept, I, and slope, s, via:

$$s_{i+1} = \frac{y_{i+1} - y_i}{x_{i+1} - x_i}, I_{i+1} = y_i - x_i s_{i+1} \qquad (2.11)$$

Subsequently the BET C parameter follows from:

$$C_i = \frac{I_i + s_i}{I_i} \qquad (2.12)$$

Eqs. 2.10-2.12 can be applied to each pair of data points of an isotherm recursively. The calculated C values as function of relative pressure are depicted in Fig. A.14 and compared with those values obtained from the previously discussed linear fitting procedure. Strikingly, for all the materials under investigation the two-point procedure yields exactly the same relative pressure at which C becomes negative as was obtained by the linear fitting method, without the laborious efforts of fitting different parts of the isotherm with different degrees of freedom. By applying this routine, not only a fundamental physical reason is given to reject data points, but also a fast mathematical calculation procedure is provided to filter out these data points effectively. The first recommendation, especially for microporous materials, is to apply this filter to the isotherm of the material under investigation. This filter will lead to a very similar relative pressure window as proposed by Rouquerol *et al.* [33], based on the work of Keii *et al.* [84]. Here it was suggested to plot $q \cdot (p_o - p)$ versus p/p_o and to limit the relative pressures to an interval where $q \cdot (p_o - p)$ shows a continuous increase. By following this approach BET surface areas were shown to be in good agreement with those obtained from molecular simulation [36]. Added benefit of the approach opted here is that C is intrinsically constrained to positive values. Also the current method can be more easily implemented in automated software for routine determination of BET surface areas, as no derivative needs to be calculated, as required for the method put forward by Rouquerol *et al.* [33].

Furthermore, it is advised to use the maximum degrees of freedom available within the window to ensure minimal variability and uncertainty in the BET area (Fig. A.15). Since the direct fitting method results in a smaller variation in BET area and confidence interval for data inside the recommended pressure window, it is recommended to use the direct fitting procedure. This conclusion is in line with recent work of Osmari *et al.*, who show that Langmuir parameters from different adsorption measurements determined using the nonlinear (direct) fitting approach yields better parameters and lower uncertainties than using different linearization schemes [71]. Furthermore they concluded that the direct method is much more robust, as it is less influenced by the in- or exclusion of a specific measured point, which can also be seen from the results presented here (Fig. A.15). However, when nonlinear parameter estimation procedures would not be at hand, the linear method but supplemented with weights, ω_l^{-1}, (Section A.15) as shown by Van Erp and Martens [37], could be used. Note that these linearization weights, ω_l, are different from those applied in the weighted direct method.

For *mesoporous materials*, the original restriction posed by Brunauer, Emmet and Teller [34] is a starting point for reasoning. Based on a large set of experimental adsorption measurements, they suggested to use $0.05 < p/p_o < 0.35$. Later, IUPAC decreased the upper limit to 0.30 [2, 3]. The upper limit can be explained by the linearized BET curve becoming more convex, as was found for microporous materials, though at significantly higher relative pressures. It is proposed here to replace this upper limit by one determined by the same mathematical procedure that was successfully applied for microporous materials using pairs of data points. The lower limit, as mentioned by the original authors [34], was put in place because of the observation that below it the transformed BET data showed for many materials strong deviations from linearity. This is most probably because of the surface heterogeneity, violating the assumption of a homogenous surface [34]. Indeed, Salvador *et al*. showed that the BET C parameter varies heavily as function of loading at low surface coverages, yielding extremely high C values for $q/q_m < 0.5$-0.7, for different mesopore containing materials [85]. These high values would erroneously indicate highly microporous materials. Also, as C and q_m are negatively correlated, one would underestimate the surface area as well (Van Erp and Martens [37]). In line with these previous reports, results indicate the lower surface area and higher C values at $p/p_o < 0.03$ -0.07, for both MIL-101(Cr) and γ-alumina (*cf.* Figs. A.11 and A.14). This indeed corresponds roughly to relative loadings $q/q_m < 0.5$-0.7. Despite the physical sense of constraining the pressure range to a minimum for q/q_m, practically this is not easily implemented because it is not trivial to determine *a priori* an exact ratio q/q_m and it

depends on the fitting result. Another option might be to eliminate exorbitantly high values of C, which is again not feasible *a priori*. Though Eq. 2.12 is helpful in determining the relative pressure for which there is a transition from positive to negative C, it does not work to determine a low relative pressure limit (Fig. A.14), because of the high values of C and strong fluctuations therein at low relative pressures. It is thus proposed to use the direct fitting method for the data up to the upper relative pressure limit determined above and to investigate the residuals as function of relative pressure; in this way, large residuals will indicate data points that require further inspection. As these residuals are scale-dependent, they should be normalized or 'Studentized'. Studentized residuals are the residuals obtained divided by their estimated standard deviation [86]. These scale-independent Studentized residuals, res_i^s, are assumed to follow a normal distribution with zero mean and standard deviation of unity [86]. Large residuals, $|\text{res}_i^s| > 2\text{-}3$ (95-99% confidence level), are very likely to be outliers and should be investigated more closely, still under the assumption that the model used is correct. It is not opted here to automatically remove a data point that gives rise to $|\text{res}_i^s| > 2\text{-}3$ as this would require the knowledge *a priori* that the BET model is a proper description, but visual inspection of these Studentized residuals might be a better aid when selecting and possibly eliminate outliers at the lowest relative pressures. For γ-alumina, indeed the data points at lowest relative pressures have the largest residuals. As depicted in Fig. A.16, the Studentized residuals are significantly larger at low relative pressures, indicating inaccurate description of adsorption by the BET equation in this region. Removing these data points increases the quality of the fit substantially and reduces the confidence interval of the estimated surface area (Fig. A.16). The fit becomes impeccable for $q/q_m > 0.9$ where indeed $p/p_o > 0.05$. This is supported by the seemingly randomly distributed Studentized residuals and the strong correspondence between the measured isotherm and fitted curve (Fig. A.16). Furthermore this can be concluded from the normal probability plots accompanying the fits (Fig. A.17). With the decreasing confidence interval the value of surface area increases gradually, as shown in Fig. A.18. Note that initially the Studentized residuals do not necessarily decrease significantly, as they are renormalized each time a measured point is eliminated. Obtaining residuals without any tailing at low relative pressures, starts occurring at $p/p_o > 0.05$ for γ-alumina, when $q/q_m \geq 0.9$, putting most emphasis on multilayer formation during the fitting procedure, the essence of the BET theory.

For MIL-101(Cr) the story is completely different. Because of the distinct kinks in the adsorption isotherm, the BET equation will inherently yield a poor description of the

adsorption behavior. This is reflected in the Studentized residuals (Fig. A.19). Thus there is no statistical incentive to remove particularly the data at low relative pressures. If one were to, despite previous statistical arguments, eliminate points of largest residuals in an iterative fashion, one would need to remove almost the entire dataset (~ 18 data points) to yield some sort of randomly distributed residuals (Figs. A.19 and A.20). The obtained fit parameter values for the latter do not represent the isotherm for MIL-101(Cr) any better than those obtained without any exclusion of data points and even have a higher uncertainty (Table A.6). This corresponds with the notion that the linearized BET curve does not show a significant linear section (see Fig. A.13). From both a statistical and physical point of view thus, for materials deviating strongly in adsorption behavior from the BET formulation as was exemplified for MIL-101(Cr), one should be very careful with the removal of data points.

One might opt to consider using the experimentally found uncertainties from adsorption measurements as weights for the determination of the BET surface area, as was previously recommended by Pendleton and Badalyan [80]. The use of this approach however, is strongly discouraged. As uncertainties are cumulative, the highest weights are given to the first data points. This in turn means that highest importance is given to the data at lowest relative pressures, putting strong emphasis on the region where surface heterogeneity might significantly interfere. As a result the obtained C parameter will be artificially increased and the BET surface area decreased. Indeed Pendleton and Badalyan obtained, for a BET-like reference sample even, lower specific surface areas than for their unweighted case, both based on the linear fitting method [80]. Because the linear fitting method puts, compared to the direct method, more emphasis on high relative pressure data, as has been shown by Van Erp and Martens [37], the undesirable influence of including experimental uncertainties as weights is likely to be even larger for the direct method.

Lastly, the above discussion on the BET surface area determination is based on the third isotherm measurement of each of the materials. For the various fitting strategies investigated the differences in specific surface area and 95% confidence interval determined from all three consecutive measurements on the same sample are minor (Section A.14), indicating the reproducibility of the BET surface area determination procedure. Furthermore, based on these repeated measurements, a 'lack-of-fit' test can be performed to quantify how well the BET-model can be fitted to describe adsorption behavior, in a similar fashion as for the estimation of kinetic reaction parameters from repeated experiments [26]. This test (Section A.17)

indicates that the proposed fitting strategy significantly improves the quality of the fit for the materials under investigation.

2.4.4. Textural characterization in literature – The case of MIL-101

As mentioned in the introduction, the large number of publications on MIL-101 calls for an investigation of the variation in reported pore volumes and surface areas [11, 12, 40-66]. Fig. 2.1 showed the scatter in BET surface area as function of the pore volumes reported in literature, whereas a clear correlation is expected between these parameters. Less than half of the cited papers indicated the relative pressure used for the pore volume determination and more than half of these used a relative pressure very close to unity. At high relative pressures ($p/p_o > 0.9$) condensation of nitrogen in inter-particle spaces may occur, and this contribution should clearly not be included in the pore volume. The extent of this depends on the particle size of the material. Therefore the pore volumes from the isotherm data available in literature are recalculated at a fixed relative pressure, $p/p_o \sim 0.4$. This might be an unusual low relative pressure, but the MIL-101 structure should already be saturated at this pressure, and the uncertainty in pore volume is lower (Fig. 2.2). Furthermore, the adsorption isotherms all overlap once rescaled with their pore volume (Fig. A.22), except for one or two samples with purposely defect-induced mesoporosity. Comparing this recalculated pore volume with the originally reported value (see Fig. A.21), shows that the literature value is significantly higher in most cases. This is not caused by the low relative pressure chosen, since the pore volume at this relative pressure is at most ~5% lower than the one calculated at the more often used p/p_o ~ 0.9 for the majority of cases (Fig. A.22). Clearly, care must be taken when drawing conclusions based on reported pore volumes in literature. When it comes to the BET surface area, for less than one third of the values reported in literature the range of relative pressures or degrees of freedom used for its determination were stated. Furthermore, BET areas were frequently reported with up to six significant digits, suggesting an accuracy that, in view of the findings in this work, is highly exaggerated (Table 2.2). For the cited literature sources the BET surface area is redetermined using the linear, direct and weighted direct method. In all cases the maximum degrees of freedom available for $p/p_o < 0.3$ were used. This because, due to the particular shape of MIL-101, there is no clear statistically valid reason to eliminate data points, as discussed above. Moreover, using the maximum degrees of freedom will decrease uncertainty.
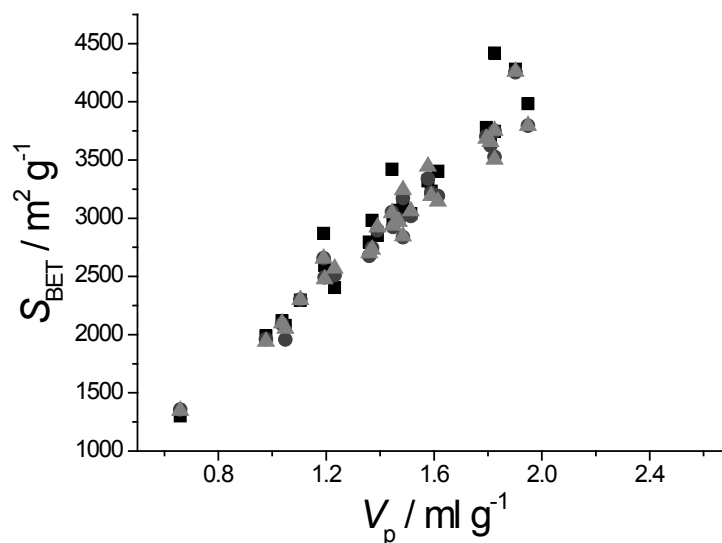
Figure 2.8: Recalculated pore volume and BET area for MIL-101(Cr), determined with the linear (■), direct (●) and weighted direct method (▲) for the literature data depicted in Fig. 2.1.

Comparison of the original and recalculated BET areas, Fig. A.23 shows again that literature values are exaggerated, albeit less pronounced than it was the case for the pore volume. Depicting the recalculated surface area as a function of the recalculated pore volume (Fig. 2.8) gives a significantly stronger correlation than for the values reported in literature (Fig. 2.1).

This example clearly shows the necessity of standardizing conditions for the determination of pore volume and surface area. Furthermore, applying the direct fitting method shows the highest correlation between surface area and pore volume (R^2 of 0.96), and the least variability in BET surface area. The weighted direct (R^2 of 0.95) and linear method (R^2 of 0.93) perform slightly worse. Hence to decrease variability of surface area between different samples of the same compound, one should ideally use the direct fitting method (nonlinear parameter estimation).

2.4.5. UNCERTAINTY IN BJH-PORE SIZE DISTRIBUTION

In Fig. 2.9 pore size distributions and their 95% confidence intervals are given for the materials under investigation.
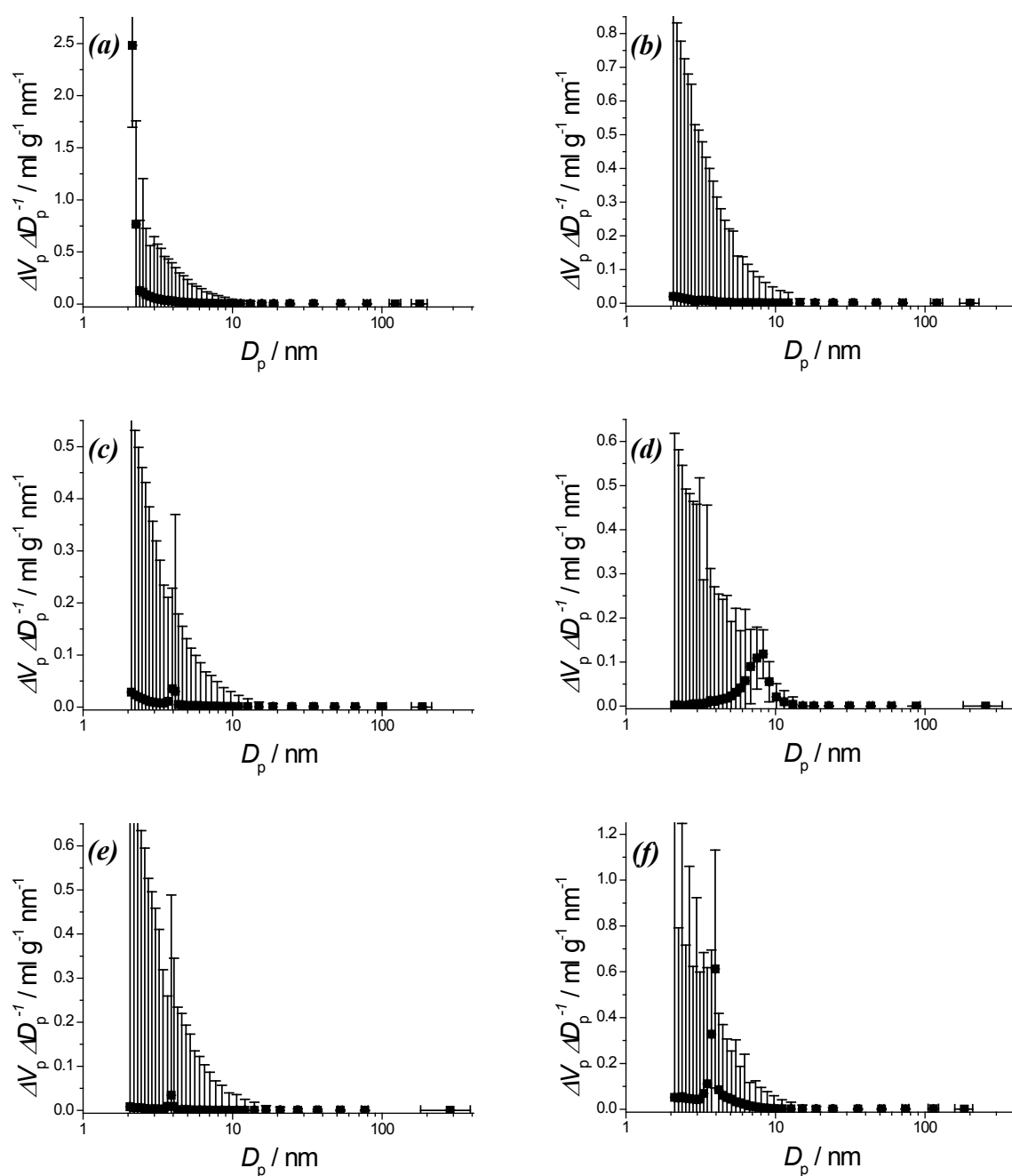
Figure 2.9: BJH pore size distribution including 95% confidence intervals for both the *x*- and *y*-coordinate based on the desorption branch of the isotherm for MIL-101(Cr) (*a*), UiO-66 (*b*), Norit RB2 (*c*), γ-alumina (*d*), Sigma-1 (*e*) for the third measurement of each material and H-ZSM-5 (*f*) with artificially created mesopores [87]. BJH-calculations purposely extended to lower relative pressure than is generally recommended (below $p/p_o = 0.42$) to show trends in distribution and uncertainty.

As first conclusion, the uncertainty in pore diameter (*x*-axis) is negligibly small for $D_p < 50$ nm. Above this pore size, the confidence intervals become significant, showing that indeed the BJH-method is not suitable for macroporous materials. This is easily rationalized when considering that relative pressures corresponding with larger pore diameters are close to unity. The uncertainty in pore diameter is roughly proportional to $|\ln^{-1}(p/p_o)|$, see Eqs. A3.4 – A3.5, and thus greatly amplified at these relative pressures. Secondly, the confidence interval for incremental pore volume per pore diameter ($\Delta V_p/\Delta D_p$) is highest at smallest pore diameters. This is due to the recursive nature of the BJH-calculation, which has its starting point at high relative pressure, and thus large pore diameter, and ends at smallest pore diameters. From Eq. A3.15, it becomes apparent that the uncertainty for a given incremental pore volume is largely influenced by the sum of uncertainties in surface areas of the pores larger than the pore size for the data point under investigation. This uncertainty is expressed in the pore volume and surface area associated with this pore size, and cumulatively propagates towards smaller pore diameters. As this accumulation will only become apparent when pore volume and surface area are of significant magnitude, removing from the calculation pores for which $D_p > 200$ nm will not generate an observable reduction in uncertainty for smaller pore sizes. Even for the microporous materials under investigation, UiO-66, Norit-RB2 and Sigma-1, that show hardly or no mesopore volume, the uncertainty is significant. Indeed, the BJH-method is not suited for the microporous region, but these results are included to show that, also for low pore volumes, the uncertainty is significant. In general the magnitude of this uncertainty mitigates firm quantitative conclusions drawn from pore size distributions. Even for the mesopore-containing materials under investigation, the 95% confidence interval becomes prohibitively large especially for small pore sizes. This occurs already for $D_p > 3.4$ nm, indicating also from the error analysis perspective that the BJH-method, based on the desorption branch, should not be used for $p/p_o < 0.42$. If one would desire to make conclusions based on the pore size distribution quantitatively, one would need to severely decrease the uncertainty therein. This might be accomplished by increasing the sample amount and by measuring significantly less points in the adsorption branch.

Furthermore, both Sigma-1 and Norit-RB2 show a small peak in the pore size distribution around 3.8 nm, which is, as explained by Groen *et al.* [39], due to the so called *tensile strength effect* (TSE). To elaborate on this in particular, a sample of mesoporous zeolite H-ZSM-5 showing distinct type-H2 hysteresis behavior (IUPAC classification) [2, 3], obtained via desilication has been included [87]. This because the TSE is particularly visible for this

type of hysteresis [4]. The forced closure of the desorption branch near $p/p_o = 0.42$ indicates the occurrence of this tensile strength effect (TSE), and does not point to a well-defined mesopore size. The BJH model applied to the adsorption branch demonstrates this (Fig. A.24) as the TSE phenomenon is absent. The TSE leads often to misinterpretation of the pore size distribution: the peak observed at around 4 nm in de BJH from the desorption branch (Fig. 2.9), does not reflect the exact porous properties of the material, but primarily the nature of the adsorptive N_2. Still publications in highly respected journals appear where the contribution of the TSE is erroneously attributed to the presence of real pores [88, 89].

Because of the smaller uncertainty in the adsorbed quantities in the adsorption branch, uncertainty in the pore volume is generally smaller for similar pore sizes. Uncertainties become increasingly large when $D_p < 2$ nm, the border to the microporous region. Again the cumulative nature of the BJH-method is demonstrated. Note that it is strictly not advocated here to apply the BJH-method to the adsorption branch of an isotherm, unless it is used to verify the existence of a tensile strength effect related artefact.

The artificially widened desorption hysteresis caused by decreasing sample mass and increasing sample cell volume (Section 2.4.1) also has a strong effect on the BJH pore size distribution, when based on the desorption branch (Fig. 2.10).

For smallest sample cell volumes (cell 1), the BJH pore size distributions for the three different sample masses used are almost identical, showing smooth curvature. For larger sample cells, the difference between the three different sample masses become increasingly larger and the distributions less smooth. Furthermore, due the artificially increased desorption hysteresis the presence of pores with diameters below 6 nm is erroneously enhanced. This adverse effect can increase the volume for $3.4 \leq D_p \leq 6$ nm up to 5 times (obtained by comparing results for smallest and largest cell volume).
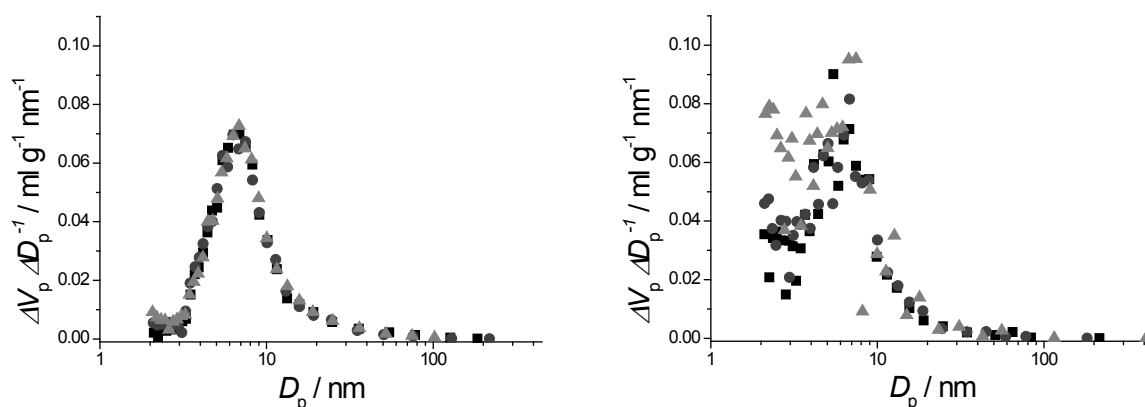
Figure 2.10: BJH-pore size distribution based on the desorption branch for the repeated measurements with γ-alumina(2) for Cell 1 (*left*) and Cell 5 (*right*) for the first(■), second(●) and third(▲) measurement (other cells can be found in the S.I. of [83]). Measurement conditions can be found in Fig. A.7. Confidence interval omitted for clarity. BJH-calculations purposely extended to lower relative pressure than is generally recommended (below $p/p_o <$ 0.42) to show trend in distribution.

2.4.6. RECOMMENDATIONS FOR ADSORPTIVE CHARACTERIZATION

To optimize the N_2 adsorption methodology for the characterization of porous materials and to improve the data analysis, the findings of the error analysis are summarized below in detail and have resulted in recommendations and guidelines collected in Table 2.3.

Regarding uncertainty in *adsorption measurements*:

- Uncertainty propagates cumulatively, and is lowest for the first point of the adsorption branch and highest for the last point measured in the desorption branch. The 95% confidence interval in the adsorption isotherms found are below ±10 ml_{STP} g^{-1} for adsorption and below ±20 ml_{STP} g^{-1} for desorption

- Uncertainty can be decreased by increasing the accuracy of the pressure measurements, the calibration of the manifold volume, by optimizing ratio of manifold and cell volume and by increasing sample mass

- A large sample cell volume and/or small sample mass can artificially and erroneously enlarge or introduce hysteresis between ad- and desorption because of reduced sensitivity to determine equilibration

For the determination of *pore volume*:

- The relative confidence interval in pore volume can be as large as $\pm 10\%$ (p/p_0 = 0.9, Sigma-1), for the measurements performed. To reduce the relative confidence interval in pore volume (p/p_0 = 0.9) to below $\pm 5\%$, one should use:
  - More than 0.5 gram for weakly adsorbing materials (low q_m and K)
  - Around 0.2-0.3 gram for moderately adsorbing materials ($K > 10$ bar^{-1} and $100 < q_m < 200$ ml$_{STP}$ g^{-1})
  - Less than 0.1 gram for strongly adsorbing materials
- For microporous materials, it is recommended to determine the pore volume at relative pressures lower than 0.9. This decreases the uncertainty in pore volume without influencing significantly the absolute value found and automatically ignores inter-particle condensation
- The relative uncertainty in pore volume is lowest when V_{man}/V_{cell} is between 2 and 3.

When it comes to determination of the *BET area*:

- The obtained BET surface area and confidence interval are strongly dependent on applied fitting strategy:
  - The difference in maximum and minimum estimated BET surface areas from a single isotherm ('variability') is limited to 20-40% if more than ten degrees of freedom are used. If less degrees are used this can increase up to ~ 400%
  - Variability is lowest for the 'direct method' (nonlinear parameter estimation) and highest for the 'linear method', attributed to the higher emphasis on points close to saturation for the latter
  - To obtain a small uncertainty in BET surface area, one should at least use three degrees of freedom (at least 5 data points) regardless of fitting strategy
  - The confidence intervals of the BET parameters from the 'direct method' are generally slightly smaller than those obtained from the 'linear method'
- Because of the strong influence of fitting strategy on BET surface area and uncertainty therein it is strongly recommended to report the pressure window, degrees of freedom and fitting method applied alongside the obtained BET surface area
- For microporous materials, it is proposed to exclude data points close to saturation, as the BET equation is unfit to describe saturation

- - By not adhering to this, one might obtain:
    - Negative values for the BET *C* parameter when applying the 'linear method' and thus unphysical results
    - Strongly enlarged uncertainties because of insensitivity towards *C* when using the 'direct method'
    - Lower values for the BET surface area for both fitting methods
  - By adhering to this, one would obtain:
    - A significant reduction in uncertainty in obtained parameters
    - A significant reduction in variability

- The contrived two-point BET method is a useful tool to determine *a priori* the upper relative pressure boundary of the BET window (close to saturation)*,* an alternative to the method reported by Rouquerol *et al.* [33])

- For mesoporous materials, it is recommended to replace the upper boundary of the relative pressure window ($p/p_o \leq 0.35$ as posed by Brunauer *et al.* [34], or $p/p_o \leq 0.30$ by IUPAC [2, 3]) with the relative pressure where the *C* parameter calculated with the two-point method becomes negative

- No method was obtained to *a priori* exclude data for the low relative pressure range where surface heterogeneity may interfere strongly for mesoporous materials especially
  - Here it is suggested to use Studentized residuals, res_i^s. Provided the model isotherm is correct, data points become eligible for possible exclusion when $|res_i^s| > 2\text{-}3$

Uncertainty in BJH-*pore size distribution*:

- The magnitude of the 95% confidence found for BJH-pore size distributions severely impedes drawing quantitative conclusions

- The artificially increased or introduced desorption hysteresis by unfit experimental operation (low sample weight and large sample volume) has a detrimental effect on the desorption branch based BJH pore size analysis

- Still the tensile-strength-effect (TSE) related artefact in desorption-branch related pore-size distributions is often overlooked, yielding erroneous conclusions on seemingly inherent material properties

o   By comparing the pore-size distribution of the ad- and desorption branch one can easily spot the presence of this artefact

Regarding interpretation and reporting of results human influences have a strong impact, as exemplified by the *case of MIL-101(Cr)*:

- Less than half of the cited papers indicate the relative pressure used for the pore volume determination for MIL-101 and of those that did, more than half erroneously overlooked inter-particle condensation and overestimated the pore volume significantly

- Less than one third of reported BET surface areas in literature were accompanied by the relative pressure window and/or degrees of freedom used for their determination

- BET areas are reported with a highly exaggerated number of insignificant digits

- Depicting the recalculated surface area as function of the recalculated pore volume gives a significantly better correlation between both than was the case for the values reported in literature, and clearly underlines the potential of standardizing conditions for the determination of pore volume and surface area

Finally, it is realized that the use of nitrogen for this type of adsorptive characterization is under discussion and argon adsorption at liquid argon temperature (87 K) may be preferred as it is slightly smaller and has no quadrupole moment unlike nitrogen [90, 91]. However the costs of liquid argon are higher and nitrogen is still deeply penetrated in daily texture characterization, making that the presented analysis is nevertheless of high relevance.

Table 2.3: Recommendations and guidelines for texture characterization using volumetric N_2 adsorption at 77 K.

When:	Recommendations

Measuring N_2 adsorption isotherms	• Use as minimal sample mass:
	  ○ 0.5 g for weak adsorption
	  ○ 0.2-0.3 g for moderate adsorption ($K > 10$ bar^{-1} and $100 < q_m < 200$ ml$_{STP}$ g^{-1})
	  ○ 0.1 g for strong adsorption
	• Use $2 \leq V_{man}/V_{cell} \leq 3$ to minimize uncertainty
	• Keep V_{cell} small (~10 ml) to avoid artificially introducing erroneous desorption behavior
	  ○ Use filler rods to decrease V_{cell}

Calculation pore volume	• Avoid including inter-particle condensation • Use a low but relevant p/p_o to reduce uncertainty, while making sure the material is saturated
Reporting pore volume	• State p/p_o used for the determination • The number of significant digits should correspond with the confidence interval of the isotherm
Calculation BET surface area	• Use the 'direct fitting' method (nonlinear estimation parameters and confidence intervals) • Before fitting, determine upper boundary of relative pressure window using the two-point BET method (for both micro- and mesoporous materials) • For mesoporous materials, investigate Studentized residuals to investigate whether low pressure data points are outliers and eligible for exclusion from fitting (due to surface heterogeneity) • Within this pressure window, use the maximum degrees of freedom available

Reporting BET surface area	• Indicate the full fitting strategy, including:
	  ○ The fitting method
	  ○ The pressure window
	  ○ The degrees of freedom
	• The number of significant digits should correspond with the confidence interval

BJH pore size distribution (if used)[a]	• Compare the pore size distribution of both the adsorption and desorption branch to make sure that any TSE-related artefact is absent • Keep V_{cell} small (~10 ml) during measurements to avoid artificially introducing desorption hysteresis, and an erroneous pore size distribution

[a] in most cases confidence interval of pore size distribution statistically undistinguishable from the null hypothesis.

2.5. CONCLUSIONS

In this contribution the influence of uncertainty in adsorptive characterization of porous solids, with special emphasis on the adsorption isotherm measurements and on the determination of pore volume, BET area and pore size distribution has been studied. Uncertainty in *adsorption measurements* can be decreased not only by increasing measuring accuracy or sample mass, but also by optimizing the ratio of manifold and cell volume (optimum at V_{man}/V_{cell} is 2 - 3). Further, a large sample cell volume and/or small sample mass can artificially and erroneously enlarge or even introduce artificially apparent hysteresis between ad- and desorption.

To reduce the relative uncertainty in the *determination of pore volume* for microporous materials it is beneficial to determine the pore volume at relative pressures lower than 0.9. When it comes to *determination of BET area*, obtained surface areas and confidence intervals are strongly dependent on applied fitting strategy. To obtain a small uncertainty in BET surface area, one should at least use three degrees of freedom (at least 5 data points) and apply the direct (nonlinear) fitting method. Excluding data points close to saturation, results in reduction in uncertainty and variability. The contrived two-point BET method is a useful tool to determine *a priori* the upper relative pressure boundary of the BET window. For mesoporous materials, it is recommended to use the same upper boundary. No method was obtained to *a priori* exclude data for the low relative pressure range where surface heterogeneity may interfere strongly but it is suggested to use Studentized residuals for to help locate this boundary.

The magnitude of the 95% confidence limits for *BJH-pore size distributions* severely impedes drawing quantitative conclusions. The artificially increased desorption hysteresis by unfit experimentation has a detrimental effect on the desorption branch based BJH pore size analysis. Regarding interpretation and reporting of results human influences have a strong impact, as exemplified by *the case of MIL-101(Cr)*. For pore volumes and especially BET surface areas reported in literature, often the relative pressure (window) used and determination strategy are not reported or plainly wrong. Using the guidelines posed in this work for the determination of both parameters, a significantly better correlation between both was obtained than was the case for the original values reported in literature.

2.6. REFERENCES

[1] F. Rouquerol, J. Rouquerol, K. Sing, Adsorption by powders & porous solids, Academic Press, London, 1999.

[2] K. Sing, D. Everett, R. Haul, L. Moscou, R. Pierotti, J. Rouquerol, T. Siemieniewska, Reporting physisorption data for gas/solid systems, Pure and Applied Chemistry, 54 (1982) 2201.

[3] R. Pierotti, J. Rouquerol, Reporting physisorption data for gas/solid systems with special reference to the determination of surface area and porosity, Pure and Applied Chemistry, 57 (1985) 603-619.

[4] F. Schüth, K.S.W. Sing, J. Weitkamp, Handbook of porous solids, Wiley-VCH, 2002.

[5] J.-R. Li, R.J. Kuppler, H.-C. Zhou, Selective gas adsorption and separation in Metal-Organic Frameworks, Chemical Society Reviews, 38 (2009) 1477-1504.

[6] S. Couck, J.F.M. Denayer, G.V. Baron, T. Rémy, J. Gascon, F. Kapteijn, An amine-functionalized MIL-53 Metal-Organic Framework with large separation power for CO_2 and CH_4, Journal of the American Chemical Society, 131 (2009) 6326-6327.

[7] C. Gücüyener, J. van den Bergh, J. Gascon, F. Kapteijn, Ethane/ethene separation turned on its head: Selective ethane adsorption on the Metal-Organic Framework ZIF-7 through a gate-opening mechanism, Journal of the American Chemical Society, 132 (2010) 17704-17706.

[8] L.J. Murray, M. Dinca, J.R. Long, Hydrogen storage in Metal-Organic Frameworks, Chemical Society Reviews, 38 (2009) 1294-1314.

[9] J. Juan-Alcaniz, J. Gascon, F. Kapteijn, Metal-Organic Frameworks as scaffolds for the encapsulation of active species: State of the art and future perspectives, Journal of Materials Chemistry, 22 (2012) 10102-10118.

[10] J. Gascon, U. Aktay, M.D. Hernandez-Alonso, G.P.M. van Klink, F. Kapteijn, Amino-based Metal-Organic Frameworks as stable, highly active basic catalysts, Journal of Catalysis, 261 (2009) 75-87.

[11] G. Férey, C. Mellot-Draznieks, C. Serre, F. Millange, J. Dutour, S. Surblé, I. Margiolaki, A chromium terephthalate-based solid with unusually large pore volumes and surface area, Science, 309 (2005) 2040-2042.

[12] G. Akiyama, R. Matsuda, H. Sato, A. Hori, M. Takata, S. Kitagawa, Effect of functional groups in MIL-101 on water sorption behavior, Microporous and Mesoporous Materials, 157 (2012) 89-93.

[13] J. Juan-Alcañiz, E.V. Ramos-Fernandez, U. Lafont, J. Gascon, F. Kapteijn, Building MOF bottles around phosphotungstic acid ships: One-pot synthesis of bi-functional polyoxometalate-MIL-101 catalysts, Journal of Catalysis, 269 (2010) 229-241.

[14] E.V. Ramos-Fernandez, C. Pieters, B. van der Linden, J. Juan-Alcaniz, P. Serra-Crespo, M.W.G.M. Verhoeven, H. Niemantsverdriet, J. Gascon, F. Kapteijn, Highly dispersed platinum in Metal Organic Framework NH_2-MIL-101(Al) containing phosphotungstic acid - characterization and catalytic performance, Journal of Catalysis, 289 (2012) 42-52.

[15] S.N. Klyamkin, E.A. Berdonosova, E.V. Kogan, K.A. Kovalenko, D.N. Dybtsev, V.P. Fedin, Influence of MIL-101 doping by ionic clusters on hydrogen storage performance up to 1900 bar, Chemistry-an Asian Journal, 6 (2011) 1854-1859.

[16] D. Jiang, L.L. Keenan, A.D. Burrows, K.J. Edler, Synthesis and post-synthetic modification of MIL-101(Cr)-NH_2 via a tandem diazotisation process, Chemical Communications, 48 (2012) 12053-12055.

[17] C.-X. Yang, X.-P. Yan, Metal-organic framework MIL-101(Cr) for high-performance liquid chromatographic separation of substituted aromatics, Analytical Chemistry, 83 (2011) 7144-7150.

[18] J.H. Cavka, S. Jakobsen, U. Olsbye, N. Guillou, C. Lamberti, S. Bordiga, K.P. Lillerud, A new zirconium inorganic building brick forming Metal Organic Frameworks with exceptional stability, Journal of the American Chemical Society, 130 (2008) 13850-13851.

[19] H. Wu, T. Yildirim, W. Zhou, Exceptional mechanical stability of highly porous zirconium Metal-Organic Framework UiO-66 and its important implications, The Journal of Physical Chemistry Letters, 4 (2013) 925-930.

[20] S. Chavan, J.G. Vitillo, D. Gianolio, O. Zavorotynska, B. Civalleri, S. Jakobsen, M.H. Nilsen, L. Valenzano, C. Lamberti, K.P. Lillerud, S. Bordiga, H_2 storage in isostructural UiO-67 and UiO-66 MOFs, Physical Chemistry Chemical Physics, 14 (2012) 1614-1626.

[21] A.D. Wiersum, E. Soubeyrand-Lenoir, Q. Yang, B. Moulin, V. Guillerm, M.B. Yahia, S. Bourrelly, A. Vimont, S. Miller, C. Vagner, M. Daturi, G. Clet, C. Serre, G. Maurin, P.L. Llewellyn, An evaluation of UiO-66 for gas-based applications, Chemistry – An Asian Journal, 6 (2011) 3270-3280.

[22] F. Vermoortele, B. Bueken, G. Le Bars, B. Van de Voorde, M. Vandichel, K. Houthoofd, A. Vimont, M. Daturi, M. Waroquier, V. Van Speybroeck, Synthesis modulation as a tool to increase the catalytic

activity of Metal-Organic Frameworks: The unique case of UiO-66(Zr), Journal of the American Chemical Society, 135 (2013) 11465-11468.

[23]   Y. Iwase, Y. Sakamoto, A. Shiga, A. Miyaji, K. Motokura, T.-r. Koyama, T. Baba, Shape-selective catalysis determined by the volume of a zeolite cavity and the reaction mechanism for propylene production by the conversion of butene using a proton-exchanged zeolite, The Journal of Physical Chemistry C, 116 (2012) 5182-5196.

[24]   H.-Y. Jeon, C.-H. Shin, H.J. Jung, S.B. Hong, Catalytic evaluation of small-pore molecular sieves with different framework topologies for the synthesis of methylamines, Applied Catalysis A: General, 305 (2006) 70-78.

[25]   Y. Kumita, J. Gascon, E. Stavitski, J.A. Moulijn, F. Kapteijn, Shape selective methanol to olefins over highly thermostable DDR catalysts, Applied Catalysis A: General, 391 (2011) 234-243.

[26]   F. Kapteijn, H.L. Bredt, E. Homburg, J.C. Mol, Kinetics of the metathesis of propene over dirhenium heptaoxide/Gamma-aluminum oxide, Industrial & Engineering Chemistry Product Research and Development, 20 (1981) 457-466.

[27]   F. Kapteijn, L. Singoredjo, N.J. Dekker, J.A. Moulijn, Kinetics of the selective catalytic reduction of nitrogen oxide (NO) with ammonia over manganese oxide (Mn_2O_3)-tungsten oxide (WO_3)/Gamma.-alumina, Industrial & Engineering Chemistry Research, 32 (1993) 445-452.

[28]   L. Zhou, Y. Guo, Q. Zhang, M. Yagi, J. Hatakeyama, H. Li, J. Chen, M. Sakurai, H. Kameyama, A novel catalyst with plate-type anodic alumina supports, $Ni/NiAl_2O_4$/gamma-Al_2O_3/alloy, for steam reforming of methane, Applied Catalysis A: General, 347 (2008) 200-207.

[29]   S. Sircar, T. Golden, M. Rao, Activated carbon for gas separation and storage, Carbon, 34 (1996) 1-12.

[30]   D. Lozano-Castello, J. Alcaniz-Monge, D. Cazorla-Amoros, A. Linares-Solano, W. Zhu, F. Kapteijn, J. Moulijn, Adsorption properties of carbon molecular sieves prepared from an activated carbon by pitch pyrolysis, Carbon, 43 (2005) 1643-1651.

[31]   C.Y. Yin, M.K. Aroua, W.M.A.W. Daud, Review of modifications of activated carbon for enhancing contaminant uptakes from aqueous solutions, Separation and Purification Technology, 52 (2007) 403-415.

[32]   A.R. Millward, O.M. Yaghi, Metal-Organic Frameworks with exceptionally high capacity for storage of carbon dioxide at room temperature, Journal of the American Chemical Society, 127 (2005) 17998-17999.

[33]   J. Rouquerol, P. Llewellyn, F. Rouquerol, Is the BET equation applicable to microporous adsorbents?, in: F.R.-R.J.R. P.L. Llewellyn, N. Seaton (Eds.) Studies in surface science and catalysis, Elsevier2007, pp. 49-56.

[34]   S. Brunauer, P.H. Emmett, E. Teller, Adsorption of gases in multimolecular layers, Journal of the American Chemical Society, 60 (1938) 309-319.

[35]   I. Langmuir, The constitution and fundamental properties of solids and liquids. Part I. Solids, The Journal of the American Chemical Society, 38 (1916) 2221-2295.

[36]   K.S. Walton, R.Q. Snurr, Applicability of the BET method for determining surface areas of Microporous Metal-Organic Frameworks, Journal of the American Chemical Society, 129 (2007) 8552-8556.

[37]   T.S. Van Erp, J.A. Martens, A standardization for BET fitting of adsorption isotherms, Microporous and Mesoporous Materials, 145 (2011) 188-193.

[38]   E.P. Barrett, L.G. Joyner, P.P. Halenda, The determination of pore volume and area distributions in porous substances. I. Computations from nitrogen isotherms, Journal of the American Chemical Society, 73 (1951) 373-380.

[39]   J.C. Groen, L.A. Peffer, J. Pérez-Ramírez, Pore size determination in modified micro-and mesoporous materials. Pitfalls and limitations in gas adsorption data analysis, Microporous and Mesoporous Materials, 60 (2003) 1-17.

[40]   P. Trens, H. Belarbi, C. Shepherd, P. Gonzalez, N.A. Ramsahye, U.H. Lee, Y.K. Seo, J.S. Chang, Coadsorption of n -hexane and benzene vapors onto the chromium terephthalate-based porous material MIL-101(Cr) an experimental and computational study, Journal of Physical Chemistry C, 116 (2012) 25824-25831.

[41]   X. Liu, H. Zhou, Y. Zhang, Y. Liu, A. Yuan, Syntheses, characterizations and adsorption properties of MIL-101/graphene oxide composites, Chinese Journal of Chemistry, 30 (2012) 2563-2566.

[42]   K. Munusamy, G. Sethia, D.V. Patil, P.B. Somayajulu Rallapalli, R.S. Somani, H.C. Bajaj, Sorption of carbon dioxide, methane, nitrogen and carbon monoxide on MIL-101(cr): Volumetric measurements and dynamic adsorption studies, Chemical Engineering Journal, 195-196 (2012) 359-368.

[43]   I. Senkovska, E. Barea, J.A.R. Navarro, S. Kaskel, Adsorptive capturing and storing greenhouse gases such as sulfur hexafluoride and carbon tetrafluoride using Metal-Organic Frameworks, Microporous and Mesoporous Materials, 156 (2012) 115-120.

[44] S.N. Kim, S.T. Yang, J. Kim, J.E. Park, W.S. Ahn, Post-synthesis functionalization of MIL-101 using diethylenetriamine: A study on adsorption and catalysis, CrystEngComm, 14 (2012) 4142-4147.

[45] M. Anbia, V. Hoseini, Development of mwcnt@MIL-101 hybrid composite with enhanced adsorption capacity for carbon dioxide, Chemical Engineering Journal, 191 (2012) 326-330.

[46] M. Anbia, V. Hoseini, Enhancement of CO_2 adsorption on nanoporous chromium terephthalate (MIL-101) by amine modification, Journal of Natural Gas Chemistry, 21 (2012) 339-343.

[47] L. Bromberg, Y. Diao, H. Wu, S.A. Speakman, T.A. Hatton, Chromium(III) terephthalate metal organic framework (MIL-101): HF-free synthesis, structure, polyoxometalate composites, and catalytic properties, Chemistry of Materials, 24 (2012) 1664-1675.

[48] H.B.T. Jeazet, C. Staudt, C. Janiak, A method for increasing permeability in O_2/N_2 separation with mixed-matrix membranes made of water-stable MIL-101 and polysulfone, Chemical Communications, 48 (2012) 2140-2142.

[49] Z. Saedi, S. Tangestaninejad, M. Moghadam, V. Mirkhani, I. Mohammadpoor-Baltork, MIL-101 Metal/Organic Framework: A highly efficient heterogeneous catalyst for oxidative cleavage of alkenes with H_2O_2, Catalysis Communications, 17 (2012) 18-22.

[50] J. Ehrenmann, S.K. Henninger, C. Janiak, Water adsorption characteristics of MIL-101 for heat-transformation applications of MOFs, European Journal of Inorganic Chemistry, 2011 (2011) 471-474.

[51] Z. Zhao, X. Li, S. Huang, Q. Xia, Z. Li, Adsorption and diffusion of benzene on chromium-based Metal Organic Framework MIL-101 synthesized by microwave irradiation, Industrial and Engineering Chemistry Research, 50 (2011) 2254-2261.

[52] Z. Zhao, X. Li, Z. Li, Adsorption equilibrium and kinetics of p-xylene on chromium-based Metal Organic Framework MIL-101, Chemical Engineering Journal, 173 (2011) 150-157.

[53] Z. Zhang, S. Huang, S. Xian, H. Xi, Z. Li, Adsorption equilibrium and kinetics of CO_2 on chromium terephthalate MIL-101, Energy and Fuels, 25 (2011) 835-842.

[54] C.Y. Huang, M. Song, Z.Y. Gu, H.F. Wang, X.P. Yan, Probing the adsorption characteristic of Metal-Organic Framework MIL-101 for volatile organic compounds by quartz crystal microbalance, Environmental Science and Technology, 45 (2011) 4490-4496.

[55] J. Shi, Z. Zhao, Q. Xia, Y. Li, Z. Li, Adsorption and diffusion of ethyl acetate on the chromium-based Metal-Organic Framework MIL-101, Journal of Chemical and Engineering Data, 56 (2011) 3419-3425.

[56] P.B. Somayajulu Rallapalli, M.C. Raj, D.V. Patil, K.P. Prasanth, R.S. Somani, H.C. Bajaj, Activated carbon MIL-101(Cr): A potential Metal-Organic Framework composite material for hydrogen storage, International Journal of Energy Research.

[57] K. Yang, Q. Sun, F. Xue, D. Lin, Adsorption of volatile organic compounds by Metal-Organic Frameworks MIL-101: Influence of molecular size and shape, Journal of Hazardous materials, 195 (2011) 124-131.

[58] D. Jiang, A.D. Burrows, K.J. Edler, Size-controlled synthesis of MIL-101(Cr) nanoparticles with enhanced selectivity for CO_2 over N_2, CrystEngComm, 13 (2011) 6916-6919.

[59] N.A. Khan, J.W. Jun, S.H. Jhung, Effect of water concentration and acidity on the synthesis of porous chromium benzenedicarboxylates, European Journal of Inorganic Chemistry, (2010) 1043-1048.

[60] N. Klein, A. Henschel, S. Kaskel, N-butane adsorption on $Cu_3(BTC)_2$ and MIL-101, Microporous and Mesoporous Materials, 129 (2010) 238-242.

[61] J. Yang, Q. Zhao, J. Li, J. Dong, Synthesis of Metal–Organic Framework MIL-101 in TMAOH-$Cr(NO)_3$-H_2BDC-H_2O and its hydrogen-storage behavior, Microporous and Mesoporous Materials, 130 (2010) 174-179.

[62] T.K. Trung, N.A. Ramsahye, P. Trens, N. Tanchoux, C. Serre, F. Fajula, G. Férey, Adsorption of C5-C9 hydrocarbons in microporous MOFs MIL-100(Cr) and MIL-101(Cr): A manometric study, Microporous and Mesoporous Materials, 134 (2010) 134-140.

[63] P. Küsgens, M. Rose, I. Senkovska, H. Fröde, A. Henschel, S. Siegle, S. Kaskel, Characterization of Metal-Organic Frameworks by water adsorption, Microporous and Mesoporous Materials, 120 (2009) 325-330.

[64] J.S. Lee, S.H. Jhung, J.W. Yoon, Y.K. Hwang, J.S. Chang, Adsorption of methane on porous metal carboxylates, Journal of Industrial and Engineering Chemistry, 15 (2009) 674-676.

[65] S.H. Jhung, J.H. Lee, J.W. Yoon, C. Serre, G. Férey, J.S. Chang, Microwave synthesis of chromium terephthalate MIL-101 and its benzene sorption ability, Advanced Materials, 19 (2007) 121-124.

[66] X.X. Huang, L.G. Qiu, W. Zhang, Y.P. Yuan, X. Jiang, A.J. Xie, Y.H. Shen, J.F. Zhu, Hierarchically mesostructured MIL-101 Metal-Organic Frameworks: Supramolecular template-directed synthesis and accelerated adsorption kinetics for dye removal, CrystEngComm, 14 (2012) 1613-1617.

[67] A. Stewart Zeolite Sigma-1Patent GB19870017794 19870728, 1988

[68] S.J. Gregg, K.S.W. Sing, Adsorption, surface area and porosity, Academic Press, London, 1982.

[69]   P.H. Emmett, S. Brunauer, The use of low temperature Van der Waals adsorption isotherms in determining the surface area of iron synthetic ammonia catalysts, Journal of the American Chemical Society, 59 (1937) 1553-1564.

[70]   A.L. McClellan, H.F. Harnsberger, Cross-sectional areas of molecules adsorbed on solid surfaces, Journal of Colloid and Interface Science, 23 (1967) 577-599.

[71]   T. Osmari, R. Gallon, M. Schwaab, E. Barbosa-Coutinho, J. Severo, J. Pinto, Statistical analysis of linear and non-linear regression for the estimation of adsorption isotherm parameters, Adsorption Science & Technology, 31 (2013) 433-458.

[72]   H. Lineweaver, D. Burk, The determination of enzyme dissociation constants, Journal of the American Chemical Society, 56 (1934) 658-666.

[73]   O.A. Hougen, K.M. Watson, Chemical process principles, Wiley, New York, 1947.

[74]   G.F. Froment, K.B. Bischoff, Chemical reactor analysis and design, 2nd ed., Wiley, New York, 1991.

[75]   C.G. Shull, The determination of pore size distribution from gas adsorption data, Journal of the American Chemical Society, 70 (1948) 1405-1410.

[76]   J.H. de Boer, B.C. Lippens, B.G. Linsen, J.C.P. Broekhoff, A. van den Heuvel, T.J. Osinga, The t-curve of multimolecular N_2-adsorption, Journal of Colloid and Interface Science, 21 (1966) 405-414.

[77]   W.D. Harkins, G. Jura, An adsorption method for the determination of the area of a solid without the assumption of a molecular area, and the area occupied by nitrogen molecules on the surfaces of solids, The Journal of Chemical Physics, 11 (1943) 431-432.

[78]   M. Kruk, M. Jaroniec, A. Sayari, Application of large pore MCM-41 molecular sieves to improve pore size analysis using nitrogen adsorption measurements, Langmuir, 13 (1997) 6267-6273.

[79]   J.R. Taylor, An introduction to error analysis, 2nd ed., University Science Books1997.

[80]   A. Badalyan, P. Pendleton, Analysis of uncertainties in manometric gas-adsorption measurements. I: Propagation of uncertainties in BET analyses, Langmuir, 19 (2003) 7919-7928.

[81]   P. Pendleton, A. Badalyan, Uncertainty in pore volumes derived from α_s-analyses and from the theory for volume filling of micropores, Colloids and Surfaces A: Physicochemical and Engineering Aspects, 300 (2007) 253-258.

[82]   A. Badalyan, P. Pendleton, Analysis of uncertainties in manometric gas-adsorption measurements. I. Uncertainty in α_s-analyses and pore volumes, Journal of Colloid and Interface Science, 326 (2008) 1-7.

[83]   M.F. De Lange, T.J.H. Vlugt, J. Gascon, F. Kapteijn, Adsorptive characterization of porous solids: Error analysis guides the way, Microporous and Mesoporous Materials, 200 (2014) 199-215.

[84]   T. Keii, T. Takagi, S. Kanetaka, A new plotting of the BET method, Analytical Chemistry, 33 (1961) 1965.

[85]   F. Salvador, C. Sánchez-Jiménez, M.J. Sánchez-Montero, A. Salvador, A review of the application of the BET equation to experimental data: The C parameter, in: B.M.J.R. F. Rodriguez-Reinoso, K. Unger (Eds.) Studies in surface science and catalysis, Elsevier2002, pp. 379-386.

[86]   R.D. Cook, S. Weisberg, Residuals and influence in regression, Chapman and Hall, New York, 1982.

[87]   S. Sartipi, K. Parashar, M. Makkee, J. Gascon, F. Kapteijn, Breaking the fischer–tropsch synthesis selectivity: Direct conversion of syngas to gasoline over hierarchical Co/H-ZSM-5 catalysts, Catalysis Science & Technology, 3 (2013) 572-575.

[88]   L.G. Qiu, T. Xu, Z.Q. Li, W. Wang, Y. Wu, X. Jiang, X.Y. Tian, L.D. Zhang, Hierarchically micro- and mesoporous Metal–Organic Frameworks with tunable porosity, Angewandte Chemie International Edition, 47 (2008) 9487-9491.

[89]   L. Li, S. Xiang, S. Cao, J. Zhang, G. Ouyang, L. Chen, C.-Y. Su, A synthetic route to ultralight hierarchically micro/mesoporous al (III)-carboxylate Metal-Organic aerogels, Nature communications, 4 (2013) 1774.

[90]   M. Thommes, Physical adsorption characterization of nanoporous materials, Chemie-Ingenieur-Technik, 82 (2010) 1059-1073.

[91]   J. Silvestre-Albero, A. Silvestre-Albero, F. Rodríguez-Reinoso, M. Thommes, Physical characterization of activated carbons with narrow microporosity by nitrogen (77.4 K), carbon dioxide (273 K) and argon (87.3 K) adsorption in combination with immersion calorimetry, Carbon, 50 (2012) 3128-3133.

APPENDIX A

ADSORPTIVE CHARACTERIZATION OF
POROUS SOLIDS

LIST OF SYMBOLS

Latin

Symbol	Description	Unit
A_{cs}	Cross-sectional area	m^2
C	Dimensionless BET parameter	-
c	Dimensionless ratio of Kelvin and pore radius	-
D	Diameter	m
E	Adsorption energy	$kJ\ mol^{-1}$
F	F-test statistic	-
I	Intercept	$g\ ml_{STP}^{-1}$
K	Langmuir adsorption equilibrium constant	bar^{-1}
M_{N2}	Molar mass of nitrogen	$g\ mol^{-1}$
N	Number	-
n	Amount	mol
N_A	Avogadro's constant	mol^{-1}
p	Pressure	bar
p	Number of parameters to be estimated	-
p/p_o	Relative pressure	-
q	Adsorbed amount	$ml_{STP}\ g^{-1}$
R	Universal gas constant	$J\ mol^{-1}\ K^{-1}$
r	Radius	m
$R(n)$	Pore aspect ratio	-
R^2	Coefficient of determination	-
res	Residual	(a)
S	Specific surface area	$m^2\ g^{-1}$
s	Slope	$g\ ml_{STP}^{-1}$
SSE	Error sum of squares	[*varies*]
SSL	Lack-of fit sum of squares	[*varies*]
SSR	Sum of squared residuals	[*varies*]
T	Temperature	K
t	Thickness of adsorbed layer	m
t	Student t-distribution	-
V	Volume	m^3
V_p	Specific pore volume	$ml\ g^{-1}$
V_l	Liquid molar volume	$m^3\ mol^{-1}$
w	Weight	g
Z	Compressibility factor	-

Greek

Symbol	Description	Unit
α	Linear correction factor	bar^{-1}

α	Confidence level (in Student's *t*-distribution)	-
β	Dimensionless ratio (see Eq. A14.3)	-
ζ	Parameter (either V_p or S_{BET})	[*varies*]
ρ	Density	g ml^{-1}
σ	Standard deviation or uncertainty	(a,b)
σ^2	Variance	(c)
σ$_t$	Surface tension	dyn cm^{-1}
ω	Statistical weight	-

Subscripts

ads	Adsorbed
BET	Brunauer, Emmett and Teller (method)
cell	Sample cell
cold	Cold fraction of the sample cell
d	Dose
D.O.F.	Degree(s) of freedom
dosed	Dosed
gas	Present in the gas phase
K	Kelvin
l	Linear
m	Monolayer
man	Manifold
nbp	Normal boiling point
p	Pore
res	Residual(s)
sample	Sample of (porous) material
sat	At saturation
STP	Standard temperature and pressure [d]
warm	Warm fraction of the sample cell

Superscripts

liq	Liquid phase
S	Studentized
vap	Vapor phase

Notes:
  (a)   Same units as the property it is related to
  (b)   Standard deviation if based solely on measured values, else uncertainty
  (c)   Squared units of the property it is related to
  (d)   273.15 K and 1 bar

Table A.1: Samples masses and cell volumes used in nitrogen adsorption measurements. Manifold volume is 24.3 ml.

Material	w_{sample} / g	V_{cell} / ml
MIL-101(Cr)	0.12	10.5
UiO-66	0.13	11.0
Sigma-1	0.15	11.1
γ-alumina	0.18	10.8
Norit RB2	0.20	10.7

As the supplementary information belonging the original publication is rather lengthy, the choice was made not depict all information in this chapter. For information omitted here, the reader is kindly referred to the original publication [1].

A.1. SAMPLE MASS AND CELL VOLUME FOR REPEATED MEASUREMENTS

Sample masses of materials used in the adsorptive investigations and sample cell volumes determined are given in Table A.1.

A.2. ERROR PROPAGATION IN NITROGEN PHYSISORPTION MEASUREMENTS

The variance in a measured nitrogen isotherm is calculated using propagation of uncertainty (see, e.g. Taylor [2]):

$$\sigma_y^2 = \sum \left(\frac{\partial y}{\partial x_i} \right)^2 \sigma_{x_i}^2 \tag{A2.1}$$

Here y is a variable calculated from i measured variables x_i and σ_y is the uncertainty in this variable y, clearly a function of the uncertainties in x_i, σ_{xi}. Applying Eq. A2.1 consecutively on all calculated variables will ultimately lead to the uncertainty the adsorbed amount as function of relative pressure.

An adsorption measurement in general starts with the determination of the volume of the sample cell, V_{cell}, which is connected to the dosing manifold. This dosing manifold is a vessel of which the volume, V_{man}, is accurately determined by the manufacturer. The determination of V_{cell} is started by pressurizing the manifold with helium and then opening the connection

between manifold and sample cell, which is at or near vacuum before connection to manifold is opened. The cell volume can then be calculated via:

$$V_{\text{cell}} = \left(\frac{p_{\text{man}}^0 - p_{\text{man}}^1}{p_{\text{cell}}^1 - p_{\text{cell}}^0} \right) V_{\text{man}} \tag{A2.2}$$

Here, p_{man} is the manifold pressure, p_{cell} is the cell pressure, and indices 1 and 0 correspond to after and before opening the connection between manifold and cell, respectively. Error propagation dictates thus that the variance in the cell volume is:

$$\sigma_{V_{\text{cell}}}^2 = \left(\frac{1}{p_{\text{cell}}^1 - p_{\text{cell}}^0} V_{man} \right)^2 \left(2\sigma_{\text{p}}^2 \right) + \left(\frac{p_{\text{man}}^0 - p_{\text{man}}^1}{\left(p_{\text{cell}}^1 - p_{\text{cell}}^0 \right)^2} V_{\text{man}} \right)^2 \left(2\sigma_{\text{p}}^2 \right) + \left(\frac{p_{\text{man}}^0 - p_{\text{man}}^1}{p_{\text{cell}}^1 - p_{\text{cell}}^0} \right)^2 \sigma_{V_{\text{man}}}^2 \tag{A2.3}$$

Here σ_{p} is the uncertainty in any of the measured pressures, irrespective of which volume it belongs to. As nitrogen adsorption measurements are performed at the normal boiling point of nitrogen (77.4 K), a part of the sample cell volume will be cooled to this temperature, called the cold volume, V_{cold}, and a part of this volume will remain at room temperature, V_{warm}. To determine both, the sample cell is now pressurized with helium, before the cooling is applied. After cooling, the pressure in the sample cell will have decreased. From this decrease, the warm part of the cell volume, V_{warm}, can be quantified by:

$$V_{\text{warm}} = \left(\frac{\dfrac{p_{\text{cell}}^0}{p_{\text{cell}}^1} - \dfrac{T_{\text{warm}}}{T_{\text{cold}}}}{1 - \dfrac{T_{\text{warm}}}{T_{\text{cold}}}} \right) V_{\text{cell}} \tag{A2.4}$$

Here T_{warm} is the temperature of the manifold, and T_{cold} is the temperature of liquid nitrogen. Hereby it is assumed that the thermal conditions are the same under helium and nitrogen and that these don't change during adsorption measurements.

The variance in the warm fraction of the cell volume can be calculated via:

$$\sigma_{V_{\text{warm}}}^2 = \left(\frac{1}{p_{\text{cell}}^1 \left(1 - \dfrac{T_{\text{warm}}}{T_{\text{cold}}} \right)} V_{\text{cell}} \right)^2 \sigma_p^2 + \left(\frac{\dfrac{p_{\text{cell}}^0}{\left(p_{\text{cell}}^1 \right)^2}}{1 - \dfrac{T_{\text{warm}}}{T_{\text{cold}}}} V_{\text{cell}} \right)^2 \sigma_p^2 + \left(\frac{T_{\text{cold}} \left(p_{\text{cell}}^0 - p_{\text{cell}}^1 \right)}{p_{\text{cell}}^1 \left(T_{\text{warm}} - T_{\text{cold}} \right)} V_{\text{cell}} \right)^2 \sigma_{T_{\text{warm}}}^2$$

$$+ \left(\frac{T_{\text{warm}} \left(p_{\text{cell}}^0 - p_{\text{cell}}^1 \right)}{p_{\text{cell}}^1 \left(T_{\text{warm}} - T_{\text{cold}} \right)^2} V_{\text{cell}} \right)^2 \sigma_{T_{\text{cold}}}^2 + \left(\frac{\dfrac{p_{\text{cell}}^0}{p_{\text{cell}}^1} - \dfrac{T_{\text{warm}}}{T_{\text{cold}}}}{1 - \dfrac{T_{\text{warm}}}{T_{\text{cold}}}} \right)^2 \sigma_{V_{\text{cell}}}^2$$

$$(A2.5)$$

Here $\sigma_{T\text{warm}}$ is the uncertainty in the measured temperature in the manifold, and $\sigma_{T\text{cold}}$ is uncertainty in the liquid nitrogen temperature. The latter is caused by minor fluctuations in ambient pressure of the surrounding atmosphere as measured periodically by the machine and thus the uncertainty in T_{cold} is back-calculated via the Antoine equation. In practice this uncertainty is rather similar to $\sigma_{T\text{warm}}$. The cold volume and variance therein are easily found via subtraction:

$$V_{\text{cold}} = V_{\text{cell}} - V_{\text{warm}} \tag{A2.6}$$

$$\sigma_{V_{\text{cold}}}^2 = \sigma_{V_{\text{cell}}}^2 + \sigma_{V_{\text{warm}}}^2 \tag{A2.7}$$

After these volume determinations, the actual measurement can be commenced. This is effectively done by evacuating the sample cell, to remove all the helium present and supplying a given pressure of nitrogen to the manifold. The connection between sample and manifold is opened and the material under investigation will start to adsorb nitrogen. After equilibration, in this analysis it is tacitly assumed that thermodynamic equilibrium is reached, the amount adsorbed for the first measured point is calculated as the difference of the total amount dosed and the amount of nitrogen pressure present in the gas-phase in the sample cell. From the second measured point and onwards this difference is augmented with the amount adsorbed for the previous point(s):

$$n_{\text{ads}} (i) = n_{\text{dosed}} (i) - n_{\text{gas}} (i) + n_{\text{ads}} (i-1) \tag{A2.8}$$

Here n_{ads} is the amount adsorbed, n_{dosed} the amount dosed from the manifold and n_{gas} is the amount present in the gas phase, all in moles. The amount present in the gas phase can be calculated via:

$$n_{gas}(i) = p_{cell}^i \left(\frac{V_{warm}}{RT_{warm}} + \frac{V_{cold}}{Z(p_{cell}^i)RT_{cold}} \right) \tag{A2.9}$$

Here Z is the compressibility factor, a correction for non-ideality, defined as:

$$Z = 1 - \alpha(T_{cold}) p_{cell}^i \tag{A2.10}$$

Here α is the linear correction factor. The amount dosed can be calculated via:

$$n_{dosed}(i) = \left(p_{man}^0(i) - p_{man}^1(i) \right) \frac{V_{man}}{RT_{warm}} = \Delta p_{man}(i) \frac{V_{man}}{RT_{warm}} \tag{A2.11}$$

For now it is tacitly assumed that a single dose will be sufficient to measure a point on the isotherm. In Section A.9 the effect of not adhering to this assumption on uncertainty is shown. The variance in n_{gas}, n_{dosed} and n_{ads} respectively can now be calculated:

$$\sigma_{n_{gas}}^2(i) = \left(\frac{V_{warm}}{RT_{warm}} + \frac{V_{cold}}{RT_{cold}Z(p_{cell}^i)} + \frac{p_{cell}^i \alpha(T) V_{cold}}{RT_{cold}(Z(p_{cell}^i))^2} \right)^2 \sigma_p^2 + \left(\frac{p_{cell}^i}{RT_{warm}} \right)^2 \sigma_{V_{warm}}^2$$

$$+ \left(\frac{p_{cell}^i V_{warm}}{R(T_{warm})^2} \right)^2 \sigma_{T_{warm}}^2 + \left(\frac{p_{cell}^i}{Z(p_{cell}^i)RT_{cold}} \right)^2 \sigma_{V_{cold}}^2 + \left(\frac{p_{cell}^i V_{cold}}{Z(p_{cell}^i)R(T_{cold})^2} \right)^2 \sigma_{T_{cold}}^2 \tag{A2.12}$$

$$\sigma_{n_{dosed}}^2(i) = \left(\frac{V_{man}}{RT_{warm}} \right)^2 2\sigma_p^2 + \left(\frac{\Delta p_{man}(i)}{R(T_{warm})^2} V_{man} \right)^2 \sigma_{T_{warm}}^2 + \left(\frac{\Delta p_{man}(i)}{RT_{warm}} \right)^2 \sigma_{V_m}^2 \tag{A2.13}$$

$$\sigma_{n_{ads}}^2(i) = \sigma_{n_{gas}}^2(i) + \sigma_{n_{dosed}}^2(i) + \sigma_{n_{ads}}^2(i-1) \tag{A2.14}$$

Clearly, the variance is of a cumulative nature. Each point is determined in parts by what has been measured the point before, hence propagating the uncertainty of each point into the next. The equipment used actually does not report the amount dosed, so to be able to calculate the uncertainty in the amount dosed, essential in this error analysis, a back-calculation of this quantity is required before proceeding, via:

$$n_{dosed}(i) = n_{ads}(i) - n_{ads}(i-1) + n_{gas}(i) - n_{gas}(i-1) \tag{A2.15}$$

Often the loading is expressed in either mmol g^{-1} or ml$_{STP}$ g^{-1}. Hence the uncertainty in sample mass has to be taken account. For the former case:

$$q(i) = \frac{n_{ads}(i)}{w_{sample}} \tag{A2.16}$$

Here w_{sample} is the sample mass used. The variance is thus:

$$\sigma_q^2(i) = \left(\frac{1}{w_{sample}}\right)^2 \sigma_{n_{ads}}^2(i) + \left(\frac{n_{ads}(i)}{(w_{sample})^2}\right)^2 \sigma_{w_{sample}}^2 \tag{A2.17}$$

Note that the variance in sample mass is often twice that based on the accuracy of the balance used. This because the sample mass is often determined as difference of the sample holder empty and filled. The uncertainty can obviously be reported in ml$_{STP}$ g^{-1} as well, just by multiplication with the molar volume at standard temperature and pressure (1 bar and 0° C). Lastly, one could also introduce the uncertainty in the relative pressure but this turns out to be negligible. Of the measured quantities pressure, temperature and mass, the standard deviation provided by the equipment's suppliers have been used. The 95% confidence interval is $\pm 1.96 \cdot \sigma_q$.

A.3. CALCULATION OF BJH-PORE SIZE DISTRIBUTION AND UNCERTAINTY THEREIN

First step in the determination of a BJH pore size distribution is the calculation of pore size, r_p, for each relative pressure. This pore size is the sum of the statistical thickness, t, herein calculated using the Harkins-Jura equation [3, 4], and inner capillary radius, r_k, determined with the Kelvin equation:

$$r_p = r_K + t \tag{A3.1}$$

$$t = \sqrt{\left(\frac{13.99}{\log_{10}\left(\frac{p_o}{p}\right) + 0.034}\right)} \tag{A3.2}$$

$$r_K = \frac{2\sigma_t V_l}{RT \ln\left(\dfrac{p_o}{p}\right)} \tag{A3.3}$$

Here σ_t represents surface tension and V_l is the liquid molar volume of nitrogen. According to the propagation of errors [2], the uncertainty in the pore radius can be calculated as function of uncertainty in relative pressure, using:

$$\sigma_t^2 = \left(\frac{\dfrac{13.99}{2}\ln(10)}{\left(\dfrac{\ln\left(\dfrac{p_o}{p}\right)}{\ln(10)} + 0.034\right)^{0.5}\left[\ln\left(\dfrac{p_o}{p}\right) + 0.034\ln(10)\right]} \right)^2 \sigma_{\frac{p}{p_o}}^2 \tag{A3.4}$$

$$\sigma_{r_K}^2 = \left(\frac{2\sigma_t V_l}{RT\left\{\ln\left(\dfrac{p_o}{p}\right)\right\}^2\left(\dfrac{p}{p_o}\right)} \right)^2 \sigma_{\frac{p}{p_o}}^2 \tag{A3.5}$$

$$\sigma_{r_p}^2 = \sigma_{r_K}^2 + \sigma_t^2 \tag{A3.6}$$

The uncertainty in relative pressure is taken from the uncertainty analysis results of adsorption isotherms, (Fig. 2.2), wherein it was not depicted because of the small values thereof. Next step is to determine the dimensionless factors for each interval between two measured points, R_i and c_i, respectively, via:

$$R = \left(\frac{\bar{r}_p}{\bar{r}_K + \Delta t}\right)^2 \tag{A3.7}$$

$$c = \frac{\bar{r}_K}{\bar{r}_p} \tag{A3.8}$$

Uncertainty herein can be calculated according to:

$$\sigma_R^2 = \left(\frac{2\overline{r}_p}{\left(\overline{r}_K + \Delta t\right)^2}\right)^2 \sigma_{\overline{r}_p}^2 + \left(\frac{2\overline{r}_p^2}{\left(\overline{r}_K + \Delta t\right)^3}\right)^2 \left(\sigma_{\overline{r}_K}^2 + \sigma_{\Delta t}^2\right) \tag{A3.9}$$

$$\sigma_c^2 = \left(\frac{\overline{r}_K}{\overline{r}_p^2}\right)^2 \sigma_{\overline{r}_p}^2 + \left(\frac{1}{\overline{r}_p}\right)^2 \left(\sigma_{\overline{r}_K}^2\right) \tag{A3.10}$$

Uncertainty in the average Kelvin- or pore radius belonging to two adjacent data points and the difference in statistical thickness can be calculated using respectively:

$$\sigma_{\overline{r}}^2 = \frac{\left(\sigma_r^2(i) + \sigma_r^2(i+1)\right)}{2^2} \tag{A3.11}$$

and

$$\sigma_{\Delta t}^2 = \sigma_t^2(i) + \sigma_t^2(i+1) \tag{A3.12}$$

The pore volume distribution can be calculated by applying following equation starting from a measured point at saturation recursively either down the ad- or desorption branch:

$$V_p(n) = R(n)\left(\Delta q(n)\frac{\rho_{STP}^{vap}}{\rho_{nbp}^{liq}} - \Delta t(n)\sum_{j=1}^{n-1} c_j S_{p,j}\right) \tag{A3.13}$$

Assuming a cylindrical pore geometry, the specific surface area of each pore increment, $S_{p,j}$, can be calculated using:

$$S_p(n) = \frac{2V_p(n)}{\overline{r}_p} \tag{A3.14}$$

For the pore volume thus, one can derive for the variance:

$$\sigma_{V_p}^2(n) = \left(\frac{\rho_{STP}^{vap}}{\rho_{nbp}^{liq}}\Delta q(n) - \Delta t(n)\sum_{j=1}^{n-1} c_j S_{p,j}\right)^2 \sigma_R^2(n) + \left(\frac{\rho_{STP}^{vap}}{\rho_{nbp}^{liq}}R(n)\right)^2 \sigma_{\Delta q}^2(n)$$
$$+ \left(R(n)\sum_{j=1}^{n-1} c_j S_{p,j}\right)^2 \sigma_{\Delta t}^2(n) + \left(R(n)\Delta t(n)\right)^2 \sum_{j=1}^{n-1}\left(S_{p,j}^2\sigma_{c_j}^2 + c_j^2\sigma_{S_{p,j}}^2\right) \tag{A3.15}$$

Here the variance of the differential volume adsorbed is given by:

$$\sigma_{\Delta q}^2 = \sigma_q^2(i) + \sigma_q^2(i+1)$$

(A3.16)

The variance in q (in $\mathrm{ml_{STP}}$ $\mathrm{g^{-1}}$) was calculated previously, and depicted in Fig. 2.2. Lastly, the variance in surface area of each pore can be calculated via:

$$\sigma_{s_p}^2(n) = \left(\frac{2V_p(n)}{\bar{r}_p^2} \right)^2 \sigma_{\bar{r}_p}^2 + \left(\frac{2}{\bar{r}_p} \right)^2 \sigma_{V_p}^2$$

(A3.17)

Often the pore size distribution is visualized with $\Delta V_p / \Delta D_p$. The variance therein can be calculated using:

$$\sigma_{\frac{\Delta V_p}{\Delta D_p}}^2 = \left(\frac{1}{\Delta D_p} \right)^2 \sigma_{\Delta V_p}^2 + \left(\frac{\Delta V_p}{\Delta D_p^2} \right)^2 \sigma_{\Delta D_p}^2$$

(A3.18)

Here the variance in ΔV_p and ΔD_p can be calculated in the same manner as for Δq (see Eq. A3.16).

A.4. CALCULATING THE CONFIDENCE INTERVAL FOR BET PARAMETERS DETERMINED WITH THE LINEAR METHOD

Recall that the monolayer capacity is calculated from:

$$q_m = \left(\frac{1}{I+S} \right), \quad C = \left(\frac{I+s}{I} \right)$$

(A4.1)

Clearly, the uncertainty in the monolayer capacity and C parameter are a function of both the uncertainty in intercept and slope. As the intercept and slope are determined via least-squares fitting, one can write for the uncertainty in these parameters [2]:

$$\sigma_I = \sigma_y \sqrt{\sum_i \frac{x_i^2}{\Delta}}$$

(A4.2)

$$\sigma_s = \sigma_y \sqrt{\frac{N}{\Delta}}$$

(A4.3)

Here x_i are the relative pressure of each data point, y_i is the left-hand side of Eq. 2.5 for that same data point and N is the total number of data points included in fitting. As there are two fitted parameters, the degrees of freedom is the total number of data points, N, decreased by two.

The uncertainty, σ_y, in predicted values and the denominator in above equations, and Δ are given, respectively by [2]:

$$\sigma_y = \sqrt{\frac{1}{N-2}\underbrace{\sum_i (y_i - A - Bx_i)^2}_{SS_{res}}} \tag{A4.4}$$

$$\Delta = N\sum_i x_i^2 - \left(\sum_i x_i\right)^2 \tag{A4.5}$$

As slope and intercept are determined from the same fit, the uncertainties are not expected to be devoid of correlation. Consequence is that in calculation of the uncertainties in BET area and C parameter, the covariance of I and s should be included:

$$\sigma_B^2 = \left(\frac{\partial B}{\partial I}\right)^2 \sigma_I^2 + \left(\frac{\partial B}{\partial s}\right)^2 \sigma_s^2 + 2\left(\frac{\partial B}{\partial I}\right)\left(\frac{\partial B}{\partial s}\right)\sigma_{I,s} \tag{A4.6}$$

Here B is either the monolayer capacity or the BET C parameter, and $\sigma_{I,S}$ is the covariance of the regression coefficients, given by:

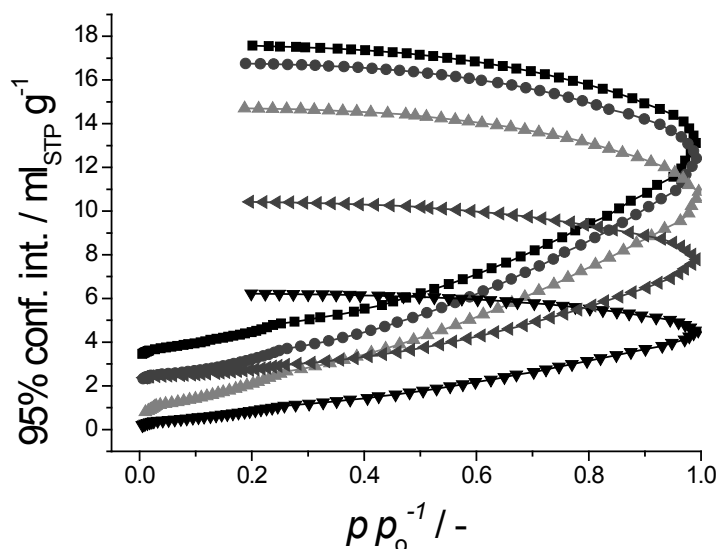$$\sigma_{I,s} = \sigma_y^2 \frac{\sum_i x_i}{\Delta} \tag{A4.7}$$

Finally, the uncertainties in the BET parameters can be calculated:

$$\sigma_{q_m}^2 = \left(\frac{1}{(I+s)^2}\right)^2 (\sigma_I^2 + \sigma_s^2) + \frac{2}{(I+s)^4}\sigma_{I,s} \tag{A4.8}$$

$$\sigma_C^2 = \left(\frac{s}{I^2}\right)^2 \sigma_I^2 + \left(\frac{1}{I}\right)^2 \sigma_s^2 - 2\frac{s}{I^3}\sigma_{I,s} \tag{A4.9}$$

The confidence interval is determined using:

$$B \pm t_{1-\frac{\alpha}{2},\text{DOF}}\,\sigma_B \tag{A4.10}$$

Figure A.1: Absolute error in measured adsorbed N_2 amount as function of relative pressure for both ad- and desorption branch of the materials under investigation, for MIL-101 (■), UiO-66 (◆), Sigma-1 (▲) , γ-alumina (▼) and Norit RB 2 (◀). For each material the third of three isotherm measurements is depicted.

Here t stands for Student's t-distribution, α is the confidence level (0.05 for a 95% confidence interval) and DOF stands for the number of degrees of freedom. Again, B stands for either q_m or C. Obviously, for the uncertainty in the BET surface area, one can write:

$$\sigma_{S_{BET}} = \sigma_{q_m} \frac{\rho_{STP}^{vap} N_A A_{CS}}{M_{N_2}} \tag{A4.11}$$

A.5. CALCULATED CONFIDENCE INTERVALS FOR NITROGEN ADSORPTION ISOTHERMS

In Fig. A.2 the confidence interval in the adsorption isotherm calculated using the propagation of uncertainties for the third isotherm measurement of each material are shown.

A.6. BREAKDOWN OF UNCERTAINTIES

It is insightful to investigate the different contributions to the 95% confidence intervals depicted in Fig. A.2, especially when one aims to improve the accuracy of adsorption measurements.
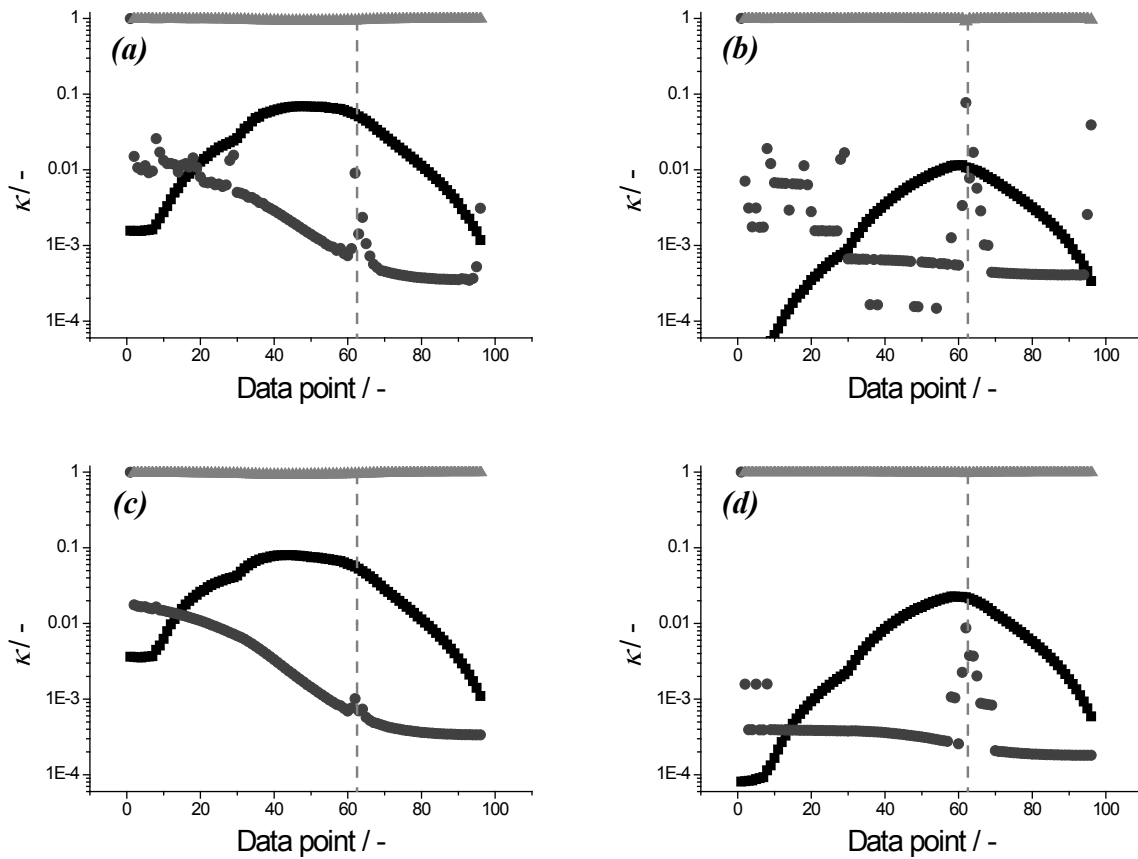
Figure A.2: Fractional contributions to the variance in the amount adsorbed, κ_{gas} (■), κ_{dosed} (●) and $\kappa_{ads}(i\text{-}1)$ (▲), calculated according to Eqs. A6.2 - A6.4 for MIL-101(Cr) (*a, b*), and UiO-66 (*c, d*) (for others see [1]) assuming either a single dose per measured point (*a, c*), or using the most stringent dosing threshold ($7 \cdot 10^{-3}$ Pa) for dosing (*b, d*), as function of the points measured. Dashed line indicates the transition from ad- to desorption.

Starting point is the variance in the isotherm, as given by Eq. A2.17, from which the fractional contributions to the variance in the adsorption measurements can be calculated. For all measurements the first term in Eq. A2.17 was found very dominant in the total variance:

$$\frac{\left(\dfrac{1}{w_{sample}}\right)^2 \sigma_{n_{ads}}^2(i)}{\sigma_q^2(i)} >> \frac{\left(\dfrac{n_{ads}(i)}{\left(w_{sample}\right)^2}\right)^2 \sigma_{w_{sample}}^2}{\sigma_q^2(i)} \tag{A6.1}$$

So, the variance in amount adsorbed, n_{ads}, has a significantly higher contribution to the overall uncertainty than the variance in weighing of the investigated samples. Consequently one can rightfully conclude that sample weighing on a balance with an accuracy of ± 0.1 mg is more

than sufficient. Unless of course a much smaller sample is used than in this work (0.1-0.2 g). In that case the right hand side term in Eq. A6.1 is no longer negligible. This situation however is to be avoided and not taken further into account here.

The variance in amount adsorbed $n_{ads}(i)$ has three contributions per measured point (see Eq. A2.14) related to the uncertainty in determination of the amount present in the gas phase, $n_{gas}(i)$, the amount dosed, $n_{dosed}(i)$, and the amount adsorbed for the previous measured point, $n_{ads}(i-1)$. To conveniently compare the different contributions to the variance in $n_{ads}(i)$, the following dimensionless fractions have been defined:

$$\kappa_{gas}(i) = \frac{\sigma^2_{n_{gas}}(i)}{\sigma^2_{n_{ads}}(i)} \tag{A6.2}$$

$$\kappa_{dosed}(i) = \frac{\sigma^2_{n_{dosed}}(i)}{\sigma^2_{n_{ads}}(i)} \tag{A6.3}$$

$$\kappa_{ads}(i-1) = \frac{\sigma^2_{n_{ads}}(i-1)}{\sigma^2_{n_{ads}}(i)} = 1 - \kappa_{dosed}(i) - \kappa_{gas}(i) \tag{A6.4}$$

These fractions are calculated for the third isotherm measurement of each of the materials, both under simplifying assumption of a single dose per measured point as well as for the most stringently incorporated dosing threshold in this work (Section A.9). Results are depicted in Fig. A.2. Clearly for all materials the largest contribution stems from that of the previous data point $\kappa_{ads}(i-1)$, which is not surprising because of the cumulative nature of the propagation of uncertainties for adsorption.

Furthermore, for low relative pressure, $p/p_o < 0.10 - 0.15$, (corresponding to the first 10-20 data points, see Fig. A.3), κ_{dosed} is larger than κ_{gas}. At higher relative pressure this relative order is reversed and the gas-phase contribution becomes more dominant. This is easily rationalized, as the gas-phase variance is strongly increasing with pressure (Eq. A2.12), whereas the variance in the amount dosed is related to the pressure difference over the manifold Δp_{man} (*cf.* Eqs. A2.13 and A9.5), which is dependent on the adsorption behavior of the material under investigation ($n_{ads}(i) - n_{ads}(i-1)$), which thus does not show a continuous increase as function of pressure. The transition point is shifted to higher pressures for more mesoporous materials (see Fig. A.2, [1]), as for these materials adsorption uptake continues up to higher relative pressures.
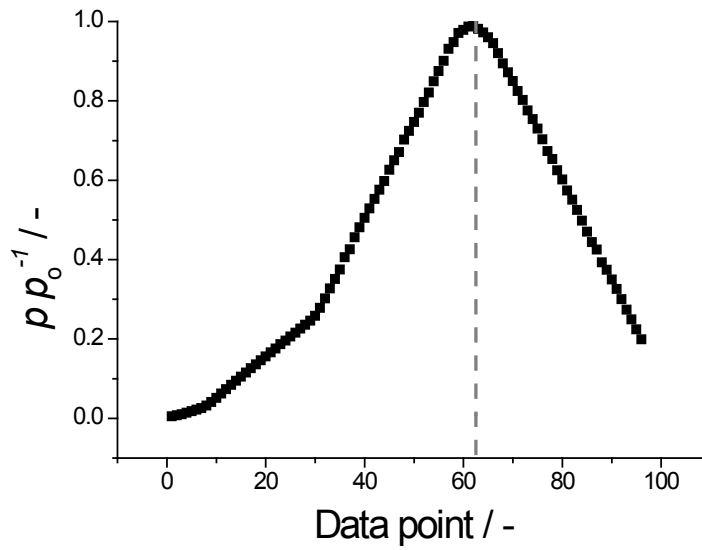
Figure A.3: Relative pressure belonging to each measured point. Dashed line indicates the transition from ad- to desorption. Taken from the third measurement of γ-alumina, but the distribution of data points over the relative pressure range is very similar for all conducted measurements.

Also, if one does not assume a single dose per measured point (Section A.9), this transition pressure is shifted to higher values (Fig. A.2, [1]). From this analysis, it can be deduced that the variance in amount present in the gas-phase, $\sigma^2_{n_{gas}}$, should be decreased if one wants to significantly decrease the uncertainty in the full adsorption measurement. If one is particularly interested in the low relative pressure regime, however, the variance in amount dosed should be targeted. The former is investigated further first.

The variance in the amount present in the gas-phase, dominantly present in the uncertainty for $p/p_o > 0.10$ - 0.15, is determined from five separate terms (Eq. A2.12), for which the fractional contributions can be calculated:

$$\kappa_{\text{gas-1}}(i) = \frac{\left(\dfrac{V_{\text{warm}}}{RT_{\text{warm}}} + \dfrac{V_{\text{cold}}}{RT_{\text{cold}}Z\left(p_{\text{cell}}^i\right)} + \dfrac{p_{\text{cell}}^i \alpha(T) V_{\text{cold}}}{RT_{\text{cold}}\left(Z\left(p_{\text{cell}}^i\right)\right)^2} \right)^2 \sigma_p^2}{\sigma_{n_{\text{gas}}}^2(i)} \qquad (A6.5)$$

$$\kappa_{\text{gas-2}}(i) = \frac{\left(\dfrac{p_{\text{cell}}^i}{RT_{\text{warm}}} \right)^2 \sigma_{V_{\text{warm}}}^2}{\sigma_{n_{\text{gas}}}^2(i)} \qquad (A6.6)$$

$$\kappa_{\text{gas-3}}(i) = \frac{\left(\dfrac{p_{\text{cell}}^{i} V_{\text{warm}}}{R\left(T_{\text{warm}}\right)^{2}}\right)^{2} \sigma_{\text{T}_{\text{warm}}}^{2}}{\sigma_{\text{n}_{\text{gas}}}^{2}(i)} \tag{A6.7}$$

$$\kappa_{\text{gas-4}}(i) = \frac{\left(\dfrac{p_{\text{cell}}^{i}}{Z\left(p_{\text{cell}}^{i}\right) R T_{\text{cold}}}\right)^{2} \sigma_{\text{V}_{\text{cold}}}^{2}}{\sigma_{\text{n}_{\text{gas}}}^{2}(i)} \tag{A6.8}$$

$$\kappa_{\text{gas-5}}(i) = \frac{\left(\dfrac{p_{\text{cell}}^{i} V_{\text{cold}}}{Z\left(p_{\text{cell}}^{i}\right) R\left(T_{\text{cold}}\right)^{2}}\right)^{2} \sigma_{\text{T}_{\text{cold}}}^{2}}{\sigma_{\text{n}_{\text{gas}}}^{2}(i)} \tag{A6.9}$$

These fractions, calculated for all the performed measurements, are depicted in Fig. A.4 for MIL-101(Cr) and UiO-66. Both from Eqs. A6.5-A5.9 and Fig. A.4 it can be seen that the gas-phase variance contributions are not sample specific and thus not depicted for the other materials.

Clearly, at low relative pressure (p/p_{o} < 0.05-0.06) the first term (Eq. A6.5) is the dominant contribution to the variance in amount present in the gas-phase, above this the fourth term is largest (Eq. A6.8). Recall however that for p/p_{o} < 0.10 - 0.15 the variance in the amount dosed is larger than variance in the amount gas phase, and that thus decreasing the contribution of Eq. A6.5 is of little use. So, for measurements that include p/p_{o} > 0.10 - 0.15, the variance in the cold part of the cell volume, $\sigma_{\text{Vcold}}^{2}$, should be decreased to make measurements more accurate.

For measurements where the region p/p_{o} < 0.10 - 0.15 is essential, one should aim at decreasing the variance in the amount dosed (Eq. A2.13 or A9.5 if single dose is not assumed). For all measurements under investigation, the dominant term for all measurements under investigation is the first (for both Eq. A2.13 and A9.5), indicating that accurate pressure measurement is key for low relative pressures.
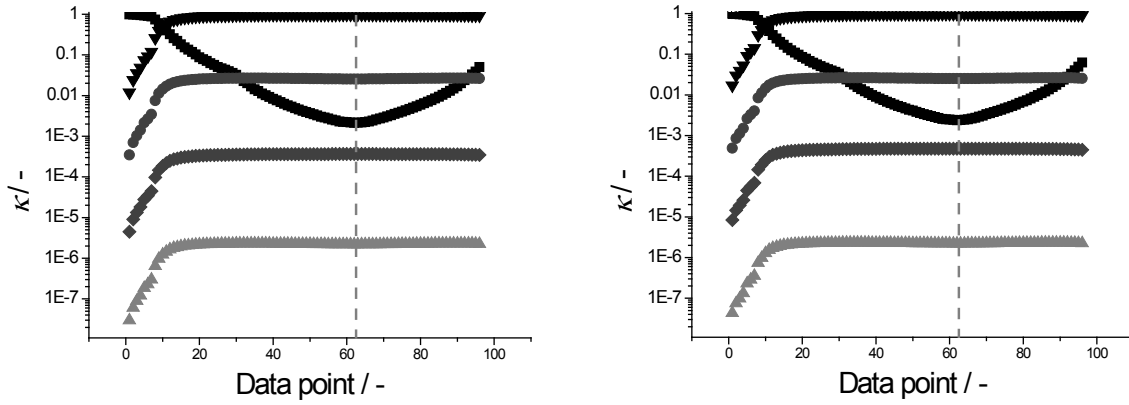
Figure A.4: Fractional contributions, κ_{gas-1} (■), κ_{gas-2} (●), κ_{gas-3} (▲), κ_{gas-4} (▼) and κ_{gas-5} (◆), to the variance in gas-phase, as calculated from Eqs. A6.5 - A6.9, for MIL-101(Cr) (*left*) and UiO-66 (*right*).

Returning to the case where the region $p/p_o > 0.10 - 0.15$ is of interest, the variance in the cold part of the cell volume should be reduced. As this is a calculated property, it is interesting to find out which measurement should be conducted more accurately. To do so the uncertainty in cold volume is broken down into two contributions (see Eq. A2.17), of which the relative importance is calculated, based on available measurement data:

$$\frac{\sigma^2_{V_{warm}}}{\sigma^2_{V_{cold}}} = 0.658 \pm 0.006 \tag{A6.10}$$

$$\frac{\sigma^2_{V_{cell}}}{\sigma^2_{V_{cold}}} = 0.342 \pm 0.006 \tag{A6.11}$$

This indicates that both volumes contribute to the variance of the cold volume, of which the warm volume is more important. If in turn the variance in the warm volume (Eq. A2.5) is investigated, it can be found, for the different measurements, that the fifth term is dominant:

$$\frac{\left(\dfrac{\dfrac{p^0_{cell}}{p^1_{cell}} - \dfrac{T_{warm}}{T_{cold}}}{1 - \dfrac{T_{warm}}{T_{cold}}} \right)^2 \sigma^2_{V_{cell}}}{\sigma^2_{V_{warm}}} = 0.973 \pm 0.004 \tag{A6.12}$$

Clearly, decreasing variance in the cell volume is crucial to increase the accuracy of the adsorption measurement, when $p/p_o > 0.1$. From Eq. A2.3 and data from the different

measurements the relative contributions to this variance from the pressure sensor and of the manifold volume can be found:

$$\frac{\left(\left(\dfrac{1}{p_{cell}^1 - p_{cell}^0}V_{man}\right)^2 + \left(\dfrac{p_{man}^0 - p_{man}^1}{\left(p_{cell}^1 - p_{cell}^0\right)^2}V_{man}\right)^2\right)\left(2\sigma_p^2\right)}{\sigma_{V_{cell}}^2} = 0.69 \pm 0.01 \quad \text{(A6.13)}$$

$$\frac{\left(\dfrac{p_{man}^0 - p_{man}^1}{p_{cell}^1 - p_{cell}^0}\right)^2 \sigma_{V_{man}}^2}{\sigma_{V_{cell}}^2} = 0.31 \pm 0.01 \quad \text{(A6.14)}$$

This indicates that a more accurate calibration of the manifold volume would help decreasing the uncertainty in adsorption experiments, as σ^2_{Vman} would be decreased. But, as was also shown for low pressure measurements, it is best to decrease the accuracy of the used pressure sensor. Lastly, as the pressure difference in the cell (p^0_{cell} - p^1_{cell}) is a function of the manifold pressure difference (p^0_{man} - p^1_{man}) and the ratio V_{man}/V_{cell} (see Eq. A2.2), one could optimize this ratio also to decrease the uncertainty. Result of this analysis is that this ratio is optimally between 2 and 3 (Section A.7).
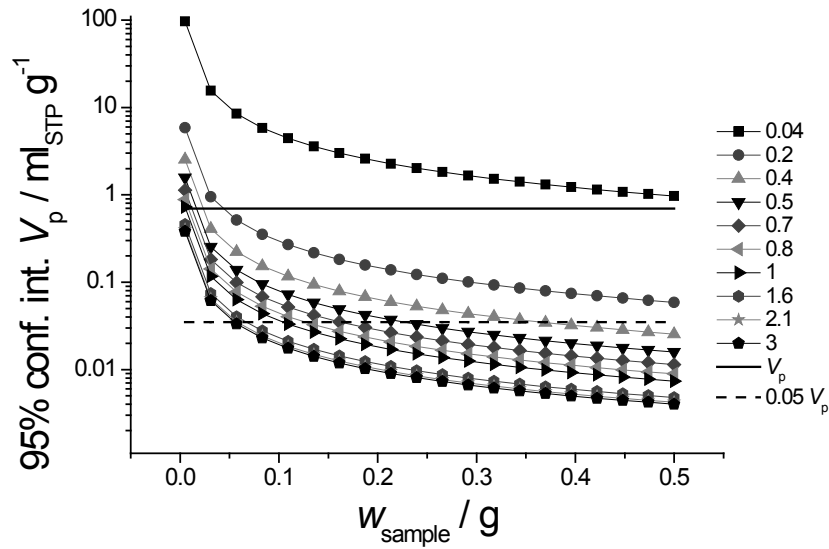
Figure A.5: 95% confidence interval for the calculated pore volume at $p/p_o = 0.9$ as function of sample mass used for a Langmuir isotherm ($q_m = 500$ ml$_{STP}$ g^{-1}, $K = 10$ bar^{-1}) for different values of V_{man}/V_{cell}. Pore volume and 5% thereof (both in ml$_{STP}$ g^{-1}) are depicted as solid and dashed line, respectively.

A.7. INFLUENCE OF EXPERIMENTAL VARIABLES ON UNCERTAINTY IN ADSORBED AMOUNT AND PORE VOLUME – THEORETICAL STUDY

The effect of the sample amount used during a measurement and the ratio of manifold and cell volume, V_{man}/V_{cell} on error propagation is investigated by calculating the uncertainty in the pore volume for a Langmuir isotherm, rewritten to incorporate relative pressure:

$$q = q_m \left(\frac{K \dfrac{p}{p_o}}{\dfrac{1}{p_o} + K \dfrac{p}{p_o}} \right) \tag{A7.6}$$

Results are depicted in Fig. A.5. The effect of sample mass is clear. If less than 0.05 gram is used, the uncertainty becomes prohibitively high. The more mass is used the better, but the decrease in uncertainty becomes less with increasing mass. This observation is explained by Eq. A2.17. The uncertainty is roughly a function of w_{sample}^{-1}, because the amount adsorbed n_{ads} is a linear function of w_{sample} as well. For low values of V_{man}/V_{cell}, thus large cell volume, the uncertainty is very high as well. This is attributed to two reasons. Firstly, a large cell volume

increases uncertainty in the amounts adsorbed and present in the gas phase (Eqs. A2.12 and A2.14). Secondly, uncertainty in the cell volume is increased severely. If the cell volume is much larger than the manifold volume, there is hardly any pressure difference in the cell when the cell volume is calculated by expanding helium (Eq. A2.2). This small pressure difference increases the uncertainty in the cell volume substantially (Eq. A2.3). A value for V_{man}/V_{cell} larger than 3 would increasingly lead to a larger uncertainty. So, to decrease the uncertainty, the sample cell would ideally be about half of the manifold volume ($2 \leq V_{man}/V_{cell} \leq 3$). Note that for these calculations, the single dose assumption was used. Uncertainties might become higher when using a dosing threshold, depending on material properties.

Above results are for one single Langmuir isotherm. The influence of both the equilibrium constant, K, and monolayer capacity, q_m, on (relative) uncertainty of the pore volume (*e.g.* pore volume filling of zeolites can described with a Langmuir-type isotherm) (see Supplementary Information (S.I.) in [1]). Clearly, for low values of K and q_m, the relative uncertainty is very high. Up to 50% for 0.05 g of material. This is because a material with low values of both parameters hardly adsorbs any nitrogen [1]. Increasing the amount of material to 0.5 g significantly decreases the relative uncertainty [1], not changing the shape of the surface. Again, this is under the assumption of single dosage. For 0.5 g, encompassing a dosing threshold, Δp_{max} of 0.07 bar, again a high relative uncertainty is seen at low K and q_m [1]. A difference, with the previous case is however, the dependency of the uncertainty on K. The uncertainty is higher than under the single dose assumption, at high values of the equilibrium constant. This is due to the fact that a high equilibrium constant mimics the properties of a microporous material and thus requires a significant number of doses for the first measured adsorption point. For the case of 0.05 g sample mass, the difference in uncertainty between single dosing and using a dosing threshold is more or less negligible [1]. Lastly, in Fig. A.6, relative confidence interval in pore volume calculated at $p/p_o = 0.9$ is given as function of $q_{sat} w_{sample}$, for easy estimation of uncertainties of performed measurements.
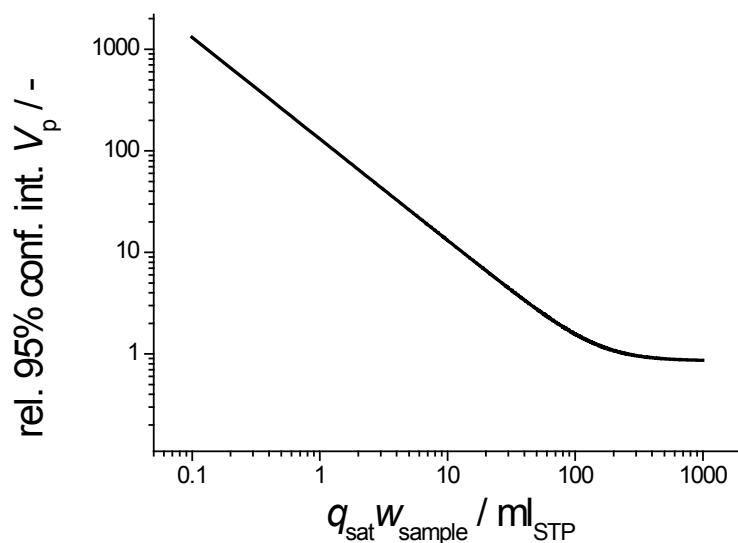
**Figure A.6:** Relative 95% confidence interval of pore volume V_p depicted as function of total amount adsorbed ($q_{sat}\, w_{sample}$). Calculated using the single dose assumption.

A.8. INFLUENCE OF EXPERIMENTAL VARIABLES ON MEASUREMENTS – EXPERIMENTAL STUDY USING γ-ALUMINA (2)

In this work the sample mass and cell volume were deliberately kept constant for the three repeated consecutive measurements (Fig. 2.2) to investigate the reproducibility of this measurement procedure. It is as important, however, to investigate the effect of sample mass and cell volume on adsorption measurements of one material. A notably different sample of γ-alumina (000-3p, Akzo Nobel), denoted as γ-alumina(2), was used for this purpose. This because γ-alumina(2) has a larger desorption hysteresis compared to the γ-alumina used in the rest of this work (CK-300) and the variation of cell volume has a notable effect especially on desorption, as will be shown. To reduce effects of possible sample inhomogeneity, the first conducted measurement of each of the five different cells contained the highest sample mass (~ 0.14 g). For the second and third measurements, from this mass ~0.05 g was removed from the previously measured sample.
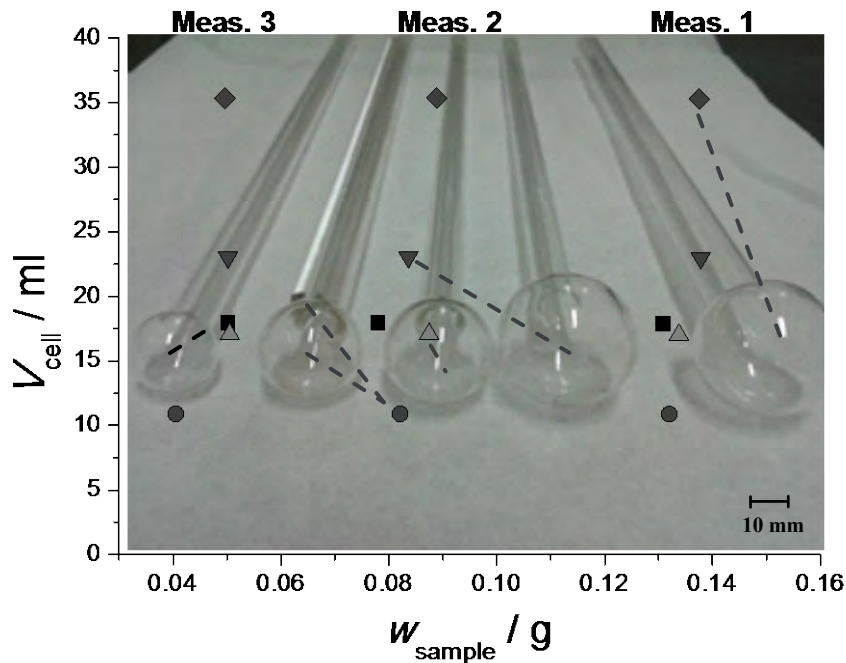
Figure A.7: Sample mass and cell volume calculated during measurements for the three separate measurements (about 0.14, 0.09 and 0.05 g for the 1st, 2nd and 3rd measurement, respectively) and the five different cells (1 (●), 2 (▲), 3 (■), 4 (▼) and 5 (◆)) used in this study. In the background an image of the different sample cells and the glass filler rod (used in Cell 1(●)) are shown. Dashed lines connect the cell volume curve with the image. Manifold volume is 24.3 ml.

Of the sample holders with different volumes (four types were available), the smallest one was used also with a supplemented a glass rod to reduce the sample holder's volume further. This yielded the five cell volumes and different sample masses for the three subsequent measurements in each cell as depicted in Fig. A.7.

Measured adsorption isotherms and calculated confidence intervals are depicted in Fig. 2.4, left for cells 1,3 and 5 and a zoom-in on the desorption hysteresis are depicted in Fig. 2.4, right (results for cells 2 and 4 can be found in [1]). In Fig. A.8 the measurement time as function of measured points is given for the smallest and largest sample cell. From this can be concluded that discrepancy between the smallest and largest cell volume in measurement time becomes significant in the adsorption branch only at high relative pressure, and becomes increasingly large at the first desorption points.
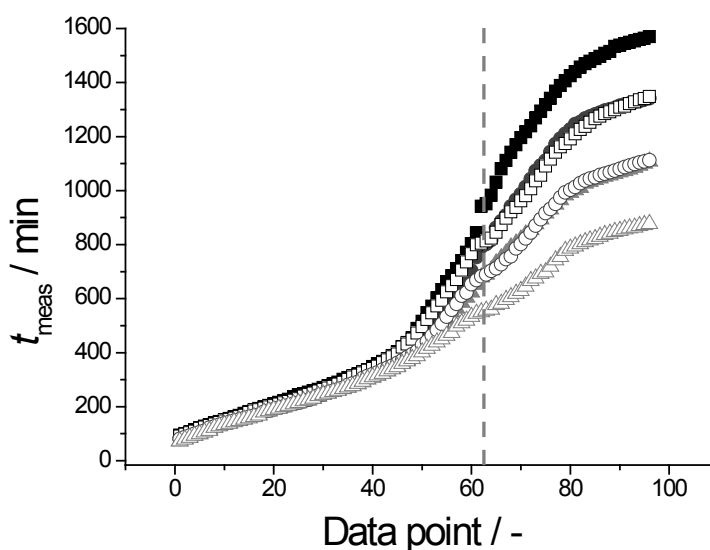
Figure A.8: Cumulative measurement time on γ-alumina(2) as function of data points for the smallest cell volume used (Cell 1, *closed symbols*) and largest cell (Cell 5, *open symbols*) for measurement 1 (■), 2 (●) and 3 (▲). Note that in the first measured point the time required for initialization and characterization of the cell, warm and cold volume is included. Dashed line indicates transition from adsorption to desorption.

This means that especially for measured points where significant amounts are ad- or desorbed (see Fig. 2.4) a large discrepancy is created by the reduced sensitivity due to a larger cell volume and/or a decreased sample mass, as at these points measurement time is significantly reduced for more pressure-insensitive measurements. This is also directly visible from the adsorption isotherms, where resemblance between the different measurements in the low relative pressure adsorption branch is generally better than it is for the higher relative pressure adsorption and the desorption branch (Fig. 2.4). Note that this effect is caused by the absolute magnitude of the sample cell volume, as it is the pressure determined in the sample cell which is used for assessing equilibrium. This is notably different from the minimum found in measurement uncertainty, as shown in (Section A.7), where an optimal ratio of manifold volume and cell volume was found ($2 \leq V_{man}/V_{cell} \leq 3$). Since the manifold volume amounts to 24.3 ml this optimal ratio is obtained with sample cell 1. As expected the derived pore volumes have a larger confidence interval for the sample cell with a larger volume and lower sample mass (see Fig. A.9). Furthermore, the variation in experimentally found pore volume increases with increasing cell volume and decreasing sample mass (see Fig. A.9 and Table A.2).
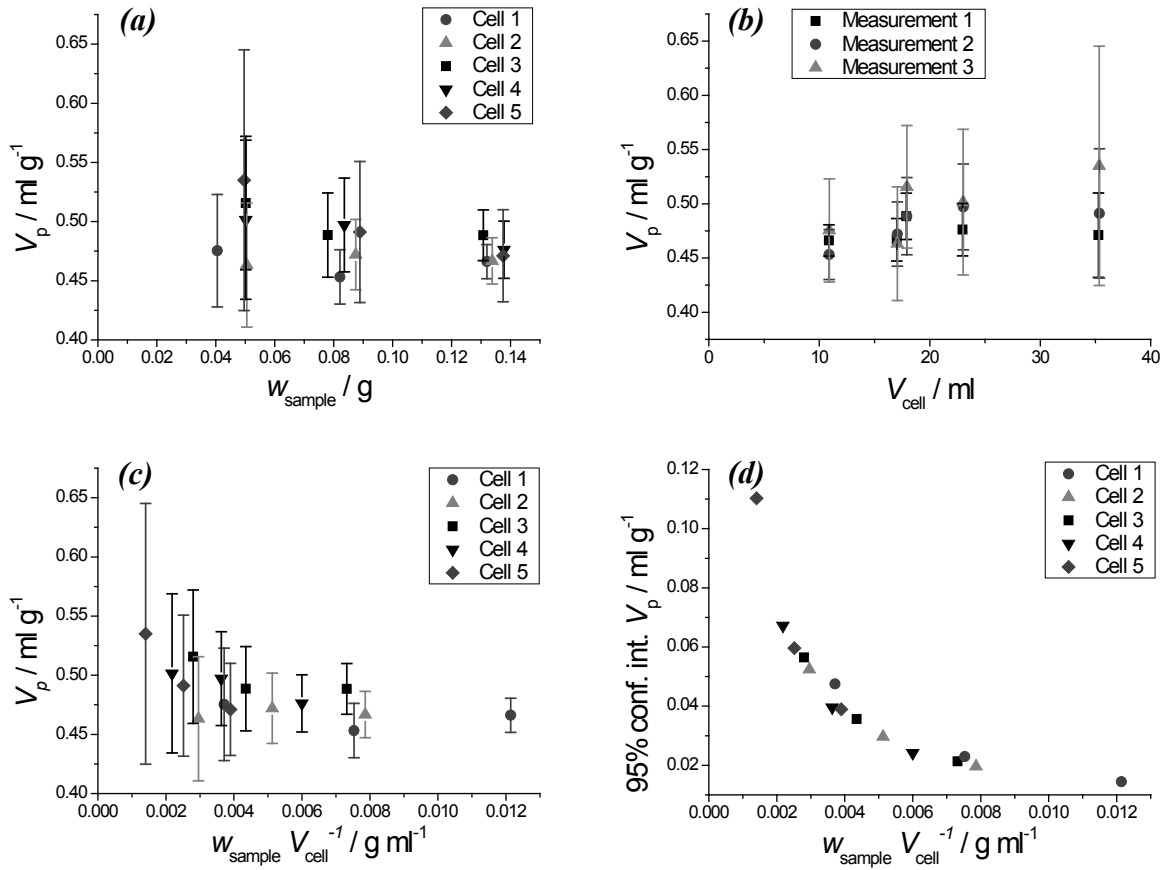
Figure A.9: Pore volume for γ-alumina(2) calculated at $p/p_o = 0.9$ as function of w_{sample} (*a*), V_{cell} (*b*) and w_{sample}/V_{cell} (*c*) and 95% confidence interval in pore volume as function of w_{sample}/V_{cell} (*d*).

Table A.2: Average pore volume for γ-alumina(2) calculated at $p/p_o = 0.9$ and standard deviation per measurement (*left,* averaged results over all cells, per measurement (sample mass)) and per sample cell (*right,* averaged over all three sample masses per used cell).

	$<V_p>$ / ml g^{-1}	σ_{meas} / ml g^{-1}		$<V_p>$ / ml g^{-1}	σ_{meas} / ml g^{-1}
Meas. 1	0.47	0.005	Cell 1	0.46	0.006
Meas. 2	0.48	0.009	Cell 2	0.47	0.002
Meas. 3	0.50	0.015	Cell 3	0.50	0.008
			Cell 4	0.49	0.007
			Cell 5	0.50	0.017

Table A.3: BET surface areas and 95% confidence intervals for γ-alumina(2) obtained for the different measurements using both the smallest (Cell 1) and largest sample cell (Cell 5) with different sample amounts using the proposed recommendations (see Table 2.3).

Cell 1	w / mg	S_{BET} / m^2 g^{-1}		$N_{D.O.F.}$ / -	$p\,p_o^{-1}{}_{min}$ / -	$p\,p_o^{-1}{}_{max}$ / -
Meas. 1	0.132	244.5	±0.37	13	0.05	0.20
Meas. 2	0.082	244.5	±0.47	14	0.06	0.21
Meas. 3	0.041	241.9	±0.46	15	0.06	0.22
Cell 5	w / mg	S_{BET} / m^2 g^{-1}		$N_{D.O.F.}$ / -	$p\,p_o^{-1}{}_{min}$ / -	$p\,p_o^{-1}{}_{max}$ / -
Meas. 1	0.138	254.4	±0.41	17	0.06	0.25
Meas. 2	0.089	251	±1.8	27	0.02	0.28
Meas. 3	0.050	273	±4.5	28	0.02	0.29

This is in line with the increasing confidence interval calculated using error propagation. Seemingly also the absolute value of the pore volume increases slightly with decreasing sample mass and increasing cell volume but this might well be due to the higher uncertainty and variation in the pore volume at these conditions.

The adsorption branches below p/p_o < 0.3 are similar for all measurements except for those measured using the largest sample cell (cell 5) (Fig. 2.4, [1]). The effect of cell volume on the BET surface is assessed by comparing obtained specific surface areas for the measurements conducted in the smallest sample cell (cell 1) with those of the largest (cell 5), using the fitting strategy as proposed in Table 2.3. Results given in Table A.3 show a clear difference between the different cell volumes. For the largest cell, the specific surface area increases with decreasing sample mass. Furthermore, the relative pressure window is widened when sample mass is decreased, indicating that the proposed constraints are becoming less effective. This is in turn caused by an alteration in the shape of the isotherm, deviating more from BET behavior. This is also reflected in the increase in confidence interval. For the smallest cell volume, these effects are absent and similar BET surface areas are obtained with comparable confidence intervals. This cell has the optimal V_{man}/V_{cell} ratio of ~2.

In conclusion, the results obtained with the smallest cell volume show the lowest uncertainty (Fig. 2.4). The pore volume determined from the measurements with different sample masses showed the least variation for this cell (Fig. A.9) and the BET surface area can be determined reproducibly (Table A.3). Also, using this cell volume, no artificially enhanced desorption hysteresis was found for the material under investigation (Fig. 2.4). As the manifold of the

adsorption equipment is 24.3 ml, it can be concluded that for this ratio $V_{man}/V_{cell} \sim 2$ optimal results are obtained. This corroborates the theoretical error analysis findings that the uncertainty is minimized for this volume ratio (Section A.7).

A.9. INFLUENCE OF DOSING ON UNCERTAINTY OF NITROGEN ADSORPTION ISOTHERMS

In the error analysis of nitrogen physisorption, it was assumed that a single dosage of nitrogen was used for each measured data point. Therefore one could write for the amount dosed for each of these data points:

$$n_{dosed}(i) = \left(p_{man}^0(i) - p_{man}^1(i) \right) \frac{V_{man}}{RT_{warm}} = \Delta p_{man}(i) \frac{V_{man}}{RT_{warm}} \tag{A9.1}$$

and for the variance in this quantity:

$$\sigma_{dosed}^2(i) = \left(\frac{V_{man}}{RT_{warm}} \right)^2 \left(2\sigma_p^2 \right) + \left(\Delta p_{man}(i) \frac{V_{man}}{RT_{warm}^2} \right)^2 \sigma_{T_{warm}}^2 + \left(\Delta p_{man}(i) \frac{1}{RT_{warm}} \right)^2 \sigma_{V_{man}}^2 \tag{A9.2}$$

By no longer adhering the single dosage assumption, the equation for the amount of moles dosed becomes slightly more complicated:

$$n_{dosed}(i) = \frac{V_{man}}{RT_{warm}} \sum_{k=1}^{N_d(i)} \Delta p_{man}^k(i) \tag{A9.3}$$

Here N_d is the number of doses used to measure point i, and Δp_{man}^k is the manifold pressure difference before and after dosing for each dose k used to determine point i. The actual number of doses is, for most commercial equipment, unfortunately not explicitly stated. This complicates the inclusion of multiple doses per point in this error propagation analysis. One could, for example, assume that a fixed number of doses would be required for each data point. This however would not represent well the actual evolution of a physisorption measurement in practice, as the number of doses is obviously strongly dependent on the amount that will be adsorbed by the sample during the measurement of that particular point.

Therefore the following is proposed:

$$N_d = ceil\left(\frac{\sum_{k=1}^{N_d(i)} \Delta p_{man}^k(i)}{\Delta p_{max}}\right) \tag{A9.4}$$

Here Δp_{max} is an arbitrarily chosen maximum manifold pressure difference during dosage and N_d is found by rounding up (ceiling) the quantity calculated on the right-hand side of the equation. Each dose k, except the last, now has that Δp^k_{man} is equal to Δp_{max}. The equation might, at first sight, look recursive as N_d is on both the left- and right-hand side. However the summation, $\sum_{k=1}^{N_d(i)} \Delta p_{man}^k(i)$, can be back-calculated if one knows the amount of moles adsorbed and present in the gas-phase respectively of measurement i, without prior knowledge of the integer value of N_d. The uncertainty in the amount adsorbed becomes only slightly more complicated when including these multiple doses:

$$\sigma_{dosed}^2(i) = \left(N_d \frac{V_{man}}{RT_{warm}}\right)^2 \left(2\sigma_p^2\right) + \left(\sum_{k=1}^{N_d(i)} \Delta p_{man}^k(i) \frac{V_{man}}{RT_{warm}^2}\right)^2 \sigma_{T_{warm}}^2 + \left(\sum_{k=1}^{N_d(i)} \Delta p_{man}^k(i) \frac{1}{RT_{warm}}\right)^2 \sigma_{V_{man}}^2 \tag{A9.5}$$

Compared with the single dose expression, the uncertainty practically only differs in the number of doses N_d, in the first term of the right-hand side, as the quantity $\sum_{k=1}^{N_d(i)} \Delta p_{man}^k(i)$ is exactly equal to Δp_{max} for the single-dose case. Furthermore, for the determination of uncertainty, one only needs the total amount dosed and the number of doses needed for this amount. The distribution of Δp^k_{man} for the k different doses is not required. In commercial adsorption equipment, proprietary algorithms are often used to adjust during measurements the quantity (Δp^k_{man}) added per dose to decrease the number of doses needed for a point. This to decrease the uncertainty and measurement time both. The finding that the pressure difference distribution is not a necessary requirement for uncertainty analysis is thus highly beneficial. Furthermore, this makes that the devised approximation of number of doses can be very similar to that of an actual measurement with respect to uncertainty propagation, provided a representative value of Δp_{max} is chosen. To this end, the uncertainty of the third measured isotherm of each material is calculated, varying the values of Δp_{max} over a broad range. Results are depicted in Fig. A.10a, c and e.
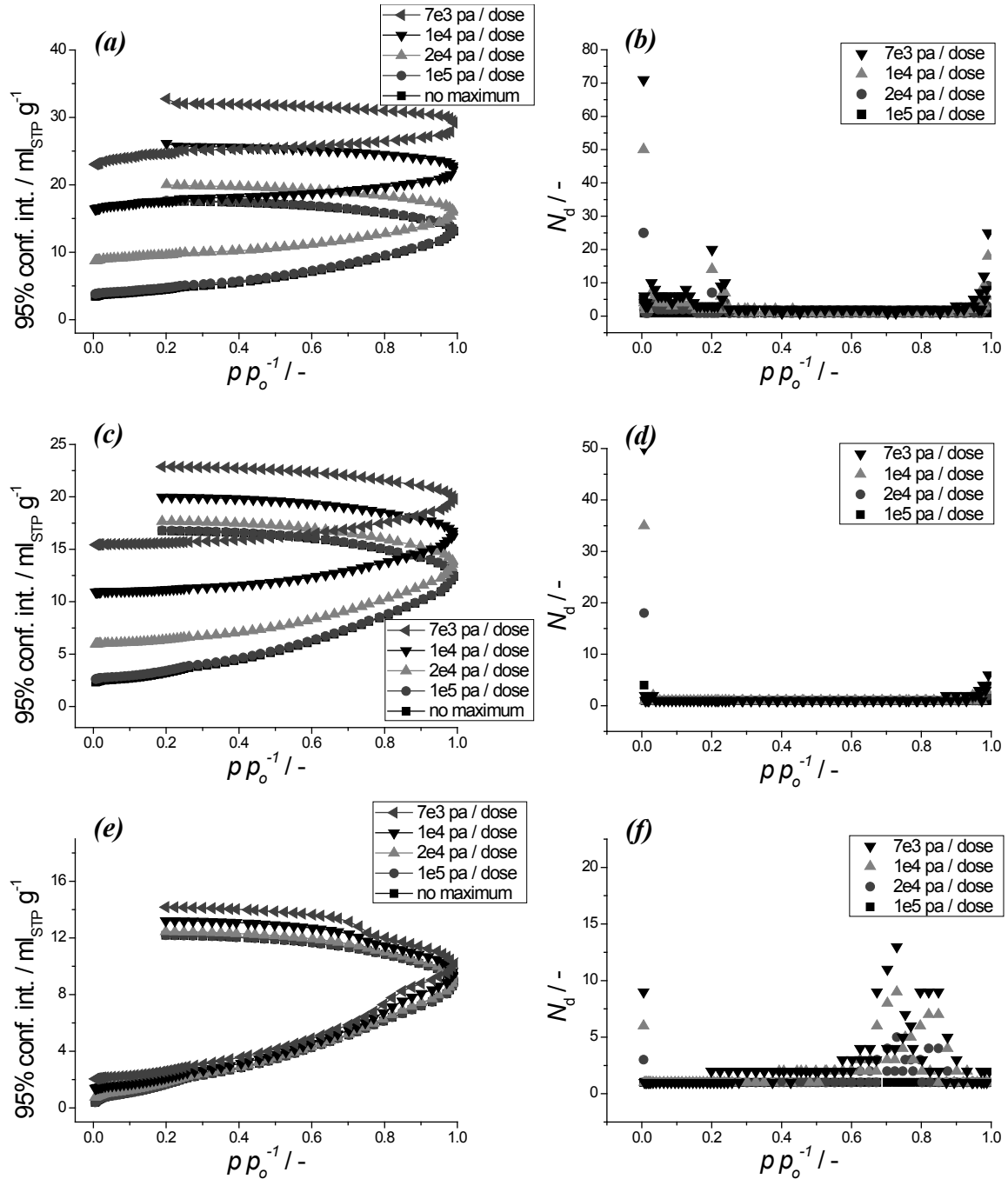
Figure A.10: (*left*) Confidence interval of the adsorbed N_2 amount as function of restrictive maximum pressure difference of the manifold during dosing of nitrogen, Δp_{max} (*a, c, e*). Number of doses calculated with posed approximation as function of relative pressure for restrictive maximum pressure difference of the manifold during dosing of nitrogen, Δp_{max} (*b, d, f*). For MIL-101(Cr) (*a, b*), UiO-66 (*c, d*) and γ-alumina (*e, f*). For each material the third of three isotherm measurements is used. Results for Norit RB and Sigma-1 can be found in [1].

Clear differences can be observed between the different materials. Clearly, due to the high adsorption capacity of the material, the confidence interval of MIL-101(Cr) is affected the most by a more stringent dosing criterion. The increased uncertainty is primarily caused by the first measured point. As the adsorption is already around 300 ml_{STP} g^{-1}, a large number of doses is required in reality. This is captured by the proposed dosing approximation earlier, as can be seen from Fig. A.10b, d and f. Up to roughly 60 doses are required to measure this point for the most stringent dosing criterion. The other points of the isotherms encompass relatively small additional amounts adsorbed, keeping the doses required mostly around one, independent of the stringency of the dosing criterion. This makes that the evolution of the uncertainty interval is very similar to that obtained from the single dose assumption from the first points onward. Current estimate is that a dosing criterion between 0.1 and 0.07 bar would yield a dosing distribution in close correspondence with an actual measurement, depending slightly on the intelligence of the dosing strategy applied during the actual measurements. If one would use the proposed approximation with even more stringent criteria, one would find that the uncertainty would scale linearly with Δp_{max}^{-1}, indicating that all except the first term in Eq. A9.2 would have become negligible, and only the number of doses would be of relevance, something deemed unlikely. For the other materials, the variation in uncertainty as function of Δp_{max} is smaller, due to a smaller amount adsorbed. A difference can be seen between microporous materials, *e.g.* UiO-66, where the influence of varying Δp_{max} is mainly visible in the first measured point, and mesoporous materials, *e.g.*, γ-alumina, where the difference is more apparent at higher relative pressures. Using 0.07 bar as criterion, the uncertainty in the pore volume of MIL-101(Cr) has become 0.042 cm^3 g^{-1}, more than double that of the uncertainty for the single dose assumption (0.017). The recalculated pore volume for 0.07 bar as criterion for all materials is given in Table A.4. So, replacing the single dose assumption with the restrictive maximum dosage, generally results in a larger increase in uncertainty for materials that have a higher adsorption capacity and thus total pore volume. However, upon comparing the uncertainty of UiO-66, Norit RB2 and γ-alumina, when Δp_{max} is 0.07 bar, the uncertainty in pore volume of the latter is roughly half that of the former two while their pore volumes are very similar. This difference is attributed to the difference in the shape of the nitrogen isotherm or pore size distribution of these materials.

Table A.4: Calculated pore volume at $p/p_o = 0.9$ and its 95% confidence interval for both the single dose assumption and a restrictive maximum dosage of 0.07 bar in the dosing manifold, for the third isotherm of each material.

| Material	V_p / cm^3 g^{-1}	95% conf. int. / cm^3 g^{-1}	
		single dose	Δp_{max} 0.07 bar
MIL-101(Cr)	1.51	± 0.017	± 0.042
UiO-66	0.43	± 0.016	± 0.028
Sigma-1	0.14	± 0.014	± 0.016
γ-alumina	0.40	± 0.011	± 0.014
Norit RB2	0.46	± 0.010	± 0.026

For Norit RB2, and even more for UiO-66, a large part of the adsorbed amount is obtained when measuring the first adsorption point. Here a large number of doses would be required, generating a relatively large uncertainty therein. For γ-alumina, the isotherm shape is different. The amount adsorbed is more gradually distributed over the pressure range than is the case for the other two materials. This means that on average for γ-alumina less doses are needed per point, even when restricting strongly the maximum allowable dose (Fig. A.10b, d and f). This explains the lower uncertainty for a similar pore volume.

A.10. DETAILED BET AREA AND CONFIDENCE INTERVAL USING THE LINEAR METHOD

In Figs. A.11 and A.12 the obtained BET values and confidence intervals are given for MIL-101(Cr), γ-Alumina and UiO-66 (for others, see the S.I. of [1]), as function of the degrees of freedom for the linear method, according to Eq. A4.10, and also for the (weighted) direct method, of which the results will be discussed in more detail in Section A.16. These are plotted versus an average relative pressure, which is simply taken by averaging the pressure of the data points used in the fit.
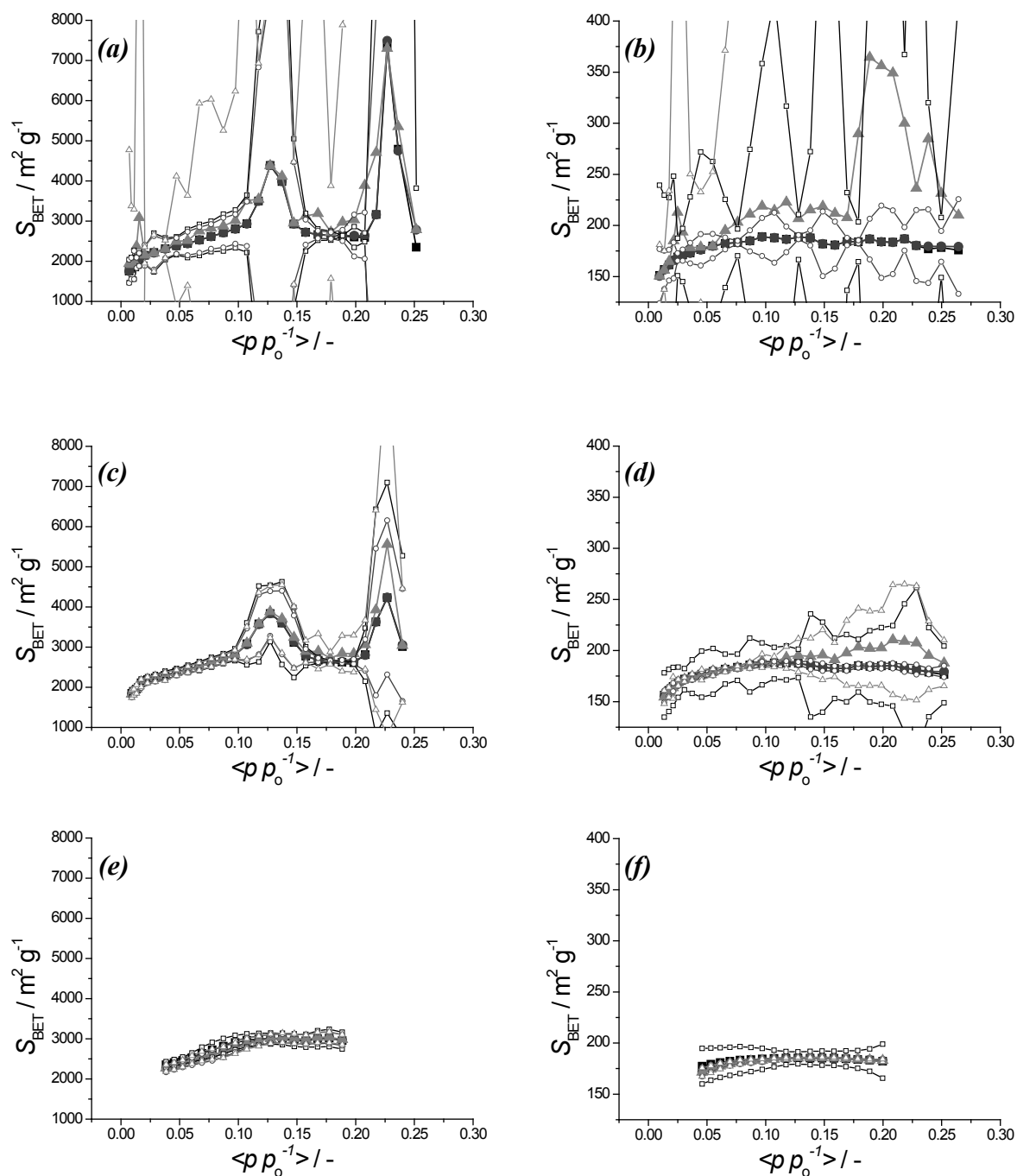
Figure A.11: Obtained BET surface area (*closed symbols*) and 95% confidence interval thereof (*open symbols*) for linear (■), direct (●) and weighted direct (▲) fitting, as function of the relative pressure, averaged over the pressure range used for fitting, for MIL-101(Cr) (*a, c, e*) and γ-Alumina (*b, d, f*) with 1 degree of freedom (*a, b*), 3 degrees of freedom (*c, d*) and 13 degrees of freedom (*e, f*). For clarity, the confidence interval at low degrees of freedom is truncated. For all calculations, the third adsorption measurement was used.
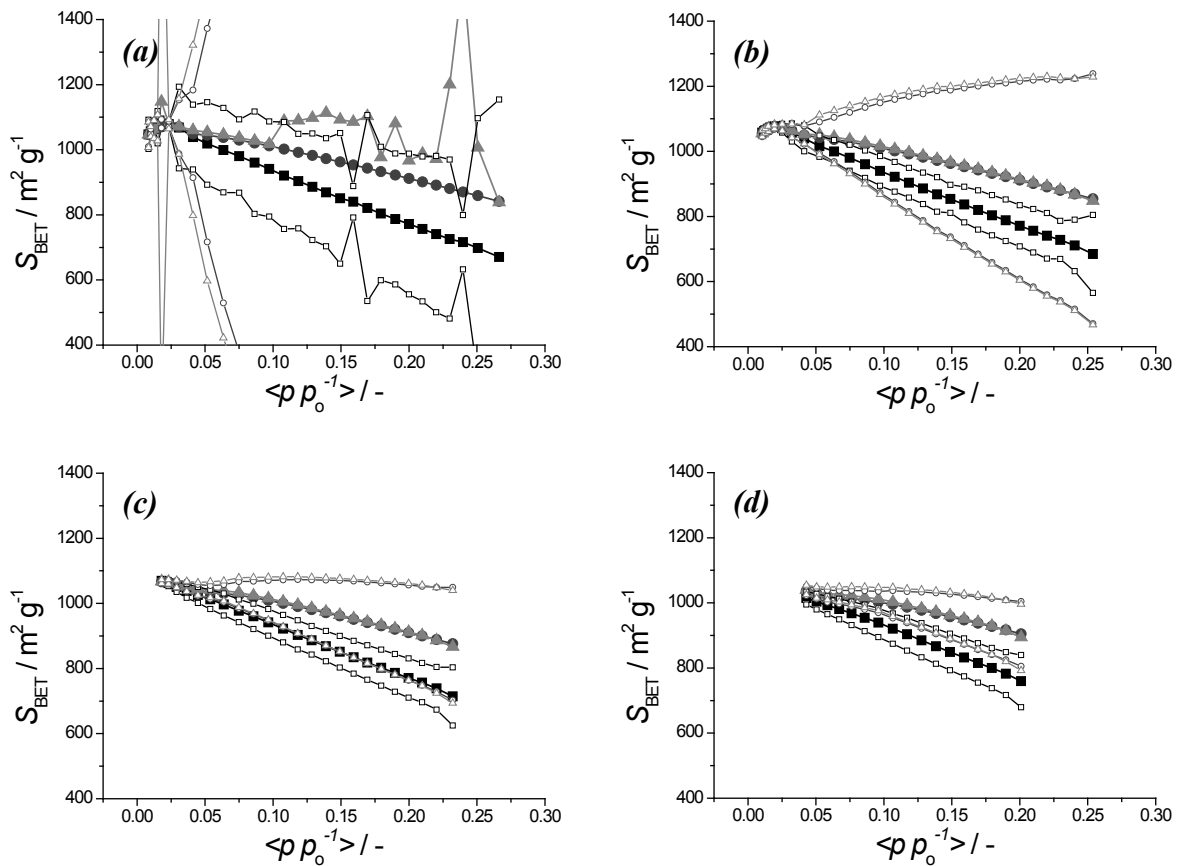
Figure A.12: Obtained BET surface area (*closed symbols*) and 95% confidence interval thereof (*open symbols*) for linear (■), direct (●) and weighted direct (▲) fitting, using different degrees of freedom, as function of the relative pressure, averaged over the pressure range used for fitting, for UiO-66, with 1 degree of freedom (*a*), 3 degrees of freedom (*b*), 7 degrees of freedom (*c*), and 13 degrees of freedom (*d*). For clarity, the confidence interval at low degrees of freedom is truncated. For all calculations, the third adsorption measurement was used.

Fig. A.13 shows the linearized BET plot for each of the materials. For clarity, a normalization by dividing each linear plot by its value at $p/p_o = 0.3$ has been applied, the upper limit of the BET pressure window as recommended by IUPAC [5, 6].
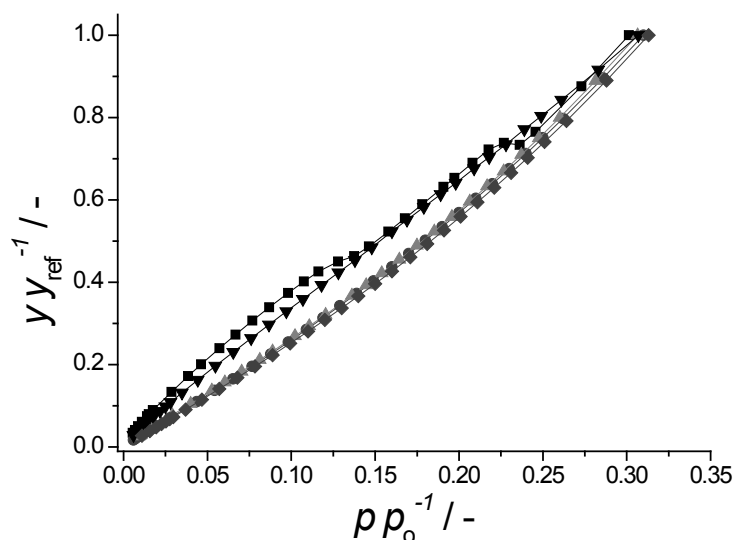
Figure A.13: Normalized linearized BET plot for the third adsorption isotherm of MIL-101 (■), UiO-66 (●), Norit RB 2 (▲), γ-alumina (▼) and Sigma-1(◆). Here y is defined as the left-hand side of Eq. 2.5 and the value for y_{ref} is taken at $p/p_o = 0.3$ (IUPAC upper bound for BET analysis [5, 6]).

In Fig. A.14 the obtained C values belonging to the fits in Figs. A.11 and A.12 and in the S.I. of [1] are depicted. Confidence intervals are omitted for clarity. The uncertainty is extremely large around the transition from positive to negative C values, but negligibly small elsewhere.
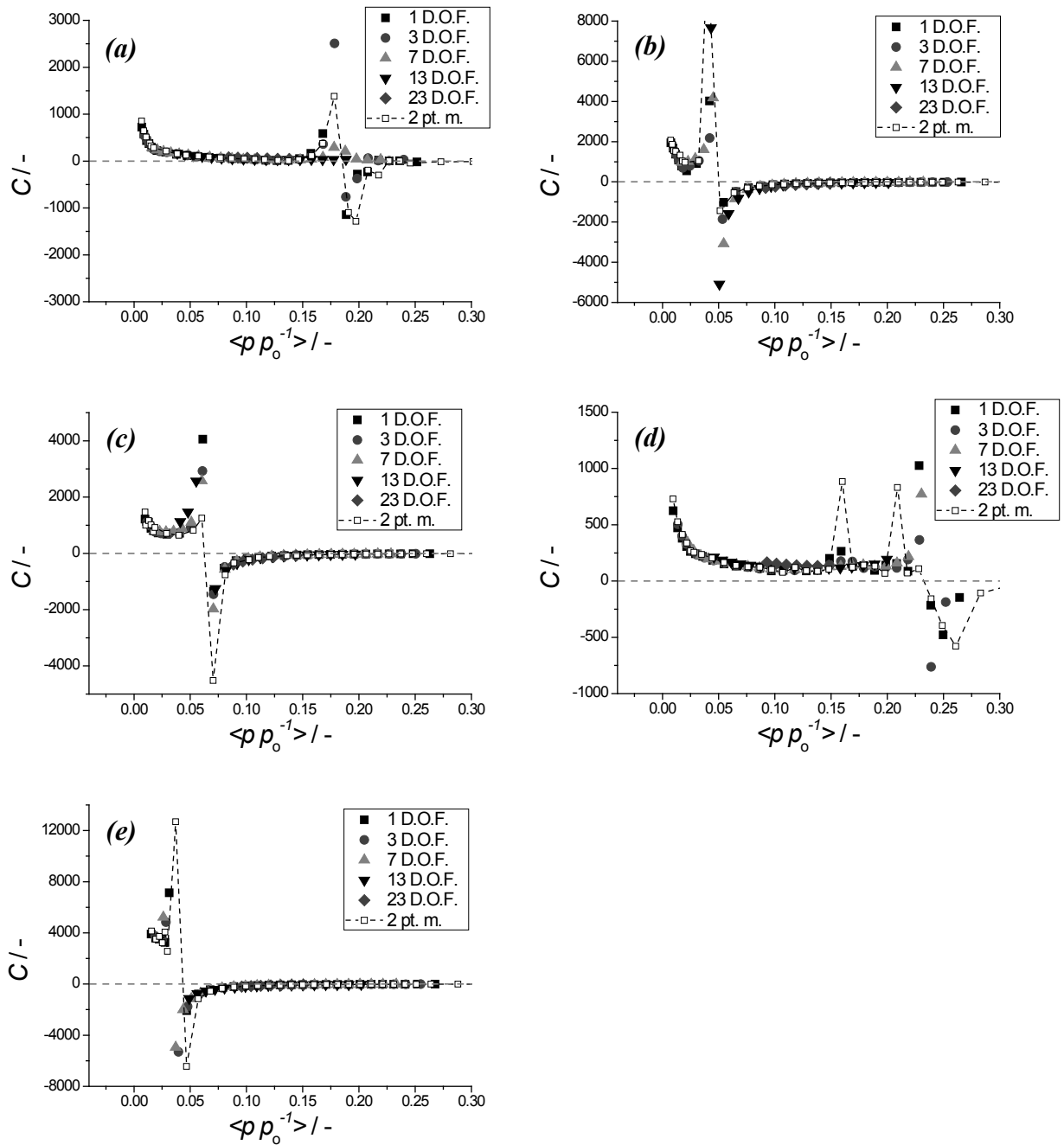
Figure A.14: Obtained C parameter values from the linear fitting method (closed symbols, for 1,3,7,13 and 23 degrees of freedom) and from direct calculation (dashed line and open squares) over the relative pressure range for MIL-101(Cr) (*a*), UiO-66 (*b*), Norit RB 2 (*c*), γ-alumina (*d*) and Sigma-1 (*e*). For all calculations, the third adsorption measurement was used. Grey dashed line corresponds to $C = 0$ (added for clarity).

Table A.5: BET surface area and absolute confidence interval obtained by the three different fitting methods for the third isotherm measured for each material and the maximum degrees of freedom in the relative pressure range limited by the IUPAC upper bound ($p/p_0 \leq 0.3$) [5, 6].

Material	Linear S_{BET} / m^2 g^{-1}	Linear 95% conf. int.	Direct S_{BET} / m^2 g^{-1}	Direct 95% conf. int.	Weighted direct S_{BET} / m^2 g^{-1}	Weighted direct 95% conf. int.
MIL-101(Cr)	2820	± 88	2680	± 87	2700	± 90
UiO-66	860	± 60	950	± 30	950	± 35
Sigma-1	270	± 53	300	± 10	290	± 11
γ-alumina	183	± 8	180	± 2	179	± 2
Norit RB2	930	± 57	1000	± 26	1000	± 29

A.11. BET – COMPARISON OF (WEIGHTED) DIRECT AND LINEAR FITTING

The uncertainties in BET values for the (weighted) direct method are obtained from the fit directly, and for the linear method as previously explained in Section A.4. In Table A.5 areas and uncertainties for maximum degrees of freedom are given for the three materials. The weights calculated according to the approach of Van Erp and Martens [7] are given in the S.I. of [1].

A.12. THE TWO-POINT BET METHOD

The calculated C values according to the two-point BET method proposed in this work, compared to those obtained from previous fitting exercises using the linear method, are given in Fig. A.14. One can clearly observe that relative pressure at which C changes from positive to negative is identical for the two-point method and the fitted results. Fitting results adhering to the applied filter for both linear and direct method show (see Fig. A.15), for the microporous materials under investigation, that adhering to the pressure window provided by the two-point method results in lower uncertainties in BET values.
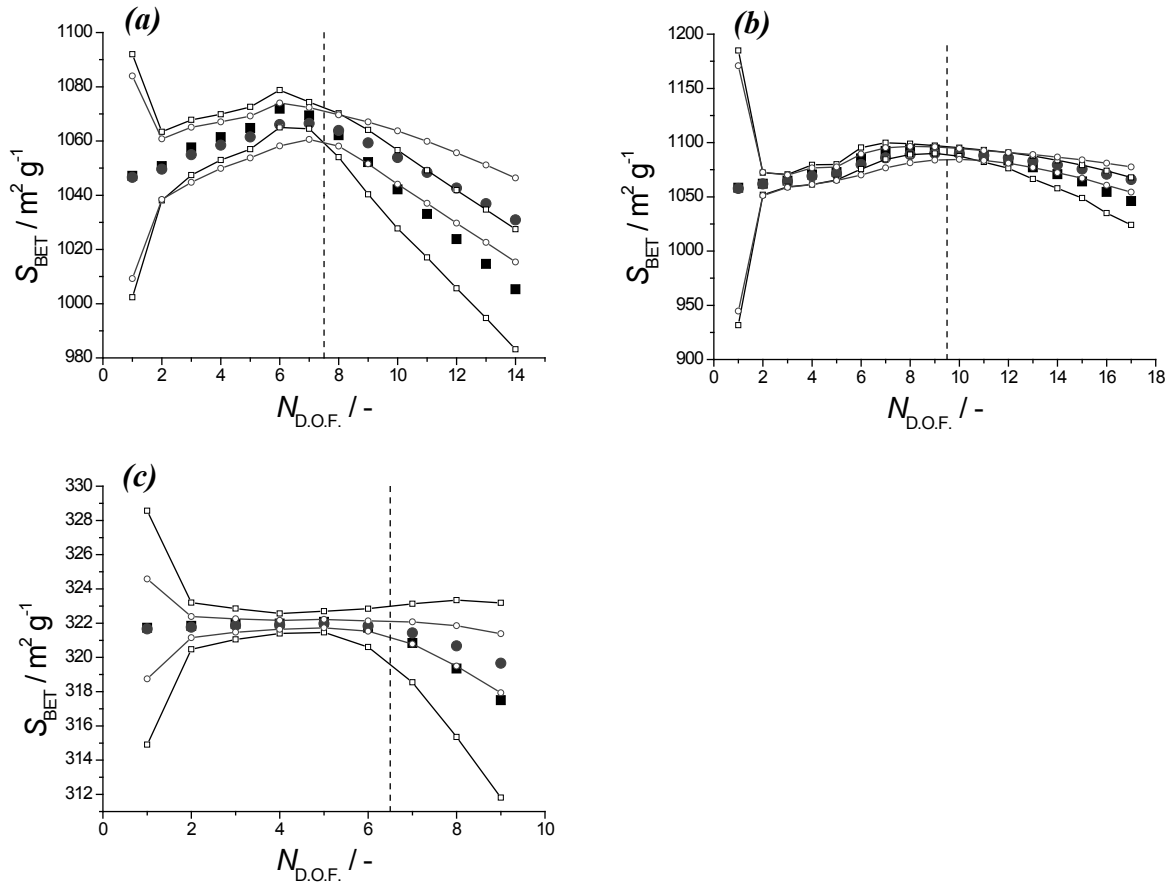
Figure A.15: BET surface area and confidence interval thereof for both direct ($\bullet$) and linear ($\blacksquare$) fitting method, for UiO-66 (*a*), Norit RB2 (*b*) and Sigma-1 (*c*), starting from the first fit available (first 3 data points) and adding an adjacent data point to the fit. Dashed line indicates the sign change of the *C* parameter, as determined by the proposed filter method. For all calculations, the third adsorption measurement was used.

A.13. STUDENTIZED RESIDUAL PLOTS AND PREDICTIONS FOR γ-ALUMINA AND MIL-101(Cr)

In Fig. A.16 the Studentized residuals and predictions based on the BET model are shown for γ-alumina, for an increasing number of excluded data points in the low relative pressure regime of the adsorption isotherm. Corresponding normal probability plots are given in Fig. A.17. Note that the Studentized residuals initially do not necessarily decrease in value, as for every time the data point with lowest relative pressure is removed the distribution changes as the removed point has the highest residual. Fig. A.18 contains the surface area and confidence interval thereof as function of these excluded points for γ-alumina.
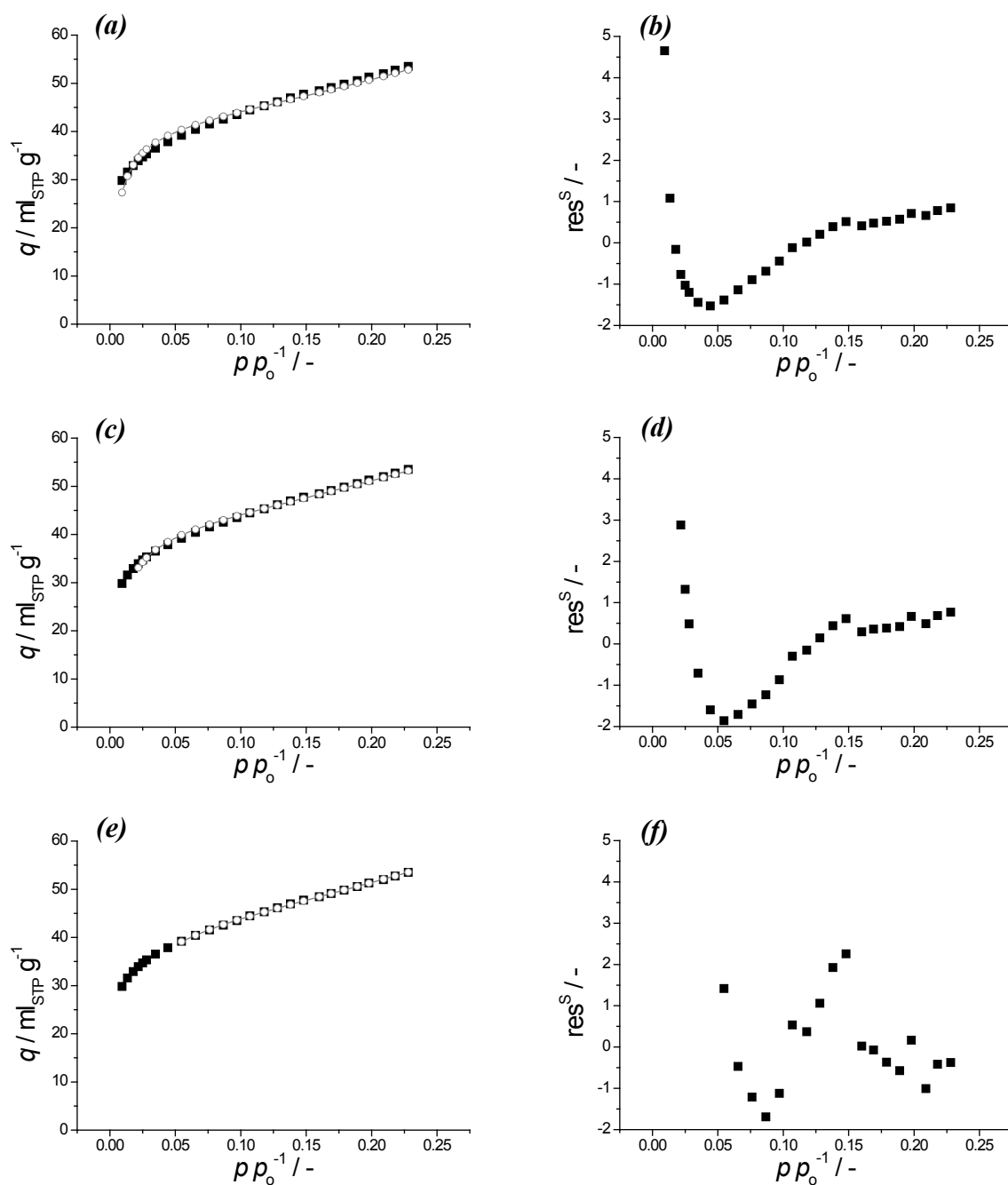
Figure A. 16: Measured adsorption isotherm for γ-alumina, after removal of points for which $C < 0$ at high relative pressures (closed symbols), and predictions (open symbols) based on direct fitting of the BET equation (*a, c, e*), and Studentized residuals (*b, d, f*), for no additional removal of data points (*a, b*), first three data points excluded (*c, d*) and first eight points excluded (*e, f*). For all calculations, the third adsorption isotherm measurement was used.
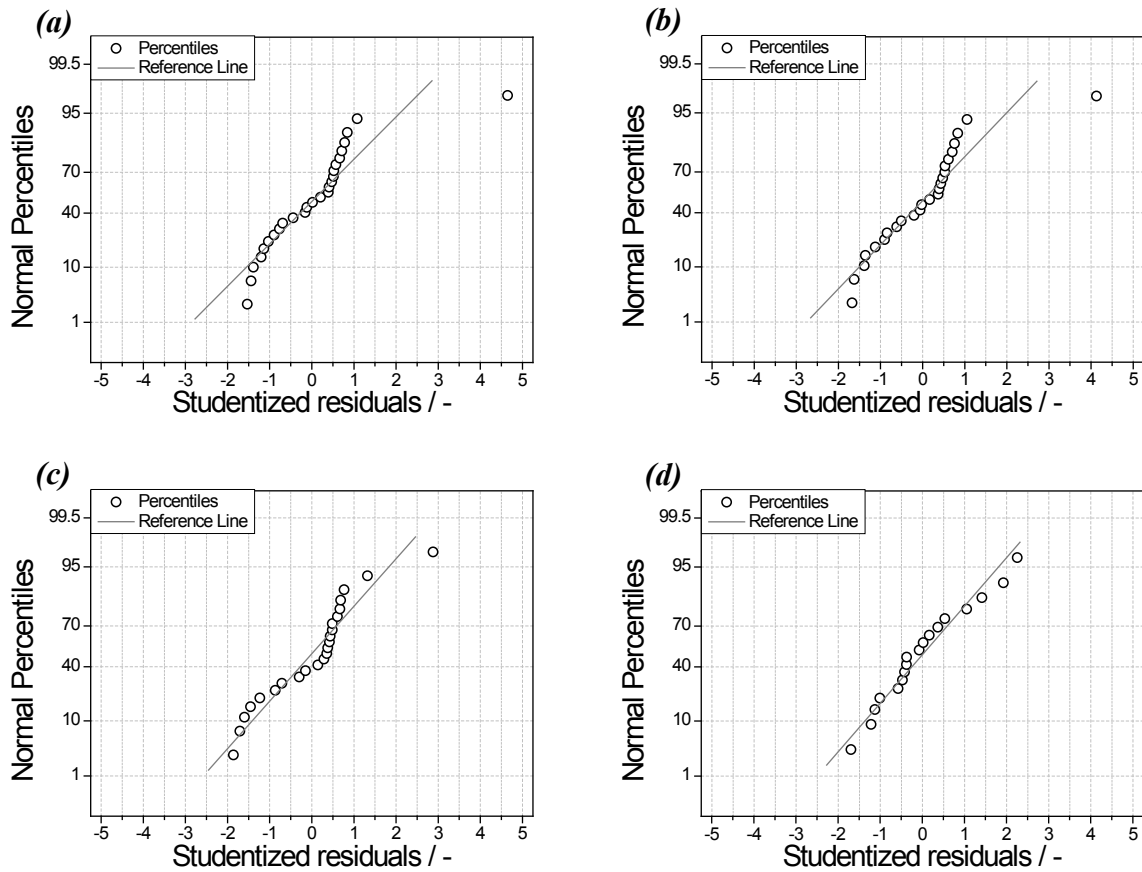
Figure A.17: Normal probability plots for γ-alumina, belonging to the different fits in Fig. A.16, for no additional removal of data points (*a*), first data point excluded (*b*), first three data points excluded (*c*) and first eight points excluded (*d*).
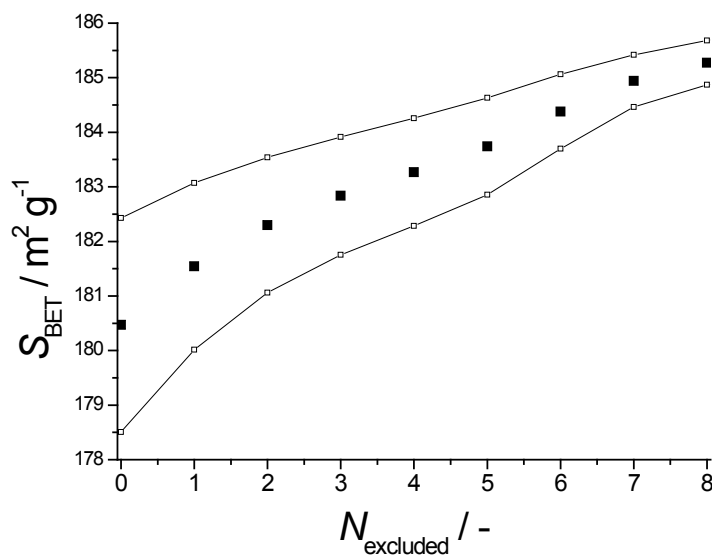
Figure A.18: Surface area of γ-alumina and confidence interval thereof, obtained with the direct method as function as in excluded data points from the low pressure regime.
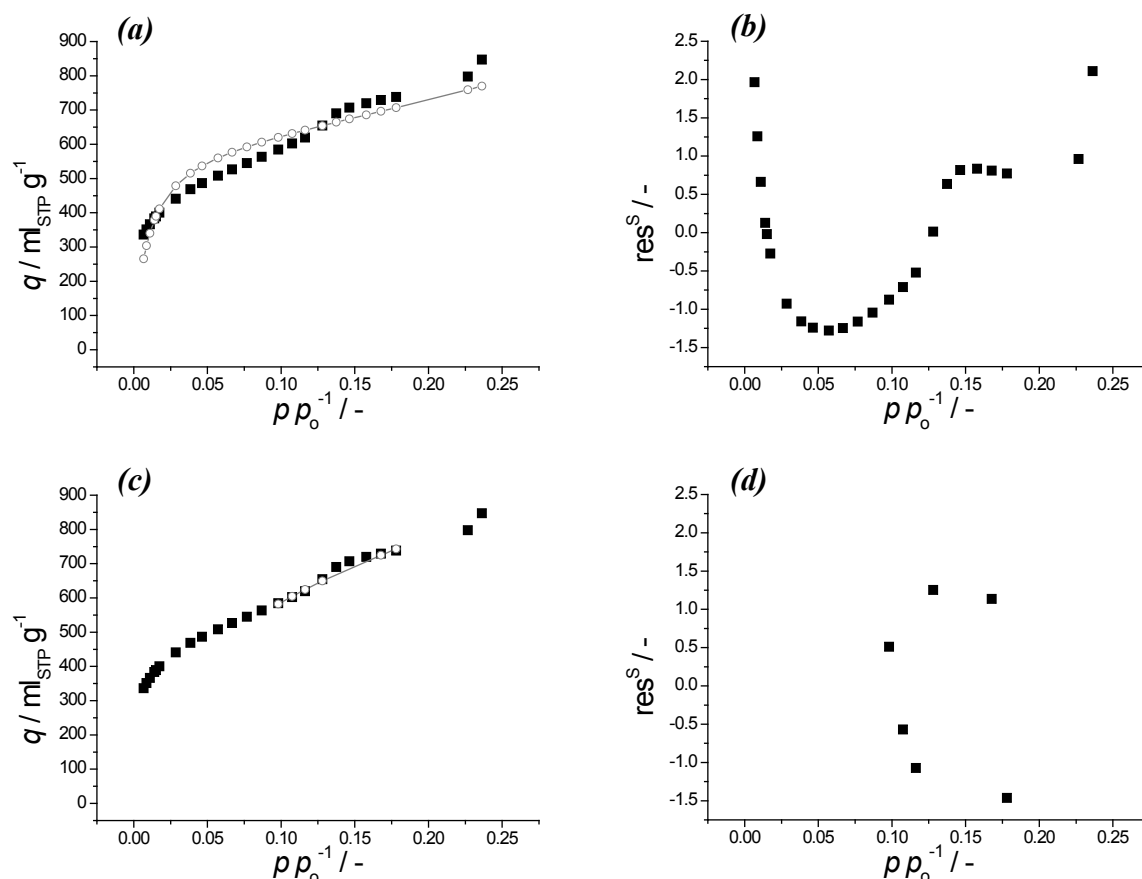
Figure A.19: Measured adsorption data for MIL-101(Cr), after removal of points for which $C < 0$, depicted in open symbols and predictions based on direct fitting of the BET equation (*a, c*), and Studentized residuals (*b, d*), for no additional removal of data points (*a, b*) and eighteen removed data points (*c, d*). For all calculations, the third adsorption measurement was used.

In Fig. A.19 Studentized residuals and BET predictions are shown for MIL-101(Cr). Accompanying normal probability plots are shown in Fig. A.20. As the residuals are large over the whole pressure range for MIL-101, because of the poor description obtained by fitting the BET equation to the isotherm of this material, there is no statistical reason to eliminate only the low pressure points. If one were to remove points with high residuals until the residual distribution is more or less random (this would require roughly eighteen points), one obtains BET parameters that are not better at characterizing the material than the starting parameters and have an even higher uncertainty (see Table A.6).
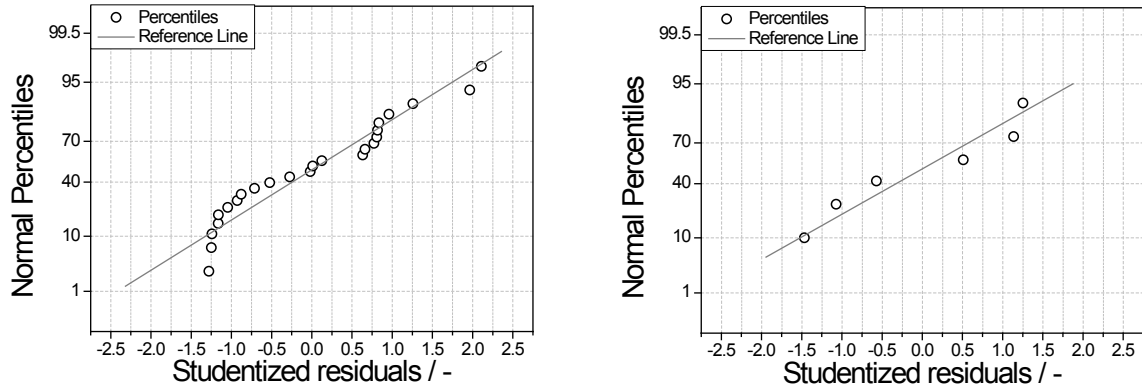
Figure A.20: Normal probability plots for MIL-101(Cr), belonging to the different fits in Fig. A.19, for no additional removal of data points (*left*) and eighteen removed data points (*right*).

Table A.6: BET surface area, C parameter and confidence intervals, obtained using the direct method, without exclusion of data points and for eighteen removed data points (belonging to Fig. A.19).

case	S_{BET} / m^2 g^{-1}	95% conf. int.	C / -	95% conf. int.
no exclusion	2680	± 87	113.26	± 0.06
18 points removed	3200	± 140	23.54	± 0.08

A.14. VARIATION OF V_P AND S_{BET} OBTAINED FROM DIFFERENT MEASUREMENTS OF THE SAME MATERIAL

For each of the three different isotherm measurements one can determine a mean and standard deviation in the derived parameter ζ (which stands either for the pore volume, V_p, or specific surface area, S_{BET}):

$$\overline{\zeta} = \frac{1}{N}\sum_{i=1}^{N}\overline{\zeta}(i) \tag{A14.1}$$

$$\sigma_\zeta^{exp} = \sqrt{\frac{1}{N-1}\sum_{i=1}^{N}\left(\zeta(i)-\overline{\zeta}\right)^2} \tag{A14.2}$$

β is defined as the ratio of the estimated 95% confidence interval (1.96 $\sigma_\zeta^{\mathrm{exp}}$) and the average value of ζ:

$$\beta = 1.96 \frac{\sigma_\zeta^{\mathrm{exp}}}{\bar{\zeta}} \qquad\qquad (A14.3)$$

The ratio β is an indicator for the relative magnitude of the variation of either V_{p} or S_{BET} compared to the absolute value of this variable. For the pore volume, results are depicted in Table A.7. From this one conclude that the variation in pore volume is small compared to its absolute value (β is small). Also, differences in the confidence intervals per measurement are minor. This indicates that nitrogen adsorption procedure yields reproducible values for the pore volume and related uncertainty. For the BET surface area determination, results for the different measurements on the same sample are given in Table A.8, for the maximum degrees of freedom for the three different fitting methods under investigation. Similar conclusions to the pore volume results can be drawn; variation in the BET surface area is small compared to its absolute value and differences in the confidence intervals per measurement are minor. This indicates that nitrogen adsorption yields reproducible values for the BET surface area and related uncertainty. Furthermore, when comparing the three different methods, no distinct differences can be observed. This indicates that all methods yield comparable inter-measurement variation in BET surface area for the materials under investigation.

When the results using unconstrained fitting strategies (Table A.8) are compared with those obtained with constrained fits for microporous (see Table A.9) and mesoporous (see Table A.10) materials, one can observe that for the constrained case, confidence intervals (either from error propagation or from variation between measurements) are in general smaller compared to the absolute value of the BET surface areas for the different materials, indicating even slightly better reproducibility of BET surface areas from different measurements of the same sample.

Table A.7: Pore volumes and 95% confidence intervals determined at $p/p_o = 0.9$ for each of the three measurements on the same sample and 95% confidence intervals therein.

Material	1st meas. V_p / cm^3 g^{-1}		2nd meas. V_p / cm^3 g^{-1}		3rd meas. V_p / cm^3 g^{-1}		1.96 $\sigma_{V_p}^{exp}$ / cm^3 g^{-1}	β / %
MIL-101(Cr)	1.49	± 0.016	1.50	± 0.016	1.51	± 0.017	± 0.017	1.15
UiO-66	0.43	± 0.016	0.43	± 0.016	0.43	± 0.016	± 0.002	0.39
Sigma-1	0.13	± 0.014	0.14	± 0.014	0.14	± 0.014	± 0.004	2.68
γ-alumina	0.39	± 0.014	0.39	± 0.014	0.40	± 0.011	± 0.004	0.93
Norit RB2	0.46	± 0.010	0.46	± 0.010	0.46	± 0.010	± 0.004	0.94

Table A.8: BET surface areas and 95% confidence intervals obtained using the maximum degrees of freedom in the relative pressure range limited by the IUPAC upper bound ($p/p_o \leq 0.3$) [5, 6] for the linear, direct and weighted direct method for all three measured isotherms on the same sample. Number of significant digits purposely slightly exaggerated to depict subtle differences between measurements.

Linear	1st meas. S_{BET} / m^2 g^{-1}		2nd meas. S_{BET} / m^2 g^{-1}		3rd meas. S_{BET} / m^2 g^{-1}		1.96 σ_{SBET}^{exp} / m^2 g^{-1}	β / %
MIL-101(Cr)	2956	±77	2948	±78	2815	±88	155	5.34
UiO-66	858	±60	858	±60	863	±60	5.3	0.62
Sigma-1	269	±52	268	±52	265	±53	3.9	1.47
γ-alumina	184	±8.5	183	±8.5	183	±8.2	2.0	1.07
Norit RB2	932	±57	924	±57	928	±57	8.0	0.87
Direct	S_{BET} / m^2 g^{-1}		S_{BET} / m^2 g^{-1}		S_{BET} / m^2 g^{-1}		1.96 σ_{SBET}^{exp} / m^2 g^{-1}	β / %
MIL-101(Cr)	2836	±81	2828	±82	2675	±88	178	6.41
UiO-66	947	±30	947	±30	953	±30	7.0	0.74
Sigma-1	295	±10	298	±10	299	±10	3.9	1.30
γ-alumina	181	±2.3	180	±2.1	180	±2.1	1.4	0.77
Norit RB2	998	±25	994	±25	1002	±25	7.3	0.73
Wgt. Dir.	S_{BET} / m^2 g^{-1}		S_{BET} / m^2 g^{-1}		S_{BET} / m^2 g^{-1}		1.96 σ_{SBET}^{exp} / m^2 g^{-1}	β / %
MIL-101(Cr)	2846	±86	2843	±88	2703	±90	161	5.74
UiO-66	945	±34	946	±34	950	±35	6.0	0.63
Sigma-1	291	±11	294	±11	294	±11	3.8	1.31
γ-alumina	181	±2.3	179	±2.1	179	±2.1	1.5	0.81
Norit RB2	1000	±29	996	±28	1004	±28	8.3	0.83

Table A.9: BET surface areas and 95% confidence intervals obtained for the microporous materials under investigation for both the linear and direct method based on the measurements on the same sample using the proposed filter for selection of the upper relative pressure limit, as proposed for microporous materials.

	1st meas.		2nd meas.		3rd meas.			
Linear	S_{BET} / m^2 g^{-1}		S_{BET} / m^2 g^{-1}		S_{BET} / m^2 g^{-1}		1.96 σ_{SBET}^{exp} / m^2 g^{-1}	β / %
UiO-66	1061	±5.6	1061	±5.8	1069	±4.9	10	0.90
Sigma-1	325	±1.0	325	±1.4	322	±1.1	3.6	1.11
Norit RB2	1098	±5.5	1089	±4.6	1094	±3.6	8.3	0.76
Direct	S_{BET} / m^2 g^{-1}		S_{BET} / m^2 g^{-1}		S_{BET} / m^2 g^{-1}		1.96 σ_{SBET}^{exp} / m^2 g^{-1}	β / %
UiO-66	1057	±6.7	1059	±6.1	1066	±5.9	10	0.91
Sigma-1	325.0	±0.3	324.9	±0.4	321.8	±0.3	3.5	1.08
Norit RB2	1091	±9.4	1084	±8.1	1090	±6.1	6.6	0.61

Table A.10: BET surface areas and 95% confidence intervals obtained for the mesoporous γ-alumina for the direct method on the three measurements on the same sample using the proposed filter for selection of the lower and upper relative pressure limit.

γ -alumina	S_{BET} / m^2 g^{-1}		$N_{D.O.F.}$ / -	$p\,p_o^{-1}{}_{min}$ / -	$p\,p_o^{-1}{}_{max}$ / -	1.96 σ_{SBET}^{exp} / m^2 g^{-1}	β / %
Meas. 1	187.1	±0.26	16	0.063	0.236	2.0	0.42
Meas. 2	185.3	±0.29	16	0.065	0.238		
Meas. 3	185.3	±0.41	16	0.055	0.228		

A.15. WEIGHTS USED FOR LINEARIZATION

Van Erp and Martens [7] have both derived and demonstrated that one can obtain, while using the direct fitting method, results almost identical to the linear fitting method, if the weights, ω_l, given in Eq. A15.1 are applied to the direct method:

$$\omega_l(i) = \left(\frac{\left.\frac{p}{p_o}\right|_i}{q_i^2 \left(1 - \left.\frac{p}{p_o}\right|_i\right)} \right)^2 \tag{A15.1}$$

Or obviously, by applying the inverse weights, $\omega_l{}^{-1}$, while using the linear fitting method, to obtain very similar results to the direct fitting method. From this one can rightfully conclude that the linear method, when compared to the direct fitting method, puts significantly more emphasis on measured points at higher relative pressure.

A.16. WEIGHTED DIRECT METHOD

The weighted direct fitting method, left out of the discussion mostly, yields fairly similar results as the regular direct method at high degrees of freedom (Figs. 2.6 and 2.7), albeit that uncertainty generally is slightly higher (*e.g.* see Table A.5). The reader is reminded once more that the weights used in the weighted direct method, are not the linearization weights, ω_l, mentioned in Section A.15. At low degrees of freedom, however, the weighted method is found to obtain higher variability and uncertainty in general (Figs. 2.6 and 2.7). This because, when for at least one of the data points the associated weight is very low, the BET values become very different from the unweighted case. Furthermore, because of the resulting poor fitting, seen for example for Sigma-1 (see S.I. of [1]), also the uncertainty of the BET values obtained is very large. This unwanted effect is mitigated when enough degrees of freedom are used. Furthermore, one might have hoped that the weighted method would yield less variability of the BET surface area determined from a single nitrogen isotherm than the unweighted method would. However, as this variability is largest at low degrees of freedom and the weighted method performs rather poorly at low degrees of freedom, there is no incentive to include these weights when fitting. At high degrees of freedom, the results obtained with the direct fitting method without and with weights are very similar, again yielding no clear incentive to include these weights. The weighted method was specifically developed to mitigate the effects of fluctuation of the relative pressure of each of the measured points on the BET parameters. These fluctuations, as can be seen from Fig. A.2, are for the measurements performed in this study, very minor, hence the variability of BET surface area determined from different isotherms of the same sample is expected to very small in this work. Hence there is again no clear incentive to use the weighted method. However, if one were to perform measurements where the number of measured points and the associated relative pressure are not fixed *a priori* but are fluctuating based on the number of doses, the weighted method might still has lowest variability of the BET area between different

measurements, as was shown by Van Erp and Martens [7]. Such measurements however, are unavailable with the equipment used in this work.

A.17. LACK-OF-FIT TEST FOR REPEATED ISOTHERM MEASUREMENTS

The lack-of-fit test is used to test whether a model is accurate to describe measured experimental data. In this particular case, to verify whether the BET-model is an appropriate representation for the measured adsorption isotherms for the different materials under investigation. The central concept is that the total sum of squared residuals (denoted SSR), obtained from fitting the model to experimental data, is the sum of two contributions:

$$\text{SSR} = \text{SSE} + \text{SSL} \tag{A17.1}$$

The first contribution is the error sum of squared residuals (SSE) and is only based on the error in measurements. The second contribution to SSR arises from the lack-of-fit of the model to describe the experiments (SSL). The former can be calculated from the measurements directly, by applying:

$$\text{SSE} = \sum_{i=1}^{n_{\text{exp}}} \sum_{j=1}^{n_{\text{rep}}(i)} \left(Y_{ij} - <Y_i> \right)^2 \tag{A17.2}$$

Here n_{rep} is the number of repeated measurements per separate x-value (here p/p_o) and n_{exp} is the number of different experiments (different x-values). For each ith experiment, an average value for the n_{rep} repeated measurements is calculated, $<Y_i>$, and from this subsequently the (squared) residuals can be determined. Note that in order to be able to estimate SSE, one requires at least two measured values for the same experimental input (in this work, at least two different values for q for the same p/p_o and the same material). This means that the three repeated isotherm measurements for a material (Fig. 2.2) are treated as a single experiment to be able to perform a lack-of-fit test. This means that the parameter estimations (fits) performed in this section are by definition based on experimental isotherms of all three measurements simultaneously. Once the SSE is determined, the SSL can be calculated from Eq. A17.1, as the SSR is obtained from the fit directly.

When the different contributions to the sum of squared residuals are known, one can calculate the *F* test-statistics according to:

$$F = \frac{\mathrm{SSL}\Big/\big(n_{\exp} - p\big)}{\mathrm{SSE}\Big/\big(N - n_{\exp}\big)} = \frac{mean(\mathrm{SSL})}{mean(\mathrm{SSE})} \tag{A17.3}$$

Here *p* is the number of parameters to be estimated in the model and *N* can be calculated according to:

$$N = \sum_{i=1}^{n_{\exp}} n_{\mathrm{rep}}(i) \tag{A17.4}$$

A model fits sufficiently, when this *F*-statistic is smaller than a criterion value based on the Fischer distribution:

$$F < F_{(1-\alpha)}\Big(\big(n_{\exp} - p\big), \big(N - n_{\exp}\big), \big(1-\alpha\big)\Big) \tag{A17.5}$$

Here α is the confidence level, set to 0.05, meaning that with 95% certainty the model yields an accurate description of the supplied experimental data, when:

$$\frac{F}{F_{0.95}} < 1 \tag{A17.6}$$

Firstly, fitting the three measurements of each material simultaneously using the direct method, and both with and without the proposed constraints, yields results as presented in Table A.11. Obtained surface areas are in line with those previously found for the individual parameter estimations for both the unconstrained and constrained case. Confidence intervals of the estimated surface areas are lowered due to the increase in measured data points. From the repeated measurements one can obtain an estimate for SSE. This is indeed only an estimate, as for the different adsorption measurements the data points are not recorded at exactly equal *p/p*$_{\mathrm{o}}$ values. This variation in *p/p*$_{\mathrm{o}}$ values of the different isotherms, which are treated as equal required for the determination of SSE, makes that the obtained values might not be 100% accurate but it at least gives a proper indication. From the SSE and the SSR of the parameter estimation the SSL and their mean-values can be calculated. All required information for the lack-of-fit test is presented in Table A.12.

Table A.11: Obtained BET surface area and 95% confidence intervals for combined fitting of three isotherm measurements simultaneously, using the direct method, for the five different materials under investigation (Fig. 2.2). Performed for the unconstrained case, where the maximum degrees of freedom is used for $p/p_o \leq 0.3$ and for the constrained case where the proposed guidelines are used to delimit the relative pressure window.

Material	Unconstrained S_{BET} / m^2 g^{-1}		Constrained S_{BET} / m^2 g^{-1}	
MIL-101	2320	±47	-	-
UiO-66	950	±17	1061	±4.1
Norit RB2	1000	±14	1088	±5.3
γ-alumina	180	±1.2	186	±1.0
Sigma-1	297	±5.6	324	±1.9

Table A.12: Lack-of-fit test results for 95% confidence level obtained by fitting the BET-equation to the repeated measurements of the five different materials under investigation (Fig. 2.2) using the direct method. Performed for the unconstrained case, where the maximum degrees of freedom is used for $p/p_o \leq 0.3$ and for the constrained case where posed guidelines are used to delimit the relative pressure window.

Material	Unconstrained mean(SSE)	mean(SSL)	F	$F(0.95)$	$F/F(0.95)$	Constrained mean(SSE)	mean(SSL)	F	$F(0.95)$	$F/F(0.95)$
MIL-101	15.8	90.7	5.74	1.65	3.48	-	-	-	-	-
UiO-66	0.95	1031	1089	1.66	658	1.40	1.12	1.18	2.66	0.45
Norit RB2	1.45	685	473	1.65	287	1.83	5.90	4.08	2.46	1.66
γ-alumina	0.040	4.48	112	1.65	68.2	0.035	0.10	2.60	2.07	1.26
Sigma-1	0.27	102	386	1.65	234	0.21	0.06	0.22	2.74	0.08

Clearly, for the unconstrained case, where the maximum degrees of freedom are used, the factor F/F_{crit} is exorbitantly high. This means that for this relative pressure range of data points the BET-model is by no means appropriate to describe the adsorption behavior of the materials under investigation. Note that, as mentioned in Section A.13, there is no statistical incentive to apply constraints for the case of MIL-101, hence the absence of the constrained results. For all other materials under investigation, Applying the recommendations to delimit the relative pressure range as proposed in this work, decreases the lack-of-fit substantially.

Table A.13: Lack-of-fit test results for 95% confidence level obtained by fitting the BET-equation to the repeated measurements for the five different cell volumes using different sample masses of γ-alumina(2) (Fig. 2.4) using the direct method. Performed for the unconstrained case, where the maximum degrees of freedom is used for $p/p_o \leq 0.3$ and for the constrained case where posed guidelines are used to delimit the relative pressure window.

|	Unconstrained					Constrained				
	mean(SSE)	mean(SSL)	F	$F(0.95)$	$F/F(0.95)$	mean(SSE)	mean(SSL)	F	$F(0.95)$	$F/F(0.95)$
Cell 1	0.075	2.8	38	1.7	22	0.084	0.21	2.55	2.18	1.17
Cell 2	0.22	4	17	2	10	0.26	1.54	6.05	2.18	2.77
Cell 3	1.20	5	4	2	2	0.98	0.29	0.30	2.18	0.14
Cell 4	1.3	4.5	3.5	1.7	2.1	0.91	0.97	1.06	2.18	0.49
Cell 5	7.1	9	1	2	1	4.0	1.36	0.34	2.18	0.16

For both Norit RB2 and γ-alumina the BET model still might not give a proper description of the experimental data. This might be attributed to a too low estimate of the pure error sum of squares (SSE) compared to the other materials. To have a better appreciation not only the same sample in the same sample tube should be considered repeatedly (which gives an impression of the measurement procedure), but also the sample should be changed, *e.g.* as is performed in Section A.8. Doing so, as indicated in Table A.13, indeed shows that the mean(SSE) is enlarged when sample masses and/or cell volumes are varied during repetition of experiments. Further, as described in Section 2.3.2, the BET-method is from a theoretical perspective not a priori expected to yield a perfect description. This exercise however, shows once more that the quality of the fit can be substantially increased when using the guidelines proposed in this work.
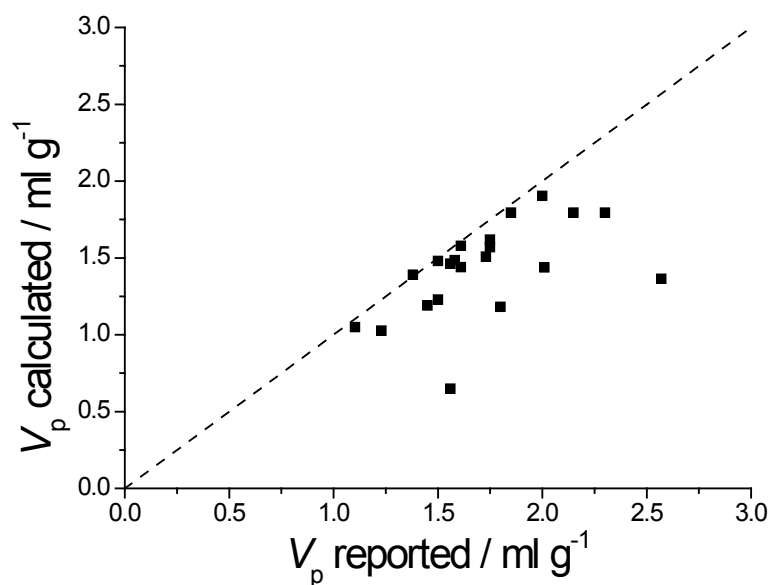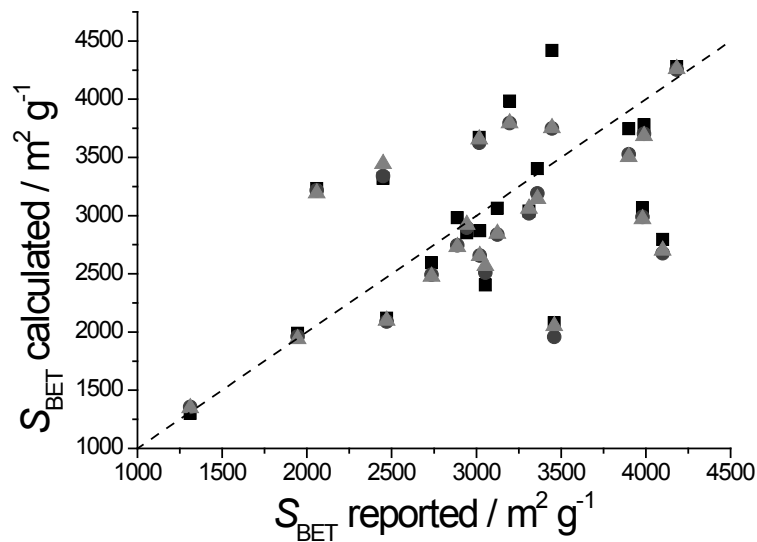
Figure A.21: Reported versus recalculated pore volume for MIL-101 from various literature sources [8-36].

A.18. RECALCULATING BET AND PORE VOLUME FOR MIL-101(Cr) RETRIEVED FROM VARIOUS LITERATURE SOURCES

In Fig. A.21 the recalculated pore volume is depicted as function of the originally reported pore volume for the literature sources under study [8-36]. Clearly, the reported volumes are significantly larger than the recalculated counterparts. Fig. A.22 contains the nitrogen adsorption isotherms for these sources, both in- and excluding a rescaling based on the pore volume. The rescaled isotherms overlap properly. In Fig. A.23 reported versus recalculated BET surface areas for the three methods used are given, for the same literature sources under study. This shows again an overprediction in general of the literature reported values, albeit less significant than for the case of the pore volume.
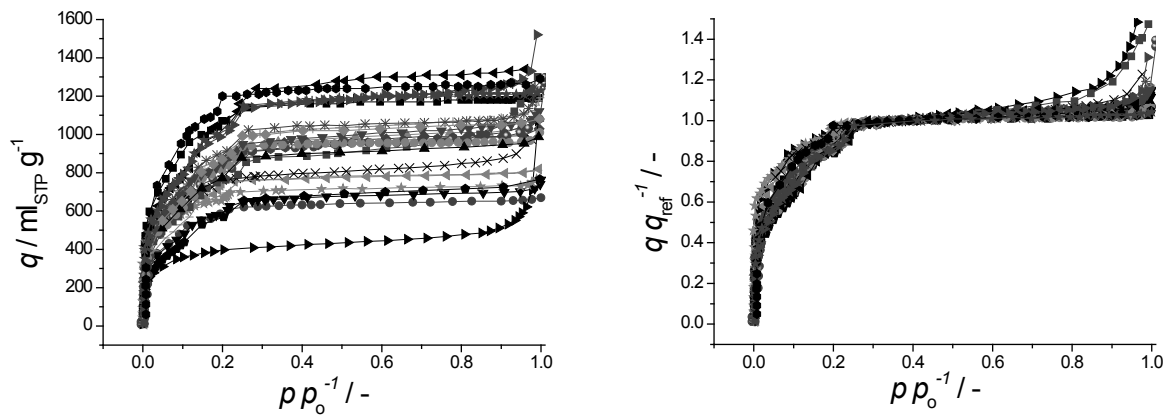
Figure A.22: Nitrogen adsorption isotherms obtained from literature (*left*) [8-36] and the same isotherms scaled with their respective quantities adsorbed at a relative pressure of 0.4 (used for the recalculation of the pore volume as well, *right*).

Figure A.23: Reported versus recalculated BET surface area, using three different fitting methods, linear (■), direct (●) and weighted direct (▲), for MIL-101 [8-36].

A.19. BJH PORE-SIZE DISTRIBUTIONS BASED ON ADSORPTION BRANCH

In Fig. A.24 the pore size distributions according to the BJH-method [37] based on the adsorption branch, including 95% confidence intervals. Calculation details are given in Section A.3.
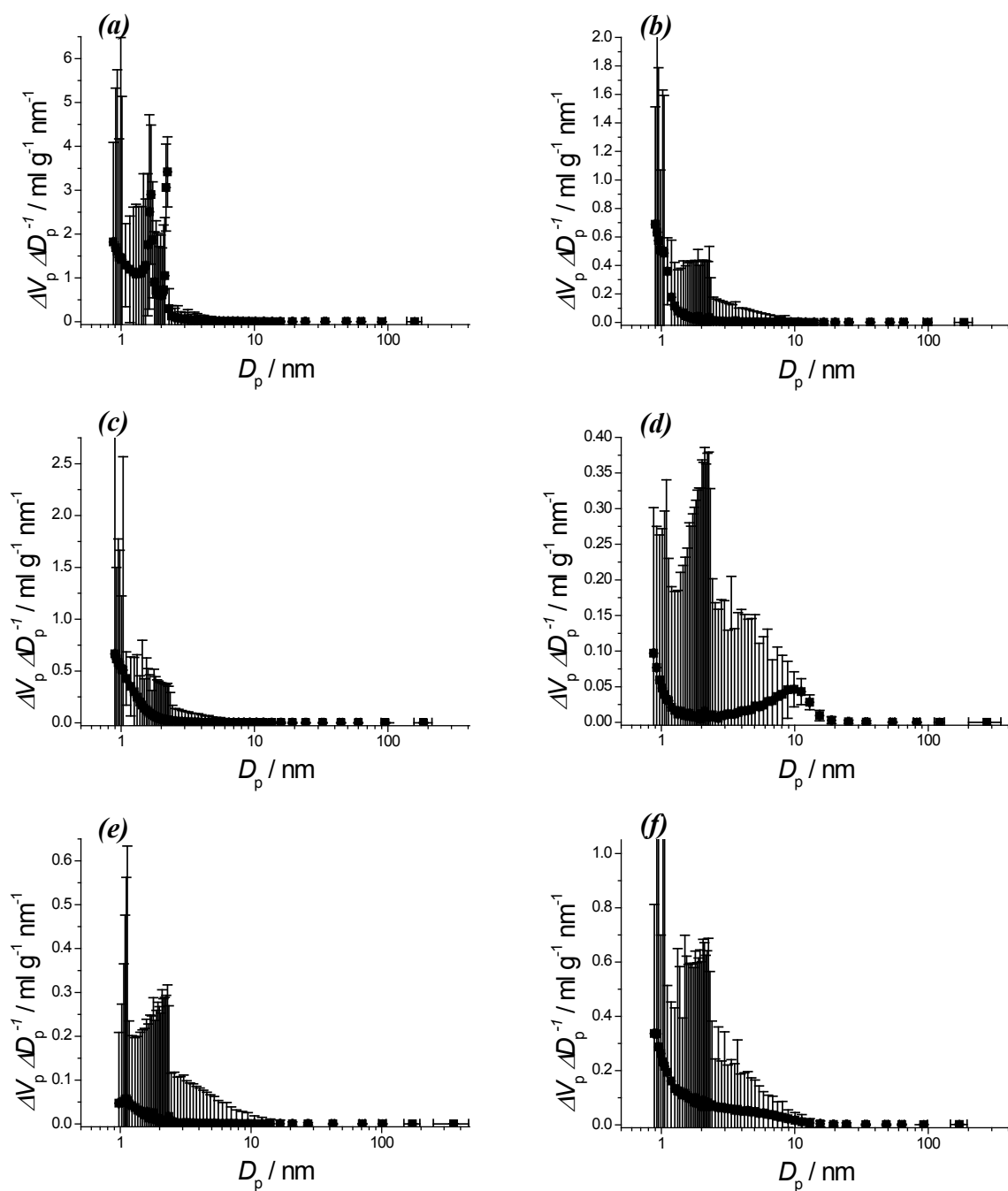
Figure A.24: BJH pore size distribution including 95% confidence intervals based on adsorption branch of the isotherm for MIL-101(Cr) (*a*), UiO-66 (*b*), Norit RB2 (*c*), γ-alumina (*d*), Sigma-1 (*e*) for the third adsorption measurement and H-ZSM-5(*f*) with artificially created mesopores [38]. BJH-calculations purposely extended to lower relative pressures to show trend in distribution and uncertainty.

A.20. REFERENCES

[1]   M.F. De Lange, T.J.H. Vlugt, J. Gascon, F. Kapteijn, Adsorptive characterization of porous solids: Error analysis guides the way, Microporous and Mesoporous Materials, 200 (2014) 199-215.
[2]   J.R. Taylor, An introduction to error analysis, 2nd ed., University Science Books, 1997.
[3]   W.D. Harkins, G. Jura, An adsorption method for the determination of the area of a solid without the assumption of a molecular area, and the area occupied by nitrogen molecules on the surfaces of solids, The Journal of Chemical Physics, 11 (1943) 431-432.
[4]   M. Kruk, M. Jaroniec, A. Sayari, Application of large pore MCM-41 molecular sieves to improve pore size analysis using nitrogen adsorption measurements, Langmuir, 13 (1997) 6267-6273.
[5]   K. Sing, D. Everett, R. Haul, L. Moscou, R. Pierotti, J. Rouquerol, T. Siemieniewska, Reporting physisorption data for gas/solid systems, Pure and Applied Chemistry, 54 (1982) 2201.
[6]   R. Pierotti, J. Rouquerol, Reporting physisorption data for gas/solid systems with special reference to the determination of surface area and porosity, Pure and Applied Chemistry, 57 (1985) 603-619.
[7]   T.S. Van Erp, J.A. Martens, A standardization for BET fitting of adsorption isotherms, Microporous and Mesoporous Materials, 145 (2011) 188-193.
[8]   P. Trens, H. Belarbi, C. Shepherd, P. Gonzalez, N.A. Ramsahye, U.H. Lee, Y.K. Seo, J.S. Chang, Coadsorption of n -hexane and benzene vapors onto the chromium terephthalate-based porous material MIL-101(Cr) an experimental and computational study, Journal of Physical Chemistry C, 116 (2012) 25824-25831.
[9]   X. Liu, H. Zhou, Y. Zhang, Y. Liu, A. Yuan, Syntheses, characterizations and adsorption properties of MIL-101/graphene oxide composites, Chinese Journal of Chemistry, 30 (2012) 2563-2566.
[10]   G. Akiyama, R. Matsuda, H. Sato, A. Hori, M. Takata, S. Kitagawa, Effect of functional groups in MIL-101 on water sorption behavior, Microporous and Mesoporous Materials, 157 (2012) 89-93.
[11]   K. Munusamy, G. Sethia, D.V. Patil, P.B. Somayajulu Rallapalli, R.S. Somani, H.C. Bajaj, Sorption of carbon dioxide, methane, nitrogen and carbon monoxide on MIL-101(Cr): Volumetric measurements and dynamic adsorption studies, Chemical Engineering Journal, 195-196 (2012) 359-368.
[12]   I. Senkovska, E. Barea, J.A.R. Navarro, S. Kaskel, Adsorptive capturing and storing greenhouse gases such as sulfur hexafluoride and carbon tetrafluoride using Metal-Organic Frameworks, Microporous and Mesoporous Materials, 156 (2012) 115-120.
[13]   S.N. Kim, S.T. Yang, J. Kim, J.E. Park, W.S. Ahn, Post-synthesis functionalization of MIL-101 using diethylenetriamine: A study on adsorption and catalysis, CrystEngComm, 14 (2012) 4142-4147.
[14]   M. Anbia, V. Hoseini, Development of mwcnt@MIL-101 hybrid composite with enhanced adsorption capacity for carbon dioxide, Chemical Engineering Journal, 191 (2012) 326-330.
[15]   M. Anbia, V. Hoseini, Enhancement of CO_2 adsorption on nanoporous chromium terephthalate (MIL-101) by amine modification, Journal of Natural Gas Chemistry, 21 (2012) 339-343.
[16]   L. Bromberg, Y. Diao, H. Wu, S.A. Speakman, T.A. Hatton, Chromium(III) terephthalate Metal Organic Framework (MIL-101): HF-free synthesis, structure, polyoxometalate composites, and catalytic properties, Chemistry of Materials, 24 (2012) 1664-1675.
[17]   H.B.T. Jeazet, C. Staudt, C. Janiak, A method for increasing permeability in O_2/N_2 separation with mixed-matrix membranes made of water-stable MIL-101 and polysulfone, Chemical Communications, 48 (2012) 2140-2142.
[18]   Z. Saedi, S. Tangestaninejad, M. Moghadam, V. Mirkhani, I. Mohammadpoor-Baltork, MIL-101 Metal-Organic Framework: A highly efficient heterogeneous catalyst for oxidative cleavage of alkenes with H_2O_2, Catalysis Communications, 17 (2012) 18-22.
[19]   J. Ehrenmann, S.K. Henninger, C. Janiak, Water adsorption characteristics of MIL-101 for heat-transformation applications of MOFs, European Journal of Inorganic Chemistry, 2011 (2011) 471-474.
[20]   Z. Zhao, X. Li, S. Huang, Q. Xia, Z. Li, Adsorption and diffusion of benzene on chromium-based Metal Organic Framework MIL-101 synthesized by microwave irradiation, Industrial and Engineering Chemistry Research, 50 (2011) 2254-2261.
[21]   Z. Zhao, X. Li, Z. Li, Adsorption equilibrium and kinetics of p-xylene on chromium-based metal organic framework MIL-101, Chemical Engineering Journal, 173 (2011) 150-157.
[22]   Z. Zhang, S. Huang, S. Xian, H. Xi, Z. Li, Adsorption equilibrium and kinetics of CO_2 on chromium terephthalate MIL-101, Energy and Fuels, 25 (2011) 835-842.
[23]   C.Y. Huang, M. Song, Z.Y. Gu, H.F. Wang, X.P. Yan, Probing the adsorption characteristic of Metal-Organic Framework MIL-101 for volatile organic compounds by quartz crystal microbalance, Environmental Science and Technology, 45 (2011) 4490-4496.

[24]   J. Shi, Z. Zhao, Q. Xia, Y. Li, Z. Li, Adsorption and diffusion of ethyl acetate on the chromium-based Metal-Organic Framework MIL-101, Journal of Chemical and Engineering Data, 56 (2011) 3419-3425.

[25]   P.B. Somayajulu Rallapalli, M.C. Raj, D.V. Patil, K.P. Prasanth, R.S. Somani, H.C. Bajaj, Activated carbon MIL-101(Cr): A potential Metal-Organic Framework composite material for hydrogen storage, International Journal of Energy Research.

[26]   K. Yang, Q. Sun, F. Xue, D. Lin, Adsorption of volatile organic compounds by Metal-Organic Frameworks MIL-101: Influence of molecular size and shape, Journal of Hazardous materials, 195 (2011) 124-131.

[27]   D. Jiang, A.D. Burrows, K.J. Edler, Size-controlled synthesis of MIL-101(Cr) nanoparticles with enhanced selectivity for CO_2 over N_2, CrystEngComm, 13 (2011) 6916-6919.

[28]   N.A. Khan, J.W. Jun, S.H. Jhung, Effect of water concentration and acidity on the synthesis of porous chromium benzenedicarboxylates, European Journal of Inorganic Chemistry, (2010) 1043-1048.

[29]   N. Klein, A. Henschel, S. Kaskel, N-butane adsorption on $Cu_3(BTC)_2$ and MIL-101, Microporous and Mesoporous Materials, 129 (2010) 238-242.

[30]   J. Yang, Q. Zhao, J. Li, J. Dong, Synthesis of Metal-Organic Framework MIL-101 in TMAOH-$Cr(NO_3)_3$-H_2BDC-H_2O and its hydrogen-storage behavior, Microporous and Mesoporous Materials, 130 (2010) 174-179.

[31]   T.K. Trung, N.A. Ramsahye, P. Trens, N. Tanchoux, C. Serre, F. Fajula, G. Férey, Adsorption of C5-C9 hydrocarbons in microporous MOFs MIL-100(Cr) and MIL-101(Cr): A manometric study, Microporous and Mesoporous Materials, 134 (2010) 134-140.

[32]   P. Küsgens, M. Rose, I. Senkovska, H. Fröde, A. Henschel, S. Siegle, S. Kaskel, Characterization of Metal-Organic Frameworks by water adsorption, Microporous and Mesoporous Materials, 120 (2009) 325-330.

[33]   J.S. Lee, S.H. Jhung, J.W. Yoon, Y.K. Hwang, J.S. Chang, Adsorption of methane on porous metal carboxylates, Journal of Industrial and Engineering Chemistry, 15 (2009) 674-676.

[34]   S.H. Jhung, J.H. Lee, J.W. Yoon, C. Serre, G. Férey, J.S. Chang, Microwave synthesis of chromium terephthalate MIL-101 and its benzene sorption ability, Advanced Materials, 19 (2007) 121-124.

[35]   G. Férey, C. Mellot-Draznieks, C. Serre, F. Millange, J. Dutour, S. Surblé, I. Margiolaki, A chromium terephthalate-based solid with unusually large pore volumes and surface area, Science, 309 (2005) 2040-2042.

[36]   X.X. Huang, L.G. Qiu, W. Zhang, Y.P. Yuan, X. Jiang, A.J. Xie, Y.H. Shen, J.F. Zhu, Hierarchically mesostructured MIL-101 Metal-Organic Frameworks: Supramolecular template-directed synthesis and accelerated adsorption kinetics for dye removal, CrystEngComm, 14 (2012) 1613-1617.

[37]   E.P. Barrett, L.G. Joyner, P.P. Halenda, The determination of pore volume and area distributions in porous substances. I. Computations from nitrogen isotherms, Journal of the American Chemical Society, 73 (1951) 373-380.

[38]   S. Sartipi, K. Parashar, M. Makkee, J. Gascon, F. Kapteijn, Breaking the fischer–tropsch synthesis selectivity: Direct conversion of syngas to gasoline over hierarchical Co/H-ZSM-5 catalysts, Catalysis Science & Technology, 3 (2013) 572-575.

CHAPTER 3

UNDERSTANDING ADSORPTION OF HIGHLY POLAR VAPORS ON MESOPOROUS MIL-100(Cr) AND MIL-101(Cr)

ABSTRACT:

The adsorption of polar vapors water and methanol on meso- and microporous Metal Organic Frameworks, MIL-100(Cr) and MIL-101(Cr), has been studied in a combined experimental and simulation approach. The results undoubtedly demonstrate that both adsorbate-adsorbent and adsorbate-adsorbate interactions rule the adsorption process. At low loadings, before all coordinatively unsaturated chromium sites are occupied, the MOF structure determines the shape of the isotherm and the molecular model used to simulate the polar sorbate is less important. A clear difference is found between fully fluorinated and hydroxylated MIL-101 structures for both methanol and water, demonstrating that partial charges on Cr drive the initial shape of the isotherm. At higher loadings, adsorbate-adsorbate interactions become much more important and the choice of especially the water model is crucial for the agreement between experimental and simulation results. The simplest SPC/E model reproduces experimental results with the best accuracy, in contrast to more advanced models like TIP5PEw, explained by the slightly stronger Coulombic interactions predicted by the former. For methanol the general TraPPE force field performs well. A composite type IV isotherm for methanol and a composite type V isotherm for water, according to the IUPAC classification, have been found. The heats of adsorption are in line with these conclusions. This effect has, to the best of our knowledge, not been observed in adsorption in microporous materials and highlights the complexity behind molecular simulations in periodic meso-structured materials.

3.1. INTRODUCTION

Synthetic crystalline micro- and mesoporous materials have been extensively researched during the last few decades [1]. Several unique aspects of these materials are responsible for their success: They have a very high and tunable adsorption capacity, active sites of different strengths can be generated in the frameworks. The size of their channels and cavities falls within the range of that of many molecules of interest, and many materials present excellent ion exchange capabilities and exciting electronic properties, ranging from insulators to conductors and semi-conductors [2, 3]. In addition, owing to their periodic nature, nano-structured materials are excellent playgrounds for scientists, since macroscopic events may be explained on the basis of interaction at molecular level.

Among the different classes, Metal Organic Frameworks (MOFs) bridge micro- and mesoporous materials and present unprecedented topological richness. The combination of organic and inorganic building blocks offers an almost infinite number of combinations, enormous flexibility in pore size, shape and structure, and unlimited opportunities for functionalization, grafting and encapsulation. These materials hold very high adsorption capacities, specific surface areas and pore volumes. Their porosity is much higher than that of their inorganic counterpart zeolites (up to 90% higher). Their thermal stability is sometimes unexpectedly high, reaching temperatures above 400°C. Obviously, MOFs have attracted much attention, the major studies have dealt with the synthesis of new structures [4], and most applications have focused on adsorption/separation [5-7], storage [8], encapsulation [9] and catalysis [10].

MOF materials like MIL-101 [11-13] and MIL-100 [12] (MIL stands for Material from Institut Lavoisier) offer tremendous possibilities for material engineers. These hybrid solid are built up from *super-tetrahedra* (ST) building units, which are formed by rigid terephthalic or trimesic acid linkers and trimeric chromium (III) oxide octahedral clusters. The resulting solids possess two types of quasi-spherical mesoporous cages limited by 12 pentagonal faces for the smaller and by 16 faces for the larger. The former so-called medium cavities are accessible through 1.2 nm (MIL-101) or 0.5 nm (MIL-100) pentagonal windows, while the latter large cavities are communicated through the same pentagonal windows and 1.5 nm (MIL-101) or 0.9 nm (MIL-100) hexagonal windows. Since the discovery of both structures,

numerous publications have reported on their excellent stability and on several perspective applications [14-23].

Since a very large number of MOFs have been synthesized to date, and many more are possible, the role of molecular simulations becomes even more important in order to screen the properties of new materials, to gain microscopic insight and to elucidate the underlying physics behind molecular interactions upon adsorption of different adsorbates. Adsorptive behavior of porous materials is indeed a key feature, since it is not only important for gas storage or separation, but also for other applications like catalysis or nano-medicine. To date, most simulation studies dealing with metal organic frameworks have focused on the adsorption and transport properties of small gases (mainly CO_2 and CH_4) in micro-porous MOFs [24-49]. When it comes to micro-mesoporous structures like MIL-101 and MIL-100, due to their unit cell complexity and to the large computational requirements, the number of simulation works is even lower [34, 50]. In addition, very little attention has been devoted to studying the interaction of polar vapors like water with MOFs, of the utmost importance for the stability for the "*real life*" application of these materials. The latter is mostly due to the complexity to describe the adsorption of such polar adsorbates, where the molecule-molecule interactions play a major role.

In this work we make a quantum leap in understanding adsorption of highly polar vapors on micro-meso-structured materials with the MIL-100 and MIL-101 topologies. Adsorption of water and methanol has been studied on both structures in a combined experimental and simulation approach: the main adsorption sites, mechanism of adsorption and the role of adsorbate-adsorbent and adsorbate-adsorbate interactions have been identified.

3.2. EXPERIMENTAL

All chemicals were obtained from Sigma–Aldrich and were used without further purification. Synthesis of MIL-101(Cr) was performed as previously reported in literature [11-13]. 1.63 g of chromium(III) nitrate, $Cr(NO_3)_3 \cdot 9H_2O$ (97%), 0.7 g of terephthalic acid, C_6H_4-1,4-$(CO_2H)_2$ (97%), 0.20 g of hydrofluoric acid, HF (40%), and 20 g of distilled water was added in a Teflon container, which was inserted in a stainless steel autoclave. The autoclave was heated for 8 h at 493 K in an oven under static conditions. After synthesis, the solid product was filtered from the synthesis solution. For activation, a solvothermal treatment was performed using ethanol (95% EtOH) at 353 K for 24 h. The resulting solid was exchanged in a 1M

solution of ammonium fluoride, NH_4F, at 343 K for 24 h and was immediately filtered off and washed with hot water. The solid was finally dried overnight at 433 K and stored under air atmosphere.

Synthesis of MIL-100(Cr) was performed in accordance with literature as well [12]. A mixture of 0.5 g chromium(VI) oxide, CrO_3, 1.05 g of trimesic acid, C_6H_3-1,3,5-$(CO_2H)_3$ (97%), 0.2 g hydrofluoric acid, HF, and 24 g of H_2O was added to a Teflon container and inserted in a stainless steel autoclave. This was then heated in an oven at 493 K for 4 days under static conditions. The resulting solid was filtered off, washed with deionized water and subsequently with acetone and finally dried overnight at 433 K and stored under air atmosphere.

Nitrogen physisorption measurements were performed at 77 K using a Quantachrome Autosorb-6B unit gas adsorption analyzer. Vapor adsorption isotherms were measured using a Quantachrome Autosorb 1C volumetric adsorption analyzer equipped with a vapor-dosing system. An equilibration time of 600 seconds has been used for all measurements. All samples were outgassed for 16 hours under vacuum at 473 K before adsorption analysis, for both nitrogen and vapor measurements. Pressures were converted to fugacities using the Peng-Robinson equation of state, valid for the low pressures in this work [51]. The isosteric heat of adsorption was estimated from isotherm measurements at 303 and 313 K. The isosteric enthalpy of adsorption, $\Delta_{ads}H$, for a given amount adsorbed, q, can be calculated from adsorption isotherms at two or more different temperatures, using [52]:

$$\Delta_{ads}H_q = R\left(\frac{\partial \ln p}{\partial \left(\frac{1}{T}\right)}\right)_q \tag{3.1}$$

Here R is the universal gas constant, p is the absolute pressure and T is the temperature. Using this equation, it is (tacitly) assumed that adsorption is fully reversible (no chemisorption occurs), that both the internal energy of the adsorbent surface and the adsorbent structure don't change during adsorption, and equilibrium is reached between adsorbent and adsorbate. Crystallinity was assessed using X-ray diffraction (XRD) with a Bruker-AXS D5005 (CoKα radiation).

3.3. SIMULATION METHODS

Both MIL-100(Cr) and MIL-101(Cr) were modeled as rigid structures, interacting with adsorptive molecules via Van der Waals and Coulombic interactions. The assumption of rigidity is often made when simulating adsorption in MOFs [53-55]. This is justified when pore dimensions exceed kinetic diameters of adsorptive molecules and when the structure does not undergo any significant adsorbent-induced deformation. The Van der Waals interactions were described by Lennard-Jones potentials, of which the parameters were taken from the DREIDING force field [56], except for chromium atoms for which UFF was used [57]. The partial charges, needed to describe the Coulombic interactions, were taken from Yazaydin [58] for the fluorinated structures. For the hydroxylated structure, the atomic charges were calculated with the code $Dmol^3$ [59] as implemented in the Accelrys software package Materials Studio [60] using the PW91 exchange-correlation functional [61] with the double numerical plus polarization (DNP) basis set. The cluster approach was employed to obtain the partial charges. The atom centered charges are those that best fit the Electrostatic Potential (ESP) of the cluster shown in Fig. B.1, which is a model of a chromium trimer in a mesoporous cage of MIL-101. It is well known that fluorine is involved in the terminal bond of the trimeric chromium species and partly substitutes the terminal water molecules attached to chromium in MIL-100 and MIL-101. Although it is not fully clear yet, it seems that the use of fluorine provides a strong interaction with chromium octahedral motif and the effective nuclei formation of MIL-101 during the hydrothermal reaction. In order to study the effect of fluorine on the adsorption of polar vapors, we employed the fully fluorinated structure of MIL-101 [58] as starting point and compared its adsorption properties with the structure where all fluorine atoms were exchanged by OH-groups. It should be stressed that in the real structure, a mixture of fluorinated and hydroxylated Cr trimers will be found. The full set of applied parameters is given in Table B.1. The original MIL-101(Cr) and MIL-100(Cr) unit cells were simplified to primitive unit cells using Materials Studio [60], by making use of symmetry. The volumes of these primitive cells are only one fourth of the original cubic cells (Table B.2) but are no longer cubic. As the initially reported cells are relatively large, MIL-101 occupies a volume of 90^3 $Å^3$, using primitive cells considerably decreases computational requirements, while describing equally well the MOF structures. Methanol was described using the transferable TraPPE force field for polar hydrocarbons [62] (Table B.3), which accurately describes vapor-liquid coexistence and is commonly used to describe methanol

adsorption in ordered porous materials [63-66]. For simulations concerning adsorption of water, there is no consensus on which molecular representation to use. Multiple models are available in literature, none of which is able to describe several arbitrarily chosen properties of water simultaneously [67]. In this work, three distinct water models were used to investigate the effect of water-water interactions during adsorption in mesoporous frameworks. Tip5Pew [68] was selected as it accurately reproduces liquid density and has been used previously for adsorption in microporous materials [63, 69]. SPC/E [70] is a relatively simple representation of water and therefore requires less computational power. This model has been applied to obtain a reasonable description of experimental adsorption data in microporous zeolites [71, 72]. The TIP4Pew [73] has been used for water adsorption because of good reproduction of bulk liquid properties [74]. All three models consider water as a rigid, non-polarizable molecule. Although these models might be less accurate in describing water properties, they require less computational efforts, a necessity considering the large unit cell size of the periodic systems under study. All three models assume a single Lennard-Jones interaction site, the oxygen, with similar parameterization. The main difference among these models is the incorporation of electrostatic interactions (Table 3.1, Fig. 3.1).

Table 3.1: Force field parameters for the water models used in this work.

Model	$\varepsilon_O k_b^{-1}$ / K	σ_O / Å	q_O / e	q_H / e	q_M / e	q_L / e
SPC/E [70]	78.2	3.1656	-0.8476	0.4238	-	-
TIP4PEw [73]	81.899	3.16435	-	0.52422	-1.04844	-
TIP5PEw [68]	89.633	3.097	-	0.241	-	-0.241
	l_{O-H} / Å	l_{O-M} / Å	l_{O-L} / Å	Θ_{H-O-H} / °	Θ_{H-O-M} / °	Θ_{L-O-L} / °
SPC/E	1	-	-	109.47	-	-
TIP4PEw	0.9572	0.125	-	104.52	52.26	-
TIP5PEw	0.9572	-	0.7	104.52	-	109.47
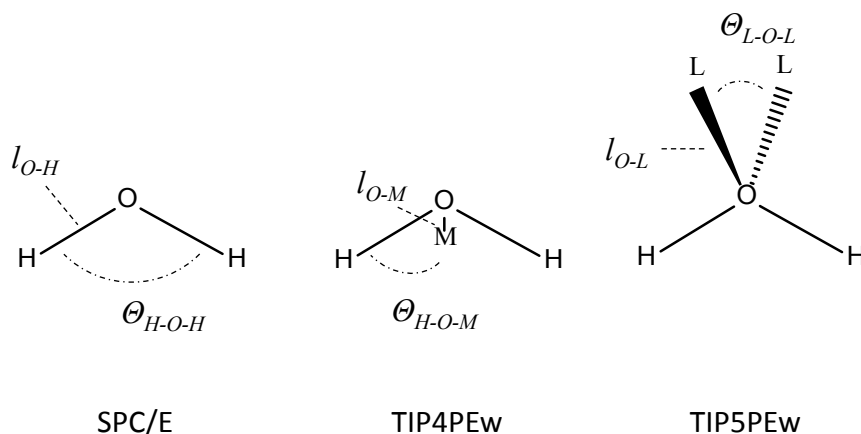
Figure 3.1: Representation of the water models used. Assigned values are presented in Table 3.1.

TIP5PEw has 2 dummy atoms to distribute the negative charge, TIP4PEw has a single dummy atom and SPC/E has the negative charge located on the oxygen atom. All mixed-pair potentials were calculated using Lorentz-Berthelot mixing rules. Lennard-Jones potentials were cut off and shifted at a radius of 12 Å. For electrostatics an Ewald summation [75] with relative precision of 10^{-6} was used for truncation of the Coulombic potentials at a radius of half the simulation box length. Adsorption isotherms were calculated using classical Monte Carlo simulations in the grand-canonical ensemble. In this ensemble, the chemical potential, volume and temperature are kept constant, allowing the number of adsorptive molecules to fluctuate. The chemical potential is fixed by fixing the fugacity. Monte Carlo moves include rotation, translation and (re-)insertion of adsorptive molecules. Heat of adsorption at zero coverage was calculated using the Widom particle insertion method in the canonical ensemble (fixed number of particles, volume and temperature) [76].
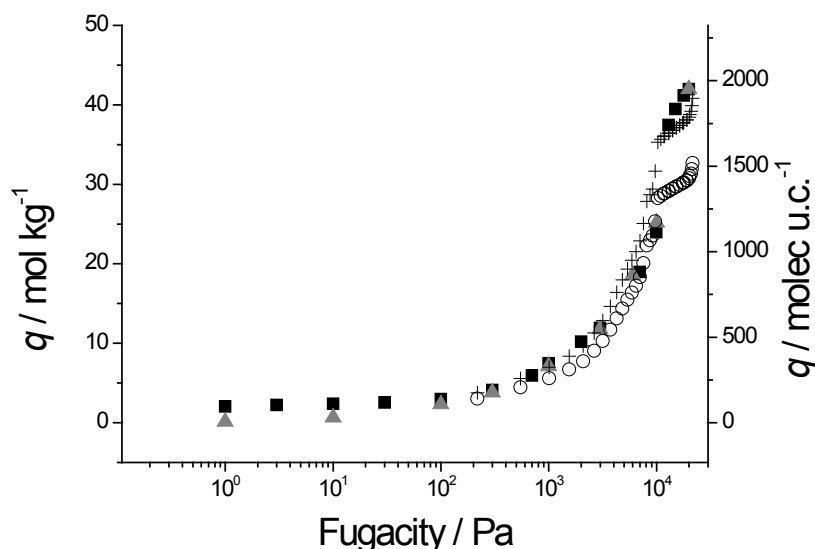
119
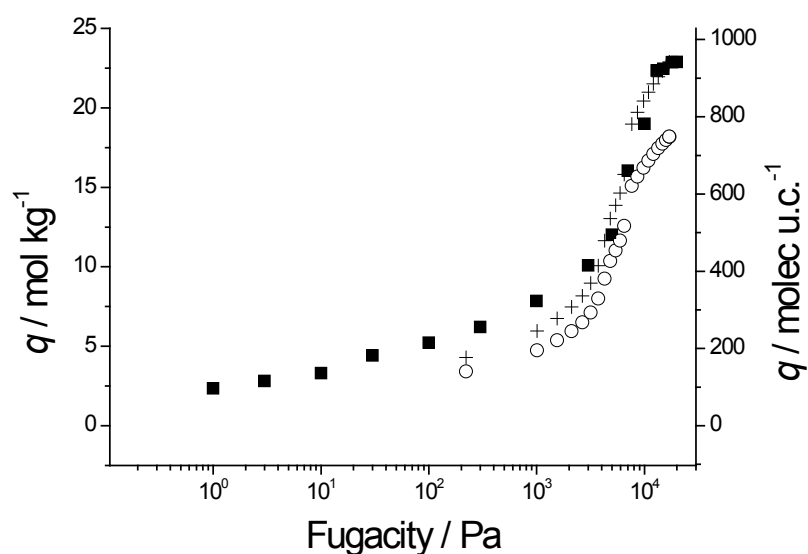
Figure 3.2: Simulated (■) and experimentally measured (○) adsorption of methanol on MIL-100(Cr) at 303 K and experimental results scaled by 5/4 (+).

The heat of adsorption at non-zero coverage was determined using the method developed by Vlugt *et al.* [77]. Radial distribution functions have been obtained by collecting and averaging the atomic positions of all atoms over more than thousand simulation cycles, after equilibration of the simulation box.

3.4. RESULTS AND DISCUSSION

The characterization results in Section B.2 show that synthesized MIL-100(Cr) and MIL-101(Cr) are both porous and crystalline. The simulated methanol adsorption results for MIL-100(Cr), together with experimental results, are depicted in Fig. 3.2. The shape of the isotherm found experimentally is reproduced with fair accuracy by simulations, though the obtained loading for simulations is higher. This comes as no surprise as the simulation uses a perfect crystal whereas the synthesized material is prone to have imperfections to a certain extent. If one scales the simulated results, common practice when combining simulations with experiments, to take into account the inaccessible porosity in the synthesized material [78-80], very good agreement is found at higher fugacities. At lower fugacities there is seemingly an overprediction of adsorption in the simulation. This might indicate that the employed partial charges are slightly too high. Polar compounds are generally sensitive to small changes in partial charges [69].

Figure 3.3: Simulated adsorption for fluorinated (■) and hydroxylated structure (▲) and experimentally measured (○) adsorption of methanol on MIL-101(Cr) at 303 K and experimental results scaled by 5/4 (+).

In Fig. 3.3 experimental methanol adsorption results are compared with simulations using both the fluorinated and the hydroxylated structure model of MIL-101. Results for both structures agree to a large extent with the scaled experimental results. At fugacities above 10^2 Pa, simulation results for both structures are very similar. Below this fugacity there is a discrepancy between the two simulation results. The difference can most likely be attributed to the partial charges of the coordinatively unsaturated chromium atoms. In the fluorinated structure these charges are higher (see Table B.1), hence the observed higher adsorption at very low fugacities. The absence of notable discrepancy between results for these two structures above 10^2 Pa shows that the effect of charge is diminished when sufficient methanol molecules have been adsorbed. The loading at this fugacity corresponds to ~140 molecules per unit cell, the total number of coordinatively unsaturated chromium sites present in the structure. If one were to extrapolate the experimentally found adsorption isotherm to lower fugacity, it would seem that this would correspond better to the hydroxylated structure. However no definitive qualitative discrimination can be made between the two structural representations of MIL-101 due to the lack of reliable experimental data at very low fugacities. The shape of the methanol isotherms on both MIL-100 and MIL-101 can be characterized by a combination of two IUPAC type IV isotherms, one corresponding to the medium and the other to the large cages, respectively [52]. This is visible when fugacity is depicted linearly, as shown in Fig. B.4.
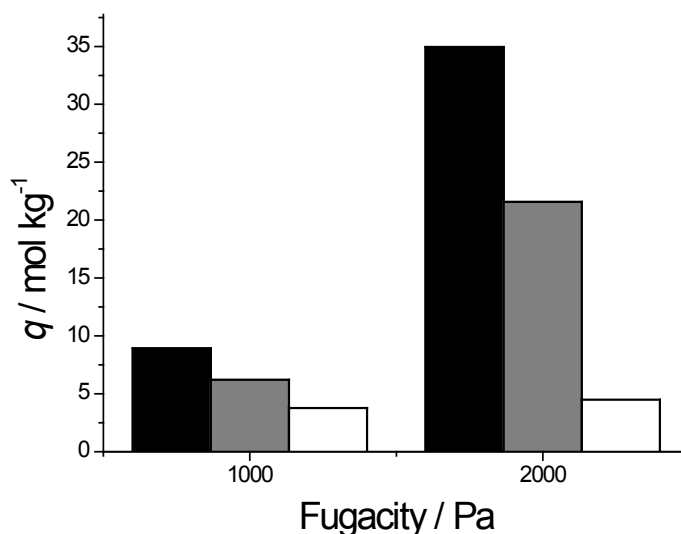
Figure 3.4: Simulated adsorption of water on fluorinated MIL-101(Cr) for two different fugacities at 303 K, for SPC/E (*black*), TIP4PEw (*grey*) and TIP5PEw (*white*).

As mentioned in the previous section, to describe water adsorption in MIL-100 and MIL-101 three distinct water models have been employed, SPC/E, TIP4PEw and TIP5PEw. To assess their individual performance, simulations have been performed using the different models for two intermediate fugacities in MIL-101(Cr). Results, shown in Fig. 3.4, clearly indicate a large difference in loading for the three different water models.

At both fugacities the loading is highest for the SPC/E model and lowest for TIP5PEw. As the Lennard-Jones interactions are quite similar for the different models, see Table 3.1, the difference is most likely due to the difference in Coulombic interactions. If one compares the dipole moments of the three models, see Table 3.2, it becomes apparent that a small increase in dipole moment leads to a significant increase in adsorption. On the other hand, every water model used underpredicts the liquid water dipole and overpredicts the water vapor dipole. This is a known problem [67], which could be circumvented by using polarizable models. However, considering the tremendous increase in computational expenditure of these models, doing so would be computationally infeasible. In the remainder of this work the SPC/E and TIP5PEw water models are used to investigate the effect of Coulombic interactions over a broad range of fugacities in both structures under study.
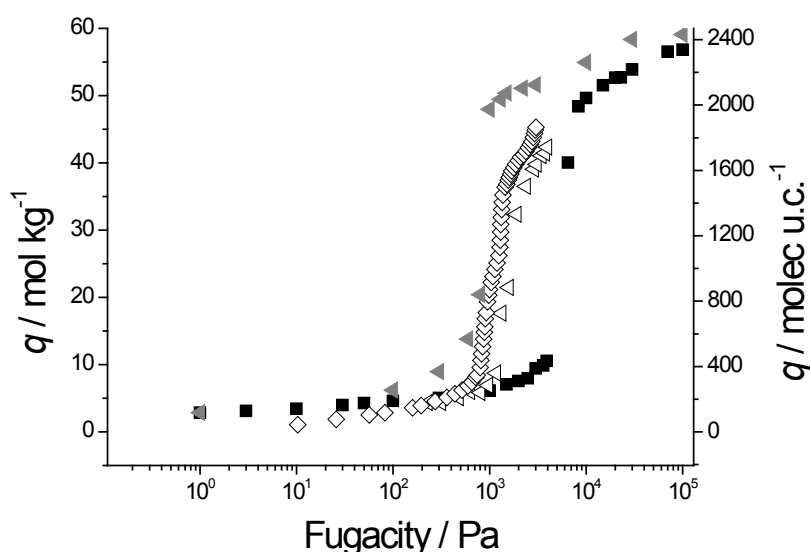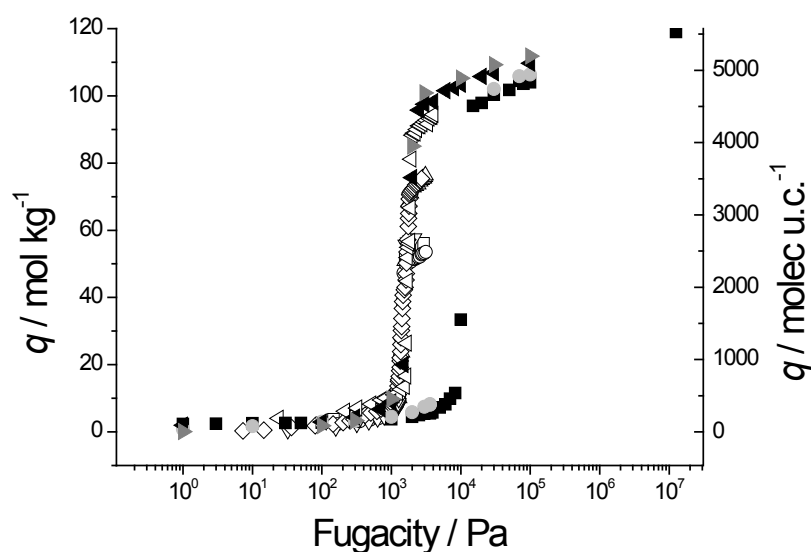
Figure 3.5: Simulated adsorption on MIL-100(Cr) using TIP5PEw (■) and SPC/E (◀) water models at 303 K. Experimental isotherms from Chang *et al.* (◁) [82] and Akiyama *et al.* (298 K, ◇) [83].

Table 3.2: Dipole moment of the used water models, compared to experimentally determined dipoles.

		Dipole moment / D
	SPC/E	2.35
Model	TIP4PEw	2.32
	TIP5PEw	2.29
	ice	3.09
Real [81]	liquid	2.95
	gas	1.85

In Fig. 3.5 the simulated adsorption results for both SPC/E and TIP5PEw, supplemented with experimental literature data for MIL-100(Cr) are shown. At low fugacities, there is no notable difference between the two models; both slightly overpredict the experimentally found adsorption. A striking difference is visible when comparing the fugacity at which both models predict the large step in uptake. For TIP5PEw this step occurs at a fugacity one order of magnitude higher than that found experimentally, while the fugacity for this step predicted with SPC/E is very close to those of the experiments. The difference can again be attributed to the different polarity of water in these models.

123

Figure 3.6: Simulated adsorption for fluorinated MIL-101(Cr) using TIP5PEw (■) and SPC/E water (◄) models and for hydroxylated MIL-101(Cr) using TIP5PEw (●) and SPC/E water (►) models at 303 K. Experimental data from Ehrenmann *et al.* (298 K, volumetrically (○) and gravimetrically(□)) [84], Küsgens *et al.* (298 K, △) [85], Akiyama *et al.* (298 K, ◇) [14], Chang *et al.* (◁) [82] and own experiments (▽).

For both fluorinated and hydroxylated MIL-101(Cr) simulated adsorption results for TIP5Ew and SPC/E, supplemented with experimental and literature data, are shown in Fig. 3.6 (low-fugacity regime shown in Fig. 3.7, for linear representation of fugacity of Figs. 3.3-3.6, see Section B.3). The experimental results in literature all show a characteristic step in water uptake at fugacities around 10^3 Pa. The quantity adsorbed at saturation, however, varies. This can be related to material quality. For MIL-101(Cr) it is known that synthesis conditions strongly influence the quality of the resulting material (*i.e.* some chromium oxide can precipitate together with the MOF) [86]. Since the only noticeable difference between the different experimental isotherms is in the saturation loading, it seems a plausible assumption that the imperfections in these materials do not play a role during adsorption. These impurities can be thought of as inaccessible parts that only effectively dilute the part of the material that is available for adsorption or as regions where formation of small amounts of non-porous phases (not noticeable by PXRD, Fig. B.3) had taken place. This assumption would justify the comparison with scaled experimental results.
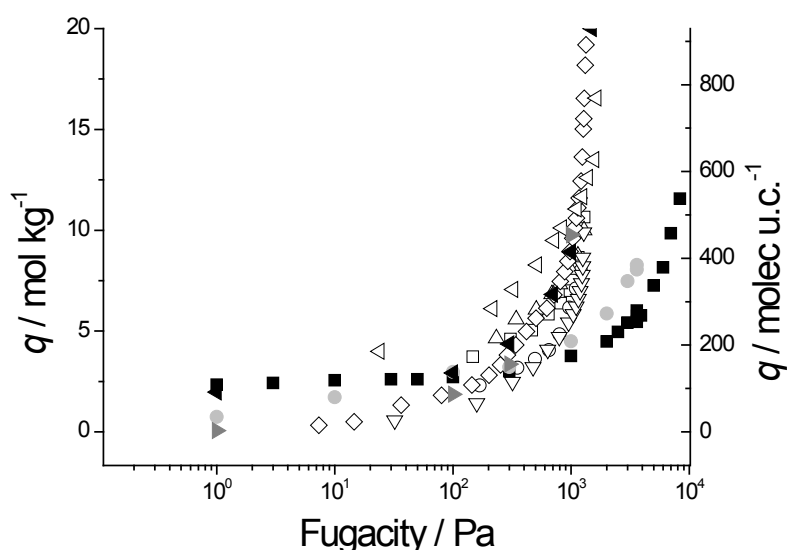
Figure 3.7: Low fugacity regime of Fig. 3.6. Simulated adsorption for fluorinated MIL-101(Cr) using TIP5PEw (■) and SPC/E water (◀) models and for hydroxylated MIL-101(Cr) using TIP5PEw (●) and SPC/E water (▶) models at 303 K. Experimental data from Ehrenmann *et al.* (298 K (○) and (□)) [84], Küsgens *et al.* (298 K, △) [85], Akiyama *et al.* (298 K, ◇) [14], Chang *et al.* (◁) [82] and own experiments (▽).

Identical to the findings for methanol on MIL-101(Cr), at loadings below 140 molecules per unit cell, there is a discrepancy between the results obtained for the hydroxylated and for the fluorinated structure. This can again be attributed to the difference in partial charges on the coordinatively unsaturated chromium sites. Above this loading threshold, the results for the hydroxylated and fluorinated structures are very similar. These conclusions hold individually for both the SPC/E and TIP5PEw model. Again, the correspondence between the hydroxylated and fluorinated structures suggest that the effect of the framework charges is negligible. As was the case for MIL-100(Cr), in MIL-101(Cr) the location of the uptake step occurs for TIP5Ew at fugacities one order of magnitude higher than those found experimentally. In contrast, as it was the case for MIL-100(Cr), when using the SPC/E model, experimental and simulation data are in good agreement. The large difference in adsorption observed as function of adsorbent polarity seems in contradiction with the statement that results for the hydroxylated and fluorinated structures are similar, as one of the key differences between these structures is in the partial charges employed. That this in fact is a paradox and not a contradiction lies in the fact that adsorbate-adsorbate interactions dominate the adsorption process once all the coordinatively unsaturated chromium sites are occupied.

This is plausible considering the achieved loading. Up to 5000 molecules of water can be present in a reduced unit cell of MIL-101(Cr), where there are only ~210 chromium sites, of which ~140 are coordinatively unsaturated. The increased dipole on SPC/E, with respect to TIP5PEw, clearly affects the affinity between water molecules. As a result, the step in adsorption occurs at a lower fugacity for SPC/E. The shape of the water isotherms on both MIL-100 and MIL-101 can be described by a combination of two IUPAC type V isotherms, one corresponding to the medium and one to the large cages, respectively [52]. The radial distribution functions at 10^2 Pa, see Section B.4, show the relative hydrophobicity of the structural fluor groups, compared to the structural hydroxyls. The ratio of water in close proximity to the unsaturated chromium over water close to the coordinated chromium sites is larger in fluorinated MIL-101 (*confer* Figs. B.9 and B.10). Water locates far away from the structural fluor groups (Fig. B.11), as evidenced by the second peak in the radial distribution corresponding to the distance between this fluor group and the oxygen of water is larger. Furthermore, these distributions indicate that the oxygen of the hydroxyl group and the hydrogen of water undergo a clear interaction in the hydroxylated structure (Fig. B.12).

The importance of adsorbate-adsorbate interactions in adsorption in these structures can also be observed in the heat of adsorption of water. As is shown in Fig. 3.8 or MIL-101(Cr), heat of adsorption drops very quickly from ~80 kJ mol^{-1} at very low loading to just above the heat of evaporation of water when loading is only slightly increased. This clearly indicates that water-water interactions rule adsorption after the chromium sites have been occupied. Expectedly, the heat of adsorption obtained by simulations using the SPC/E model are closer to the ones observed experimentally, in contrast to the TIP5PEw model. The heat of evaporation of bulk water at room temperature predicted by these two models, 48.9 kJ mol^{-1} and 43.4 kJ mol^{-1} for SPC/E [67] and TIP5Pew [68] respectively, explain the difference in heat of adsorption. In addition, before all coordinatively saturated chromium sites are occupied, the heat of adsorption observed for the hydroxylated structure is lower than that for the fluorinated one.
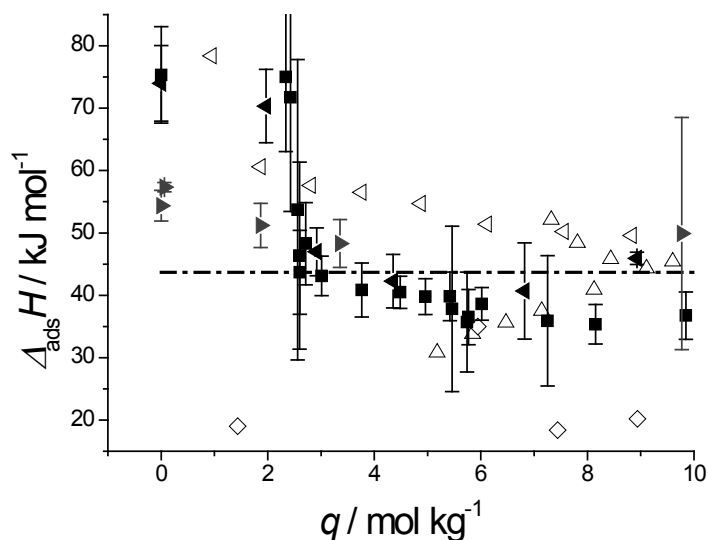
Figure 3.8: Simulated heat of adsorption of water for fluorinated MIL-101(Cr) for TIP5PEw (■) and SPC/E (◄) and for hydroxylated MIL-101(Cr) using SPC/E (►) at 303 K. Complemented by measured isosteric heat of adsorption from Chang *et al.* (◁) [82] and estimated heat of adsorption from Küsgens *et al.* (△)[85] and Akiyama *et al.* (◇) [14]. Dashed line indicates enthalpy of evaporation of water (at 303 K) [87]. Error bars indicate 95 % confidence interval.

For MIL-100(Cr), results depicted in Fig. 3.9 for water, the heat of adsorption decreases more gradually as a function of loading. These results demonstrate that structure-adsorbate interactions are relatively of more importance for MIL-100(Cr) at low to intermediate loadings: since the size of the MIL-100(Cr) cavities is smaller, thus less water molecules are adsorbed at saturation and thus the structure-adsorbate interactions become more important than in the case of MIL-101(Cr).
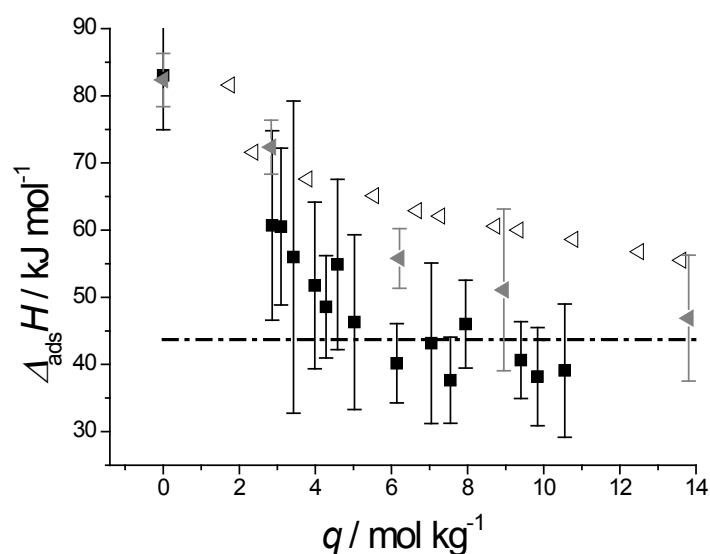
Figure 3.9: Simulated heat of adsorption of water on MIL-100(Cr) using TIP5PEw (■) and SPC/E (◀) water models at 303 K. Complemented by measured heat of adsorption on MIL-100(Fe) from Chang *et al.* (◁) [82]. Dashed line indicates enthalpy of evaporation of water (at 303 K) [87]. Error bars indicate 95 % confidence interval.

Heats of adsorption of methanol in MIL-100 and MIL-101, Figs. 3.10 and 3.11, show similar trends as for water: the heat of adsorption decreases from high values to values close to the heat of evaporation over a moderate increase in loading. The experimentally calculated heats of adsorption are in very good agreement with those found with simulations.

Fig. 3.12 shows the location of water molecules in both the medium and the large cage as function of loading (for methanol this is shown in Fig. B.13). Fig. 3.13 shows water located close to a supertetrahedron (Fig. B.14 for methanol).
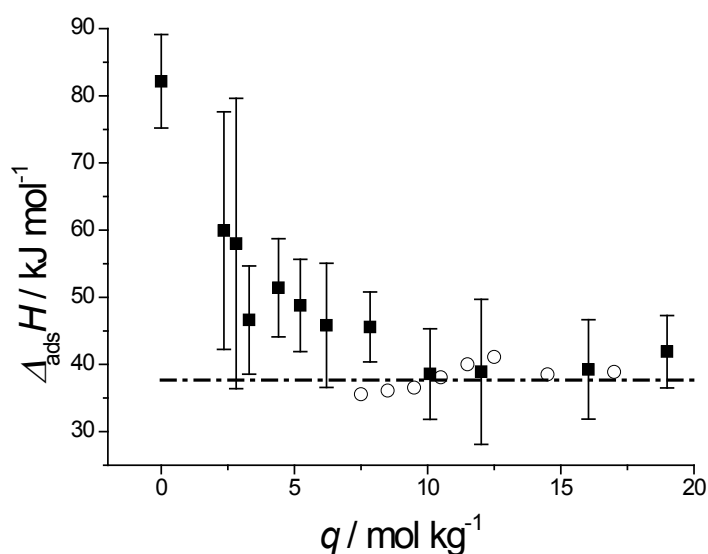
Figure 3.10: Simulated heat of adsorption of methanol on MIL-100(Cr) (■) and estimated isosteric heat of adsorption (using Eq. 3.1) (O). Dashed line indicates enthalpy of evaporation of methanol (at 303 K) [87]. Error bars indicate 95 % confidence interval.

Figure 3.11: Simulated heat of adsorption of methanol on fluorinated (■) and hydroxylated (▲) MIL-101(Cr) and estimated isosteric heat of adsorption (using Eq. 3.1) (O). Dashed line indicates enthalpy of evaporation of methanol (at 303 K) [87]. Error bars indicate 95 % confidence interval.
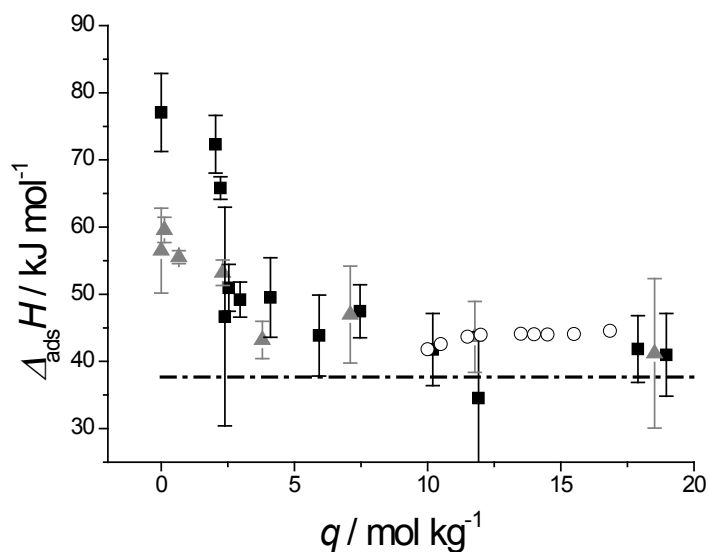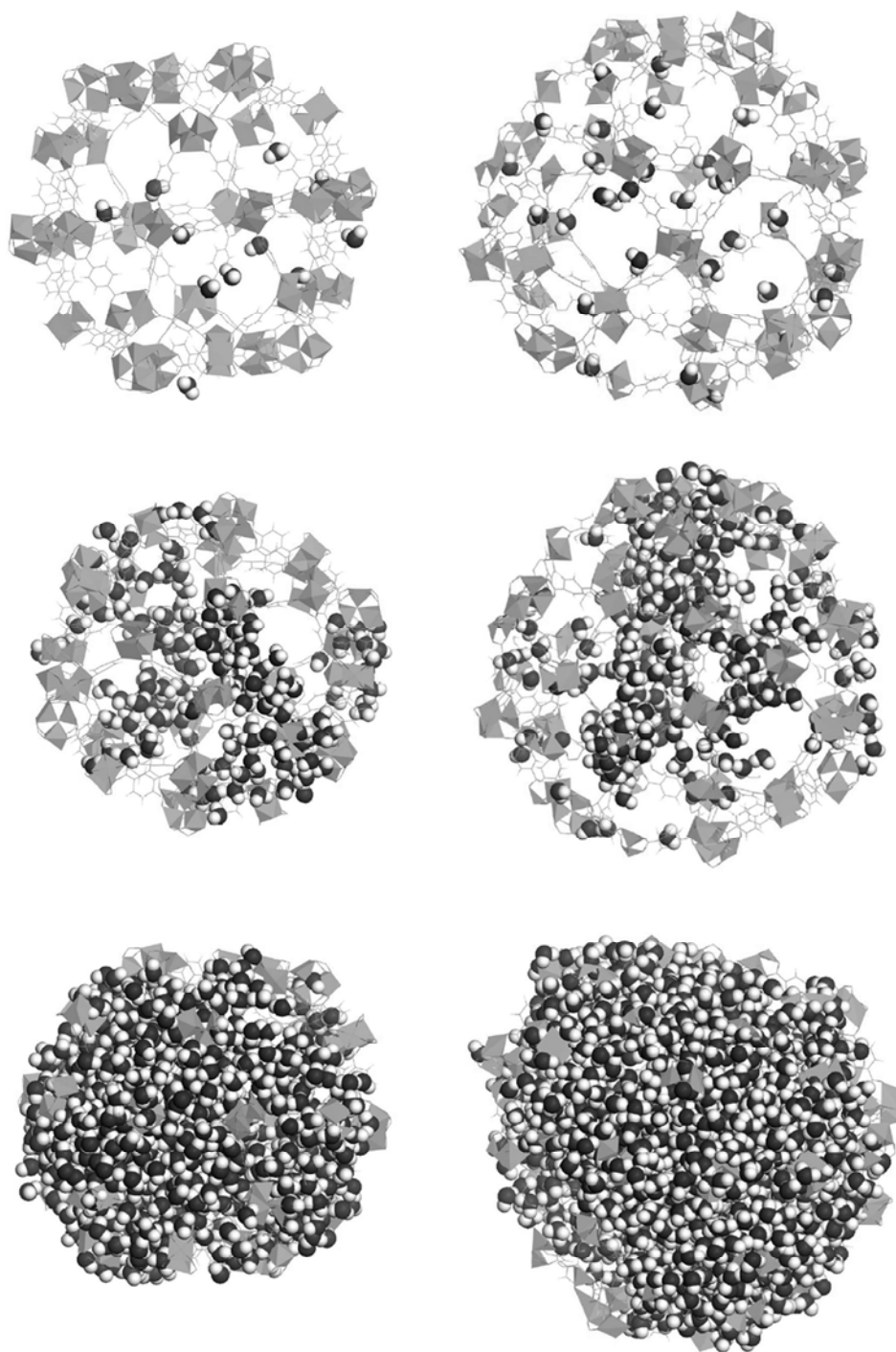
Figure 3.12: Water (SPC/e model, 303 K) located in medium (*left*) and large cage (*right*) for 1 Pa (*top*), 15 kPa (*middle*) and 30 kPa (*bottom*). Water shown with Van der Waals radii, chromium as polyhedra, and the organic ligands as lines. For a depiction in colors, the reader is kindly referred to the original text [88].
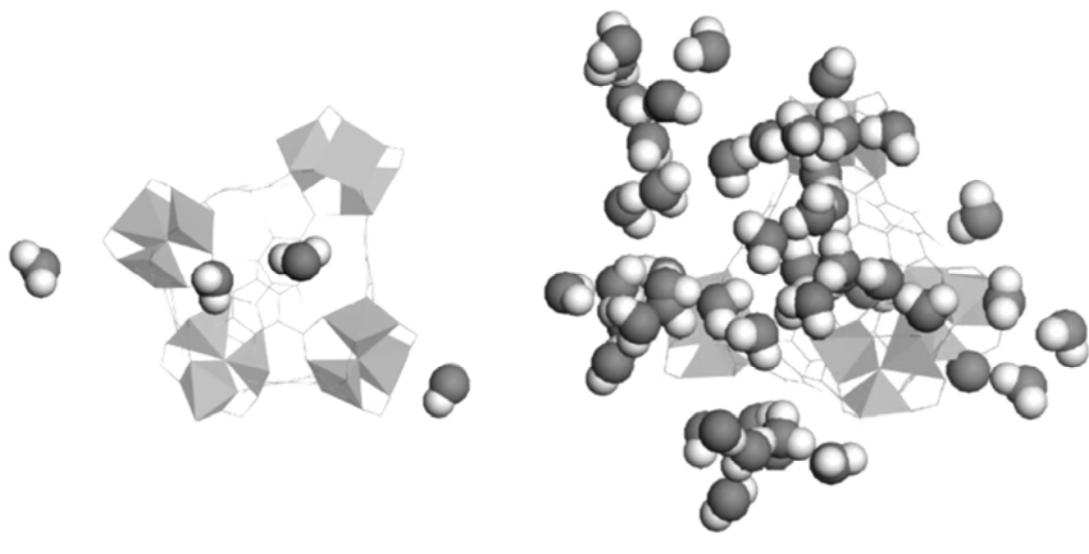
Figure 3.13: Water (SPC/E, 303 K) located close to a supertetrahedron, at 1 Pa (*left*) and 15 kPa (*right*). Water shown with Van der Waals radii, chromium as polyhedra, and the organic ligands as lines. For a depiction in colors, the reader is kindly referred to the original text [88].

Combined with the adsorption results, an adsorption process can be deduced. At low loading, below ~140 molecules per unit cell, the adsorbate molecules are only located next to the coordinatively unsaturated chromium atoms. As loading increases, adsorbate molecules start clustering around the molecules that were already present at these chromium sites, thus filling the windows of the cavities. When loading is increased further, the adsorbate molecules start filling the cavities completely. Overall this leads to a composite type IV isotherm for methanol and type V for water, according to the IUPAC classification [52].

3.5. CONCLUSIONS

Adsorption of polar vapors on mesoporous MOFs has been studied by a combination of experimental and simulation techniques. Our results undoubtedly demonstrate that both adsorbate-adsorbent and adsorbate-adsorbate interactions rule the adsorption process. At low loadings, before all coordinatively unsaturated chromium sites are occupied, the structure determines the shape of the isotherm and the water model is less important. A clear difference is found between fully fluorinated and hydroxylated MIL-101 structures for both methanol and water, demonstrating that Cr partial charges drive the initial shape of the isotherm. At higher loadings, adsorbate-adsorbate interactions become much more important and the choice of water model determines the agreement between experimental and simulated results. In this sense, the simplest SPC/E model reproduces experimental results with the best

131

accuracy in contrast to more advanced methods like TIP5PEw, attributed to the slightly higher Coulombic interactions predicted by the former. A composite type IV isotherm for methanol and a composite type V isotherm for water, according to the IUPAC classification have been found. The heat of adsorption results are in line with these conclusions. This is effect has, to the best of our knowledge, not been observed in adsorption in microporous materials and highlights the complexity behind molecular simulations in periodic meso-structured materials.

3.6. REFERENCES

[1]   F. Schuth, W. Schmidt, Microporous and mesoporous materials, Advanced Materials, 14 (2002) 629-638.
[2]   A. Corma, State of the art and future challenges of zeolites as catalysts, Journal of Catalysis, 216 (2003) 298-312.
[3]   A. Corma, H. Garcia, Zeolite-based photocatalysts, Chemical Communications, (2004) 1443-1459.
[4]   D.J. Tranchemontagne, J.L. Mendoza-Cortes, M. O'Keeffe, O.M. Yaghi, Secondary building units, nets and bonding in the chemistry of Metal-Organic Frameworks, Chemical Society Reviews, 38 (2009) 1257-1283.
[5]   J.R. Li, R.J. Kuppler, H.C. Zhou, Selective gas adsorption and separation in Metal-Organic Frameworks, Chemical Society Reviews, 38 (2009) 1477-1504.
[6]   S. Couck, J.F.M. Denayer, G.V. Baron, T. Remy, J. Gascon, F. Kapteijn, An amine-functionalized MIL-53 Metal-Organic Framework with large separation power for CO_2 and CH_4, Journal of the American Chemical Society, 131 (2009) 6326-6327.
[7]   C. Gücüyener, J. van den Bergh, J. Gascon, F. Kapteijn, Ethane/ethene separation turned on its head: Selective ethane adsorption on the Metal Organic Framework ZIF-7 through a gate-opening mechanism, Journal of the American Chemical Society, 132 (2010) 17704-17706.
[8]   L.J. Murray, M. Dinca, J.R. Long, Hydrogen storage in Metal-Organic Frameworks, Chemical Society Reviews, 38 (2009) 1294-1314.
[9]   J. Juan-Alcaniz, J. Gascon, F. Kapteijn, Metal-Organic Frameworks as scaffolds for the encapsulation of active species: State of the art and future perspectives, Journal of Materials Chemistry, 22 (2012) 10102-10118.
[10]   J. Gascon, U. Aktay, M.D. Hernandez-Alonso, G.P.M. van Klink, F. Kapteijn, Amino-based Metal-Organic Frameworks as stable, highly active basic catalysts, Journal of Catalysis, 261 (2009) 75-87.
[11]   G. Férey, C. Mellot-Draznieks, C. Serre, F. Millange, J. Dutour, S. Surblé, I. Margiolaki, A chromium terephthalate-based solid with unusually large pore volumes and surface area, Science, 309 (2005) 2040-2042.
[12]   P.L. Llewellyn, S. Bourrelly, C. Serre, A. Vimont, M. Daturi, L. Hamon, G. De Weireld, J.-S. Chang, D.-Y. Hong, Y. Kyu Hwang, S. Hwa Jhung, g.r. Férey, High uptakes of CO_2 and CH_4 in mesoporous Metal-Organic Frameworks MIL-100 and MIL-101, Langmuir, 24 (2008) 7245-7250.
[13]   J. Juan-Alcañiz, E.V. Ramos-Fernandez, U. Lafont, J. Gascon, F. Kapteijn, Building MOF bottles around phosphotungstic acid ships: One-pot synthesis of bi-functional polyoxometalate-MIL-101 catalysts, Journal of Catalysis, 269 (2010) 229-241.
[14]   G. Akiyama, R. Matsuda, H. Sato, A. Hori, M. Takata, S. Kitagawa, Effect of functional groups in MIL-101 on water sorption behavior, Microporous and Mesoporous Materials, 157 (2012) 89-93.
[15]   D. Jiang, L.L. Keenan, A.D. Burrows, K.J. Edler, Synthesis and post-synthetic modification of MIL-101(Cr)-NH$_2$ via a tandem diazotisation process, Chemical Communications, 48 (2012) 12053-12055.
[16]   J. Juan-Alcaniz, M. Goesten, A. Martinez-Joaristi, E. Stavitski, A.V. Petukhov, J. Gascon, F. Kapteijn, Live encapsulation of a keggin polyanion in NH$_2$-MIL-101(Al) observed by in situ time resolved x-ray scattering, Chemical Communications, 47 (2011) 8578-8580.
[17]   S.N. Klyamkin, E.A. Berdonosova, E.V. Kogan, K.A. Kovalenko, D.N. Dybtsev, V.P. Fedin, Influence of MIL-101 doping by ionic clusters on hydrogen storage performance up to 1900 bar, Chemistry-an Asian Journal, 6 (2011) 1854-1859.
[18]   E.V. Ramos-Fernandez, C. Pieters, B. van der Linden, J. Juan-Alcaniz, P. Serra-Crespo, M.W.G.M. Verhoeven, H. Niemantsverdriet, J. Gascon, F. Kapteijn, Highly dispersed platinum in Metal Organic

Framework NH_2-MIL-101(Al) containing phosphotungstic acid - characterization and catalytic performance, Journal of Catalysis, 289 (2012) 42-52.

[19] C.-X. Yang, X.-P. Yan, Metal-Organic Framework MIL-101(Cr) for high-performance liquid chromatographic separation of substituted aromatics, Analytical Chemistry, 83 (2011) 7144-7150.

[20] A. Dhakshinamoorthy, M. Alvaro, P. Horcajada, E. Gibson, M. Vishnuvarthan, A. Vimont, J.-M. Greneche, C. Serre, M. Daturi, H. Garcia, Comparison of porous iron trimesates basolite F300 and MIL-100(Fe) as heterogeneous catalysts for lewis acid and oxidation reactions: Roles of structural defects and stability, Acs Catalysis, 2 (2012) 2060-2065.

[21] J. Juan-Alcaniz, M.G. Goesten, E.V. Ramos-Fernandez, J. Gascon, F. Kapteijn, Towards efficient polyoxometalate encapsulation in MIL-100(Cr): Influence of synthesis conditions, New Journal of Chemistry, 36 (2012) 977-987.

[22] E. Soubeyrand-Lenoir, C. Vagner, J.W. Yoon, P. Bazin, F. Ragon, Y.K. Hwang, C. Serre, J.-S. Chang, P.L. Llewellyn, How water fosters a remarkable 5-fold increase in low-pressure CO_2 uptake within mesoporous MIL-100(Fe), Journal of the American Chemical Society, 134 (2012) 10174-10181.

[23] S. Wuttke, P. Bazin, A. Vimont, C. Serre, Y.-K. Seo, Y.K. Hwang, J.-S. Chang, G. Ferey, M. Daturi, Discovering the active sites for C3 separation in MIL-100(Fe) by using operando IR spectroscopy, Chemistry-a European Journal, 18 (2012) 11959-11967.

[24] M. Arici, O.Z. Yesilel, S. Keskin, M. Tas, A three-dimensional silver(I) framework assembled from 3,3 '-thiodipropionate: Synthesis, structure and molecular simulations for hydrogen gas adsorption, Polyhedron, 45 (2012) 103-106.

[25] E. Atci, S. Keskin, Atomically detailed models for transport of gas mixtures in ZIF membranes and ZIF/polymer composite membranes, Industrial & Engineering Chemistry Research, 51 (2012) 3091-3100.

[26] S. Calero, J. Jose Gutierrez-Sevillano, E. Garcia-Perez, Effect of the molecular interactions on the separation of nonpolar mixtures using Cu-BTC Metal-Organic Framework, Microporous and Mesoporous Materials, 165 (2013) 79-83.

[27] S. Calero, A. Martin-Calvo, S. Hamad, E. Garcia-Perez, On the performance of Cu-BTC Metal Organic Framework for carbon tetrachloride gas removal, Chemical Communications, 47 (2011) 508-510.

[28] J.M. Castillo, T.J.H. Vlugt, S. Calero, Understanding water adsorption in Cu-BTC Metal-Organic Frameworks, Journal of Physical Chemistry C, 112 (2008) 15934-15939.

[29] C. Chmelik, J. Kaerger, M. Wiebcke, J. Caro, J.M. van Baten, R. Krishna, Adsorption and diffusion of alkanes in CuBTC crystals investigated using infra-red microscopy and molecular simulations, Microporous and Mesoporous Materials, 117 (2009) 22-32.

[30] A.N. Dickey, A.O. Yazaydin, R.R. Willis, R.Q. Snurr, Screening CO_2/N_2 selectivity in Metal-Organic Frameworks using Monte Carlo simulations and ideal adsorbed solution theory, Canadian Journal of Chemical Engineering, 90 (2012) 825-832.

[31] I. Erucar, S. Keskin, Screening Metal-Organic Framework-based mixed-matrix membranes for CO_2/CH_4 separations, Industrial & Engineering Chemistry Research, 50 (2011) 12606-12616.

[32] I. Erucar, S. Keskin, Computational screening of Metal Organic Frameworks for mixed matrix membrane applications, Journal of Membrane Science, 407 (2012) 221-230.

[33] E. Haldoupis, T. Watanabe, S. Nair, D.S. Sholl, Quantifying large effects of framework flexibility on diffusion in MOFs: CH_4 and CO_2 in ZIF-8, ChemPhysChem, 13 (2012) 3449-3452.

[34] L. Hamon, N. Heymans, P.L. Llewellyn, V. Guillerm, A. Ghoufi, S. Vaesen, G. Maurin, C. Serre, G. De Weireld, G.D. Pirngruber, Separation of CO_2-CH_4 mixtures in the mesoporous MIL-100(Cr) MOF: Experimental and modelling approaches, Dalton Transactions, 41 (2012) 4052-4059.

[35] H. Huang, W. Zhang, D. Liu, B. Liu, G. Chen, C. Zhong, Effect of temperature on gas adsorption and separation in ZIF-8: A combined experimental and molecular simulation study, Chemical Engineering Science, 66 (2011) 6297-6305.

[36] N. Lamia, M. Jorge, M.A. Granato, F.A. Almeida Paz, H. Chevreau, A.E. Rodrigues, Adsorption of propane, propylene and isobutane on a Metal-Organic Framework: Molecular simulation and experiment, Chemical Engineering Science, 64 (2009) 3246-3259.

[37] A. Lyubchyk, I.A.A.C. Esteves, F.J.A.L. Cruz, J.P.B. Mota, Experimental and theoretical studies of supercritical methane adsorption in the MIL-53(Al) metal organic framework, Journal of Physical Chemistry C, 115 (2011) 20628-20638.

[38] A. Martin-Calvo, F.D. Lahoz-Martin, S. Calero, Understanding carbon monoxide capture using Metal Organic Frameworks, Journal of Physical Chemistry C, 116 (2012) 6655-6663.

[39] C. Petit, L. Huang, J. Jagiello, J. Kenvin, K.E. Gubbins, T.J. Bandosz, Toward understanding reactive adsorption of ammonia on Cu-MOF/graphite oxide nanocomposites, Langmuir, 27 (2011) 13043-13051.

[40]   N.A. Ramsahye, T. Thuy Khuong, S. Bourrelly, Q. Yang, T. Devic, G. Maurin, P. Horcajada, P.L. Llewellyn, P. Yot, C. Serre, Y. Filinchuk, F. Fajula, G. Ferey, P. Trens, Influence of the organic ligand functionalization on the breathing of the porous iron terephthalate Metal Organic Framework type material upon hydrocarbon adsorption, Journal of Physical Chemistry C, 115 (2011) 18683-18695.

[41]   N. Rosenbach, Jr., A. Ghoufi, I. Deroche, P.L. Llewellyn, T. Devic, S. Bourrelly, C. Serre, G. Ferey, G. Maurin, Adsorption of light hydrocarbons in the flexible MIL-53(Cr) and rigid MIL-47(V) metal-organic frameworks: A combination of molecular simulations and microcalorimetry/gravimetry measurements, Physical Chemistry Chemical Physics, 12 (2010) 6428-6437.

[42]   F. Salles, S. Bourrelly, H. Jobic, T. Devic, V. Guillerm, P. Llewellyn, C. Serre, G. Ferey, G. Maurin, Molecular insight into the adsorption and diffusion of water in the versatile hydrophilic/hydrophobic flexible MIL-53(Cr) MOF, Journal of Physical Chemistry C, 115 (2011) 10764-10776.

[43]   F. Salles, H. Jobic, T. Devic, P.L. Llewellyn, C. Serre, G. Ferey, G. Maurin, Self and transport diffusivity of CO_2 in the Metal-Organic Framework MIL-47(V) explored by quasi-elastic neutron scattering experiments and molecular dynamics simulations, Acs Nano, 4 (2010) 143-152.

[44]   R.A. Sarmiento-Perez, L. Marleny Rodriguez-Albelo, A. Gomez, M. Autie-Perez, D.W. Lewis, A. Rabdel Ruiz-Salvador, Surprising role of the BDC organic ligand in the adsorption of CO_2 by MOF-5, Microporous and Mesoporous Materials, 163 (2012) 186-191.

[45]   D. Wu, C. Wang, B. Liu, D. Liu, Q. Yang, C. Zhong, Large-scale computational screening of Metal-Organic Frameworks for CH_4/H_2 separation, AIChE Journal, 58 (2012) 2078-2084.

[46]   Q. Yang, H. Jobic, F. Salles, D. Kolokolov, V. Guillerm, C. Serre, G. Maurin, Probing the dynamics of CO_2 and CH_4 within the porous zirconium terephthalate UiO-66(Zr): A synergic combination of neutron scattering measurements and molecular simulations, Chemistry-a European Journal, 17 (2011) 8882-8889.

[47]   Q. Yang, S. Vaesen, M. Vishnuvarthan, F. Ragon, C. Serre, A. Vimont, M. Daturi, G. De Weireld, G. Maurin, Probing the adsorption performance of the hybrid porous MIL-68(Al): A synergic combination of experimental and modelling tools, Journal of Materials Chemistry, 22 (2012) 10210-10220.

[48]   W. Zhuang, D. Yuan, D. Liu, C. Zhong, J.-R. Li, H.-C. Zhou, Robust Metal-Organic Framework with an octatopic ligand for gas adsorption and separation: Combined characterization by experiments and molecular simulation, Chemistry of Materials, 24 (2012) 18-25.

[49]   D. Dubbeldam, R. Krishna, S. Calero, A.Ö. Yazaydın, Computer-assisted screening of ordered crystalline nanoporous adsorbents for separation of alkane isomers, Angewandte Chemie International Edition, 51 (2012) 11867-11871.

[50]   Y.F. Chen, R. Babarao, S.I. Sandler, J.W. Jiang, Metal Organic Framework MIL-101 for adsorption and effect of terminal water molecules: From quantum mechanics to molecular simulation, Langmuir, 26 (2010) 8743-8750.

[51]   B.E. Poling, J.M. Prausnitz, J.P. O'Connel, The properties of gases and liquids, 5th ed., McGraw-Hill, 2001.

[52]   F. Rouquerol, J. Rouquerol, K. Sing, Adsorption by powders & porous solids, Academic Press, London, 1999.

[53]   T. Duren, Y.-S. Bae, R.Q. Snurr, Using molecular simulation to characterise Metal-Organic Frameworks for adsorption applications, Chemical Society Reviews, 38 (2009) 1237-1247.

[54]   S. Keskin, J. Liu, R.B. Rankin, J.K. Johnson, D.S. Sholl, Progress, opportunities, and challenges for applying atomically detailed modeling to molecular adsorption and transport in Metal-Organic Framework materials, Industrial & Engineering Chemistry Research, 48 (2008) 2355-2371.

[55]   J.-R. Li, Y. Ma, M.C. McCarthy, J. Sculley, J. Yu, H.-K. Jeong, P.B. Balbuena, H.-C. Zhou, Carbon dioxide capture-related gas adsorption and separation in Metal-Organic Frameworks, Coordination Chemistry Reviews, 255 (2011) 1791-1823.

[56]   S.L. Mayo, B.D. Olafson, W.A. Goddard, DREIDING: A generic force field for molecular simulations, The Journal of Physical Chemistry, 94 (1990) 8897-8909.

[57]   A.K. Rappe, C.J. Casewit, K.S. Colwell, W.A. Goddard, W.M. Skiff, UFF, a full periodic table force field for molecular mechanics and molecular dynamics simulations, Journal of the American Chemical Society, 114 (1992) 10024-10035.

[58]   A.Ö. Yazaydın, Internal communication, 2011.

[59]   B. Delley, From molecules to solids with the DMol 3 approach, Journal of Chemical Physics, 113 (2000) 7756-7764.

[60]   Materials studio v4.4, accelrys software inc. (c), san diego, ca, 2009.

[61]   J.P. Perdew, Generalized gradient approximations for exchange and correlation: A look backward and forward, Physica B: Physics of Condensed Matter, 172 (1991) 1-6.

[62] B. Chen, J.J. Potoff, J.I. Siepmann, Monte Carlo calculations for alcohols and their mixtures with alkanes. Transferable potentials for phase equilibria. 5. United-atom description of primary, secondary, and tertiary alcohols, The Journal of Physical Chemistry B, 105 (2001) 3093-3104.

[63] J. Kuhn, J.M. Castillo-Sanchez, J. Gascon, S. Calero, D. Dubbeldam, T.J.H. Vlugt, F. Kapteijn, J. Gross, Adsorption and diffusion of water, methanol, and ethanol in all-silica DD3R: Experiments and simulation, The Journal of Physical Chemistry C, 113 (2009) 14290-14301.

[64] A. Nalaparaju, X.S. Zhao, J.W. Jiang, Molecular understanding for the adsorption of water and alcohols in hydrophilic and hydrophobic zeolitic Metal-Organic Frameworks, The Journal of Physical Chemistry C, 114 (2010) 11542-11550.

[65] R.P. Lively, M.E. Dose, J.A. Thompson, B.A. McCool, R.R. Chance, W.J. Koros, Ethanol and water adsorption in methanol-derived ZIF-71, Chemical Communications, 47 (2011) 8667-8669.

[66] J. Zang, S. Chempath, S. Konduri, S. Nair, D.S. Sholl, Flexibility of ordered surface hydroxyls influences the adsorption of molecules in single-walled aluminosilicate nanotubes, The Journal of Physical Chemistry Letters, 1 (2010) 1235-1240.

[67] B. Guillot, A reappraisal of what we have learnt during three decades of computer simulations on water, Journal of Molecular Liquids, 101 (2002) 219-260.

[68] S.W. Rick, A reoptimization of the five-site water potential (TIP5P) for use with Ewald sums, Journal of Chemical Physics, 120 (2004) 6085-6093.

[69] J.M. Castillo, T.J.H. Vlugt, S.a. Calero, Understanding water adsorption in Cu-BTC Metal-Organic Frameworks, The Journal of Physical Chemistry C, 112 (2008) 15934-15939.

[70] H.J.C. Berendsen, J.R. Grigera, T.P. Straatsma, The missing term in effective pair potentials, The Journal of Physical Chemistry, 91 (1987) 6269-6271.

[71] S. Henninger, F. Schmidt, H.M. Henning, Characterisation and improvement of sorption materials with molecular modeling for the use in heat transformation applications, Adsorption, (2011) 1-11.

[72] É. Csányi, Z.Ható, T. Kristóf, Molecular simulation of water removal from simple gases with zeolite Naa, Journal of Molecular Modeling, 18 (2012) 2349-2356.

[73] H.W. Horn, W.C. Swope, J.W. Pitera, J.D. Madura, T.J. Dick, G.L. Hura, T. Head-Gordon, Development of an improved four-site water model for biomolecular simulations: TIP4P-Ew, Journal of Chemical Physics, 120 (2004) 9665-9678.

[74] S. Paranthaman, F.-X. Coudert, A.H. Fuchs, Water adsorption in hydrophobic MOF channels, Physical Chemistry Chemical Physics, 12 (2010) 8123-8129.

[75] P.P. Ewald, Die berechnung optischer und elektrostatischer gitterpotentiale, Annalen der Physik, 369 (1921) 253-287.

[76] A.L. Myers, P.A. Monson, Adsorption in porous materials at high pressure: Theory and experiment, Langmuir, 18 (2002) 10261-10273.

[77] T.J.H. Vlugt, E. García-Pérez, D. Dubbeldam, S. Ban, S. Calero, Computing the heat of adsorption using molecular simulations: The effect of strong coulombic interactions, Journal of Chemical Theory and Computation, 4 (2008) 1107-1118.

[78] E. García-Pérez, J. Gascón, V.c. Morales-Flórez, J.M. Castillo, F. Kapteijn, S.a. Calero, Identification of adsorption sites in Cu-BTC by experimentation and molecular simulation, Langmuir, 25 (2009) 1725-1731.

[79] D. Dubbeldam, H. Frost, K.S. Walton, R.Q. Snurr, Molecular simulation of adsorption sites of light gases in the Metal-Organic Framework IRMOF-1, Fluid Phase Equilibria, 261 (2007) 152-161.

[80] S. Surblé, F. Millange, C. Serre, T. Düren, M. Latroche, S. Bourrelly, P.L. Llewellyn, G. Férey, Synthesis of MIL-102, a chromium carboxylate Metal-Organic Framework, with gas sorption analysis, Journal of the American Chemical Society, 128 (2006) 14889-14896.

[81] IAPWS, Guideline on the Use of Fundamental Physical Constants and Basic Constants of Water, September (2001).

[82] J.-S. Chang, Porous metal(III) carboxylates as multifunctional adsorbents and catalytic materials, iCeMS-ERATO Symposium, July 26th, 2012.

[83] G. Akiyama, R. Matsuda, S. Kitagawa, Highly porous and stable coordination polymers as water sorption materials, Chemistry Letters, 39 (2010) 360-361.

[84] J. Ehrenmann, S.K. Henninger, C. Janiak, Water adsorption characteristics of MIL-101 for heat-transformation applications of MOFs, European Journal of Inorganic Chemistry, 2011 (2011) 471-474.

[85] P. Küsgens, M. Rose, I. Senkovska, H. Fröde, A. Henschel, S. Siegle, S. Kaskel, Characterization of Metal-Organic Frameworks by water adsorption, Microporous and Mesoporous Materials, 120 (2009) 325-330.

[86] D.-Y. Hong, Y.K. Hwang, C. Serre, G. Férey, J.-S. Chang, Porous chromium terephthalate MIL-101 with coordinatively unsaturated sites: Surface functionalization, encapsulation, sorption and catalysis, Advanced Functional Materials, 19 (2009) 1537-1552.

[87]   D.W. Green, R.H. Perry, Perry's chemical engineers' handbook, 8th ed., McGraw-Hill, 2008.

[88]   M.F. De Lange, J.-J. Gutierrez-Sevillano, S. Hamad, T.J.H. Vlugt, S. Calero, J. Gascon, F. Kapteijn, Understanding adsorption of highly polar vapors on mesoporous MIL-100(Cr) and MIL-101(Cr): Experiments and molecular simulations, The Journal of Physical Chemistry C, 117 (2013) 7613-7622.
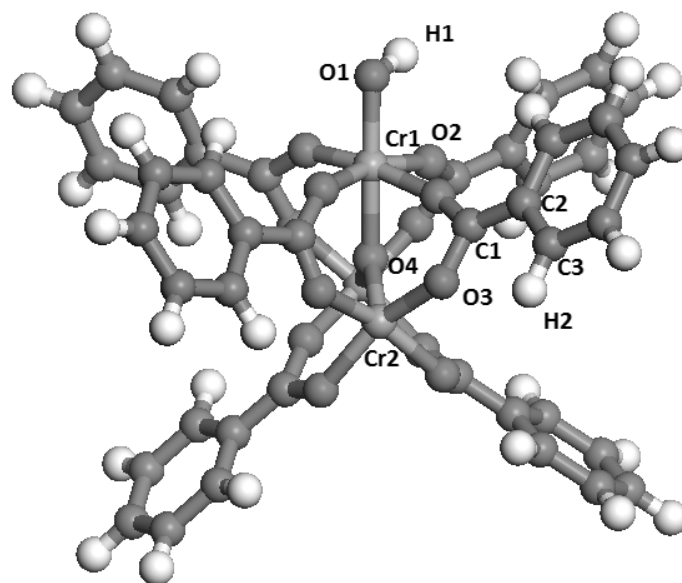
APPENDIX B

UNDERSTANDING ADSORPTION OF
HIGHLY POLAR VAPORS ON MESOPOROUS
MIL-100(Cr) AND MIL-101(Cr)

Figure B.1: Structure of the cluster employed to calculate the atomic charges of MIL-101-OH. The numbers are used as a help to identify the atomic charges of the atoms reported in Table B.1. Same labels apply for fluorinated MIL-101 and MIL-100, only O1-H1 is replaced by F. For a more insightful depiction in colors, the reader is kindly referred to the original text [1].

B.1. FORCE FIELD PARAMETERS

The structure of the cluster employed to calculate the atomic charges of MIL-101-OH is shown in Fig. B.1. The atomic charges and Lennard-Jones parameters for all atoms of the structures used in this study are listed in Table. B.1. Table B.2 contains the unit cell parameters and total number of structure atoms present for both the cubic and primitive unit cells of the three structures under study. In Table B.3 the force field parameters for methanol are shown. The force field parameters of the different water models are given in Table 3.1.

Table B.1: Lennard-Jones parameters and partial charges used. For MIL-101 and MIL-100 charges are obtained from Yazaydin, for MIL-101-OH they are calculated by performing a ESP fitting of the electrostatic potential calculated with a PW91/DNP calculation of the cluster shown in Fig. B.1.

Atom	$\varepsilon\, k_b^{-1}$ [2, 3]	σ [2, 3]	Charges / e		
	K	Å	MIL-101[4]	MIL-100[4]	MIL-101-OH
Cr1	7.54829	2.69319	1.35	1.62	1.28
Cr2	7.54829	2.69319	1.619	1.859	1.44
O1	-	-	-	-	-0.76
O2	48.1581	3.03315	-0.574	-0.731	-0.58
O3	48.1581	3.03315	-0.438	-0.587	-0.65
O4	48.1581	3.03315	-0.853	-1.28	-0.67
C1	47.8562	3.47299	0.496	0.848	0.74
C2	47.8562	3.47299	-0.07	-0.274	-0.12
C3	47.8562	3.47299	-0.058	0.11	-0.1
F	36.4834	3.0932	-0.547	-0.566	-
H1	-	-	-	-	0.35
H2	7.64893	2.84642	0.108	0.1	0.16

Table B.2: Unit cell parameters of MIL-100 and MIL-101 for both the cubic and primitive unit cell.

Unit cell parameters	MIL-101		MIL-100		MIL-101-OH	
	Cubic	Primitive	Cubic	Primitive	Cubic	Primitive
a, b, c / Å	89	63	73	52	89	63
α, β, γ / °	90	60	90	60	90	60
Structure atoms / -	14416	3604	11152	2788	14688	3672

Table B.3: Parameters used to describe methanol, as taken from the TraPPE force field [5].

Atom	$\varepsilon\, k_b^{-1}$ / K	σ / Å	Charge / e
CH3-alc	98	3.75	0.265
O-alc	93	3.02	-0.7
H-alc	-	-	0.435
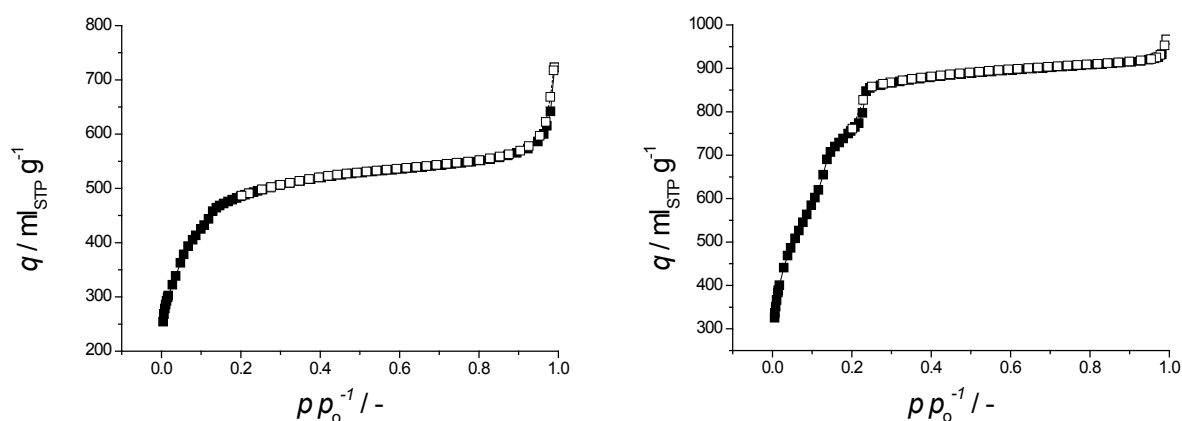
Figure B.2: Nitrogen adsorption isotherms (77 K) of MIL-100(Cr) (*left*) and MIL-101(Cr) (*right*). Open symbols for adsorption, closed for desorption. Here p_o is the saturated vapor pressure at measurement temperature and STP refers to standard temperature and pressure (0 ^{o}C, 1 bar).
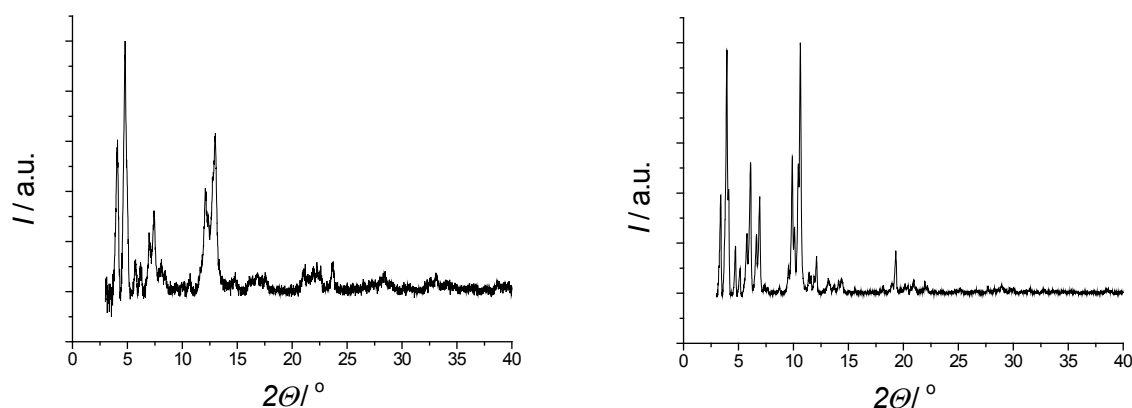
Figure B.3: X-ray diffraction patterns of MIL-100(Cr) (*left*) and MIL-101(Cr) (*right*).

B.2. CHARACTERIZATION OF SYNTHESIZED MATERIALS

Nitrogen adsorption isotherms (Fig. B.2) and XRD patterns (Fig. B.3) for both MIL-100(Cr) and MIL-101(Cr) are shown. These figures both indicate the successful synthesis of both materials. Measured methanol isotherms on both materials are shown in Fig. B.4.
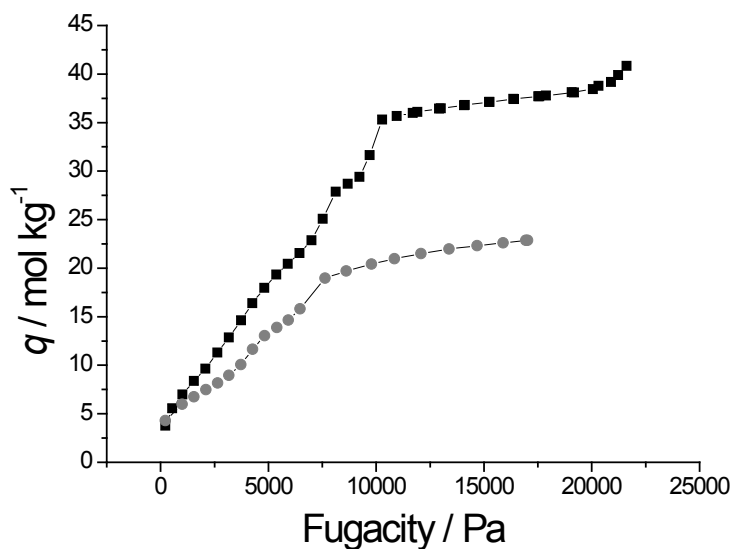
Figure B.4: Measured adsorption isotherms of methanol (303 K) on MIL-100 (●) and MIL-101 (■).
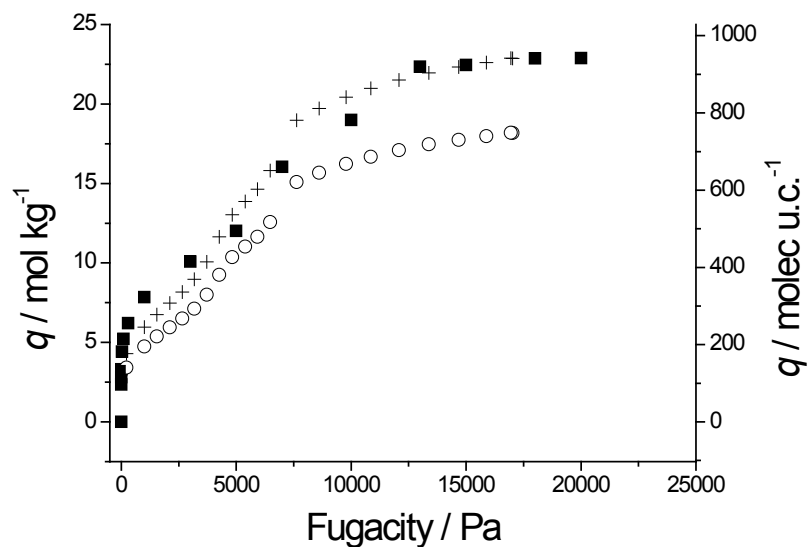
Figure B.5: Simulated (■) and experimentally measured (○) adsorption of methanol on MIL-100(Cr) at 303 K and experimental results scaled by 5/4 (+) (linear representation).

B.3. LINEAR REPRESENTATION OF ISOTHERMS

Linear representation of fugacity for Figs. 3.3 - 3.6 are shown in Figs. B.5 - B.8, respectively.
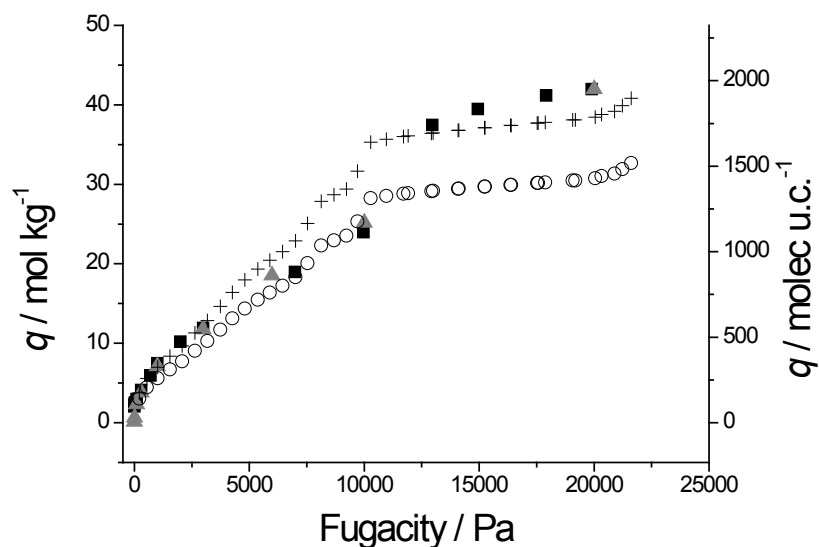
Figure B.6: Simulated adsorption for fluorinated (■) and hydroxylated structure (▲) and experimentally measured (○) adsorption of methanol on MIL-101(Cr) at 303 K and experimental results scaled by 5/4 (+) (linear representation).
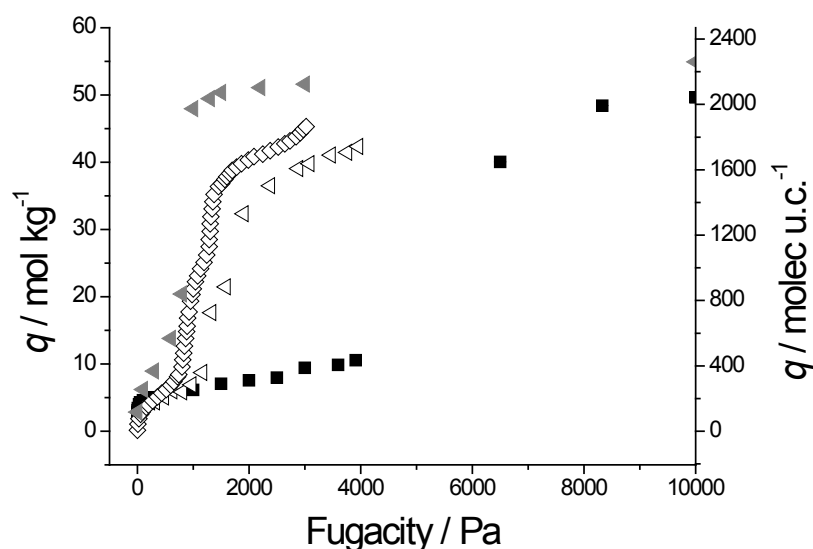
Figure B.7: Simulated adsorption on MIL-100(Cr) using TIP5PEw (■) and SPC/E (◄) water models at 303 K. Experimental isotherms from Chang *et al.* (◁) [6] and Akyiama *et al.* (298K, ◇) [7] (linear representation).
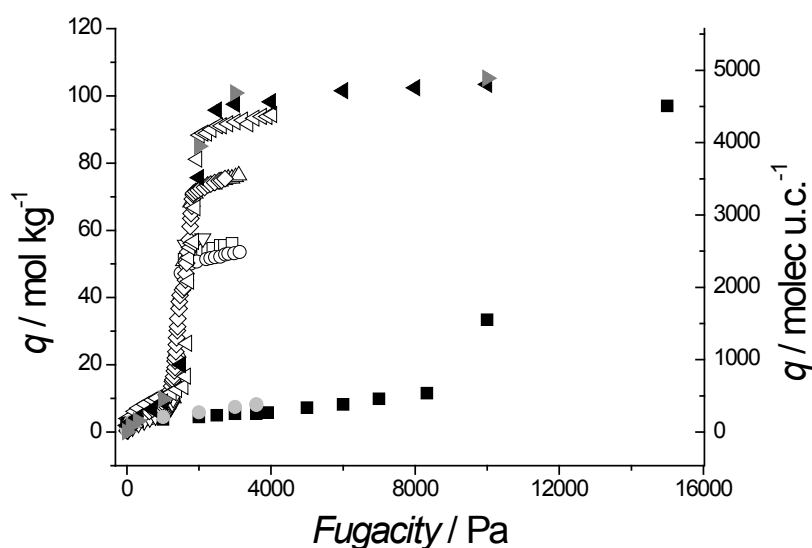
Figure B.8: Simulated adsorption for fluorinated MIL-101(Cr) using TIP5PEw (■) and SPC/E water (◄) models and for hydroxylated MIL-101(Cr) using TIP5PEw (●) and SPC/E water (►) models at 303 K. Experimental data from Ehrenmann *et al.* (298 K, volumetrically (○) and gravimetrically (□)) [8], Küsgens *et al.* (298 K, △) [9], Akiyama *et al.* (298 K, ◇) [10], Chang *et al.* (◁) [6] and own experiments (▽) (linear representation).

B.4. RADIAL DISTRIBUTION FUNCTIONS

Figs. B.9 and B.10 show the distance between water and structural chromium sites for fluorinated and hydroxylated MIL-101(Cr) respectively. In Fig. B.11 the distance between structural fluor and water is shown (fluorinated MIL-101(Cr)) and in Fig. B.12 the distance between the structural OH-groups and water is shown (hydroxylated MIL-101(Cr)).
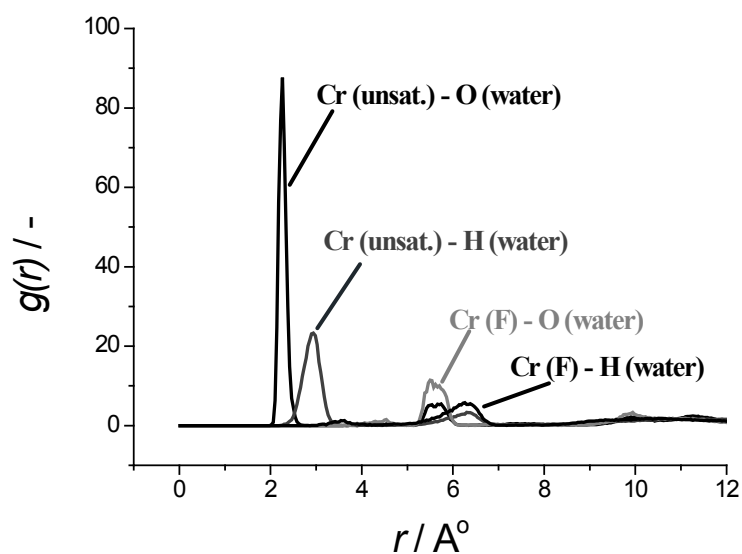
Figure B.9: Radial distribution function of water in fluorinated MIL-101. Distance between water and chromium sites.
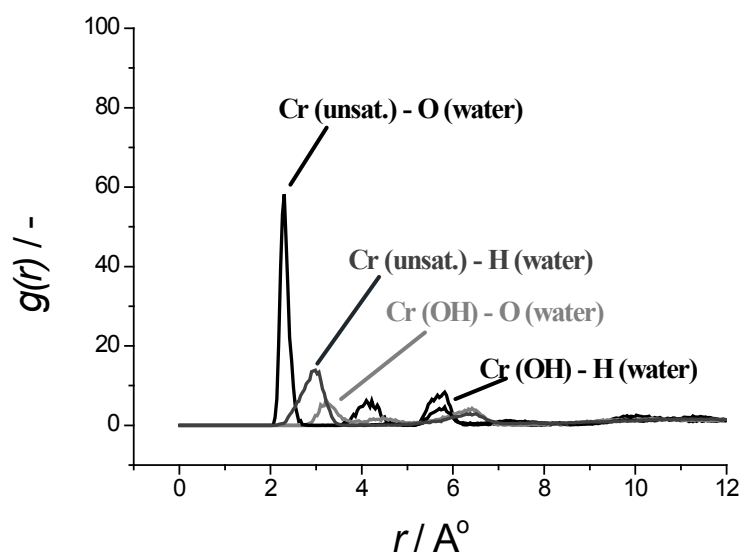
Figure B.10: Radial distribution function of water in hydroxylated MIL-101. Distance between water and chromium sites.
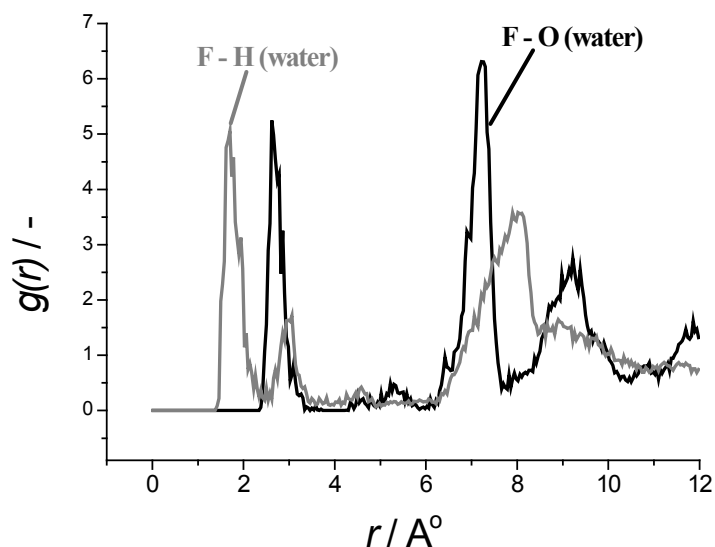
Figure B.11: Radial distribution function of water in fluorinated MIL-101. Distance between water and structural fluor group.
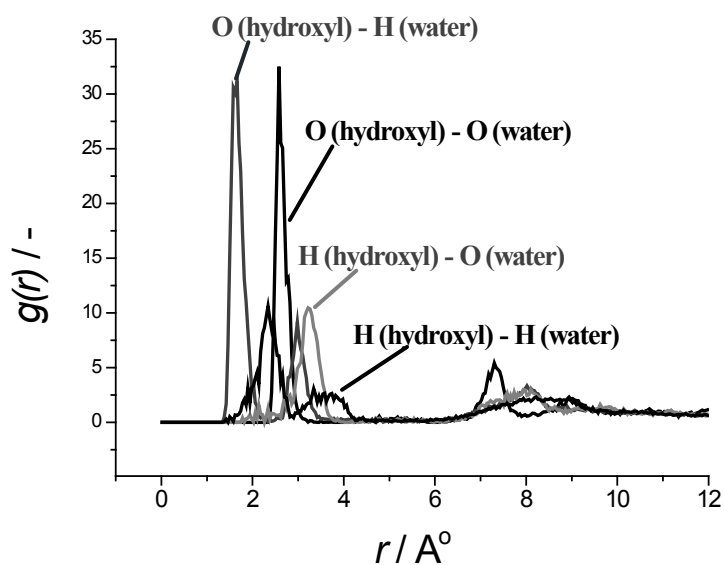
Figure B.12: Radial distribution function of water in hydroxylated MIL-101. Distance between water and structural hydroxyl group.

B.5. LOCATION OF ADSORBED METHANOL

Fig. B.13 shows the filling of the medium and large cage of MIL-101(Cr) with methanol at different fugacities. Fig. B.14 shows the location of methanol molecules close to MIL-101(Cr)'s supertetrahedron.
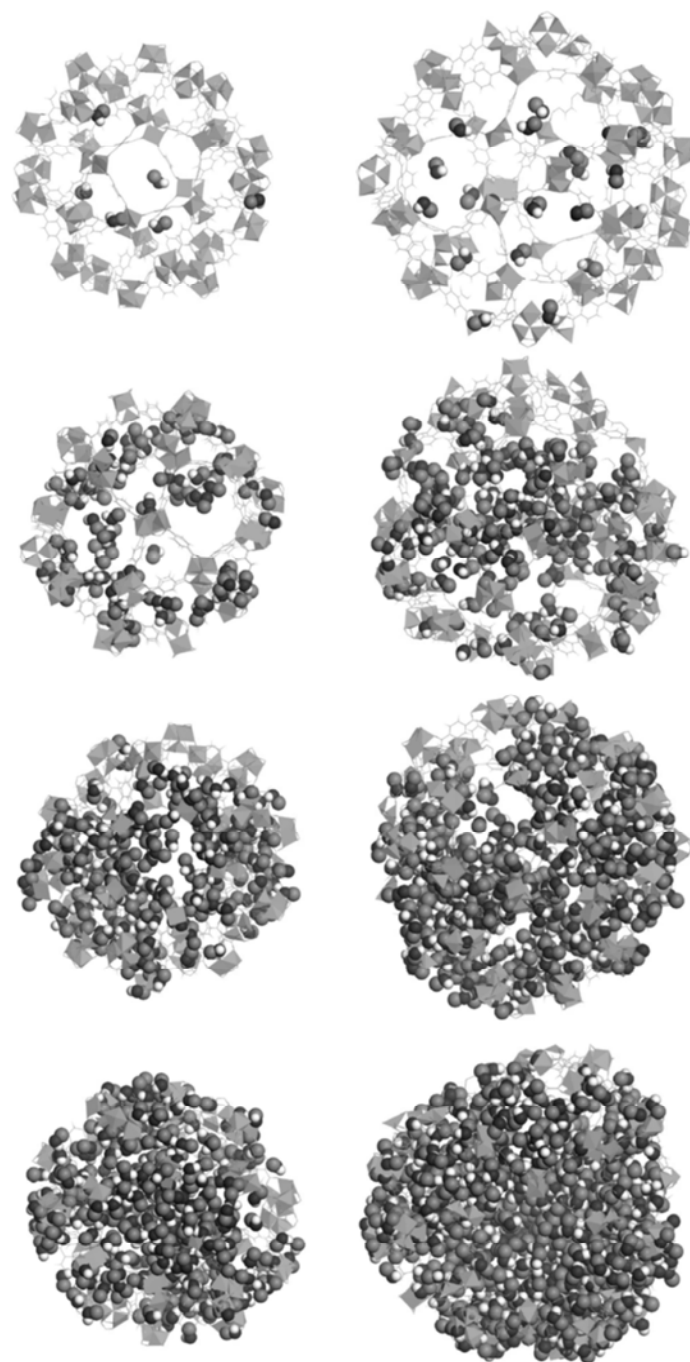
Figure B.13: Methanol located in medium (*left*) and large cage (*right*) for 1 Pa (*top*), 3 kPa (*second from top*), 10 kPa (*second from bottom*) and 15 kPa (*bottom*). Methanol shown with Van der Waals radii, chromium as polyhedra, and the organic ligands as lines. For a depiction in colors, the reader is kindly referred to the original text [1].
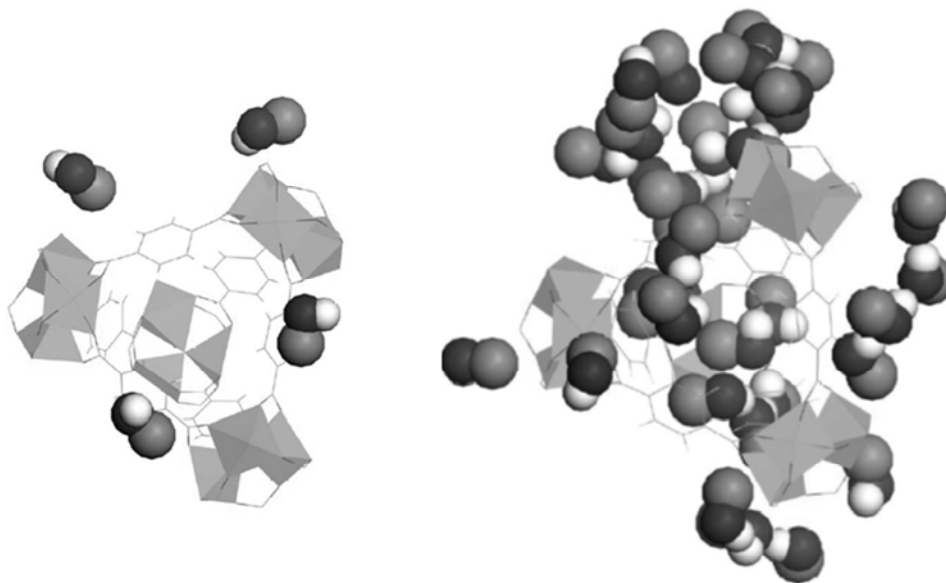
Figure B.14: Methanol located close to a supertetrahedron, at 1 Pa (*left*) and 3 kPa (*right*). Methanol shown with Van der Waals radii, chromium as polyhedra, and the organic ligands as lines. For a depiction in colors, the reader is kindly referred to the original text [1].

B.6. REFERENCES

[1]   M.F. De Lange, J.-J. Gutierrez-Sevillano, S. Hamad, T.J.H. Vlugt, S. Calero, J. Gascon, F. Kapteijn, Understanding adsorption of highly polar vapors on mesoporous MIL-100(Cr) and MIL-101(Cr): Experiments and molecular simulations, The Journal of Physical Chemistry C, 117 (2013) 7613-7622.

[2]   S.L. Mayo, B.D. Olafson, W.A. Goddard, DREIDING: A generic force field for molecular simulations, The Journal of Physical Chemistry, 94 (1990) 8897-8909.

[3]   A.K. Rappe, C.J. Casewit, K.S. Colwell, W.A. Goddard, W.M. Skiff, UFF, a full periodic table force field for molecular mechanics and molecular dynamics simulations, Journal of the American Chemical Society, 114 (1992) 10024-10035.

[4]   A.Ö. Yazaydin, Internal communication, 2011.

[5]   B. Chen, J.J. Potoff, J.I. Siepmann, Monte Carlo calculations for alcohols and their mixtures with alkanes. Transferable potentials for phase equilibria. 5. United-atom description of primary, secondary, and tertiary alcohols, The Journal of Physical Chemistry B, 105 (2001) 3093-3104.

[6]   J.-S. Chang, Porous metal(III) carboxylates as multifunctional adsorbents and catalytic materials, iCeMS-ERATO Symposium, July 26th, 2012.

[7]   G. Akiyama, R. Matsuda, S. Kitagawa, Highly porous and stable coordination polymers as water sorption materials, Chemistry Letters, 39 (2010) 360-361.

[8]   J. Ehrenmann, S.K. Henninger, C. Janiak, Water adsorption characteristics of MIL-101 for heat-transformation applications of MOFs, European Journal of Inorganic Chemistry, 2011 (2011) 471-474.

[9]   P. Küsgens, M. Rose, I. Senkovska, H. Fröde, A. Henschel, S. Siegle, S. Kaskel, Characterization of Metal-Organic Frameworks by water adsorption, Microporous and Mesoporous Materials, 120 (2009) 325-330.

[10] G. Akiyama, R. Matsuda, H. Sato, A. Hori, M. Takata, S. Kitagawa, Effect of functional groups in MIL-101 on water sorption behavior, Microporous and Mesoporous Materials, 157 (2012) 89-93.

CHAPTER 4

ADSORPTION DRIVEN HEAT PUMPS – THE POTENTIAL OF MOFS

ABSTRACT:

The potential of Metal Organic Frameworks (MOFs) as adsorbents in adsorption driven allocation of heat and cold is thoroughly assessed. With global energy consumption continuously increasing and a large percentage being used for allocation of heat and cold, the use of adsorption driven heat pumps and chillers is being revisited during the last few years. In this Chapter, the feasibility and the potential benefits of replacing conventional sorbents by porous crystalline Metal-Organic Frameworks is critically explored. First, the state of the art in stability and adsorptive properties of MOFs in relation to heat pumps is summarized. After selection of the most adequate working pairs (MOF-adsorbate), the potential of MOFs in these applications is evaluated, comparing their thermodynamic efficiency with current commercial adsorbents. The great promise that stable MOFs hold for this application is demonstrated in this work, as they exhibit higher thermodynamic efficiency and volumetric working capacity than conventional sorbents and may often be regenerated at lower desorption temperatures.

4.1. INTRODUCTION

Global energy consumption shows a continuous rise, despite the increased tangibility of (anthropogenic) global climate change [1]. Large contributors are households, which are responsible worldwide for about one third of this world energy consumption, mainly for heating and cooling [2]. The building sector accounted for 25% of the total global energy consumption in 2010, predominantly for space heating and hot water production, respectively 53% and 16% of this sector [3]. These energy demands for heating, and especially cooling, are forecasted to increase significantly in the coming years [2]. Significantly reducing the energy expenditures for heating and cooling will have a large impact on the total energy consumption.

When energy supply and demand are in phase, *e.g.* for air-conditioning, refrigeration and hot water production, thermally driven heat pumps can be employed, sustainably utilizing the available energy (*e.g.* solar or waste heat), a clear advantage over devices based on vapor compression [4]. There are multiple possible working principles for such thermally driven heat pumps (see Chapter 1). Central in this work is the adsorption driven heat pump, which has the advantages that low driving or regeneration temperatures (< 100 $^{\circ}$C) can be employed efficiently, [5-9] fitting the available temperatures of the desired energy sources, *e.g.* solar or industrial waste heat and environmentally benign working fluids (*e.g.* water) can be used. Already commercially available adsorption driven heat pumps and chillers employ silica gel or zeolite based adsorbents in conjunction with water as working fluid [10-17]. Among the different commercial adsorbents, the FAM (Functional Adsorbent Material Zeolite) Z-series, commercialized by Mitsubishi plastics as the AQSOA^{tm} series [18] show most suitable adsorption characteristics (Chapter 1). It is clear that large commercial interest in the development of new adsorption based devices exists, and that the market for such devices is expected to grow as performance improves [11]. One way of achieving this is by the application and development of new adsorbents. Here a relatively novel class of materials, *i.e.* Metal-Organic Frameworks (MOFs) is investigated for this purpose.

When energy supply and demand are out of phase, temporary energy storage is required. Among the different options, thermochemical storage is interesting, as it requires significantly less volume to store the same amount of energy [19, 20] compared to systems based on latent [21] or sensible energy [22]. As mentioned in Chapter 1, material properties for adsorption

driven heat pumps and adsorption based thermochemical storage are very similar. Thus, it makes sense to also investigate the feasibility of MOFs in energy storage, an application considered as alternative in this work. Another alternative application is the open cycle adsorption based desiccant air-conditioning, which could be potentially more energetically efficient than conventional air-conditioning (Chapter 1). The potential advantages of MOFs in both applications is concisely discussed in Section 4.8. As the main focus is the assessment of the performance of MOFs in adsorption driven heat pumps, this will be discussed firstly and significantly more elaborated.

In the scope of this work, the state of the art in MOF science with regard to stability and adsorption behavior for the aforementioned working fluids is given first (Sections 4.2-4.5). With this information in hand, a selection of suitable candidates will be made. In the second part of this work the thermodynamic efficiency and storage capacity for these materials will be determined and compared to conventional sorbents (Sections 4.6-4.7). A comprehensive summary and a detailed future perspective are elaborated in Section 4.9.

To be able to understand, and to possibly tune, the adsorption of vapors in MOFs, one should have insight in the mechanism of adsorption. This will be described firstly concerning the experimental and simulation point of view (Section 4.2). Of the utmost importance for the targeted application is further knowledge about the solvothermal (in)stability, as will be discussed secondly in a clear and concise manner (Section 4.3). Subsequently, an overview of known adsorption behavior (Section 4.4), results in a selection of the most promising MOFs in Section 4.5. This will comprise all four selected working fluids, water (Section 4.4.1), methanol (Section 4.4.2), ethanol (Section 4.4.3) and ammonia (Section 4.4.4), though water will be dominantly present in the discussion, as it has received by far the most attention in scientific literature. Because of the numerous symbols used in various figures and equations, and large amount abbreviations are used throughout this chapter, both a list of symbols and a list of abbreviations can be found in Appendix C.

4.2. ADSORPTION MECHANISM

According to Canivet *et al*. three different mechanisms for water adsorption in MOFs can be distinguished [23]:

- Adsorption on metallic cluster; This modifies the first coordination sphere of the metal ion (irreversible)
- Layer or cluster adsorption in pores (reversible)
- Capillary condensation in pores (irreversible)

Note that reversibility here is defined by thermodynamics and is not meant to include irrevocable loss of structural fidelity (instability), which is discussed separately (Section 4.3). As most MOFs consist of aromatic ligands, which are hydrophobic in nature, cluster adsorption is prevalent over layer formation when water is concerned. Clusters of water can be formed around three different types of sites. Firstly, for MOFs that have coordinatively unsaturated sites (cus) on the metal ions after solvent removal, water can be clustered around those sites. As mentioned already, the first water molecule will then be irreversibly adsorbed, modifying the coordination sphere of said ion. Terminal groups on the metal-ions of the cluster, when present, are predominantly hydroxido-species that can also act as nucleation sites for clustering of water. Finally, hydrophilic functional groups can be attached to the organic ligand, adding additional nucleation sites.

Whether fully reversible cluster-based adsorption or irreversible capillary condensation occurs, will depend on pore size. In pores with a diameter smaller than a certain critical diameter, D_c, water adsorption occurs solely by cluster formation, for pore diameters larger than D_c, water is adsorbed due to capillary condensation, preceded by cluster adsorption [23, 24]. The former case yields continuous reversible adsorption, whereas the latter will result in a hysteretic difference between ad- and desorption behavior, due to the thermodynamic irreversibility of capillary condensation [23, 24]. According to Coasne *et al.*, this critical pore diameter can be expressed as [25, 26]:

$$D_c = \frac{4\sigma T_c}{T_c - T} \qquad (4.1)$$

Here σ is the approximate size of a water molecule (0.28 nm), T_c is the critical temperature of water and T is the actual temperature. For water at room temperature *e.g.*, this yields a critical diameter of 2 nm [23, 24].

In a previous communication, we have shown computationally that mesoporous MIL-100(Cr) and MIL-101(Cr), with cavities bigger than the above mentioned critical diameter, indeed show capillary condensation, preceded by clustering of water molecules around the coordinatively unsaturated chromium sites [27] (Chapter 3). The crux of describing experimentally found adsorption behavior computationally lies in properly accounting for water-water interactions for pores with diameter larger than D_c, water-framework interactions are of little significance [27] (Chapter 3). Correctly describing these water-water interactions is not at all trivial. In scientific literature, there is a plethora of different molecular descriptions of the water molecule available, none of which is capable of accurately describe all properties of this molecule [28]. To obtain a sound molecular description of adsorption in microporous materials, showing reversible, cluster-based adsorption, structure-water interactions should be tuned with scrutiny, in sharp contrast to mesoporous materials. *E.g.*, Castillo *et al.* have shown, using classical force fields, that simulating water adsorption in Cu-BTC is extremely sensitive to attributed partial charges, responsible for electrostatic interactions between host and guest, and that subsequently considerate tuning is required to match computational results with experiments [29]. Using similar methods, without tuning, satisfying predictions were obtained for Al(OH)(1,4-ndc) [30]. Ghosh *et al.* found for UiO-66(Zr) that, employing Monte Carlo simulations [31] and classical force fields, the structure is significantly more hydrophobic *in silico* than in reality [32]. By inducing defects via replacing an organic ligand with OH-groups, a significantly more hydrophilic structure can be obtained, though a small hysteresis with experimental results remains [32]. Zang *et al.* found, in line with previously discussed results, that classical force fields cannot describe water adsorption in copper-based MOFs [33]. When employing more accurate and computationally more expensive DFT-derived force fields, at best a fair coherence with experiments is obtained [33]. This in contrast to *e.g.* CO_2-adsorption in nanoporous materials, which is seemingly nearly perfectly reproduced with these DFT-derived force fields [34, 35]. In the same line, Lin *et al.* have developed a different DFT-derived force field for CO_2-adsorption in MOF-74(Zn,Mg), showcasing accurate reproduction of adsorption measurements *in silico* [36]. The same protocol, however, only exhibits reasonable reproduction of water adsorption in these materials, in line with the findings of Zang *et al.* [36].

Based on the preceding discussion, it seems difficult to describe with computational methods of varying complexity the experimentally determined adsorption data. This can only mean that these computational methods are not mature enough for *in silico* design or computational screening. This in sharp contrast with *e.g.* H_2 storage [37] or CO_2 capture [38, 39], where screening methods are more precise.

For alcohols, coherence of simulated and experimentally observed adsorption is much more easily obtained, even when using classical force fields [27, 40-43]. Mechanistically speaking, when compared to water, alcohols show in general a less sharp uptake profile in MOFs due to their lower polarity [27], and lowered repulsion from the aromatic ligands. Furthermore, seemingly chemisorption is not observed in literature for alcohols.

In case of ammonia, most data available in the literature come from *in silico* studies. Snurr *et al.* have elaborately discussed NH_3 adsorption in MOFs using quantum-chemistry derived force fields [44-46], showing that in principle a steep uptake can be achieved, at usefully low (relative) pressure, for various frameworks [44]. These studies, however, did not consider chemisorption effects and instability of the investigated MOFs towards ammonia (Section 4.4.4), thus limiting the relevance of these adsorption predictions for performance assessment. Furthermore, there are little to no experimental adsorption measurements available to benchmark these predictions.

4.3. STABILITY

For application in AHP/ADCs, MOF stability is of utmost importance. Degradation under prolonged exposure to the adsorptive of choice is unacceptable. Especially regarding water, this is a limiting constraint for application. Before discussing the factors that determine the differences in structural stability in detail, different levels of hydrothermal stability will be defined. Subsequently, an overview will be presented of techniques to increase stability of MOFs, be it *in situ* or post-synthetic, with focus on their potential use for AHP/ADCs. In a recent review on water stability in MOFs, Burtch *et al.* conveniently defined four successive levels of stability [47]:

- Thermodynamic stability (Th.S.)
  - Stable after long-term exposure to aqueous solutions
- High kinetic stability (H.K.)

- o Stable after exposure to high relative humidity
- o Decomposes after short exposure to liquid water

- Low kinetic stability (L.K.)
  - o Stable after exposure to low relative humidity only

- Unstable (Uns.)
  - o Any exposure to moisture will cause loss of structural integrity

Eligibility to the thermodynamic stability level is considered by the authors after demonstrated structural survival after exposure at least seven days for pure water and at least one day for boiling or basic/acidic conditions [47]. For the subsequent levels, proof requires significantly less stringency. Analysis of the extent of degradation, after exposure to applied conditions, should minimally consist of the retention of crystallinity (using *e.g.* X-ray diffraction) and porosity (using adsorptive characterization) [47]. In fact, the authors recommend to use the BET-analysis for this quantification specifically, but in light of our recent work on the inconsistencies that can arise when determining a specific surface area using this method [48] (Chapter 2), we here advocate to use adsorption capacities (at saturation) instead. Although one could debate whether stability after one week exposure to liquid water at ambient conditions truly can only be caused by intrinsic thermodynamic stability and which temperature and relative humidity thresholds define the discrimination between low and high kinetic stability, this classification suits well to discriminate between different MOF structures on a qualitative level. Adhering to this classification, eligibility for AHP/ADCs can only be considered for the first two levels (thermodynamic and high kinetic stability). As a material employed in AHP/ADCs has to endure a large number of adsorption-desorption cycles, stability over many of these cycles has to be demonstrated in addition. This is especially true for the structures that show high kinetic stability only, but should be checked for all MOFs of interest. One should take into account that determining the relative stability of any structure is indeed a clear function of the application (conditions) envisaged.

Water can potentially damage metal-oxide clusters through ligand-displacement, where a ligand is replaced by a water molecule, or by forming a metal-hydroxide bond and a (partially) protonated ligand [49]. Whether and to what extent these will occur is a function of several factors, as first explored in the pioneering work of Low *et al.*, using a combined experimental and computational approach [49]. These factors can be subdivided in two main categories. Firstly, there are factors determining whether an irreversible reaction of water

within the MOF structure is thermodynamically favorable [47]. Secondly, of interest especially for structures for which water reactions are energetically favorable, there are factors that determine whether this reaction will occur (kinetics/steric hindrance) [47]. Note that whilst these factors are discussed individually, they cannot always be completely separated in reality [50]. The factors identified in literature in the former category, determining the energetic feasibility of degradation reactions, revolve around the strength of the interaction of the inorganic cluster with the surrounding organic ligands, most often the structure's heel of Achilles, and the stability of the cluster towards water [47, 50].

The most important aspects considered below that control the hydrolytic stability are the valence of the metal ions, the nature of the metal, the filling of the coordination sphere of the inorganic cluster and its pK_a. The (formal) valence of the metal ion is of importance, as MOFs that incorporate trivalent metal ions, seem to be more stable than bivalent metal ions [47, 49, 50]. Low *et al.* have shown amongst others, that bivalent MOF-5 (Zn_4O^{6+}-*cluster*), Cu-BTC (Cu_2^{4+}-*paddlewheel*) and MOF-508B (Zn_2^{4+}-*paddlewheel*) are significantly less stable than trivalent MIL-53(Al, Cr) (MOH^{2+}-*chain*) or MIL-101 (Cr_3OX^{6+}-*cluster*, X = OH⁻ or F⁻). Note however, that not only the metal valence is varied, but also the metal species amongst others, skewing the comparison. Furthermore, high chemical stability is ascribed to tetravalent Zr/Hf-based MOFs [47, 51-54].

Another key aspect is the metal-ligand bond strength. As MOF coordination is perceived to be governed by Lewis acid/base chemistry [47, 50], MOFs comprising imidazolate ligands (pK_a ~ 18-19) exhibit a higher hydrothermal stability than carboxylates (pK_a ~ 4) [49, 50]. This is in line with the findings of Li *et al.*, who suggested based on literature [55-57] that the pK_a of the ligand is an indicator for the relative strength of the ligand-metal bond; for instance, acetic acid (pK_a ~ 4) and tetrazole (pK_a ~ 4-5) ligands are more easily replaced by water than more basic ligands, such as triazoles (pK_a ~ 9-10) and pyrazoles (pK_a ~ 14-15) [58].

Furthermore, metal ions that show sixfold coordination tend to be more stable than those that have fourfold coordination. The latter, according to Low *et al.*, is because the denser filling of the coordination sphere in case of the former, and makes coordination of water to the metal-ion more difficult [49]. So, *e.g.*, MOF-5 (fourfold coordination) is less stable than MOF-74 (Zn, fivefold coordinated when desolvated) [59].

In addition, the nature of the metal species plays an important role in stability [47, 49, 50]. Tan *et al.* have recently investigated, in a multi-faceted spectroscopic study, the relative

stability of bivalent metal ions in isostructural M(BDC)(TED/DABCO)$_{0.5}$ incorporating Cu, Zn, Ni and Co ions [60, 61]. It was found that hydrolysis occurs of the Cu-based MOF, ligand replacement of the TED ligands by water takes place for the Zn- and Co-based structures, whereas incorporation of Ni results in a relatively more stable structure [60, 61]. Bivalent, fourfold coordinated, copper paddlewheel-based MOFs show moderate stability [62, 63]. Depending on conditions, Cu-BTC can survive, with only minor degradation, prolonged exposure to water vapor for multiple weeks, but the structure is never fully retained [52]. Interestingly, it was recently demonstrated that this degradation can be nearly fully repaired by treatment with ethanol [64]. The Zn-BTC cluster, which has identical coordination environment as that of Cu-BTC, collapses upon solvent removal [65], indicating that Cu-based clusters are relatively less unstable than the zinc based topology.

Not surprisingly, based on the preceding discussion, Cychosz and Matzger found that zinc-acetate based MOFs exhibit poor water stability [62], due to the bivalent Zn-ion, the fourfold coordination and an acidic ligand. In the isoreticular IRMOF-series, all comprising the Zn$_4$O-cluster, the zinc-acetate based MOF is notorious for degrading in the presence of water. Although these materials are hydrophobic, they degrade in the presence of even low moisture concentrations [66]. The cluster is hydrated and subsequently the ligands are easily replaced [67]. Based on various computational approaches on IRMOF-1, it was found that the critical water content for degradation is somewhere between 4 and 6 % wt. [68-70]. In accordance with the stability factors discussed above, MIL-100(Cr), comprising trivalent, sixfold coordinated, chromium clusters, was found to be completely water stable, according to Cychosz and Matzger [62], as well as tetravalent zirconium atom-containing UiO-66 [51, 52, 71], both in line with the findings of Low *et al.* [49]. MIL-100(Cr) and especially MIL-101(Cr) derivatives are predominantly used for catalysis in aqueous media, made possible by the high hydrothermal stability of these structures [72]. In fact, in part due to its excellent stability MIL-101(Cr) has been examined for a plethora of different applications [73]. Kang *et al.* demonstrated that MIL-53(Cr) is more stable towards water than MIL-53(Al), which is in turn more stable than isotypic MIL-47(V), which decomposes rapidly in the presence of liquid water [74].

Based on the preceding, one might expect MIL-101(Al)-based materials to be stable as well. Unfortunately, NH$_2$-MIL-101(Al) is transformed to NH$_2$-MIL-53(Al), the thermodynamically stable phase [75], upon contact with liquid water [76]. The aforementioned stability of MIL-53(Al) is thought to be due to sterically more shielded one-dimensional inorganic building

units in MIL-53 compared to the open ones of MIL-101 to provide sufficient protection against water in the case of Al^{3+} (and Fe^{3+}) [75, 77, 78]. In addition, according to Kang *et al.*, MIL-53(Al) slowly decomposes in liquid water (80 $^{\circ}$C) as well [74]. More specifically, Bezverkhyy *et al.* demonstrated that a γ-AlO(OH)-phase is formed at the exterior of MIL-53(Al) crystals under reflux conditions, consuming part of the MOF [79]. A maximum conversion of around 20% can be achieved (after 10 hours), which results in a layer of 100-200 nm thickness consisting of crumpled sheets (3 nm) [79]. At this conversion level, the layer becomes impermeable, which is not necessarily the case for shorter reaction times [79]. Qian *et al.* reported, in contrast, that MIL-53(Al) is hydrothermally stable [80], although a maximum reduction in pore volume of about 25% can be observed. In addition, the XRD reflections that were attributed to the γ-AlO(OH)-phase [79], can be also observed albeit only after three days at 100 $^{\circ}$C [80]. As the MIL-53(Al) samples were synthesized under different conditions [79, 80], the rate of degradation might be due to differences in material quality. The effect of flexibility on stability is not taken into account in the preceding discussion. This is assumed to be of less importance [49].

Attempts have been made by researchers to enhance the water stability of MOFs, mostly by influencing kinetic factors. By preventing water molecules from entering the pores of the MOF entirely ("pore hydrophobicity" [47]) or by hindering water molecules to group around the inorganic cluster ("internal hydrophobicity" [47]), thermodynamically unstable clusters can be made stable from a kinetic perspective. Interesting techniques to improve the external or pore hydrophobicity of MOF materials have been developed recently. Yang and Park have strongly enhanced the water-tolerance of notoriously unstable MOF-5 by creating a carbon layer at the external surface of the material using pyrolysis [81]. Gadipelli and Guo also obtained more water-stable MOF-5 particles by thermal annealing slightly below the structure's decomposition temperature [82].

Wu *et al.* stabilized MOF-5 by incorporating the MOF in mesoporous silica SBA-15 [83]. Yang *et al.* have created a Carbon nanotube-MOF-5 hybrid material which shows higher adsorptive uptake of H_2 and hydrothermal stability, because of the water repelling nature of the carbon material [84]. This core-shell approach can also be applied to MOF structures, as was shown by Li *et al.* [85]. A mixed ligand core of bio-MOF-11/14 was prepared after which a shell was created of pure bio-MOF-14. In this way the CO_2 capacity of bio-MOF-11 was largely retained, whilst the core's water intolerance was mitigated by the stable bio-MOF-14 outer shell [85, 86]. Liu *et al.* have created, using solvent-assisted ligand exchange, a

158

hydrophobic exterior shell on ZIF-8 particles, making the structure more resistant towards hydrothermal conditions [87]. These approaches have indeed significantly increased the lifetime of the targeted MOF to ambient moisture by using a shielding exterior layer to prevent water from entering the structure entirely. Although exterior shielding in a hydrophobic matrix can potentially be extremely beneficial for using water-unstable (or hydrophilic) MOFs for *e.g.* gas separation in mixed matrix membranes, [88-95] this approach obviously fails to be of use in AHP/ADCs.

Rao and co-workers developed an interesting method to functionalize the exterior surface with aromatic hydrocarbons in such a way that only bulk water is repelled but water vapor can still potentially enter [96]. De Coste *et al.* have used plasma-enhanced chemical vapor deposition (PECVD) of perfluorohexane to enhance water stability of Cu-BTC. It was found that the perfluorohexane groups are oriented such in the structure that clustering of water is prohibited, explaining the increase in stability observed [97].

Interpenetrated growth of crystals, or catenation, can also result in an increased inherent water stability of MOFs, as was demonstrated for MOF-508 (Zn(BDC)(BPY)$_{0.5}$) [98]. Uncatenated MOF-508, even with decorated methyl-groups, loses almost all porosity whilst twofold interpenetrated MOF-508, without any water repellent functional groups retains full adsorption capacity after exposure to water [98]. The increased stability is attributed to an inherent higher thermodynamic stability of catenated structures and a significantly reduced water adsorption capacity [98].

The road most often travelled to increase hydrothermal stability is by ligand functionalization. Here the focus lies on making the material more hydrophobic, predominantly by utilizing organic ligands with water-repellent functionalities during MOF synthesis [57, 86, 99-120]. Post-functionalization of MOFs [121-124], a powerful technique to overcome the limitations of "isoreticular" synthesis in creating new MOF materials [125], has been applied less frequently [76, 126-129]. Unfortunately, the downside of these two approaches is that the majority of the materials that have undergone this functionalization no longer adsorb appreciable amounts of water. Thus the improved hydrophobicity that might even be beneficial for certain applications, such as CO_2 capture and storage [58], renders the material useless for AHP/ADCs when water is the adsorptive of choice. Interestingly, there are MOFs with repellent functions that nevertheless retain water adsorption after modification [57, 99, 103, 107, 108]. For other adsorptives, *e.g.* methanol, hydrothermal stability is obviously not

particularly important, as long as the material does not degrade when contacted with ambient humidity (for handling purposes).

A somewhat paradoxical method to increase hydrothermal stability, is the introduction of hydrophilic amine groups, as was shown for aminated MOF-5(Zn) (IRMOF-3) [130, 131]. The observed increase in stability was shown to be due to the stabilizing effect of the hydrogen-bonding interaction between hydrogen of the amine and oxygen of adjacent carboxylates [132]. Another reason is thought to be the creation of alternative adsorption sites on the organic ligand, which can reduce the water concentration at the inorganic cluster [133].

A more suitable approach to enhance stability might be the (partial) exchange of metal-ions. Bellarosa *et al*., in a computational study, interchanged Zn with Be in the M_4O-core of IRMOFs, making the material much more tolerant towards water, due to an increase in the activation energy barrier for hydrolysis [134]. Indeed, also experimentally, it was found that MOF-5(Be) is more stable against humidity than MOF-5(Zn) [135]. Substitution of only a part of the metal ions (doping) in a MOF crystal might also be a possibility [136]. Doping MOF-5(Zn) with Ni-ions increases the water (vapor) tolerance of the parent structure [137, 138].

In conclusion, Burtch *et al.* identified the qualitative stability of over 200 structures, of which they found roughly 10% to exert thermodynamic stability, 60% high kinetic stability, 20% low kinetic stability and only 10% unstable towards water [47]. Currently however, there are more than 20.000 MOF structures known [47], of which the majority is based on bivalent metal ions. These have in general (hydrothermal) stability issues [139, 140]. This means that the percentages above are by no means representative and it can safely be assumed that the fraction of unstable structures is strongly underestimated. As summarized concisely (*vide supra*), there are pathways that may lead to stabilization of MOFs, but the majority of these aim at avoiding any water adsorption in the structure, making them useless for the application at hand.

To end with a positive note, there exist MOF structures that show sufficient water stability for application in AHP/ADCs, and of which the adsorptive behavior will be assessed in the next section. Solvothermal stability for methanol and ethanol is seemingly thought to be less of an issue for MOFs [141] and is henceforth not investigated in such detail in academia. Studies concerning MOF (in)stability towards ammonia are seldom conducted. Stability will thus be

discussed alongside ammonia adsorption, (Section 4.4.4), as detailed insights on degradation mechanisms seem to be mostly limited to water.

4.4. ADSORPTIVE PROPERTIES

A comprehensive overview of different MOF structures and their water, methanol, ethanol and ammonia adsorption behavior is listed in Tables 4.1-4.4, respectively. For each of the individual structures, the parameter α is indicated, defined by Canivet *et al.* [24] as the relative pressure at which half of the structure is filled with a working fluid of choice. This indicator may help in differentiating materials with uptake in- and outside of the operating window. For water as adsorptive, $\alpha < 0.05$ indicates that a material would be too hydrophilic, whereas for $\alpha > 0.45$ a material is too hydrophobic. The α-value by Canivet *et al.* [24] is thus used to distinguish between hydrophobicity and hydrophilicity instead of the quantitative Weitkamp hydrophobicity index [142] which has been employed for a variety of adsorbents [143-147]. This as the former is more easily related to the application at hand and the latter is more difficult to determine as it comprises measuring the co-adsorption of water and toluene (or methylcyclohexane). Drawback of the chosen method is that α changes as a function of temperature (see Eq. 4.21) and should thus preferably be measured at or close to room temperature.

Furthermore, the maximum uptake of the working fluid, q_{max} (per unit mass), listed in Tables 4.1-4.4, is invaluable for an initial assessment of feasibility. Although, for application, it is preferred to compare materials based on capacity per unit volume (W_{max}, Section 4.7), q_{max} does not require information on material density and is thus more easily determined. As the benchmark materials display, for water, $0.2 < q_{max} < 0.3$ g g^{-1} (Fig. 1.4, Chapter 1) and have generally speaking a higher (crystallographic) density than MOFs (Table 4.6), MOFs displaying $q_{max} < 0.2$ can already be deemed unsatisfactory for application.

These tables are further supplemented with the enthalpy of adsorption, $\Delta_{ads}H$, the pore volume based on N$_2$ adsorption, V_p, and remarks about material stability, indicated when available. In the case of water, for publications which contain no clear indication about hydro(thermal) stability, the classification of Burtch *et al.* has been used where possible [47]. The specific surface areas (BET) of these materials are ignored, since without the actual conditions used to determine these, and they are often omitted in practice, surface areas are by no means a proper indicator/comparator [48]. The main findings from literature will be discussed individually.

For water (Table 4.1) tri- and tetravalent MOFs are subdivided into existing cluster configurations and discussed first, followed by bivalent zeolite-imidazolate frameworks (ZIFs) and pillared MOFs and the presumably less stable remaining bivalent Zn- and Cu-based MOFs, whereafter a set of miscellaneous structures is listed. For the remaining adsorptives, this subdivision is not explicitly made due to significantly less availability of literature.

4.4.1. WATER ADSORPTION (TABLE 4.1)

Mesoporous MIL-101(Cr) [148] has received significant attention for application in heat pumps in literature (*confer* Table 4.1), owing to its robustness and high capacity. Indeed up to 1.4 g_{H2O} g^{-1} can be adsorbed in MIL-101 [149]. Unfortunately a significant fraction of this loading is achieved at $p/p_o > 0.4$, which decreases the material's applicability in AHP/ADCs. Because of the large pore sizes of MIL-101(2.9, 3.4 nm), capillary condensation occurs at these undesirably high relative pressures. These large pore sizes are also responsible for an undesired desorption hysteresis. By functionalizing (part of) the organic ligands, one can make the internal surface more hydrophilic. The addition of NO_2- [24, 149, 150], NH_2- [24, 149, 150] or SO_3H-groups [149] to MIL-101(Cr) shifts the step in adsorption to lower p/p_o, where α is highest for unfunctionalized MIL-101(Cr) and lowest for MIL-101(Cr)-SO_3H. For the amino-, and nitro functionalized MOFs, the location of the step in desorption is hardly altered. As reasoned by Canivet *et al*., because of the presence of hydrophilic groups, more water molecules adsorb before capillary condensation occurs, effectively reducing the actual volume to be filled during condensation and thus reducing the p/p_o required for this condensation [24]. During desorption, however, the filled volumes are very similar, resulting in desorption occurring at similar p/p_o for all functionalized and unfunctionalized materials. For MIL-101(Cr)-SO_3H the hysteretic difference in p/p_o between the ad- and desorption branch is significantly enhanced, because water is more difficult to remove due to the strong interaction of the sulfonic groups with water. Subsequently for adequate desorption, lower p/p_o, and thus higher desorption temperature is required compared to the other MIL-101(Cr)-based materials, highly undesired for AHP/ADCs. Note that the strong interactions of H_2O with the sulfonate-group are not adequately captured in the reported isosteric heats of adsorption, due to the irreversible nature of these interactions.

MIL-100(Cr) [151], containing the same inorganic cluster as MIL-101(Cr) but trimesic acid instead of terephthalic acid as linker, contains smaller mesoporous cages (2.5, 2.9 nm) than

MIL-101(Cr). These smaller cages make that the step in adsorption is beneficially shifted to lower p/p_o ($\alpha \sim 0.3$-0.35 [152, 153], where $\alpha > 0.4$ for MIL-101), while retaining a large water capacity (up to 0.8 g_{H2O} g^{-1}) [152]. Attempts to decorate MIL-100(Cr) with hydrophilic moieties have been directed towards modification of the chromium-oxide cluster via grafting with organic components [153] or counterion-replacement [152] and replacement of chromium with other metals [154]. This because of the difficulty of creating additional functional groups on trimesic acid (1,3,5-benzene dicarboxylic acid). Grafting the *cus*-sites in MIL-100(Cr) with either (mono, di and tri-)ethylene glycols or ethylene diamine results in a negligible decrease of α [153]. However, replacing fluoride-counterions with sulfate does result in an appreciable decrease in p/p_o required for adsorption ($\alpha \sim 0.25$) [152]. The effect of changing from chromium to either iron or aluminium does not seem to have a clear effect on adsorption behavior (*confer* Fig. 4.1). Seemingly small variations in p/p_o for which the steps in adsorption occur, are caused by the difference in measurement equipment rather than by the metal present in MIL-100. The fact that the metal in the inorganic cluster is of little importance in these large mesoporous cavities is in line with the capillary condensation mechanism, driven by water-water interactions [27]. In conclusion, mesoporous MIL-100 and MIL-101 show high water uptake capacities and decent stability (see Table 4.1) for application in AHP/ADCs, but most of the uptake occurs at high p/p_o, limiting the applicability to narrow operation windows, *i.e.* a small 'temperature lifts' (see Section 4.7.3). Functionalizing these materials has been shown to have little impact.

Another MOF investigated for application in adsorption driven transformation of heat is titanium(IV)-based amino-functionalized microporous MIL-125(Ti) [155]. Not only is the step in adsorption uptake beneficially shifted to lower p/p_o [24, 156], the amine-group makes MIL-125(Ti)-NH$_2$ more stable towards aqueous solutions [156]. According to the authors, this is similar to the increased stability of MOF-5 upon incorporation of amino-moieties explained above [130, 132]. Although MIL-125(Ti)-NH$_2$ is thermally stable up to ~550 K, Jeremias *et al.* have shown that upon cycling between ad- (5.6 kPa H$_2$O, 40 °C) and desorption (5.6 kPa H$_2$O, 140 °C) a continuous decrease in working capacity can be observed, resulting in a 17% decrease in maximum water loading after 40 cycles [157]. As the stability of MOFs in contact with water vapor is a function of both vapor pressure and temperature [49], cycling thus between milder conditions might increase cyclic stability. On that note, given the stepwise isotherm of MIL-125(Ti)-NH$_2$, desorption could be operated at far lower temperatures (70-90 °C, depending on conditions).
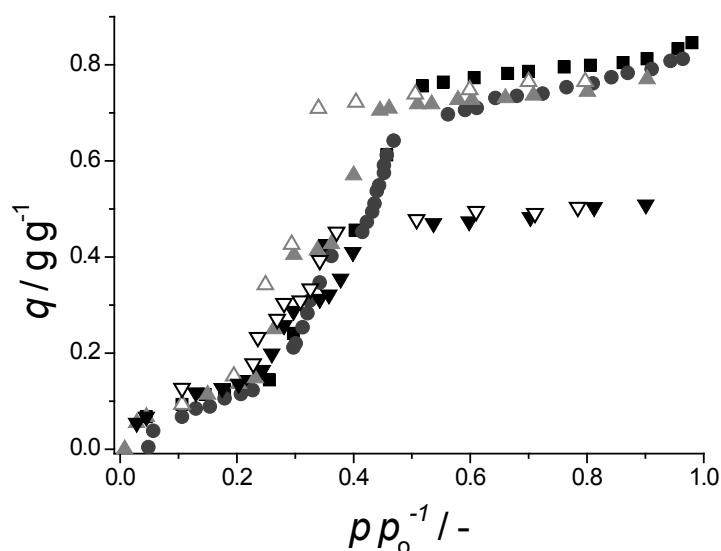
Figure 4.1: Adsorption isotherms for MIL-100 (Fe (▲) and Al (▼)) measured at 298 K, including measurements from Küsgens *et al.* (■) [158] and Akiyama *et al.* (●) [152] Open symbols depict adsorption, closed desorption and p_o is the saturated vapor pressure at measurement temperature. Adapted from Ref [159].

Next to the possible positive effect this might have on cyclic stability, this would also increase thermodynamic efficiency. CAU-1(Al) [160], which is isostructural to MIL-125(Ti)-NH$_2$ but contains μ_2-methoxy-species instead of bridging μ_2-oxygen, shows increased hydrophobicity, most likely due to these methoxy-species. The different post-functionalization reactions performed on the amino-moiety increase the undesired hydrophobicity of this MOF further.

Zirconium(IV)-based MOFs are, as mentioned previously, known to be stable when subjected to water. This is reflected in the number of entries in Table 4.1, for *e.g.* UiO-66(Zr) and derivatives [53], that have been explored for application in heat pumps [157]. Of this series, especially UiO-66(Zr)-NH$_2$ shows interesting water adsorption behavior for AHP/ADCs. Compared to MIL-125(Ti)-NH$_2$, cyclic stability is worse, however. Under equal cycling conditions, the decrease in water capacity is significantly larger for UiO-66(Zr)-NH$_2$, as a 38% reduction in adsorption capacity is observed over 40 cycles [157]. This is in contrast with previous findings, which claim that UiO-66(Zr)-NH$_2$ is stable when exposed to water vapor [51, 52]. The difference in stability might be due to rapid changes in temperature introduced in the cyclic measurements or to the elongated exposure to water vapor compared to other procedures. Alternatively, it could be due to defect chemistry. It has been demonstrated for UiO-66 and derivatives that, depending on synthesis conditions, the number

of organic ligands connected to the inorganic cluster can be much lower than in a perfect crystal (down to 8, where 12 represents the ideal material) [32, 161-163]. More defects have a positive effect on adsorption capacity [161], decrease hydrophobicity [32] but have an adverse effect on thermal stability [162, 164]. It is perfectly possible that these defects also have an adverse effect on the material's tolerance towards water, or that the thermal stability in defected UiO-66(Zr)-NH$_2$ is no longer sufficient. Dwelling on the latter, it has been demonstrated that the amino-group decreases the thermal stability of the UiO-66 structure [51].

De Coste *et al.* reported for UiO-67(Zr), isostructural to UiO-66(Zr) but with elongated BPDC-ligands, instability towards water vapor [51]. This decreased stability was claimed to be due to the torsional strain experienced in the crystalline structure of UiO-67(Zr), making it more susceptible to structural breakdown [51]. In a more recent publication, Mondloch and co-workers reported that this instability may be caused by surface-tension driven collapse of the structure during activation [165]. When the water present in UiO-67(Zr) is solvent-exchanged with acetone prior to thermal activation, the materials displayed no degradation. Without this intermediate step, activation causes (nearly) complete structural breakdown for these two compounds [165]. In addition, DFT-calculations suggest an apparent stability of the UiO-67(Zr)-cluster towards hydrolytic attack, making this mechanism plausible [165]. Others have erroneously claimed that the lowered water capacity of UiO-67(Zr) compared to UiO-66(Zr) is due to hydrophobic domains within the structure, devoid of water at saturation capacity [157]. Defect chemistry is probably of less influence on UiO-67(Zr), as missing linker defects are not as frequently observed for this structure as for UiO-66(Zr) [161, 163]. Unfortunately though, during cyclic operation in AHP/ADCs, solvent-exchange is not an option to prevent collapse during the thermal desorption step, making that in any case, UiO-67(Zr) might not be suitable for application, at least when water is employed as working fluid.

In a more recent study, Furukawa *et al.* investigated water adsorption and stability of a set of novel MOFs incorporating the same Zr-cluster as in the UiO-series, connected by a variety of linkers [166], some of which show remarkable water uptake and stability. As repeated isotherm measurements were performed separated only by brief intermediate evacuation at room temperature, no distinction can be made between intrinsic instability and strong binding of water to certain sites. *E.g.*, the authors found a strong decrease in adsorption capacity of water-stable zeolite 13X after the first cycle, because brief evacuation at room temperature is unsufficient to desorb the strongly adsorbed water in the structure. This is especially relevant,

as many of these novel MOFs have intrinsically a coordination number lower than 12, which means that they have coordinatively unsaturated sites which might bind water strongly. Nonetheless, especially MOF-801(Zr) and MOF-841(Zr) show high reversibility of water adsorption with favorable S-shaped isotherms. This reversibility is also reflected in the moderate values reported for the isosteric heat of adsorption, making them excellent candidates for AHP/ADCs, assuming, for now, that cyclic thermal regeneration of these materials does not cause degradation, as was shown to be the case for UiO-66(Zr) and UiO-67(Zr) materials. Kaskel *et al.* reported a set of zirconium- and hafnium-based MOFs and investigated water uptake [54, 167, 168]. DUT-52(Zr), DUT-53(Zr), DUT-67(Zr) and DUT-68(Zr) show interesting stepwise adsorption behavior [167, 168]. Unfortunately, for DUT-52(Zr) and DUT-53(Zr), the sorption hysteresis loop is not fully closed during desorption, losing a large part of the working capacity [167]. This is less of an issue for DUT-67(Zr) and DUT-68(Zr), which however have the steps in uptake at somewhat inconveniently high relative pressures ($\alpha \geq 0.35$), limiting the material to low temperature lift applications [168]. DUT-67(Hf) and DUT-68(Hf) have nearly identical adsorption behavior as their zirconium-counterparts [168]. The adsorption capacity however, when expressed per unit mass of adsorbent, is lower as hafnium is a heavier element than zirconium. NU-1000(Zr) has the highest water adsorption capacity (on a weight basis) of all zirconium-based MOFs in Table 4.1, but the material is too hydrophobic ($\alpha = 0.75$) [169]. In addition, it has been reported to collapse upon activation when water is present in the pores, as was also the case for UiO-67(Zr) [165]. Using solvent-assisted ligand incorporation (SALI) in post synthesis, hydrophobic organic molecules of varying length were added to unsaturated metal sites (SALI-n) to increase water-repellent behavior [169]. By adding instead hydrophilic chains, the material properties might be tuned towards application in AHP/ADCs. The effect of these added ligands on the stability towards activation in the presence of water is unclear however.

The MOFs discussed so far have in common that the inorganic cluster has a defined number of metal ions (3-8) and the ligands make that the resulting MOF has a three-dimensional structure. There are, however, MOFs that contain polymeric metal-hydroxide or metal-oxide chains extending infinitely in one dimension. Of these, metal-hydroxide containing MIL-53 [170, 171] is arguably the most well-known, because of its stability and reversible structural expansion upon adsorption of different guests. This effect, often referred to as "breathing" [172], has an adverse effect on adsorption, as it often introduces undesired hysteretic behavior [24, 173] in spite of being microporous ($D_c < 2$ nm). Further, the water capacity of MIL-53

and derived materials is disappointingly low and the step in uptake is at unfeasibly high p/p_o for AHP/ADCs. Vanadium-based MIL-47 [174], a rigid MOF with similar structure as MIL-53, is devoid of "breathing" effects and might be of interest. Unfortunately, this structure is far less stable when contacted with H_2O than MIL-53(Cr, Al) [74], and deteriorates even when the structure is decorated with hydrophobic fluorine-groups [175].

A more recently developed metal-hydroxide chain-containing MOF is CAU-10(Al)-H [176]. CAU-10(Al)-H contains isophthalic acid as organic linker and *cis*-connected AlO_6-polyhedra, containing helical chains, whereas MIL-53 contains terephthalic acid and *trans*-connected polyhedra forming linear chains [176]. CAU-10(Al)-H shows a very favorable steep uptake step at $p/p_o = 0.18$ and a decent capacity of ~ 38 % wt. [176]. This uptake resembles a kind of phase change to a highly regular arrangement of water molecules in the structure into a state in between liquid and solid [177] (Chapter 6). Furthermore, the material is stable under repetitive water adsorption, has reasonably low heat of adsorption and can be even grown directly on heat exchanger (aluminium) surfaces, making it an excellent candidate for AHP/ADCs [177]. Fröhlich *et al.* have shown that CAU-10(Al)-H does not lose any capacity over 700 adsorption cycles, showing its extreme stability compared to other MOFs [178]. The resulting coating is stable during repetitive adsorption as well (at least 5 isotherms with any loss of capacity) [177]. Decorating CAU-10(Al) with either hydrophilic or hydrophobic moieties introduces a significantly less favorable adsorption performance. Replacing aromatic isophthalic acid with aliphatic *trans*-1,4-cyclohexane-dicarboxylic acid (CAU-13(Al)) also yields a steep step in uptake albeit with low capacity (0.16 g g^{-1}) [179]. Al-fumarate, containing Al-OH chains linked together by fumaric acid is another MOF with a favorable isotherm for adsorption driven reallocation of heat and cold [180]. The isotherm is similar in shape and uptake as that of CAU-10(Al)-H but the step occurs at slightly higher p/p_o. Further, Jeremias *et al.* were able to grow this MOF on supports using the thermal gradient method they have developed [181]. Unfortunately, the resulting material is not perfectly stable when exposed to repeated adsorption cycles, as a ~13% loss in capacity can be observed over the first 40 adsorption cycles [180]. On the other hand the coated material virtually did not show any further loss of capacity between 1500 and 4500 cycles, making the material still interesting for application [180].

MOF-74 [59] (firstly named CPO-27 [182] or M/DOBDC [183]) is another example of metal-chain based MOFs. The oxygen atoms present in the M-O-M-chains originate from the OH-groups of the dihydroxy-terephthalic acid ligands, which thus are not available for any

specific host-guest interactions. Although MOF-74 can be synthesized with a variety of metal ions (M = Zn, Mg, Ni or Co), water adsorption behavior is strikingly similar (for M = Mg, Ni, Co) [166, 183, 184]. Adsorption occurs primarily at very low p/p_o, due to the irreversible adsorption of H_2O molecules on the cus-sites of the metal incorporated in the structure. The structure of MOF-74(Zn) was shown, with the aid of molecular modelling, to collapse at 10% relative humidity (at 300 K), in line with the reported instability of many other zinc-based MOFs, as discussed previously. Dietzel *et al.*, however, claim that for Zn-based MOF-74, based on temperature dependent PXRD experiments, the crystal structure can be fully recovered upon dehydration, though in the process several structural intermediates are observed [182]. For MOF-74(Co), dehydration is fully reversible as well, though no intermediate structures are formed [182]. Chmelik *et al.* showed for MOF-74(Co) that brief exposure, in the order of seconds, to ambient (moist) air makes the material impermeable to any guest molecule [185]. Exposure to methanol can reverse this adverse effect [185]. The structural retention upon dehydration also holds for MOF-74(Ni). Though when oxygen is present, crystallinity is irreversibly lost, even at mild regeneration temperatures [186]. The porosity of MOF-74(Mg) is lost irreversibly when exposed to humid air [52]. In any case though, very high temperatures are required to desorb the water, explaining why Furukawa *et al.* observed a decrease in adsorption in repeated cycles, employing only mild intermittent regeneration [166]. The preceding indicates that making conclusive remarks about hydrothermal stability is not always straightforward and paradoxical or contradictory remarks may be reported in different sources. Regardless of the (in-)stability of MOF-74, adsorption behavior is not appealing for application in heat transformation and storage, primarily due to the high temperature required for regeneration.

Zeolitic imidazolate frameworks (ZIFs) are a subclass of MOFs known for excellent stability [187]. ZIFs consist of imidazolate ligands that connect individual metal ions in a three-dimensional fashion. The inherent absence of metal-oxide or hydroxide groups on the inorganic cluster and the aromatic nature of imidazoles make that ZIFs are inherently hydrophobic without added functionality. Most notably, hydrophobic ZIF-8 can become increasingly hydrophilic by exchanging methyl-imidazolate ligands with methyl-triazolate ligands [188]. After full ligand exchange, the material (named MAF-7) has favorable water adsorption characteristics for application in AHP/ADCs, albeit that the hysteresis loop does not fully close anymore [188]. As upon this functionalization only one carbon-atom in the aromatic ring of the ligand is replaced by a nitrogen-atom, no reduction in porosity and thus

in adsorption capacity (based on volume) occurs, contrary to functionalization attempts performed for most dicarboxylic acid based MOFs, where bulky functional groups often reduce the available volume for adsorption. In addition, MAF-7(Zn) has been successfully directly grown on structured zinc oxide, without the addition of any solvent, which is very beneficial for application [189]. On top of that, these materials are relatively robust, as it takes multiple days to degrade these materials in boiling water [190].

As mentioned, hydrothermally unstable MOFs can be modified to be more tolerant towards water (vapor). This has been demonstrated by the group of Walton in great detail for pillared MOFs [57, 103, 108, 184, 191]. Pillared MOFs consist of metal-ions, so far all bivalent, linked together in two dimensions by one ligand and in the third dimension by a second ligand (pillars). Notable example is the DMOF [192] (or DABCO-MOF) series. This family consists of metal ions (mostly zinc) coordinated in two dimensions using terephthalate derivates, DABCO (1,4-diazabicyclo[2.2.2]octane) is used to extend the structure in the third dimension. Without or with a variety of functional groups on the terephthalate moiety (NH_2-, Br-, Cl-, OH-, NO_2-, Naphthyl-), the DMOF structure is irreversibly lost upon water adsorption [57, 103, 184]. However, when all vacant positions on the terephthalic acid ligand are replaced with methyl-groups, the structure, named DMOF-TM2, is stable towards water for at least three adsorption cycles [57], while with less methyl-groups instability is still observed [57, 103]. Surprisingly, the material is not fully water repellent and adsorption of water in DMOF-TM2 contains a distinct step ($\alpha = 0.26$) with sufficient loading for application. More recently, this MOF has also been synthesized using different metal ions. The materials become increasingly hydrophobic (measured by the step in the isotherm) when including cobalt ($\alpha = 0.35$), nickel ($\alpha = 0.45$) or copper ($\alpha = 0.55$) ions [108]. Additionally, due to the flexible nature of these frameworks, there seem to be some hysteretic effects which are unfavorable for application [108]. Also for other pillared MOFs, methylation may increase stability (see Table 4.1), but these materials are either too hydrophobic in nature or show low adsorption capacity [108, 191].

Of all cupper-based MOFs, Cu-BTC (also referred to as HKUST-1) shows highest water capacity [43, 107, 158, 183, 184]. Unfortunately, Cu-BTC and most likely other MOFs containing Cu-paddlewheel clusters, are only moderately stable when subjected to water [107, 183, 184]. Notable exception being $Cu_2(dmcapz)_2$, which seems to undergo a reversible structural transition upon water adsorption [193]. Unfortunately for application, the benefits of the stepwise adsorption branch are nullified by a strong, not fully closing, hysteresis loop,

due to this structural transition [193]. The higher stability seems to be due to the ligand used. The pyrazolato-moiety at one end of the ligand (higher *pKa* compared to carboxylates, thus more stable) and the carboxylate oxygen shielded by methyl-groups are considered to contribute to the increased stability compared to other Cu-based MOFs.

Zn-based MOFs often exhibit limited hydrothermal stability. There are however, notable exceptions. Zn-trimesate, containing of zinc-oxide clusters, shows an exceptionally high hydrothermal stability for zinc-based MOFs [194]. Even after 40 adsorption-desorption cycles, its water adsorption capacity, on itself somewhat low for application (20 % wt.), is retained [194]. MFU-4(Zn), containing a rare Zn_5Cl_4-based cluster, exhibits a peculiar linear water adsorption isotherm with a capacity of 0.55 g_{H2O} g^{-1} ($\alpha = 0.25$) and no loss in capacity after water adsorption [195]. Though a linear isotherm, as rare as it is, is better suited for application in AHP/ADCs than Type-I isotherms, a stepwise isotherm is still preferred. $Zn_4O(dmcapz)_3$, which has the same inorganic cluster as water-unstable MOF-5, shows sufficient adsorption capacity and remarkable water stability, due to the dmcapz-ligand [196]. However, the material is too hydrophobic for application. Stability is in line with the claimed water stability of a series Zn-pyrazolate derivates reported by Wade *et al*. [197]. Another method of increasing stability of MOFs with the Zn_4O-cluster, is by fluorination of the organic ligand [198]. Unfortunately, the reported Zn-based MOF is extremely hydrophobic ($\alpha = 0.9$), due to addition of these fluorine-groups [198]. The amino-acid derived Zn-based MOFs reported by Kundu *et al*. were found to be stable as well [199, 200], but also their adsorption characteristics are not very appealing for AHP/ADCs.

ISE-1(Ni), arguably the first MOF specifically designed for application in AHP/ADCs, has only a marginal water capacity (0.18 g g^{-1}) and is seemingly devoid of stepwise uptake [201]. It is however stable upon repeated adsorption cycles, unlike many other bivalent metal-ion (Cu, Zn) containing MOFs [49]. A set of isostructural Ni-based MOFs with increasing ligand length has been reported by Padial *et al*. [202]. Unfortunately this set of materials shows a clear trade-off between capacity and hydrophobicity, as the increase in capacity coincides with an increase in α. They are seemingly stable though, as was the case for ISE-1(Ni). The remaining MOFs in the miscellaneous section of Table 4.1 either are too hydrophobic or hydrophilic or show a low capacity.

Table 4.1: MOFs examined for water adsorption in scientific literature. Maximum capacity (q_{max}), relative pressure for which capacity is 50% of q_{max} (α), pore volume (V_p), enthalpy of adsorption ($\Delta_{ads}H$) and remarks about stability are included where possible.

Material	Ligand	α[a] / -	q_{max} / g g^{-1}	$-\Delta_{ads}H$ / kJ mol^{-1}	V_p[b] / cm^3 g^{-1}	Stability[c]	REF
$M_3(\mu_3\text{-O})(X)(cus)_2$[d]							
MIL-101(Cr)	TPA	0.45	1	-	-	(Th.S.-hi[47])[49, 148, 149, 158, 203-206]	[150]
MIL-101(Cr)-NH$_2$	NH$_2$-TPA	0.42	1.05	43[e]	1.6	6.3% loss in S_{BET} after 40 ads. cycles	[150]
MIL-101(Cr)-pNH$_2$[f]	(NH$_2$)-TPA	0.41	1	43[e]	1.3	6.3% loss in S_{BET} after 40 ads. cycles	[150]
MIL-101(Cr)-NO$_2$	NO$_2$-TPA	0.5	0.45	46[e]	0.6	25% loss in S_{BET} after 40 ads. cycles	[150]
MIL-101(Cr)-pNO$_2$[f]	(NO$_2$)-TPA	0.48	0.6	48[e]	1.0	20% loss in S_{BET} after 40 ads. cycles	[150]
MIL-101(Cr)	TPA	0.44	1	-	1.1	3.2% loss in q_{max} after 40 ads. cycles	[204]
MIL-101(Cr)	"	0.46	1.3	52-40[g]	1.6	(Th.S.-hi[47])[49, 148, 149, 158, 203-206]	[158]
MIL-101(Cr)	"	0.48	1.4	70-35[g]	1.58	(Th.S.-hi[47])[49, 148, 149, 158, 203-206]	[149]
MIL-101(Cr)-NH$_2$	NH$_2$-TPA	0.42	0.95	75-38[g]	1.27	(H.K.-hi[47])[149, 150]	[149]
MIL-101(Cr)-NO$_2$	NO$_2$-TPA	0.48	0.65	38-20[g]	1.19	(L.K.-hi[47])[149, 150]	[149]
MIL-101(Cr)-SO$_3$H	SO$_3$H-TPA	0.28	0.95	60-35[g]	0.94	(Th.S.-hi[47])[149, 207]	[149]
MIL-101(Cr)	TPA	0.47	0.87	-	1.22	(Th.S.-hi[47])[49, 148, 149, 158, 203-206]	[24]
MIL-101(Cr)-NH$_2$	NH$_2$-TPA	0.35	0.9	-	0.97	(H.K.-hi[47])[149, 150]	[24]
MIL-101(Cr)-NO$_2$	NO$_2$-TPA	0.45	0.7	-	0.95	(L.K.-hi[47])[149, 150]	[24]
MIL-101(Cr)	TPA	0.45[h]	0.4	-	-	(Th.S.-hi[47])[49, 148, 149, 158, 203-206]	[208]
+ POM incorporated	"	0.42[h]	0.5	-	-	-	[208]
MIL-101(Al)-NH$_2$	NH$_2$-TPA	0.35	0.43	-	1.67	Rapidly degrades upon exposure to vapor	[76]
MIL-101(Al)-URPh	URPh-TPA	0.40	0.36	-	0.83	More slowly degrades upon exposure to vapor	[76]
MIL-100(Cr)	BTC	0.36[i]	0.4	-	0.77	(Th.S.-med[47])[62, 152, 209]	[153]
Grafted w. EG	"	0.35[i]	0.43	-	0.47	-	[153]
Grafted w. DEG	"	0.35[i]	0.42	-	0.50	-	[153]
Grafted w. TEG	"	0.35[i]	0.33	-	0.53	-	[153]
Grafted w. EN	"	0.35[i]	0.37	-	0.42	~2% loss in q_{max} after	[153]

						20 ads. cycles	
MIL-100(Cr) (X=F)	"	0.3	0.8	48[j]	0.93	Stable after 2000 ads. cycles	[152]
MIL-100(Cr) (X=Cl)	"	0.31	0.6	48-49[j]	0.70	-	[152]
MIL-100(Cr) (X=SO$_4$)	"	0.25	0.6	48-49[j]	0.70	-	[152]
MIL-100(Fe)	"	0.35	0.79	65-40[g]	0.82	(H.K.-hi[47])[154, 158, 203, 210, 211]	[158]
MIL-100(Fe)	"	0.29	0.75	90-50[g]	0.85	6.4% loss in Δq after 40 ads. cycles	[154]
MIL-100(Al)	"	0.28	0.5	80-42[g]	0.8	6.6% loss in Δq after 40 ads. cycles	[154]
Ti$_8$(μ$_2$-O)$_8$(μ$_2$-OH)$_4$							
MIL-125(Ti)	TPA	0.25	0.36	-	0.47	(L.K.-lo[47])[156, 212]	[24]
MIL-125(Ti)-NH$_2$	NH$_2$-TPA	0.2	0.45	-	0.51	(H.K.-hi[47])[156, 157, 212]	[24]
MIL-125(Ti)-NH$_2$	"	0.19	0.35	95-45[g]	0.45	~17% loss in q_{max} after 40 ads. cycles	[157]
MIL-125(Ti)	TPA	0.35	0.30	-	0.60	Unstable during H$_2$O adsorption	[156]
MIL-125(Ti)-NH$_2$	NH$_2$-TPA	0.2	0.52	-	0.67	Stable in aqueous solution (48 h)	[156]
Al$_8$(μ$_2$-OCH$_3$)$_8$(μ$_2$-OH)$_4$							
CAU-1(Al)	NH$_2$-TPA	0.38	0.55		0.64	-	[160]
CAU-1(Al)-NHCH$_3$	NHCH$_3$.TPA	0.48	0.40		0.53	-	[160]
CAU-1(Al)-NHCOCH$_3$	NHCOCH$_3$.TPA	0.26	0.25		0.30	-	[160]
M$_6$(μ$_3$-O)$_{4+x}$(μ$_3$-OH)$_{4-x}$							
UiO-66(Zr)	TPA	0.33	0.36	-	0.41	(H.K.-hi[47])[51, 53, 166, 184, 210, 211, 213, 214]	[24]
UiO-66(Zr)-NH$_2$	NH$_2$-TPA	0.15	0.36	-	0.35	(H.K.-hi[47])[51, 157, 184, 211, 215, 216]	[24]
UiO-66(Zr)	TPA	0.25	0.45	-	0.52	2% loss in S_{BET} after 1 ads. cycle	[184]
UiO-66(Zr)-NH$_2$	NH$_2$-TPA	0.16	0.36	-	0.57	no loss in S_{BET} after 1 ads. cycle	[184]
UiO-66(Zr)	TPA	0.25	0.5	45-20[g]	0.77	(H.K.-hi[47])[51, 53, 166, 184, 210, 211, 213, 214]	[157]
UiO-66(Zr)-NH$_2$	NH$_2$-TPA	0.15	0.45	120-60[g]	0.70	~38% loss in q_{max} after 40 ads. cycles	[157]
UiO-67(Zr)	BPDC	0.6	0.18	75-50[g]	0.97	(H.K.-hi[47])[51, 165, 213, 214]	[157]
UiO-67(Zr)	"	0.5	0.29	-	-	> 99% loss in S_{BET} after 1 cycle	[51]
UiO-66(Zr)-BIPY	BIPY	0.2	0.23	-	-	> 99% loss in S_{BET} after 1 cycle	[51]
UiO-66(Zr)	TPA	0.34	0.43	-	0.49	Slight decr. q_{max}/	[166]

						strong H_2O ads	
UiO-66(Zr)	TPA	0.35	0.37	-	0.52	(H.K.-hi[47])[51, 53, 166, 184, 210, 211, 213, 214]	[217]
UiO-66(Zr)-CH₃	CH₃-TPA	0.29	0.31	-	0.51	Stable after 1 ads. cycle	[217]
UiO-66(Zr)-(CH₃)₂	(CH₃)₂-TPA	0.43	0.23	-	0.40	Stable after 1 ads. cycle	[218]
UiO-66(Zr)	TPA	0.26	0.45	-	0.55	(H.K.-hi[47])[51, 53, 166, 184, 210, 211, 213, 214]	[215]
UiO-66(Zr)-NH₂	NH₂-TPA	0.16	0.34	-	0.52	(H.K.-hi[47])[51, 157, 184, 211, 215, 216]	[215]
UiO-66(Zr)-1,4-Napthyl	1,4-NDC	0.25	0.26	-	0.40	No loss in crystallinity after ads.	[215]
UiO-66(Zr)-NO₂	NO₂-TPA	0.18	0.37	-	0.42	No loss in crystallinity after ads.	[215]
UiO-66(Zr)-2,5-(OMe)₂	(OMe)₂-TPA	0.2	0.42	-	0.38	No loss in crystallinity after ads.	[215]
UiO-66(Zr)-(COOH)₂	(COOH)₂-TPA	0.15[k]	0.27	-	0.21	No loss in q_{max} after 2 ads. cycles	[219]
MOF-801(Zr)	FA	0.09	0.36	62-47[g]	0.45	Stable after 5 ads. cycles	[166]
MOF-802(Zr)	PZDC	0.4	0.09	-	<0.01	Stable after 5 ads. cycles	[166]
MOF-804(Zr)	(OH)₂-TPA	0.4	0.23	-	0.46	Unstable/strong H_2O ads.	[166]
MOF-805(Zr)	(OH)₂-NDC	0.31	0.33	-	0.48	Unstable/strong H_2O ads.	[166]
MOF-806(Zr)	(OH)₂-BPDC	0.1	0.34	-	0.85	Unstable/strong H_2O ads.	[166]
MOF-808(Zr)	BTC	0.3	0.59	-	0.84	Unstable/strong H_2O ads.	[166]
MOF-841(Zr)	MTB	0.22	0.51	58-42[g]	0.53	Stable after 5 ads. cycles	[166]
PIZOF-2(Zr)	(OMe)₂-PEDB	0.75	0.68	-	0.67	Unstable/strong H_2O ads.	[166]
DUT-67(Zr)	TDC	0.22	0.50	-	0.60	Unstable/strong H_2O ads..	[166]
DUT-51(Zr)	DTTDC	0.63	0.55	-	1.08	23% reduction in q_{N2} after 12 h in liq.	[167]
DUT-52(Zr)	2,6-NDC	0.35	0.24	-	0.54	-	[54]
1DUT-84(Zr)	2,6-NDC	0.38	0.12	-	0.27	-	[54]
DUT-53(Hf)	2,6-NDC	0.38	0.22	-	0.31	-	[54]
DUT-67(Zr)	TDC	0.35	0.41	-	0.44	Survives HCl sol. (1 mol L⁻¹), 3 days	[168]
DUT-67(Hf)	TDC	0.35	0.29	-	0.33	Survives HCl sol. (1 mol L⁻¹), 3 days	[168]
DUT-68(Zr)	TDC	0.40	0.34	-	0.41	Survives HCl sol. (1 mol L⁻¹), 3 days	[168]

DUT-68(Hf)	TDC	0.38	0.29	-	0.34	Survives HCl sol. (1 mol L^{-1}), 3 days	[168]
DUT-69(Zr)	TDC	0.30	0.26	-	0.31	Survives HCl sol. (1 mol L^{-1}), 1 day	[168]
DUT-69(Hf)	TDC	0.28	0.20	-	0.22	-	[168]
NU-1000(Zr)	TBAPy	0.75	1.0	-	1.4	Stable after 1 ads. cycle	[169]
+ SALI-1	CF$_3$CO$_2^-$	0.80	0.9	-	1	Stable after 1 ads. cycle	[169]
+ SALI-3	CF$_3$(CF$_2$)$_2$CO$_2^-$	0.80	0.7	-	0.8	Stable after 1 ads. cycle	[169]
+ SALI-7	CF$_3$(CF$_2$)$_6$CO$_2^-$	0.85	0.45	-	0.6	Stable after 1 ads. cycle	[169]
+ SALI-9	CF$_3$(CF$_2$)$_8$CO$_2^-$	0.85	0.35	-	0.6	Stable after 1 ads. cycle	[169]
[M(μ$_2$-OH)]$_n$							
MIL-53(Cr)	TPA	0.15	0.1	60-40[1]	-	(H.K.-hi[47])[74]	[173]
MIL-53(Al)	"	0.09	0.14	-	0.51	(H.K.-hi[47])[49, 74, 80]	[24]
MIL-53(Al)-NH$_2$	NH$_2$-TPA	0.08	0.04	-	0.37	-	[24]
MIL-53(Ga)	TPA	0.05	0.02	-	0.47	-	[24]
MIL-53(Ga)-NH$_2$	NH$_2$-TPA	-	0.02	-	-	-	[24]
MIL-53(Al)	TPA	0.30	0.09	-	-	(H.K.-hi[47])[49, 74, 80]	[220]
MIL-53(Fe)-(COOH)$_2$	(COOH)$_2$-TPA	0.05	0.16	-	-	-	[220]
MIL-53(Al)-OH	OH-TPA	0.75	0.40	-	-	-	[220]
MIL-53(Al)-(OH)$_{.68}$(NH$_2$)$_{.32}$	NH$_2$-/OH-TPA	0.80	0.36	-	-	-	[221]
MIL-53(Al)-(OH)$_{0.53}$(NH$_2$)$_{.47}$	NH$_2$-/OH-TPA	0.88	0.23	-	-	-	[221]
MIL-53(Al)-(OH)$_{0.34}$(NH$_2$)$_{.66}$	NH$_2$-/OH-TPA	0.02	0.11	-	-	-	[221]
MIL-53(Al)-Cl	Cl-TPA	0.18	0.14	-	0.32	-	[222]
MIL-53(Al)-Br	Br-TPA	0.50	0.11	-	0.14	-	[222]
MIL-53(Al)-CH$_3$	CH$_3$-TPA	0.25	0.11	-	0.32	-	[222]
MIL-53(Al)-NO$_2$	NO$_2$-TPA	0.10	0.12	-	0.34	-	[222]
MIL-53(Al)-(OH)$_2$	(OH)$_2$-TPA	0.65	0.42	-	0.07	-	[222]
MIL-53(Al)-F	F-TPA	0.80	0.07	-	0.48	No reduction in Hexane capacity after 1 ads. cycle	[175]
MIL-53(Al)-F$_2$	F$_2$-TPA	0.70	0.23	-	0.16	-	[223]
MIL-47(V)-F	F-TPA	0.60	0.18	-	0.36	~50% reduction in Hexane capacity after 1 ads. cycle	[175]
MIL-47(V)-F$_2$	F$_2$-TPA	0.70	0.18	-	0.34	-	[223]
MIL-53(Al)-NH$_2$	NH$_2$-TPA	0.02	0.09	-	-	-	[220]
MIL-53(Al)$_{ionothermal}$	TPA	0.15	0.08	-	0.36	-	[224]
MIL-53(Al)-SO$_3$H	SO$_3$H-TPA	0.45	0.45	-	-	Stable over 3 ads. cycles	[225]

Al(OH)-(1,4-NDC)	1,4-NDC	0.45	0.16	-	0.22	-	[226]
DUT-4(Al)	2,6-NDC	0.65	0.52	-	0.79	Unstable during first ads. cycle	[158]
MIL-68(In)	TPA	0.58	0.32	-	0.42	-	[24]
MIL-68(In)-NH$_2$	NH$_2$-TPA	0.44	0.32	-	0.30	-	[24]
CAU-10(Al)-H	IPA	0.18	0.35	53.5$^{(Ch. 6)[g]}$	0.27	No capacity loss over 700 ads. cycles	[178]
CAU-10(Al)-H	IPA	0.18	0.38	53.5$^{(Ch. 6)[g]}$	0.28	Survives liq. water (18 h)	[176]
CAU-10(Al)-CH$_3$	CH$_3$-IPA	0.45	0.18	-	-	Survives liq. water (18 h)	[176]
CAU-10(Al)-OCH$_3$	OCH$_3$-IPA	0.25	0.08	-	-	Survives liq. water (18 h)	[176]
CAU-10(Al)-NO$_2$	NO$_2$-IPA	0.32	0.17	-	0.21	Survives liq. water (18 h)	[176]
CAU-10(Al)-NH$_2$	NH$_2$-IPA	0.16	0.23	-	-	Survives liq. water (18 h)	[176]
CAU-10(Al)-OH	OH-IPA	0.16	0.30	-	-	Survives liq. water (18 h)	[176]
CAU-13(Al)	CDC	0.22	0.16	-	0.15	-	[179]
Al-fumarate	FA	0.27	0.45	50-42$^{[g]}$	0.48	~ 13% loss in Δq over 40 ads. cycles	[180]
[M$_2$O$_2$]$_n$							
MOF-74(Mg)	(OH)$_2$-TPA	0.02	0.63	-	0.65	83% loss in S_{BET} after 1 cycle	[184]
MOF-74(Mg)	"	0.05	0.60	-	0.53	Unstable/strong H$_2$O ads.	[166]
MOF-74(Ni)	"	0.05	0.51	-	0.49	Unstable/strong H$_2$O ads.	[166]
MOF-74(Co)	"	0.05	0.49	-	0.46	Unstable/strong H$_2$O ads.	[166]
MOF-74(Ni)	"	0.02	0.54	-	-	Little loss in q_{CO2} after H$_2$O ads.	[183]
ZIFs							
ZIF-8(Zn)	mIm	-	-	-	0.49	(Th.S.-hi[47])[49, 62, 158, 187, 227]	[188]
SIM-1(Zn)	mImca	0.27	0.14	-	0.30	-	[24]
MAF-4(ZIF-8)	mIm	-	-	-	0.65	(Th.S.-hi[47])[49, 62, 158, 187, 227]	[188]
MAF-4$_{.76}$-7$_{.24}$	mIm/mTz	0.85	0.4	-	0.64	-	[188]
MAF-4$_{.49}$-7$_{.51}$	mIm/mTz	0.62	0.43	-	0.65	-	[188]
MAF-4$_{.23}$-7$_{.77}$	mIm/mTz	0.37	0.43	-	0.64	-	[188]
MAF-7(Zn)	mTz	0.27	0.43	-	0.65	-	[188]
ZIF-71(Zn)	dcIm	-$^{[h]}$	-	-	0.39	-	[228]
ZIF-90(Zn)	Ica	0.35$^{[h]}$	0.32	-	0.49	(H.K.-med[47])[227]	[228]
CoNIm	NIm	0.55$^{[i]}$	0.16	-	-	-	[229]
Pillared MOFs: M(II)(L$_a$)(L$_b$)$_{0.5}$							
DMOF(Zn)	TPA/DABCO	0.30	0.09	-	0.75	100% loss in S_{BET} after 90% R.H.	[184]
DMOF(Zn)-NH$_2$	NH$_2$-	0.30	0.08	-	0.58	100% loss in S_{BET} after	[184]

	TPA/DABCO					90% R.H.	
DMOF(Zn)-Br	Br-TPA/DABCO	0.45	0.05	-	0.53	100% loss in S_{BET} after 90% R.H.	[103]
DMOF(Zn)-Cl₂	Cl₂-TPA/DABCO	0.35	0.07	-	0.45	100% loss in S_{BET} after 90% R.H.	[103]
DMOF(Zn)-OH	OH-TPA/DABCO	0.30	0.11	-	0.54	100% loss in S_{BET} after 90% R.H.	[103]
DMOF(Zn)-NO₂	NO₂-TPA/DABCO	0.40	0.14	-	0.53	97% loss in S_{BET} after 90% R.H.	[103]
DMOF(Zn)-N	NDC/DABCO	-	-	-	0.57	26% loss in S_{BET} after 90% R.H.	[103]
DMOF(Zn)-A	ADC/DABCO	0.30	0.27	-	0.33	4% loss in S_{BET} after 90% R.H.	[103]
DMOF-TM1(Zn) (mixed linker)	TMBDC/TPA/DABCO	0.44	0.27	-	0.53	30% loss in S_{BET} after 90% R.H.	[103]
DMOF-TM2(Zn)	TMBDC/DABCO	0.26	0.43	-	0.51	Stable over 3 ads. cycles	[57]
DMOF-TM(Co)	TMBDC/DABCO	0.35	0.40	-	0.49	3.4% loss in S_{BET} after 1 cycle	[108]
DMOF-TM(Ni)	TMBDC/DABCO	0.45	0.40	-	0.48	2.5% loss in S_{BET} after 1 cycle	[108]
DMOF-TM(Cu)	TMBDC/DABCO	0.55	0.42	-	0.46	4.9% loss in S_{BET} after 1 cycle	[108]
Cd(BTTB)[m]	BTTB	0.50	0.27	-	0.19	100% loss in S_{BET} after 90% R.H.	[191]
Zn(BTTB)[m]	BTTB	0.70	0.22	-	0.25	100% loss in S_{BET} after 90% R.H.	[191]
Zn(BTTB)(BDC)[m]	BTTB/TPA	0.50	0.09	-	0.21	50% loss in S_{BET} after 90% R.H.	[191]
Ni(BTTB)[m]	BTTB	0.80	0.02	-	0.20	no loss in S_{BET} after 90% R.H.	[191]
Co(BTTB)(BPY)	BTTB/BPY	0.30	0.01	-	0.40	no loss in S_{BET} after 90% R.H.	[191]
Zn(BTTB)(BPY)	BTTB/BPY	0.70	0.27	-	0.38	no loss in S_{BET} after 90% R.H.	[191]
Co(BTTB)(AZPY)	BTTB/AZPY	0.55	0.25	-	0.39	56% loss in S_{BET} after 90% R.H.	[191]
Zn(BTTB)(AZPY)		0.55	0.20	-	0.36	43% loss in S_{BET} after 90% R.H.	[191]
Co(BTTB)(DMBPY)	BTTB/DMBPY	0.85	0.20	-	0.29	0.2% loss in S_{BET} after 90% R.H.	[108]
Zn(BTTB)(DMBPY)	BTTB/DMBPY	0.85	0.22	-	0.27	1.2% loss in S_{BET} after 90% R.H.	[108]
Cu₂(pzdc)₂pyz	Pzdc/pyz	0.10[k]	0.12	-	-	-	[230]
Cu₂(pzdc)₂bpy	Pzdc/bpy	0.09[k]	0.17	-	-	-	[230]
Cu₂(pzdc)₂bpe	Pzdc/bpe	0.08[k]	0.29	-	-	-	[230]
Copper based MOFs (remainder)							
CuBTC	BTC	0.1	0.5	-	0.62	26% loss in S_{BET} after 1 cycle	[107, 184]
CuMBTC	CH₃-BTC	0.30	0.18	-	0.50	Loss of crystallinity	[107]

						after 90% R.H.	
CuEBTC	C$_2$H$_5$-BTC	0.15	0.18	-	0.46	Loss of crystallinity after 90% R.H.	[107]
Cu-BTC	BTC	0.15[n]	0.54	-	-	(L.K.-hi[47])[49, 62, 158, 184, 209, 210, 231]	[43]
Cu-BTC	"	0.1	0.5	-	0.72	(L.K.-hi[47])[49, 62, 158, 184, 209, 210, 231]	[158]
Cu-BTC	"	0.5	0.72	-	-	Unstable when contacted with H$_2$O	[183]
Cu$_2$(dmcapz)$_2$	dmcapz	0.33	0.22	-	0.23	Reversible structural change upon ads.	[193]
Cu$_2$(pmpmd)$_2$ (CH$_3$OH)$_4$(opd)$_2$	pmpmd /opd	0.15	0.20	-	-	-	[232]
Zinc based MOFs (remainder)							
Zn-Trimesate	BTC	0.10[k]	0.2	-	-	Stable after 40 cycles (hydrothermal)	[194]
Zn$_2$(bptc)	Bptc	0.18	0.16	-	-	-	[233]
MFU-4(Zn)	BBTA	0.25	0.55	-	-	No loss in q_{max} after 1 ads. cycle.	[195]
ThrZnOAc	Thr	0.25	0.15	-	-	-	[199]
AlaZnOAc	Ala	0.88	0.25	-	-	-	[199]
AlaZnCl	"	0.25	0.16	-	-	Stable for 6 months in H$_2$O	[200]
AlaZnBr	"	0.60	0.14	-	-	Stable for 6 months in H$_2$O	[200]
ValZnOAc	Val	0.78	0.25	-	-	-	[199]
ValZnCl	"	0.45	0.07	-	-	Stable for 6 months in H$_2$O	[200]
(H$_2$dab)[Zn$_2$(ox)$_3$]	ox/dab	0.70	0.23	-	-	-	[234]
Zn(NDI-H)	NDI-H	0.45[i]	0.45	-	0.65	Survives liq. water (24 h)	[197]
Zn(NDI-SEt)	NDI-SEt	0.41[i]	0.25	-	0.39	-	[197]
Zn(NDI-SOEt)	NDI-SOEt	0.26[i]	0.30	-	0.38	-	[197]
Zn(NDI-SO$_2$Et)	NDI-SO$_2$Et	0.35[i]	0.25	-	0.31	-	[197]
Zn$_4$O(dmcapz)$_3$	dmcapz	0.85	0.45	-	0.43	Mild degradation after H$_2$O ads.	[196]
Zn$_4$O(bfbpdc)$_3$(bpy)$_{.5}$	bfbpdc/bpy	0.92	0.50	-	0.59	Stable upon exposure to water (vapor)	[198]
Zn$_2$(bptc)	Bptc	0.18	0.16	-	-	-	[233]
Miscellaneous MOFs							
CAU-3(Al)	TPA	0.63	0.51	-	0.64	-	[235]
CAU-3(Al)-NH$_2$	NH$_2$-TPA	0.67	0.50	-	0.53	-	[235]
CAU-6(Al)	NH$_2$-TPA	0.09	0.40	-	0.25	(L.K.-lo[47])[166]	[236]
CALF-25(Ba)	PytPh	0.60	0.09	45[g]	-	Stable over 4 ads. cycles	[99]
ISE-1(Ni)	BTC/btre	0.15[o]	0.18	-	0.51	Stable over 10 ads. cycles	[201]
JUC-110(Cd)	THIPC	0.2	0.11	-	-	Survives boiling water	[237]

177

						(10 days)	
Ni₈(L1)₆	L1	0.9	0.45	-	0.52	Stable over 3 ads. cycles	[202]
Ni₈(L2)₆	L2	0.8	0.63	-	0.52	Mild degradation after H₂O ads.	[202]
Ni₈(L3)₆	L3	0.4	0.99	-	1.21	Stable over 3 ads. cycles	[202]
Ni₈(L4)₆	L4	0.45	0.9	-	0.97	Stable over 3 ads. cycles	[202]
Ni₈(L5)₆	L5	0.7	1.12	-	1.25	Stable over 3 ads. cycles	[202]
Ni₈(L5-(CH₃)₂)₆	L5-(CH₃)₂	0.72	0.70	-	-	-	[202]
Ni₈(L5-(CF₃)₂)₆	L5-(CF₃)₂	0.85	0.86	-	-	-	[202]
([Ni(L6)₂]·4H₂O)ₙ	L6	0.11	0.12	-	-	Stable after 1 ads. cycle	[238]
[Cd(L'1)(Cl)](H2O)	L'1	0.9	0.38	-	-	-	[239]
[Cd(L'2)(Cl)](H2O)	L'2	0.1	0.09	-	-	-	[239]
[Cd₂(L'2)₂(Br)₂](H₂O)₃	L'2	0.5	0.04	-	-	-	[239]
[Cd(L'3)(Cl)](H₂O)₂	L'3	0.15	0.11	-	-	-	[239]
[Cd(L7)(DMF)]	L7	0.1	0.15	-	-	Stable in boiling water, 1 day	[240]
[Co(DPE)]·0.5DPE	DPE	0.45	0.20	-	0.14	-	[241]
[Dy(ox)(Bpybc)(H2O)]	Ox/ Bpybc	0.60	0.25	-	-	-	[242]
[PbL₂]·2DMF·6H₂O	L	0.8	0.24			-	[243]

Notes: [a] p/p_o for which $q = 0.5\, q_{max}$. Measured at 298 K unless otherwise noted. [b] Based on N_2 adsorption (at 77 K). Reported values are used where possible. Otherwise these are estimated from N_2 isotherms. [c] For entries which do not contain clear statements regarding stability, the classification of Burtch *et al.* has been used, including the confidence expressed by the authors (hi(gh),lo(w) or med(ium)) and the references on which their verdict has been based [47]. [d] X = F,OH. [e] Average value from isosteric method for $q < 0.1$ g g⁻¹. [f] *p* stands for partial, indicating that ~ 78% mol. of the linkers is functionalized, and ~ 22% is plain TPA. [g] Isosteric heat of adsorption, calculated with Eq. 4.22. [h] Measured at 308 K. [i] Measured at 293 K. [j] Based on Dubinin-Radushkevich (DR) analysis [244] for second ($0.3 < p/p_o < 0.4$) and third step ($0.5 < p/p_o < 0.7$). [k] Measured at 303 K. [l] Determined by microcalorimetry. [m] not a pillared MOF, added for comparison with others. [n] Measured at 323 K. [o] Measured at 313 K.

As a general observation, for MOFs of which water adsorption is reported in multiple literature sources, both *α* and uptake capacity seem to vary. The latter is mostly due to variation in material quality. The former however can be caused by a variety of reasons, *e.g.* measurements are conducted differently (static, under flow *etc.*). In some isotherms condensation effects start occurring already at $p/p_o \sim 0.9$, implying that the p_o value might be inaccurate. Furthermore, as water adsorption measurements are generally relatively time consuming, there is a large fluctuation in the concentration of data points in reported isotherms, making that stepwise uptake is shown in various resolutions. Also, minor shifts in *α* are to be expected as a function of measurement temperature (Eq. 4.21). In addition, as indicated by Ghosh *et al.*, also a shift in uptake might be observed due to defects [32]. One

should take this into consideration when browsing through the different entries of the same structure in Table 4.1.

4.4.2. METHANOL ADSORPTION (TABLE 4.2)

Not surprisingly, for MIL-101(Cr), one of the most reported MOFs in literature, methanol adsorption has been investigated [141]. The isotherm is nearly linear and the high saturation capacity is reached at $p/p_o \sim 0.4$, making the material suitable for application in AHP/ADCs [141]. MIL-53(Cr) shows a clear step in the desired relative pressure range [173]. Unfortunately, this step comprises only part of the (moderate) adsorption capacity. Furthermore, the enthalpy of adsorption is relatively high compared to the enthalpy of evaporation of methanol.

Both hydrophobic ZIF-8 and ZIF-71 and hydrophilic ZIF-91 show decent uptake of methanol in a narrow relative pressure range [228], indicating that water adsorption is more sensitive to the interior decoration of the pore space than is the case for alcohols. By exchanging methyl-imidazolate ligands (ZIF-8 or MAF-4(Zn)) with methyl-triazolate ligands to form (MAF-7(Zn)) the step in adsorption can be tuned to lower relative pressures [190], as was shown for water adsorption previously [188].

Cu-BTC displays a fair capacity for methanol but adsorption occurs at low relative pressures, making regeneration energetically costly [43]. $Cu_2(dmcapz)_2$ shows a very favorable step in adsorption, making it potentially interesting for application [193]. However, this steep adsorption step is due to a structural transition, and requires high temperatures to be reversed. Therefore, under isothermal conditions, hysteresis during desorption does not fully close. $Cu_4O(OH)_2(Me_2trzpba)_4$ also shows high methanol capacity but suffers from a large desorption hysteresis as well. DABCO (TED)-based MOF $Zn(BDC)(TED)_{0.5}$, notoriously unstable in the presence of water, shows a good uptake of methanol at relevant relative pressures and only has a mild hysteresis [245]. Enthalpy of adsorption is in the same order of magnitude as MIL-53(Cr). The instability though, might be the reason why others indicate inferior adsorption properties for seemingly the same compound [246]. Most of the remaining MOFs in Table 4.2 either suffer from unfavorable adsorption behavior or unsatisfactory capacity.

Table 4.2: MOFs examined for methanol adsorption in scientific literature. Maximum capacity (q_{max}), relative pressure for which capacity is 50% of q_{max} (α), pore volume (V_p), enthalpy of adsorption ($\Delta_{ads}H$) and remarks about stability are included where possible.

Material	Ligand	α[a] / -	q_{max} / g g^{-1}	$-\Delta_{ads}H$ / kJ mol^{-1}	V_p[b] / cm^3 g^{-1}	Stability	REF
MIL-101(Cr)	TPA	0.25	1.15	-	-	-	[141]
MIL-53(Cr)	"	0.18	0.40	65-42[c]	-	-	[173]
Al(OH)-(1,4-NDC)	1,4-NDC	0.05	0.16	-	0.22	-	[226]
ZIF-8(Zn)	mIm	0.15[d]	0.34	-	0.63	-	[228]
ZIF-71(Zn)	dcIm	0.25[d]	0.27	-	0.39	-	[228]
ZIF-90(Zn)	Ica	0.07[d]	0.29	-	0.49	-	[228]
ZIF-68(Zn)	nIm/bIm	0.25[e]	0.28	-	0.44	-	[247]
MAF-4(ZIF-8)	mIm	0.18	0.40	-	-	Stable in boiling methanol (7 days)	[190]
MAF-5(Zn)	eim	0.25	0.20	-	-	Stable in boiling methanol (7 days)	[190]
MAF-7(Zn)	mTz	0.07	0.40	-	-	Stable in boiling methanol (7 days)	[190]
Cu-BTC	BTC	0.05	0.60	-	-	-	[141]
Cu-BTC	"	0.01[e]	0.55	-	-	-	[43]
Cu$_2$(pmpmd)$_2$ (CH$_3$OH)$_4$(opd)$_2$	pmpmd /opd	0.55	0.50	-	-	-	[232]
Cu$_2$(dmcapz)$_2$	dmcapz	0.05	0.19	-	0.23	Revers. structural change upon ads.	[193]
Cu$_4$O(OH)2(Me2trzpba)$_4$	Me2trzpba	0.18	0.45	-	0.58	-	[248]
Cu$_2$(pzdc)$_2$(dpyg)	Pzdc/dpyg	0.30	0.11	-	-	-	[249]
MAF-2(Cu)	etz	0.05	0.16	-	-	-	[250]
Zn(BDC)(TED)$_{0.5}$	TPA/TED	0.15[f]	0.50	-	-	-	[41]
Zn(BDC)(TED)$_{0.5}$	"	0.14	0.50	60-41[g]	-	-	[245]
Zn$_2$(BDC)$_2$(dabco)	BDC/dabco	0.01	0.21	-	-	-	[246]
Zn$_2$(NDC)$_2$(dabco)	1,4-NDC/dabco	<0.01	0.16	-	-	-	[246]
Zn$_5$O$_2$(bpdc)$_4$	bpdc	0.10	0.15	-	-	-	[251]
ThrZnOAc	Thr	0.10	0.15	-	-	-	[199]
AlaZnOAc	Ala	0.15	0.12	-	-	-	[199]
ValZnOAc	Val	0.5	0.06	-	-	-	[199]
(H$_2$dab)[Zn$_2$(ox)$_3$]	ox/dab	0.35	0.32	-	-	-	[234]
Zn$_2$(bptc)	Bptc	<0.01	0.10	-	0.15	-	[233]
Zn(tbip)	Tbip	0.30	0.11	-	0.13	-	[252]
Co(pybz)$_2$	pybz	0.05	0.23	-	-	-	[253]
CoDPE	DPE	0.50	0.11	-	0.14	-	[241]
Co$_3$(fa)$_6$	FA	0.04[f]	0.10	-	0.14	-	[254]
JUC-110(Cd)	THIPC	<0.01	0.06	-	-	-	[237]
Cd(4-btapa)$_2$(NO$_3$)$_2$	4-btapa	0.50	0.10	-	-	-	[255]
[Cd(L7)(DMF)]	L7	<0.01	0.11	-	-	-	[240]
Mn-formate	FA	0.08	0.14	-	-	-	[256]
([Ni(L6)$_2$]·4H$_2$O)$_n$	L6	0.22	0.13	-	-	Stable for 1 cycle	[238]
[Dy(ox)(Bpybc)(H2O)]	Ox/ Bpybc	0.80	0.10	-	-	-	[242]
([Eu(CAM)(HCAM)$_2$Mn$_2$(H$_2$O)$_4$])$_n$	(H)CAM	<0.01	0.26	-	-	-	[257]

Notes:[a] p/p_o for which $q = 0.5\ q_{max}$, measured at 298 K unless otherwise mentioned. [b] Based on N_2 adsorption (at 77 K). Reported values are used where possible. Otherwise these are estimated from N_2 isotherms. [c] Determined by microcalorimetry. [d] Measured at 308 K. [e] Measured at 323 K. [f] Measured at 303 K. [g] Isosteric heat of adsorption, calculated with Eq. 4.22.

4.4.3. ETHANOL ADSORPTION (TABLE 4.3)

MIL-101(Cr) shows adsorption behavior that can be described as the combination of two Type I isotherms, one at low and one at intermediate relative pressure, and an outstanding capacity [258]. Furthermore, it has been shown that for at least 20 adsorption/desorption cycles of ethanol, MIL-101(Cr) remains stable [258]. The Type I isotherm at low relative pressure unfortunately means that relatively high desorption temperature is required for full regeneration. MIL-100(Cr) shows uptake at lower relative pressures, at the expense of lower capacity [258]. Ethanol adsorption in MIL-53(Cr) shows very similar isotherm shape and step location, as was found for methanol [173]. As was the case for methanol, the enthalpy of adsorption for ethanol is somewhat high, compared to the enthalpy of evaporation for this structure [173]. Bipyridyl-based UiO exhibits high ethanol capacity, albeit at a low relative pressure ($\alpha = 0.05$) [259]. The structure was deemed stable, as after ethanol adsorption and after soaking the material in water or methanol the structure does not show degradation in the X-ray diffraction pattern [259]. This in shear contrast with DeCoste *et al.*, who reported that the bipyridyl-moiety makes the resulting UiO-derivative instable towards methanol exposure [51].

The aforementioned family of ZIFs shows steep uptake at somewhat lower relative pressures than for methanol [228]. The same was found for ethanol adsorption in Cu-BTC [43], but, like for methanol, the uptake is located at undesirably low relative pressures. Zn(BDC)(TED)$_{0.5}$, as was found for methanol, shows a step-like uptake of ethanol with a good capacity [245]. Most of the remaining MOFs in Table 4.3 either suffer from unfavorable adsorption behavior or unsatisfactory capacity.

Table 4.3: MOFs examined for ethanol adsorption in scientific literature. Maximum capacity (q_{max}), relative pressure for which capacity is 50% of q_{max} (α), pore volume (V_p), enthalpy of adsorption ($\Delta_{ads}H$) and remarks about stability are included where possible.

Material	Ligand	$\alpha^{[a]}$ / -	q_{max} / g g^{-1}	$-\Delta_{ads}H$ / kJ mol^{-1}	$V_p^{[b]}$ / cm^3 g^{-1}	Stability	REF
MIL-100(Cr)	BTC	0.1	0.6	-	-	-	[258]
MIL-101(Cr)	TPA	0.18	1.1	-	-	Stable over 20 ads. cycles	[258]
MIL-53(Cr)	TPA	0.18	0.36	70-48[c]	-	-	[173]
UiO(bipy)	bipy	0.05[d]	0.70	-	1.05	Stable over 1 ads. cycle	[259]
ZIF-8(Zn)	mIm	0.07[e]	0.28	-	0.63	-	[228]
ZIF-71(Zn)	dcIm	0.13[e]	0.28	-	0.39	-	[228]
ZIF-90(Zn)	Ica	0.04[e]	0.28	-	0.49	-	[228]
ZIF-68(Zn)	nIm/bIm	0.05[f]	0.26	-	0.44	-	[247]
Cu-BTC	BTC	<0.01[f]	0.57	-	-	-	[43]
MAF-2(Cu)	etz	0.05	0.25	-	-	-	[250]
Zn(BDC)(TED)$_{0.5}$	TPA/TED	0.09	0.4	66-41[g]	-	-	[245]
(H$_2$dab)[Zn$_2$(ox)$_3$]	ox/dab	0.45	0.26	-	-	-	[234]
Zn$_2$(BDC)$_2$(dabco)	BDC/dabco	0.01	0.33	-	-	-	[246]
Zn$_2$(NDC)$_2$(dabco)	1,4-NDC/dabco	<0.01	0.20	-	-	-	[246]
[Co(L)(DPE)]·0.5DPE	DPE	-	-	-	0.14	-	[241]
Co$_3$(fa)$_6$	FA	<0.01[h]	0.11	-	0.14	-	[254]
JUC-110(Cd)	THIPC	-	-	-	-	-	[237]
[Cd(L7)(DMF)]	L7	<0.01	0.06	-	-	Stable in boiling ethanol, 1 day	[240]
([Ni(L6)$_2$]·4H$_2$O)$_n$	L6	0.09	0.07	-	-	Stable after 1 measurement	[238]
[Dy(ox)(Bpybc)(H2O)]	Ox/ Bpybc	-	-	-	-	-	[242]
([Eu(CAM)(HCAM)$_2$Mn$_2$(H$_2$O)$_4$])$_n$	(H)CAM	<0.01	0.26	-	-	-	[257]

Notes: [a] p/p_o for which $q = 0.5\ q_{max}$, measured at 298 K unless otherwise mentioned. [b] Based on N$_2$ adsorption (at 77 K). Reported values are used where possible. Otherwise these are estimated from N$_2$ isotherms. [c] Determined by microcalorimetry. [d] Measured at 293 K. [e] Measured at 308 K. [f] Measured at 323 K. [g] Isosteric heat of adsorption, calculated with Eq. 4.22. [h] Measured at 303 K.

4.4.4. AMMONIA ADSORPTION (TABLE 4.4)

The availability of ammonia adsorption data in literature, see Table 4.4, is quite limited, and the research scope for this adsorptive is entirely different. Investigations are tailored towards the capture of toxic gaseous compounds [260-262], explaining why in many cases only (trace) ammonia adsorption capacities from breakthrough experiments, where NH$_3$ is diluted to concentrations down to 1000 mg m^{-3} [260, 261, 263], are presented. It is clear that, from these data, assessment for AHP/ADCs would be difficult. MOF stability towards ammonia seems to be at least a similar issue as was found for water. All Zn$_4$O-cluster based MOFs under study

seem to degrade completely upon contact with ammonia [264, 265]. Also HKUST-1 seems to completely degrade during NH_3 adsorption [266]. Though according to Borfecchia *et al.*, NH_3 adsorption on dry HKUST-1 only results in strong chemisorption of ammonia on Cu(II), distorting the framework, but without loss of crystallinity [267]. Only in the simultaneous presence of water and ammonia a strong detrimental effect on the structure should be observed [267]. In contrast, MIL-100(Fe) is more stable towards ammonia, as after breakthrough experiments with ammonia under dry or humid conditions, no significant loss in porosity can be observed from breakthrough experiments, employing MOF-carbon composites [268]. UiO-66(Zr), post-functionalized with various combinations of exotic side-groups, also seem to show reversible adsorption (up to $p/p_o \sim 0.12$), indicated by the apparent closed hysteresis loop [269]. This actually indicates another issue with the assessment of ammonia for AHP/ADCs. As many standard set-ups can only measure up to roughly 1.2 bar, yielding a relative pressure of ~ 0.12 at room temperature, only a small part of the ammonia isotherm is commonly reported. This is especially troublesome as the application window is $0.15 < p/p_o < 0.55$ for ammonia (Chapter 1). Therefore the volume that could be filled with ammonia (liquid density of ammonia is ~ 0.77 g ml^{-1} at STP (0 ^{o}C, 1 bar)) is significantly smaller than the reported pore volume in all entries of Table 4.4. Therefore, in this study, ammonia is disregarded as potential working fluid and future measurements should be conducted, for NH_3-tolerant MOFs, at higher relative pressures (*e.g.* by decreasing measurement temperature).

Table 4.4: MOFs examined for ammonia adsorption in scientific literature. Maximum capacity (q_{max}), relative pressure for which capacity is 50% of q_{max} (α), pore volume (V_p), enthalpy of adsorption ($\Delta_{ads}H$) and remarks about stability are included where possible.

| Material	Ligand	α[a] / -	q_{max} / g g^{-1}	$-\Delta_{ads}H$ / kJ mol^{-1}	V_p[b] / cm^3 g^{-1}	Stability	REF
UiO-66(Zr)-A	(NH$_2$)$_{.67}$-/(NH$_3^+$Cl$^-$)$_{.33}$-TPA	<0.01	0.10[c]	-	-	Stable/Reversible ads.	[269]
UiO-66(Zr)-B	(NH$_3^+$Cl$^-$)$_{.30}$/(hma)$_{.50}$-/(azi)$_{.20}$-TPA	<0.01	0.11[c]	-	-	Stable/Reversible ads.	[269]
UiO-66(Zr)-C	(NH$_3^+$Cl$^-$)$_{.33}$/(hma)$_{.11}$-/(azi)$_{.56}$-TPA	0.01	0.15[e]	-	-	Stable/Reversible ads.	[269]
UiO-66(Zr)-NH$_2$	NH$_2$-TPA	-[d]	0.06[e]	-	0.46	-	[261]
UiO-66(Zr)	TPA	-	0.03[f]	-	-	-	[270]
UiO-66(Zr)-NH$_2$	NH$_2$-TPA	-	0.06[f]	-	-	-	[270]
UiO-66(Zr)-NO$_2$	NO$_2$-TPA	-	0.03[f]	-	-	-	[270]
UiO-66(Zr)-OH	OH-TPA	-	0.10[e]	-	-	-	[270]
UiO-66(Zr)-(OH)$_2$	(OH)$_2$-TPA	-	0.04[e]	-	-	-	[270]
UiO-66(Zr)-SO$_3$H	SO$_3$H-TPA	-	0.04[e]	-	-	-	[270]
UiO-66(Zr)-(COOH)$_2$	(COOH)$_2$-TPA	-	0.05[e]	-	-	-	[270]
DMOF(Zn)	TPA/DABCO	-	<0.01[f]	-	-	-	[270]
DMOF(Zn)-A	ADC/DABCO	-	<0.01[f]	-	-	-	[270]
DMOF(Zn)-TM2	TMBDC/DABCO	-	<0.01[f]	-	-	-	[270]
Zn(BTTB)	BTTB	-	0.08[f]	-	-	-	[270]
Cu(BTB)	BTB	-	0.04[f]	-	-	-	[270]
MOF-74(Zn)	(OH)$_2$-TPA	-	0.09[g]	-	0.39	-	[263]
MOF-74(Zn)	"	-[d]	0.06[f]	-	0.28	-	[260]
MOF-74(Ni)	"	-[d]	0.04[f]	-	0.31	-	[260]
MOF-74(Mg)	"	-[d]	0.13[f]	-	0.56	-	[260]
MOF-74(Co)	"	-[d]	0.10[f]	-	0.45	-	[260]
Cu-BTC	BTC	-[h]	0.11[c]	85-65[i]	-	Loss in q_{max} after 1 cycle	[266]
MOF-199(Cu)	"	-	0.09[g]	-	0.75	-	[263]
MOF-5(Zn)	TPA	<0.01	0.20[c]	-	1.39	Complete loss of porosity	[264]
MOF-5(Zn)	TPA	-	<0.01[g]	-	1.22	-	[263]
MOF-177(Zn)	BTB	0.01	0.20[c]	-	1.63	Complete loss of porosity	[264]
MOF-177(Zn)	BTB	-	0.04[g]	-	1.59	-	[263]
MOF-05(Zn)-OH	2,6-NDC-4,8-(OH)$_2$/BTB	<0.01	0.28[c]	-	2.01	Severe loss of crystallinity	[265]
DUT-6(Zn)	2,6-NDC/BTB	<0.01	0.21[c]	-	-	Severe loss of crystallinity	[265]
IRMOF-3(Zn)	NH$_2$-TPA	-	0.11[g]	-	1.07	-	[263]
IRMOF- 62(Zn)	dacba	-	0.02[g]	-	0.99	-	[263]

Notes: [a] p/p_o for which $q = 0.5\ q_{max}$, measured at 298 K unless noted otherwise. [b] Based on N_2 adsorption (at 77 K). Reported values are used where possible. Otherwise these are estimated from N_2 isotherms. [c] Measured until $p/p_o \sim 0.11$ ($p \sim 1.2$ bar). [d] Measured at 293 K. [e] Dynamic adsorption capacity determined from breakthrough experiments with 2000 mg m^{-3} NH_3 in inert carrier). [f] Dynamic adsorption capacity determined from breakthrough experiments $\sim$1000 mg m^{-3} NH_3 in inert carrier). [g] Dynamic adsorption capacity determined from breakthrough experiments $\sim$1% NH_3 in inert carrier). [h] Measured at 313 K. [i] Isosteric heat of adsorption, calculated with Eq. 4.22.

4.5. MOF EVALUATION AND SELECTION

When regarding water as adsorptive, stability is more of an issue than for alcohols. Nonetheless, there are MOFs that have shown to be (relatively) stable under cyclic water adsorption. In order of increasing stability, these are Al-fumarate [180], MIL-100(Fe) [154], MIL-101(Cr) [204] and CAU-10(Al)-H [178]. In addition, there are MOFs that, at least, have not shown to be unstable under several adsorption cycles. Of these, DMOF-TM2(Zn) [57], MOF-801(Zr) [166] and MOF-841(Zr) [166] have interesting adsorption behavior. The former, due the absence of information on enthalpy of adsorption, will not be considered further in Sections 4.6-4.7 of this chapter. The latter two, MOF-801(Zr) and MOF-841(Zr) comprise the same Zr-cluster as UiO-66 [166] that was demonstrated to degrade under cyclic operations [157]. Whether this might also hold for MOF-801(Zr) and MOF-841(Zr), which contain the same cluster, is unclear and for the time being these structures are assumed stable for the further purposes of this work. Adsorption isotherms of these interesting materials, selected for the performance assessment in Sections 4.6-4.7, are shown in Fig. 4.2.
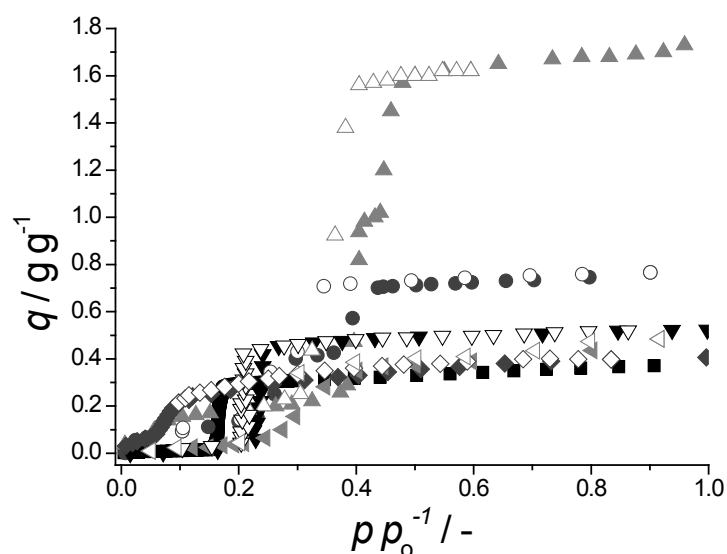
Figure 4.2: Water adsorption isotherms (298 K) for CAU-10(Al)-H (■), MIL-100(Fe) (●), MIL-101(Cr) (▲), Al-fumarate (◄), MOF-841(Zr) (▼) and MOF-801(Zr) (◆). From own exp. (Chapter 6) and lit. sources [27, 154, 166, 180]. Closed symbols depict adsorption, open desorption.

Methanol (Table 4.2) or ethanol (Table 4.3) adsorption in MOFs, when compared to that of water, is far less reported. Where for previous generations of MOFs methanol was the polar adsorptive of choice, in more recent works water seems to be preferred. This pivot in adsorption, loosely coinciding with the highly appreciated work of Küsgens *et al.* in 2009 [158], makes that for a few MOF structures, the adsorption behavior is analyzed of both water and methanol. Furthermore, information on stability is limited, and will be assumed less of an issue than for water or ammonia. Two structures were found to have at least moderate suitability for application in AHP/ADCs when alcohols are employed as working fluid, namely MIL-53(Cr) [173] and $Zn(BDC)(TED)_{0.5}$ [245]. For both the adsorption enthalpy was reported as function of loading. The latter is a must for detailed performance characterization (Section 4.6). The seemingly most favorable isotherm for methanol is that of ZIF-71(Zn), though no information about adsorption enthalpy or desorption hysteresis could be retrieved [228]. The isotherms of these materials, selected for the performance assessment in Sections 4.6-4.7, are shown in Fig. 4.3.
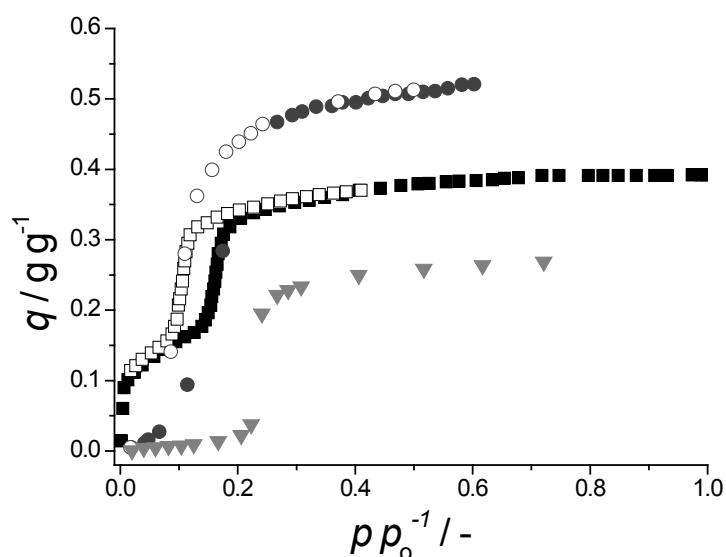
Figure 4.3: Methanol adsorption isotherms for MIL-53(Cr) (■), Zn(BDC)(TED)$_{0.5}$ (●) and ZIF-71(Zn) (▼). From lit. sources [173, 228, 245]. Closed symbols depict adsorption, open desorption.

Table 4.5: Molecule size, sigma, Critical temperature and critical diameter (at 298 K) of working fluids, calculated according to Eq. 4.1.

Vapor	σ / nm	T_c / K [271]	D_c / nm
Water	0.28	647.1	2.1
Methanol	0.36	512.6	3.5
Ethanol	0.45	513.9	4.3
Ammonia	0.29	405.7	4.4

Both MIL-53(Cr) and Zn(BDC)(TED)$_{0.5}$ show undesirable hysteresis, unexpected based upon pore size alone. As can be seen from Table 4.5, the critical diameter is significantly higher than the pore sizes of these materials. This is likely caused by the flexibility of these frameworks. It is often observed that "breathing" behavior induced by adsorption of various guest molecules often coincides with hysteresis in microporous materials [272-302], unexpected based on pore size alone. For most materials, of which alcohol and water adsorption is known, α decreases for adsorptives in the order of water > methanol > ethanol, in line with increased size, and thus confinement effect, when strong flexibility effects and enhanced hydrophobicity are absent. Compare *e.g.* the locations of the step in uptake for water, methanol and ethanol of MIL-100(Cr) (α = 0.45-0.48, α = 0.25 and α = 0.18, respectively). This means that for alcohols, MOFs with larger pore sizes could be used than

187

for water. MIL-101, which has a large portion of uptake for water at an undesirably high α, has the uptake of methanol almost completely at $\alpha < 0.3$. Advantageously, and in line with values for D_c (Table 4.5), there is no notable hysteresis loop for methanol in MIL-101(Cr). Unfortunately, due to the lower polarity of methanol though, the shape of the initial part of the isotherm ($\alpha < 0.1$) has become IUPAC Type I [303, 304] where for water this part ($\alpha < 0.3$) was more like Type III/V [303, 304]. This means that either a high desorption temperature should be exerted for full regeneration, or the working capacity will be lowered compared to the adsorption capacity. The number of viable MOF-alcohol working pairs is low in comparison to water-based working pairs, for which there are interesting candidates available already. However, the feasibility to employ larger pore sizes without introducing hysteresis and the decreased issues with stability can trigger further investigation. For the time being, however, the current assessment is somewhat limited due to the lack of information on uptake behavior and adsorption enthalpies. The reader is reminded lastly, that, for ammonia adsorption, no suitable candidates were found at all.

4.6. PERFORMANCE ASSESSMENT

MOFs with suitable adsorption characteristics and devoid of instability issues were identified in Sections 4.3-4.5 and are listed in Section 4.6.1. Feasibility for application of these structures in adsorption driven heat pumps are assessed in more detail in Sections 4.6-4.7. MOF performance will be compared to selected benchmark materials to further elucidate the possible benefits of using MOFs for the application at hand. To do so, a more detailed understanding of an ideal heat pump cycle is required (Section 4.6.2). Based on this cycle, the governing equations of the thermodynamic model can subsequently be described (Section 4.6.3). This model requires some thermodynamic properties as input. Their determination and/or estimation is briefly mentioned (Section 4.6.4), followed by a detailed discussion of the results (Section 4.7). Ultimately, other possible niche-applications for materials that can reversibly adsorb water are described, including a brief assessment of the potential of MOFs in these (Section 4.8).

4.6.1. SELECTED WORKING PAIRS

The MOFs that show promise for application in adsorption driven allocation of heat and cold are listed in Table 4.6. Of these materials, pore and window size and crystallographic density

are indicated when known. Most MOFs are combined with water as working fluid. Only MIL-53(Cr) and Zn(BDC)(DABCO)$_{0.5}$ are suitable candidates when methanol is employed. The list is completed with selected or benchmark materials.

For water as working fluid, these are commercially applied AQSOA-Z01 [15] and -Z05 [17], both AlPO$_4$-5-based zeotypes (Z01 is partially iron-exchanged) with the AFI-structure, AQSOA-Z02, based on the SAPO-34 zeotype (CHA-structure), and silica gel (Grade 40, Davidson) [305].

For methanol as working fluid, research in academia has focused primarily on various activated carbons[306-312]. Here G32-H has been selected as reference, as it shows a good working capacity under varying working conditions and has been properly characterized for AHP/ADCs [307]. These materials will be subjected in this section to a thorough thermodynamics-based comparison to critically assess the feasibility of MOFs. In addition to the structural parameters in Table 4.6, the loading-averaged enthalpy change upon adsorption, has also been listed, as this is a proper comparator for the adsorption energetics of different working pairs (Eq. 4.24), in addition to the volumetric saturation capacity (W_{sat}).

From Table 4.6 it can be concluded that the selected MOFs have a greater variety in pore sizes than the benchmark materials. Furthermore, in general, the average enthalpy of adsorption is lower for MOFs than for benchmark materials (for water). This is a primary indication that employing MOFs might energetically be more efficient as less energy is required for regeneration (desorption, Section 4.6.3). Additionally, it appears that larger pore sizes lead to lower average enthalpies of adsorption for water as working fluid. This can be easily rationalized. For a larger pore size, there are larger voids within a structure. This in turn means that on average, water molecules interact more with other water molecules than with the pore surface for these larger pores. This results in an enthalpy of adsorption that is closer to the evaporation enthalpy of water.

Table 4.6: Selected MOFs and benchmark materials for performance assessment in Section 4.6-4.7. Pore structure, window and pore size, crystal density, loading averaged enthalpy of adsorption and saturation volume adsorbed, per volume of adsorbent, are indicated where meaningful.

Material	Pore structure	d_{window} / Å[a]	d_{pore} / Å[a]	ρ_c / g ml^{-1}[b]	$<-\Delta_{ads}H>$ / kJ mol^{-1}[c]	W_{sat} / ml ml^{-1}[d]	REF
				MOFs			
CAU-10(Al)-H	1-D	5.6	-	1.15	53.5	0.43	[166, 176] (Chapter 6)
MIL-101(Cr)	3-D	12, 15	27, 34	0.48	45.5	0.82	[27, 148, 313]
MIL-100(Fe)	3-D	5, 9	24, 29	0.72	50.6	0.55	[151, 154]
Al-fumarate	1-D	-	-	0.71 $^{b.d.}$	42.8 [e]	0.34 $^{b.d.}$	[180]
MOF-841(Zr)	3-D	9.2	13.3	1.05	50.4	0.55	[166]
MOF-801(Zr)	3-D	4.8, 5.6, 7.4	8	1.59	58.4	0.63	[166]
MIL-53(Cr)	1-D, flexible	7 to 13	-	1.50 ^{np} - 1.14 ^{lp}	51.5 ^{MeOH}	0.56 ^{lp}	[24, 173]
Zn(BDC)(DABCO)$_{0.5}$	3-D, flexible	3.2, 4.8, 7.5 ^{lp}	3.2, 4.8, 7.5 ^{lp}	1.42 ^{np} - 1.35 ^{lp}	42.8 ^{MeOH}	0.89 ^{lp}	[245, 314]
				Benchmarks			
AQSOA-Z01	1-D	7.4	8.3	1.75 [f]	56.1	0.42	[315, 316]
AQSOA-Z02	3-D	3.7	7.4	1.43	57.0	0.45	[315, 317]
AQSOA-Z05	1-D	7.4	8.3	1.75	52.6	0.39	[315, 316]
Silica gel	3-D, irregular	-	-	0.72 $^{b.d.}$	55.7	0.22 $^{b.d.}$	[305]
Act. Carbon	3-D, irregular	<6, 8, 12 ^{N2}	-	2.17 $^{r.d.}$	43.0 ^{MeOH}	1.05 $^{r.d.}$	[307, 308]

Notes: [a] As reported, unless noted otherwise. [b] Crystal density, determined from crystallographic structure, unless noted otherwise. [c] Average enthalpy of adsorption, as calculated with Eq. 4.24, over the loading range for which the enthalpy (or else isosteric heat) of adsorption is determined. Value is for water as adsorptive, unless noted otherwise. [d] Saturation capacity (in g g^{-1}) is converted using the crystal density of the material, where possible, and liquid density of the working fluid [e] The reported isosteric heat of adsorption at higher loadings [180] becomes lower than the evaporation enthalpy of water, yielding this unphysically low average. [f] AQSOA-Z01 is a partially Fe-exchanged AlPO$_4$-5 material. However the fraction of iron is not accurately reported and is thus neglected in the density calculations. b.d. Is the bulk density. r.d. is the real density. np is the narrow pore configuration. lp is the large pore configuration. N_2 Derived from pore-size distribution of N$_2$ physisorption isotherm (at 77 K).

Lastly, the crystallographic density of MOFs is lower than of benchmark zeotypes, especially for large pore size structures. This is important in comparing different materials. It is customary to present adsorption capacities of porous materials per unit mass of material, but this results in a skewed evaluation, as the volume of material required to trap a certain amount of working fluid is a more important parameter. Hence the crystallographic density is used to convert to amount adsorbed on a volumetric basis as has been done for the water isotherms of selected MOFs (Fig. 4.2) in Fig. 4.4.
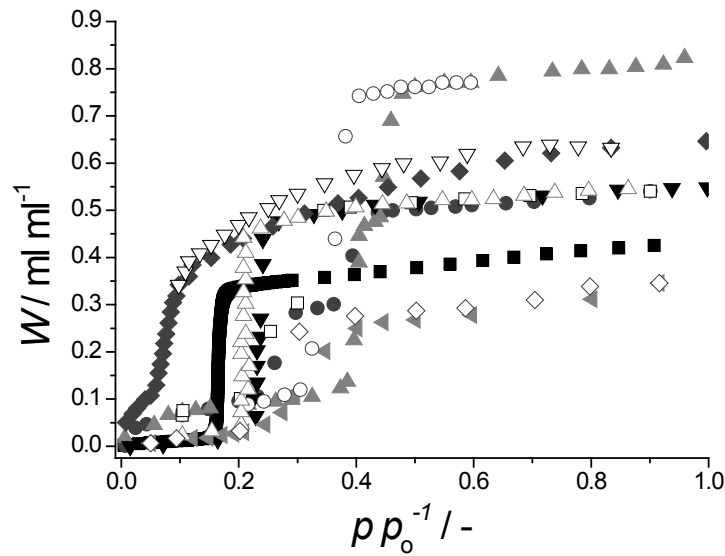
Figure 4.4: Adsorption isotherms for CAU-10(Al)-H (■), MIL-100(Fe) (●), MIL-101(Cr) (▲), Al-fumarate (◄), MOF-841(Zr) (▼) and MOF-801(Zr) (◆) represented in ml of H_2O (*liq*) per ml of (dry) MOF. Liquid water and MOF Crystal densities were used for the conversion from Fig. 4.2, except for Al-fumarate for which the powder density had to be used [180]. Closed symbols depict adsorption, open desorption.

Clearly, the adsorption capacities of interesting materials vary less in magnitude when compared per unit volume of material. In fact, one could argue that the bulk density of the material would be more appropriate to perform this conversion than the density of a (perfect) crystal. The bulk density, ρ_b, depends on the bulk porosity, ε_b, of the sample under investigation:

$$\rho_b = \rho_c \left(1 - \varepsilon_b\right) \tag{4.2}$$

Often, if not always, the bulk density is omitted for the materials reported in Section 4.4. In addition, these measurements are almost exclusively performed on powder samples. Thus, even if the bulk density is known, the porosity is expected to be different than in actual application, where coatings or pellets should be used. In these applications, the bulk porosity depends primarily on the configuration (coatings, pellets) chosen and hardly, if at all, on the material chosen.
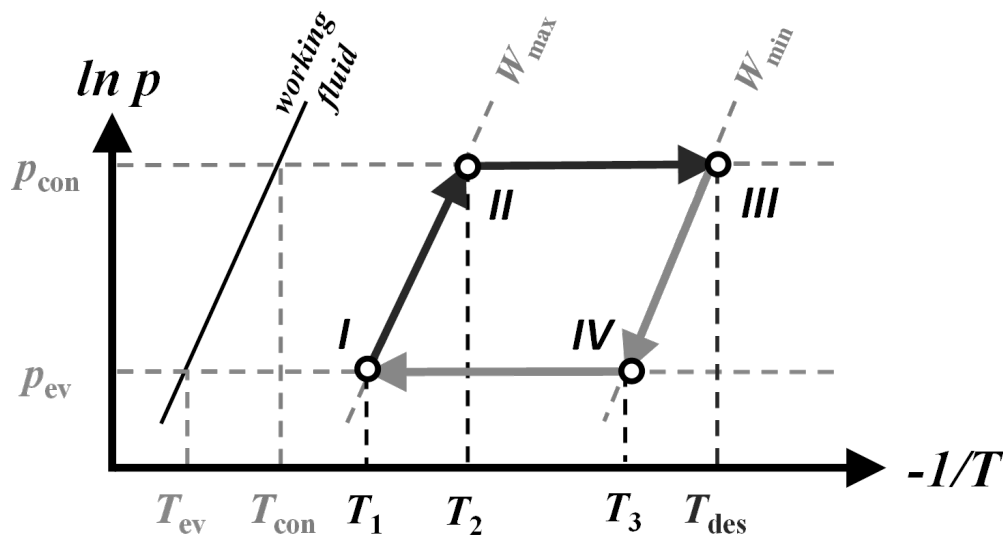
Figure 4.5: Isosteric cycle diagram of an adsorption heat pump cycle, including the vapor pressure of the chosen working fluid (*black diagonal line*), minimum and maximum isosteres, lines of equal loading, W_{min} and W_{max} (*grey diagonal dashed lines*), temperature and pressure of the evaporator (T_{ev}, p_{ev}) and condenser (T_{con}, p_{con}) (*both with horizontal and vertical grey lines*), desorption temperature (T_{des}, *grey vertical dashed line*) and intermediate cycle temperatures (T_1, T_2 and T_3, *vertical black dashed lines*).

4.6.2. HEAT PUMP CYCLE

An adsorption driven heat pump cycle consists of four steps, two for adsorption and two for desorption. These steps are briefly explained with the aid of the cycle diagram (Fig. 4.5).

In this diagram, the *x*-axis indeed is shown as *-1/T*, which is typically done in literature [318-324] to ensure both that the isosteric lines are straight (*ln p* versus *1/T* ensures this) and that the lowest temperature is at the left end of the figure. Starting from a fully saturated adsorbent (*point I*), these four steps are consecutively:

- Isosteric compression (*I-II*):
  The adsorbent is fully saturated (W_{max}) and requires regeneration or desorption of working fluid. Before the working fluid can be released to the condenser, pressure needs to be increased from p_{ev} to p_{con}. This is realized by heating the adsorbent from T_1 to T_2. During this stage, ideally, no working fluid is desorbed and the adsorbent vessel is disconnected from both the condenser and evaporator.

- Isobaric desorption (*II-III*):

  Adsorbent heating is continued. Because the adsorbent vessel is connected to the condenser in this stage, working fluid is allowed to desorb and no further pressure increase occurs. This process is stopped when desorption temperature (T_{des}) is reached and the adsorbent loading is minimal (W_{min}). The desorbed working fluid (W_{max} - W_{min}) is condensed, releasing heat to the environment in the condenser (Q_{con}, Fig. 1.1).

- Isosteric expansion (*III-IV*):

  The adsorbent is regenerated and can be used for adsorption. However first the pressure needs to be reduced to p_{ev} by cooling the vessel from T_{des} to T_3, again isosterically and disconnected from condenser and evaporator.

- Isobaric adsorption (*IV-I*):

  Cooling is continued. Because the adsorbent vessel is connected to the evaporator in this stage, working fluid is allowed to adsorb and no further pressure decrease occurs. This process is stopped when T_1 is reached and the adsorbent loading is maximal again (W_{max}). The adsorbed working fluid (W_{max} - W_{min}) has withdrawn heat from the environment at a low temperature in the evaporator by its evaporation (Q_{ev}, Fig. 1.1), while releasing heat in the adsorber at an intermediate temperature level upon adsorption.

The energy required for trajectories *I-II* and *II-III* combined is the energy required for desorption (Q_{des}, Fig. 1.1), the energy released during trajectories *III-IV* and *IV-I* is equal to the adsorption energy (Q_{ads}, Fig. 1.1). For practical reasons, in most cases it is chosen to equate T_1, often called (minimum) temperature of adsorption (T_{ads}), to the condenser temperature, T_{con} [322, 325]. The remaining temperatures and pressures used in this cycle cannot be all independently chosen. The condenser and evaporator pressure are inherently linked to their respective temperatures by the vapor-liquid equilibrium of the selected working fluid. For a given working pair, T_2 is related to T_{con} via the maximum loading isostere (W_{max}). This means that, for a given working pair, T_2 is fixed by choosing the condenser temperature (and pressure). T_3 and T_{des} are related through the minimum loading isostere (W_{min}) and T_3 is fixed when the evaporator temperature is selected. In summary, for a given working pair, the operational conditions are fully fixed when evaporator, condenser and (maximum) desorption temperature are chosen. Generally speaking, one can use this cycle for two purposes, heating up or cooling down, as schematically indicated in Fig. 4.6.
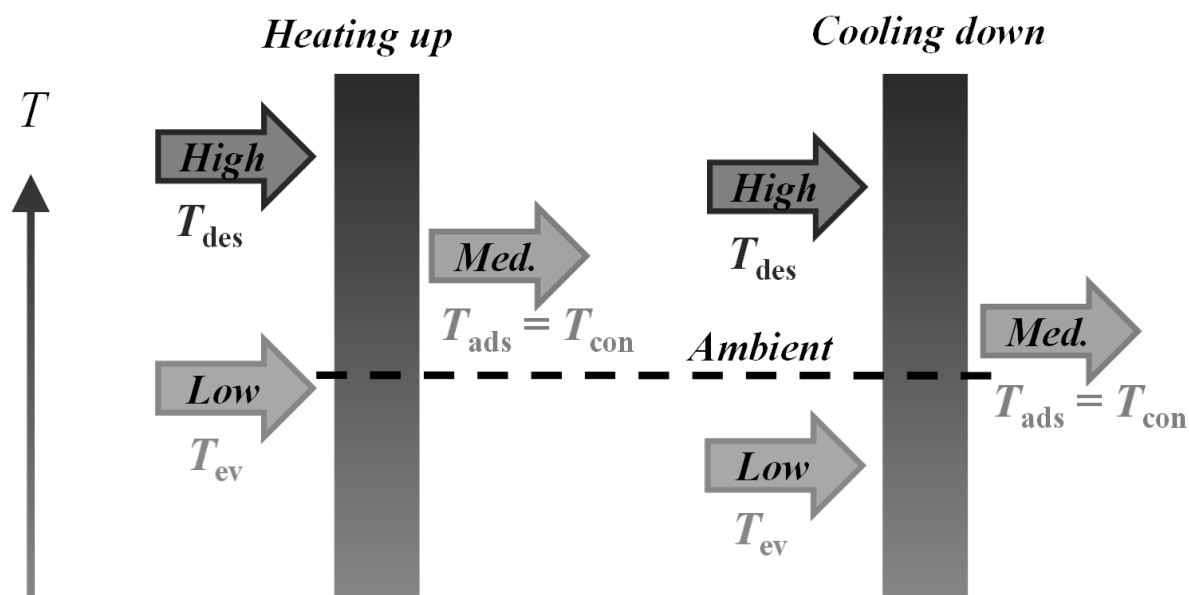
Figure 4.6: Modes of operation of an heat pump cycle. Heating up (*left*) and cooling down (*right*). Arrows indicate the flow of energy to or from the heat pump cycle (*rectangle*) at a high, medium or low temperature level. Corresponding temperatures (T_{des}, T_{ads}, T_{con} and T_{ev}) of Fig. 4.5 indicated. Dashed line represents ambient temperature.

When using the cycle for heating, energy at a high temperature (used for regeneration of the sorbent) is transferred to an intermediate temperature (via condensation and adsorption). The energy withdrawn from the environment at ambient (low) temperature (during evaporation) is also released at the intermediate temperature. The energy withdrawn at the ambient (low) temperature, can in principle be employed without effort and this is the reason why a heat pump has a higher energy efficiency in transferring energy from high to medium temperatures than a simple heat exchanger.

For cooling purposes, energy withdrawal by evaporation at a low temperature is desired. This is why the temperature of the low level is sub-ambient for cooling processes. The energy at high temperature, used for regeneration of the cycle, is used as input energy to generate this cooling effect. The energy delivered at the medium temperature level is not effectively used when cooling using this cycle. The temperatures at which the evaporator and condenser are operated depend on the actual application. The employed operational temperatures used to assess the performance of MOFs in comparison to selected benchmark materials, for different applications, are listed in Table 4.7 and are comparable to those used by others [307, 318, 320, 322, 324-327].

Table 4.7: Employed operational temperatures in this work for the four different applications considered.

	Heat pump	Refrig. I	Refrig. II	Ice making[a]
T_{ev} / K	288	283	278	268
T_{con} / K	318	303	303	298

[a]   Water cannot be employed as working fluid for ice making, due to freezing.

Heat pumps are considered here as a single application, cooling is subdivided in three different applications. Refrigeration (R.F.)-I could be used for *e.g.* air-conditioning purposes, whereas R.F.-II could be used for *e.g.* an actual refrigerator. Both are included (Section 4.7) to highlight the effect of the minor differences in the evaporation temperature on material comparison. The desorption temperature can be independently varied to find an optimum between working capacity and energy efficiency, as will be discussed in detail (Section 4.7). On a more critical note, one might argue that the evaporation temperature of the heat pump condition is at the high end of the spectrum of commonly applied temperatures (270-288 K mostly). The choice for this somewhat high temperature (288 K) was made as most MOFs have an isotherm (Fig. 4.2) with a step in adsorption such that the working capacity at lower temperatures will likely become negligible, as will become clear from the results (MOF-801(Zr) is the exception). This temperature however is by no means practically unfeasible.

4.6.3. THERMODYNAMIC MODEL

Here the necessary equations to describe the heat pump cycle from a thermodynamic perspective are presented, starting with the coefficient of performance (COP), which is the commonly adopted parameter to describe energetic efficiency [4, 323, 325]. The COP is defined as the useful energy output divided by the energy required as input. For heating this becomes:

$$COP_H = \frac{-\left(Q_{con} + Q_{ads}\right)}{Q_{regen}} \tag{4.3}$$

Here Q_{con} is the energy released during condensation, and $Q_{sorption}$ the energy released during adsorption, both have a negative value as energy is withdrawn from the adsorption cycle, and Q_{regen} is the energy required for regeneration of adsorbent, a positive quantity as energy is added to the system. For cooling, the coefficient of performance becomes:

$$\text{COP}_C = \frac{Q_{ev}}{Q_{regen}} \tag{4.4}$$

Here Q_{ev} is the energy withdrawn by the evaporator. The energy withdrawn by the evaporator and released by the condenser can be calculated with knowledge of the enthalpy of evaporation, $\Delta_{vap}H$ (Fig. 1.3) by respectively:

$$Q_{ev} = -\frac{\Delta_{vap}H\left(T_{ev}\right)m_{sorbent}\Delta W}{M_w} \tag{4.5}$$

$$Q_{con} = \frac{\Delta_{vap}H\left(T_{con}\right)m_{sorbent}\Delta W}{M_w} \tag{4.6}$$

Here $m_{sorbent}$ is the amount of adsorbent used in the adsorption cycle. From here onwards this quantity is omitted making that the quantities of energy, Q_i, are defined per unit of mass of the adsorbent used. ΔW is the working capacity, defined as the difference in working fluid between the maximum and minimum isosteres (W_{max} - W_{min}, see Fig. 4.6). Note that because of the limited temperature difference between T_{ev} and T_{con}, Q_{ev} and Q_{con} are almost equal in magnitude but opposite in sign.

The calculation of the energy required during the regeneration is more tedious as it comprises both isosteric compression (*I-II*) and isobaric desorption (*II-III*) [325]. The energy required for isosteric heating can be determined with [325]:

$$Q_{\text{I-II}} = \int_{T_{con}}^{T_2} c_p^{\text{effective}}\left(T\right)dT + \int_{T_{con}}^{T_2} W_{max}c_p^{\text{wf}}\left(T\right)dT \tag{4.7}$$

Here c_p^{wf} is the heat capacity of the chosen working fluid and $c_p^{\text{effective}}$ is the effective heat capacity of the adsorbent (sorbent) and heat exchanger (hx), defined as [325]:

$$c_p^{\text{effective}}\left(T\right) = c_p^{\text{sorbent}}\left(T\right) + \frac{m_{hx}}{m_{sorbent}}c_p^{\text{hx}}\left(T\right) \tag{4.8}$$

The mass of heat exchanger, m_{hx}, is defined relative to the mass of adsorbent used. In practice, the heat exchanger area (~mass) can be increased to increase heat transfer, at the cost of thermodynamic efficiency, and can thus be an important tuning parameter. As the heat and mass transport properties of MOFs are scarcely known to the best of our knowledge, this tuning cannot be performed in reality. Hence, for a comparison based on intrinsic MOF

properties the mass of heat exchanger is assumed zero in the efficiency calculations. The energy required for isobaric desorption is determined with [325]:

$$
Q_{\text{II-III}} = \int_{T_2}^{T_{\text{des}}} c_p^{\text{effective}}(T)dT +
$$
$$
\int_{T_2}^{T_{\text{des}}} \frac{W_{\max} + W_{\min}}{2} c_p^{\text{wf}}(T)dT - Q_{\text{sorption}}
$$

(4.9)

Q_{sorption} is the energy released during adsorption of the working fluid and can be calculated with:

$$
Q_{\text{sorption}} = \frac{1}{M_{\text{w}}} \int_{W_{\min}}^{W_{\max}} \Delta_{\text{ads}} H(W)dW
$$

(4.10)

Here M_w is the molar mass of the working fluid and $\Delta_{\text{ads}}H$ the enthalpy of adsorption, which often has a significant dependence on loading (W). The estimation of $\Delta_{\text{ads}}H$ will be discussed in more detail further on this manuscript. Finally, combining the energy required isosteric compression and isobaric desorption yields the total energy required for regeneration:

$$
Q_{\text{regen}} = Q_{\text{I-II}} + Q_{\text{II-III}}
$$

(4.11)

The energy gained during the adsorption stage is a combination of the energy gained during isosteric expansion ($Q_{\text{III-IV}}$) and isobaric adsorption ($Q_{\text{IV-I}}$):

$$
Q_{ads} = Q_{III-IV} + Q_{IV-I}
$$

(4.12)

The relation for the energy gain during isosteric expansion is similar to that of isosteric compression (Eq. 4.7):

$$
Q_{\text{III-IV}} = \int_{T_{\text{des}}}^{T_3} c_p^{\text{effective}}(T)dT + \int_{T_{\text{des}}}^{T_3} W_{\max} c_p^{\text{wf}}(T)dT
$$

(4.13)

For isobaric adsorption, in line with Eq. 4.9, one could obtain:

$$
Q_{\text{IV-I}} = \int_{T_3}^{T_{\text{con}}} c_p^{\text{effective}}(T)dT +
$$
$$
\int_{T_3}^{T_{\text{con}}} \frac{W_{\max} + W_{\min}}{2} c_p^{\text{wf}}(T)dT + Q_{\text{sorption}}
$$

(4.14)

One can observe from the above that the energy required for regeneration (Q_{regen}) will be very similar in magnitude to the energy gained during adsorption (Q_{sorption}). Furthermore, as the enthalpy of adsorption should physically be larger in absolute magnitude than the enthalpy of evaporation, Q_{con} will be not be larger than Q_{sorption}. This means, for a single adsorption vessel, that:

$$1 \leq \mathrm{COP_H} \leq 2 \qquad\qquad (4.15)$$

In fact, for $\mathrm{COP_H} = 1$ there is no incentive to use a heat pump at all and a simple heat exchanger should be utilized. Applying similar logic ($Q_{\mathrm{ev}} \leq Q_{\mathrm{regen}}$) one can conclude for cooling purposes that:

$$\mathrm{COP_C} \leq 1 \qquad\qquad (4.16)$$

In fact, when using multiple adsorption beds, one could use parts of the energy released during adsorption of one bed for partial regeneration of another bed [322, 325, 328, 329]. Although this energy recovery might aid in exceeding the posed limits on the coefficient of performance (Eqs. 4.15-4.16) with proper design and operation, it is not taken into account in this work. This simply because the extent of energy recovery between adsorbers depends on system design and can in principle be done for any working pair. Omission of any heat recovery is assumed not to modify the intrinsic material comparison aimed at in this work.

4.6.4. THERMODYNAMIC PROPERTIES

The model, as presented (Section 4.6.3) to describe the performance of a given working pair in an adsorption heat pump cycle requires the knowledge of thermodynamic properties. Firstly, for both working fluids (H_2O, CH_3OH) the enthalpy of evaporation, vapor pressure (see Fig. 1.3) and heat capacity (Fig. C.1) are accurately known [271].

For the adsorbent, information on the heat capacity is also required (Section 4.6.4.1). In addition, for each adsorbent-working fluid pair, information is needed on the loading dependence on both temperature and pressure. For this purpose, the concept of characteristic curves is conveniently adopted (Section 4.6.4.2) [244, 325, 330-332]. Lastly, information on the enthalpy of adsorption as a function of loading is needed (Section 4.6.4.3). The information required for the adsorbents and adsorbent-working fluid pairs is more tedious to obtain than is the case for pure fluid properties, and requires proper explanation.

4.6.4.1. ADSORBENT HEAT CAPACITY

As highlighted above, the heat capacity of the adsorbent is necessary to assess the coefficient of performance in AHP/ADCs. Mu and Walton investigated the heat capacity of MOFs in great detail in comparison with zeolites and other materials. Their results (Fig. 4.7) indicate that for most of the materials under investigation one could roughly state that [333]:

$$0.6 \leq c_p^{sorbent} \leq 1.4 \left[\frac{J}{gK} \right] \qquad (4.17)$$

Although the materials studied by Mu and Walton do not correspond with those selected in this work, their findings, which are largely in line with the heat capacities reported by Pirngruber *et al.* [209], serve as a proper indication for the unknown heat capacities. Based on these results, $c_p^{sorbent}$ is assumed to be 1 J g^{-1} K^{-1} regardless of temperature, except for Al-fumarate ($c_p^{sorbent} \sim 1.1$ J g^{-1} K^{-1}) [180] and activated carbon ($c_p^{sorbent} \sim 0.95$ J g^{-1} K^{-1}) [307] for which the specific heat capacity is known. A small sensitivity analysis exercise can be performed, employing a simplified equation of the energy required for regeneration:

$$Q_{regen} \approx c_p^{sorbent} \Delta T - \frac{1}{M_w} \langle \Delta_{ads} H \rangle \Delta W \qquad (4.18)$$

With Eq. 4.18 one can estimate Q_{regen} for a heat capacity, *e.g.* of 1.0 and 1.4 J K^{-1} g^{-1}, as will be done for the conditions for which the influence of $c_p^{sorbent}$ will be the highest. This means a temperature difference, ΔT, of 75 K, the largest used in the results section (Section 4.7), and a loading difference, ΔW, of 0.2 g g^{-1}, the minimal value for which coefficients of performance are presented (Fig. 4.10). Using the lowest, still physically sound, average adsorption enthalpy of the materials under investigation for water as working fluid, (-45.5 kJ mol^{-1} for MIL-101(Cr), Table 4.6), indicates that a difference of 0.4 J g^{-1} K^{-1} in the used $c_p^{sorbent}$ will result roughly only in a 5% change in Q_{regen}. For methanol, using the average adsorption enthalpy of Zn(BDC)(DABCO)$_{0.5}$ (-42.8 kJ mol^{-1}, Table 4.6) the change in Q$_{regen}$ will be roughly 8%. For larger adsorption enthalpies and loading differences and smaller temperature differences these changes will become even less significant. Furthermore, the neglect of the influence of the working fluid heat capacity in Eq. 4.18 for simplicity reasons further indicates that the effect of $c_p^{sorbent}$ on the magnitude of Q_{regen} and $Q_{sorption}$ are exaggerated in this analysis and that thus employing a fixed sorbent heat capacity of 1.0 J g^{-1} K^{-1} for all adsorbents will not significantly affect the performance comparison of the different materials under investigation.
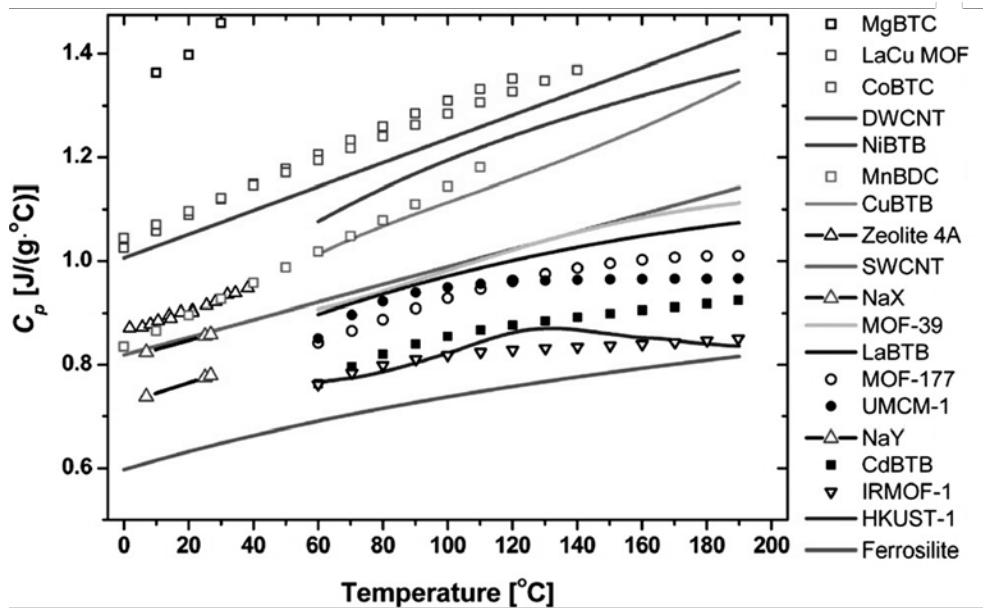
Figure 4.7: Specific heat capacity as function of temperature for MOFs, coordination polymers, carbon nanotubes, zeolites, and minerals. Reprinted with permission from Ref. [333]. Literature data included for MgBTC [334], LaCu MOF [335], CoBTC [336], DWCNT [337], MnBDC [338], Zeolite 4A [339], SWCNT [337], NaX [340], NaY[340] and Ferrosilite [341]. For a representation in color, the reader is kindly referred to Ref. [333].

4.6.4.2. CHARACTERISTIC CURVE

The amount adsorbed in a porous material at equilibrium is a function of both pressure and temperature. Most often adsorption isotherms are measured for one or more given temperatures. These temperatures are frequently around room temperature (298 K), thus lower than *e.g.* the temperatures applied for desorption in AHP/ADCs. This means that these isotherms, on which the data in Sections 4.4-4.5 are based, cannot directly be used in the adopted model (Section 4.6.3). To circumvent this, the concept of the characteristic curve is adopted [244, 325, 330-332]. Central in this theory is the use of the Polanyi adsorption potential [342-344], which is the molar Gibbs free energy of adsorption with opposite sign, defined as:

$$A = RT \ln\left(\frac{p_o(T)}{p}\right) \tag{4.19}$$

Here p_o is the temperature-dependent vapor pressure of the adsorbate of choice. The amount adsorbed should be expressed as volume occupied by the adsorbed phase. As the density of

the adsorbed phase is often not known, the liquid phase density is often used as approximation:

$$W = \frac{q(p,T)}{\rho_{\text{liq}}^{\text{wf}}(T)}$$

(4.20)

Here q is the mass adsorbed, W is the volume liquid adsorbed and $\rho_{\text{liq}}^{\text{wf}}$ the liquid density of the same adsorbate. If so-called temperature invariance of W is assumed, all measured adsorption data should collapse onto one single "characteristic curve". In practice, this assumption can easily be verified by performing this transformation for more than one isotherm (or isobar). This results in the fact that for each amount of volume adsorbed, W, there is one value of the adsorption potential, A, and each A-W combination corresponds to an isostere (*e.g.*, W_{max} and W_{min} in Fig. 4.5). Computationally, this means that each combination of pressure (p, T) can be converted to a single adsorption potential, A, for which the volume adsorbed W can be determined easily via interpolation of the characteristic curve. For a selection of MOFs and the AQSOA-series, this transformation has been performed and the resulting curves are shown in Fig. 4.8 (other samples in Fig. C.2).
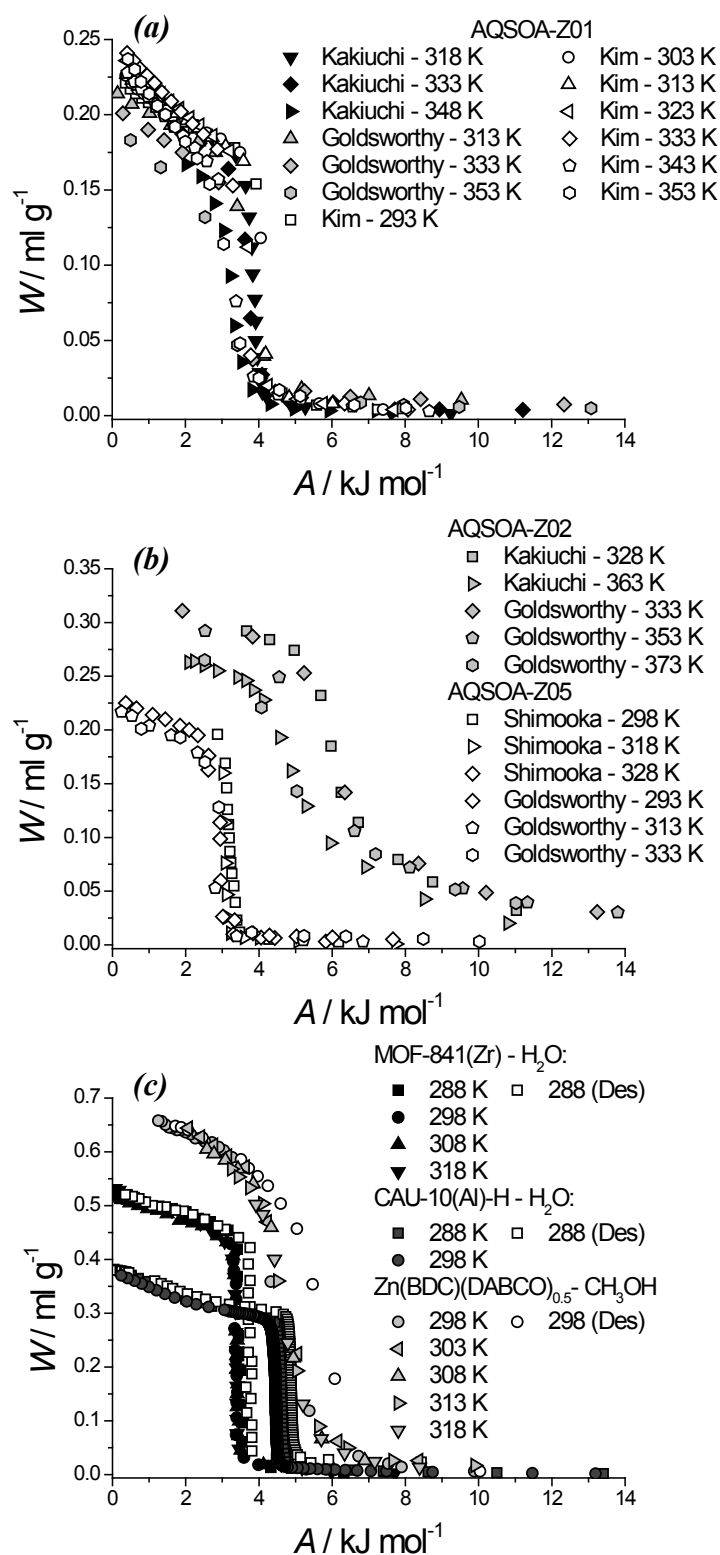
Figure 4.8: Characteristic curves determined using Eqs. 4.19-4.20, using adsorption isotherms from various literature sources, for AQSOA-Z01-water [15, 345, 346] (*a*), AQSOA-Z02-water [16, 345] and AQSOA-Z05-water [17, 345] (*b*) and MOF-841(Zr)-water [166], CAU-10(Al)-H and Zn(BDC)(DABCO)$_{0.5}$-methanol [245] (*c*).

Clearly, for the MOFs shown, Fig. 4.8c, this 'characteristic curve' concept works properly. The same can be said for AQSOA-Z05, Fig. 4.8b. However for AQSOA-Z01 (Fig. 4.8a), and even more for AQSOA-Z02, (Fig. 4.8b), this concept does not perfectly hold. A clear shift in the curve towards lower adsorption potentials can be observed when temperature is increased. AQSOA-Z02, which is actually SAPO-34, displays a structural contraction upon water adsorption, reducing the unit cell volume roughly 2% at room temperature [317]. This contraction might be different at the elevated temperatures encountered in Fig. 4.8, which could make hydration less favorable [347].

The fact that the volume adsorbed does not display temperature invariance as function of adsorption potential makes that simple interpolation of the characteristic curve cannot be executed for AQSOA-Z01 and Z02. As for these materials isotherms are in fact measured at elevated temperatures (up to 373 K), the isotherms could in principle be used directly. To make the temperature-span continuous, the isotherms are interpolated for these compounds. The details of this procedure and the effect this has on working capacity and coefficient of performance are displayed in Section C.3.

Lastly, as was hinted at in Section 4.4, the relative pressure to indicate the step in uptake, α, changes as function of temperature of the isotherm. Using Eq. 4.19, one can derive an expression to exactly calculate the shift in α when comparing two isotherms at temperature T_1 and T_2, respectively, under the assumption of temperature invariance of W:

$$\alpha_2 = \alpha_1^{\frac{T_1}{T_2}} \tag{4.21}$$

Here α_1 and α_2 are the relative pressures of the step in uptake for isotherms measured at respectively T_1 and T_2. Clearly, this dependency of α on temperature should be considered when comparing results from different temperatures.

4.6.4.3. ENTHALPY OF ADSORPTION

For MIL-53(Cr) and MIL-101(Cr), $\Delta_{ads}H(W)$ is accurately known from calorimetric measurements. For the other structures calorimetric data is not available and thus the isosteric enthalpy of adsorption will be used.

The isosteric enthalpy of adsorption can be calculated, from adsorption isotherms at two or more different temperatures, using [348]:

$$\Delta_{\text{ads}} H_{\text{W}} = R \left(\frac{\partial \ln p}{\partial \left(\frac{1}{T} \right)} \right)_{\text{W}} \tag{4.22}$$

Using this equation, it is (tacitly) assumed that adsorption is fully reversible (no chemisorption occurs), neither the internal energy of the adsorbent surface nor the adsorbent structure is altered during adsorption, and equilibrium is reached between adsorbent and adsorbate. The isosteric enthalpy of adsorption is reported alongside the isotherms at different temperatures for most adsorbents, for other this quantity is calculated (all are shown in Fig. C.4). It can be noticed that the maximum adsorbed volume for which $\Delta_{\text{ads}}H(W)$ is known, denoted by $W_{\text{max}}^{\Delta H}$, is sometimes smaller than the adsorption capacity in the adsorbent (W_{max}). In the case when $W_{\text{max}} > W_{\text{max}}^{\Delta H}$, it is assumed that the enthalpy of adsorption will become equal to that of evaporation, and Eq. 4.10 is expanded to include this phenomenon:

$$Q_{\text{sorption}} = \frac{1}{M_{\text{w}}} \int_{W_{\text{min}}^{\Delta H}}^{W_{\text{max}}^{\Delta H}} \Delta_{\text{ads}} H(W) dW$$
$$+ \frac{1}{M_{\text{w}}} \left(W_{\text{max}} - W_{\text{max}}^{\Delta H} \right) \Delta_{\text{vap}} H \tag{4.23}$$

The same can in principle be applied when $W_{\text{min}} < W_{\text{min}}^{\Delta H}$, though this situation occurred less frequently in this study. Lastly, the loading averaged enthalpy of adsorption, as reported in Table 4.6, is calculated using full range of the enthalpy of adsorption as function of adsorbed volume (from $W_{\text{min}}^{\Delta H}$ to $W_{\text{max}}^{\Delta H}$):

$$\left\langle \Delta_{\text{ads}} H \right\rangle = \frac{\int_{W_{\text{min}}^{\Delta H}}^{W_{\text{max}}^{\Delta H}} \Delta_{\text{ads}} H(W) dW}{W_{\text{max}}^{\Delta H} - W_{\text{min}}^{\Delta H}} \tag{4.24}$$

The loading-dependent enthalpy of adsorption, as used in this work, is shown for all materials under investigation in Fig. C.4.

4.7. RESULTS AND DISCUSSION

The potential of selected MOFs for application in adsorption driven heat pumps and chillers is assessed from a thermodynamic perspective, and compared with commercially used benchmark materials. Firstly, the total energy storage capacity is compared (Section 4.7.1), after which the performance is determined for different applications, using the operating conditions as specified in Table 4.7 (Section 4.7.2). Additionally, the concept of temperature lift is used to further explain the potential of MOFs (Section 4.7.3).

4.7.1. CAPACITY

From Table 4.6 it becomes clear that, per volume of material, most MOFs adsorb more working fluid than commercially used sorbents (AQSOAs and Silica Gel). The activated carbon-methanol pair, however, even supersedes MOFs in volumetric working fluid adsorption, but one should note that the amount of energy for condensation or evaporation depends on the enthalpy of evaporation of the working fluid, which is obviously lower for methanol. The maximum energy that can be released in the condenser per cycle, Q_{con}, is calculated for full adsorption capacity of each material. This is shown in Fig. 4.9, top.

Clearly the activated carbon-methanol pair has a lower energy capacity, because of the lower enthalpy of evaporation of methanol. Where ~ 2.4 kJ ml^{-1} is released for water, only ~ 0.9 kJ ml^{-1} (both at 298 K) is obtained for methanol. This makes that the activated carbon-methanol pair is somewhere in between MOFs and AQSOAs with regards the volume-specific energy released/withdrawn. This effect further worsens the MOF-methanol pairs in comparison. Another interesting property to compare is the total amount of energy generated by adsorption, which is calculated using Eq. 4.23 from zero to saturation loading for all adsorbent-working pairs. Results are shown in Fig. 4.9, bottom, both per unit volume and per unit mass.

205
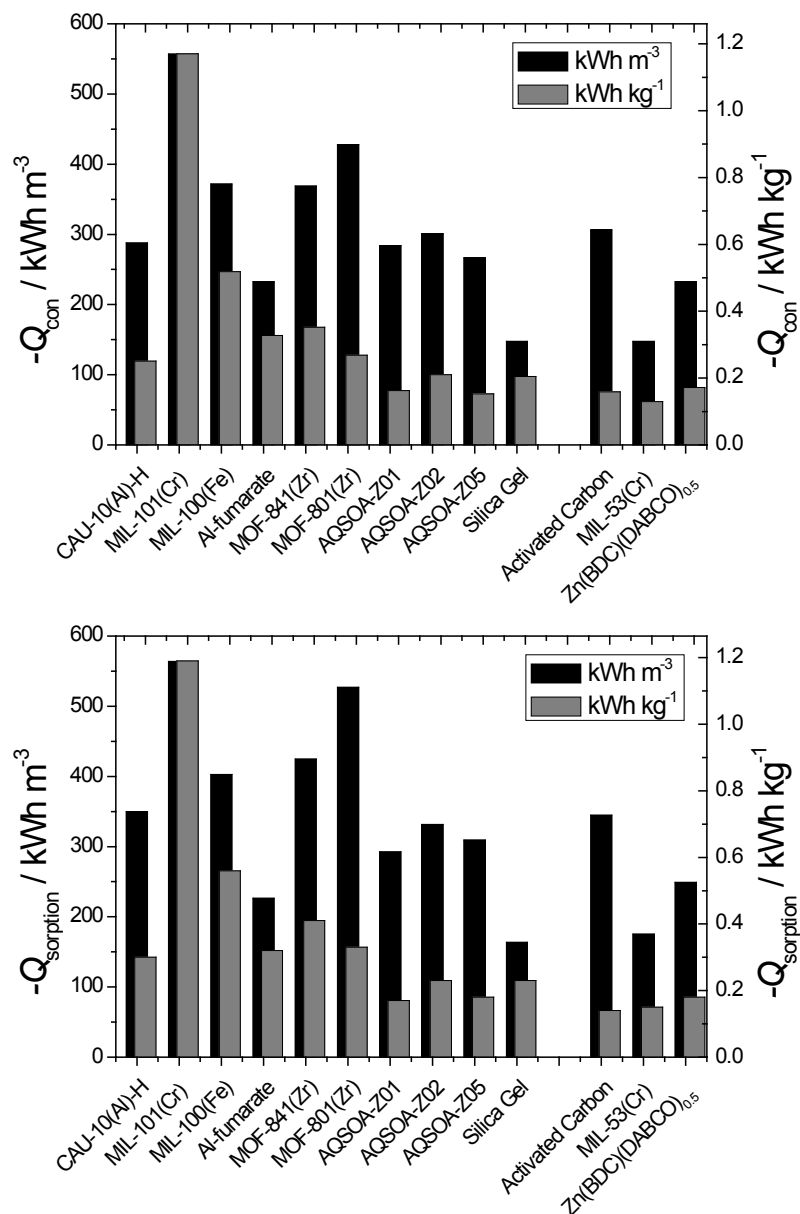
Figure 4.9: Total amount of energy released in the condenser (at 298 K), Q_{con}, when the full working fluid capacity is condensed (*top*) and total amount of energy released during adsorption, $Q_{sorption}$, by fully saturating the adsorbent with working fluid, both per unit MOF volume, using the densities (lp for flexible MOFs) listed in Table 4.6, (*black bars, left x-axis*) and per unit mass (*grey bars, right x-axis*). The last three adsorbents are calculated with methanol as working fluid, for the other water is used.

In accordance with the previous discussion, mass-specific $Q_{sorption}$ is generally found larger for MOFs than for benchmark sorbents and methanol-based working pairs. In comparison, volumetric $Q_{sorption}$ of the AQSOA-series are roughly equal to that of activated carbon-methanol, though Q_{con} has been found larger for the latter. This is because for the AQSOA-

water working pairs the ratios of enthalpy of adsorption to evaporation is higher than for most other materials. Though this fact might be beneficial for energy storage, and this will be explored in Section 4.8.1, this will have a negative influence on the coefficient of performance in AHP/ADCs, as will be demonstrated. Further, by reporting mass-based adsorptive energy content comparison becomes skewed. The high mass-based uptake of MIL-101(Cr), which in fact has the lowest density amongst compared materials, would show vastly higher values than all other materials if performance would be reported in kWh kg^{-1} (Fig. 4.9). When the results are compared on a volumetric basis, MIL-101(Cr) still exhibits the highest $Q_{sorption}$, but the difference with other materials is less pronounced. In conclusion, the energy content of MOFs can be larger than that of benchmark sorbents. Whether this potential can be harnessed under practical conditions will be discussed in the following section.

4.7.2. EFFICIENCY COMPARISON

For heat pump application and refrigeration I and II (conditions in Table 4.7), both the volumetric working capacity, ΔW, and coefficient of performance (heating for heat pump, cooling for refrigeration I & II) have been determined as function of desorption temperature, T_{des}. For materials that show suitable uptake under applied conditions, results are shown in Fig. 4.10. For those that do not show suitable uptake, results are shown Fig. C.5. In addition, because of the limited number of MOFs that can operate under ice making conditions (using methanol), results for this application are shown in the appendix as well (Fig. C.6).

For heat pump conditions, Fig. 4.10a, b, employing water as working fluid, it becomes apparent that AQSOA-Z02 can be operated with lower desorption temperatures than MOF-801(Zr). Above 373 K, ΔW is almost equal for both components (~ 0.3 ml ml^{-1}), the same holds for COP$_H$ (~ 0.7). Activated carbon-methanol shows higher ΔW, especially at elevated desorption temperatures, but since methanol has a lower evaporation enthalpy, the nett condensable/evaporable energy per cycle is lower, as at 393 K activated carbon G32-H still contains methanol. Increasing temperature might still thus improve performance. However, as reported by Hu *et al.*, methanol undergoes thermal decomposition at higher temperatures and thus increasing temperature over 403 K is not very practical [349]. In comparison, for 366 K $\leq T_{des} \leq$ 380 K, Zn(BDC)(DABCO)$_{0.5}$ has a larger ΔW and a greater efficiency than activated carbon, both employing methanol. MIL-53(Cr) however, because only part of its methanol capacity is used, shows a lower uptake. In addition, both MOF-methanol pairs show little to no release of working fluid for $T_{des} \geq$ 370 K, mitigating the need to go to higher desorption

temperatures. Because the adsorption potential for the adsorbed (maximum capacity) state is already quite high (A_{ads} = 4.6 kJ mol^{-1}), many adsorbents do not contain significant adsorbed working fluid volume, making that a negligible working capacity is obtained regardless of desorption strategy. By decreasing the evaporator temperature further, thus increasing A_{ads} (Eq. 4.19), even more structures become useless, as during the adsorption stage the materials are hardly loaded with working fluid.

For refrigeration I, Fig. 4.10c, d, especially MOF-841(Zr) stands out. Saturation capacity is reached at conveniently low desorption temperatures (T_{des} ~ 333 K) making that either waste or solar energy can be efficiently utilized. Compared to AQSOA-Z01, which requires a similar desorption temperature, ΔW is almost doubled (0.48 versus 0.26 ml ml^{-1}) and its efficiency is higher (COP$_H$ of 0.83 and 0.72, respectively). The higher efficiency can be explained by the (average) enthalpy of adsorption, being -50.4 and -56.1 kJ mol^{-1} for MOF-841(Zr) and AQSOA-Z01, respectively (Table 4.6). This in turn can be attributed to the higher porosity of the former, as per unit volume less adsorption sites are present, making that water interacts more with water in this particular structure than it would in AQSOA-Z01. In contrast thus to the heat pump conditions, for refrigeration I clearly there are MOFs that outperform benchmark materials with respect to both (energetic) capacity and thermodynamic efficiency. This difference can be attributed to the lower adsorption potential of the adsorption stage (A_{ads} = 3.1 kJ mol^{-1}) for Refrigeration I, which allows structures with higher α-values to be practically utilized.

When higher desorption temperatures can be utilized, also CAU-10(Al)-H (T_{des} ~ 345 K) or MOF-801(Zr) (T_{des} ~ 355 K) show higher capacity than, and similar efficiency as, benchmark materials AQSOA-Z01 and Z02, respectively. This is of particular interest because the organic ligands used for these materials, isophthalic acid [350] for CAU-10(Al)-H and fumaric acid [351] for MOF-801(Zr) are already produced on an industrial scale. In contrast, 4,4',4",4'''-Methanetetrayltetrabenzoic acid (MTB), the ligand used to synthesize MOF-841(Zr) is not produced on any commercial scale, to the best of our knowledge.

For refrigeration II, Fig. 4.10e, f, the lower evaporator temperature (278 K instead of 283 K) or higher adsorption potential of the adsorption stage (A_{ads} = 4.0 instead of 3.1 kJ mol^{-1}) makes that MOF-841(Zr) and AQSOA-Z01 can no longer be utilized. CAU-10(Al)-H is under these conditions the best performing adsorbent, followed by MOF-801(Zr) and AQSOA-Z02.

For ice-making conditions, the discussion can be brief. Activated carbon outperforms the two MOF-methanol working pairs (Fig. C.6) over the whole range of desorption temperatures, only for T_{des} ~ 345 K, Zn(BDC)(DABCO)$_{0.5}$ has a capacity similar to that of the activated carbon. So, based on these results, there is no clear incentive to use MOF-methanol working pairs for this specific application.

From Fig. 4.10 one can observe that an increase in COP is often observed at lower T_{des} than is needed for a significant working capacity, ΔW. This can be reasoned by the small effect of the effective heat capacity. The heat capacity of the heat exchange surface is ignored in this evaluation, as this generates better intrinsic adsorbent performance comparison. As the heat capacity of the adsorbent has a small influence (Section 4.6.4.1) on the total energy balance, any nonzero ΔW constitutes already a Q_{regen} (and $Q_{sorption}$) with a magnitude in the same order as Q_{ev}/Q_{con}. This yields as result that directly a coefficient of performance can be observed, whilst the (volumetric) working capacity might be still negligibly small. This is thus a direct effect of ignoring the heat capacity of the heat conduction surface. To envisage the effect of the latter, the coefficient of performance for MOF-841(Zr)-water has been calculated for increasing magnitude of $c_p^{effective}$ with the conditions of refrigeration I (Fig. 4.10c, d), and shown in Fig. 4.11. Clearly, when $c_p^{effective}$ is increased, the coefficient of performance does not increase at lower T_{des} than ΔW anymore. Furthermore, the COP decreases as relatively more energy is required for heating up. The desorption temperature corresponding with the optimum COP$_c$ is not significantly influenced by the effective heat capacity. The decrease with higher T_{des} however is stronger for larger $c_p^{effective}$. This because increasing temperature does not significantly release more working fluid but energy is nonetheless still required for further temperature increase. This is obviously more cumbersome when $c_p^{effective}$ is higher (more heat exchanger mass is present). The influence of $c_p^{effective}$ on COP increases with decreasing ΔW, lower enthalpy of adsorption and higher T_{des}, obviously. Coming back to the results shown in Fig. 4.10, more specifically to further elucidate the effect of operational temperatures on performance, the concept of 'temperature lift' will be introduced and utilized.

209
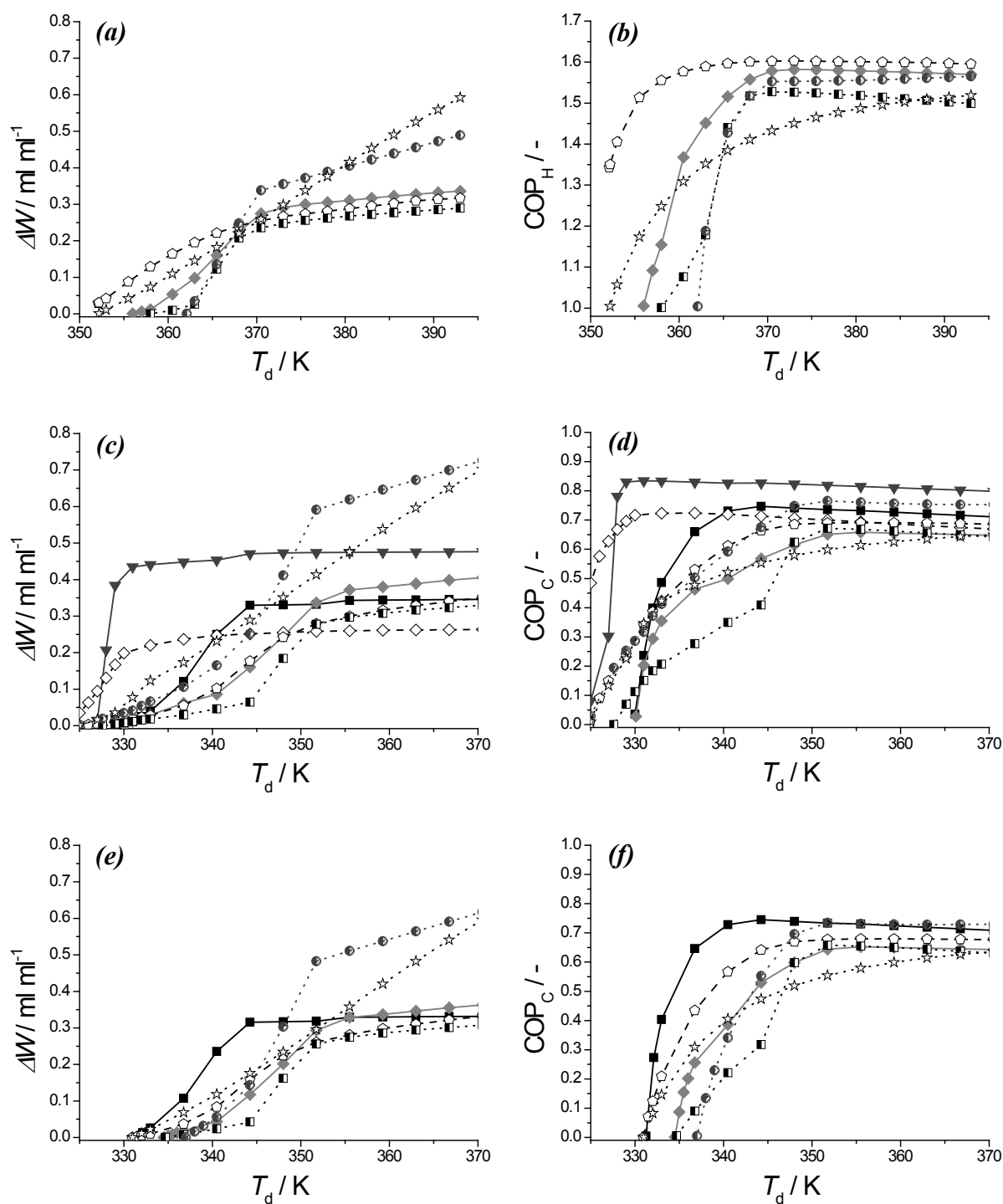
Figure 4.10: Working volume adsorbed per volume adsorbent, ΔW, (*a, c, e*) and COP (*b, d, f*) as function of desorption temperature, T_{des}, for heat pump (T_{ev} = 288 K, T_{ads} = 318 K, *a, b*), R.F.-I, (T_{ev} = 283 K, T_{ads} = 303 K, *c, d*) and R.F.-II (T_{ev} = 278 K, T_{ads} = 303 K, *e, f*). MOF-water working pairs, CAU-10(Al)-H (■), MOF-841(Zr) (▼) and MOF-801(Zr) (◆) with full lines. Benchmark-water pairs, AQSOA-Z01 (◇) and Z02 (⬠) with dashed lines. Methanol-based working pairs, MIL-53(Cr) (◨), Zn(BDC)(DABCO)$_{0.5}$ (◐) and Activated Carbon (✪) with dotted lines.
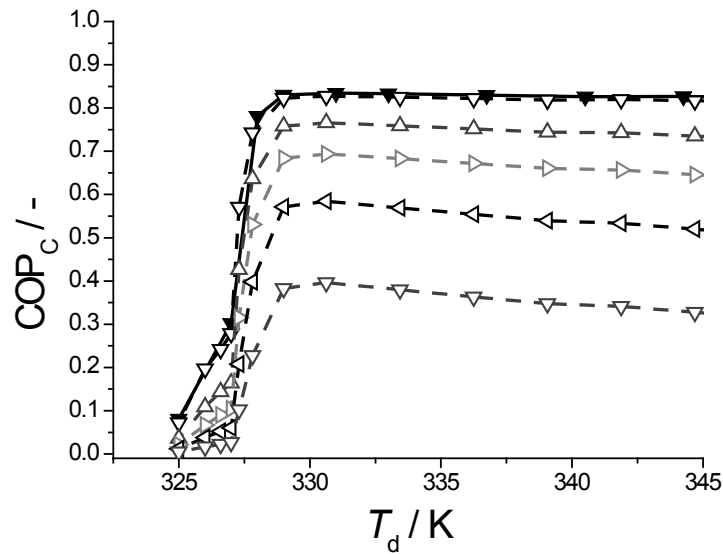
Figure 4.11: Coefficient of performance for cooling for MOF-841-water for conditions of refrigeration I, (T_{ev} = 283 K, T_{con} = 303 K) with varying effective heat capacity. For $c_p^{effective}$ = 1 (same as in Fig. 4.10c, d, ▼), $c_p^{effective}$ = 1.4 (▽), $c_p^{effective}$ = 5 (△), $c_p^{effective}$ = 10 (▷), $c_p^{effective}$ = 20 (◁) and $c_p^{effective}$ = 50 (▽).

4.7.3. TEMPERATURE LIFT

The temperature lift during the adsorption half-cycle can be defined as the difference between T_{con} and T_{ev} [325]. During desorption this is the difference between T_{des} and T_{con} [325]. Here focus is on the former, which can be interpreted as the temperature gain during adsorption for heat pumps, or the achievable decrease in temperature for cooling purposes. For a condenser temperature of 303 K and a fixed desorption temperature (373 K), the temperature of the evaporator is varied to envisage the effect of temperature lift on the energy withdrawal per volume of adsorbent per cycle. Results for all adsorbents are shown in Fig. 4.12.

For low temperature lifts, $\Delta T_{lift} \leq 12$ K, MIL-101(Cr) has the highest volumetric energy capacity ($\sim$ 500 kWh m^{-3}). For higher required temperature lifts, $12 \leq \Delta T_{lift} \leq 20$ K, MOF-841(Zr) is the adsorbent of choice ($\sim$ 350 kWh m^{-3}). For higher temperature lifts, CAU-10(Al)-H ($20 \leq \Delta T_{lift} \leq 26$ K) or MOF-801(Zr) can be efficiently utilized ($\sim$ 250 and $\sim$280 kWh m^{-3}, respectively). In fact it seems that CAU-10(Al)-H would have similar performance as AQSOA-Z02 over a wide range of temperature lifts. However, CAU-10(Al)-H can be regenerated at a significantly lower desorption temperature (see Fig. 4.10) than either AQSOA-Z02 or MOF-801(Zr).
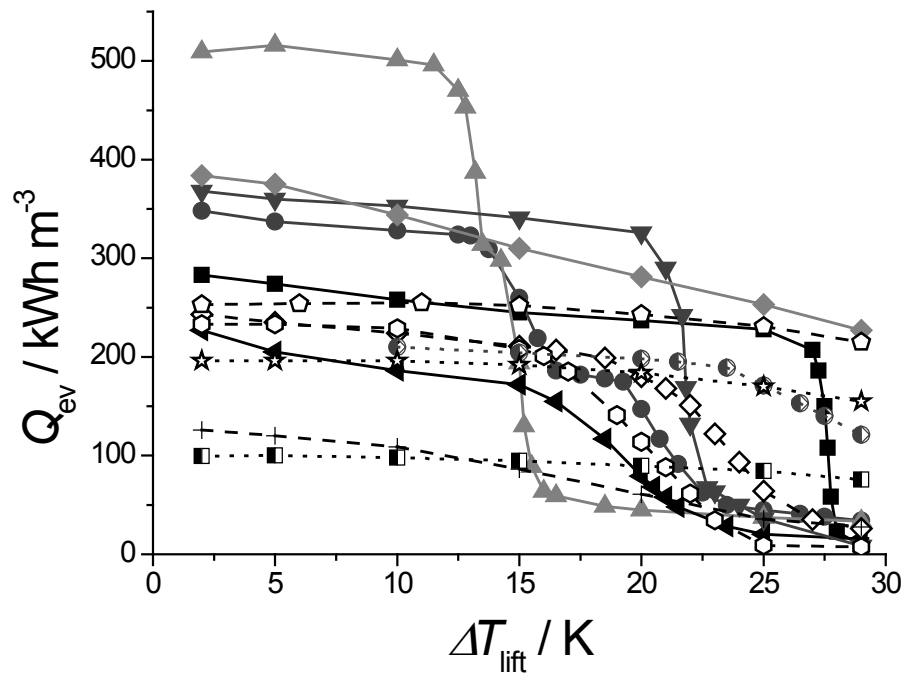
Figure 4.12: Energy withdrawn from the evaporator as function of temperature lift during adsorption, obtained by varying T_{ev} when $T_{des} = 373$ K and $T_{con} = 303$ K. MOF-water working pairs, CAU-10(Al)-H (■), MIL-100(Fe) (●), MIL-101(Cr) (▲), Al-fumarate (◀), MOF-841(Zr) (▼) and MOF-801(Zr) (◆) with solid lines. Benchmark-water pairs, Silica Gel (+), AQSOA-Z01 (◇), Z02 (⬠), and Z05 (◯) with dashed lines. Methanol-based working pairs, MIL-53(Cr) (▣), Zn(BDC)(DABCO)$_{0.5}$ (◖) and Activated Carbon (✩) with dotted lines.

To dwell on that, the required desorption temperature increases in order of: MIL-101(Cr) < MOF-841(Zr) < CAU-10(Al)-H < AQSOA-Z02 < MOF-801(Zr) (derived from Fig. 4.10), perfectly in line with the maximum achievable temperature lift. The coefficient of performance for cooling purposes also decreases with this maximum achievable temperature lift of each material; MIL-101(Cr, COP$_c$ ~ 0.89) > MOF-841(Zr, COP$_c$ ~ 0.79) > CAU-10(Al)-H (COP$_c$ ~ 0.72) > AQSOA-Z02 (COP$_c$ ~ 0.69) > MOF-801(Zr, COP$_c$ ~ 0.68). Thus, over a wide range of temperature lifts, MOFs can be more efficiently applied than currently available adsorbents. To allow for efficient heat removal by the evaporator, the immediate surroundings of the evaporator (*e.g.* the inside of a refrigerator) should have a (slightly) higher temperature, T_{ev}'. The reverse is true for the surroundings of the condenser, which should be lower than T_{con} (T_{con}'). The effective temperature lift thus, $T_{ev}' - T_{con}'$, is lower than that mentioned in the preceding discussion. Allowing thus for efficient heat transfer in condenser and evaporator, will diminish part of the maximum achievable temperature lift.

The above results can be, at least qualitatively, reasoned with the aid of pore size. A larger pore size means that pores are filled at lower adsorption potential, A_{ads}, (or higher α) making that the maximum temperature lift is reduced. Because of the same reason, the material is efficiently regenerated at lower adsorption potential of desorption, A_{des} (or lower desorption temperature). Because of the larger pore volume of structures with larger pores, the volumetric adsorption capacity is also increased (see Fig. 4.4, Table 4.6) and thus also Q_{ev} per volume of material. Lastly, because of a larger pore volume, the average adsorption enthalpy is lower, as previously mentioned, making thermodynamic efficiency greater. This discussion is based on MOF-water working pairs, and because water is very sensitive to specific adsorption sites, this rationale cannot be quantified fully with only the pore sizes of different materials. For methanol (or other working fluids), although less data are available, it can be safely assumed that this qualitative rationale also holds. The volumetric energy density for methanol, however, has been found lower in comparison to water as working fluid, because of the lower enthalpy of evaporation.

In short thus, for AHP/ADCs, MOFs offer from the thermodynamic perspective a significant improvement of thermodynamic efficiency and released/withdrawn energy per unit volume per cycle over a wide range of desired temperature lifts. This because of the large variation of pore sizes and possible tuning of adsorption sites. However, heat and mass transfer, left out of the comparison in this work as this is scarcely investigated for MOFs, are also important for actual application. If the characteristic cycle times for the above mentioned MOFs would be significantly longer than for conventional materials, application would still not be feasible. As the configuration of the employed adsorbent (powder, pellets, granules or coatings) play a determining role [306, 352-355], dynamic studies should be performed in conjunction with shaping MOF adsorbents. As with MOFs one has the ability to employ larger pore sizes, one may expect that diffusion inside these materials is faster than more narrow pore zeolites. Unfortunately, as studies on thermal transport of MOFs are mainly limited to water-unstable MOF-5 [356-360], it is difficult predict a priori whether MOFs might display shorter cycle times for a given configuration. Lastly, as the COPs reported in this work are based on thermodynamic equilibrium, which essentially means with infinite cycle times, in reality efficiency will be lower than determined here. In fact, there is an optimal cycle time to obtain a maximal power per unit volume (J s^{-1} m^{-3}) where the efficiency is maximal at infinite cycle time [361]. Furthermore, since in an actual adsorption cycle a certain amount of working fluid is required to desorb in the isosteric compression stage to achieve the pressure increase from

p_{ev} to p_{con}, the actual working capacity is reduced compared to the ideal working capacity used in this work, and thus also the coefficient of performance. The magnitude of this decrease can be mitigated by allowing for only a small empty volume in the adsorption vessel [362, 363]. Before concluding this communication with a summary and outlook (Section 4.9), alternative applications in which MOF adsorbents could potentially be employed are briefly discussed. All of these applications utilize water as working fluid.

4.8. ALTERNATIVE APPLICATIONS

Adsorption driven allocation of heat or cold is not the only application based on the reversible ad- and desorption of a working fluid. In this section, two major alternative applications will be discussed briefly, and the potential of applying MOFs in these will be concisely assessed. These are thermochemical energy storage (Section 4.8.1) and open cycle dehumidification for air conditioning (Section 4.8.2).

4.8.1. THERMOCHEMICAL ENERGY STORAGE

As mentioned in Chapter 1, temporary energy storage is required when energy supply and demand are out of phase. Especially thermochemical storage is interesting, as it requires significantly less volume to store the same amount of energy [19, 20] compared to systems based on latent [21] or sensible energy [22]. Conceptually, sorption-based thermochemical storage follows the same cycle as a heat pump, with the exception that the adsorption and desorption process are separated by storage time [325]. The relevant energy is comprised by the sorption energy and the latent heat of the sorbent. As during desorption, or charging, the adsorbent is heated, this latent heat could thus also be employed, in theory, during the exothermic adsorption stage for additional energy. However, depending on system insulation and storage time, only a fraction of the sensible heat can be recovered [325]. This contribution will be omitted here, as it constitutes only a small fraction the total energy anyways, and the amount of stored energy will be equated to $Q_{sorption}$. The amount of storable energy is thus a function of operational conditions, as is the case for AHP/ADCs, making that the volumetric storage capacity is lower than the values indicated in Fig. 4.9, bottom. This fact is sometimes forgotten when materials are compared, as mentioned by Stach *et al.* [364].
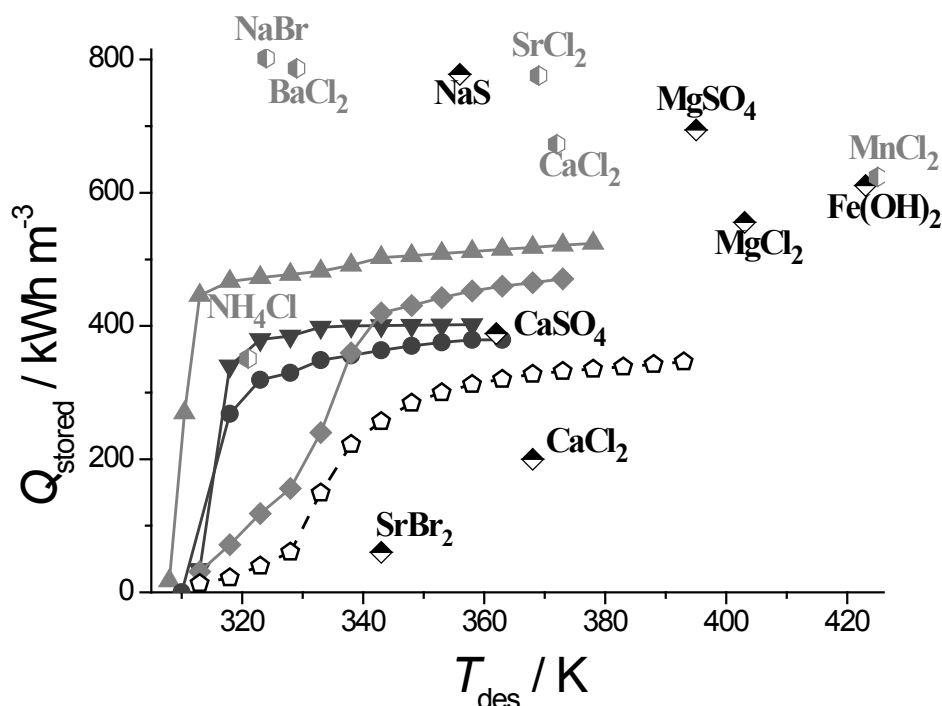
Figure 4.13: Storable energy density as function of T_{des} for T_{ev} = 283 K and T_{con} = 293 K. MOF-water working pairs, MIL-100(Fe) (●), MIL-101(Cr) (▲), MOF-841(Zr) (▼) and MOF-801(Zr) (◆) shown with solid lines. AQSOA-Z02(⬠) with dashed lines. Inorganic salts, used for comparison, in combination with water (◆) for SrBr$_2$ [365-367], CaCl$_2$ [365, 368], CaSO$_4$ [369, 370], NaS [369, 371, 372], MgSO$_4$ [365, 373, 374], MgCl$_2$ [365, 375] and Fe(OH)$_2$ [369, 370], and in combination with NH$_3$ (◖) for NH$_4$Cl [20, 376], NaBr [20, 376], BaCl$_2$ [20, 376], SrCl$_2$ [20, 376], CaCl$_2$ [20, 376] and MnCl$_2$ [20, 376].

Another difference in practical operation, is that relatively small temperature lifts of adsorption can be used, down to ~10 K [325, 377, 378], which makes (see Fig. 4.12) that the potential of MOFs can optimally be employed. For T_{con} = 283 K, an often employed temperature when thermochemical storage is considered [373, 375, 378], and T_{ev} = 293 K [325], sufficient for residential heating, $Q_{sorption}$ as function of desorption temperature can be calculated. Results are shown in Fig. 4.13 for the more promising MOFs, based on Figs. 4.9 and 4.12, and compared with inorganic salts that in combination with water or NH$_3$ are commonly employed for energy storage at similar desorption or driving temperatures [20, 365, 369]. Clearly, most of the inorganic salt-fluid combinations exhibit larger volumetric storage density than those of the porous adsorbents. Note that these quantities are based on the pure salt-solvate densities and that these salts are non-porous, some even become liquid upon hydration. Both aspects may induce transport limitations and slow down the response time.

Embedding these in porous solids is considered [379-383], decreasing the energy density. Therefore, to calculate an effective (energy) density, a bulk porosity of 50% is often assumed [20, 375]. In Fig. 4.13 however, this has not been done (MOFs and salt-solvates are employed both with 0% porosity). As MOFs are indeed porous, a lower effective bulk porosity than 0.5 might be used in practice, making that energy densities become more in line with those of inorganic salts. Compared to especially water-salt combinations, MOFs have the advantage that lower desorption temperatures can be used, for low temperature lifts. In addition, some of these salts, *e.g.* $MgCl_2$, exhibit display significant degradation over a few ad- and desorption cycles [384]. Lastly, other zeolites were not considered in this section, in spite of investigations for thermal energy storage, because these generally exhibit lower energy densities (110 and 160 kWh m^{-3} for NaX and LiX, respectively [385]) and often require higher desorption temperatures than the adsorbents presented in Fig. 4.13.

4.8.2. OPEN CYCLE AIR-CONDITIONING

As already mentioned (Chapter 1), the great advantage of open system air-conditioning by desiccation [8, 9, 386, 387] is that water vapor can be removed directly from the ambient air, whereas the closed devices require cooling down of the incoming air to temperatures below the dew point [388]. The concept revolves around the direct adsorption of water vapor from ambient air, an effective way of dehumidification. The solid adsorbent is commonly coated on the internal channels of a rotating wheel, called either a sorption rotor or desiccant wheel. Devices employing either zeolites, zeotypes or silica gel are already commercially available [18, 389, 390]. The actual operation of desiccant wheel dehumidification is more complex than the heat pump cycle, and the operating conditions depend on outside climate and season [8, 391-393]. Detailed performance characterization of materials in open cycle desiccation is entirely different from AHP/ADCs and is considered out of scope for this work. However, desired adsorbent properties are similar to those for AHP/ADCs; sufficient stability towards water and suitable adsorptive properties. Additionally, as the adsorbent will be exposed to the ambient, fouling resistance by *e.g.* microbes should be considered. As a difference, the adsorption uptake is allowed to occur at higher relative α's (or relative humidity, R.H.) than is the case for heat pumps [388]. So, all AQSOA-materials are used for open cycle dehumidification, whilst AQZOA-Z05, the material with the highest α, is not used for application in AHP/ADCs [18]. This means that MOFs with a high volumetric capacity (*e.g.*, MOF-841, MIL-100 and MIL-101) can in principle be efficiently utilized for this purpose.
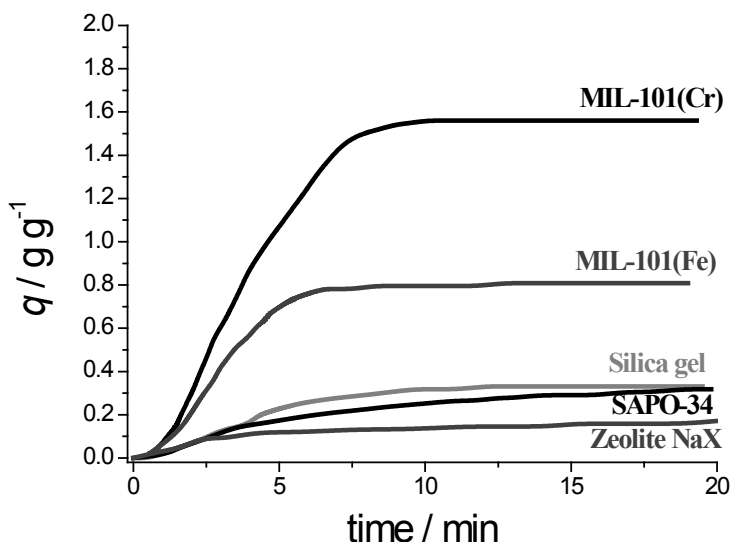
Figure 4.14: Water adsorption uptake profiles of adsorbent materials MIL-101(Cr), MIL-100(Fe), silica gel, SAPO-34, and zeolite NaX at 30 °C in a humid N_2 flow. Test conditions are adsorption at 30 °C, R.H. 60%; and flow rate of N_2, 200 mL min^{-1}. Adapted with permission from Ref. [203].

This has been demonstrated by Seo *et al.*, who showed that the rate mass uptake (R.H. = 60%) per unit mass of material, for MIL-101 is far greater than for other adsorbents, including SAPO-34 (Fig. 4.14) [203]. This also clearly indicates a potential advantage of MOFs in dehumidification applications over commonly used adsorbents. Guo *et al.* further underlined this potential. They claimed, based on an array of different MOFs in comparison with alumina, their industrial adsorbent of choice for dehumidification, that all MOFs have superior total capacities, and some also display superior breakthrough behavior, so faster kinetics [394]. In addition, cyclic regeneration for MOFs can be achieved with significantly less energy (lower T_{des}), all in line with preceding findings (desiccant, AHP/ADC) [394].

4.9. SUMMARY AND FUTURE PERSPECTIVES

4.9.1. SUMMARY

The potential of MOFs as adsorbents in adsorption driven allocation of heat and cold has been thoroughly assessed in this work. The adsorption mechanism of water on MOFs is known. Water initially adsorbs at specific hydrophilic sites (uncoordinated metal sites, OH-groups on inorganic clusters or functional groups on the organic ligand). Subsequently, additional water clusters around these initially adsorbed water molecules, after which the pores are filled via volume filling ($d_p < D_c$) or capillary condensation ($d_p > D_c$). *In silico* prediction of water adsorption in MOFs is deemed not yet mature enough for accurate selection of MOF structures. For alcohols the adsorption mechanism is somewhat similar, although the adsorption behavior is often devoid of steep steps in uptake. In this case, *in silico* prediction seems to work better, as the behavior of methanol is well described by classical force fields.

Stability of MOFs with respect to water has been researched in a plethora of communications. Various factors that (co-)determine the structural stability have been posed, of which the most important are the metal species, its valence, coordination number and degree of filling of the coordination sphere, and the metal-ligand bond strength. Additionally, structural defects can play an important role on stability. Further, degradation reactions do not always occur in the bulk of the material. In some cases only an exterior shell is degraded, forming an impervious layer, preserving the bulk of the material. Surface tension of water might also have adverse effects on stability for MOFs with elongated ligands. Lastly, MOFs that have been claimed to be stable towards water vapor, have been shown to degrade under repeated ad- and desorption cycles. The preceding highlights the complexity of influences on water stability. Nonetheless, there are MOFs that exhibit the level of hydrothermal stability required for application in AHP/ADCs. Of these structures, some show the interesting stepwise water uptake behavior for this target application. These are CAU-10(Al)-H, MIL-100(Fe), MIL-101(Cr), MOF-801(Zr), MOF-841(Zr) and Al-fumarate, of which the performance is thoroughly assessed in Sections 4.6-4.7 of this work. Especially CAU-10(Al)-H stands out with respect to stability, as no degradation was observed for over 700 adsorption cycles [178]. For methanol stability is seemingly less of an issue. However, the list of structures for which methanol adsorption has been investigated (at more than one temperature) is too limited for a proper evaluation. Only the performance of MIL-53(Cr) and Zn(BDC)(DABCO)$_{0.5}$ could be assessed. These

structures exhibit the desired stepwise uptake of methanol, although this is caused by the structural flexibility of the frameworks, making that an undesired hysteresis-loop is observed. Lastly, for ammonia, because of stability issues and subsequent limited adsorption data, no suitable candidate could be identified. Of the available adsorption data, a significant part is used for trace removal, which is characterized by very low partial pressures of working fluid, making the bulk of the retrieved studies of little use for detailed assessment.

A thermodynamic model of the ideal adsorption heat pump cycle has been adopted, with the aim to assess the performance of MOFs for adsorption driven allocation of heat and cold in an accurate and objective manner. Per unit volume, MOFs can in total store more energy, Q_{sorption}, and release more energy per cycle ($Q_{\text{ev}}/Q_{\text{con}}$) when water is the working fluid of choice. Especially the latter is desired for the application at hand. Also, especially for cooling applications, MOFs clearly have been shown to display improved capacity and thermodynamic efficiency. Over a wide range of required temperature lifts for application, MOFs display higher capacity and efficiency than benchmark materials. The specific material that has optimal performance depends on the desired temperature lift. For low temperature lifts, $\Delta T_{lift} \leq 12$ K, MIL-101(Cr) has the highest energy capacity per unit volume MOF (~ 500 kWh m^{-3}). For higher required temperature lifts, $12 \leq \Delta T_{\text{lift}} \leq 20$ K, MOF-841(Zr) is the adsorbent of choice (~ 350 kWh m^{-3}). For higher temperature lifts, CAU-10(Al)-H ($20 \leq \Delta T_{\text{lift}} \leq 26$ K) or MOF-801(Zr) can be efficiently utilized (~ 250 and ~ 280 kWh m^{-3}, respectively). The required desorption temperature increases, for the investigated adsorbent-water pairs, in the order: MIL-101(Cr) < MOF-841(Zr) < CAU-10(Al)-H < AQSOA-Z02 < MOF-801(Zr). Lastly, thermodynamic efficiency follows the same trend: MIL-101(Cr, COP$_c$ ~ 0.89) > MOF-841(Zr, COP$_c$ ~ 0.79) > CAU-10(Al)-H (COP$_c$ ~ 0.72) > AQSOA-Z02(COP$_c$ ~ 0.69) > MOF-801(Zr, COP$_c$ ~ 0.68). These trends can be directly related to the material's pore size. A larger pore size means that pores are generally filled at higher α, thus at lower adsorption potential for adsorption, A_{ads}, making that the maximum temperature lift is reduced, but the material is efficiently regenerated at lower adsorption potential for desorption, A_{des}, as well. A larger pore volume leads to an increased volumetric adsorption capacity. Because of a larger pore volume, the average adsorption enthalpy is lower resulting in a higher thermodynamic efficiency.

Furthermore, MOFs have great potential for the efficient direct dehumidification of air for air-conditioning purposes. For energy storage applications, focus should be especially on low desorption temperature applications, as MOF-water pairs are likely to be more competitive in

this range. In this work, however, no better performance with respect to commonly used inorganic salts has been identified in terms of energy storage capacity.

4.9.2. FUTURE PERSPECTIVES

Focus of this work is on the thermodynamic ('static') properties of MOFs in relation to allocation of heat and cold, as these are most abundantly available. For successful application, however, also the dynamics of the MOF-working fluid pair are important. The latter depends heavily on the macroscopic structure of the MOF chosen in the heat exchange application. Furthermore, MOFs are commonly synthesized and characterized on the (sub-)gram scale, while actual heat pumps contain adsorbent material in the order of kilograms. To help put things in perspective, seven subsequent stages are defined that will eventually lead to application:

- Stage 0 – Stability: As primary requirement, MOFs should be tolerant towards the working fluid of choice. This should be ensured before anything else.
- Stage 1 – Adsorptive properties: Based on primary vapor adsorption measurement(s), the shape of an isotherm can be envisaged. From this initial feasibility can be assessed.
- Stage 2 – Thermodynamic efficiency and working capacity: With knowledge of the enthalpy of adsorption, preferably directly from calorimetric measurements or else calculated isosteric enthalpy (from isotherms at more than one temperature) and (crystallographic) density of a material, the efficiency and volumetric (working) capacity can be assessed as has been done extensively in Sections 4.6-4.7.
- Stage 3 – Shaping of materials: The previous stages have in common that they can be assessed on as-synthesized powders. As dynamics of heat and mass transfer (Stage 4) are dependent on the chosen configuration of the employed adsorbent (*e.g.* pellets, granules or coatings) shaping is in order.
- Stage 4 – Heat and mass transfer of shaped materials: Based on the morphology chosen in stage 3, the effective heat and mass transfer rates should be determined to assess the dynamics of the MOF-working pair.
- Stage 5 – Scale up of synthesis: Previous stages can be performed on the (sub-)gram scale. For actual application, the synthesis should be properly scaled up, to allow for large-scale performance testing.

- Stage 6 – Large-scale evaluation of shaped systems: The performance of a large-scale system should be ensured before commercialization. Additionally, based on the performance and the results of stage 5, an economic evaluation will ultimately determine the feasibility of the MOF-working fluid combination.

This classification will help assess at which stage MOFs combined with the working fluid of choice are. Furthermore, guidelines and considerations can be posed for focus of future work.

AMMONIA – STAGE 0

For very few MOFs, if any, it has been convincingly demonstrated that they reversibly adsorb significant amounts of ammonia with structural retention. The number of different MOF structures for which this has been examined is far lower than for water. The cause of instability with respect to ammonia has received little attention. It is therefore not clear whether there exists a justifiable expectation for ammonia-stable MOFs. If any desire exists to employ MOF-ammonia working pairs in heat pumps, focus should be on resolving instability of MOFs towards ammonia.

ALCOHOLS – STAGE 2

Interesting adsorption properties have been reported for several MOFs with respect to methanol/ethanol, namely for ZIFs (ZIF-8, -68, -71 and -90), MIL-53(Cr) and $Zn(BDC)(DABCO)_{0.5}$. Of the ZIFs, little to no information on either desorption or enthalpy of adsorption is known, making practical assessment impossible. Of the latter two, the energy capacity turned out to be lower than for water-MOF pairs. Because of the higher vapor pressure of methanol and to a lesser extent ethanol, dynamics might be faster than for water, so a lower energetic capacity does not necessarily exclude a viable application. However, for most conditions the methanol-MOF pairs exhibited lower coefficients of performance (COP) than methanol-activated carbon. Regarding the to be avoided adsorption-desorption hysteresis alcohols require larger pore diameters than water (3.5 nm for methanol, 4.3 nm for ethanol, and 2 nm for water). So, larger pore sizes could be used for MOF-alcohol pairs than for water and for alcohols focus should be on exploring adsorption on additional MOF structures, especially comprising larger pore size structures to obtain more efficient alcohol-based working pairs.

WATER – STAGE 3/4:

In Section 4.7 it has been demonstrated convincingly that water-MOF working pairs exist with higher capacity and thermodynamic efficiency than benchmark sorbents. Shaping of these materials should be focused on, in conjunction with measurements on heat and mass transfer dynamics. For packed bed systems, heat transfer is often limiting, making coatings an optimal configuration [352, 353, 395]. Most work regarding MOF coatings has focused on the creation of thin films [396-401], of which the thickness is generally on the submicron-scale, orders of magnitude off for target application. However, there are studies focusing on creating thick MOF films (>100 micron), suited for application. These are based direct crystallization on the surface, without the need for a physical binder material [177, 180, 181]. Furthermore, MAF-4 has been grown directly from and on structured ZnO [189], and Al-based MOFs have been formed directly on and from structured alumina-supports [402]. These and other [403, 404] examples highlight the potential of direct growth of MOFs on various structured supports. Alternatively, granules or pellets [359, 405-408] can be utilized. For benchmark materials AQSOA-Z01 [409, 410], AQSOA-Z02 [411-413] and silica gel [413, 414] the adsorption dynamics of water have been determined and serve as a good basis for comparison.

Though there are few accounts of their large-scale synthesis [415-417], MOFs potentially offer advantages, as environmentally benign [418-421], room temperature [422-429] and even solvent-free synthesis [430-435] protocols have been developed. In comparison, zeolite and zeotype synthesis often requires relatively expensive sacrificial organic templates [436-441], as is the case for the synthesis of SAPO-34 (AQSOA-Z02) [442-444] and AlPO-5(AQSOA-Z01/Z05) [445-447].

In short, MOFs with water as working fluid show improved thermodynamic efficiency and volumetric adsorption capacity in comparison to commercially available benchmark materials for adsorption driven allocation of heat and cold. MOF potential is further strengthened by the availability of low temperature, environmentally benign and even solvent-free synthesis protocols and the possibility of synthesizing these materials directly on heat exchanger surfaces. MOFs thus have a bright future for application in adsorption driven heat pumps and chillers.

4.10. REFERENCES

[1]   M. Höök, X. Tang, Depletion of fossil fuels and anthropogenic climate change - a review, Energy Policy, 52 (2013) 797-809.

[2]   M. Isaac, D.P. van Vuuren, Modeling global residential sector energy demand for heating and air conditioning in the context of climate change, Energy Policy, 37 (2009) 507-521.

[3]   International Energy Agency, World energy outlook. 2011, 696.
        http://www.iea.org/publications/freepublications/publication/weo2011_web.pdf (accessed 17-01-2015).

[4]   M.J. Moran, H.N. Shapiro, Fundamentals of engineering thermodynamics, 5th ed., Wiley, 2006.

[5]   W. Wongsuwan, S. Kumar, P. Neveu, F. Meunier, A review of chemical heat pump technology and applications, Applied Thermal Engineering, 21 (2001) 1489-1519.

[6]   W. Wu, X. Zhang, X. Li, W. Shi, B. Wang, Comparisons of different working pairs and cycles on the performance of absorption heat pump for heating and domestic hot water in cold regions, Applied Thermal Engineering, 48 (2012) 349-358.

[7]   C.A. Balaras, G. Grossman, H.-M. Henning, C.A. Infante Ferreira, E. Podesser, L. Wang, E. Wiemken, Solar air conditioning in Europe - an overview, Renewable and Sustainable Energy Reviews, 11 (2007) 299-314.

[8]   H.-M. Henning, Solar assisted air conditioning of buildings - an overview, Applied Thermal Engineering, 27 (2007) 1734-1749.

[9]   H.M. Henning, T. Erpenbeck, C. Hindenburg, I.S. Santamaria, The potential of solar energy use in desiccant cooling cycles, International Journal of Refrigeration, 24 (2001) 220-229.

[10]   Y.M. Yonezawa, Masao; Oku, Kenzo; Nakano, Hiroki; Okumura, Shin-ichi; Yoshihara, Motoshi; Sakai, Akiyoshi; Morikawa, Atsushi Adsorption refrigeration system.United States Patent 4881376, 1989

[11]   F. Meunier, Adsorption heat powered heat pumps, Applied Thermal Engineering, 61 (2013) 830-836.

[12]   R.Z. Wang, R.G. Oliveira, Adsorption refrigeration - an efficient way to make good use of waste heat and solar energy, Progress in Energy and Combustion Science, 32 (2006) 424-458.

[13]   Invensor. http://www.invensor.com/en/technology/cooling-system.htm (accessed 17-01-2015).

[14]   B. Dawoud, P. Hoefle, A. Bornmann, S. Chmielewski, C. Marburger Vacuum sorption apparatus.Unites States Patent 8544293, 2013

[15]   H. Kakiuchi, S. Shimooka, M. Iwade, K. Oshima, M. Yamazaki, S. Terada, H. Watanabe, T. Takewaki, Novel water vapor adsorbent FAM-Z01 and its applicability to an adsorption heat pump, Kagaku Kogaku Ronbunshu, 31 (2005) 361-364.

[16]   H. Kakiuchi, S. Shimooka, M. Iwade, K. Oshima, M. Yamazaki, S. Terada, H. Watanabe, T. Takewaki, Water vapor adsorbent FAM-Z02 and its applicability to adsorption heat pump, Kagaku Kogaku Ronbunshu, 31 (2005) 273-277.

[17]   S. Shimooka, K. Oshima, H. Hidaka, T. Takewaki, H. Kakiuchi, A. Kodama, M. Kubota, H. Matsuda, The evaluation of direct cooling and heating desiccant device coated with FAM, Journal of Chemical Engineering of Japan, 40 (2007) 1330-1334.

[18]   MITSUBISHI PLASTICS, Zeolitic water vapor adsorbent: AQSOA.
        http://www.aaasaveenergy.com/products/001/pdf/AQSOA_1210E.pdf (accessed 17-01-2015).

[19]   J. Hadorn, Advanced storage concepts for active solar energy - IEA SHC task 32 2003-2007, Eurosun—1st international conference on solar heating, cooling and buildings. Lisbon2008.

[20]   N. Yu, R.Z. Wang, L.W. Wang, Sorption thermal storage for solar energy, Progress in Energy and Combustion Science, 39 (2013) 489-514.

[21]   A. Fernandez, M. Martínez, M. Segarra, I. Martorell, L. Cabeza, Selection of materials with potential in sensible thermal energy storage, Solar Energy Materials and Solar Cells, 94 (2010) 1723-1729.

[22]   A. Sharma, V. Tyagi, C. Chen, D. Buddhi, Review on thermal energy storage with phase change materials and applications, Renewable and Sustainable Energy Reviews, 13 (2009) 318-345.

[23]   J. Canivet, A. Fateeva, Y. Guo, B. Coasne, D. Farrusseng, Water adsorption in MOFs: Fundamentals and applications, Chemical Society Reviews, (2014).

[24]   J. Canivet, J. Bonnefoy, C. Daniel, A. Legrand, B. Coasne, D. Farrusseng, Structure–property relationships of water adsorption in Metal–Organic Frameworks, New Journal of Chemistry, 38 (2014) 3102.

[25]   B. Coasne, K.E. Gubbins, R.J.-M. Pellenq, Temperature effect on adsorption/desorption isotherms for a simple fluid confined within various nanopores, Adsorption, 11 (2005) 289-294.

[26]   B. Coasne, A. Galarneau, R.J.M. Pellenq, F. Di Renzo, Adsorption, intrusion and freezing in porous silica: The view from the nanoscale, Chemical Society Reviews, 42 (2013) 4141-4171.

[27]   M.F. De Lange, J.-J. Gutierrez-Sevillano, S. Hamad, T.J.H. Vlugt, S. Calero, J. Gascon, F. Kapteijn, Understanding adsorption of highly polar vapors on mesoporous MIL-100(Cr) and MIL-101(Cr): Experiments and molecular simulations, The Journal of Physical Chemistry C, 117 (2013) 7613-7622.

[28]   B. Guillot, A reappraisal of what we have learnt during three decades of computer simulations on water, Journal of Molecular Liquids, 101 (2002) 219-260.

[29]   J.M. Castillo, T.J.H. Vlugt, S.a. Calero, Understanding water adsorption in Cu−BTC Metal−Organic Frameworks, The Journal of Physical Chemistry C, 112 (2008) 15934-15939.

[30]   S. Paranthaman, F.-X. Coudert, A.H. Fuchs, Water adsorption in hydrophobic MOF channels, Physical Chemistry Chemical Physics, 12 (2010) 8123-8129.

[31]   D. Dubbeldam, A. Torres-Knoop, K.S. Walton, On the inner workings of Monte Carlo codes, Molecular Simulation, 39 (2013) 1253-1292.

[32]   P. Ghosh, Y.J. Colon, R.Q. Snurr, Water adsorption in UiO-66: The importance of defects, Chemical Communications, (2014).

[33]   J. Zang, S. Nair, D.S. Sholl, Prediction of water adsorption in copper-based Metal–Organic Frameworks using force fields derived from dispersion-corrected DFT calculations, The Journal of Physical Chemistry C, 117 (2013) 7519-7525.

[34]   H. Fang, P. Kamakoti, J. Zang, S. Cundy, C. Paur, P.I. Ravikovitch, D.S. Sholl, Prediction of CO_2 adsorption properties in zeolites using force fields derived from periodic dispersion-corrected DFT calculations, The Journal of Physical Chemistry C, 116 (2012) 10692-10701.

[35]   H. Fang, P. Kamakoti, P.I. Ravikovitch, M. Aronson, C. Paur, D.S. Sholl, First principles derived, transferable force fields for CO_2 adsorption in Na-exchanged cationic zeolites, Physical Chemistry Chemical Physics, 15 (2013) 12882-12894.

[36]   L.-C. Lin, K. Lee, L. Gagliardi, J.B. Neaton, B. Smit, Force-field development from electronic structure calculations with periodic boundary conditions: Applications to gaseous adsorption and transport in Metal–Organic Frameworks, Journal of Chemical Theory and Computation, 10 (2014) 1477-1488.

[37]   Y.J. Colón, D. Fairen-Jimenez, C.E. Wilmer, R.Q. Snurr, High-throughput screening of porous crystalline materials for hydrogen storage capacity near room temperature, The Journal of Physical Chemistry C, 118 (2014) 5383-5389.

[38]   C.E. Wilmer, R.Q. Snurr, Towards rapid computational screening of Metal-Organic Frameworks for carbon dioxide capture: Calculation of framework charges via charge equilibration, Chemical Engineering Journal, 171 (2011) 775-781.

[39]   M. Fernandez, P.G. Boyd, T.D. Daff, M.Z. Aghaji, T.K. Woo, Rapid and accurate machine learning recognition of high performing Metal Organic Frameworks for CO_2 capture, The Journal of Physical Chemistry Letters, 5 (2014) 3056-3060.

[40]   R.P. Lively, M.E. Dose, J.A. Thompson, B.A. McCool, R.R. Chance, W.J. Koros, Ethanol and water adsorption in methanol-derived ZIF-71, Chemical Communications, 47 (2011) 8667-8669.

[41]   Y.F. Chen, J.Y. Lee, R. Babarao, J. Li, J.W. Jiang, A highly hydrophobic Metal−Organic Framework $Zn(BDC)(TED)_{0.5}$ for adsorption and separation of CH_3OH/H_2O and CO_2/CH_4: An integrated experimental and simulation study, The Journal of Physical Chemistry C, 114 (2010) 6602-6609.

[42]   K. Zhang, L. Zhang, J. Jiang, Adsorption of C1–C4 alcohols in Zeolitic Imidazolate Framework-8: Effects of force fields, atomic charges, and framework flexibility, The Journal of Physical Chemistry C, 117 (2013) 25628-25635.

[43]   T.R.C. Van Assche, T. Duerinck, J.J. Gutiérrez Sevillano, S. Calero, G.V. Baron, J.F.M. Denayer, High adsorption capacities and two-step adsorption of polar adsorbates on copper–benzene-1,3,5-tricarboxylate Metal–Organic Framework, The Journal of Physical Chemistry C, 117 (2013) 18100-18111.

[44]   D. Yu, P. Ghosh, R.Q. Snurr, Hierarchical modeling of ammonia adsorption in functionalized Metal-Organic Frameworks, Dalton Transactions, 41 (2012) 3962-3973.

[45]   K.C. Kim, D. Yu, R.Q. Snurr, Computational screening of functional groups for ammonia capture in Metal–Organic Frameworks, Langmuir, 29 (2013) 1446-1456.

[46]   P. Ghosh, K.C. Kim, R.Q. Snurr, Modeling water and ammonia adsorption in hydrophobic Metal–Organic Frameworks: Single components and mixtures, The Journal of Physical Chemistry C, 118 (2013) 1102-1110.

[47]   N.C. Burtch, H. Jasuja, K.S. Walton, Water stability and adsorption in Metal–Organic Frameworks, Chemical Reviews, 114 (2014) 10575-10612.

[48]   M.F. De Lange, T.J.H. Vlugt, J. Gascon, F. Kapteijn, Adsorptive characterization of porous solids: Error analysis guides the way, Microporous and Mesoporous Materials, 200 (2014) 199-215.

224

[49] J.J. Low, A.I. Benin, P. Jakubczak, J.F. Abrahamian, S.A. Faheem, R.R. Willis, Virtual high throughput screening confirmed experimentally: Porous coordination polymer hydration, Journal of the American Chemical Society, 131 (2009) 15834-15842.

[50] N.u. Qadir, S.A.M. Said, H.M. Bahaidarah, Structural stability of Metal Organic Frameworks in aqueous media - controlling factors and methods to improve hydrostability and hydrothermal cyclic stability, Microporous and Mesoporous Materials, 201 (2015) 61-90.

[51] J.B. DeCoste, G.W. Peterson, H. Jasuja, T.G. Glover, Y.-g. Huang, K.S. Walton, Stability and degradation mechanisms of Metal-Organic Frameworks containing the $Zr_6O_4(OH)_4$ secondary building unit, Journal of Materials Chemistry A, 1 (2013) 5642-5650.

[52] J.B. DeCoste, G.W. Peterson, B.J. Schindler, K.L. Killops, M.A. Browe, J.J. Mahle, The effect of water adsorption on the structure of the carboxylate containing Metal-Organic Frameworks Cu-BTC, Mg-MOF-74, and UiO-66, Journal of Materials Chemistry A, 1 (2013) 11922-11932.

[53] J.H. Cavka, S. Jakobsen, U. Olsbye, N. Guillou, C. Lamberti, S. Bordiga, K.P. Lillerud, A new zirconium inorganic building brick forming Metal Organic Frameworks with exceptional stability, Journal of the American Chemical Society, 130 (2008) 13850-13851.

[54] V. Bon, I. Senkovska, M.S. Weiss, S. Kaskel, Tailoring of network dimensionality and porosity adjustment in Zr- and Hf-based MOFs, CrystEngComm, 15 (2013) 9572-9577.

[55] H.J. Choi, M. Dinca, A. Dailly, J.R. Long, Hydrogen storage in water-stable Metal-Organic Frameworks incorporating 1,3- and 1,4-benzenedipyrazolate, Energy & Environmental Science, 3 (2010) 117-123.

[56] V. Colombo, S. Galli, H.J. Choi, G.D. Han, A. Maspero, G. Palmisano, N. Masciocchi, J.R. Long, High thermal and chemical stability in pyrazolate-bridged Metal-Organic Frameworks with exposed metal sites, Chemical Science, 2 (2011) 1311-1319.

[57] H. Jasuja, N.C. Burtch, Y.-g. Huang, Y. Cai, K.S. Walton, Kinetic water stability of an isostructural family of zinc-based pillared Metal–Organic Frameworks, Langmuir, 29 (2012) 633-642.

[58] P. Li, J. Chen, J. Zhang, X. Wang, Water stability and competition effects toward CO_2 adsorption on Metal Organic Frameworks, Separation & Purification Reviews, 44 (2014) 19-27.

[59] N.L. Rosi, J. Kim, M. Eddaoudi, B. Chen, M. O'Keeffe, O.M. Yaghi, Rod packings and Metal−Organic Frameworks constructed from rod-shaped secondary building units, Journal of the American Chemical Society, 127 (2005) 1504-1518.

[60] K. Tan, N. Nijem, P. Canepa, Q. Gong, J. Li, T. Thonhauser, Y.J. Chabal, Stability and hydrolyzation of Metal Organic Frameworks with paddle-wheel SBUs upon hydration, Chemistry of Materials, 24 (2012) 3153-3167.

[61] Y.J. Chabal, K. Tan, N. Nijem, S. Zuluaga, Y. Gao, J. Li, T. Thonhauser, Water interactions in Metal Organic Frameworks, CrystEngComm, 17 (2015) 247-260.

[62] K.A. Cychosz, A.J. Matzger, Water stability of microporous coordination polymers and the adsorption of pharmaceuticals from water, Langmuir, 26 (2010) 17198-17202.

[63] Z. Zhang, Z.-Z. Yao, S. Xiang, B. Chen, Perspective of microporous Metal-Organic Frameworks for CO_2 capture and separation, Energy & Environmental Science, (2014).

[64] G. Majano, O. Martin, M. Hammes, S. Smeets, C. Baerlocher, J. Pérez‐Ramírez, Solvent‐mediated reconstruction of the Metal-Organic Framework HKUST-1 (Cu_3BTC_2), Advanced Functional Materials, 24 (2014) 3855-3865.

[65] M.K. Bhunia, J.T. Hughes, J.C. Fettinger, A. Navrotsky, Thermochemistry of paddle wheel MOFs: Cu-HKUST-1 and Zn-HKUST-1, Langmuir, 29 (2013) 8140-8145.

[66] S.S. Kaye, A. Dailly, O.M. Yaghi, J.R. Long, Impact of preparation and handling on the hydrogen storage properties of $Zn_4O(1,4-benzenedicarboxylate)_3$ (MOF-5), Journal of the American Chemical Society, 129 (2007) 14176-14177.

[67] M. De Toni, R. Jonchiere, P. Pullumbi, F.-X. Coudert, A.H. Fuchs, How can a hydrophobic MOF be water-unstable? Insight into the hydration mechanism of IRMOFs, ChemPhysChem, 13 (2012) 3497-3503.

[68] L. Bellarosa, J.M. Castillo, T. Vlugt, S. Calero, N. López, On the mechanism behind the instability of isoreticular Metal-Organic Frameworks (IRMOFs) in humid environments, Chemistry - A European Journal, 18 (2012) 12260-12266.

[69] J.A. Greathouse, M.D. Allendorf, The interaction of water with MOF-5 simulated by molecular dynamics, Journal of the American Chemical Society, 128 (2006) 10678-10679.

[70] S.S. Han, S.-H. Choi, A.C.T. van Duin, Molecular dynamics simulations of stability of Metal-Organic Frameworks against H_2O using the reaxff reactive force field, Chemical Communications, 46 (2010) 5713-5715.

[71] C. Gomes Silva, I. Luz, F.X. Llabrés i Xamena, A. Corma, H. García, Water stable Zr–benzenedicarboxylate Metal–Organic Frameworks as photocatalysts for hydrogen generation, Chemistry – A European Journal, 16 (2010) 11133-11138.

[72] A. Dhakshinamoorthy, A.M. Asiri, H. Garcia, Catalysis by Metal-Organic Frameworks in water, Chemical Communications, 50 (2014) 12800-12814.

[73] S. Bhattacharjee, C. Chen, W.-S. Ahn, Chromium terephthalate Metal-Organic Framework MIL-101: Synthesis, functionalization, and applications for adsorption and catalysis, RSC Advances, 4 (2014) 52500-52525.

[74] I.J. Kang, N.A. Khan, E. Haque, S.H. Jhung, Chemical and thermal stability of isotypic Metal-Organic Frameworks: Effect of metal ions, Chemistry – A European Journal, 17 (2011) 6437-6442.

[75] E. Stavitski, M. Goesten, J. Juan-Alcañiz, A. Martinez-Joaristi, P. Serra-Crespo, A.V. Petukhov, J. Gascon, F. Kapteijn, Kinetic control of Metal-Organic Framework crystallization investigated by time-resolved in situ x-ray scattering, Angewandte Chemie International Edition, 50 (2011) 9624-9628.

[76] T. Wittmann, R. Siegel, N. Reimer, W. Milius, N. Stock, J. Senker, Enhancing the water stability of Al-MIL-101-NH$_2$ via postsynthetic modification, Chemistry– A European Journal, 21 (2015) 314-323.

[77] S. Bauer, C. Serre, T. Devic, P. Horcajada, J.r.m. Marrot, g.r. Férey, N. Stock, High-throughput assisted rationalization of the formation of Metal Organic Frameworks in the iron(III) aminoterephthalate solvothermal system, Inorganic Chemistry, 47 (2008) 7568-7576.

[78] T. Wittmann, R. Siegel, N. Reimer, W. Milius, N. Stock, J. Senker, Enhancing the water stability of Al-MIL-101-NH$_2$ via postsynthetic modification, Chemistry – A European Journal, 21 (2015) 314-323.

[79] I. Bezverkhyy, G. Ortiz, G. Chaplais, C. Marichal, G. Weber, J.-P. Bellat, MIL-53(Al) under reflux in water: Formation of γ-AlO(OH) shell and H$_2$BDC molecules intercalated into the pores, Microporous and Mesoporous Materials, 183 (2014) 156-161.

[80] X. Qian, B. Yadian, R. Wu, Y. Long, K. Zhou, B. Zhu, Y. Huang, Structure stability of Metal-Organic Framework MIL-53(Al) in aqueous solutions, International Journal of Hydrogen Energy, 38 (2013) 16710-16715.

[81] S.J. Yang, C.R. Park, Preparation of highly moisture-resistant black-colored Metal Organic Frameworks, Advanced Materials, 24 (2012) 4010-4013.

[82] S. Gadipelli, Z. Guo, Postsynthesis annealing of MOF-5 remarkably enhances the framework structural stability and CO$_2$ uptake, Chemistry of Materials, (2014).

[83] C.-M. Wu, M. Rathi, S.P. Ahrenkiel, R.T. Koodali, Z. Wang, Facile synthesis of MOF-5 confined in SBA-15 hybrid material with enhanced hydrostability, Chemical Communications, 49 (2013) 1223-1225.

[84] S.J. Yang, J.Y. Choi, H.K. Chae, J.H. Cho, K.S. Nahm, C.R. Park, Preparation and enhanced hydrostability and hydrogen storage capacity of cnt@MOF-5 hybrid composite, Chemistry of Materials, 21 (2009) 1893-1897.

[85] T. Li, J.E. Sullivan, N.L. Rosi, Design and preparation of a core–shell Metal–Organic Framework for selective CO$_2$ capture, Journal of the American Chemical Society, 135 (2013) 9984-9987.

[86] T. Li, D.-L. Chen, J.E. Sullivan, M.T. Kozlowski, J.K. Johnson, N.L. Rosi, Systematic modulation and enhancement of CO$_2$:N$_2$ selectivity and water stability in an isoreticular series of BIO-MOF-11 analogues, Chemical Science, 4 (2013) 1746-1755.

[87] X. Liu, Y. Li, Y. Ban, Y. Peng, H. Jin, H. Bux, L. Xu, J. Caro, W. Yang, Improvement of hydrothermal stability of ZeoliticImidazolate Frameworks, Chemical Communications, 49 (2013) 9140-9142.

[88] B. Zornoza, C. Tellez, J. Coronas, J. Gascon, F. Kapteijn, Metal Organic Framework based mixed matrix membranes: An increasingly important field of research with a large application potential, Microporous and Mesoporous Materials, 166 (2013) 67-78.

[89] B. Zornoza, A. Martinez-Joaristi, P. Serra-Crespo, C. Tellez, J. Coronas, J. Gascon, F. Kapteijn, Functionalized flexible MOFs as fillers in mixed matrix membranes for highly selective separation of CO$_2$ from CH$_4$ at elevated pressures, Chemical Communications, 47 (2011) 9522-9524.

[90] O.G. Nik, X.Y. Chen, S. Kaliaguine, Functionalized Metal Organic Framework-polyimide mixed matrix membranes for CO$_2$/CH$_4$ separation, Journal of Membrane Science, 413 (2012) 48-61.

[91] H.B.T. Jeazet, C. Staudt, C. Janiak, Metal–Organic Frameworks in mixed-matrix membranes for gas separation, Dalton Transactions, 41 (2012) 14003-14027.

[92] E.V. Perez, K.J. Balkus Jr, J.P. Ferraris, I.H. Musselman, Mixed-matrix membranes containing MOF-5 for gas separations, Journal of Membrane Science, 328 (2009) 165-173.

[93] T. Rodenas, I. Luz, G. Prieto, B. Seoane, H. Miro, A. Corma, F. Kapteijn, F.X.L. i Xamena, J. Gascon, Metal–Organic Framework nanosheets in polymer composite materials for gas separation, Nature materials, (2014).

[94] T. Rodenas, M. van Dalen, E. García-Pérez, P. Serra-Crespo, B. Zornoza, F. Kapteijn, J. Gascon, Visualizing MOF mixed matrix membranes at the nanoscale: Towards structure-performance

relationships in CO_2/CH_4 separation over NH_2-MIL-53(Al)@ PI, Advanced Functional Materials, 24 (2014) 249-256.

[95] Y. Yoo, V. Varela-Guerrero, H.-K. Jeong, Isoreticular Metal−Organic Frameworks and their membranes with enhanced crack resistance and moisture stability by surfactant-assisted drying, Langmuir, 27 (2011) 2652-2657.

[96] K.P. Rao, M. Higuchi, K. Sumida, S. Furukawa, J. Duan, S. Kitagawa, Design of superhydrophobic porous coordination polymers through the introduction of external surface corrugation by the use of an aromatic hydrocarbon building unit, Angewandte Chemie, 126 (2014) 8364-8369.

[97] J.B. Decoste, G.W. Peterson, M.W. Smith, C.A. Stone, C.R. Willis, Enhanced stability of Cu-BTC MOF via perfluorohexane plasma-enhanced chemical vapor deposition, Journal of the American Chemical Society, 134 (2012) 1486-1489.

[98] H. Jasuja, K.S. Walton, Effect of catenation and basicity of pillared ligands on the water stability of MOFs, Dalton Transactions, 42 (2013) 15421-15426.

[99] J.M. Taylor, R. Vaidhyanathan, S.S. Iremonger, G.K.H. Shimizu, Enhancing water stability of Metal–Organic Frameworks via phosphonate monoester linkers, Journal of the American Chemical Society, 134 (2012) 14338-14340.

[100] J.M. Taylor, K.W. Dawson, G.K.H. Shimizu, A water-stable Metal-Organic Framework with highly acidic pores for proton-conducting applications, Journal of the American Chemical Society, 135 (2013) 1193-1196.

[101] T. Wu, L. Shen, M. Luebbers, C. Hu, Q. Chen, Z. Ni, R.I. Masel, Enhancing the stability of Metal-Organic Frameworks in humid air by incorporating water repellent functional groups, Chemical Communications, 46 (2010) 6120-6122.

[102] C. Yang, U. Kaipa, Q.Z. Mather, X. Wang, V. Nesterov, A.F. Venero, M.A. Omary, Fluorous Metal-Organic Frameworks with superior adsorption and hydrophobic properties toward oil spill cleanup and hydrocarbon storage, Journal of the American Chemical Society, 133 (2011) 18094-18097.

[103] H. Jasuja, Y.-g. Huang, K.S. Walton, Adjusting the stability of Metal-Organic Frameworks under humid conditions by ligand functionalization, Langmuir, 28 (2012) 16874-16880.

[104] T.-H. Chen, I. Popov, O. Zenasni, O. Daugulis, O.Š. Miljanić, Superhydrophobic perfluorinated Metal-Organic Frameworks, Chemical Communications, 49 (2013) 6846-6848.

[105] C. Serre, Superhydrophobicity in highly fluorinated porous Metal-Organic Frameworks, Angewandte Chemie International Edition, 51 (2012) 6048-6050.

[106] J. Yang, A. Grzech, F.M. Mulder, T.J. Dingemans, Methyl modified MOF-5: A water stable hydrogen storage material, Chemical Communications, 47 (2011) 5244-5246.

[107] Y. Cai, Y. Zhang, Y. Huang, S.R. Marder, K.S. Walton, Impact of alkyl-functionalized BTC on properties of copper-based Metal-Organic Frameworks, Crystal Growth & Design, 12 (2012) 3709-3713.

[108] H. Jasuja, Y. Jiao, N.C. Burtch, Y.-g. Huang, K.S. Walton, Synthesis of cobalt, nickel, copper, and zinc-based water stable pillared Metal-Organic Frameworks, Langmuir, 30 (2014) 14300-14307.

[109] T.A. Makal, X. Wang, H.-C. Zhou, Tuning the moisture and thermal stability of Metal–Organic Frameworks through incorporation of pendant hydrophobic groups, Crystal Growth & Design, 13 (2013) 4760-4768.

[110] Z. Zhang, Y. Zhao, Q. Gong, Z. Li, J. Li, MOFs for CO_2 capture and separation from flue gas mixtures: The effect of multifunctional sites on their adsorption capacity and selectivity, Chemical Communications, 49 (2013) 653-661.

[111] D. Ma, Y. Li, Z. Li, Tuning the moisture stability of Metal-Organic Frameworks by incorporating hydrophobic functional groups at different positions of ligands, Chemical Communications, 47 (2011) 7377-7379.

[112] J.-W. Zhang, C.-C. Zhao, Y.-P. Zhao, H.-Q. Xu, Z.-Y. Du, H.-L. Jiang, Metal-Organic Frameworks with improved moisture stability based on a phosphonate monoester: Effect of auxiliary n-donor ligands on framework dimensionality, CrystEngComm, 16 (2014) 6635-6644.

[113] J.H. Im, N. Ko, S.J. Yang, H.J. Park, J. Kim, C.R. Park, Enhanced water stability and CO_2 gas sorption properties of a methyl functionalized titanium Metal-Organic Framework, New Journal of Chemistry, 38 (2014) 2752-2755.

[114] J.-H. Wang, M. Li, D. Li, An exceptionally stable and water-resistant Metal-Organic Framework with hydrophobic nanospaces for extracting aromatic pollutants from water, Chemistry – A European Journal, 20 (2014) 12004-12008.

[115] D.-Y. Ma, X. Li, X.-G. Wu, X.-Q. Chen, Z.-R. Xu, F.-D. Liu, D.-F. Huang, H.-F. Guo, Improving the moisture stability of a 3D zinc-organic framework by incorporating methyl groups into the auxiliary ligand: Synthesis, characterization, luminescence and catalytic properties, Journal of Molecular Structure.

[116] Y. Lin, Q. Zhang, C. Zhao, H. Li, C. Kong, C. Shen, L. Chen, An exceptionally stable functionalized Metal-Organic Framework for lithium storage, Chemical Communications, (2014).

[117] C. Racles, S. Shova, M. Cazacu, D. Timpu, New highly ordered hydrophobic siloxane-based coordination polymers, Polymer, 54 (2013) 6096-6104.

[118] L.-H. Xie, M.P. Suh, Flexible Metal-Organic Framework with hydrophobic pores, Chemistry – A European Journal, 17 (2011) 13653-13656.

[119] M.H. Weston, A.A. Delaquil, A.A. Sarjeant, O.K. Farha, J.T. Hupp, S.T. Nguyen, Tuning the hydrophobicity of zinc dipyridyl paddlewheel Metal-Organic Frameworks for selective sorption, Crystal Growth & Design, 13 (2013) 2938-2942.

[120] Z. Lu, H. Xing, R. Sun, J. Bai, B. Zheng, Y. Li, Water stable Metal–Organic Framework evolutionally formed from a flexible multidentate ligand with acylamide groups for selective CO_2 adsorption, Crystal Growth & Design, 12 (2012) 1081-1084.

[121] D. Farrusseng, J. Canivet, A. Quadrelli, Design of functional Metal–Organic Frameworks by post-synthetic modification, in: D. Farrusseng (Ed.) Metal-organic frameworks: Applications from catalysis to gas storage, Wiley-VCH Verlag GmbH & Co. KGaA2011, pp. 23-48.

[122] K.K. Tanabe, S.M. Cohen, Postsynthetic modification of Metal-Organic Frameworks - a progress report, Chemical Society Reviews, 40 (2011) 498-519.

[123] S.M. Cohen, Postsynthetic methods for the functionalization of Metal–Organic Frameworks, Chemical Reviews, 112 (2011) 970-1000.

[124] Z. Wang, S.M. Cohen, Postsynthetic modification of Metal-Organic Frameworks, Chemical Society Reviews, 38 (2009) 1315-1329.

[125] M.G. Goesten, F. Kapteijn, J. Gascon, Fascinating chemistry or frustrating unpredictability: Observations in crystal engineering of Metal-Organic Frameworks, CrystEngComm, 15 (2013) 9249-9257.

[126] J.G. Nguyen, S.M. Cohen, Moisture-resistant and superhydrophobic Metal-Organic Frameworks obtained via postsynthetic modification, Journal of the American Chemical Society, 132 (2010) 4560-4561.

[127] J. Aguilera-Sigalat, D. Bradshaw, A colloidal water-stable MOF as a broad-range fluorescent pH sensor via post-synthetic modification, Chemical Communications, 50 (2014) 4711-4713.

[128] S. Aguado, J. Canivet, Y. Schuurman, D. Farrusseng, Tuning the activity by controlling the wettability of MOF eggshell catalysts: A quantitative structure–activity study, Journal of Catalysis, 284 (2011) 207-214.

[129] J. Canivet, S. Aguado, C. Daniel, D. Farrusseng, Engineering the environment of a catalytic Metal-Organic Framework by postsynthetic hydrophobization, ChemCatChem, 3 (2011) 675-678.

[130] J. Gascon, U. Aktay, M.D. Hernandez-Alonso, G.P.M. van Klink, F. Kapteijn, Amino-based Metal-Organic Frameworks as stable, highly active basic catalysts, Journal of Catalysis, 261 (2009) 75-87.

[131] S. Rostamnia, H. Xin, Basic isoreticular Metal-Organic Framework (IRMOF-3) porous nanomaterial as a suitable and green catalyst for selective unsymmetrical Hantzsch coupling reaction, Applied Organometallic Chemistry, 28 (2014) 359-363.

[132] D. Kim, T.B. Lee, S.B. Choi, J.H. Yoon, J. Kim, S.-H. Choi, A density functional theory study of a series of functionalized Metal-Organic Frameworks, Chemical Physics Letters, 420 (2006) 256-260.

[133] L. Bellarosa, J.J. Gutierrez-Sevillano, S. Calero, N. Lopez, How ligands improve the hydrothermal stability and affect the adsorption in the IRMOF family, Physical Chemistry Chemical Physics, 15 (2013) 17696-17704.

[134] L. Bellarosa, S. Calero, N. Lopez, Early stages in the degradation of Metal-Organic Frameworks in liquid water from first-principles molecular dynamics, Physical Chemistry Chemical Physics, 14 (2012) 7240-7245.

[135] S. Hausdorf, F. Baitalow, T. Böhle, D. Rafaja, F.O.R.L. Mertens, Main-group and transition-element IRMOF homologues, Journal of the American Chemical Society, 132 (2010) 10978-10981.

[136] Y. Han, J.-R. Li, Y. Xie, G. Guo, Substitution reactions in Metal-Organic Frameworks and metal-organic polyhedra, Chemical Society Reviews, 43 (2014) 5952-5981.

[137] H. Li, W. Shi, K. Zhao, H. Li, Y. Bing, P. Cheng, Enhanced hydrostability in Ni-doped MOF-5, Inorganic Chemistry, 51 (2012) 9200-9207.

[138] J.-M. Yang, Q. Liu, W.-Y. Sun, Shape and size control and gas adsorption of Ni(II)-doped MOF-5 nano/microcrystals, Microporous and Mesoporous Materials, 190 (2014) 26-31.

[139] T. Devic, C. Serre, High valence 3p and transition metal based MOFs, Chemical Society Reviews, 43 (2014) 6097-6115.

[140] M. Bosch, M. Zhang, H.-C. Zhou, Increasing the stability of Metal-Organic Frameworks, Advances in Chemistry, 2014 (2014).

[141] F. Jeremias, D. Fröhlich, C. Janiak, S.K. Henninger, Water and methanol adsorption on MOFs for cycling heat transformation processes, New Journal of Chemistry, 38 (2014) 1846-1852.

[142] C.H. Berke, A. Kiss, P. Kleinschmit, J. Weitkamp, Der hydrophobizitäts-index: Eine neue methode zur charakterisierung der oberflächeneigenschaften zeolithischer adsorbentien, Chemie Ingenieur Technik, 63 (1991) 623-625.

[143] J. Stelzer, M. Paulus, M. Hunger, J. Weitkamp, Hydrophobic properties of all-silica zeolite Beta, Microporous and Mesoporous Materials, 22 (1998) 1-8.

[144] A.W. Heinen, J.A. Peters, H.v. Bekkum, Competitive adsorption of water and toluene on modified activated carbon supports, Applied Catalysis A: General, 194–195 (2000) 193-202.

[145] N. Ketcome, N. Grisdanurak, S. Chiarakorn, Silylated rice husk MCM-41 and its binary adsorption of water-toluene mixture, Journal of Porous Materials, 16 (2009) 41-46.

[146] A.H. Yonli, I. Gener, S. Mignard, Comparative study of the hydrophobicity of BEA, HZSM-5 and HY zeolites determined by competitive adsorption, Microporous and Mesoporous Materials, 132 (2010) 37-42.

[147] L. Vanoye, A. Favre-Réguillon, P. Munno, J.F. Rodríguez, S. Dupuy, S. Pallier, I. Pitault, C. De Bellefon, Methanol dehydration over commercially available zeolites: Effect of hydrophobicity, Catalysis Today, 215 (2013) 239-242.

[148] G. Férey, C. Mellot-Draznieks, C. Serre, F. Millange, J. Dutour, S. Surblé, I. Margiolaki, A chromium terephthalate-based solid with unusually large pore volumes and surface area, Science, 309 (2005) 2040-2042.

[149] G. Akiyama, R. Matsuda, H. Sato, A. Hori, M. Takata, S. Kitagawa, Effect of functional groups in MIL-101 on water sorption behavior, Microporous and Mesoporous Materials, 157 (2012) 89-93.

[150] A. Khutia, H.U. Rammelberg, T. Schmidt, S. Henninger, C. Janiak, Water sorption cycle measurements on functionalized MIL-101Cr for heat transformation application, Chemistry of Materials, 25 (2013) 790-798.

[151] G. Férey, C. Serre, C. Mellot-Draznieks, F. Millange, S. Surblé, J. Dutour, I. Margiolaki, A hybrid solid with giant pores prepared by a combination of targeted chemistry, simulation, and powder diffraction, Angewandte Chemie International Edition, 43 (2004) 6296-6301.

[152] G. Akiyama, R. Matsuda, S. Kitagawa, Highly porous and stable coordination polymers as water sorption materials, Chemistry Letters, 39 (2010) 360-361.

[153] M. Wickenheisser, F. Jeremias, S.K. Henninger, C. Janiak, Grafting of hydrophilic ethylene glycols or ethylenediamine on coordinatively unsaturated metal sites in MIL-100(Cr) for improved water adsorption characteristics, Inorganica Chimica Acta, 407 (2013) 145-152.

[154] F. Jeremias, A. Khutia, S.K. Henninger, C. Janiak, MIL-100(Al, Fe) as water adsorbents for heat transformation purposes - a promising application, Journal of Materials Chemistry, 22 (2012) 10148-10151.

[155] M. Dan-Hardi, C. Serre, T. Frot, L. Rozes, G. Maurin, C. Sanchez, G. Férey, A new photoactive crystalline highly porous titanium(IV) dicarboxylate, Journal of the American Chemical Society, 131 (2009) 10857-10859.

[156] S.-N. Kim, J. Kim, H.-Y. Kim, H.-Y. Cho, W.-S. Ahn, Adsorption/catalytic properties of MIL-125 and NH_2-MIL-125, Catalysis Today, 204 (2013) 85-93.

[157] F. Jeremias, V. Lozan, S.K. Henninger, C. Janiak, Programming mofs for water sorption: Amino-functionalized MIL-125 and UiO-66 for heat transformation and heat storage applications, Dalton Transactions, 42 (2013) 15967-15973.

[158] P. Küsgens, M. Rose, I. Senkovska, H. Fröde, A. Henschel, S. Siegle, S. Kaskel, Characterization of Metal-Organic Frameworks by water adsorption, Microporous and Mesoporous Materials, 120 (2009) 325-330.

[159] C. Janiak, S.K. Henninger, Porous coordination polymers as novel sorption materials for heat transformation processes, Chimia, 67 (2013) 419-424.

[160] T. Ahnfeldt, D. Gunzelmann, J. Wack, J. Senker, N. Stock, Controlled modification of the inorganic and organic bricks in an Al-based MOFS by direct and post-synthetic synthesis routes, CrystEngComm, 14 (2012) 4126-4136.

[161] M.J. Katz, Z.J. Brown, Y.J. Colón, P.W. Siu, K.A. Scheidt, R.Q. Snurr, J.T. Hupp, O.K. Farha, A facile synthesis of UiO-66, Uio-67 and their derivatives, Chemical Communications, 49 (2013) 9449-9451.

[162] G.C. Shearer, S. Chavan, J. Ethiraj, J.G. Vitillo, S. Svelle, U. Olsbye, C. Lamberti, S. Bordiga, K.P. Lillerud, Tuned to perfection: Ironing out the defects in Metal-OrganicFramework UiO-66, Chemistry of Materials, 26 (2014) 4068-4071.

[163] S. Øien, D.S. Wragg, H. Reinsch, S. Svelle, S. Bordiga, C. Lamberti, K.P. Lillerud, Detailed structure analysis of atomic positions and defects in zirconium Metal-Organic Frameworks, Crystal Growth & Design, (2014).

[164]   L. Valenzano, B. Civalleri, S. Chavan, S. Bordiga, M.H. Nilsen, S. Jakobsen, K.P. Lillerud, C. Lamberti, Disclosing the complex structure of UiO-66 Metal Organic Framework: A synergic combination of experiment and theory, Chemistry of Materials, 23 (2011) 1700-1718.

[165]   J.E. Mondloch, M.J. Katz, N. Planas, D. Semrouni, L. Gagliardi, J.T. Hupp, O.K. Farha, Are Zr_6-based MOFs water stable? Linker hydrolysis vs. Capillary-force-driven channel collapse, Chemical Communications, 50 (2014) 8944-8946.

[166]   H. Furukawa, F. Gándara, Y.-B. Zhang, J. Jiang, W.L. Queen, M.R. Hudson, O.M. Yaghi, Water adsorption in porous Metal-Organic Frameworks and related materials, Journal of the American Chemical Society, 136 (2014) 4369-4381.

[167]   V. Bon, V. Senkovskyy, I. Senkovska, S. Kaskel, Zr(IV) and Hf(IV) based Metal-Organic Frameworks with reo-topology, Chemical Communications, 48 (2012) 8407-8409.

[168]   V. Bon, I. Senkovska, I.A. Baburin, S. Kaskel, Zr-and Hf-based Metal-Organic Frameworks: Tracking down the polymorphism, Crystal Growth & Design, 13 (2013) 1231-1237.

[169]   P. Deria, J.E. Mondloch, E. Tylianakis, P. Ghosh, W. Bury, R.Q. Snurr, J.T. Hupp, O.K. Farha, Perfluoroalkane functionalization of NU-1000 via solvent-assisted ligand incorporation: Synthesis and CO_2 adsorption studies, Journal of the American Chemical Society, 135 (2013) 16801-16804.

[170]   C. Serre, F. Millange, C. Thouvenot, M. Noguès, G. Marsolier, D. Louër, G. Férey, Very large breathing effect in the first nanoporous chromium(III)-based solids: MIL-53 or $CrIII(OH) \cdot \{O_2C-C_6H_4-CO_2\} \cdot \{HO_2C-C_6H_4-CO_2H\}_x \cdot H_2O_y$, Journal of the American Chemical Society, 124 (2002) 13519-13526.

[171]   G. Férey, M. Latroche, C. Serre, F. Millange, T. Loiseau, A. Percheron-Guégan, Hydrogen adsorption in the nanoporous metal-benzenedicarboxylate $M(OH)(O_2C-C_6H_4-CO_2)$ ($M = Al^{3+}$, Cr^{3+}), MIL-53, Chemical Communications, 9 (2003) 2976-2977.

[172]   T. Loiseau, C. Serre, C. Huguenard, G. Fink, F. Taulelle, M. Henry, T. Bataille, G. Férey, A rationale for the large breathing of the porous aluminum terephthalate (MIL-53) upon hydration, Chemistry - A European Journal, 10 (2004) 1373-1382.

[173]   S. Bourrelly, B.A. Moulin, A. Rivera, G. Maurin, S. Devautour-Vinot, C. Serre, T. Devic, P. Horcajada, A. Vimont, G. Clet, M. Daturi, J.-C. Lavalley, S. Loera-Serna, R. Denoyel, P.L. Llewellyn, G.R. Férey, Explanation of the adsorption of polar vapors in the highly flexible Metal Organic Framework MIL-53(Cr), Journal of the American Chemical Society, 132 (2010) 9488-9498.

[174]   K. Barthelet, J. Marrot, D. Riou, G. Férey, A breathing hybrid organic–inorganic solid with very large pores and high magnetic characteristics, Angewandte Chemie, 114 (2002) 291-294.

[175]   S. Biswas, T. Rémy, S. Couck, D. Denysenko, G. Rampelberg, J.F. Denayer, D. Volkmer, C. Detavernier, P. Van Der Voort, Partially fluorinated MIL-47 and Al-MIL-53 frameworks: Influence of functionalization on sorption and breathing properties, Physical Chemistry Chemical Physics, 15 (2013) 3552-3561.

[176]   H. Reinsch, M.A. van der Veen, B. Gil, B. Marszalek, T. Verbiest, D. de Vos, N. Stock, Structures, sorption characteristics, and nonlinear optical properties of a new series of highly stable aluminum MOFs, Chemistry of Materials, 25 (2012) 17-26.

[177]   M. De Lange, C. Ottevanger, M. Wiegman, T. Vlugt, J. Gascon, F. Kapteijn, Crystals for sustainability–structuring Al-based MOFs for the allocation of heat and cold, CrystEngComm, 17 (2015) 281-285.

[178]   D. Fröhlich, S.K. Henninger, C. Janiak, Multicycle water vapour stability of microporous breathing MOF aluminium isophthalate CAU-10-H, Dalton Transactions, (2014).

[179]   F. Niekiel, J. Lannoeye, H. Reinsch, A.S. Munn, A. Heerwig, I. Zizak, S. Kaskel, R.I. Walton, D. de Vos, P. Llewellyn, A. Lieb, G. Maurin, N. Stock, Conformation-controlled sorption properties and breathing of the aliphatic Al-MOF [Al(OH)(CDC)], Inorganic Chemistry, 53 (2014) 4610-4620.

[180]   F. Jeremias, D. Frohlich, C. Janiak, S.K. Henninger, Advancement of sorption-based heat transformation by a metal coating of highly-stable, hydrophilic aluminium fumarate MOF, RSC Advances, 4 (2014) 24073-24082.

[181]   F. Jeremias, S.K. Henninger, C. Janiak, High performance Metal-Organic Framework coatings obtained via thermal gradient synthesis, Chemical Communications, 48 (2012) 9708-9710.

[182]   P.D.C. Dietzel, R.E. Johnsen, R. Blom, H. Fjellvåg, Structural changes and coordinatively unsaturated metal atoms on dehydration of honeycomb analogous microporous Metal-Organic Frameworks, Chemistry – A European Journal, 14 (2008) 2389-2397.

[183]   J. Liu, Y. Wang, A.I. Benin, P. Jakubczak, R.R. Willis, M.D. LeVan, CO_2/H_2O adsorption equilibrium and rates on Metal−Organic Frameworks: HKUST-1 and Ni/DOBDC, Langmuir, 26 (2010) 14301-14307.

[184]   P.M. Schoenecker, C.G. Carson, H. Jasuja, C.J.J. Flemming, K.S. Walton, Effect of water adsorption on retention of structure and surface area of Metal–Organic Frameworks, Industrial & Engineering Chemistry Research, 51 (2012) 6513-6519.

[185] C. Chmelik, A. Mundstock, P.D.C. Dietzel, J. Caro, Idiosyncrasies of CO_2(DHTP): In situ-annealing by methanol, Microporous and Mesoporous Materials, 183 (2014) 117-123.

[186] P.D.C. Dietzel, B. Panella, M. Hirscher, R. Blom, H. Fjellvag, Hydrogen adsorption in a nickel based coordination polymer with open metal sites in the cylindrical cavities of the desolvated framework, Chemical Communications, (2006) 959-961.

[187] K.S. Park, Z. Ni, A.P. Côté, J.Y. Choi, R. Huang, F.J. Uribe-Romo, H.K. Chae, M. O'Keeffe, O.M. Yaghi, Exceptional chemical and thermal stability of Zeolitic Imidazolate Frameworks, Proceedings of the National Academy of Sciences, 103 (2006) 10186-10191.

[188] J.-P. Zhang, A.-X. Zhu, R.-B. Lin, X.-L. Qi, X.-M. Chen, Pore surface tailored sod-type Metal-Organic Zeolites, Advanced Materials, 23 (2011) 1268-1271.

[189] J.-B. Lin, R.-B. Lin, X.-N. Cheng, J.-P. Zhang, X.-M. Chen, Solvent/additive-free synthesis of porous/zeolitic Metal Azolate Frameworks from metal oxide/hydroxide, Chemical Communications, 47 (2011) 9185-9187.

[190] A.-X. Zhu, R.-B. Lin, X.-L. Qi, Y. Liu, Y.-Y. Lin, J.-P. Zhang, X.-M. Chen, Zeolitic Metal Azolate Frameworks (MAFs) from $ZnO/Zn(OH)_2$ and monoalkyl-substituted imidazoles and 1,2,4-triazoles: Efficient syntheses and properties, Microporous and Mesoporous Materials, 157 (2012) 42-49.

[191] J.R. Karra, H. Jasuja, Y.-G. Huang, K. Walton, Structural stability of BTTB-based Metal-Organic Frameworks under humid conditions, Journal of Materials Chemistry A, (2014).

[192] Z. Wang, K.K. Tanabe, S.M. Cohen, Accessing postsynthetic modification in a series of Metal-Organic Frameworks and the influence of framework topology on reactivity, Inorganic Chemistry, 48 (2009) 296-306.

[193] E. Quartapelle Procopio, T. Fukushima, E. Barea, J.A.R. Navarro, S. Horike, S. Kitagawa, A soft copper(II) porous coordination polymer with unprecedented aqua bridge and selective adsorption properties, Chemistry – A European Journal, 18 (2012) 13117-13125.

[194] T. Birsa Čelič, M. Mazaj, N. Guillou, E. Elkaïm, M. El Roz, F. Thibault-Starzyk, G. Mali, M. Rangus, T. Čendak, V. Kaučič, N. Zabukovec Logar, Study of hydrothermal stability and water sorption characteristics of 3-dimensional Zn-based trimesate, The Journal of Physical Chemistry C, 117 (2013) 14608-14617.

[195] S. Biswas, M. Grzywa, H.P. Nayek, S. Dehnen, I. Senkovska, S. Kaskel, D. Volkmer, A cubic coordination framework constructed from benzobistriazolate ligands and zinc ions having selective gas sorption properties, Dalton Transactions, (2009) 6487-6495.

[196] C. Montoro, F. Linares, E. Quartapelle Procopio, I. Senkovska, S. Kaskel, S. Galli, N. Masciocchi, E. Barea, J.A.R. Navarro, Capture of nerve agents and mustard gas analogues by hydrophobic robust MOF-5 type Metal–Organic Frameworks, Journal of the American Chemical Society, 133 (2011) 11888-11891.

[197] C.R. Wade, T. Corrales-Sanchez, T.C. Narayan, M. Dincă, Postsynthetic tuning of hydrophilicity in pyrazolate MOFs to modulate water adsorption properties, Energy & Environmental Science, 6 (2013) 2172-2177.

[198] A. Santra, I. Senkovska, S. Kaskel, P.K. Bharadwaj, Gas storage in a partially fluorinated highly stable three-dimensional porous Metal–Organic Framework, Inorganic Chemistry, 52 (2013) 7358-7366.

[199] T. Kundu, S.C. Sahoo, R. Banerjee, Relating pore hydrophilicity with vapour adsorption capacity in a series of amino acid based Metal Organic Frameworks, CrystEngComm, 15 (2013) 9634-9640.

[200] T. Kundu, S.C. Sahoo, S. Saha, R. Banerjee, Salt metathesis in three dimensional Metal-Organic Frameworks (MOFs) with unprecedented hydrolytic regenerability, Chemical Communications, 49 (2013) 5262-5264.

[201] S.K. Henninger, H.A. Habib, C. Janiak, MOFs as adsorbents for low temperature heating and cooling applications, Journal of the American Chemical Society, 131 (2009) 2776-2777.

[202] N.M. Padial, E. Quartapelle Procopio, C. Montoro, E. López, J.E. Oltra, V. Colombo, A. Maspero, N. Masciocchi, S. Galli, I. Senkovska, S. Kaskel, E. Barea, J.A.R. Navarro, Highly hydrophobic isoreticular porous Metal–Organic Frameworks for the capture of harmful volatile organic compounds, Angewandte Chemie International Edition, 52 (2013) 8290-8294.

[203] Y.-K. Seo, J.W. Yoon, J.S. Lee, Y.K. Hwang, C.-H. Jun, J.-S. Chang, S. Wuttke, P. Bazin, A. Vimont, M. Daturi, S. Bourrelly, P.L. Llewellyn, P. Horcajada, C. Serre, G. Férey, Porous materials: Energy-efficient dehumidification over hierachically porous Metal–Organic Frameworks as advanced water adsorbents, Advanced Materials, 24 (2012) 710-710.

[204] J. Ehrenmann, S.K. Henninger, C. Janiak, Water adsorption characteristics of MIL-101 for heat-transformation applications of MOFs, European Journal of Inorganic Chemistry, 2011 (2011) 471-474.

[205] D.-Y. Hong, Y.K. Hwang, C. Serre, G. Férey, J.-S. Chang, Porous chromium terephthalate MIL-101 with coordinatively unsaturated sites: Surface functionalization, encapsulation, sorption and catalysis, Advanced Functional Materials, 19 (2009) 1537-1552.

[206] Y. Hu, C. Song, J. Liao, Z. Huang, G. Li, Water stable Metal-Organic Framework packed microcolumn for online sorptive extraction and direct analysis of naproxen and its metabolite from urine sample, Journal of Chromatography A, 1294 (2013) 17-24.

[207] G. Akiyama, R. Matsuda, H. Sato, M. Takata, S. Kitagawa, Cellulose hydrolysis by a new porous coordination polymer decorated with sulfonic acid functional groups, Advanced Materials, 23 (2011) 3294-3297.

[208] Y.I. Aristov, Challenging offers of material science for adsorption heat transformation: A review, Applied Thermal Engineering, 50 (2013) 1610-1618.

[209] G.D. Pirngruber, L. Hamon, S. Bourrelly, P.L. Llewellyn, E. Lenoir, V. Guillerm, C. Serre, T. Devic, A method for screening the potential of MOFs as CO_2 adsorbents in pressure swing adsorption processes, ChemSusChem, 5 (2012) 762-776.

[210] E. Soubeyrand-Lenoir, C. Vagner, J.W. Yoon, P. Bazin, F. Ragon, Y.K. Hwang, C. Serre, J.-S. Chang, P.L. Llewellyn, How water fosters a remarkable 5-fold increase in low-pressure CO_2 uptake within mesoporous MIL-100(Fe), Journal of the American Chemical Society, 134 (2012) 10174-10181.

[211] D. Cunha, M. Ben Yahia, S. Hall, S.R. Miller, H. Chevreau, E. Elkaïm, G. Maurin, P. Horcajada, C. Serre, Rationale of drug encapsulation and release from biocompatible porous Metal–Organic Frameworks, Chemistry of Materials, 25 (2013) 2767-2776.

[212] S. Vaesen, V. Guillerm, Q. Yang, A.D. Wiersum, B. Marszalek, B. Gil, A. Vimont, M. Daturi, T. Devic, P.L. Llewellyn, A robust amino-functionalized titanium (IV) based MOF for improved separation of acid gases, Chemical Communications, 49 (2013) 10082-10084.

[213] V. Guillerm, F. Ragon, M. Dan‑Hardi, T. Devic, M. Vishnuvarthan, B. Campo, A. Vimont, G. Clet, Q. Yang, G. Maurin, A series of isoreticular, highly stable, porous zirconium oxide based Metal-Organic Frameworks, Angewandte Chemie International Edition, 51 (2012) 9267-9271.

[214] Q. Yang, V. Guillerm, F. Ragon, A.D. Wiersum, P.L. Llewellyn, C. Zhong, T. Devic, C. Serre, G. Maurin, CH_4 storage and CO_2 capture in highly porous zirconium oxide based Metal–Organic Frameworks, Chemical Communications, 48 (2012) 9831-9833.

[215] G.E. Cmarik, M. Kim, S.M. Cohen, K.S. Walton, Tuning the adsorption properties of UiO-66 via ligand functionalization, Langmuir, 28 (2012) 15606-15613.

[216] M. Kandiah, M.H. Nilsen, S. Usseglio, S. Jakobsen, U. Olsbye, M. Tilset, C. Larabi, E.A. Quadrelli, F. Bonino, K.P. Lillerud, Synthesis and stability of tagged UiO-66 Zr-mofs, Chemistry of Materials, 22 (2010) 6632-6640.

[217] H. Jasuja, J. Zang, D.S. Sholl, K.S. Walton, Rational tuning of water vapor and CO_2 adsorption in highly stable Zr-based mofs, Journal of Physical Chemistry C, 116 (2012) 23526-23532.

[218] H. Jasuja, K.S. Walton, Experimental study of CO_2, CH_4, and water vapor adsorption on a dimethyl-functionalized UiO-66 framework, The Journal of Physical Chemistry C, 117 (2013) 7062-7068.

[219] Q. Yang, S. Vaesen, F. Ragon, A.D. Wiersum, D. Wu, A. Lago, T. Devic, C. Martineau, F. Taulelle, P.L. Llewellyn, H. Jobic, C. Zhong, C. Serre, G. De Weireld, G. Maurin, A water stable Metal-Organic Framework with optimal features for CO_2 capture, Angewandte Chemie International Edition, 52 (2013) 10316-10320.

[220] A. Shigematsu, T. Yamada, H. Kitagawa, Wide control of proton conductivity in porous coordination polymers, Journal of the American Chemical Society, 133 (2011) 2034-2036.

[221] T. Yamada, Y. Shirai, H. Kitagawa, Synthesis, water adsorption, and proton conductivity of solid-solution-type Metal–Organic Frameworks $Al(OH)(BDC-OH)_x(BDC-NH_2)_{1-x}$, Chemistry – An Asian Journal, 9 (2014) 1316-1320.

[222] S. Biswas, T. Ahnfeldt, N. Stock, New functionalized flexible Al-MIL-53-x (x = -Cl, -Br, -CH$_3$, -NO$_2$, -(OH)$_2$) solids: Syntheses, characterization, sorption, and breathing behavior, Inorganic Chemistry, 50 (2011) 9518-9526.

[223] S. Biswas, S. Couck, D. Denysenko, A. Bhunia, M. Grzywa, J.F.M. Denayer, D. Volkmer, C. Janiak, P. Van Der Voort, Sorption and breathing properties of difluorinated MIL-47 and Al-MIL-53 frameworks, Microporous and Mesoporous Materials, 181 (2013) 175-181.

[224] J. Liu, F. Zhang, X. Zou, G. Yu, N. Zhao, S. Fan, G. Zhu, Environmentally friendly synthesis of highly hydrophobic and stable MIL-53 MOF nanomaterials, Chemical Communications, 49 (2013) 7430-7432.

[225] M.G. Goesten, J. Juan-Alcañiz, E.V. Ramos-Fernandez, K.B. Sai Sankar Gupta, E. Stavitski, H. van Bekkum, J. Gascon, F. Kapteijn, Sulfation of Metal-Organic Frameworks: Opportunities for acid catalysis and proton conductivity, Journal of Catalysis, 281 (2011) 177-187.

[226] A. Comotti, S. Bracco, P. Sozzani, S. Horike, R. Matsuda, J. Chen, M. Takata, Y. Kubota, S. Kitagawa, Nanochannels of two distinct cross-sections in a porous Al-based coordination polymer, Journal of the American Chemical Society, 130 (2008) 13664-13672.

[227] S. Han, Y. Huang, T. Watanabe, Y. Dai, K.S. Walton, S. Nair, D.S. Sholl, J.C. Meredith, High-throughput screening of Metal–Organic Frameworks for CO_2 separation, ACS Combinatorial Science, 14 (2012) 263-267.

[228] K. Zhang, R.P. Lively, M.E. Dose, A.J. Brown, C. Zhang, J. Chung, S. Nair, W.J. Koros, R.R. Chance, Alcohol and water adsorption in Zeolitic Imidazolate Frameworks, Chemical Communications, 49 (2013) 3245-3247.

[229] B.P. Biswal, T. Panda, R. Banerjee, Solution mediated phase transformation (rho to sod) in porous Co-Imidazolate based Zeolitic Frameworks with high water stability, Chemical Communications, 48 (2012) 11868-11870.

[230] A. Kondo, T. Daimaru, H. Noguchi, T. Ohba, K. Kaneko, H. Kanoh, Adsorption of water on three-dimensional pillared-layer Metal Organic Frameworks, Journal of Colloid and Interface Science, 314 (2007) 422-426.

[231] A. Rezk, R. Al-Dadah, S. Mahmoud, A. Elsayed, Experimental investigation of Metal Organic Frameworks characteristics for water adsorption chillers, Proceedings of the Institution of Mechanical Engineers, Part C: Journal of Mechanical Engineering Science, 227 (2013) 992-1005.

[232] G.-B. Li, L. Li, J.-M. Liu, T. Yang, C.-Y. Su, A $CdSO_4$-type 3D Metal-Organic Framework showing coordination dynamics on Cu^{2+} axial sites: Vapochromic response and guest sorption selectivity, Crystal Growth & Design, 13 (2013) 1518-1525.

[233] X. Lin, A.J. Blake, C. Wilson, X.Z. Sun, N.R. Champness, M.W. George, P. Hubberstey, R. Mokaya, M. Schröder, A porous framework polymer based on a zinc(II) 4,4'-bipyridine-2,6,2',6'-tetracarboxylate: Synthesis, structure, and "zeolite-like" behaviors, Journal of the American Chemical Society, 128 (2006) 10745-10753.

[234] M. Sadakiyo, T. Yamada, H. Kitagawa, Hydroxyl group recognition by hydrogen-bonding donor and acceptor sites embedded in a layered Metal-Organic Framework, Journal of the American Chemical Society, 133 (2011) 11050-11053.

[235] H. Reinsch, M. Feyand, T. Ahnfeldt, N. Stock, CAU-3: A new family of porous MOFs with a novel Al-based brick: $[Al_2(OCH_3)4(O_2C$-x-$CO_2)]$ (x = aryl), Dalton Transactions, 41 (2012) 4164-4171.

[236] H. Reinsch, B. Marszalek, J. Wack, J. Senker, B. Gil, N. Stock, A new Al-MOF based on a unique column-shaped inorganic building unit exhibiting strongly hydrophilic sorption behaviour, Chemical Communications, 48 (2012) 9486-9488.

[237] T. Borjigin, F. Sun, J. Zhang, K. Cai, H. Ren, G. Zhu, A microporous Metal-Organic Framework with high stability for GC separation of alcohols from water, Chemical Communications, 48 (2012) 7613-7615.

[238] C. Hou, Q. Liu, P. Wang, W.-Y. Sun, Porous Metal-Organic Frameworks with high stability and selective sorption for CO_2 over N_2, Microporous and Mesoporous Materials, 172 (2013) 61-66.

[239] T. Kundu, S.C. Sahoo, R. Banerjee, Variable water adsorption in amino acid derivative based homochiral Metal Organic Frameworks, Crystal Growth & Design, 12 (2012) 4633-4640.

[240] Y. Huang, X. Zheng, J. Duan, W. Liu, L. Zhou, C. Wang, L. Wen, J. Zhao, D. Li, A highly stable multifunctional three-dimensional microporous framework: Excellent selective sorption and visible photoluminescence, Dalton Transactions, 43 (2014) 6811-6818.

[241] C. Hou, Q. Liu, T.-a. Okamura, P. Wang, W.-Y. Sun, Dynamic porous Metal-Organic Frameworks: Synthesis, structure and sorption property, CrystEngComm, 14 (2012) 8569-8576.

[242] J.-K. Sun, M. Ji, C. Chen, W.-G. Wang, P. Wang, R.-P. Chen, J. Zhang, A charge-polarized porous Metal-Organic Framework for gas chromatographic separation of alcohols from water, Chemical Communications, 49 (2013) 1624-1626.

[243] X.-M. Lin, T.-T. Li, L.-F. Chen, L. Zhang, C.-Y. Su, Two ligand-functionalized Pb(II) Metal-Organic Frameworks: Structures and catalytic performances, Dalton Transactions, 41 (2012) 10422-10429.

[244] M.M. Dubinin, The potential theory of adsorption of gases and vapors for adsorbents with energetically nonuniform surfaces, Chemical Reviews, 60 (1960) 235-241.

[245] J.Y. Lee, D.H. Olson, L. Pan, T.J. Emge, J. Li, Microporous Metal-Organic Frameworks with high gas sorption and separation capacity, Advanced Functional Materials, 17 (2007) 1255-1262.

[246] K. Uemura, Y. Komagawa, Y. Yamasaki, H. Kita, Characterization of organic solvents adsorption/desorption on hydrophobic porous coordination polymers and their micro-crystals aggregation on mullite support, Desalination, 234 (2008) 1-8.

[247] S. Van der Perre, T. Van Assche, B. Bozbiyik, J. Lannoeye, D.E. De Vos, G.V. Baron, J.F.M. Denayer, Adsorptive characterization of the ZIF-68 Metal-Organic Framework: A complex structure with amphiphilic properties, Langmuir, 30 (2014) 8416-8424.

[248] J. Lincke, D. Lässig, J. Moellmer, C. Reichenbach, A. Puls, A. Moeller, R. Gläser, G. Kalies, R. Staudt, H. Krautscheid, A novel copper-based MOF material: Synthesis, characterization and adsorption studies, Microporous and Mesoporous Materials, 142 (2011) 62-69.

[249]   R. Kitaura, K. Fujimoto, S.-I. Noro, M. Kondo, S. Kitagawa, A pillared-layer coordination polymer network displaying hysteretic sorption: $[Cu_2(PZDC)_2(DPYG)]_n$ (PZDC = pyrazine-2,3-dicarboxylate; DPYG=1,2-di(4-pyridyl)glycol), Angewandte Chemie, 114 (2002) 141-143.

[250]   J.-P. Zhang, X.-M. Chen, Exceptional framework flexibility and sorption behavior of a multifunctional porous cuprous triazolate framework, Journal of the American Chemical Society, 130 (2008) 6010-6017.

[251]   Q.-R. Fang, G.-S. Zhu, Z. Jin, M. Xue, X. Wei, D.-J. Wang, S.-L. Qiu, A novel Metal-Organic Framework with the diamondoid topology constructed from pentanuclear zinc−carboxylate clusters, Crystal Growth & Design, 7 (2007) 1035-1037.

[252]   L. Pan, B. Parker, X. Huang, D.H. Olson, Lee, J. Li, Zn(TBIP) (H_2TBIP = 5-tert-butyl isophthalic acid): A highly stable guest-free microporous Metal Organic Framework with unique gas separation capability, Journal of the American Chemical Society, 128 (2006) 4180-4181.

[253]   M.-H. Zeng, Y.-X. Tan, Y.-P. He, Z. Yin, Q. Chen, M. Kurmoo, A porous 4-fold-interpenetrated chiral framework exhibiting vapochromism, single-crystal-to-single-crystal solvent exchange, gas sorption, and a poisoning effect, Inorganic Chemistry, 52 (2013) 2353-2360.

[254]   K. Li, D.H. Olson, J.Y. Lee, W. Bi, K. Wu, T. Yuen, Q. Xu, J. Li, Multifunctional microporous MOFs exhibiting gas/hydrocarbon adsorption selectivity, separation capability and three-dimensional magnetic ordering, Advanced Functional Materials, 18 (2008) 2205-2214.

[255]   S. Hasegawa, S. Horike, R. Matsuda, S. Furukawa, K. Mochizuki, Y. Kinoshita, S. Kitagawa, Three-dimensional porous coordination polymer functionalized with amide groups based on tridentate ligand: Selective sorption and catalysis, Journal of the American Chemical Society, 129 (2007) 2607-2614.

[256]   M. Arnold, P. Kortunov, D.J. Jones, Y. Nedellec, J. Kärger, J. Caro, Oriented crystallisation on supports and anisotropic mass transport of the Metal-Organic Framework manganese formate, European Journal of Inorganic Chemistry, 2007 (2007) 60-64.

[257]   Z. Niu, S. Fang, J.-G. Ma, X.-P. Zhang, P. Cheng, Enhancement of adsorption selectivity for MOFs under mild activation and regeneration conditions, Chemical Communications, 50 (2014) 7797-7799.

[258]   A. Rezk, R. Al-Dadah, S. Mahmoud, A. Elsayed, Investigation of ethanol/Metal Organic Frameworks for low temperature adsorption cooling applications, Applied Energy, 112 (2013) 1025-1031.

[259]   L. Li, S. Tang, C. Wang, X. Lv, M. Jiang, H. Wu, X. Zhao, High gas storage capacities and stepwise adsorption in a UiO type Metal-Organic Framework incorporating lewis basic bipyridyl sites, Chemical Communications, 50 (2014) 2304-2307.

[260]   T. Grant Glover, G.W. Peterson, B.J. Schindler, D. Britt, O. Yaghi, MOF-74 building unit has a direct impact on toxic gas adsorption, Chemical Engineering Science, 66 (2011) 163-170.

[261]   G.W. Peterson, J.B. DeCoste, F. Fatollahi-Fard, D.K. Britt, Engineering UiO-66-NH_2 for toxic gas removal, Industrial & Engineering Chemistry Research, 53 (2013) 701-707.

[262]   J.B. DeCoste, G.W. Peterson, Metal-Organic Frameworks for air purification of toxic chemicals, Chemical Reviews, (2014).

[263]   D. Britt, D. Tranchemontagne, O.M. Yaghi, Metal-Organic Frameworks with high capacity and selectivity for harmful gases, Proceedings of the National Academy of Sciences, 105 (2008) 11623-11627.

[264]   D. Saha, S. Deng, Ammonia adsorption and its effects on framework stability of MOF-5 and MOF-177, Journal of Colloid and Interface Science, 348 (2010) 615-620.

[265]   I. Spanopoulos, P. Xydias, C.D. Malliakas, P.N. Trikalitis, A straight forward route for the development of Metal-Organic Frameworks functionalized with aromatic -OH groups: Synthesis, characterization, and gas (N_2, Ar, H_2, CO_2, CH_4, NH_3) sorption properties, Inorganic Chemistry, 52 (2013) 855-862.

[266]   C. Petit, S. Wrabetz, T.J. Bandosz, Microcalorimetric insight into the analysis of the reactive adsorption of ammonia on Cu-MOF and its composite with graphite oxide, Journal of Materials Chemistry, 22 (2012) 21443-21447.

[267]   E. Borfecchia, S. Maurelli, D. Gianolio, E. Groppo, M. Chiesa, F. Bonino, C. Lamberti, Insights into adsorption of NH_3 on KHUST-1 Metal-Organic Framework: A multitechnique approach, The Journal of Physical Chemistry C, 116 (2012) 19839-19850.

[268]   C. Petit, T.J. Bandosz, Synthesis, characterization, and ammonia adsorption properties of mesoporous Metal–Organic Framework (MIL(Fe))–graphite oxide composites: Exploring the limits of materials fabrication, Advanced Functional Materials, 21 (2011) 2108-2117.

[269]   W. Morris, C.J. Doonan, O.M. Yaghi, Postsynthetic modification of a Metal-Organic Framework for stabilization of a hemiaminal and ammonia uptake, Inorganic Chemistry, 50 (2011) 6853-6855.

[270]   H. Jasuja, G.W. Peterson, J.B. Decoste, M.A. Browe, K.S. Walton, Evaluation of MOFs for air purification and air quality control applications: Ammonia removal from air, Chemical Engineering Science, 124 (2015) 118-124.

[271]   D.W. Green, R.H. Perry, Perry's chemical engineers' handbook, 8th ed., McGraw-Hill, 2008.

234

[272] A.J. Fletcher, K.M. Thomas, M.J. Rosseinsky, Flexibility in Metal-Organic Framework materials: Impact on sorption properties, Journal of Solid State Chemistry, 178 (2005) 2491-2510.

[273] B. Chen, S. Ma, F. Zapata, F.R. Fronczek, E.B. Lobkovsky, H.-C. Zhou, Rationally designed micropores within a Metal-Organic Framework for selective sorption of gas molecules, Inorganic Chemistry, 46 (2007) 1233-1236.

[274] S. Bureekaew, S. Shimomura, S. Kitagawa, Chemistry and application of flexible porous coordination polymers, Science and Technology of Advanced Materials, 9 (2008) 014108.

[275] J.-P. Zhang, S. Kitagawa, Supramolecular isomerism, framework flexibility, unsaturated metal center, and porous property of Ag(I)/Cu(I) 3,3',5,5'-tetrametyl-4,4'-bipyrazolate, Journal of the American Chemical Society, 130 (2008) 907-917.

[276] P.K. Thallapally, J. Tian, M. Radha Kishan, C.A. Fernandez, S.J. Dalgarno, P.B. McGrail, J.E. Warren, J.L. Atwood, Flexible (breathing) interpenetrated Metal-Organic Frameworks for CO_2 separation applications, Journal of the American Chemical Society, 130 (2008) 16842-16843.

[277] S.-i. Noro, D. Tanaka, H. Sakamoto, S. Shimomura, S. Kitagawa, S. Takeda, K. Uemura, H. Kita, T. Akutagawa, T. Nakamura, Selective gas adsorption in one-dimensional, flexible CuII coordination polymers with polar units, Chemistry of Materials, 21 (2009) 3346-3355.

[278] Z. Wang, S.M. Cohen, Modulating metal−organic frameworks to breathe: A postsynthetic covalent modification approach, Journal of the American Chemical Society, 131 (2009) 16675-16677.

[279] A.V. Neimark, F.-X. Coudert, A. Boutin, A.H. Fuchs, Stress-based model for the breathing of Metal-Organic Frameworks, The Journal of Physical Chemistry Letters, 1 (2009) 445-449.

[280] S. Couck, J.F.M. Denayer, G.V. Baron, T. Rémy, J. Gascon, F. Kapteijn, An amine-functionalized MIL-53 Metal-Organic Framework with large separation power for CO_2 and CH_4, Journal of the American Chemical Society, 131 (2009) 6326-6327.

[281] H. Chun, J. Seo, Discrimination of small gas molecules through adsorption: Reverse selectivity for hydrogen in a flexible Metal−Organic Framework, Inorganic Chemistry, 48 (2009) 9980-9982.

[282] H.J. Park, M.P. Suh, Stepwise and hysteretic sorption of N_2, O_2, CO_2, and H_2 gases in a porous Metal-Organic Framework [$Zn_2(BPNDC)_2(BPY)$], Chemical Communications, 46 (2010) 610-612.

[283] D. Tanaka, A. Henke, K. Albrecht, M. Moeller, K. Nakagawa, S. Kitagawa, J. Groll, Rapid preparation of flexible porous coordination polymer nanocrystals with accelerated guest adsorption kinetics, Nat Chem, 2 (2010) 410-416.

[284] S. Shimomura, R. Matsuda, S. Kitagawa, Flexibility of porous coordination polymers strongly linked to selective sorption mechanism, Chemistry of Materials, 22 (2010) 4129-4131.

[285] K.L. Mulfort, O.K. Farha, C.D. Malliakas, M.G. Kanatzidis, J.T. Hupp, An interpenetrated framework material with hysteretic CO_2 uptake, Chemistry – A European Journal, 16 (2010) 276-281.

[286] B. Chen, S. Xiang, G. Qian, Metal-Organic Frameworks with functional pores for recognition of small molecules, Accounts of Chemical Research, 43 (2010) 1115-1124.

[287] A. Boutin, F.o.-X. Coudert, M.-A. Springuel-Huet, A.V. Neimark, G.r. Férey, A.H. Fuchs, The behavior of flexible MIL-53(Al) upon CH_4 and CO_2 adsorption, The Journal of Physical Chemistry C, 114 (2010) 22237-22244.

[288] K. Uemura, Y. Yamasaki, F. Onishi, H. Kita, M. Ebihara, Two-step adsorption on jungle-gym-type porous coordination polymers: Dependence on hydrogen-bonding capability of adsorbates, ligand-substituent effect, and temperature, Inorganic Chemistry, 49 (2010) 10133-10143.

[289] R. Grunker, I. Senkovska, R. Biedermann, N. Klein, M.R. Lohe, P. Muller, S. Kaskel, A highly porous flexible Metal-Organic Framework with corundum topology, Chemical Communications, 47 (2011) 490-492.

[290] A. Kondo, H. Kajiro, H. Noguchi, L. Carlucci, D.M. Proserpio, G. Ciani, K. Kato, M. Takata, H. Seki, M. Sakamoto, Y. Hattori, F. Okino, K. Maeda, T. Ohba, K. Kaneko, H. Kanoh, Super flexibility of a 2D Cu-based porous coordination framework on gas adsorption in comparison with a 3D framework of identical composition: Framework dimensionality-dependent gas adsorptivities, Journal of the American Chemical Society, 133 (2011) 10512-10522.

[291] C. Reichenbach, G. Kalies, J. Lincke, D. Lässig, H. Krautscheid, J. Moellmer, M. Thommes, Unusual adsorption behavior of a highly flexible copper-based MOF, Microporous and Mesoporous Materials, 142 (2011) 592-600.

[292] Y.-Y. Liu, S. Couck, M. Vandichel, M. Grzywa, K. Leus, S. Biswas, D. Volkmer, J. Gascon, F. Kapteijn, J.F.M. Denayer, M. Waroquier, V. Van Speybroeck, P. Van Der Voort, New VIV-based Metal-Organic Framework having framework flexibility and high CO_2 adsorption capacity, Inorganic Chemistry, 52 (2012) 113-120.

[293] A. Shigematsu, T. Yamada, H. Kitagawa, Selective separation of water, methanol, and ethanol by a porous coordination polymer built with a flexible tetrahedral ligand, Journal of the American Chemical Society, 134 (2012) 13145-13147.

[294]   B. Mu, F. Li, Y. Huang, K.S. Walton, Breathing effects of CO_2 adsorption on a flexible 3D lanthanide Metal-Organic Framework, Journal of Materials Chemistry, 22 (2012) 10172-10178.

[295]   P. Kanoo, R. Matsuda, R. Kitaura, S. Kitagawa, T.K. Maji, Topological difference in 2D layers steers the formation of rigid and flexible 3D supramolecular isomers: Impact on the adsorption properties, Inorganic Chemistry, 51 (2012) 9141-9143.

[296]   N. Nijem, H. Wu, P. Canepa, A. Marti, K.J. Balkus, T. Thonhauser, J. Li, Y.J. Chabal, Tuning the gate opening pressure of Metal–Organic Frameworks (MOFs) for the selective separation of hydrocarbons, Journal of the American Chemical Society, 134 (2012) 15201-15204.

[297]   N. Klein, H.C. Hoffmann, A. Cadiau, J. Getzschmann, M.R. Lohe, S. Paasch, T. Heydenreich, K. Adil, I. Senkovska, E. Brunner, S. Kaskel, Structural flexibility and intrinsic dynamics in the $M_2(2,6-NDC)_2(DABCO)$ (M = Ni, Cu, Co, Zn) metal-organic frameworks, Journal of Materials Chemistry, 22 (2012) 10303-10312.

[298]   D.H. Hong, M.P. Suh, Selective CO_2 adsorption in a Metal-Organic Framework constructed from an organic ligand with flexible joints, Chemical Communications, 48 (2012) 9168-9170.

[299]   S. Yang, X. Lin, W. Lewis, M. Suyetin, E. Bichoutskaia, J.E. Parker, C.C. Tang, D.R. Allan, P.J. Rizkallah, P. Hubberstey, N.R. Champness, K. Mark Thomas, A.J. Blake, M. Schröder, A partially interpenetrated Metal–Organic Framework for selective hysteretic sorption of carbon dioxide, Nat Mater, 11 (2012) 710-716.

[300]   L. Han, Y. Yan, F. Sun, K. Cai, T. Borjigin, X. Zhao, F. Qu, G. Zhu, Single- and double-layer structures and sorption properties of two microporous Metal-Organic Frameworks with flexible tritopic ligand, Crystal Growth & Design, 13 (2013) 1458-1463.

[301]   B. Liu, Y. Li, L. Hou, G. Yang, Y.-Y. Wang, Q.-Z. Shi, Dynamic Zn-based Metal-Organic Framework: Stepwise adsorption, hysteretic desorption and selective carbon dioxide uptake, Journal of Materials Chemistry A, 1 (2013) 6535-6538.

[302]   S. Sanda, S. Parshamoni, S. Konar, Third-generation breathing Metal-Organic Framework with selective, stepwise, reversible, and hysteretic adsorption properties, Inorganic Chemistry, 52 (2013) 12866-12868.

[303]   R. Pierotti, J. Rouquerol, Reporting physisorption data for gas/solid systems with special reference to the determination of surface area and porosity, Pure and Applied Chemistry, 57 (1985) 603-619.

[304]   K. Sing, D. Everett, R. Haul, L. Moscou, R. Pierotti, J. Rouquerol, T. Siemieniewska, Reporting physisorption data for gas/solid systems, Pure and Applied Chemistry, 54 (1982) 2201.

[305]   R.L. Yeh, T.K. Ghosh, A.L. Hines, Effects of regeneration conditions on the characteristics of water vapor adsorption on silica gel, Journal of Chemical and Engineering Data, 37 (1992) 259-261.

[306]   L. Gordeeva, Y. Aristov, Dynamic study of methanol adsorption on activated carbon ACM-35.4 for enhancing the specific cooling power of adsorptive chillers, Applied Energy, 117 (2014) 127-133.

[307]   S.K. Henninger, M. Schicktanz, P.P.C. Hügenell, H. Sievers, H.M. Henning, Evaluation of methanol adsorption on activated carbons for thermally driven chillers part I: Thermophysical characterisation, International Journal of Refrigeration, 35 (2012) 543-553.

[308]   M. Schicktanz, P. Hügenell, S.K. Henninger, Evaluation of methanol/activated carbons for thermally driven chillers, part II: The energy balance model, International Journal of Refrigeration, 35 (2012) 554-561.

[309]   E. Anyanwu, C. Ezekwe, Design, construction and test run of a solid adsorption solar refrigerator using activated carbon/methanol, as adsorbent/adsorbate pair, Energy Conversion and Management, 44 (2003) 2879-2892.

[310]   L. Wang, J. Wu, R. Wang, Y. Xu, S. Wang, Experimental study of a solidified activated carbon-methanol adsorption ice maker, Applied Thermal Engineering, 23 (2003) 1453-1462.

[311]   M. Pons, P. Grenier, Experimental data on a solar-powered ice maker using activated carbon and methanol adsorption pair, Journal of solar energy engineering, 109 (1987) 303-310.

[312]   G. Cacciola, G. Restuccia, L. Mercadante, Composites of activated carbon for refrigeration adsorption machines, Carbon, 33 (1995) 1205-1210.

[313]   J.-S. Chang, Porous metal(III) carboxylates as multifunctional adsorbents and catalytic materials, iCeMS-ERATO Symposium, July 26th, 2012.

[314]   D.N. Dybtsev, H. Chun, K. Kim, Rigid and flexible: A highly porous Metal–Organic Framework with unusual guest-dependent dynamic behavior, Angewandte Chemie, 116 (2004) 5143-5146.

[315]   International Zeolite Association - database of zeolite structures.http://www.iza-structure.org/databases/ (accessed 17-01-2015).

[316]   A.J. Mora, A.N. Fitch, M. Cole, R. Goyal, R.H. Jones, H. Jobic, S.W. Carr, The structure of the calcined aluminophosphate $ALPO_4$-5 determined by high-resolution X-ray and neutron powder diffraction, Journal of Materials Chemistry, 6 (1996) 1831-1835.

[317] D.S. Wragg, R.E. Johnsen, P. Norby, H. Fjellvåg, The adsorption of methanol and water on SAPO-34: In situ and ex situ x-ray diffraction studies, Microporous and Mesoporous Materials, 134 (2010) 210-215.

[318] R.E. Critoph, Performance limitations of adsorption cycles for solar cooling, Solar Energy, 41 (1988) 21-31.

[319] F. Meunier, Solid sorption: An alternative to CFCs, Heat Recovery Systems and CHP, 13 (1993) 289-295.

[320] F. Meunier, S.C. Kaushik, P. Neveu, F. Poyelle, A comparative thermodynamic study of sorption systems: Second law analysis, International Journal of Refrigeration, 19 (1996) 414-421.

[321] F. Meunier, Solid sorption heat powered cycles for cooling and heat pumping applications, Applied Thermal Engineering, 18 (1998) 715-729.

[322] M. Pons, F. Poyelle, Adsorptive machines with advanced cycles for heat pumping or cooling applications: Cycles á adsorption pour pompes á chaleur ou machines frigor: Figues, International Journal of Refrigeration, 22 (1999) 27-37.

[323] M. Pons, F. Meunier, G. Cacciola, R.E. Critoph, M. Groll, L. Puigjaner, B. Spinner, F. Ziegler, Thermodynamic based comparison of sorption systems for cooling and heat pumping: Comparaison des performances thermodynamique des systèmes de pompes à chaleur à sorption dans des applications de refroidissement et de chauffage, International Journal of Refrigeration, 22 (1999) 5-17.

[324] Y.I. Aristov, M.M. Tokarev, V.E. Sharonov, Universal relation between the boundary temperatures of a basic cycle of sorption heat machines, Chemical Engineering Science, 63 (2008) 2907-2912.

[325] T. Nunez, Henning, H.-M., Mittelbach, W.,, Adsorption cycle modeling: Characterization and comparison of materials, International Sorption Heat pump Conference1998.

[326] S.K. Henninger, F.P. Schmidt, H.M. Henning, Water adsorption characteristics of novel materials for heat transformation applications, Applied Thermal Engineering, 30 (2010) 1692-1702.

[327] I.I. El-Sharkawy, M. Hassan, B.B. Saha, S. Koyama, M.M. Nasr, Study on adsorption of methanol onto carbon based adsorbents, International Journal of Refrigeration, 32 (2009) 1579-1586.

[328] L.M. Sun, Y. Feng, M. Pons, Numerical investigation of adsorptive heat pump systems with thermal wave heat regeneration under uniform-pressure conditions, International Journal of Heat and Mass Transfer, 40 (1997) 281-293.

[329] M.A. Lambert, B.J. Jones, Review of regenerative adsorption heat pumps, Journal of Thermophysics and Heat Transfer, 19 (2005) 471-485.

[330] M. Dubinin, Physical adsorption of gases and vapors in micropores, Progress in surface and membrane science, 9 (1975) 1-70.

[331] R.K. Agarwal, J.A. Schwarz, Analysis of high pressure adsorption of gases on activated carbon by potential theory, Carbon, 26 (1988) 873-887.

[332] K. Yang, B. Xing, Adsorption of organic compounds by carbon nanomaterials in aqueous phase: Polanyi theory and its application, Chemical Reviews, 110 (2010) 5989-6008.

[333] B. Mu, K.S. Walton, Thermal analysis and heat capacity study of Metal-Organic Frameworks, The Journal of Physical Chemistry C, 115 (2011) 22748-22754.

[334] L.F. Song, C.H. Jiang, J. Zhang, L.X. Sun, F. Xu, Y.Q. Tian, W.S. You, Z. Cao, L. Zhang, D.W. Yang, Heat capacities and thermodynamic properties of MgBTC, Journal of Thermal Analysis and Calorimetry, 101 (2010) 365-370.

[335] X.-C. Lv, Z.-C. Tan, X.-H. Gao, Z.-H. Zhang, L.-N. Yang, J.-N. Zhao, L.-X. Sun, T. Zhang, Synthesis and thermodynamic properties of a Metal-Organic Framework:$[LaCu_6(\mu\text{-}OH)_3(GLY)IM_6](ClO_4)_6$, Thermochimica Acta, 450 (2006) 102-104.

[336] C.H. Jiang, L.F. Song, J. Zhang, L.X. Sun, F. Xu, F. Li, Q.Z. Jiao, Z.G. Sun, Y.H. Xing, Y. Du, J.L. Zeng, Z. Cao, Thermodynamic properties and heat capacities of Co(BTC)1/3 (DMF) (HCOO), Journal of Thermal Analysis and Calorimetry, 102 (2010) 1087-1093.

[337] G.G. Silva, A.W. Musumeci, A.P. Gomes, J.-W. Liu, E.R. Waclawik, G.A. George, R.L. Frost, M.A. Pimenta, Characterization of commercial double-walled carbon nanotube material: Composition, structure, and heat capacity, Journal of materials science, 44 (2009) 3498-3503.

[338] L.F. Song, C.H. Jiang, C.L. Jiao, J. Zhang, L.X. Sun, F. Xu, Q.Z. Jiao, Y.H. Xing, Y. Du, Z. Cao, F.L. Huang, Heat capacities and thermodynamic properties of one manganese-based MOFs, Journal of Thermal Analysis and Calorimetry, 102 (2010) 1161-1166.

[339] L. Qiu, V. Murashov, M.A. White, Zeolite 4A: Heat capacity and thermodynamic properties, Solid State Sciences, 2 (2000) 841-846.

[340] L. Qiu, P.A. Laws, B.-Z. Zhan, M.A. White, Thermodynamic investigations of zeolites NAX and NaY, Canadian Journal of Chemistry, 84 (2006) 134-139.

[341] L. Cemič, E. Dachs, Heat capacity of ferrosilite, $Fe_2Si_2O_6$, Physics and Chemistry of Minerals, 33 (2006) 457-464.

[342]   M. Polanyi, Verhandlungen der Deutschen Physekalischen Gesellschaft, 16 (1914).

[343]   M. Polanyi, Section iii. - theories of the adsorption of gases. A general survey and some additional remarks. Introductory paper to section iii, Transactions of the Faraday Society, 28 (1932) 316-333.

[344]   M. Polanyi, Verh. D. D. Phys. Ges., 18, 55, 1916. F. Goldmann & m. Pblanyi, Z. phys. Chem, 132 (1928) 321.

[345]   M. Goldsworthy, Measurements of water vapour sorption isotherms for RD silica gel, AQSOA-Z01, AQSOA-Z02, AQSOA-z05 and CECA zeolite 3A, Microporous and Mesoporous Materials, 196 (2014) 59-67.

[346]   Y.-D. Kim, K. Thu, K.C. Ng, Adsorption characteristics of water vapor on ferroaluminophosphate for desalination cycle, Desalination, 344 (2014) 350-356.

[347]   D.A. Woodcock, P. Lightfoot, L.A. Villaescusa, M.-J. Díaz-Cabañas, M.A. Camblor, D. Engberg, Negative thermal expansion in the siliceous zeolites chabazite and ITQ-4: A neutron powder diffraction study, Chemistry of Materials, 11 (1999) 2508-2514.

[348]   F. Rouquerol, J. Rouquerol, K. Sing, Adsorption by powders & porous solids, Academic Press, London, 1999.

[349]   E.J. Hu, A study of thermal decomposition of methanol in solar powered adsorption refrigeration systems, Solar Energy, 62 (1998) 325-329.

[350]   R. J. Sheehan, Terephthalic acid, dimethyl terephthalate, and isophthalic acid, Ullmann's encyclopedia of industrial chemistry, Wiley-VCH Verlag GmbH & Co. KGaA2000.

[351]   K. Lohbeck, H. Haferkorn, W. Fuhrmann, N. Fedtke, Maleic and fumaric acids, Ullmann's encyclopedia of industrial chemistry, Wiley-VCH Verlag GmbH & Co. KGaA2000.

[352]   L. Marletta, G. Maggio, A. Freni, M. Ingrasciotta, G. Restuccia, A non-uniform temperature non-uniform pressure dynamic model of heat and mass transfer in compact adsorbent beds, International Journal of Heat and Mass Transfer, 45 (2002) 3321-3330.

[353]   G. Restuccia, A. Freni, G. Maggio, A zeolite-coated bed for air conditioning adsorption systems: Parametric study of heat and mass transfer by dynamic simulation, Applied Thermal Engineering, 22 (2002) 619-630.

[354]   A.G. Fedorov, R. Viskanta, Analysis of transient heat/mass transfer and adsorption/desorption interactions, International Journal of Heat and Mass Transfer, 42 (1999) 803-819.

[355]   Y.I. Aristov, Adsorption dynamics in adsorptive heat transformers: Review of new trends, Heat Transfer Engineering, 35 (2014) 1014-1027.

[356]   B.L. Huang, A.J.H. McGaughey, M. Kaviany, Thermal conductivity of Metal-Organic Framework 5 (MOF-5): Part I. Molecular dynamics simulations, International Journal of Heat and Mass Transfer, 50 (2007) 393-404.

[357]   B.L. Huang, Z. Ni, A. Millward, A.J.H. McGaughey, C. Uher, M. Kaviany, O. Yaghi, Thermal conductivity of a Metal-Organic Framework (MOF-5): Part II. Measurement, International Journal of Heat and Mass Transfer, 50 (2007) 405-411.

[358]   D. Liu, J. Purewal, J. Yang, A. Sudik, S. Maurer, U. Mueller, J. Ni, D. Siegel, MOF-5 composites exhibiting improved thermal conductivity, International Journal of Hydrogen Energy, 37 (2012) 6109-6117.

[359]   J. Purewal, D. Liu, J. Yang, A. Sudik, D. Siegel, S. Maurer, U. Müller, Increased volumetric hydrogen uptake of MOF-5 by powder densification, International Journal of Hydrogen Energy, 37 (2012) 2723-2727.

[360]   Y. Ming, H. Chi, R. Blaser, C. Xu, J. Yang, M. Veenstra, M. Gaab, U. Müller, C. Uher, D.J. Siegel, Anisotropic thermal transport in MOF-5 composites, International Journal of Heat and Mass Transfer, 82 (2015) 250-258.

[361]   H. Chua, K. Ng, A. Malek, T. Kashiwagi, A. Akisawa, B. Saha, Modeling the performance of two-bed, sillica gel-water adsorption chillers, International Journal of Refrigeration, 22 (1999) 194-204.

[362]   A.M.W. Wojcik Structured zeolites in heat pump systems.Ph.D. Thesis, TU Delft, 2002.

[363]   M. Tatlıer, A. Erdem-Şenatalar, When do thin zeolite layers and a large void volume in the adsorber limit the performance of adsorption heat pumps?, Microporous and Mesoporous Materials, 54 (2002) 89-96.

[364]   H. Stach, J. Mugele, J. Jänchen, E. Weiler, Influence of cycle temperatures on the thermochemical heat storage densities in the systems water/microporous and water/mesoporous adsorbents, Adsorption, 11 (2005) 393-404.

[365]   P. Tatsidjodoung, N. Le Pierrès, L. Luo, A review of potential materials for thermal energy storage in building applications, Renewable and Sustainable Energy Reviews, 18 (2013) 327-349.

[366]   S. Mauran, H. Lahmidi, V. Goetz, Solar heating and cooling by a thermochemical process. First experiments of a prototype storing 60kWh by a solid/gas reaction, Solar Energy, 82 (2008) 623-636.

[367]   G. Tanguy, P. Papillon, C. Paulus, Seasonal storage coupled to solar combisystem: Dynamic simulations for process dimensioning, Proceeding of Eurosun. Graz, Austria, (2010).

[368]   S. Hennaut, S. Thomas, P. Andre, E. Courbon, T. Le Berigot, M. Frère, Pré-dimensionnement par simulations dynamiques d'un réacteur de stockage thermochimique assurant l'autonomie d'un système solaire combiné, Congrès Français de Thermique 2011-Energie Solaire et Thermique-Perpignan-24-27 Mai 2011, (2011).

[369]   Y. Ding, S. Riffat, Thermochemical energy storage technologies for building applications: A state-of-the-art review, International Journal of Low-Carbon Technologies, 8 (2013) 106-116.

[370]   K. Visscher, J. Veldhuis, Comparison of candidate materials for seasonal storage of solar heat through dynamic simulation of building and renewable energy system, Ninth International IBPSA Conference, Montréal, Canada2005.

[371]   R. De Boer, W. Haije, J. Veldhuis, Determination of structural, thermodynamic and phase properties in the Na$_2$S–H$_2$O system for application in a chemical heat pump, Thermochimica Acta, 395 (2002) 3-19.

[372]   R.d. Boer, W. Haije, J. Veldhuis, S. Smeding, Solid-sorption cooling with integrated thermal storage-the sweat prototype, Proceedings of the 3rd International Heat Powered Cycles Conference (HPC 2004), Larnaca, Cyprus2004.

[373]   V. Van Essen, H. Zondag, J.C. Gores, L. Bleijendaal, M. Bakker, R. Schuitema, W. Van Helden, Z. He, C. Rindt, Characterization of MgSO$_4$ hydrate for thermochemical seasonal heat storage, Journal of solar energy engineering, 131 (2009) 041014.

[374]   V. van Essen, L. Bleijendaal, B. Kikkert, H. Zondag, M. Bakker, P. Bach, Development of a compact heat storage system based on salt hydrates, Proceedings of the EUROSUN2010.

[375]   H. Zondag, B. Kikkert, S. Smeding, R.d. Boer, M. Bakker, Prototype thermochemical heat storage with open reactor system, Applied Energy, 109 (2013) 360-365.

[376]   T. Li, R. Wang, J.K. Kiplagat, A target-oriented solid-gas thermochemical sorption heat transformer for integrated energy storage and energy upgrade, AIChE Journal, 59 (2013) 1334-1347.

[377]   B. Mette, H. Kerskes, H. Drück, H. Müller-Steinhagen, New highly efficient regeneration process for thermochemical energy storage, Applied Energy, 109 (2013) 352-359.

[378]   F. Bertsch, B. Mette, S. Asenbeck, H. Kerskes, H. Müller-Steinhagen, Low temperature chemical heat storage-an investigation of hydration reactions, Effstock conference, Stockholm2009.

[379]   Y.I. Aristov, G. Restuccia, M.M. Tokarev, G. Cacciola, Selective water sorbents for multiple applications, 10. Energy storage ability, Reaction Kinetics and Catalysis Letters, 69 (2000) 345-353.

[380]   D. Zhu, H. Wu, S. Wang, Experimental study on composite silica gel supported CaCl$_2$ sorbent for low grade heat storage, International Journal of Thermal Sciences, 45 (2006) 804-813.

[381]   H. Wu, S. Wang, D. Zhu, Effects of impregnating variables on dynamic sorption characteristics and storage properties of composite sorbent for solar heat storage, Solar Energy, 81 (2007) 864-871.

[382]   A. Jabbari-Hichri, S. Bennici, A. Auroux, Water sorption heats on silica-alumina-based composites for interseasonal heat storage, Journal of Thermal Analysis and Calorimetry, 118 (2014) 1111-1118.

[383]   H. Liu, K. Nagano, J. Togawa, A composite material made of mesoporous siliceous shale impregnated with lithium chloride for an open sorption thermal energy storage system, Solar Energy, 111 (2015) 186-200.

[384]   O. Opel, H. Rammelberg, M. Gérard, W. Ruck, Thermochemical storage materials research-TGA/DSC-hydration studies, Proceedings of the international conference for sustainable energy storage2011.

[385]   J. Jänchen, D. Ackermann, H. Stach, W. Brösicke, Studies of the water adsorption on zeolites and modified mesoporous materials for seasonal storage of solar heat, Solar Energy, 76 (2004) 339-344.

[386]   G. Grossman, Solar-powered systems for cooling, dehumidification and air-conditioning, Solar Energy, 72 (2002) 53-62.

[387]   K. Daou, R.Z. Wang, Z.Z. Xia, Desiccant cooling air conditioning: A review, Renewable and Sustainable Energy Reviews, 10 (2006) 55-77.

[388]   X. Zheng, T. Ge, R. Wang, Recent progress on desiccant materials for solid desiccant cooling systems, Energy, 74 (2014) 280-294.

[389]   Munters, Honeycombe wheels & desiccant options (product leaflet). http://webdh.munters.com/webdh/BrochureUploads/Brochure-%20Wheel%20and%20Desiccant%20options.pdf (accessed 17-01-2015).

[390]   Klingenburg, New development sorption rotor HUGO (product leaflet). http://www.klingenburg-usa.com/news/hugo.html (accessed 17-01-2015).

[391]   M. Kanoglu, M. Özdinç ÇarpInlIoglu, M. YildIrIm, Energy and exergy analyses of an experimental open-cycle desiccant cooling system, Applied Thermal Engineering, 24 (2004) 919-932.

[392]   X.J. Zhang, Y.J. Dai, R.Z. Wang, A simulation study of heat and mass transfer in a honeycombed rotary desiccant dehumidifier, Applied Thermal Engineering, 23 (2003) 989-1003.

[393] W. Wang, L. Wu, Z. Li, Y. Fang, J. Ding, J. Xiao, An overview of adsorbents in the rotary desiccant dehumidifier for air dehumidification, Drying Technology, 31 (2013) 1334-1345.

[394] P. Guo, A.G. Wong-Foy, A.J. Matzger, Microporous coordination polymers as efficient sorbents for air dehumidification, Langmuir, 30 (2014) 1921-1925.

[395] G. Kolios, J. Frauhammer, G. Eigenberger, Efficient reactor concepts for coupling of endothermic and exothermic reactions, Chemical Engineering Science, 57 (2002) 1505-1510.

[396] D. Zacher, O. Shekhah, C. Woll, R.A. Fischer, Thin films of Metal-Organic Frameworks, Chemical Society Reviews, 38 (2009) 1418-1429.

[397] A.l. Bétard, R.A. Fischer, Metal-Organic Framework thin films: From fundamentals to applications, Chemical Reviews, 112.2 (2011) 1055-1083.

[398] O. Shekhah, A. Cadiau, M. Eddaoudi, Fabrication and non-covalent modification of highly oriented thin films of a zeolite-like Metal–Organic Framework (ZMOF) with rho topology, CrystEngComm, 17 (2015) 290-294.

[399] B.K. Keitz, C.J. Yu, J.R. Long, R. Ameloot, Lithographic deposition of patterned Metal–Organic Framework coatings using a photobase generator, Angewandte Chemie International Edition, 53 (2014) 5561-5565.

[400] D. Witters, S. Vermeir, R. Puers, B.F. Sels, D.E. De Vos, J. Lammertyn, R. Ameloot, Miniaturized layer-by-layer deposition of Metal-Organic Framework coatings through digital microfluidics, Chemistry of Materials, 25 (2013) 1021-1023.

[401] J. Zhao, B. Gong, W.T. Nunn, P.C. Lemaire, E.C. Stevens, F.I. Sidi, P.S. Williams, C.J. Oldham, H.J. Walls, S.D. Shepherd, Conformal and highly adsorptive Metal-Organic Framework thin films via layer-by-layer growth on ALD-coated fiber mats, Journal of Materials Chemistry A, (2015).

[402] J. Reboul, S. Furukawa, N. Horike, M. Tsotsalas, K. Hirai, H. Uehara, M. Kondo, N. Louvain, O. Sakata, S. Kitagawa, Mesoscopic architectures of porous coordination polymers fabricated by pseudomorphic replication, Nature materials, 11 (2012) 717-723.

[403] E.V. Ramos-Fernandez, M. Garcia-Domingos, J. Juan-Alcañiz, J. Gascon, F. Kapteijn, MOFs meet monoliths: Hierarchical structuring Metal Organic Framework catalysts, Applied Catalysis A: General, 391 (2011) 261-267.

[404] J. Gascon, S. Aguado, F. Kapteijn, Manufacture of dense coatings of $Cu_3(BTC)_2$ (HKUST-1) on α-alumina, Microporous and Mesoporous Materials, 113 (2008) 132-138.

[405] A. Dailly, E. Poirier, Evaluation of an industrial pilot scale densified MOF-177 adsorbent as an on-board hydrogen storage medium, Energy & Environmental Science, 4 (2011) 3527-3534.

[406] T. Remy, S.A. Peter, S. Van der Perre, P. Valvekens, D.E. De Vos, G.V. Baron, J.F. Denayer, Selective dynamic CO_2 separations on Mg-MOF-74 at low pressures: A detailed comparison with 13X, The Journal of Physical Chemistry C, 117 (2013) 9301-9310.

[407] L. Arnold, G. Averlant, S. Marx, M. Weickert, U. Müller, J. Mertel, C. Horch, M. Peksa, F. Stallmach, Metal Organic Frameworks for natural gas storage in vehicles, Chemie Ingenieur Technik, 85 (2013) 1726-1733.

[408] J. Schell, N. Casas, R. Blom, A.I. Spjelkavik, A. Andersen, J.H. Cavka, M. Mazzotti, MCM-41, MOF and UiO-67/MCM-41 adsorbents for pre-combustion CO_2 capture by PSA: Adsorption equilibria, Adsorption, 18 (2012) 213-227.

[409] A. Sapienza, I.S. Glaznev, S. Santamaria, A. Freni, Y.I. Aristov, Adsorption chilling driven by low temperature heat: New adsorbent and cycle optimization, Applied Thermal Engineering, 32 (2012) 141-146.

[410] A. Myat, N. Kim Choon, K. Thu, Y.-D. Kim, Experimental investigation on the optimal performance of zeolite–water adsorption chiller, Applied Energy, 102 (2013) 582-590.

[411] S. Santamaria, A. Sapienza, A. Frazzica, A. Freni, I.S. Girnik, Y.I. Aristov, Water adsorption dynamics on representative pieces of real adsorbers for adsorptive chillers, Applied Energy, 134 (2014) 11-19.

[412] A. Frazzica, G. Füldner, A. Sapienza, A. Freni, L. Schnabel, Experimental and theoretical analysis of the kinetic performance of an adsorbent coating composition for use in adsorption chillers and heat pumps, Applied Thermal Engineering, 73 (2014) 1022-1031.

[413] I. Glaznev, D. Ovoshchnikov, Y. Aristov, Effect of residual gas on water adsorption dynamics under typical conditions of an adsorption chiller, Heat Transfer Engineering, 31 (2010) 924-930.

[414] Y.I. Aristov, I.S. Glaznev, I.S. Girnik, Optimization of adsorption dynamics in adsorptive chillers: Loose grains configuration, Energy, 46 (2012) 484-492.

[415] Y.-K. Seo, J.W. Yoon, J.S. Lee, U. Lee, Y.K. Hwang, C.-H. Jun, P. Horcajada, C. Serre, J.-S. Chang, Large scale fluorine-free synthesis of hierarchically porous iron (III) trimesate MIL-100 (Fe) with a zeolite mtn topology, Microporous and Mesoporous Materials, 157 (2012) 137-145.

[416] F. Ragon, P. Horcajada, H. Chevreau, Y.K. Hwang, U.-H. Lee, S.R. Miller, T. Devic, J.-S. Chang, C. Serre, In situ energy-dispersive X-ray diffraction for the synthesis optimization and scale-up of the porous zirconium terephthalate UiO-66, Inorganic Chemistry, 53 (2014) 2491-2500.

[417] A.G. Marquez, P. Horcajada, D. Grosso, G. Ferey, C. Serre, C. Sanchez, C. Boissiere, Green scalable aerosol synthesis of porous Metal-Organic Frameworks, Chemical Communications, 49 (2013) 3848-3850.

[418] V. Agostoni, P. Horcajada, V. Rodriguez-Ruiz, H. Willaime, P. Couvreur, C. Serre, R. Gref, 'Green'fluorine-free mesoporous iron (III) trimesate nanoparticles for drug delivery, Green Materials, 1 (2013) 209-217.

[419] F. Zhang, J. Shi, Y. Jin, Y. Fu, Y. Zhong, W. Zhu, Facile synthesis of MIL-100(Fe) under HF-free conditions and its application in the acetalization of aldehydes with diols, Chemical Engineering Journal, 259 (2015) 183-190.

[420] A. Garcia Marquez, P. Horcajada, D. Grosso, G. Ferey, C. Serre, C. Sanchez, C. Boissiere, Green scalable aerosol synthesis of porous Metal-Organic Frameworks, Chemical Communications, 49 (2013) 3848-3850.

[421] A. García Márquez, A. Demessence, A.E. Platero-Prats, D. Heurtaux, P. Horcajada, C. Serre, J.-S. Chang, G. Férey, V.A. de la Peña-O'Shea, C. Boissière, D. Grosso, C. Sanchez, Green microwave synthesis of MIL-100(Al, Cr, Fe) nanoparticles for thin-film elaboration, European Journal of Inorganic Chemistry, 2012 (2012) 5165-5174.

[422] Y. Mao, J. Li, W. Cao, Y. Ying, L. Sun, X. Peng, Pressure-assisted synthesis of HKUST-1 thin film on polymer hollow fiber at room temperature toward gas separation, ACS applied materials & interfaces, 6 (2014) 4473-4479.

[423] N. Motakef-Kazemi, S.A. Shojaosadati, A. Morsali, in situ synthesis of a drug-loaded MOF at room temperature, Microporous and Mesoporous Materials, 186 (2014) 73-79.

[424] M. Díaz-García, Á. Mayoral, I. Díaz, M. Sánchez-Sánchez, Nanoscaled M-MOF-74 materials prepared at room temperature, Crystal Growth & Design, 14 (2014) 2479-2487.

[425] G. Zahn, H.A. Schulze, J. Lippke, S. König, U. Sazama, M. Fröba, P. Behrens, A water-born Zr-based porous coordination polymer: Modulated synthesis of Zr-fumarate MOF, Microporous and Mesoporous Materials, 203 (2015) 186-194.

[426] N. Nordin, A. Ismail, A. Mustafa, P. Goh, D. Rana, T. Matsuura, Aqueous room temperature synthesis of Zeolitic Imidazole Framework 8 (ZIF-8) with various concentrations of triethylamine, RSC Advances, 4 (2014) 33292-33300.

[427] E.L. Bustamante, J.L. Fernández, J.M. Zamaro, Influence of the solvent in the synthesis of Zeolitic Imidazolate Framework-8 (ZIF-8) nanocrystals at room temperature, Journal of Colloid and Interface Science, 424 (2014) 37-43.

[428] D.J. Tranchemontagne, J.R. Hunt, O.M. Yaghi, Room temperature synthesis of Metal-Organic Frameworks: MOF-5, MOF-74, MOF-177, MOF-199, and IRMOF-0, Tetrahedron, 64 (2008) 8553-8557.

[429] J. Cravillon, S. Münzer, S.-J. Lohmeier, A. Feldhoff, K. Huber, M. Wiebcke, Rapid room-temperature synthesis and characterization of nanocrystals of a prototypical Zeolitic Imidazolate Framework, Chemistry of Materials, 21 (2009) 1410-1412.

[430] A. Pichon, A. Lazuen-Garay, S.L. James, Solvent-free synthesis of a microporous Metal-Organic Framework, CrystEngComm, 8 (2006) 211-214.

[431] I. Stassen, N. Campagnol, J. Fransaer, P. Vereecken, D. De Vos, R. Ameloot, Solvent-free synthesis of supported ZIF-8 films and patterns through transformation of deposited zinc oxide precursors, CrystEngComm, 15 (2013) 9308-9311.

[432] C. Mottillo, Y. Lu, M.-H. Pham, M.J. Cliffe, T.-O. Do, T. Friščić, Mineral neogenesis as an inspiration for mild, solvent-free synthesis of bulk microporous Metal-Organic Frameworks from metal (Zn, Co) oxides, Green Chemistry, 15 (2013) 2121-2131.

[433] K. Müller‑Buschbaum, F. Schönfeld, The utilisation of solvent-free synthesis for the reaction of cobalt with imidazole: MOF conversion from $[Co_3(IM)_6(IMH)_2]$ via $[Co_4(IM)_8(IMH)]$ to $[Co(IM)_2]$, Zeitschrift fur Anorganische und Allgemeine Chemie, 637 (2011) 955-960.

[434] M. Lanchas, S. Arcediano, A.T. Aguayo, G. Beobide, O. Castillo, J. Cepeda, D. Vallejo-Sánchez, A. Luque, Two appealing alternatives for MOFs synthesis: Solvent-free oven heating vs. Microwave heating, RSC Advances, 4 (2014) 60409-60412.

[435] M.J. Cliffe, C. Mottillo, R.S. Stein, D.-K. Bučar, T. Friščić, Accelerated aging: A low energy, solvent-free alternative to solvothermal and mechanochemical synthesis of Metal–Organic materials, Chemical Science, 3 (2012) 2495-2500.

[436] R. Chal, C. Gérardin, M. Bulut, S. van Donk, Overview and industrial assessment of synthesis strategies towards zeolites with mesopores, ChemCatChem, 3 (2011) 67-81.

241

[437]   L. Ren, L. Zhu, C. Yang, Y. Chen, Q. Sun, H. Zhang, C. Li, F. Nawaz, X. Meng, F.-S. Xiao, Designed copper–amine complex as an efficient template for one-pot synthesis of Cu-SSZ-13 zeolite with excellent activity for selective catalytic reduction of NO_x by NH_3, Chemical Communications, 47 (2011) 9789-9791.

[438]   H.S. Cho, R. Ryoo, Synthesis of ordered mesoporous MFI zeolite using CMK carbon templates, Microporous and Mesoporous Materials, 151 (2012) 107-112.

[439]   E.R. Cooper, C.D. Andrews, P.S. Wheatley, P.B. Webb, P. Wormald, R.E. Morris, Ionic liquids and eutectic mixtures as solvent and template in synthesis of zeolite analogues, Nature, 430 (2004) 1012-1016.

[440]   Z. Yang, Y. Xia, R. Mokaya, Zeolite ZSM/5 with unique supermicropores synthesized using mesoporous carbon as a template, Advanced Materials, 16 (2004) 727-732.

[441]   C.S. Cundy, P.A. Cox, The hydrothermal synthesis of zeolites: History and development from the earliest days to the present time, Chemical Reviews, 103 (2003) 663-702.

[442]   G. Liu, P. Tian, Y. Zhang, J. Li, L. Xu, S. Meng, Z. Liu, Synthesis of SAPO-34 templated by diethylamine: Crystallization process and Si distribution in the crystals, Microporous and Mesoporous Materials, 114 (2008) 416-423.

[443]   Y. Xu, P.J. Maddox, J.W. Couves, The synthesis of SAPO-34 and CoSAPO-34 from a triethylamine-hydrofluoric acid-water system, Journal of the Chemical Society, Faraday Transactions, 86 (1990) 425-429.

[444]   A.M. Prakash, S. Unnikrishnan, Synthesis of SAPO-34: High silicon incorporation in the presence of morpholine as template, Journal of the Chemical Society, Faraday Transactions, 90 (1994) 2291-2296.

[445]   R.D. Gougeon, E.B. Brouwer, P.R. Bodart, L. Delmotte, C. Marichal, J.-M. Chézeau, R.K. Harris, Solid-state NMR studies of the as-synthesized $ALPO_4$-5/TPAF microporous aluminophosphate, The Journal of Physical Chemistry B, 105 (2001) 12249-12256.

[446]   F. Jiang, Z. Tang, J. Zhai, J. Ye, J. Han, Synthesis of $ALPO_4$-5 crystals using TBAOH as template, Microporous and Mesoporous Materials, 92 (2006) 129-133.

[447]   Y. Wan, C.D. Williams, C.V. Duke, J.J. Cox, Systematic studies on the effect of water content on the synthesis, crystallisation, conversion and morphology of $ALPO_4$-5 molecular sieve, Journal of Materials Chemistry, 10 (2000) 2857-2862.

APPENDIX C

ADSORPTION DRIVEN HEAT PUMPS – THE
POTENTIAL OF MOFS

LIST OF SYMBOLS

Latin

Symbol	*Meaning*	*Units*
A	Adsorption potential	kJ mol^{-1}
COP	Coefficient of performance	-
c_p	Heat capacity	J g^{-1} K^{-1} / J mol^{-1} K^{-1}
D	Diameter	nm
m	mass	g
M_w	Molar mass	g mol^{-1}
p	Pressure	bar
p/p_o	Relative pressure	-
p_o	Saturation pressure	bar
q	Amount adsorbed	g g^{-1}
Q	Energy	kJ mol^{-1} [a]
R	Gas constant	J K^{-1} mol^{-1}
T	Temperature	K
V_p	Pore volume	ml(liq.) g^{-1}
W	Liquid volume adsorbed	ml(liq.) g^{-1} [b]

Greek

Symbol	*Meaning*	*Units*
α	p/p_o for which $q = 0.5\ q_{max}$	-
$\Delta_{ads}H$	Enthalpy of adsorption	kJ mol^{-1}
$\Delta_{vap}H$	Enthalpy of evaporation	kJ mol^{-1}
ε	Porosity	-
ρ	Density	g ml^{-1}
σ	Molecule size	nm

Subscripts

1	Of point 1 (in Fig. 4.5)
2	Of point 2 (in Fig. 4.5)
3	Of point 3 (in Fig. 4.5)
4	Of point 4 (in Fig. 4.5)
ads	Adsorber
b	Bulk
c	Critical (point)
c	Crystal(line)
C	Cooling (COP)
con	Condenser
des	Desorption
ev	Evaporator
H	Heating (COP)
hx	Heat exchanger

liq	Liquid
max	Maximum
min	Minimum
regen	Regeneration
sat	At saturation
sorbent	Adsorbent
sorption	Adsorption
W	For volume W adsorbed

Superscripts

effective	Effective
hx	Heat exchanger
sorbent	adsorbent
wf	Working fluid
ΔH	For which $\Delta_{ads}H$ is known

Notes: [a] Except for Figs. 4.9, 4.12 and 4.13 where Q's are displayed per ml sorbent (ρ_c used for conversion). [b] Except for Figs. 4.4, 4.10 and C.5, where W is displayed in ml ml^{-1} sorbent (ρ_c used for conversion).

ABBREVIATIONS

MOF TERMINOLOGY

CAU – Christian Albrechts University. Cus – Coordinatively unsaturated site. DMOF – DABCO MOF. DUT – Dresden University of Technology. MAF – Metal Azolate Framework. MFU – Metal-organic Framework Ulm University. MIL – Material Institut Lavoisier. NU – Northwestern University. PIZOF – Porous Interpenetrated Zirconium–Organic Frameworks. SALI – Solvent-Assisted Ligand Exchange. UiO – University of Oslo. ZIF – Zeolitic Imidazolate Framework.

LIGANDS

4-btapa – 1,3,5-benzene tricarboxylic acid tris-[N-(4-pyridyl)amide]. ADC – 9,10-anthracenedicarboxylic acid. Ala – alanine. Azi – aziridine. AZPY – azopyridine. BBTA – 1H,5H-benzo(1,2-d:4,5-d')bistriazole. BDC – 1,4-benzene dicarboxylic acid (TPA). bfbpdc – 2,2'-bistrifluoromethyl-biphenyl-4,4'-dicarboxylic acid. bIm – benzimidazole. BIPY – 2,2'-bipyridine-5,5'-dicarboxylate. BPDC – 4,4'-biphenyldicarboxylic acid. bpe – trans-1,2-bis(4-pyridyl)ethylene. bptc – 4,4'-bipyridine-2,6,2',6'-tetracarboxylic acid. bpy – 4,4'-bipyridine. Bpybc – 1,1'-bis(4-carboxybenzyl)-4,4'-bipyridine. BTB – benzene tribenzoate. BTC – 1,3,5-benzene tricarboxylic acid. Btre – 1,2-bis(1,2,4-triazol-4-yl)ethane. BTTB –4,4',4'',4''-

benzene-1,2,4,5-tetrayltetrabenzoic acid. CAM – chelidamic acid. CDC – trans-1,4-cyclohexane dicarboxylic acid. Dab – 1,4-diamino-butane. DABCO – 1,4-diazabicyclo[2.2.2]octane (TED). dacba – diacetylene-1,4-bis(4-benzoic acid). dcIm – dichloroimidazole. DMBPY – 2,2'-dimethyl 4,4'-bipyridine. dmcapz – 3,5-dimethyl-4-carboxypyrazole. DPE – 1,2-di(4-pyridyl)ethylene. Dpyg – 1,2-di(4-pyridyl)glycol. DTTDC - dithieno[3,2-b;20,30-d]-thiophene-2,6-dicarboxylate. Eim – 2-ethylimidazole. etz – 3,5-diethyl-1,2,4-triazolate. FA – fumaric acid. Hma – hemiaminal. Ica – imidazole-2-carboxaldehyde. IPA – isopthalic acid (1,3-benzene dicarboxylic acid). L – N-(4-carboxyphenyl) isonicotinamide 1-oxide. L'1 – 2-((pyridin-4-yl)methylamino)-4-methylpentanoic acid. L'2 – 2-(pyridin-4-yl)methylamino)-3-hydroxypropanoic acid. L'3 – 2-((pyridin-4-yl)methylamino)-3-hydroxybutanoic acid. L1 – 1H-pyrazole-4-carboxylic acid. L2 – 4-(1H-pyrazole-4-yl)benzoic acid. L3 – 4,4'-benzene-1,4-diylbis(1H-pyrazole). L4 – 4,4'-buta-1,3-diyne-1,4-diylbis(1H-pyrazole). L5 – 4,4'-(benzene-1,4-diyldiethyne-2,1-diyl)bis(1H-pyrazole). L6 – 3,5-di(pyridine-4-yl)benzoic acid. L7 – 5-(4-pyridyl)-isophthalic acid. Me$_2$trzpba – 4-(3,5-dimethyl-4H-1,2,4-triazol-4-yl)benzoate. mIm – 2-methyl-imidazole. mImca – 4-methyl-5-imidazolecarboxaldehyde. MTB – 4,4',4",4"'-Methanetetrayltetrabenzoic acid. mTz – 3-methyl-1,2,4-triazole. NDC – Naphthalenedicarboxylic acid. NDI – 2,7-bis(3,5-dimethyl-1H-pyrazol-4-yl)benzo[lmn][3,8]phenanthroline-1,3,6,8(2H,7H)-tetraone. NIm – 2-Nitro-imidazole. OAc – Acetoxy. opd – o-phthalic acid. Ox – oxalate. PEDB – 4,4'-(1,4-phenylenebis(ethyne-2,1-diyl))dibenzoic acid. pmpmd – N,N'-bis (4- pyridylmethyl) phenyldiimide. pybz – 4-(4-pyridyl)benzoate. PytPh – pyrene-1,3,6,8-tetraphosphonate. pyz – pyrazine. PZDC – 1H-pyrazole-3,5-dicarboxylic acid. TBAPy – ,3,6,8-tetrakis(p-benzoic-acid)pyrene. Tbip – 5-tert-butyl isophthalic acid. TDC – thiophene-2,5-dicarboxylic acid. TED – triethylenediamine (DABCO). THIPC – (S)-4,5,6,7-tetrahydro-1H-imidazo[4,5-c]pyridine-6-carboxylate. Thr – threonine. TMBDC – 2,3,5,6-tetramethyl-1,4-benzenedicarboxylic acid. TPA – Terephthalic acid (BDC). URPh – phenylurea. Val – valine.

MISCELLANEOUS

ADC – Adsorption Driven Chiller. ads – adsorption. AHP – Adsorption driven Heat Pump. BT. – Obtained from breakthrough experiments. DEG – diethylene glycol. des – desorption. EG – ethylene glycol. EN – ethylenediamine. FAM Z – Functional Adsorbent Material Zeolite. H.K. – High kinetic stability. L.K. – Low Kinetic stability. POM – polyoxometalate. R.H. – relative humidity. TEG – tryethylene glycol. Th.S. – Thermodynamic Stability. Uns. – Unstable.
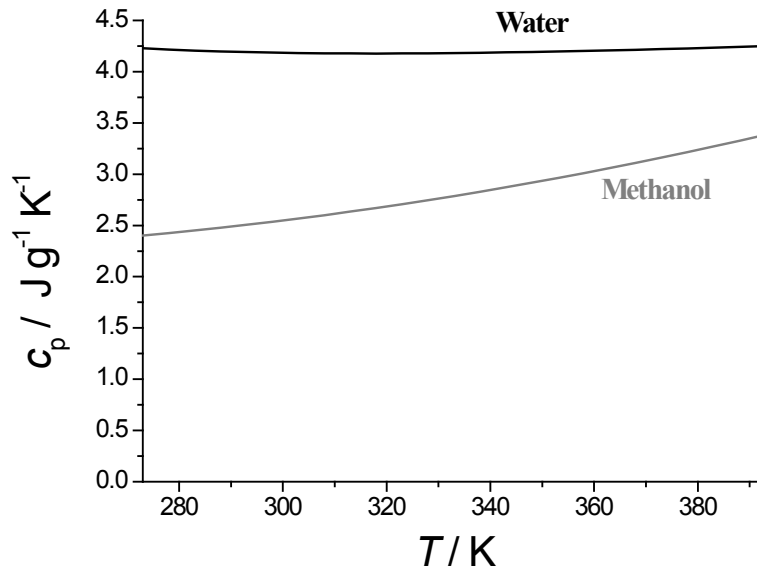
Figure C.1: Heat capacity of water and methanol as function of temperature. Data from Ref. [1].

Table C. 1: Coefficients used in Eq. C1.1 to calculate working fluid heat capacities.

	C_1 / J kmol^{-1} K^{-1}	C_2 / J kmol^{-1} K^{-2}	C_3 / J kmol^{-1} K^{-3}	C_4 / J kmol^{-1} K^{-4}	C_5 / J kmol^{-1} K^{-5}
Water	$2.76 \cdot 10^5$	$-2.09 \cdot 10^3$	8.13	$-1.41 \cdot 10^{-2}$	$9.37 \cdot 10^{-6}$
Methanol	$1.06 \cdot 10^5$	$-3.62 \cdot 10^2$	$9.38 \cdot 10^{-1}$	0	0

C.1. WORKING FLUID HEAT CAPACITY

The specific heat capacity of the employed working fluids in Part II of the review, water and methanol, are shown as function of temperature in Fig. C.1. In fact, these curves were calculated with Eq. C1.1, the coefficients for which are given in Table C.1 [1]:

$$c_p = \left(C_1 + C_2 T + C_3 T^2 + C_4 T^3 + C_5 T^4 \right) M_w^{-1} \tag{C1.1}$$
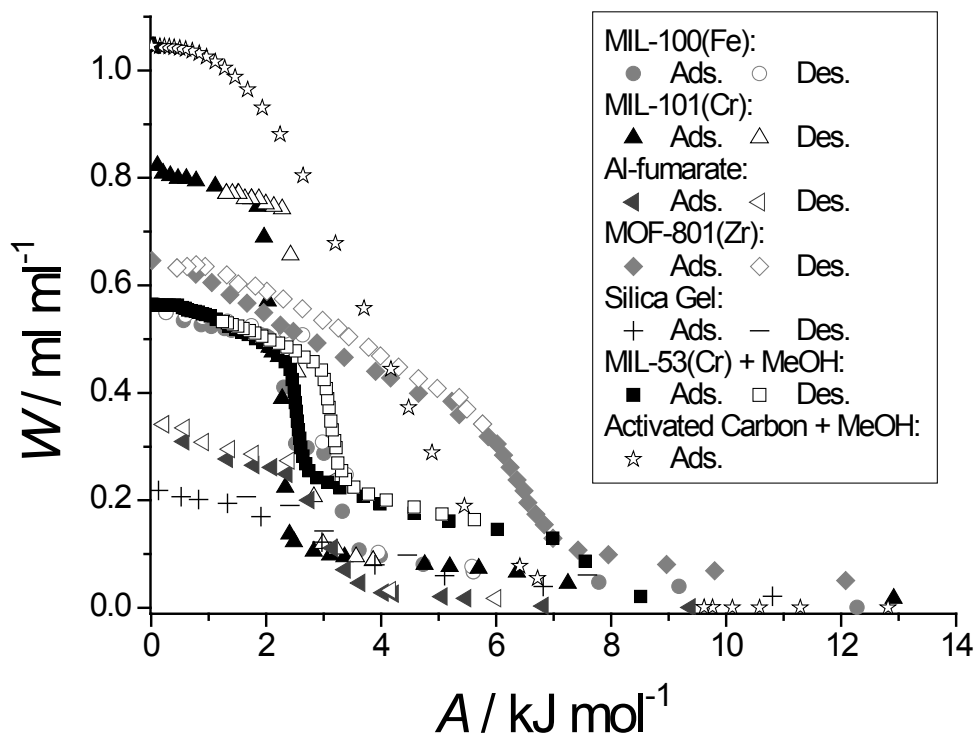
Figure C.2: Characteristic curves for materials not shown in main text. Data from literature for water and MIL-101(Cr) [2], MIL-100(Fe) [3], Al-fumarate [4], MOF-801(Zr) [5] and Silica gel [6], and for methanol and MIL-53(Cr) [7] and activated carbon (G32-H) [8].

C.2. CHARACTERISTIC CURVES

All characteristic curves not shown in the main text are given in Fig. C.2.

C.3. LINEAR INTERPOLATION SCHEME AND RESULTS FOR AQSOA-Z01 AND Z02

As indicated in the main text, the adsorption data of AQSOA-Z01 and Z02 do no collapse onto a single characteristic curve. Thus, there are three reported "characteristic curves" (W_1, W_2 and W_3) [9] measured at 3 different temperatures (T_1, T_2 and T_3), or adsorption potentials (A_1, A_2 and A_3). To span the amount adsorbed, W, for a large range of temperatures, especially important for desorption, a simple interpolation scheme has been devised. For $T \leq T_1$, amount adsorbed is simply calculated by adsorption potential, A, via:

$$W = W_1(A) \tag{C3.1}$$

For $T_1 < T \leq T_2$, the amount adsorbed can be determined via:

$$W = \left(\frac{T_2 - T}{T_2 - T_1} \right) W_1(A) + \left(\frac{T - T_1}{T_2 - T_1} \right) W_2(A) \tag{C3.2}$$

Equally, when $T_2 < T \leq T_3$, the amount adsorbed can be determined via:

$$W = \left(\frac{T_3 - T}{T_3 - T_2} \right) W_2(A) + \left(\frac{T - T_2}{T_3 - T_2} \right) W_3(A) \tag{C3.3}$$

Lastly, for $T > T_3$:

$$W = W_3(A) \tag{C3.4}$$

This scheme applies to both the ad- and desorption stage. For both AQSOA-Z01 and Z02 results in the main text are only shown for this linear interpolation scheme, the difference between said scheme and using either T_1, T_2 or T_3 for the calculation is given in Fig. C.3 for AQSOA-Z01 (heat pump conditions) and Z02 (refrigeration I).
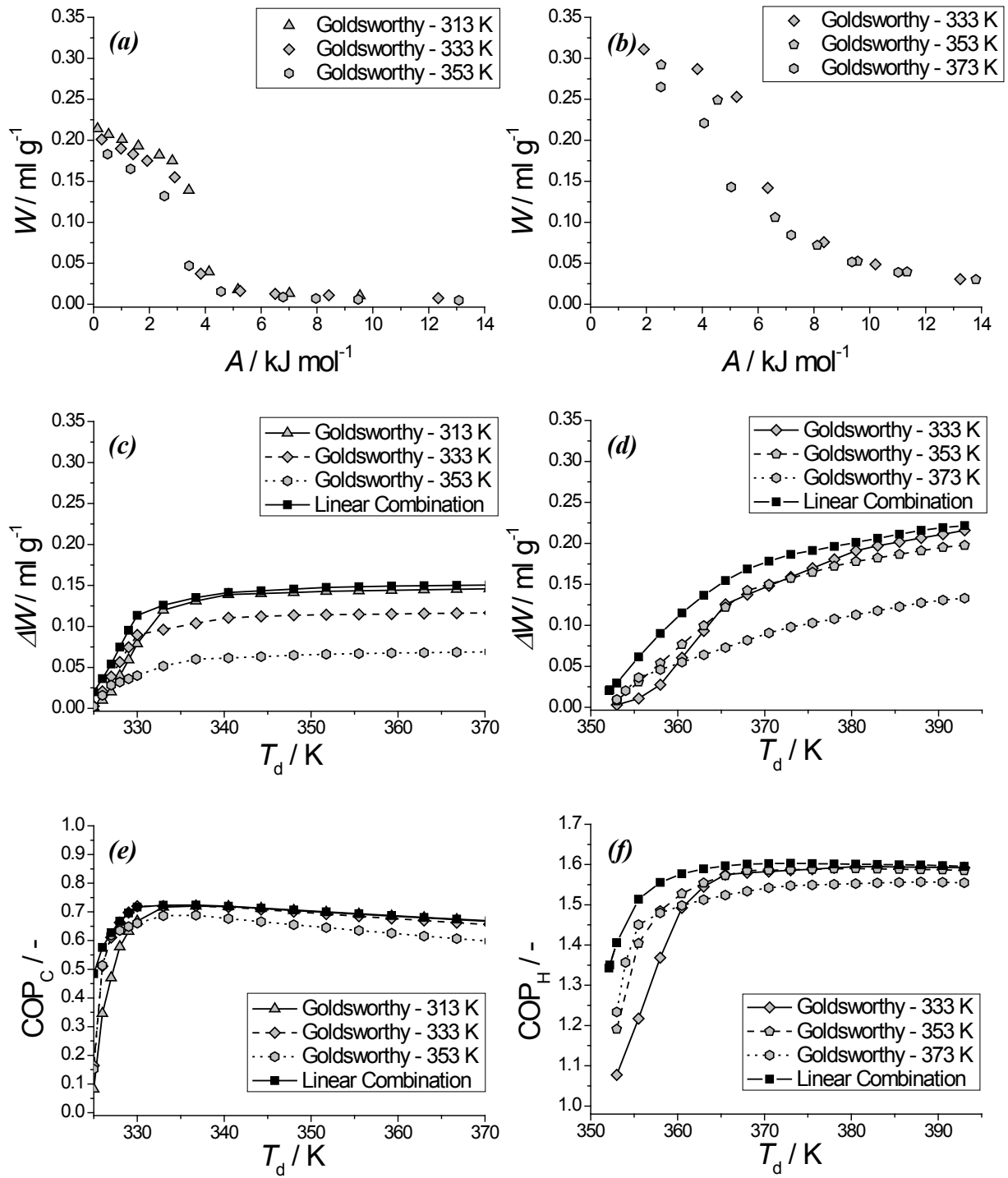
Figure C.3: Characteristic curves for different temperatures (*a, b*), working capacity (*c, d*) and coefficient of performance (*e, f*) for AQSOA-Z01 (*a, c, e*, refrigeration I) and AQSOA-Z02 (*b, d, f*, heat pump conditions).
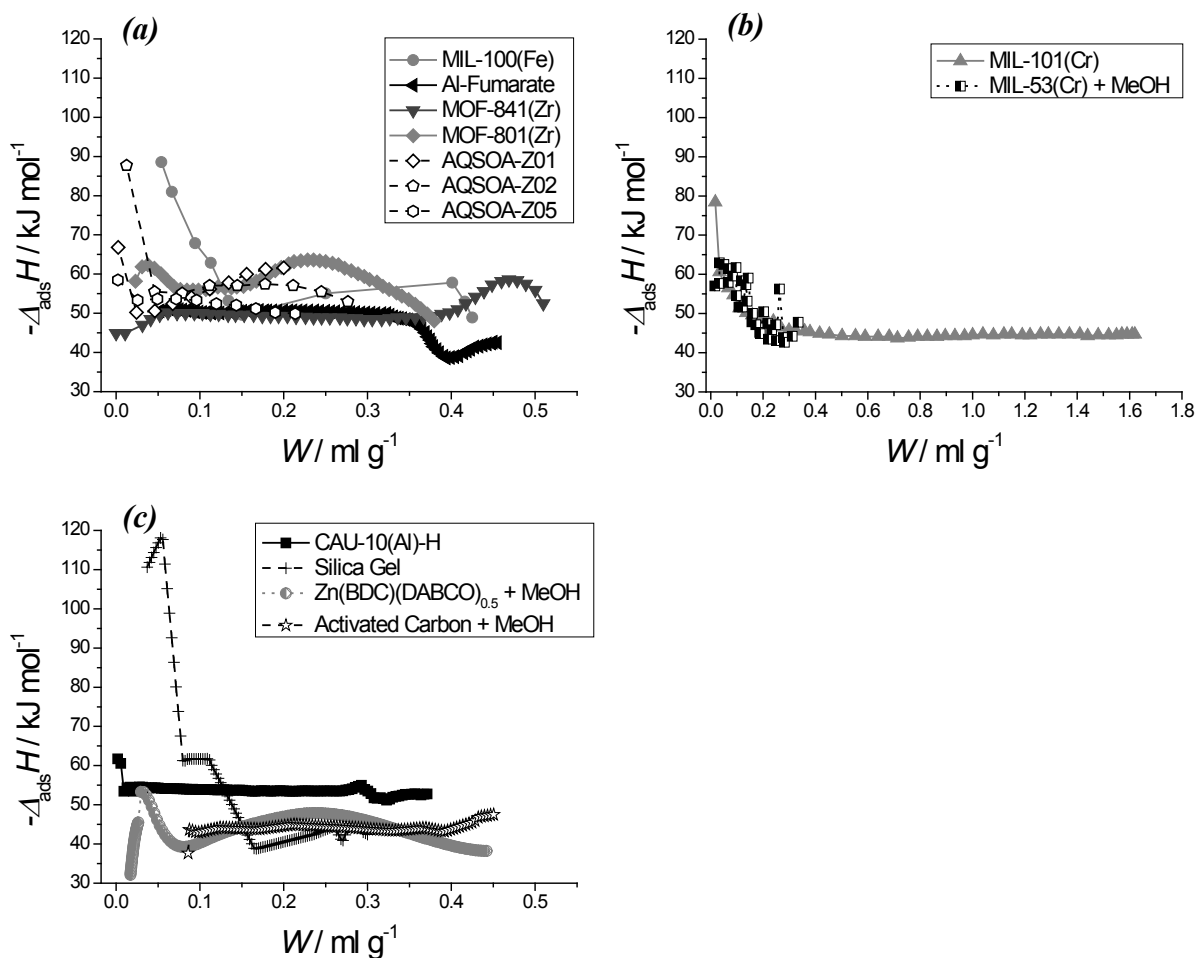
Figure C.4: Loading dependent enthalpy of adsorption for calorimetric measurements (*a*), approximated by the isosteric enthalpy of adsorption both as reported by other authors (*b*) and calculated in this work, based upon reported adsorption data (*c*). Data from literature for MIL-101(Cr) [2], MIL-53(Cr) [7], MIL-100(Fe) [3], Al-fumarate [4], MOF-841(Zr) [5], MOF-801(Zr) [5], AQSOA-Z01, Z02 and Z05 [9], Silica gel [6], Zn(BDC)(DABCO)$_{0.5}$ [10] and activated carbon (G32-H) [8].

C.4. ENTHALPY OF ADSORPTION

In Fig. C.4, the loading dependent enthalpy of adsorption as used in this work is shown for all materials under consideration.
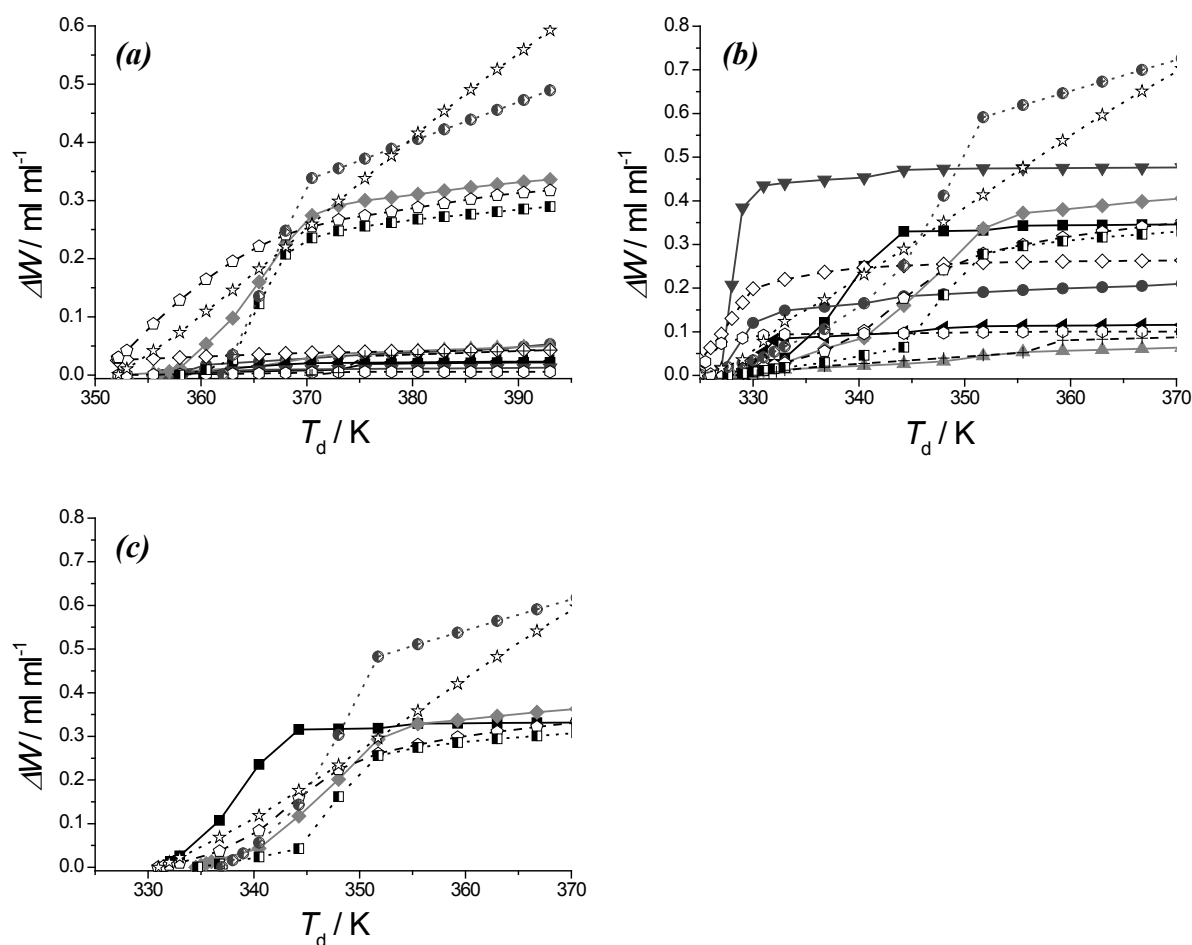
Figure C.5: Working volume adsorbed per volume adsorbent, ΔW, as function of desorption temperature, T_{des}, for heat pump (T_{ev} = 15 ^{o}C, T_{ads} = 45 ^{o}C, *a*), refrigeration I, (T_{ev} = 10 ^{o}C, T_{ads} = 30 ^{o}C, *b*) and refrigeration II (T_{ev} = 5 ^{o}C, T_{ads} = 30 ^{o}C, *c*). MOF-water working pairs, CAU-10(Al)-H (■), MIL-100(Fe) (●), MIL-101(Cr) (▲), Al-fumarate (◀), MOF-841(Zr) (▼) and MOF-801(Zr) (◆) with full lines. Benchmark-water pairs, Silica Gel (+), AQSOA-Z01 (◇), Z02(⬠), and Z05 (○) with dashed lines. Methanol-based working pairs, MIL-53(Cr) (▯), Zn(BDC)(DABCO)$_{0.5}$ (◖) and Activated Carbon (☆) with dotted lines.

C.5. WORKING CAPACITY OF ALL MATERIALS

For all materials considered, the working capacity under the three different conditions is given in Fig. C.5. In the main text, the poorly performing materials are omitted. For those, the COP is not reported as for low working capacities this is not a very meaningful quantity.
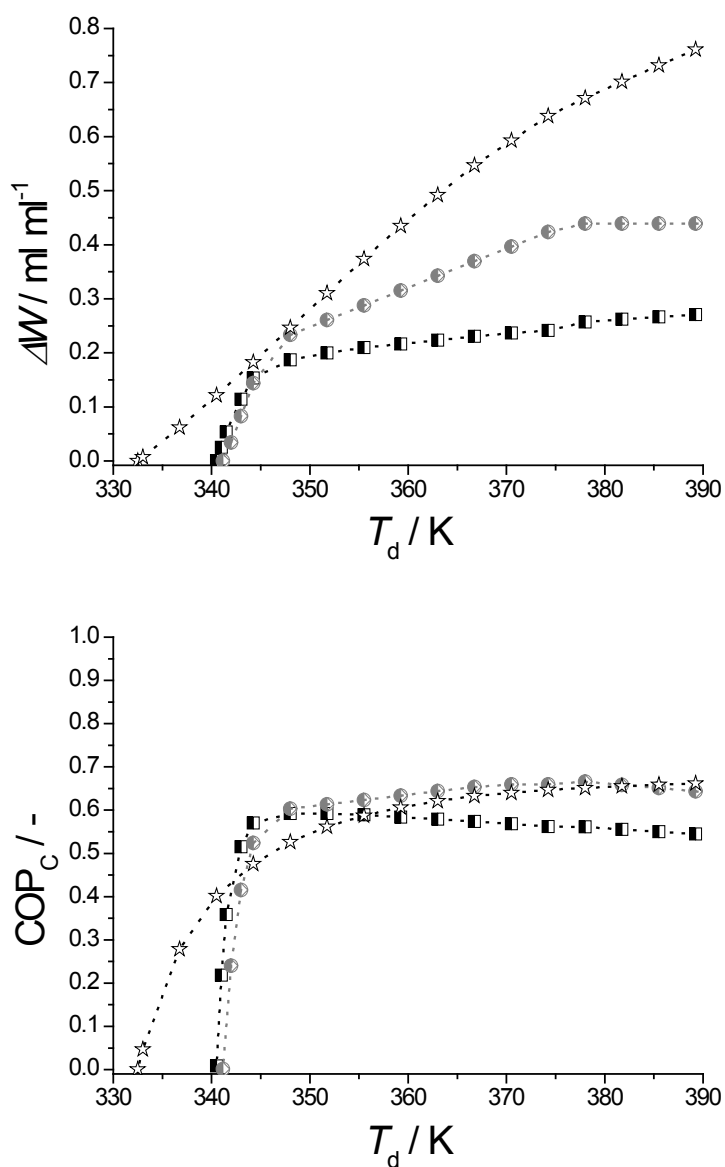
Figure C.6: Working volume adsorbed per volume adsorbent, ΔW (*top*) and coefficient of performance (*bottom*) as function of desorption temperature, T_{des}, for ice making (T_{ev} = -5 ^{o}C, T_{ads} = 25 ^{o}C). Only methanol-based working pairs, MIL-53(Cr) (▣), Zn(BDC)(DABCO)$_{0.5}$ (◖) and Activated Carbon (✿), are depicted.

C.6. WORKING CAPACITY AND COP FOR ICE-MAKING CONDITIONS

In Fig. C.6, the working capacity and COP at Ice-making conditions are given. As the evaporator is at subzero temperature, only methanol is considered as working fluid.

C.7. REFERENCES

[1]   D.W. Green, R.H. Perry, Perry's chemical engineers' handbook, 8th ed., McGraw-Hill, 2008.

[2]   J.-S. Chang, Porous metal(III) carboxylates as multifunctional adsorbents and catalytic materials, iCeMS-ERATO Symposium, July 26th, 2012.

[3]   F. Jeremias, A. Khutia, S.K. Henninger, C. Janiak, MIL-100(Al, Fe) as water adsorbents for heat transformation purposes - a promising application, Journal of Materials Chemistry, 22 (2012) 10148-10151.

[4]   F. Jeremias, D. Frohlich, C. Janiak, S.K. Henninger, Advancement of sorption-based heat transformation by a metal coating of highly-stable, hydrophilic aluminium fumarate MOF, RSC Advances, 4 (2014) 24073-24082.

[5]   H. Furukawa, F. Gándara, Y.-B. Zhang, J. Jiang, W.L. Queen, M.R. Hudson, O.M. Yaghi, Water adsorption in porous Metal-Organic Frameworks and related materials, Journal of the American Chemical Society, 136 (2014) 4369-4381.

[6]   R.L. Yeh, T.K. Ghosh, A.L. Hines, Effects of regeneration conditions on the characteristics of water vapor adsorption on silica gel, Journal of Chemical and Engineering Data, 37 (1992) 259-261.

[7]   S. Bourrelly, B.a. Moulin, A. Rivera, G. Maurin, S. Devautour-Vinot, C. Serre, T. Devic, P. Horcajada, A. Vimont, G. Clet, M. Daturi, J.-C. Lavalley, S. Loera-Serna, R. Denoyel, P.L. Llewellyn, G.r. Férey, Explanation of the adsorption of polar vapors in the highly flexible Metal Organic Framework MIL-53(Cr), Journal of the American Chemical Society, 132 (2010) 9488-9498.

[8]   S.K. Henninger, M. Schicktanz, P.P.C. Hügenell, H. Sievers, H.M. Henning, Evaluation of methanol adsorption on activated carbons for thermally driven chillers part I: Thermophysical characterisation, International Journal of Refrigeration, 35 (2012) 543-553.

[9]   M. Goldsworthy, Measurements of water vapour sorption isotherms for RD silica gel, AQSOA-Z01, AQSOA-Z02, AQSOA-Z05 and CECA zeolite 3A, Microporous and Mesoporous Materials, 196 (2014) 59-67.

[10]   J.Y. Lee, D.H. Olson, L. Pan, T.J. Emge, J. Li, Microporous Metal-Organic Frameworks with high gas sorption and separation capacity, Advanced Functional Materials, 17 (2007) 1255-1262.

CHAPTER 5

STRUCTURING Al-BASED MOFS FOR THE ALLOCATION OF HEAT AND COLD

ABSTRACT:

Several Al-based MOFs of the CAU family have been investigated for application in adsorption driven allocation of heat and cold. The special water adsorption behavior of CAU-10-H makes it ideal for this application. For increased performance, CAU-10-H crystals have been grown directly on both γ-alumina and metallic aluminium. Crystal growth on these surfaces can be controlled by the addition of acids.

5.1. INTRODUCTION

In combatting global warming, reduction of the energy consumption associated with the allocation of heat and cold can be of great importance. In the Netherlands, *e.g.*, roughly 38% of primary energy was consumed for these purposes, a total of $1.3 \cdot 10^{18}$ J in 2010 [1], the majority of which was generated by fossil fuels. In order to reduce CO_2 emissions, a transition to low-grade waste thermal energy, solar or geothermal energy for heat and cold allocation is highly desired. This can be achieved with adsorption driven heat pumps (AHPs) and -chillers (ADCs). These devices, pioneered by Faraday in 1848 [2], are based on reversible ad- and desorption of a working fluid [2, 3], instead of conventional vapor-compression [4]. Additionally, when H_2O is used as working fluid, AHPs/ADCs are intrinsically environmentally benign, a clear improvement over CFCs/HFCs used in vapor-compression counterparts. The heart of an AHP or ADC is the solid adsorbent, conventionally some type of zeolite or silica gel. In recent years however, metal-organic frameworks (MOFs) have gained increased attention in this field [3, 5-8], because of their tunable adsorption behavior and high loading capacity. For an acceptable operation window, a sorbent for AHPs/ADCs should adsorb a significant amount of H_2O at $0.05 \leq p/p_o \leq 0.3\text{-}0.35$ [3, 9, 10]. Furthermore, the adsorption isotherm should ideally have an s-shape and be devoid of hysteretic behavior, to enable desorption at low temperatures [9]. Obviously, the material should be stable and not degrade when subjected to H_2O. This is not a trivial requirement, as many MOFs degrade under (prolonged) exposure to water [11-15], Chapter 4. Last but not least, once an interesting adsorbent has been identified, heat- and mass transfer from and to the adsorbent should be optimized at the device level in order to realize a high specific power (Wg^{-1}). In case of zeolites, the use of coatings results in an improved performance over a packed bed (pellets) [16-19], because of superior heat transfer. In case of MOFs, deduced from scarce information on thermal conductivity [20, 21], it is likely that heat transfer will be a limiting factor as well. Thus, for application in AHPs/ADCs, it is highly desirable that the chosen material can be deposited on a heat exchanger-surface. Because of its natural abundance and low toxicity, aluminium would be a cost-effective metal to be used both as heat conducting surface and as metal-source for the MOF to be grown upon this interface. Recently, novel Al-based MOFs have been reported by Stock *et al.* [22-27], which have been investigated for application in adsorption-driven heat pumps in this communication. A series of potentially interesting CAU materials (CAU stands for Christian-Albrechts-Universität) were initially screened. In a

second step, the most interesting adsorbent based on its H_2O adsorption isotherm, has been interfaced on Al-based substrates. From the available Al-based CAUs, CAU-3 and CAU-6 were excluded *a priori* due to their high hydrophobicity and hydrophilicity, respectively [26, 27].

5.2. EXPERIMENTAL

5.2.1. MATERIALS

2-Aminoterephthalic acid (Aldrich, 99%), 2,5-hydroxyterephthalic acid (Aldrich, 97%), 4,4′-benzophenonedicarboxylic acid (TCI, 95%), isophthalic acid (Aldrich, 99%), 5-aminoisophthalic acid (Aldrich, 94%), 5-hydroxyisophthalic acid (TCI, 97%) $AlCl_3·6H_2O$ (Aldrich, 99%), $Al_2(SO_4)_3·18H_2O$ (Aldrich, 98%), α-alumina beads (~4mm, Alfa Aesar, 99%), γ-alumina beads (1-3 mm, 000-3p, Akzo Nobel), metallic aluminium foil (0.5 mm thick, Mateck, 99.999%), NaOH (Aldrich, 98%), methanol (Aldrich, 99.8%), DMF (Aldrich, 99.8%), acetic acid (Aldrich, 99.7%) and HCl solution (37% wt., Aldrich) were purchased from respective suppliers and were used without any further purification.

5.2.2. SYNTHESIS OF DIFFERENT CAU-MATERIALS

CAU-1

The synthesis of CAU-1 was performed according to literature [22], by suspending 379 mg of 2-aminoterephthalic acid and 1507 mg of $AlCl_3·6H_2O$ in 20 mL of methanol in a 30 mL Teflon insert. The mixture was heated for 5 hours at 125 °C. To sustain the pressure, the insert was put in a steel autoclave. The residue after filtration was a yellow powder. The as-synthesized powder was washed overnight with 500 mL of deionized water three times. The final suspension was filtered and the product was dried in air.

CAU-1-(OH)$_2$

Again literature procedure was followed to synthesize CAU-1-(OH)$_2$ [28]. A mixture of 1048 mg of $AlCl_3·6H_2O$, 299 mg of 2,5-hydroxyterephthalic acid, 36 mg of NaOH and 10 mL methanol was fitted in a 30 mL Teflon insert, which was placed in a stainless steel autoclave. Hereafter, the autoclave was placed in an oven for 5 hours at 125 °C. A yellow product was obtained after filtration. The synthesized product was thoroughly washed five times on the filter paper with demineralized water. The residue was dried in air to obtain CAU-1-(OH)$_2$.

CAU-8

The synthesis of CAU-8 was performed according to literature [29]. In a 30 mL Teflon insert, 2000 mg of 4,4′-benzophenonedicarboxylic acid, 2466 mg of $Al_2(SO_4)_3 \cdot 18H_2O$, 8 mL of deionized H_2O and 12 mL of DMF were mixed to a suspension. The insert was placed in an autoclave and heated up in the oven to 140 °C in 1 hour. The autoclave was kept at this temperature for 12 hours and then cooled down to room temperature. The reaction was followed by a filtration step. The obtained powder was thoroughly washed with 40 mL of DMF (Aldrich, 99.8%). After another filtration, the white solid was washed with water. Finally, the powder was dried in air.

CAU-10-H

According to literature [25], CAU-10-H was synthesized by adding 160 mg of isophthalic acid, 640 mg of $Al_2(SO_4)_3 \cdot 18H_2O$, 0.8 mL of DMF and 3.2 mL of H_2O to a Teflon insert, sealed within a stainless steel autoclave. The insert was placed in an oven, which was kept at 135 °C for 12 hours. The product, obtained from filtering, was dispersed in deionized water by sonication. The dispersion was filtered again and the white powder was dried in air under ambient conditions.

CAU-10-NH$_2$

A mixture of 360 mg of 5-aminoisophthalic acid (Aldrich, 94%), 477.6 mg of $AlCl_3 \cdot 6H_2O$ (Aldrich, 99%), 1.2 mL of DMF (Aldrich, 99.8%) and 4.8 mL of deionized H_2O was made to synthesize CAU-10-NH$_2$, as described in literature [25]. This mixture was made in a Teflon insert, which was placed in a stainless steel autoclave. The autoclave was kept at 120 °C for 12 hours in an oven. A pale pink solid was obtained. In similarity to the work-up of CAU-10-H, the solid was dispersed in deionized water by sonication for 30 minutes. The dispersion was filtered off and the residue was dried in air to obtain the final product.

CAU-10-OH

For the synthesis of CAU-10-OH, as adopted from literature [25], 4 mL of DMF and 16 mL of deionized H_2O with 1000 mg of 5-hydroxyisophthalic acid and 1352 mg of $AlCl_3 \cdot 6H_2O$ were mixed in a 30 mL Teflon insert within a steel autoclave. The autoclave was placed in an oven which was set to 120 °C for 12 hours. The residue of the following filtration was redispersed in deionized water by sonication for 30 minutes. After a final filtration, the product was obtained by drying in air.

5.2.3. SYNTHESIS OF CAU-10-H ON ALUMINA SUPPORTS

Synthesis of CAU-10-H on either α- or γ-alumina was performed by using the aluminium ions leached from the supports directly, effectively replacing $Al_2(SO_4)_3 \cdot 18H_2O$ by a molar equivalent amount of Al_2O_3. To have a satisfying amount of beads and to compensate for the fact that, effectively, not all alumina is involved in the reaction, this equivalent amount is doubled. This results in a Teflon insert filled with ~190 mg of either α- or γ-alumina, 160 mg of isophthalic acid, 0.8 mL of DMF and 3.2 mL of deionized H_2O. Additionally, to some of the synthesis mixtures either 0.11 ml acetic acid or 0.16 ml HCl solution (37% wt.) was added. The Teflon insert was then placed in a stainless steel autoclave and kept at 135 °C for 12 hours inside an oven. As there is an anticipated amount of excess organic linker on the alumina beads after synthesis, these were washed overnight with DMF to remove any unreacted isophthalic acid and subsequently washed overnight with H_2O to remove the DMF. Finally the beads were dried at 100 °C in air overnight.

5.2.4. SYNTHESIS OF CAU-10-H ON METALLIC ALUMINIUM

An aluminium square plate of 20 by 20 mm (~550 mg) with the corners cut off was placed in a Teflon insert. The molar ratios and reaction conditions were equivalent to the hydrothermal syntheses with γ-alumina (Section 5.2.3). Thus, again the decision was made to double the amount of moles of aluminium because evidently not all aluminium present will participate in the reaction. Due to the large amount of aluminium, the synthesis liquid volume is enlarged compared to Sections 5.2.2 and 5.2.3. To the Teflon insert containing the aluminium plate (~550 mg), 850 mg of isophthalic acid, 4.2 ml of DMF and 17 ml of deionized H_2O were added. Additionally, to some of the synthesis mixtures either 1.7 ml acetic acid or 1.7 ml HCl solution (37% wt.) was added. The Teflon insert was then placed in a stainless steel autoclave and kept at 135 °C for 12 hours inside an oven. Subsequently these plates were washed overnight with DMF and subsequently washed overnight with H_2O to remove the DMF. Finally the beads were dried at 100 °C in air overnight.

5.2.5. CHARACTERIZATION

N_2 adsorption at 77 K was measured on a Quantachrome Autosorb-6B with equilibration time of 2 minutes. Prior to adsorption measurements, samples were degassed for 16 hours at temperatures varying between 150 °C and 250 °C under vacuum. The exact temperature of degassing was chosen in accordance with TGA data of a specific sample.

H_2O adsorption was measured on a Quantachrome Autosorb-1 with an equilibration time of 10 minutes, with installed vapor capability. Pretreatment was the same as for N_2 adsorption. For the repeated adsorption measurements, samples were pretreated *ex situ* between subsequent measurements.

XRD measurements were carried out on a PANalytical X'pert PRO diffractometer. The machine used a Co-$K\alpha$ X-ray source, operating at 45 kV and 40 mA. Thermo-gravimetric analysis (TGA) was measured on a Mettler Toledo TGA/SDTA 851e. The samples were heated in air from room temperature to 800 °C with a rate of 5 °C/h. The measurement device is equipped with simultaneous differential thermal analysis (SDTA). Scanning electron microscopy (SEM) microscopy was performed with either Philips XL20 or Jeol JSM 6010AL.

5.3. RESULTS AND DISCUSSION

Characterization and water adsorption behavior of the different CAU-materials synthesized are discussed both in Section 5.3.1. The most promising material is selected for further studies attempting to grow this MOF subsequently on aluminium oxide beads (Section 5.3.2) and metallic aluminium plate supports (Section 5.3.3)

5.3.1. SYNTHESIS OF DIFFERENT CAU-MATERIALS

CAU-1, CAU-1-$(OH)_2$, CAU-8, CAU-10-H, CAU-10-NH_2 and CAU-10-OH have been synthesized successfully, based on both X-ray diffraction patterns and nitrogen adsorption isotherms (Fig. 5.1). Congruency of both analyses with those reported is found [22-25]. TGA- and SDTA analyses further confirm purity of the obtained materials (Fig. D.1).
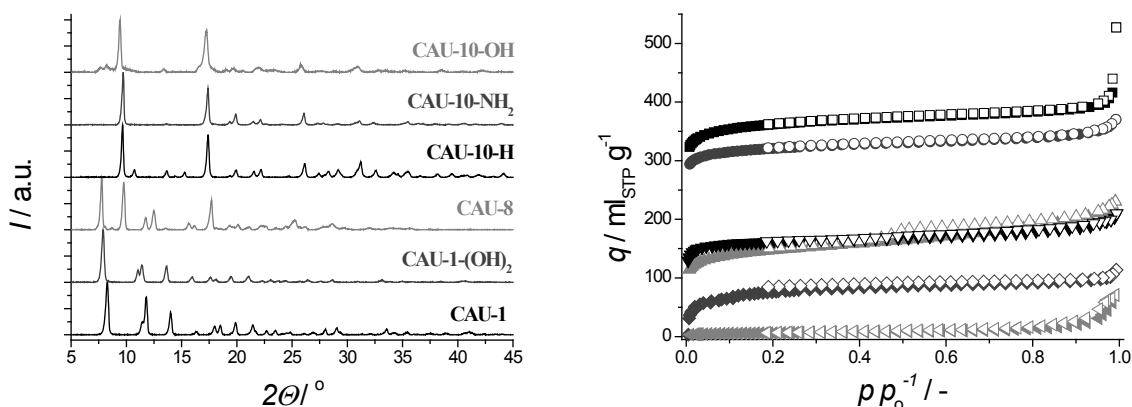
Figure 5.1: X-ray diffraction patterns of all synthesized materials (*left*) and N_2 physisorption at 77 K (*right*) for CAU-1 (■), CAU-1-(OH)$_2$ (●), CAU-8 (▲), CAU-10-H (▼), CAU-10-NH$_2$ (◆) and CAU-10-OH (◀). Closed symbols represent adsorption, open desorption. STP refers to standard pressure and temperature (0 $^{\circ}$C, 1 bar) and p_o to the saturated vapor pressure at measurement temperature.

Table 5.1: Reported and measured pore volumes of materials under investigation, all determined at $p/p_o = 0.5$.

Material	V_p (lit.) / ml g^{-1}	V_p (this work) / ml g^{-1}
CAU-1	0.64 [22]	0.61
CAU-1-(OH)$_2$	0.50 [28]	0.50
CAU-8	0.23 [29]	0.25
CAU-10-H	0.25 [25]	0.25
CAU-10-NH$_2$	-	0.13
CAU-10-OH	-	-

Lastly, the calculated pore volumes (Table 5.1), which, following the guidelines of Chapter 2, are nearly identical to those reported in literature, especially when considering the uncertainties that are present in these materials (Chapter 2). The exception here is CAU-10-NH$_2$, for which the original authors could not accurately measure the N_2 uptake due to slow equilibration. This apparently was less of an issue for the sample synthesized and characterized in this work. The water adsorption isotherms of these materials are shown in Fig. 5.2.
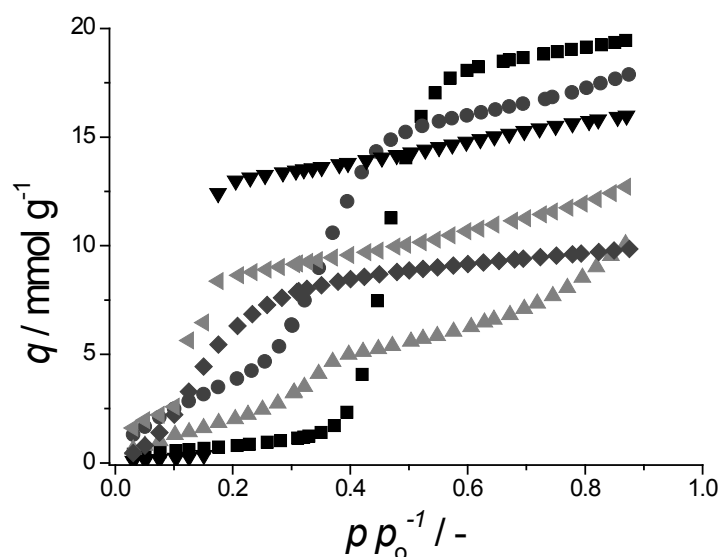
Figure 5.2: Water adsorption isotherms at 298 K of CAU-1 (■), CAU-1-(OH)$_2$ (●), CAU-8 (▲), CAU-10-H (▼), CAU-10-NH$_2$ (◆) and CAU-10-OH (◀).

Clearly, CAU-1, containing octameric $[Al_8(OH)_4 (OCH_3)_8]^{12+}$ clusters connected with 2-aminoterephthalic acid ligands, displays a beneficial S-shaped isotherm, but the amount adsorbed at $p/p_o \leq 0.35$ is rather low. When the organic ligand is changed to 2,5-hydroxyterephthalic acid (CAU-1-(OH)$_2$), adsorption is moderately higher for $p/p_o \leq 0.35$, but the undesired inclination in adsorption at low p/p_o would require an undesirably high temperature in the desorption step. CAU-8, consisting of $[Al-OH]^{2+}$ chains connected through 4,4′-benzophenonedicarboxylic acid, shows a very particular adsorption behavior, the isotherm seemingly being composed of two separate type III isotherms (IUPAC-classification) [30, 31]. The low uptake at $p/p_o \leq 0.35$, however, renders it of little use for the application at hand. On the other hand, the very narrow step in p/p_o for CAU-10-H, comprised of $[Al-OH]^{2+}$ chains linked together by isophthalic acid, makes it an ideal material for the target application. Functionalization of this framework with either amino- or hydroxyl-groups results in a less desired behavior due to the inclined adsorption at low p/p_o. Summarizing, in view of its outstanding thermal stability (Fig. D.1), its isotherm shape, its large adsorption capacity and the absence of hysteresis, CAU-10-H is a promising adsorbent for application in adsorption driven allocation of heat and cold. Furthermore, with an average isosteric heat of adsorption of about -53.5 kJ mol^{-1} (Chapter 4), regeneration of CAU-10-H is less energy-intensive than of current benchmark adsorbents used in ADH/ADC's [32], and commercialized by Mitsubishi Plastics, *e.g.* FAM Z01 [33], Z02 [34] and Z05 [35]. In

comparison, CAU-10-H shows the same advantageous S-shaped isotherm as FAM Z01 and Z05, but has a higher adsorption capacity.

5.3.2. CAU-10-H ON ALUMINA SUPPORTS

In order to further explore the applicability of CAU-10-H, the growth of this MOF on different surfaces was studied in detail. The procedure to create a coating of CAU-10-H, based on the work of Reboul *et al.* [36], is to dissolve aluminium ions from the support, directing crystal growth towards the interface with the linker in solution (without adding an additional aluminium-source). In addition, to facilitate crystal growth, the effect of adding either acetic or hydrochloric acid is investigated. Both low pH and carboxylate species aid in the dissolution of metal ions from oxides [37]. Furthermore, carboxylic acids are commonly used as modulators in the synthesis of MOF crystals [38-41], and the addition of HCl has been found beneficial in the synthesis of certain MOFs [42].

Applying the proposed synthesis protocol to γ-alumina beads (Section 5.2.3) proved successful in forming crystals attached to the external surface, as can be seen from SEM microscopy shown in Fig. 5.3. The surface coverage becomes more homogeneous when acetic acid is added and even more homogeneity is observed when HCl is used. For HCl, the surface seems to be completely covered with crystals. TGA/SDTA confirms that there is no excess of organic ligands present (Fig. D.3) and that the thermal stability of the crystals is equal to that of CAU-10-H. We speculate that the use of a non-coordinating, stronger acid is more beneficial because: (i) dissolution of Al is more efficient at lower pH and (ii) slower deprotonation of the linker and the absence of other coordinating moieties (like acetates) favor the formation of more homogeneous, smaller crystals. Furthermore, it might be the case that formation of HCl-DMF complexes could have a beneficial effect on growth kinetics, as was shown for other Al-based MOFs [43]. Assuming that, after solvent removal, all weight loss is due to decomposition of the MOF on the support, the loading of CAU-10-H would be roughly 33, 34, and 38 wt.% for the beads without acid, with acetic acid, and with HCl, respectively. XRD-analysis of these beads (Fig. 5.4) confirms that these crystals are CAU-10-H.
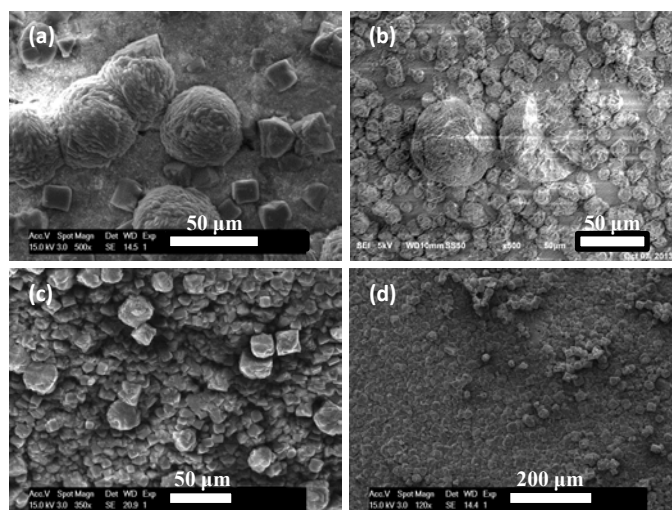
Figure 5.3: SEM images of CAU-10-H synthesized on γ-alumina beads without any acid (*a*), with addition of acetic acid (*b*) and with addition of hydrochloric acid (*c,d*).
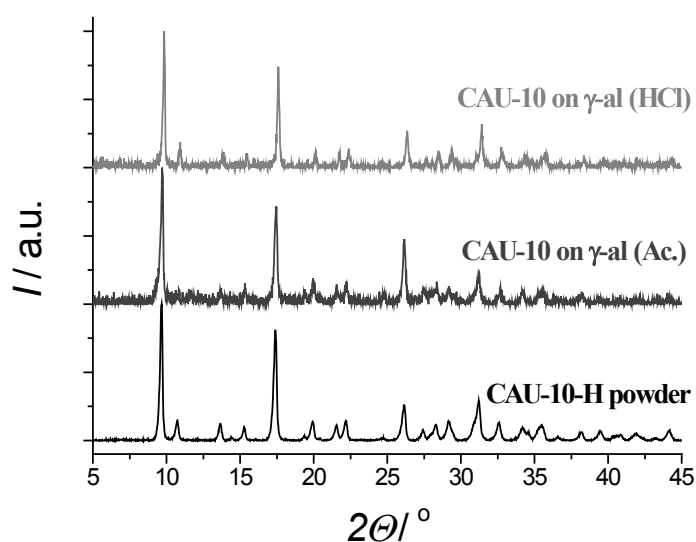
Figure 5.4: X-ray diffraction patterns of synthesized CAU-10-H and CAU-10-H synthesized on γ-alumina either with acetic acid or hydrochloric acid. No clear pattern could be collected from a bead after synthesis without any acid addition.

All coated supports with CAU-10-H contain more micropores, at the expense of mesoporosity, compared to parent γ-alumina (Fig. D.4). More importantly, the characteristic step in H_2O adsorption is retained for these beads (Fig. 5.5).
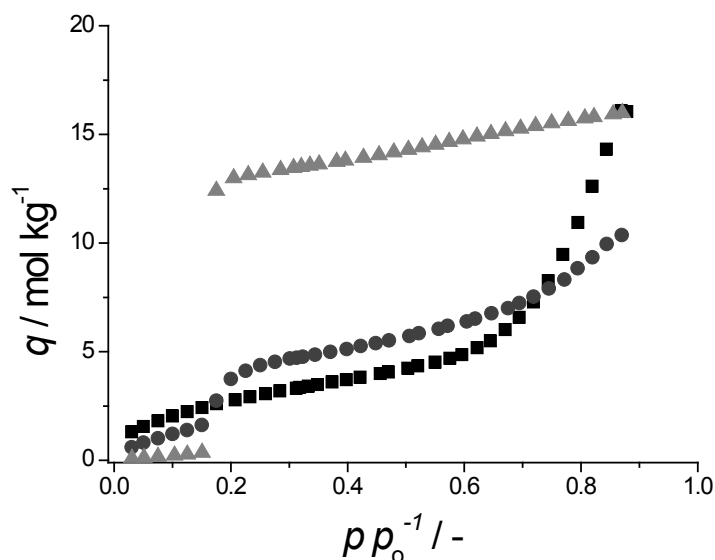
Figure 5.5: H_2O adsorption isotherms at 298 K of γ-alumina (■), CAU-10-H on γ-alumina with HCl (●) and for comparison CAU-10-H of the pure powder sample (▲).

Cracking a bead of CAU-10-H (HCl synthesis) showed that growth occurs exclusively on the external surface, as the interior seemed devoid of any crystals (Fig. D.7). This means in turn that achievable loading of such beads depends on the surface-to-volume ratio.

Syntheses on α-alumina were found unsuccessful (Fig. D.5). Crystal growth, if any, could hardly be observed on these supports. This is attributed to the higher stability of α-alumina compared to γ-alumina, and thus the higher resistance to acid leaching.

5.3.3. CAU-10-H ON METALLIC ALUMINIUM

The promising results of CAU-10-H supported on γ-alumina serve as starting point for further investigation, as porous metal-oxides themselves are not good heat conductive interfaces. For AHPs/ADCs, it is desired to have a MOF-layer grown directly on a metallic support. For CAU-10-H, one could opt to create a layer of Al_2O_3 on top of an aluminium surface prior to synthesis, so that the oxide-layer can be converted into MOF crystals. Here, attempts have been made to directly grow CAU-10-H crystals on top of aluminium without any pre-treatment, by extracting the metal ions required for the MOF from the support. Again, the effect of acid addition was studied (see Section 5.2.3 for details). Note that, on any aluminium surface exposed to atmospheric oxygen, a natural oxide layer of around 4 nm is present [44].
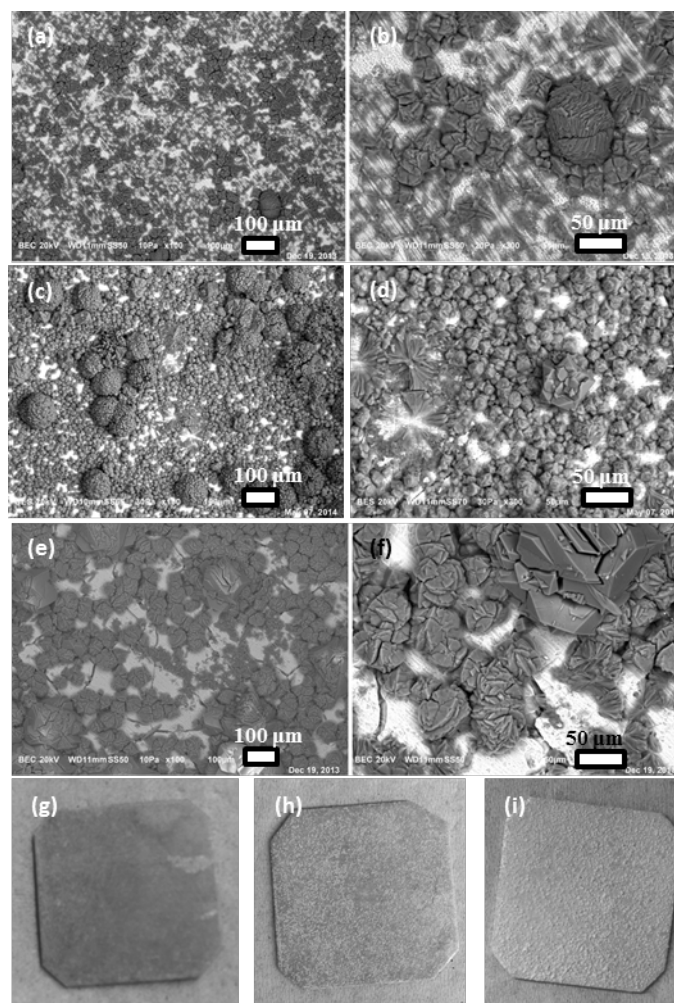
Figure 5.6: SEM-images of CAU-10 synthesized directly on metallic aluminium both without using any additional acid during synthesis (*a,b*), using acetic acid (*c,d*) and using hydrochloric acid (*e,f*). Photographs of (2 by 2 cm) aluminium plates after synthesis without acid (*g*), with acetic acid (*h*) and with hydrochloric acid (*i*).

As indicated by SEM microscopy in Fig. 5.6, crystals are formed on the metal surface. Similar to what was found for γ-alumina beads, the introduction of acid improves coverage. This can even be concluded by regular images of the Al-support after synthesis (Fig. 5.6g-i). Furthermore, it seems for the synthesis where HCl is added, that there are microscopic grooves on the aluminium surface, due to the dissolution of Al^{3+} ions. Most likely, aluminium is dissolved preferentially from local aluminium crystal boundaries in the metallic support.
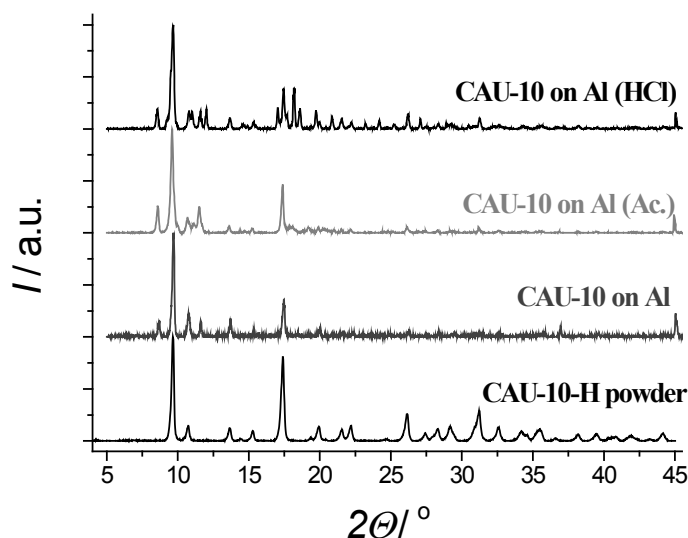
Figure 5.7: XRD diffraction patterns of synthesized CAU-10-H (powder) and CAU-10-H synthesized on metallic aluminium, using no acid, acetic acid or hydrochloric acid.

Comparing the hydrochloric acid-aided syntheses of γ-alumina and metallic aluminium, the crystal size of the rhombic particles on the latter seems larger, and there are more crystal agglomerates. Future endeavors should be directed to optimizing further homogeneous crystal growth on the surface. XRD confirms the presence of CAU-10-H (Fig. 5.7), albeit that there seem to be a minor reflection contribution of an unknown secondary crystal phase, also observed when HCl is added to the bulk synthesis of CAU-10-H (Fig. D.9).

During the experiments leading to the discovery of CAU-10-H, it was stated that a secondary phase was observed for molar ratio of Al^{3+}:Ligand > 3, however no characterization of this secondary phase was given for comparison [25].

To assess the adsorptive capacities of the CAU-10-H coating, the hydrochloric acid-aided synthesis was repeated on an aluminium plate that was *a priori* rolled into a cylindrical shape, to make the resulting coating measurable in a volumetric adsorption set-up. Subsequently, five water ad- and desorption measurements were performed, as shown in Fig. 5.8.

The shape of the adsorption isotherm of CAU-10-H coated on aluminium is strikingly similar to that of the bulk-phase (Fig. 5.2). The only minor difference is the stronger inclination of adsorbed water at p/p_o > 0.2, after the steep step in water uptake. Furthermore, an observed closure of the desorption loop at $p/p_o \sim$ 0.35, not attributable to the CAU-10-H structure, is likely to be due to water condensation in mesopores [45].

267
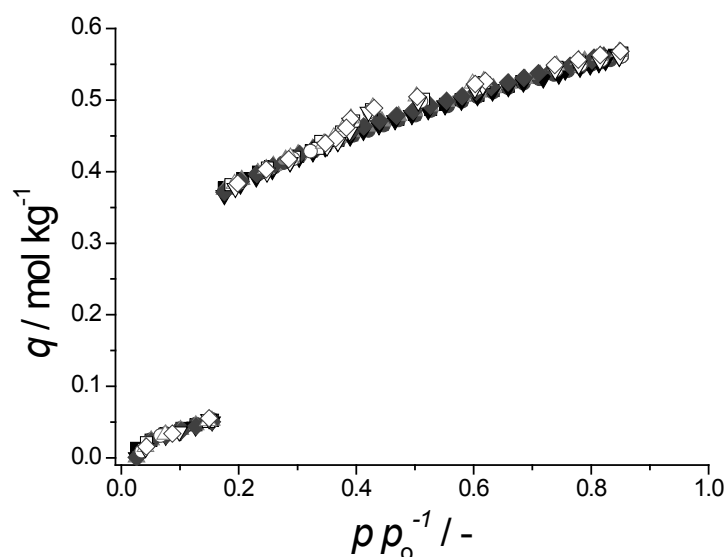
Figure 5.8: Repeated H_2O adsorption isotherms at 298 K of CAU-10 supported on a metallic aluminium plate. First (■), second (●), third (▲), fourth (▼) and fifth (♦) measurement. Closed symbols depict adsorption, open desorption. Loading presented per total mass of sample (Al substrate + CAU-10-H).

Whether this mesoporosity is caused by the secondary phase observed or by condensation of water in inter-particle spaces is unclear. More importantly, there is no desorption hysteresis in the region of the large step in water uptake, a feature highly desirable for the target application. Furthermore, these measurements indicate clearly that there is no loss of capacity, as the adsorption behavior is identical for all measurements. This makes that the coated CAU-10-H is perfectly stable, at least for 5 cycles of ad- and desorption of water.

Note that the quantity adsorbed is based on the total mass of the sample (MOF and aluminium plate). Due to the synthesis procedure and the fact that both substrate and MOF contain aluminium, direct quantification of the loading of CAU-10-H turned out to be difficult. As MOF crystals are grown on a flat metal surface rather than in a porous medium, expressing the content of MOF as (weight-)fraction relative to bulk aluminium would not yield a representative figure of merit. These measurements however, do indicate that with a coating as in Fig. 5.8 up to 38 kJ of heat can be withdrawn in the evaporator of an AHP/ADC per square meter of coated aluminium surface.

5.4. CONCLUSIONS

Of the aluminium-based Metal-Organic Frameworks (MOFs) investigated for application in adsorption driven heat pumps (AHPs) and chillers (ADCs), CAU-10-H has shown to have ideal adsorptive properties. Growth of CAU-10-H crystals directly on γ-alumina supports was achieved by using aluminium ions from the substrate as metal source for the MOF. Addition of acids improves the growth of these crystals. Especially hydrochloric acid has a beneficial effect on surface coverage and homogeneity of the formed crystal size and shape. The same approach has been successfully applied to coat CAU-10-H directly on metallic aluminium, which is highly desired for the target application. Again HCl has a beneficial effect on crystal growth. The adsorptive properties of CAU-10-H are similar to that of the bulk material and the coating showed to be stable in at least 5 water adsorption-desorption cycles.

5.5. REFERENCES

[1]   Agentschap NL, Warmte in Nederland, publ. Nr. 2necw1003.
        http://www.rvo.nl/sites/default/files/Warmte%20en%20Koude%20NL%202NECW1202%20jan13.pdf
        (accessed 17-01-2015).
[2]   R. Critoph, Y. Zhong, Review of trends in solid sorption refrigeration and heat pumping technology,
        Proceedings of the Institution of Mechanical Engineers, Part E: Journal of Process Mechanical
        Engineering, 219 (2005) 285-300.
[3]   S.K. Henninger, F. Jeremias, H. Kummer, C. Janiak, MOFs for use in adsorption heat pump processes,
        European Journal of Inorganic Chemistry, (2011) n/a-n/a.
[4]   M.J. Moran, H.N. Shapiro, Fundamentals of engineering thermodynamics, 5th ed., Wiley, 2006.
[5]   S.K. Henninger, H.A. Habib, C. Janiak, MOFs as adsorbents for low temperature heating and cooling
        applications, Journal of the American Chemical Society, 131 (2009) 2776-2777.
[6]   C.R. Wade, T. Corrales-Sanchez, T.C. Narayan, M. Dincă, Postsynthetic tuning of hydrophilicity in
        pyrazolate MOFs to modulate water adsorption properties, Energy & Environmental Science, 6 (2013)
        2172-2177.
[7]   G. Akiyama, R. Matsuda, S. Kitagawa, Highly porous and stable coordination polymers as water
        sorption materials, Chemistry Letters, 39 (2010) 360-361.
[8]   G. Akiyama, R. Matsuda, H. Sato, A. Hori, M. Takata, S. Kitagawa, Effect of functional groups in
        MIL-101 on water sorption behavior, Microporous and Mesoporous Materials, 157 (2012) 89-93.
[9]   Y.I. Aristov, Challenging offers of material science for adsorption heat transformation: A review,
        Applied Thermal Engineering, 50 (2013) 1610-1618.
[10]   M. Wickenheisser, F. Jeremias, S.K. Henninger, C. Janiak, Grafting of hydrophilic ethylene glycols or
        ethylenediamine on coordinatively unsaturated metal sites in MIL-100(cr) for improved water
        adsorption characteristics, Inorganica Chimica Acta, 407 (2013) 145-152.
[11]   J.J. Low, A.I. Benin, P. Jakubczak, J.F. Abrahamian, S.A. Faheem, R.R. Willis, Virtual high throughput
        screening confirmed experimentally: Porous coordination polymer hydration, Journal of the American
        Chemical Society, 131 (2009) 15834-15842.
[12]   P.M. Schoenecker, C.G. Carson, H. Jasuja, C.J.J. Flemming, K.S. Walton, Effect of water adsorption on
        retention of structure and surface area of Metal-Organic Frameworks, Industrial & Engineering
        Chemistry Research, 51 (2012) 6513-6519.
[13]   P. Küsgens, M. Rose, I. Senkovska, H. Fröde, A. Henschel, S. Siegle, S. Kaskel, Characterization of
        Metal-Organic Frameworks by water adsorption, Microporous and Mesoporous Materials, 120 (2009)
        325-330.

[14]   K.A. Cychosz, A.J. Matzger, Water stability of microporous coordination polymers and the adsorption of pharmaceuticals from water, Langmuir, 26 (2010) 17198-17202.

[15]   F. Jeremias, V. Lozan, S.K. Henninger, C. Janiak, Programming MOFs for water sorption: Amino-functionalized MIL-125 and UiO-66 for heat transformation and heat storage applications, Dalton Transactions, 42 (2013) 15967-15973.

[16]   G. Restuccia, A. Freni, G. Maggio, A zeolite-coated bed for air conditioning adsorption systems: Parametric study of heat and mass transfer by dynamic simulation, Applied Thermal Engineering, 22 (2002) 619-630.

[17]   L. Bonaccorsi, P. Bruzzaniti, L. Calabrese, A. Freni, E. Proverbio, G. Restuccia, Synthesis of SAPO-34 on graphite foams for adsorber heat exchangers, Applied Thermal Engineering, 61 (2013) 848-852.

[18]   B. Dawoud, Water vapor adsorption kinetics on small and full scale zeolite coated adsorbers; a comparison, Applied Thermal Engineering, 50 (2013) 1645-1651.

[19]   M. Tatlıer, B. Tantekin-Ersolmaz, A. Erdem-Şenatalar, A novel approach to enhance heat and mass transfer in adsorption heat pumps using the zeolite–water pair, Microporous and Mesoporous Materials, 27 (1999) 1-10.

[20]   B.L. Huang, Z. Ni, A. Millward, A.J.H. McGaughey, C. Uher, M. Kaviany, O. Yaghi, Thermal conductivity of a Metal-Organic Framework (MOF-5): Part II. Measurement, International Journal of Heat and Mass Transfer, 50 (2007) 405-411.

[21]   D. Liu, J. Purewal, J. Yang, A. Sudik, S. Maurer, U. Mueller, J. Ni, D. Siegel, MOF-5 composites exhibiting improved thermal conductivity, International Journal of Hydrogen Energy, 37 (2012) 6109-6117.

[22]   T. Ahnfeldt, N. Guillou, D. Gunzelmann, I. Margiolaki, T. Loiseau, G. Férey, J. Senker, N. Stock, $[Al_4(OH)_2(OCH_3)_4(H_2N-BDC)_3]\cdot x\ H_2O$: A 12-connected porous Metal-Organic Framework with an unprecedented aluminum-containing brick, Angewandte Chemie International Edition, 48 (2009) 5163-5166.

[23]   T. Ahnfeldt, J. Moellmer, V. Guillerm, R. Staudt, C. Serre, N. Stock, High-throughput and time-resolved energy-dispersive X-ray diffraction (EDXRD) study of the formation of $CAU-1-(OH)_2$: Microwave and conventional heating, Chemistry-a European Journal, 17 (2011) 6462-6468.

[24]   H. Reinsch, M. Krüger, J. Marrot, N. Stock, First keto-functionalized microporous Al-based Metal-Organic Framework: $[Al(OH)(O_2C-C_6H_4-CO-C_6H_4-CO_2)]$, Inorganic Chemistry, 52 (2013) 1854-1859.

[25]   H. Reinsch, M.A. van der Veen, B. Gil, B. Marszalek, T. Verbiest, D. de Vos, N. Stock, Structures, sorption characteristics, and nonlinear optical properties of a new series of highly stable aluminum MOFs, Chemistry of Materials, 25 (2012) 17-26.

[26]   H. Reinsch, M. Feyand, T. Ahnfeldt, N. Stock, CAU-3: A new family of porous MOFs with a novel Al-based brick: $[Al_2(OCH_3)_4(O_2C-x-CO_2)]$ (x = aryl), Dalton Transactions, 41 (2012) 4164-4171.

[27]   H. Reinsch, B. Marszalek, J. Wack, J. Senker, B. Gil, N. Stock, A new Al-MOF based on a unique column-shaped inorganic building unit exhibiting strongly hydrophilic sorption behaviour, Chemical Communications, 48 (2012) 9486-9488.

[28]   T. Ahnfeldt, J. Moellmer, V. Guillerm, R. Staudt, C. Serre, N. Stock, High-throughput and time-resolved energy-dispersive x-ray diffraction (EDXRD) study of the formation of $CAU-1-(OH)_2$: Microwave and conventional heating, Chemistry – A European Journal, 17 (2011) 6462-6468.

[29]   H. Reinsch, M. Krüger, J. Marrot, N. Stock, First keto-functionalized microporous Al-based Metal-Organic Framework:$[Al(OH)(O_2C-C_6H_4-CO-C_6H_4-CO_2)]$, Inorganic chemistry, 52 (2013) 1854-1859.

[30]   K. Sing, D. Everett, R. Haul, L. Moscou, R. Pierotti, J. Rouquerol, T. Siemieniewska, Reporting physisorption data for gas/solid systems, Pure and Applied Chemistry, 54 (1982) 2201.

[31]   R. Pierotti, J. Rouquerol, Reporting physisorption data for gas/solid systems with special reference to the determination of surface area and porosity, Pure and Applied Chemistry, 57 (1985) 603-619.

[32]   M. Goldsworthy, Measurements of water vapour sorption isotherms for RD silica gel, AQSOA-Z01, AQSOA-Z02, AQSOA-Z05 and CECA zeolite 3A, Microporous and Mesoporous Materials, 196 (2014) 59-67.

[33]   H. Kakiuchi, S. Shimooka, M. Iwade, K. Oshima, M. Yamazaki, S. Terada, H. Watanabe, T. Takewaki, Novel water vapor adsorbent FAM-Z01 and its applicability to an adsorption heat pump, Kagaku Kogaku Ronbunshu, 31 (2005) 361-364.

[34]   H. Kakiuchi, S. Shimooka, M. Iwade, K. Oshima, M. Yamazaki, S. Terada, H. Watanabe, T. Takewaki, Water vapor adsorbent FAM-Z02 and its applicability to adsorption heat pump, Kagaku Kogaku Ronbunshu, 31 (2005) 273-277.

[35]   S. Shimooka, K. Oshima, H. Hidaka, T. Takewaki, H. Kakiuchi, A. Kodama, M. Kubota, H. Matsuda, The evaluation of direct cooling and heating desiccant device coated with FAM, Journal of Chemical Engineering of Japan, 40 (2007) 1330-1334.

[36] J. Reboul, S. Furukawa, N. Horike, M. Tsotsalas, K. Hirai, H. Uehara, M. Kondo, N. Louvain, O. Sakata, S. Kitagawa, Mesoscopic architectures of porous coordination polymers fabricated by pseudomorphic replication, Nature materials, 11 (2012) 717-723.

[37] W. Stumm, R. Wollast, Coordination chemistry of weathering: Kinetics of the surface-controlled dissolution of oxide minerals, Reviews of Geophysics, 28 (1990) 53-69.

[38] A. Schaate, P. Roy, A. Godt, J. Lippke, F. Waltz, M. Wiebcke, P. Behrens, Modulated synthesis of Zr-based Metal-Organic Frameworks: From nano to single crystals, Chemistry – A European Journal, 17 (2011) 6643-6651.

[39] H. Guo, Y. Zhu, S. Wang, S. Su, L. Zhou, H. Zhang, Combining coordination modulation with acid-base adjustment for the control over size of Metal-Organic Frameworks, Chemistry of Materials, 24 (2012) 444-450.

[40] J.M. Chin, E.Y. Chen, A.G. Menon, H.Y. Tan, A.T.S. Hor, M.K. Schreyer, J. Xu, Tuning the aspect ratio of NH_2-MIL-53(Al) microneedles and nanorods via coordination modulation, CrystEngComm, 15 (2013) 654-657.

[41] A. Morsali, M.A. Alavi, Synthesis and characterization of different nanostructured copper (II) Metal-Organic Frameworks by ligand functionalization and modulation method, CrystEngComm, 16 (2014) 2246-2250.

[42] M.J. Katz, Z.J. Brown, Y.J. Colón, P.W. Siu, K.A. Scheidt, R.Q. Snurr, J.T. Hupp, O.K. Farha, A facile synthesis of UiO-66, UiO-67 and their derivatives, Chemical Communications, 49 (2013) 9449-9451.

[43] M.G. Goesten, P.C. Magusin, E.A. Pidko, B. Mezari, E.J. Hensen, F. Kapteijn, J. Gascon, Molecular promoting of aluminum Metal-Organic Framework topology MIL-101 by n, n-dimethylformamide, Inorganic Chemistry, 53 (2014) 882-887.

[44] T. Campbell, R.K. Kalia, A. Nakano, P. Vashishta, S. Ogata, S. Rodgers, Dynamics of oxidation of aluminum nanoclusters using variable charge molecular-dynamics simulations on parallel computers, Physical Review Letters, 82 (1999) 4866-4869.

[45] M. Thommes, S. Mitchell, J. Pérez-Ramírez, Surface and pore structure assessment of hierarchical MFI zeolites by advanced water and argon sorption studies, The Journal of Physical Chemistry C, 116 (2012) 18816-18823.

APPENDIX D

STRUCTURING Al-BASED MOFS FOR THE
ALLOCATION OF HEAT AND COLD
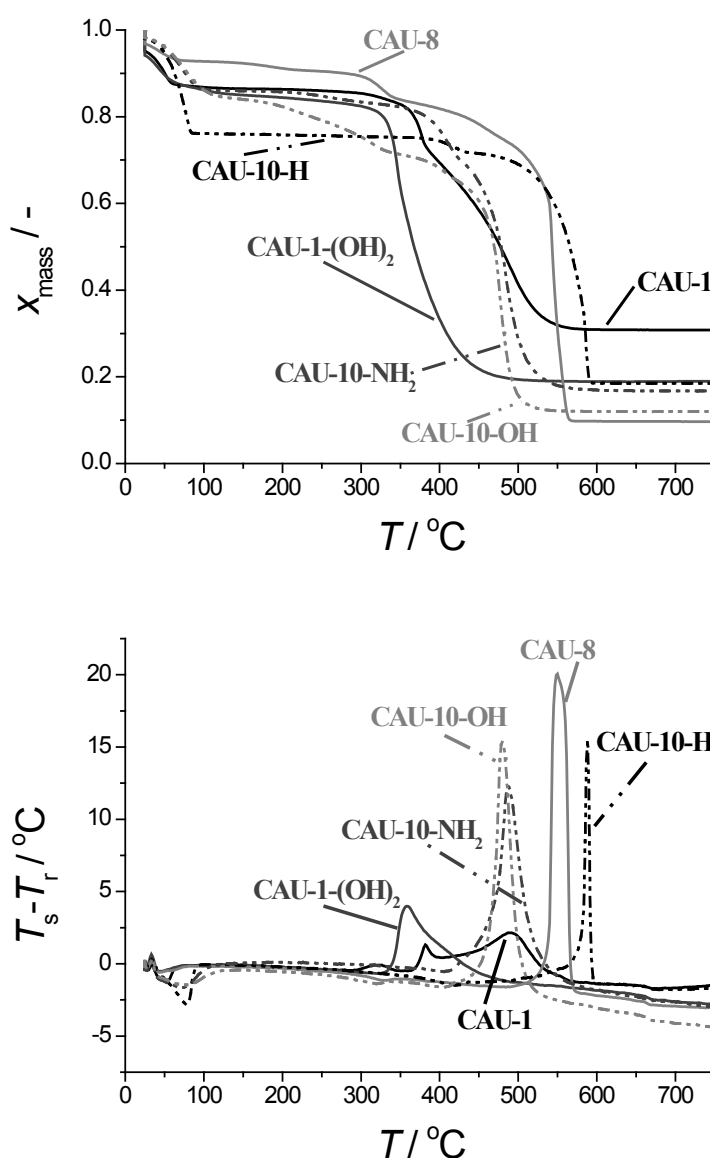
Figure D.1: TGA- (*top*) and SDTA- (*bottom*) profiles of CAU-1 (*black solid*), CAU-1-(OH)$_2$ (*dark-grey solid*), CAU-8 (*grey solid*), CAU-10-H (*black dash-dot-dot*), CAU-10-NH$_2$ (*dark-grey dash-dot-dot*) and CAU-10-OH (*grey dash-dot-dot*). Measured in a flow of 100 ml min^{-1} air with a heating rate of 5 $^{\circ}$C min^{-1}. T_s stands for sample temperature and T_r for reference temperature.

D.1. SYNTHESIS OF DIFFERENT CAU-MATERIALS

TGA-and SDTA-profiles (Fig. D.1) of synthesized CAU-1, CAU-1-(OH)$_2$, CAU-8, CAU-10-H, CAU-10-NH$_2$ and CAU-10-OH and SEM images of CAU-10-H powder (Fig. D.2) are shown here.
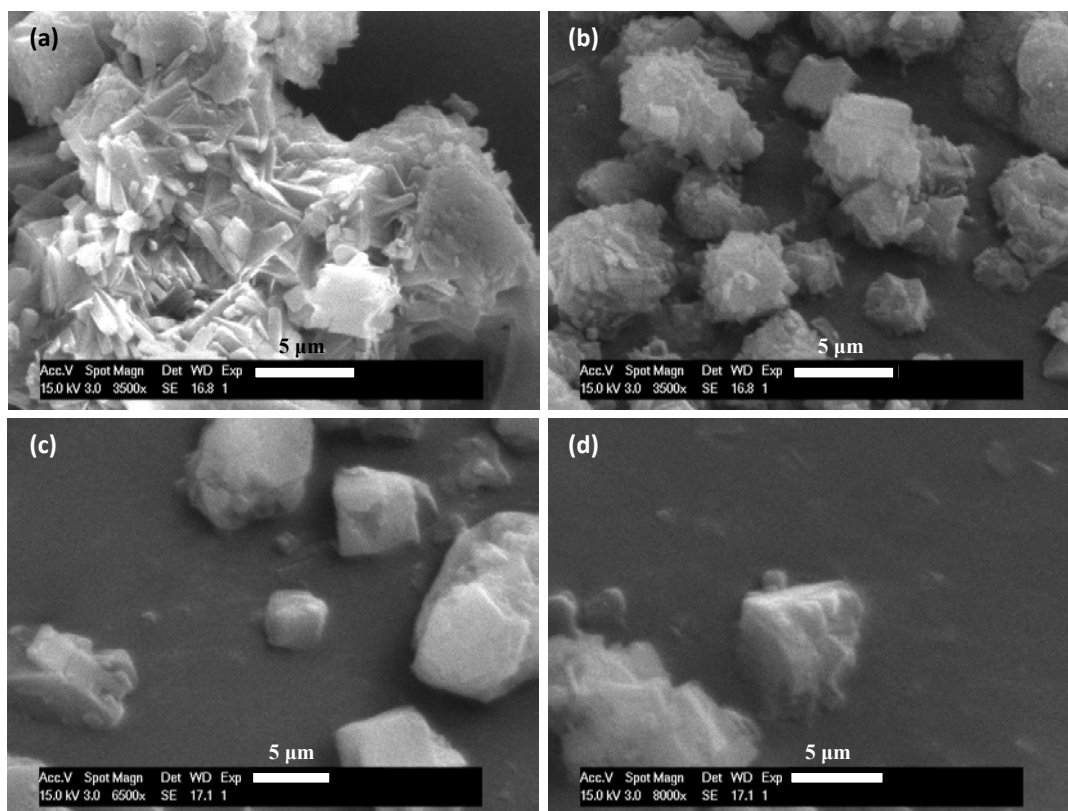
Figure D.2: Various SEM images of synthesized CAU-10-H powder.

D.2. CAU-10-H ON ALUMINA SUPPORTS

This section contains TGA-/SDTA-profiles (Fig. D.3) and N2 adsorption isotherms (Fig D.4) of CAU-10-H on γ-alumina. TGA -profiles of syntheses of CAU-10-H on α-alumina show that the employment of this support does not lead to observable crystal growth (Fig. D.5). Low magnification SEM pictures of γ-alumina beads (Fig. D.6) and of the interior of a purposely cracked open bead (Fig.D.7) are presented as well. Furthermore, it can be seen that there are two crystal shapes present on the surface, as shown in Fig. D.8. Both rhombic crystals, roughly 5-15 µm diameter, and larger spherical crystals, about 40-60 µm in size, appear on the surface. Without acid the latter seems predominant, with acetic acid and even more with HCl, rhombic crystals become more present. Crystals obtained from bulk synthesis of CAU-10-H resemble rhombic crystals (Fig. D.2), though the average size is slightly smaller (2- 5 µm).
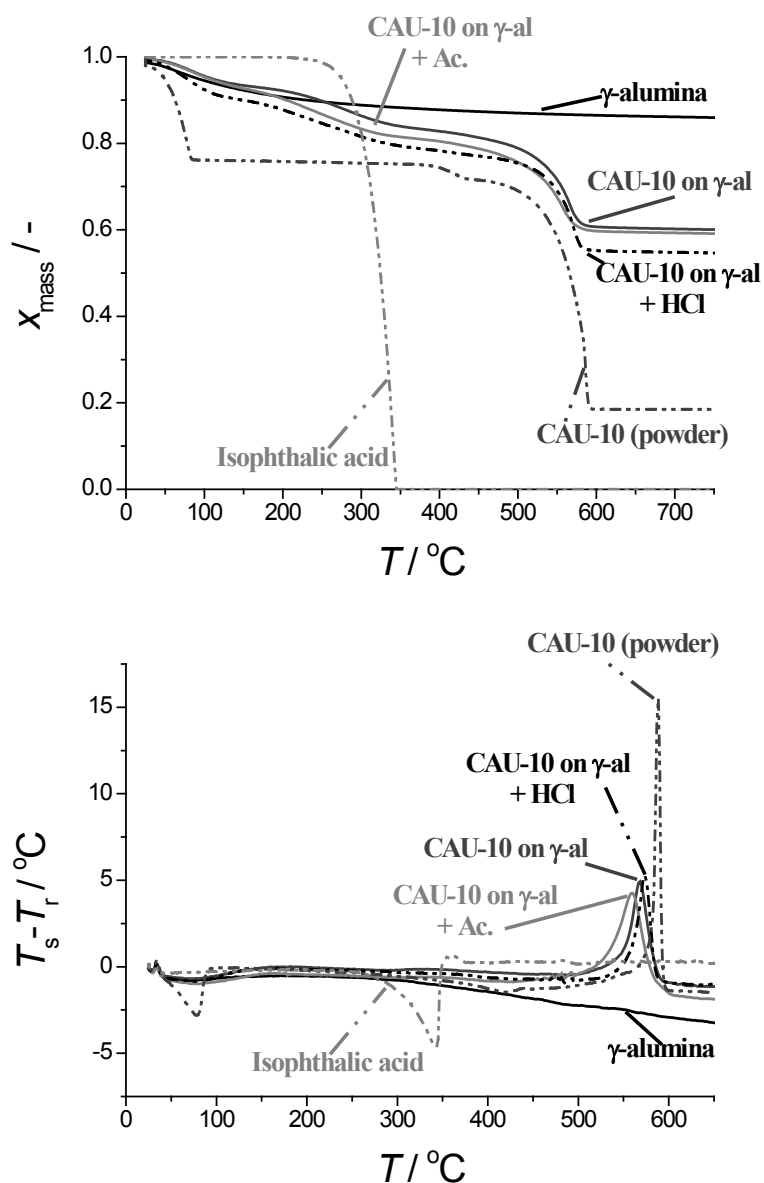
Figure D.3: TGA- (*top*) and SDTA- (*bottom*) profiles of γ-alumina (*black solid*), CAU-10 on γ-alumina (*dark-grey solid*), CAU-10 on γ-alumina with the addition of acetic acid (Ac.) (*grey solid*), CAU-10 on γ-alumina with the addition of hydrochloric acid (HCl) (*black dash-dot-dot*), CAU-10 powder (*dark-grey dash-dot-dot*) and isophthalic acid (*grey dash-dot-dot*). Measured in a flow of 100 ml min^{-1} air with a heating rate of 5 ^{o}C min^{-1}. T_s stands for sample temperature and T_r for reference (set-point) temperature.
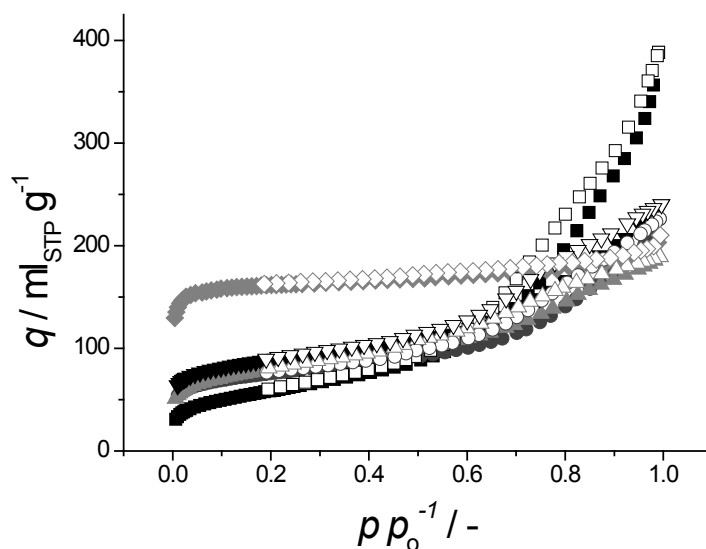
Figure D.4: Nitrogen adsorption isotherms at 77 K for γ-alumina (■), CAU-10-H on γ-alumina w/o addition of acid (●), CAU-10-H on γ-alumina with acetic acid (▲), CAU-10-H on γ-alumina with HCl (▼) and for comparison CAU-10-H of the pure powder sample (◆). Solid symbols adsorption, open symbols desorption branch.
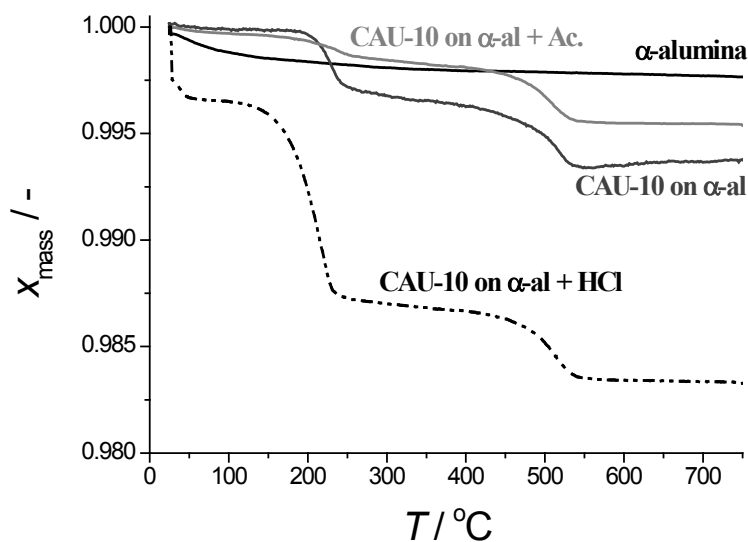
Figure D.5: TGA-profiles of α-alumina (*black solid*), CAU-10 on α-alumina (*dark-grey solid*), CAU-10 on α-alumina with the addition of acetic acid (Ac.) (*grey solid*), CAU-10 on α-alumina with the addition of hydrochloric acid (HCl) (*black dash-dot-dot*). Measured in a flow of 100 ml min^{-1} air with a heating rate of 5 °C min^{-1}. T_s stands for sample temperature and T_r for reference (set-point) temperature.
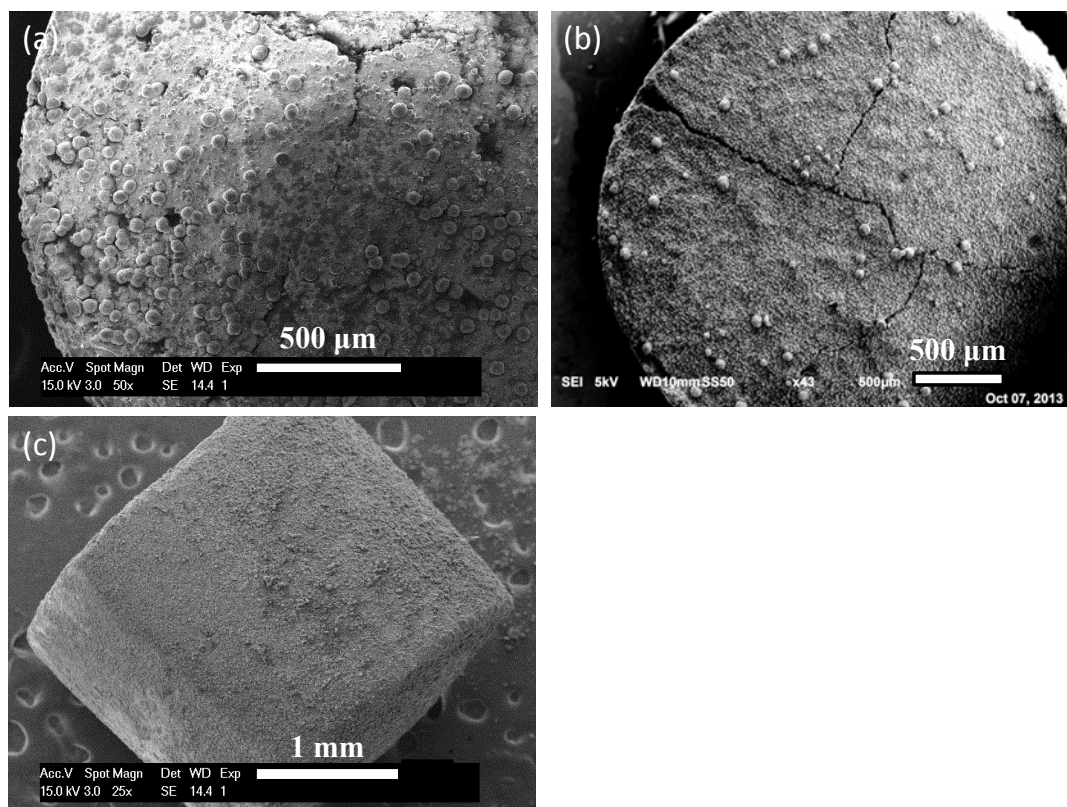
Figure D.6: SEM images (low magnification) of CAU-10-H synthesized on γ-alumina beads without any acid (*a*), with addition of acetic acid (*b*) and with addition of hydrochloric acid (*c*).
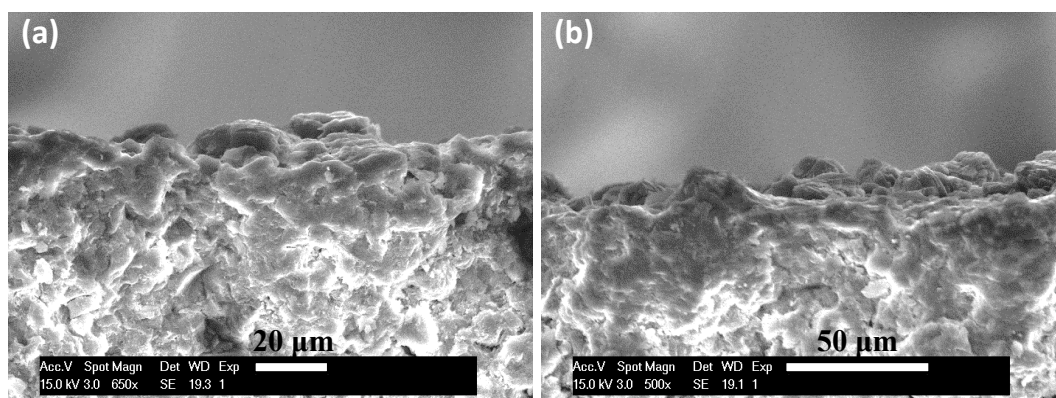
Figure D.7: SEM images of exterior surface layer (*a*) and interior (*b*) of a cracked open bead of CAU-10-H containing γ-alumina (HCl synthesis).
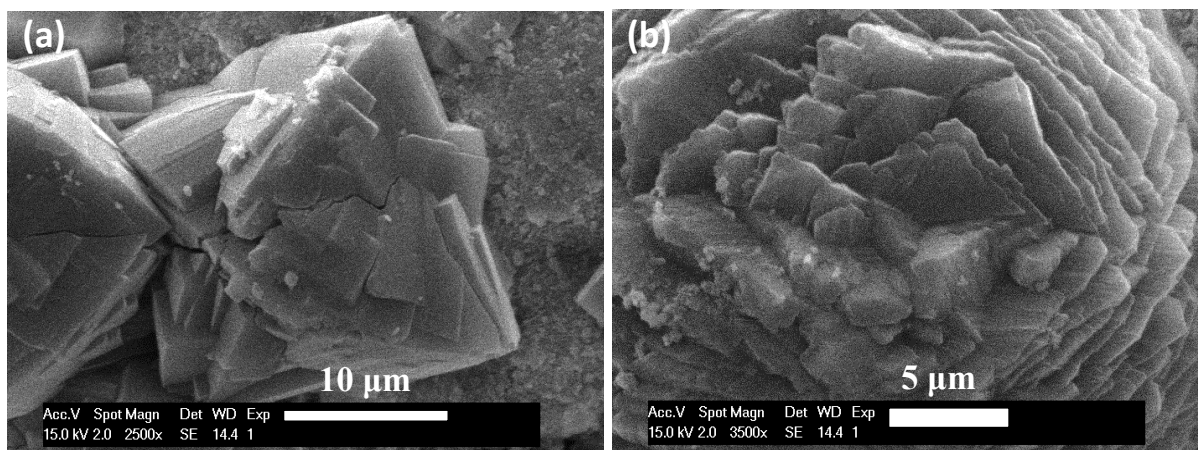
Figure D.8: SEM images of the two different crystal shapes present; rhombic (*a*) and spherical (*b*). Taken from synthesis without added acid on γ-alumina.
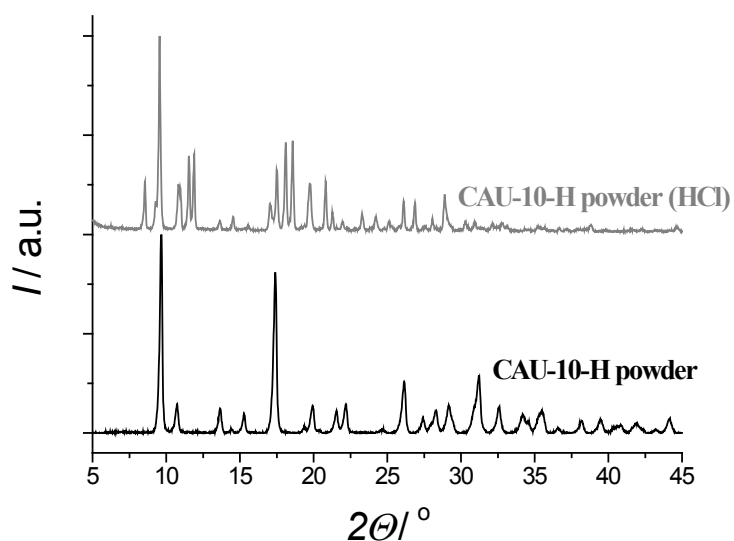
Figure D.9: XRD diffraction patterns of synthesized CAU-10-H (powder) with (*top*) and without addition of hydrochloric acid (*bottom*). Measured with Co-*Kα* radiation.

D.3. CAU-10-H ON METALLIC ALUMINIUM

The effect on the addition of HCl to powder synthesis of CAU-10-H is shown in Fig. D.9.

CHAPTER 6

MANUFACTURE OF DENSE CAU-10-H COATINGS ON ALUMINIUM SUPPORTS – OPTIMIZATION AND CHARACTERIZATION

ABSTRACT:

CAU-10-H displays a very suitable step-wise water adsorption behavior for application in adsorption driven heat pumps and chillers. For actual application, the manufacture of coatings of this material on thermally conductive surfaces is highly desired. Direct, single-step, crystallization of CAU-10-H on either metallic or anodized aluminium yields significant amount of byproduct(s) and inhomogeneous substrate coverage. Although an adequate pretreatment of the substrates before crystallization improves the quality of obtained coatings, significant improvements are achieved when crystal nucleation and growth are separated. More specifically, application of a reactive seeding approach with anodized aluminium leads to full coverage of the substrate surface, high MOF loading, homogeneous layer thickness, narrow crystal size distribution, good stability and high purity of the crystalline phase. In addition to this advancement on coating technology, it is demonstrated, based on structural refinement, that the excellent water adsorption behavior of CAU-10-H is not due to structural changes, in contrast to previous claims. The step-wise water uptake at a specific relative pressure reads like a phase change, resulting in a regularly ordered adsorbed water phase in between liquid and solid water.

6.1. INTRODUCTION

Adsorption driven heat pumps and chillers, AHP/ADC's, have great potential for reducing primary energy consumption and mitigating associated CO_2 emissions and anthropogenic climate change (Chapter 4). Devices based on this principle can potentially employ low grade thermal energy, *e.g.* solar or industrial waste heat, to sustainably supply cooling and heating, making use of the reversible ad- and desorption of, preferably, water. Compared to commercially applied adsorbents, CAU-10-H [1] shows a higher volumetric adsorption capacity and thermodynamic efficiency with water as working fluid (Chapter 4). CAU-10-H contains isophthalic acid as organic linker and *cis*-connected AlO_6-polyhedra, forming helical chains. The resulting structure has unidirectional pores. This MOF consists of abundantly available aluminium and isophthalic acid, both of which are produced industrially on a large scale [2], placing this MOF among the most commercially viable ones. Furthermore, its synthesis does not require an expensive sacrificial template, in contrast to *e.g.* the zeotype structures of the AQSOA-series [3-5] used in commercially available devices of Mitsubishi [6-12]. The potential of CAU-10-H is further strengthened by the fact that the material is perfectly stable towards water and has not shown any sign of degradation over 700 repeated adsorption/desorption cycles [13], a feature not commonly encountered for MOFs when exposed to water (Chapter 4). Altogether, these considerations confirm CAU-10-H as a commercially viable adsorbent for application in adsorption driven heat pumps and chillers. For successful implementation however, heat and mass transfer should be fast enough to allow for high volume-specific power output. A promising way to achieve this is by coating a thermally conductive surface with the adsorbent of choice. *E.g.*, the AQSOA-series are coated on a heat exchanger by using a binder [5, 6]. Ideally though, a binderless method is preferred as the binder does not only add to the cost of a device, but also dilutes the active material, decreasing the overall efficiency of the system. When MOFs are considered specifically, (organic) binders cannot be removed by combustion after coating, as this would also cause oxidation of the ligand of the MOF itself. Therefore, a coating by directly crystallizing the MOF, here CAU-10-H, on a thermally conductive surface is preferred [14]. Previous results already indicated that CAU-10-H coatings can be formed directly on metallic aluminium (*m-Al*) supports ([15], Chapter 5). With addition of HCl to the reaction mixture, a higher surface loading was achieved. However, incomplete surface coverage and a broad range of crystal sizes were observed. Furthermore, HCl addition induced the formation of unidentified by-

product(s). The aim of this study is to optimize the properties of the formed crystalline layer of CAU-10-H on aluminium substrates. Desired properties for this layer are full coverage of the surface, high MOF loading, homogeneous layer thickness, narrow crystal size distribution, sufficient stability under working conditions and high purity of the crystalline phase. In this work, a systematic study of different synthesis parameters has been performed. As a result, an optimized method for the synthesis of homogeneous CAU-10-H coatings is presented. Finally, in order to unravel whether the steep water uptake profile of CAU-10-H is due to a structural rearrangement (or 'breathing') that could lead to *e.g.* destruction of the coatings and/or pellets used in a prospective device we further studied this aspect.

6.2. EXPERIMENTAL

6.2.1. MATERIALS

Two different types of substrates were applied. Metallic aluminium (*m-Al*) substrates with a thickness of 0.5 mm and a purity of 99.9999 % were purchased from Mateck GmbH. Anodized aluminium (*a-Al*) substrates (Durapor 15) with a thickness of 0.5 mm were purchased from Polychromal B.V. According to the manufacturer's specification, the aluminium oxide layer is 15 μm thick. For all syntheses, substrates were cut into squares of 20 x 20 mm with corners cut-off. Typically, the weight was ~0.54 g and ~0.58 g for metallic and anodized aluminium substrates, respectively. The substrates were used either pretreated or as received. Isophthalic acid, 1,3-H_2BDC (99 %), aluminium sulfate octadecahydrate, $Al_2(SO_4)_3 \cdot 18H_2O$ (ACS reagent $\geq$ 99.8 %), N,N-dimethylformamide for synthesis, DMF (anhydrous 99.8 %), N,N-dimethylformamide for post-processing, DMF (puriss p.a., ACS reagent $\geq$ 99.8 %), hydrochloric acid, HCl (ACS reagent, 37 % in water), acetone (ACS reagent, $\geq$ 99.5 %) and methanol (anhydrous 99.8 %) were purchased from Sigma-Aldrich and used without further purification. Deionized water with a conductivity of 0.12 μS was prepared using a MILIPORE MILI-Q.

6.2.2. POWDER SYNTHESIS

CAU-10-H powder was synthesized using two different approaches, one employing conventional heating, the other using microwave heating. The main difference in synthesis protocols lies in the employed reaction time, which is generally significantly lower when microwave irradiation is used [16-18]. Further, since the employed Teflon inserts have a

larger volume, which needs to be filled by roughly half for the thermocouple to be in contact with liquid, the volume of the synthesis solution is significantly larger in the case of microwave synthesis. The molar ratios of reactants are however equal to those of the conventional approach. The post-processing after both methods is identical.

CONVENTIONAL SYNTHESIS

CAU-10-H was synthesized according to Reinsch *et al.* [1]. 1,3-H_2BDC (1.0 mmol, 0.16 g), $Al_2(SO_4)_3 \cdot 18H_2O$ (1.0 mmol, 0.64 g), DMF (10.6 mmol, 0.76 g) and deionized water (3.3 ml) were added to a Teflon insert with a capacity of 45.0 ml. The Teflon insert was closed with a lid, sealed in an autoclave, and heated in a convection oven (Heraeus T6, 5 °C/min) to the required reaction temperature (135 °C), left for 12 h and then allowed to cool to ambient temperature. Stirring was not applied during synthesis.

MICROWAVE SYNTHESIS

1,3-H_2BDC (12.9 mmol, 2.1 g), $Al_2(SO_4)_3 \cdot 18H_2O$ (12.9 mmol, 8.6 g), DMF (137 mmol, 10.0 g) and deionized water (42.4 ml) were added to a Teflon insert with a capacity of 90 ml. The vessel was sealed, equipped with a thermocouple and placed in the microwave oven (Milestone MultiSYNTH, 300 W, 10 °C/min). The reaction mixture was heated to the required reaction temperature (135 °C), left for 1 h at this temperature and then allowed to cool to ambient temperature. Stirring was not applied during synthesis.

POST-PROCESSING (POWDER)

After synthesis and cooling to ambient temperature the reaction mixture was filtered using a diaphragm vacuum pump (Vacuubrand MZ 2C, 1.7 m³/h), a Büchner funnel with filtration paper (GVS Maine Magna, nylon membrane filter, type: plain, pore size 0.45 μm, diameter 90 mm) and a side arm filtering flask. The loaded filter paper was dried in a muffle oven at 100 °C for about 20 min. Then, the filtration residue was transferred from the filtration paper into a beaker where it was submerged in about 20 ml DMF at room temperature overnight. The suspension was again filtered and dried as above. The filtration residue was then submerged in about 20 ml deionized water at room temperature overnight. After filtration and drying, the powder was stored in a sample vial.

6.2.3. FORMATION OF CAU-10-H ON SUBSTRATES

Three synthesis pathways have been followed in order to optimize the formation of CAU-10-H on aluminium substrates: (i) the single-step direct synthesis, adopted from previous work ([15], Chapter 5) and two multi-step procedures in order to separate crystal nucleation and growth, (ii) reactive [19] and (iii) thermal [20]. All substrates and possible solids obtained in the reaction solution (*i.e.* filtration residue) were activated following an identical protocol.

SUBSTRATE PRETREATMENT

As-received substrates might contain impurities. Furthermore, pretreatment might be necessary to enhance reactivity of the substrate before synthesis. To this end, two different substrate pretreatment methods have been applied, based on previously reported procedures of Arnold *et al*. [21] and Bux *et al*. [22]:

- *Method A:* The substrates were placed in a flask and submerged in 25 ml of acetone for at least 30 min at room temperature. The substrates were rinsed with deionized water and subsequently submerged in 25 ml deionized water for at least 30 min at room temperature. Afterwards, the substrates were rinsed again with deionized water and dried in a muffle oven at 100 °C for 1 h and stored in sample bottles.

- *Method B*: The substrates were placed in a flask and submerged in 25 ml of acetone for at least 30 min at room temperature. The substrates were rinsed with deionized water and subsequently submerged in 25 ml diluted HCl solution (6 % in water) for 30 min at room temperature. The substrates were rinsed with deionized water and subsequently submerged in 25 ml deionized water for at least 30 min at room temperature. Afterwards, the substrates were rinsed again with deionized water and dried in a muffle oven at 100 °C for 1 h and stored in sample bottles.

DIRECT SYNTHESIS COATING

In attempts to optimize the quality of CAU-10-H coatings on aluminium-supports, process parameters and synthesis mixture compositions were varied systematically. Starting point is the synthesis protocol found most successful in previous studies (Chapter 5, [15]), for both metallic (*m-Al*) and anodized (*a-Al*) aluminium substrates, either pre-treated or as received. A given substrate was placed in a Teflon insert with a capacity of 45.0 ml. Subsequently, a certain reaction mixture was added to the insert. Standard composition is 1,3-H_2BDC (5.2 mmol, 0.86 g), deionized water (17.0 ml), DMF (4.2 ml) and HCl_{aq} (1.7 ml, 37% in water).

The Teflon insert was then closed with a lid, sealed in an autoclave, and heated to the required reaction temperature in a convection oven (Heraeus T6, 5 °C/min) for a given reaction time. For the standard synthesis protocol, reaction temperature is 135 °C and reaction time is 12 h. This, in combination with the above-mentioned standard synthesis mixture composition, will be referred to as "standard synthesis protocol" (SSP). Using these conditions as starting point, *e.g.* the amount of added DMF was reduced (75%, 50%, 25%, 0%), the amount of HCl was varied (200%, 50%, 0%), additional aluminium source ($Al_2(SO_4)_3 \cdot 18H_2O$) was added (up to 3 g) and reaction time was altered, one variation at a time. When the amount of HCl solution is altered, the amount of deionized water is adjusted to keep the total amount of water molecules constant. After reaction, the autoclave was removed from the oven and allowed to cool to ambient temperature. The reaction mixture including the substrate was subjected to post-processing (*vide infra*).

REACTIVE SEEDING COATING

The reactive seeding approach is based on the methodology applied by Hu *et al.*, who used it to create MIL-53(Al) membranes on alumina supports [19]. The approach revolves around two distinct steps. In the first, small MOF crystals (seeds) are attached to the surface via a synthetic reaction. In the second, these seeds are grown to large crystals in the presence of MOF synthesis precursors under hydrothermal conditions.

For the reactive seeding step, pretreated substrates were placed in a Teflon insert with a capacity of 45.0 ml. Subsequently, 1,3-H_2BDC (5.2 mmol, 0.86 g), DMF (4.2 ml), HCl (37 % in water, 1.7 ml) and deionized water (17.0 ml) were added. For *a-Al*, no HCl was added and the amount of deionized water was adjusted to keep the total amount of water molecules constant. The Teflon insert was closed with a lid, sealed in an autoclave, and heated in a convection oven (Heraeus T6, 5 °C/min) to the required reaction temperature (135 °C). Stirring was not applied during synthesis. The time allowed for reactive seeding, t_{rs} was varied from 1 to 4 h. After reaction, the autoclave was removed from the oven and allowed to cool to ambient temperature. The seeded substrate was thoroughly rinsed with DMF and deionized water and subsequently dried in an oven (Heraeus, T5042) at 100 °C for 1 h. This seeded substrate was weighed and stored in a sample vial, until used in the second step.

For secondary growth, the seeded substrates were placed once more in a Teflon insert with a capacity of 45.0 ml. Either of two different precursor solutions, without added acidity, were used keeping volume of water constant, employing a dilution ratio (DR) of either 2 or 5,

respectively, for the other reactants, compared to conventional synthesis. For a dilution ratio of 2, the following was thus added: $1,3$-H_2BDC (2.6 mmol, 0.43 g), $Al_2(SO_4)_3 \cdot 18H_2O$ (2.6 mmol, 1.7 g), DMF (2.2 ml), deionized water (17.0 ml). For a ratio of 5, this becomes: $1,3$-H_2BDC (1.0 mmol, 0.17 g), $Al_2(SO_4)_3 \cdot 18H_2O$ (1.0 mmol, 0.69 g), DMF (0.84 ml, 0.80 g), deionized water (17.0 ml). The Teflon insert was closed with a lid, sealed in an autoclave, and heated in a convection oven (Heraeus T6, 5 °C/min) to the required reaction temperature (135 °C). After a reaction time of 12 h, the autoclave was removed from the oven and allowed to cool to ambient temperature. The reaction mixture with the substrate was post-processed as described previously.

THERMAL SEEDING COATING

The thermal seeding approach is adapted from Guerrero *et al.*, who applied this method for the creation of HKUST-1 membranes on porous supports [20]. The procedure consists of three steps: seed formation, attachment of seeds to the substrate surface and secondary growth.

The used seeds are those created *via* microwave heating (Section 6.2.2). Three different seed solutions are employed. Solution 1 is the reaction mixture, after cooling down and without further treatment (for a yield of ~ 65%, as commonly observed for conventional synthesis [1], this would be roughly 3 wt.% CAU-10-H). For the other solutions, CAU-10-H powder was processed after synthesis as before. Seed solutions 2 and 3 contain CAU-10-H seeds dispersed in deionized water, respectively with 2.5 and 5 wt.% MOF. Prior to the seeding experiments, the selected seed solution was sonicated in an ultrasonic bath (VGT-1730QT, 100 W, 40 kHz) for 1 min to break down agglomerates.

For the attachment of seeds, pretreated substrates were heated in a convection oven (Heraeus T6, 5 °C/min) at 200 °C for 15 min. While the substrates are still inside the oven, a selected seed solution was dropped on the surface of the hot substrates using a pipette until the surface was completely covered with the solution (2-6 ml, roughly). The substrates were kept inside the oven for 15 min to allow for complete evaporation of the solvent. To enable complete coverage of the substrate surface with seed crystals, this procedure had to be repeated two more times when seed solution 1 was used. In contrast, only one thermal seeding step was required when either solution 2 or 3, only containing CAU-10-H seeds in water, was used. The seeded substrates were then rinsed with deionized water, to remove excess material and

not attached seeds, and subsequently dried in an oven (Heraeus T5042) at 100 °C for 1 h. The secondary growth step is the same for thermal and reactive seeding (*vide supra*).

POST-PROCESSING

After completion of an experiment, the reaction mixture was allowed to cool to ambient temperature. Subsequently, this mixture was filtered using a diaphragm vacuum pump (Vacuubrand MZ 2C, 1.7 m3/h), a Büchner funnel with filtration paper (GVS Maine Magna, nylon membrane filter, type: plain, pore size 0.45 μm, diameter 90 mm) and a side arm filtering flask. After filtration, the substrate covered with MOF and the loaded filter paper were treated individually. The substrates were submerged in DMF overnight at room temperature. The solvent was decanted. Then, the substrate was rinsed with deionized water and submerged in about 20 ml of deionized water overnight at room temperature. Afterwards, the water was decanted and the substrate was rinsed with deionized water and dried in a muffle oven at 100 °C overnight. After drying, the substrate was weighted and stored in a sample vial. The filtration residue was processed in the same way as regular powder samples (Section 6.2.2).

6.2.4. CHARACTERIZATION METHODS

X-RAY DIFFRACTION (XRD)

XRD patterns were collected with a PANalytical X'pert PRO diffractometer using a Co-*Kα* X-ray source with a Ni-filter, operating at 45 kV and 40 mA in Bragg-Brentano geometry. Measurements were carried out at angles $5 \leq 2\theta \leq 90\,^{\circ}$. A divergence slit of 0.3, a scan speed of 0.4 s per step and an increment of 0.02 were defined. Sample rotation was used for MOF powders. Diffraction patterns of coated substrates have been normalized employing the maximum peak height observed for $2\theta \leq 40^{\circ}$, disregarding reflections from the aluminium substrate in the normalization, to better envisage the formed structure(s). Especially for substrates with a low coverage, reflections of CAU-10-H and possible byproduct(s) would be hardly visible otherwise. For selected powder sample(s), a special sample holder has been employed that can be sealed with an X-ray transparent, leak-tight dome (type A100 B33, Bruker), to be able to measure dehydrated samples, dried and loaded onto the holder in a glove box.

X-RAY REFINEMENT PROCEDURE

The powder X-ray diffraction pattern of hydrated CAU-10-H has been indexed successfully with the X-Cell algorithm [23] implemented in the Reflex Plus module of the Accelrys Material Studio software package [24]. Both an automated powder extinction class and crystallographic considerations led to space group $I4_1$ of hydrated CAU-10-H, which is identical to that reported for anhydrous CAU-10-H [1]. Pawley fitting was performed for the refinement of the unit cell parameters, for which $a = b = 21.3021$ Å, $c = 10.709$ Å, and $\beta = \gamma = \alpha = 90°$ was obtained. In the first refinement step, zero offset, the scale factor, six background terms and profile parameters were refined. The profiles have been modeled as a pseudo-Voigt function. The resulting unit cell, along with the initial structure model constructed, based on the structure model of anhydrous CAU-10-H [1], was subsequently the basis for further structure refinement. Taking into account that lattice parameters change only slightly compared to the anhydrous form, all atomic positions in the framework were fixed during refinement. Based on the results of the Void analysis performed using Platon [25], four water molecules per formula unit were assumed. Accordingly, 32 water molecules were added to the unit cell. The water molecules were treated as rigid bodies and their positions were subjected to simulated annealing using the Reflex Plus module of Material Studio [24]. A completely unrestricted refinement of the water guest molecules resulted in meaningful locations within the pore channels of CAU-10-H.

SCANNING ELECTRON MICROSCOPY (SEM)

Scanning electron micrographs were obtained with a Jeol JSM 6010AL. For (coated) substrates, backscattered electron imaging (shadowed images) was applied at low vacuum mode (pressure of 30 Pa) operating with a high voltage of 20 kV, working distance (WD) 9 – 12 mm and spot size typically adjusted to 50. With this set of parameters, the yield of back-scattered electrons could be increased and charging effects could be minimized, and highest resolution for the images were obtained. For powder samples, secondary electron imaging was applied with a voltage of 5-10 kV typically, with a fixed working distance of 10 mm and a spot size of 50. Samples were sputtered with gold before analysis to minimize charging effects.

INFRARED SPECTROSCOPY (IR)

IR spectra were recorded with a Thermo Fisher Scientific, type Nicolet 8700 FT-IR in reflectance mode. The measurements were performed in a spectral range of 400 to 4000 cm^{-1} using a mid-IR source. 124 scans were recorded for each spectrum. IR spectra for loaded substrates were obtained without further additional drying. Both the background and the spectrum of the bare substrates (measured once per substrate) were subtracted from the spectra of CAU-10-H synthesized on supports. For CAU-10-H powder, the background was recorded every measurement using KBr powder. Again measurements were performed in reflectance mode.

THERMO-GRAVIMETRIC ANALYSIS (TGA)

Thermo-gravimetric analyses were performed using a Mettler Toledo TGA/SDTA 851e / SF / 1100°C with a resolution of 1 μg. The substrates were cut into small pieces (30 - 80 mg) and inserted into alumina crucibles with a capacity of 30 μl. The samples were heated from 25 to 800 °C in a flow of air (100 ml/min). A heating rate of 5 °C/min was applied. Simultaneous differential thermal analysis (SDTA) provides information on whether endo- or exothermic effects drive the differences in the recorded mass during TGA experiments.

NITROGEN PHYSISORPTION (N$_2$)

Nitrogen physisorption measurements (at 77 K) were performed with a Micrometrics TriStar III. The loaded substrates were cut into rectangles of 20 x 5 mm and inserted into a sample tube with a diameter of 12 mm. MOF powders were inserted, without further modification, in a sample tube with a diameter of 9 mm. In both cases, pretreatment consisted of evacuation for 16 h at 150 °C using a Micrometrics VacPrep 061 with a heating rate of 10 °C/min.

VOLUMETRIC WATER ADSORPTION

Water adsorption isotherms were measured on a Micrometrics 3Flex, routinely at 298 K. Pretreatment consisted of evacuation for 16 h at 150 °C using a Quantachrome MasterPrep with a heating rate of 5 °C/min. A second isotherm was measured at 288 K, for the calculation of the isosteric enthalpy of adsorption.

The isosteric enthalpy of adsorption, $\Delta_{ads}H$, for a given amount adsorbed, q, can be calculated from adsorption isotherms at two or more different temperatures, using [26]:

$$\Delta_{ads}H_q = R\left(\frac{\partial \ln p}{\partial \left(\frac{1}{T}\right)}\right)_q \tag{6.1}$$

Here R is the universal gas constant, p is the absolute pressure and T is the temperature. Using this equation, it is (tacitly) assumed that adsorption is fully reversible (no chemisorption occurs), that both the internal energy of the adsorbent surface and the adsorbent structure don't change during adsorption, and equilibrium is reached between adsorbent and adsorbate.

GRAVIMETRIC WATER ADSORPTION

Cyclic ad- and desorption measurements were performed with a Rubotherm magnetic suspension balance (resolution 0.01 mg), in combination with a vapor dosing unit. The evaporator temperature (vapor dosing unit) was fixed at 22 °C, whilst the measurement temperature (sample chamber) was alternated between 45 and 75 °C. Both the vapor dosing and the measurement temperature were controlled with thermostat baths (Julabo FP25-Me and FP 50-Me, respectively). Pretreatment was performed and monitored in situ. Evacuation was applied at 150 °C until no further decrease in mass could be observed (< 4 h, generally).

6.3. RESULTS AND DISCUSSION

Firstly the results of bulk (powder) synthesis of CAU-10-H are discussed (Section 6.3.1). This to be able to compare with CAU-10-H coated on substrates and to unravel whether the structure is indeed flexible, as claimed before [13]. The crystals formed are used as seeds in the thermal seeding approach. Subsequently, coatings obtained by direct synthesis (Section 6.3.2) are discussed. Thereafter, the benefits of employing two multi-step approaches, reactive (Section 6.3.3) and thermal (Section 6.3.4) seeding are discussed. Lastly, selected substrates are characterized and compared in detail (Section 6.3.5).

6.3.1. POWDER SYNTHESIS

From both conventional and microwave synthesis, pure CAU-10-H is obtained (Figs. E.1,2, Appendix E). The adsorption capacity of N_2 and H_2O is seemingly somewhat larger for the material obtained by microwave synthesis (Fig. E.3).
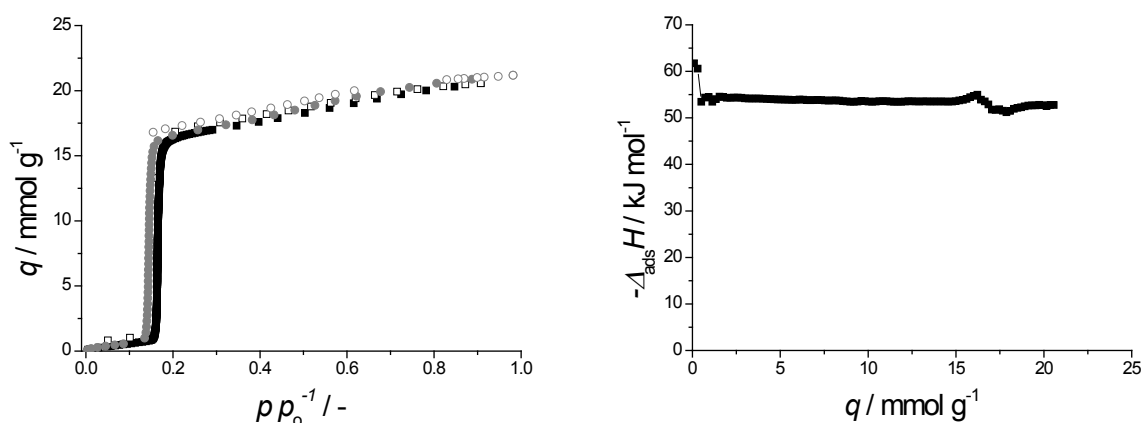
Figure 6.1: Water adsorption isotherms of CAU-10-H, obtained from microwave synthesis, at 298 (■) as well as 288 K (●) (*left*) and isosteric enthalpy of adsorption (*right*, calculated with Eq. 6.1). Closed symbols indicate adsorption, open symbols desorption, and p_o is the saturated vapor pressure of water at measurement temperature.

As the difference in capacity is larger for N_2, which is measured at significantly lower temperatures, this can be attributed to diffusional limitations in the material obtained from conventional synthesis. This is further made plausible by the fact that for N_2 the adsorption hysteresis is not fully closed at $p/p_o \leq 0.4$ for conventional synthesis (Fig. E.3), another indicator for possible diffusional limitations [27]. The fact that microwave synthesis, on average, results in smaller particle sizes is commonly observed for MOF crystals [16-18, 28, 29]. SEM images reveal that although the size of the smaller crystals present are roughly the same order of size, that for conventional synthesis, more and larger crystal agglomerates exist, likely to cause the observed diffusional limitations (Fig. E.4). Water adsorption measured at a second temperature, for CAU-10-H(MW), see Fig. 6.1, allows for the calculation of the isosteric enthalpy of adsorption.

As already noted in Chapter 4, the reversible step in uptake, at $p/p_o \sim 0.15$ makes CAU-10-H a great candidate for adsorption driven allocation of cold especially. The isosteric enthalpy of adsorption at the steep step in water uptake, $1 < q < 16$ mmol g^{-1}, is nearly constant (about -54 kJ mol^{-1}) and close to the evaporation enthalpy of water (~41 kJ mol^{-1} at measurement temperature), making regeneration in adsorption driven heat pumps and chillers relatively energy efficient (Chapter 4). Because only two isotherms were used, the uncertainty in the isosteric heat could not be calculated. However, with water as the adsorptive, this turns out to be only 3-4 kJ mol^{-1}, when additional isotherms are available [30].
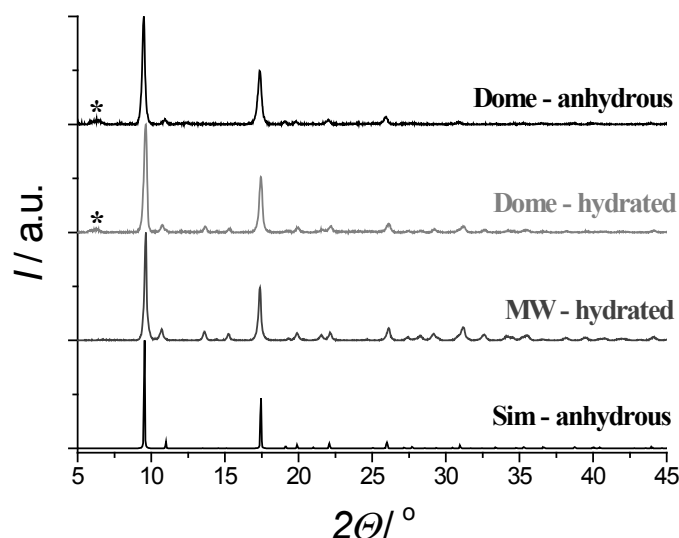
Figure 6.2: XRD patterns of CAU-10-H synthesized using microwave synthesis, without further drying (MW - hydrated), the same sample inserted in sample holder with dome without (Dome - hydrated) and with drying (Dome - anhydrous). The simulated XRD pattern of the reported anhydrous crystal structure reported by Reinsch *et al.* (Sim - anhydrous) is given for comparison [1].

It had been speculated that this step uptake is caused by reversible structural rearrangements upon water adsorption due to flexibility of the crystal structure [13]. This flexibility, sometimes called "breathing", is observed for a plethora of MOFs and often gives rise to undesired hysteresis between the adsorption and desorption branches of the isotherm (Chapter 4). This hysteresis is (nearly) absent for CAU-10-H (Fig. 6.1, [13]). Though Fröhlich *et al.* based their findings on (minor) changes in the X-ray diffraction pattern upon hydration, no comments were made on the actual structural rearrangement of CAU-10-H upon hydration [13]. To elucidate this matter, XRD patterns have been determined for anhydrous and hydrated CAU-10-H using a leak-tight dome. These results are given in Fig. 6.2 and compared to the simulated pattern of the original, anhydrous, crystalline structure reported by Reinsch *et al.* [1]. Comparing the pattern of hydrated CAU-10-H(MW) with and without dome, one can observe that the utilization of the dome induces a small hump in the diffraction pattern ($2\theta \sim 6°$,*), which will be further ignored. Further, the peak intensity is slightly lowered when the dome is employed, though the peak locations remain at the same location and relative intensities remain virtually unchanged. The location of the principal reflection ($2\theta \sim 9.5°$) undergoes only a minor shift upon hydration. After hydration, two minor reflections ($2\theta \sim 14.6, 15.1°$) become visible. The same two findings formed the basis for ascription of

293

water-induced flexibility in CAU-10-H by Fröhlich *et al*. [13]. However, the refined unit cell parameters for the hydrated state (a = 21.30, c = 10.71 Å) are only marginally different from those obtained for anhydrous CAU-10-H (a = 21.55, c = 10.38 Å) [1], resulting in a nearly negligible unit cell volume expansion of 0.8% upon water adsorption. Furthermore, the space group of CAU-10-H is unchanged ($I4_1$), concluding that CAU-10-H cannot be considered a "breathing MOF". The absence of flexibility might be beneficial, as it has been shown for *e.g.* MIL-53(Al)-NH$_2$ that the large change in unit cell volume upon adsorption causes MOF pellets to break down to powder [31]. This might also happen for coated MOFs, resulting in detachment that would be detrimental for actual application. However the absence of flexibility requires an alternative explanation for the appearance of the two noted minor reflections ($2\theta \sim$ 14.6, 15.1°). To this end, a completely unrestricted refinement of the water guest molecules is performed based on the obtained X-ray diffraction pattern of hydrated CAU-10-H. In this refinement, water molecules were treated as rigid bodies. The resulting XRD pattern of the refined structure (Fig. E.5, Table E.1) is excellently in line with experiments. Especially, the intensities of reflections in the region $13 \leq 2\theta \leq 16°$, the interval that was shown to be most sensitive to the location of guest water molecules, becomes more pronounced. The optimal refinement does not only yield better agreement with experiments, but also results in filling of water molecules in the MOF channels without unphysical steric hindrance (Fig. 6.3). Water molecules are seemingly located preferentially close to oxygen-atoms of the aluminium-hydroxide chains of the frameworks. This makes perfect sense as these the OH-groups present are the primary interaction sites for polar adsorptive molecules, thus the initial water molecules should adsorb and then cluster at these sites [32]. The fact that the position of these molecules could be refined by XRD indicates that water is adsorbed in a very regular and immobile fashion, a rare feature for MOFs, and that behavior of the adsorbed phase is distinctly different from bulk liquid water. This is further strengthened by the molar entropy of the adsorbed state ($\sim$58 J mol^{-1} K^{-1}, calculations in Section E.1), which is significantly lower than that of liquid water (70 J mol^{-1} K^{-1} [33]), though still somewhat larger than that of solid water (45 J mol^{-1} K^{-1} [33]). Unfortunately, hydrogen-atoms cannot be refined based on X-ray diffraction techniques, neither on the Al-OH chains nor on water itself, thus further details on specific host-guest interactions cannot be obtained employing this technique. Nonetheless, as the structure of hydrated CAU-10-H has been unveiled, focus is shifted to the main topic of this chapter, the improvement CAU-10-H coatings on aluminium-based supports.
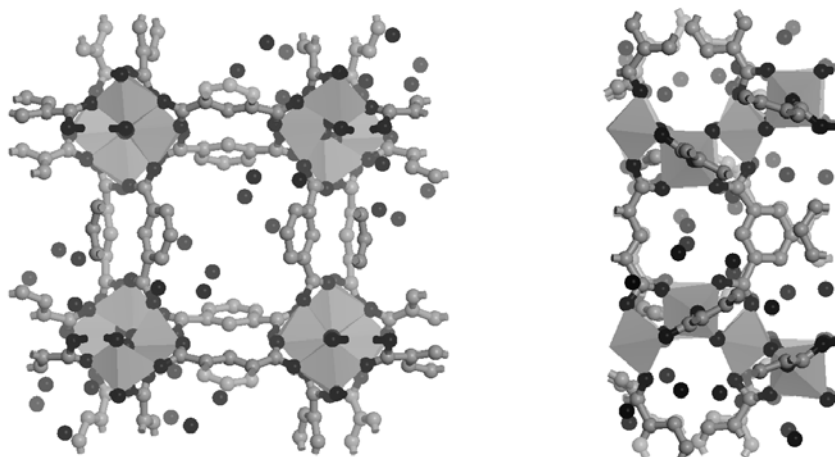
Figure 6.3: Crystallographic structure, including guest water molecules, of hydrated CAU-10-H as obtained with the Rietveld refinement, viewed along the [0 0 1]-plane (*left*) and the [0 1 0]-plane (*right*). Aluminium atoms depicted with grey polyhedrons, carbon atoms with gray spheres and oxygen atoms with black spheres. Hydrogen atoms are not depicted.

6.3.2. DIRECT SYNTHESIS COATING

In addition to the metallic aluminium (*m-Al*) substrates employed in previous studies (Chapter 5, [15]), the effect of using anodized aluminium substrates having a porous (*a-Al*) layer has been investigated. This, as previous studies on porous γ-Al$_2$O$_3$ supports revealed that high loadings of CAU-10-H with homogeneous crystal size distributions could be obtained (Chapter 5, [15]). As no aluminium-source is added to the synthesis mixture, crystal growth can only occur by extraction of Al-ions from the support [34]. This process turned out to be more efficient for γ-alumina-containing supports than for metallic aluminium (Chapter 5, [15]). As metallic supports display higher thermal conductivity and are desired for the actual application, it was evident to employ aluminium supports with an (anodized) aluminium-oxide layer. The oxide layer is 15 μm thick in case of *a-Al*, whereas on metallic aluminium an oxidic skin layer of only 4 nm exists [35]. Furthermore, anodized oxide layers are composed of amorphous alumina, if not calcined thoroughly [36], which might further increase reactivity compared to γ-alumina. Characterization of the pristine supports by XRD and SEM images is presented in Fig. 6.4.
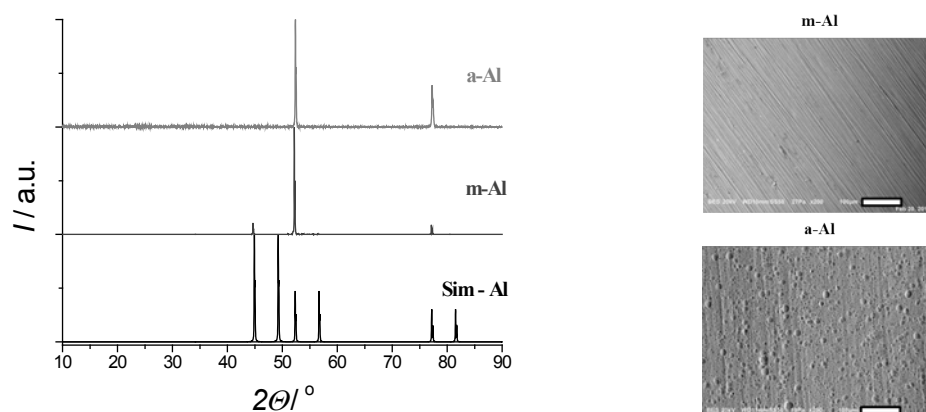
Figure 6.4: XRD patterns of bare *m-Al* and *a-Al* supports and a simulated metallic aluminium pattern (*left*) and SEM images of the same bare supports (*right*, scale bar represents 100 μm).

Comparing the XRD patterns of both *m-Al* and *a-Al* to that of a simulated aluminium pattern reveals that preferential orientation exists for the aluminium in both substrates. Lastly, no reflections were observed for the anodized layer itself, confirming that it is indeed composed of amorphous alumina. SEM microscopy unveils a distinct difference in physical appearance of the substrates. Where *m-Al* shows unidirectional grooves across the surface, the surface of *a-Al* contains spherical blisters, as result of the anodization process. Because of the anodization, *a-Al* substrates display mesoporosity and have a small water adsorption capacity (Fig. E.6), features absent for *m-Al*.

Initial experiments to increase coverage of CAU-10-H on aluminium utilized the supports as received, *i.e.* without pretreatment. As pretreatment has a more profound effect on anodized aluminium (*vide infra*), focus is on metallic aluminium for these experiments. As all Al-ions are extracted from the support in case of the standard synthesis protocol (SSP), it might well be that the availability of these ions is a limiting factor for crystal growth. Hence it might make sense to add additional aluminium. To this end different amounts of $Al_2(SO_4)_3 \cdot 18H_2O$, the same precursor used for bulk CAU-10-H, have been added to the synthesis mixture. This addition has an adverse effect on surface coverage (Figs. E.7-8). With increasing amount of added aluminium, less CAU-10-H can be found on the surface of the support, and more in the solution. Additionally, at higher Al-content in the synthesis solution, the undesired secondary crystalline phase is more dominantly observed, a finding in concert with that of the work of Reinsch *et al.* for bulk powder synthesis [1].
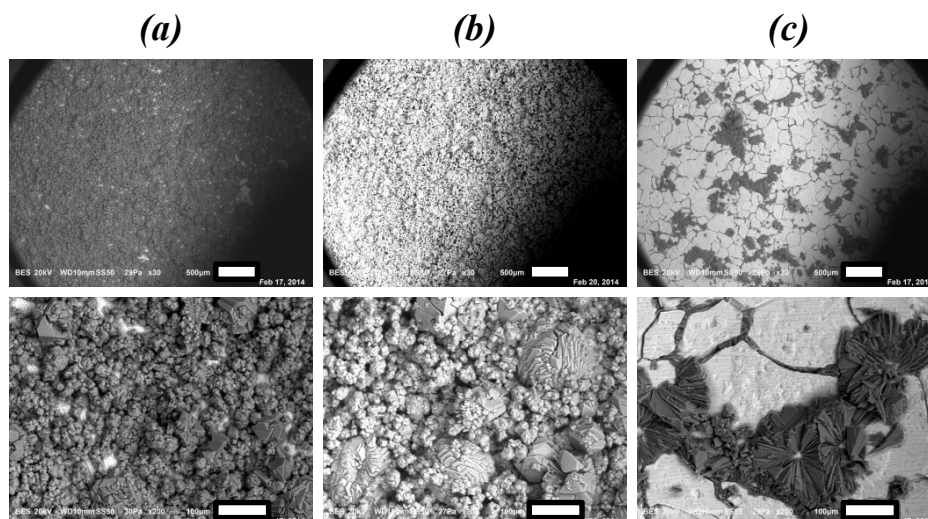
Figure 6.5: SEM images of directly synthesized CAU-10-H on *m-Al* (without pretreatment) using 50% HCl (*a*), 100% HCl (*b*, SSP) and 200% HCl (*c*) (*top* scale bar represents 500 μm, *bottom* scale bar represents 100 μm).

Another method of influencing crystal growth is by varying the amount of hydrochloric acid added. HCl induces stronger dissolution of Al-ions from a given support [37] and has been found to influence the crystallization kinetics of certain MOFs [38, 39]. SEM images of CAU-10-H synthesized on *m-Al* with 50, 100 and 200% HCl, with respect to the standard synthesis protocol, are presented in Fig. 6.5. Halving the amount of added HCl (Fig. 6.5a) results in a slightly lower coverage. For both syntheses, an undesired broad crystal size distribution is observed (Fig. 6.5a, b). Interestingly, when the amount of HCl is doubled (Fig. 6.5c), coverage is greatly reduced and crystals seemingly appear only along grooves, likely created by the preferential dissolution of Al^{3+} ions from local aluminium crystal boundaries in the metallic support, as was observed in a previous study (Chapter 5, [15]). X-ray diffraction (Fig. E.9) does not only indicate a reduced crystal coverage when 200% HCl is employed, but also a large fraction of the crystals belong to the unidentified secondary phase, also observed previously (Chapter 5, [15]). As lower pH results in a faster release of Al^{3+}-ions, the added HCl will lead to promotion of the secondary phase, similar as in experiments with high concentrations of aluminium sulfate. Using 100% HCl for syntheses on anodized aluminium results in severe dissolution of the substrate itself (Fig. E.10). In a second attempt under the same conditions the substrate did not fully dissolve, but very broad reflections of CAU-10-H were observed (Fig. E.9), indicating that the excess of Al due to dissolution of the anodized layer leads to mostly amorphous material. SEM images reveal indeed a foam-like morphology of the product with very inhomogeneous substrate coverage (Fig. E.11). Without the use of

any HCl this is not observed, though the *a-Al* substrate is not fully covered (Fig. E.11), and significant amounts of crystalline byproducts are observed (Fig. E.9). Clearly, the anodized layer makes the substrate surface more reactive. The added isophthalic acid linker is thus more than sufficient to extract Al^{3+}-ions from the support. The utilization of additional acids thus is not a necessity and actually has an adverse effect on the formation of MOF crystals on *a-Al* substrates. Hence, the standard synthesis protocol is adjusted for all further experiments employing anodized aluminium, excluding the addition of any additional acid (SSPa).

Furthermore, the DMF:H_2O ratio can be adjusted to regulate growth kinetics. The reduction of DMF leads to increased crystal growth and nucleation in the synthesis of MIL-53(Al)-NH_2, a MOF that also contains aluminium-hydroxide chains [40]. Also, a water-based synthesis would be more environmentally benign. When the amount of DMF is slightly reduced for syntheses on *m-Al*, crystal size distribution becomes more homogeneous (Fig. E.12) but more byproduct(s) are formed (Fig. E.13). For DMF contents below 25% of the standard protocol no crystals are formed (Figs. E.12-13). The TGA and SDTA profiles of the filtration residue indicate the presence of a large amount of recrystallized isophthalic acid (Fig. E.14). For *a-Al*, crystallization apparently becomes more homogeneous with decreasing amounts of DMF (Fig. E.15), though for all experiments large fractions of the crystals formed on the surface consist of byproduct(s) (Fig. E.13).

Lastly, reduction of temperature might yield more controlled crystal growth [41-44]. Unfortunately, when synthesis is performed at a slightly lowered temperature of 115 ^{o}C, no satisfactory crystal growth is obtained (Fig. E.16). The same holds for experiments at room temperature, even after prolonged reaction times. The effect of reaction time on syntheses at 135 ^{o}C is shown in Fig. 6.6 for metallic aluminium substrates. Clearly, increased reaction times result in larger crystals on the surface. Unfortunately though, coverage becomes more and more inhomogeneous for reaction times longer than 12 h. Apparently Ostwald-ripening [45] occurs. This unwanted phenomenon limits the use of longer crystallization times. Furthermore, byproduct formation is increased when longer reaction times are employed (Fig. E.17).
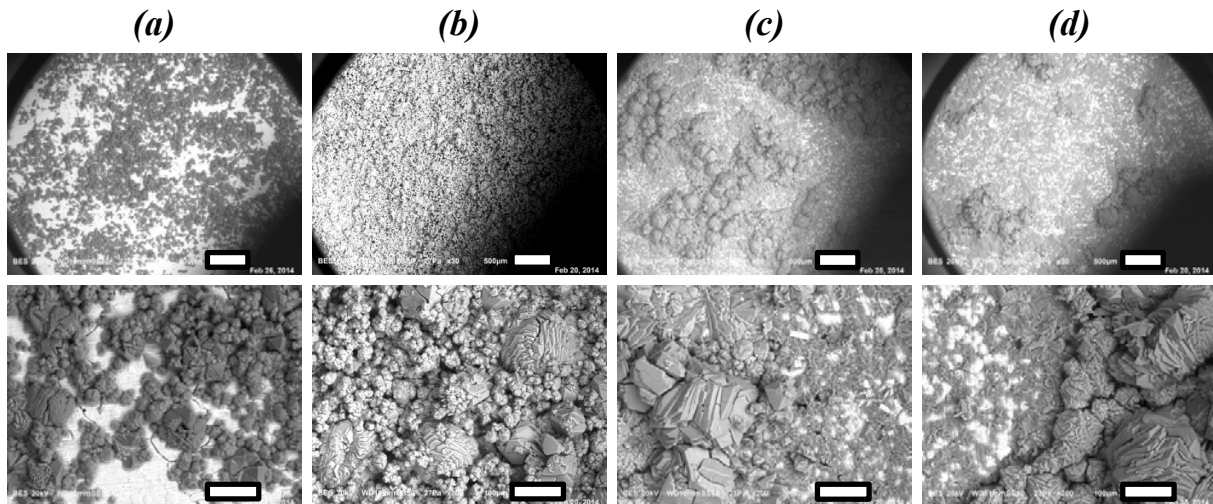
Figure 6.6: SEM images for CAU-10-H synthesized directly on *m-Al* (without pretreatment), for 6 (*a*), 12 (*b*, SSP), 18 (*c*) and 24 (*d*) h of reaction time (*top*, scale bar represents 500 μm, *bottom*, scale bar represents 100 μm).

SURFACE PRETREATMENT

Previous experiments, especially those employing *a-Al* and HCl (Fig. E.9), might indicate that differences exist between different substrate samples, driven perhaps by varying levels of impurities present. This issue might be mitigated by proper pretreatment of the substrate. Pretreatment, in the context of this work, can have two possible effects. Firstly, it removes possible pollutants present on the substrate surface that might have an adverse effect on synthesis [21, 46-48]. Secondly, it can be employed to create additional OH-groups, in order to improve reactivity [21, 22, 49, 50]. To this end, two separate substrate pretreatment methods are employed systematically on both metallic and anodized aluminium. Method A (M.A.), which involves treatment with acetone to remove impurities, is used for the primary purpose. Method B (M.B.) involves the previous step followed by treatment in diluted HCl solution (6% in H_2O) to create additional OH groups. For *m-Al* substrates, surface coverage and crystal size distributions seem hardly altered when either of the pretreatment methods is applied (Fig. E.18). This is notably different for anodized aluminium substrates. SEM pictures (Fig. 6.7) reveal that coverage is systematically increased from untreated (Fig 6.7a) to samples pretreated with method A (Fig. 6.7b) and further with method B (Fig. 6.7c). The difference might well be attributed to the fact that the metallic aluminium substrate of *a-Al*, has a very high quality (99.9999 % purity), and introduction of impurities by the anodization process is highly likely.
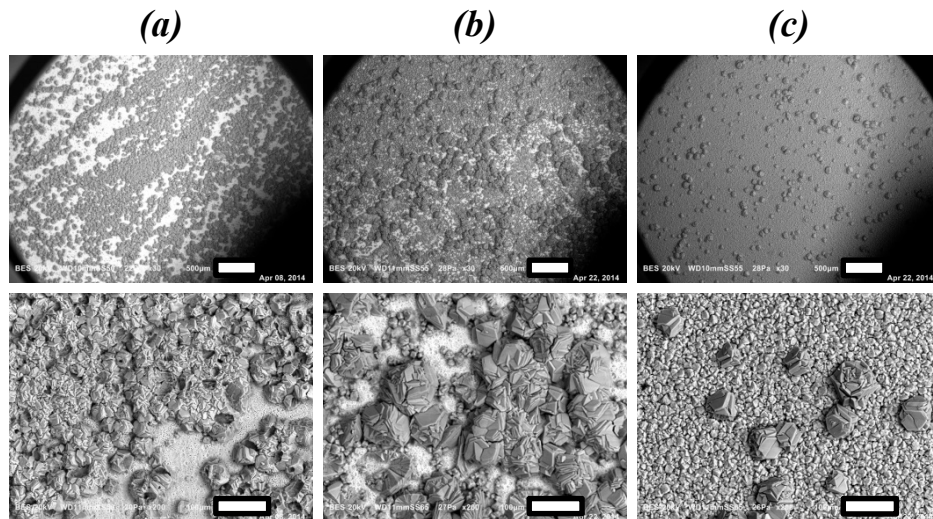
Figure 6.7: SEM images for CAU-10-H synthesized directly on *a-Al*, indicating the effect of pretreatment. Results for untreated (*a*), method A (*b*) and method B (*c*) (*top*, scale bar represents 500 μm, *bottom*, scale bar represents 100 μm).
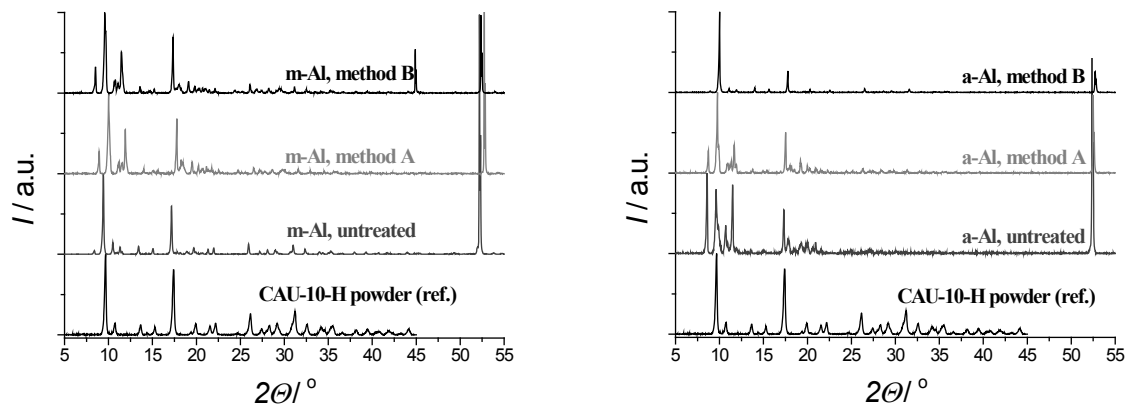
Figure 6.8: XRD patterns for CAU-10-H synthesized directly on *m-Al* (*left*) and *a-Al* (*right*), indicating the effect of pretreatment. Results for untreated samples and after treatment with method A or method B.

In addition, XRD patterns (Fig. 6.8) indicate that, as pretreatment becomes more severe, the formed CAU-10-H layer increases in purity and byproduct formation is hampered. For metallic aluminium, especially pretreatment method B induces byproduct formation (Fig. 6.8), and thus should be avoided when these substrates are utilized. The effect of pretreatment method A for *m-Al* and especially method B for *a-Al*, has a beneficial effect on reproducibility, as indicated by the XRD patterns of three repeated syntheses under identical conditions (Fig. 6.9).
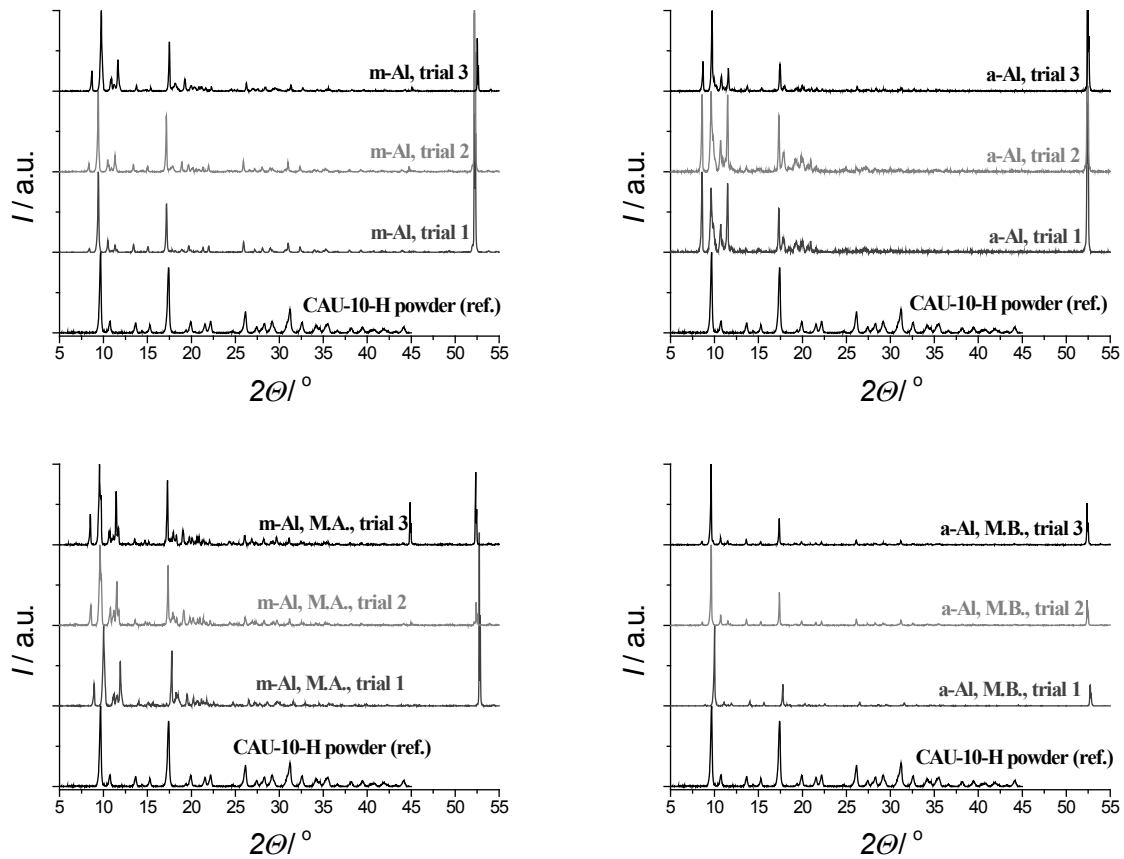
Figure 6.9: XRD patterns for CAU-10-H synthesized directly on *m-Al* (*left,* SSP) and *a-Al* (*right,* SSPa) for three separate synthesis trials, without substrate pretreatment (*top*) and after pretreatment (*bottom*, method A for *m-Al*, B for *a-Al*) .

Clearly, for untreated *a-Al* several differences between the XRD patterns of the samples of the three trials can be observed, whereas the XRD patterns for the three trials employing pretreated (method B) supports are much more identical. For sample *m-Al* this can also be observed, but both without and with treatment more impurities can be observed. SEM images confirm these trends (Figs. E.19-22). Longer reaction times, up to 14 or 16 h, using pretreated samples, also lead to unwanted Ostwald-ripening behavior and to a higher population of additional crystalline phase(s) (Figs. E.23-27), as found for untreated *m-Al* (Fig. 6.6).

To separate crystal nucleation and growth, creating additional degrees of freedom in the synthesis of CAU-10-H on aluminium substrates, multi-stage strategies have been adopted revolving around the deposition of small crystals (seeds) in one step and the subsequent growth of those crystals. Specifically two different approaches have been followed, as given in experimental, from Hu *et al.* [19] and Guerrero *et al.* [20].

6.3.3 REACTIVE SEEDING COATING

First step in the reactive seeding approach is the formation of small MOF crystals on the support. To this end, a relatively short synthesis, between 1 and 4 h, is performed on pretreated *m-Al* (method A) and pretreated *a-Al* (method B). The concentrations are those defined under the standard synthesis protocol (SSP, Section 6.2.3), except for *a-Al* where HCl is omitted from the synthesis mixture (SSPa). A seed reaction time of 1 or 2 h results in negligible coverage on either of the supports (Fig. E.28). For reaction times of 3 and especially 4 h, small crystals can be observed on the surface of both substrates (Fig. 6.11, top), and confirmed by XRD to be CAU-10-H (Fig. 6.10, left). These seeded substrates are deemed suitable for secondary growth. For secondary growth, reactant concentrations are lower with respect to bulk powder synthesis to hamper crystal nucleation in the liquid phase. When a dilution ratio (using water) of 2 is employed, incomplete and inhomogeneous substrate coverage is observed on both substrates for both 3 and 4 h of seed reaction time (Fig. E.29). The crystals formed on the substrate surface seemingly are pure CAU-10-H for *a-Al* substrates (Fig. E.30). For *m-Al* substrates, the XRD pattern indicates the presence of unwanted byproduct(s). High purity CAU-10-H crystals are obtained after filtration of the synthesis solutions (Fig. E.30). These results clearly indicate that crystallization is too rapid when a dilution ratio of 2 is employed, resulting in detachment of CAU-10-H from supports and possibly facilitating nucleation and growth in the synthesis solution. Increasing the dilution ratio to 5 significantly increases coverage and homogeneity of the formed layers (Fig. 6.11) and phase purity (Fig. 6.10). Moreover, this is highly desired from a synthesis yield point of view, since most of the reactants are used to manufacture the coating, and the amount of detached crystals and unreacted reactants is minimized.

Remarkably, layers formed on anodized aluminium after 4 h of synthesis exhibit an excellent quality. A dense, homogeneous coverage of phase-pure CAU-10-H is created (Fig. 6.11d). The obtained quality is far better than that from syntheses performed in one step (Section 6.3.3), indicating the potential of separating crystal nucleation and growth for the creation of MOF coatings on substrates.
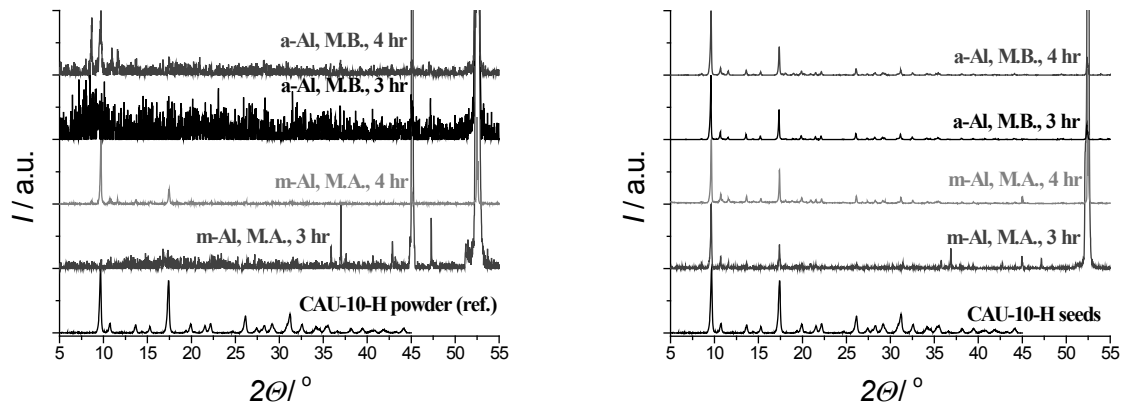
Figure 6.10: XRD patterns of substrates after reactive seeding (*left*) and secondary growth with a precursor dilution ratio of 5 (*right*), for pretreated *m-Al* (method A) and pretreated *a-Al* (method B), employing a reactive seeding time of 3 or 4 h.
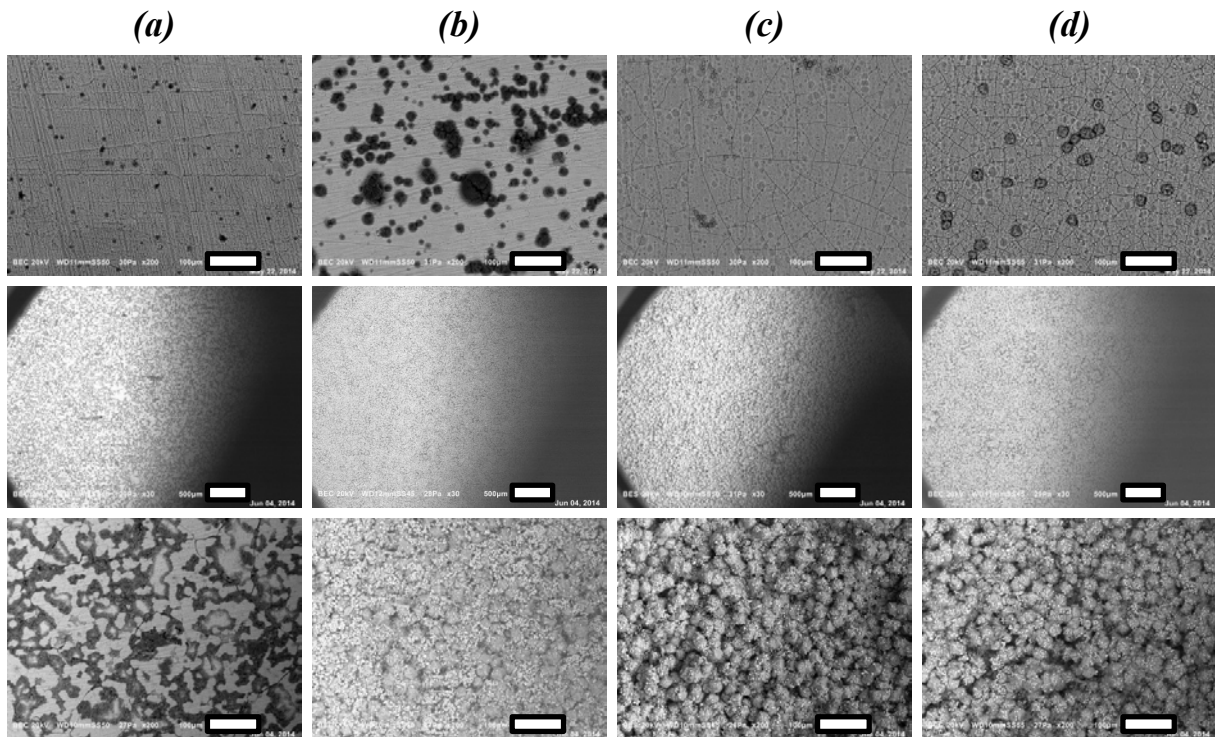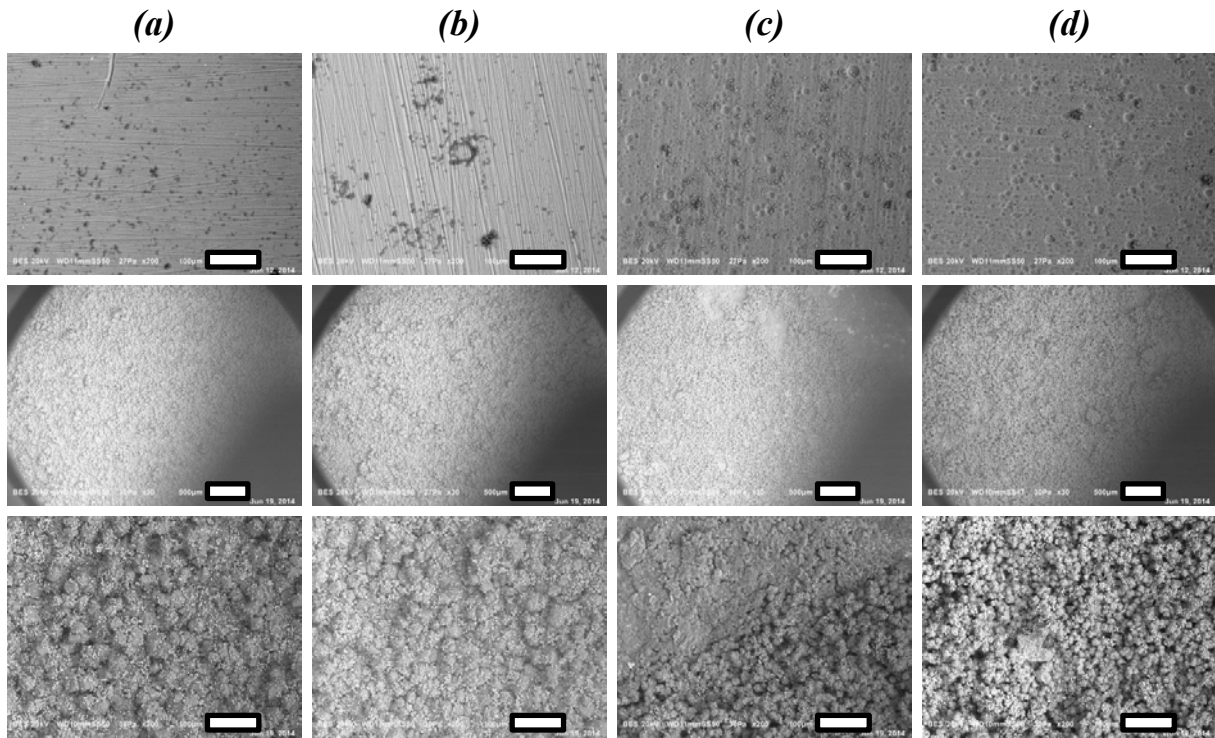

Figure 6.11: SEM images of CAU-10-H synthesized by reactive seeding and secondary growth with a precursor dilution ratio of 5, for pretreated *m-Al* (method A) employing a reaction time for the seeding step of 3 (*a*) and 4 (*b*) h and for pretreated *a-Al* (method B), employing a reaction time for the seeding step of 3 (*c*) and 4 (*d*) h. Substrates after reactive seeding (*top*, scale bar represents 100 μm) and after secondary growth (*middle*, scale bar indicates 500 μm, *bottom*, scale bar represents 100 μm).

6.3.4. THERMAL SEEDING COATING

The first step in thermal seeding is the creation of seeds synthesized via microwave heating, of which the characterization is discussed previously (Section 6.3.1). Utilizing the solution obtained from microwave reaction directly (solution 1) fails to properly deposit seeds on either of the pretreated supports, even after repetitive addition of the seed solution (Fig. E.31). This is notably different for seed solutions 2 and 3, containing 2.5% and 5% wt. of CAU-10-H crystals dispersed in water, respectively, as seeds are clearly visible on the pretreated supports (Fig. 6.12, top). For secondary growth, only a dilution ratio of 5 has been employed, based on the experience with reactive seeding (Section 6.3.3). The pretreated substrates after secondary growth show decent coverage (Fig. 6.12) and phase purity (Fig. 6.13). Compared to coverage obtained with reactive seeding, the crystal size distribution seems slightly less homogeneous and there appear to be some areas with lower coverage. This might be attributed to the less intimate contact of seeds with the support in this method, than using reactive seeding. Nonetheless, also in this approach coverage, crystal homogeneity and phase purity are superior to those obtained via direct synthesis (Section 6.3.2), once again underlining that separating crystal nucleation and growth is extremely suited for the creation of MOF coatings on substrates.

Figure 6.12: SEM images of CAU-10-H synthesized by thermal seeding and secondary synthesis, for pretreated *m-Al* (method A), employing seed solution 2 (*a*) and 3 (*b*) and for pretreated *a-Al* (method B) employing seed solution 2 (*c*) and 3 (*d*). Substrates after thermal seeding and cleaning (*top*, scale bar indicates 100 μm) and after secondary growth, employing a dilution ratio of 5 (*middle*, scale bar indicates 500 μm, *bottom*, scale bar indicates 100 μm).
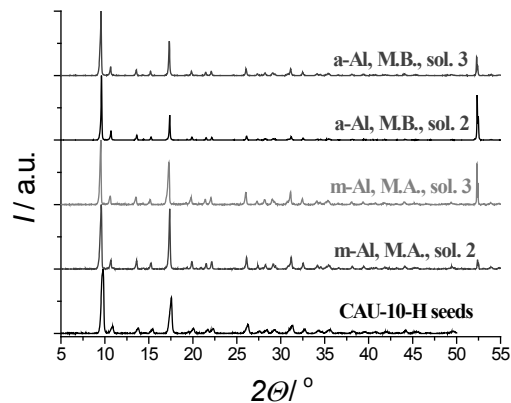
Figure 6.13: XRD patterns of used CAU-10-H seeds and substrates after thermal seeding and secondary growth, for pretreated *m-Al* (method A) and pretreated *a-Al* (method B), using seed solution 2 and 3 and a dilution ratio of 5.

6.3.5. COMPARISON

COATING METHODS

In many of the performed syntheses, a significant amount of crystalline byproduct is formed, of which the crystalline structure is not known. Recently it was reported that MIL-53(Al) is converted to non-porous γ-AlO(OH) (boehmite) when exposed to water at elevated temperatures [51]. Furthermore, under reaction conditions, insoluble $Al(OH)_3$ might precipitate [52, 53]. Unfortunately, none of the XRD patterns of these phases, or of those resulting from the recrystallization of any of the precursors corresponds to the ones of the formed byproduct(s) (Fig. E.32). The same holds for either α- or γ-alumina [54]. As the secondary phase(s) could not be isolated, the identity will remain unknown.

However, compared to results obtained in previous work ([15], Chapter 5), significant advances have been made with respect to homogeneity in both substrate coverage and size distribution of the deposited CAU-10-H crystals. Furthermore, byproduct formation has been minimized in this work. These advancements have been achieved by proper substrate pretreatment, employment of anodized alumina on the surface layer and the separation of crystal nucleation and growth. Especially, reactive seeding on pretreated *a-Al* has been shown to be a promising route, based on SEM microscopy and X-ray diffraction patterns. These techniques however, do not give any information on adsorption capacity and (cyclic) stability, nor on the chemical composition of the coating. To elucidate this, further characterization has been performed for a selection of samples. Specifically, CAU-10-H obtained by direct synthesis (DS.) on untreated (UT.) *a-Al* and *m-Al* and on pretreated *a-Al* (method B, M.B.) and *m-Al* (method A, M.A.) are compared with the samples obtained by the reactive seeding (RS.) approach on both pretreated *a-Al* and *m-Al*. Infrared spectra have been recorded for these samples (Fig. 6.14, bottom) and compared with those of CAU-10-H (powder) *a-Al* and *m-Al* (Fig. 6.14, top). The spectrum of CAU-10-H contains a sharp absorbance at 3685 cm^{-1}, attributed to the OH-vibrations of the hydroxide groups on the aluminium oxide-hydroxide chains [1]. Furthermore, the CH-vibration at the aromatic ring at 3075 cm^{-1} is clearly observed [1]. Lastly, the bands at 755 cm^{-1} and 724 cm^{-1} are characteristic for 1,3-substituted benzene-rings (out-of-plane-deformation of C-H bonds) and the band at around 1685 cm^{-1} indicates that DMF might be present inside the pores [1]. For anodized aluminium, the observed broad band between 3660 and 2940 cm^{-1} corresponds to the OH-vibrations of the aluminium hydroxide, and further indicates hydrogen bonding from water present inside the porous layer [55], despite the drying process applied (Section 6.2.3). The band around 1600

cm^{-1} corresponds to the Al=O stretch vibrations of double-bonded oxygen [55]. The two bands at roughly 1230 and 980 cm^{-1} correspond to Al-OH bending vibrations, of which the latter is likely to be from the surface layer [55]. IR spectra of CAU-10-H coated substrates after secondary synthesis (Fig. 6.14, bottom) show similarity with the recorded spectrum for bulk CAU-10-H (Fig. 6.14, top). However, there are notable differences as well. Specially, a shoulder is observed at slightly lower wavenumber than the sharp absorbance at 3685 cm^{-1}, which is attributed to the OH-stretch vibrations of the MOF. This shoulder is more predominantly perceived for substrates coated by direct synthesis (DS.) method, for which it is known that a significant amount of byproduct is formed. Hence, it is plausible that the byproduct contains OH-groups as well. Furthermore, the CH-vibration of the aromatic ring at 3075 cm^{-1} is generally less strongly observed when more byproduct is formed, an indication that the formed byproduct might contain no, or at least less, isophthalic acid. The peaks belonging to Al=O (stretch) and Al-OH (bend) of the anodized support at 1600, 1230 and 980 cm^{-1} are no longer distinguishable. At this point it should be noted that in addition to the background spectrum, the spectrum of the bare substrate (Fig. 6.14, bottom) is subtracted as well (Section 6.2.4), which is the reason for this. Between the absorbances at 3685 cm^{-1} and 3075 cm^{-1}, the spectrum is convex for metallic aluminium substrates. This is because the synthesis reaction creates a significant amount of additional Al-OH groups on the surface itself due to leaching. These are clearly not present in the pristine *m-Al* support and are thus not subtracted. This phenomenon is not present for the *a-Al* supports. In fact, for untreated (UT.) *a-Al* after direct synthesis (DS.) this part of the spectrum is concave. Seemingly, compared to the pristine anodized support, Al-OH groups have diminished, due to leaching of this reactive substrate, even without the presence of HCl.
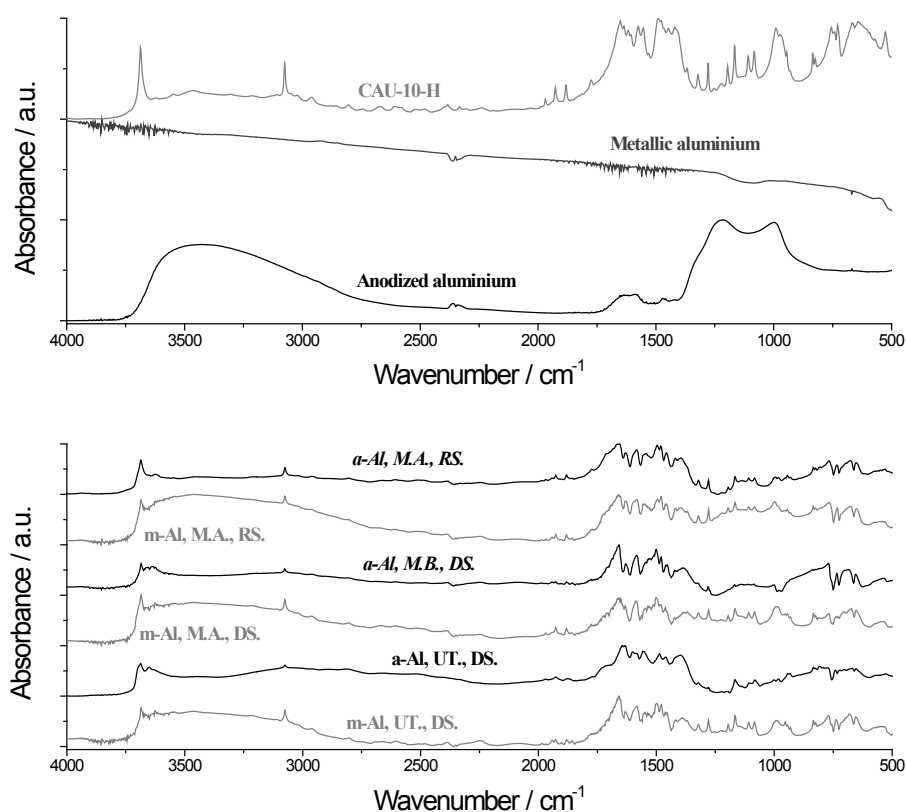
Figure 6.14: IR spectra of bulk CAU-10-H (conventional) and pristine *m-Al* and *a-Al* (*top*) and of selected syntheses (*bottom*). Specifically, CAU-10-H obtained by direct synthesis (DS.) on untreated (UT.) *a-Al* and *m-Al* and on pretreated *a-Al* (M.B.) and *m-Al* (M.A.), and by reactive seeding (RS.) on both pretreated *a-Al* and *m-Al* are shown (*a-Al* in *black lines*, *m-Al* in *grey lines*).

Thermo-gravimetric analysis (Fig. 6.15) is congruent with the qualitative indications by SEM analysis. The decrease in mass between 500 and 600 ^{o}C, which represents exothermic oxidation of the organic ligand, is largest for reactive seeding on *a-Al*. This is also observed in the SDTA profile (Fig. 6.15, right). This profile further indicates some solvent loss at low temperatures (< 150 ^{o}C). Notable exception is the profile for the direct synthesis on pretreated *a-Al*, which shows a broad endothermic peak between 300 and 500 ^{o}C, followed by a low signal for the exothermic oxidation. The onset of this curve at 300 ^{o}C might indicate the evaporation of isophthalic acid (Fig. E.14), although compared to the pure linker, this process is severely diffusion limited and therefore spread out over a wide temperature range. XRD (Fig. 6.8) does not indicate the presence of crystalline isophthalic acid, in agreement with a dispersed phase.
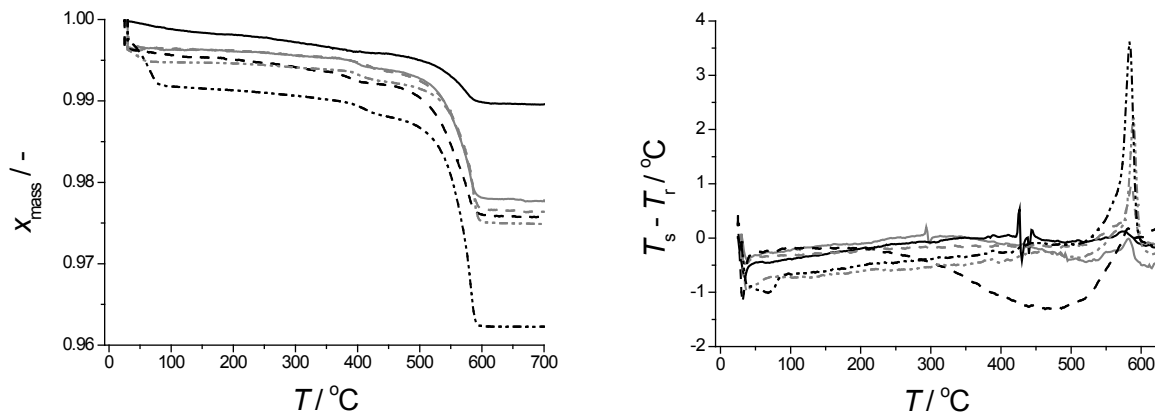
Figure 6.15: TGA (*left*) and SDTA (*right*) profiles for *a-Al* (*black lines*) and *m-Al* (*grey lines*) for untreated (*solid lines*) and pretreated (*dashed lines*) substrates obtained after direct synthesis and after reactive seeding (*dot-dashed lines*) employing pretreated substrates only.
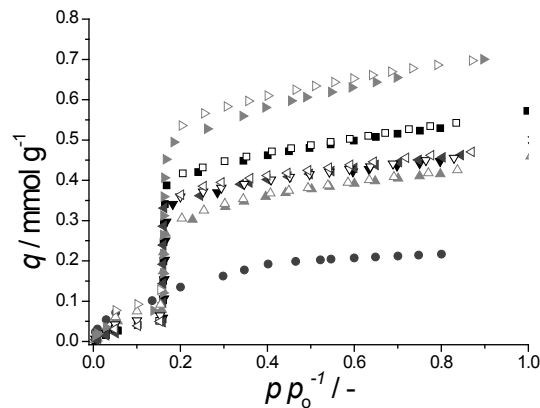
Figure 6.16: H_2O adsorption isotherms (298 K) for direct synthesis on untreated *m-Al* (■) and *a-Al* (●) and on pretreated *m-Al* (method A) (▲) and *a-Al* (method B) (▼) and for reactive seeding on pretreated *m-Al* (method A) (◀) and *a-Al* (method B) (▶). Loading, *q*, is given per total mass of sample (substrate + MOF coating).

Water adsorption isotherms on the selected coated substrates are given in Fig. 6.16. The *a-Al* substrate coated with CAU-10-H by reactive seeding shows the highest water adsorption capacity, displaying a significantly improved capacity compared to the other substrates and previous work ([15], Chapter 5). Nitrogen adsorption isotherms display strong diffusional limitations and henceforth do not offer a solid basis for detailed interpretation (Fig. E.33).

In the preceding, based on various characterization methods, conclusions regarding purity, surface coverage and crystal size distribution and adsorption capacity have been drawn. Ideally one would like to supplement this with a quantification of the amount of CAU-10-H present for selected samples. This desire is not so easily fulfilled, as *e.g.* methods based on quantitative elemental analysis cannot differentiate between aluminium present in the support and in the MOF structure. Hence further assumptions would be necessary, *e.g.* that all carbon atoms present in the sample belong to CAU-10-H on the substrate. As aluminium is predominantly present in the sample, because of the thickness of the dense support with respect to the porous coated layer, the uncertainty in the quantity of carbon present is anticipated to be large. Here it is chosen to display trends in CAU-10-H based on three simple and rather unsophisticated methods, all with inherent drawbacks.

- Firstly, dried substrates are weighed before and after synthesis. The difference can be attributed to the deposition of (crystalline) material on the surface. This method likely underestimates loading as during synthesis and/or pretreatment aluminium may have leached from the surface and subsequently dissolved in the synthesis liquid.

- Secondly, one could estimate the amount of CAU-10-H on the substrate by the weight loss observed between 450 and 700 ^{o}C, assuming that all the weight loss observed (Fig. 6.15) is caused by burning the organic ligand and subsequently that all decomposed ligands were incorporated in the CAU-10-H structure.

- Thirdly, by stating that the step in water adsorption (Fig. 6.16) is solely caused by CAU-10-H on the substrate surface and assuming that this has the same specific adsorption capacity as bulk MOF powder (Fig. 6.1), one can calculate the amount of MOF present on the substrate surface. However, to fit a substrate in a sample holder for water adsorption, it had to be cut into strips of ~ 8 mm wide. This procedure might have caused loss of crystals on the cutting edge, making that the observed capacity is a lower estimate. This effect would apply even more strongly to the TGA-analysis, as the samples required had to be cut to even smaller pieces (Section 6.2.4).

Nonetheless, the resulting estimated MOF loadings of these analyses are given in Table 6.1, per unit of substrate surface. Comparing first the observed loading of CAU-10-H on the two different substrates for the same synthesis method, the amount of MOF is systematically significantly lower for *a-Al*. This can easily be rationalized, as leaching from the reactive anodized amorphous aluminium oxide occurs more readily than from metallic aluminium.

Table 6.1: Indicative amounts of CAU-10-H present on selected substrates, estimated from substrate weighing, TGA analysis and volumetric water adsorption.

Synthesis method	substrate	Loading / mg cm^{-2}		
		Weighing	TGA	H_2O ads.
Direct, no pretreatment	m-Al	4.8	2.4	4.0
	a-Al[a]	2.3	1.0	n.d.
Direct, with pretreatment	m-Al[b]	7.2	2.6	2.8
	a-Al[c]	4.0	2.8	3.6
Reactive seeding[d]	m-Al[b]	3.4	2.8	3.3
	a-Al[c]	0.98	4.4	5.0

[a] Without HCl. [b] Method A. [c] Method B. [d] With pretreatment, seed reaction time 4 h. *n.d.* is not determinable.

This implies that by weighing no clear indication can be obtained on the amount of CAU-10-H present on a substrate. The MOF loadings determined by TGA and by water adsorption show similar trends and a fair agreement, although the quantity obtained by analyzing TGA is always lower than for H_2O adsorption. This could well be because of the necessity to cut these plates to manageable sizes. If this is the case, the loading indicated by H_2O adsorption also underestimates the actual MOF loading, as the substrates have to be cut, but to lesser extent (*vide supra*).

Nonetheless, based on water adsorption, a 25% increase in capacity has been achieved with reactive seeding on pretreated *a-Al* compared to the direct synthesis on untreated *m-Al*, the protocol used in previous work ([15], Chapter 5). This means that up to 48 kJ of heat can be withdrawn in the evaporator of an AHP/ADC per square meter of coated anodized aluminium surface (for metallic aluminium this is only 38 kJ ([15], Chapter 5). On top of that, reactive seeding leads to a more homogenous coverage of crystals and a significantly narrower crystal size distribution as well as enhanced purity of CAU-10-H.

PERFORMANCE

Lastly, cyclic water ad- and desorption has been performed gravimetrically for both bulk CAU-10-H (conventional synthesis) and reactive seeding on *a-Al* to assess stability of the coated substrate (Fig. 6.17). Clearly both bulk CAU-10-H and the substrate do not lose adsorption capacity over nine cycles. For the bulk powder this is expected as Fröhlich *et al.* already demonstrated that adsorption capacity of CAU-10-H is retained over 700 cycles [13].
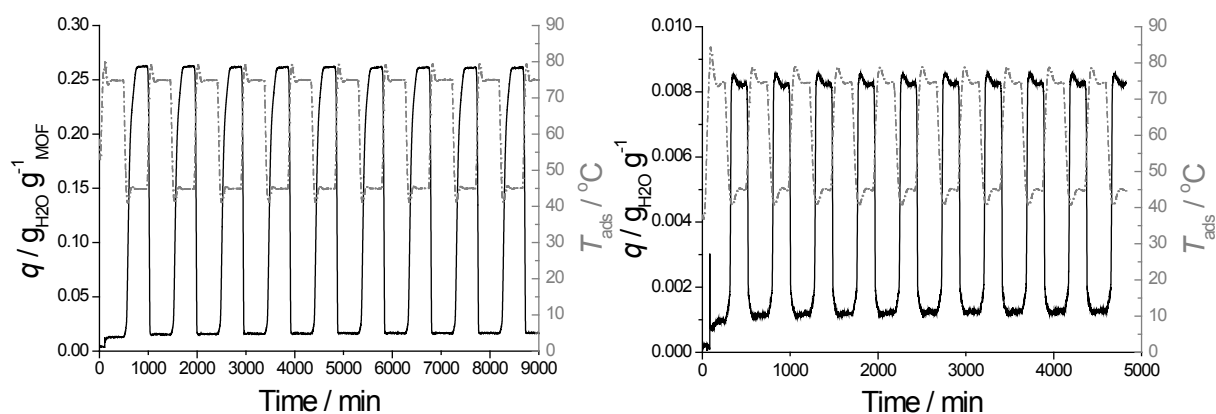
Figure 6.17: Cyclic gravimetric water adsorption measurements upon temperature step changes between 45 and 75 °C at a fixed water vapor pressure (26 mbar) for bulk CAU-10-H powder (conventional synthesis, *left*) and CAU-10-H synthesized on pretreated *a-Al* (method B) using reactive seeding (*right*). Adsorbed amount of water (*left y-axis, black solid line*) and temperature (*right y-axis, dark gray dashed line*) both as function of time. Amount adsorbed is indicated per gram of total sample, including the mass of the support for the coated *a-Al*.

Clearly, stability is not compromised when this MOF is coated on a substrate, a feature indispensable for application in adsorption driven heat pumps and chillers. Furthermore, the response of the amount adsorbed on a temperature step change is significantly more rapid for the coated sample, indicating that heat and mass transfer are enhanced when a coated substrate is employed, in comparison to powder. The loading, however, expressed per unit mass of sample, is significantly lower for the substrate than for the bulk powder. This is because the aluminium substrate has a thickness of ~ 0.5 mm, whereas the coatings have a thickness in the order of 60-120 μm (SEM images), so most of the sample mass comes from the bulk aluminium. For application in AHP/ADC devices a thermodynamic optimization analysis of the coating thickness with respect to the support thickness should be performed, considering not only capacity, but also heat and mass transport.

In summary, reactive seeding on pretreated *a-Al* results in CAU-10-H coatings that fulfill every requirement for application in adsorption driven heat pumps and chillers (Section 6.1), namely: full coverage of the substrate surface, high MOF loading, homogeneous layer thickness, narrow crystal size distribution, sufficient stability and high purity of the crystalline phase. However, the number of necessary steps starting from metallic aluminium: (i) anodization, (ii) pretreatment, (iii) reactive seeding and (iv) secondary growth may hamper scalability of these coatings. In this sense, it might be beneficial to integrate some of the steps,

especially merging anodization and pretreatment should be feasible. Additionally, the employed anodized layer was selected because of commercial availability, not because it necessarily holds optimal properties for MOF attachment. Optimizing anodization conditions and combining this step with the seeding step might thus further improve the manufacture of CAU-10-H coatings.

6.4. CONCLUSIONS

Based on XRD patterns of both the anhydrous and hydrated state and subsequent structural refinement, CAU-10-H does not exhibit structural changes upon water adsorption, in contrast to earlier literature. Minor changes in the XRD pattern (reflections at $2\theta \sim 14.6, 15.1^{o}$ become more intense) upon CAU-10-H hydration are due to an ordered arrangement of water molecules within the structure. Refinement indicates that water preferentially adsorbs close to the OH-groups on the structure's helical Al-OH chains. The step-wise water uptake at a specific relative pressure reads like a phase change, resulting in a regularly ordered adsorbed water phase in between liquid and solid water.

When it comes to the manufacture of CAU-10-H coatings on aluminium substrates, syntheses on metallic aluminium (*m-Al*) with varying manufacture conditions did not result in a notable increase in coating quality. In fact, any deviation from the standard synthesis protocol (SSP) leads to worse coatings. Addition of aluminium to the synthesis solution leads to crystal nucleation in the liquid phase and to detachment of crystals formed on the surface. Increasing the acidity by HCl addition leads to promotion of unwanted byproduct(s) formation, as does the reduction of DMF concentration. Prolonged reaction times lead to unwanted Ostwald ripening and crystal detachment. Reduction of temperature leads to insignificant substrate coverage. The porous amorphous aluminium oxide layer of anodized aluminium (*a-Al*) is more reactive and thus crystallization on the surface is easier. However, a significant amount of byproduct(s) is formed, attributed to the higher content of extracted aluminium-ions near the surface. In addition, the use of HCl during synthesis causes (partial) dissolution of this substrate and must be avoided.

Substrate pretreatment improves both reproducibility and coating quality of CAU-10-H on both *m-Al* and *a-Al* substrates. For *m-Al* substrates cleaning with acetone (method A) yields optimal results. For *a-Al*, additionally the substrate should be contacted with a diluted HCl solution (6% in water) (method B) for optimal results. Despite the improvement achieved,

obtained coatings are still suboptimal in coverage, homogeneity of crystal sizes and purity. In many cases an unwanted, unknown byproduct, which has neither been identified nor isolated, is formed next to CAU-10-H.

Separation of crystal nucleation and growth yields significantly improved quality, showcased by the high purity and homogeneous crystal size distribution obtained by both thermal and reactive seeding on pretreated substrates. Especially reactive seeding in conjunction with pretreated *a-Al* (method B) yields full coverage of the substrate surface, a homogeneous layer thickness, narrow crystal size distribution, and high purity of the crystalline phase. This method leads to the highest water adsorption capacity observed of all coated substrates. Lastly, the coating created with this method does not lose capacity upon repeated water adsorption-desorption cycles and responds much faster to temperature changes than bulk CAU-10-H powder.

6.5. REFERENCES

[1]   H. Reinsch, M.A. van der Veen, B. Gil, B. Marszalek, T. Verbiest, D. de Vos, N. Stock, Structures, sorption characteristics, and nonlinear optical properties of a new series of highly stable aluminum MOFs, Chemistry of Materials, 25 (2012) 17-26.

[2]   R. J. Sheehan, Terephthalic acid, dimethyl terephthalate, and isophthalic acid, Ullmann's encyclopedia of industrial chemistry, Wiley-VCH Verlag GmbH & Co. KGaA2000.

[3]   H. Kakiuchi, S. Shimooka, M. Iwade, K. Oshima, M. Yamazaki, S. Terada, H. Watanabe, T. Takewaki, Novel water vapor adsorbent FAM-Z01 and its applicability to an adsorption heat pump, Kagaku Kogaku Ronbunshu, 31 (2005) 361-364.

[4]   H. Kakiuchi, S. Shimooka, M. Iwade, K. Oshima, M. Yamazaki, S. Terada, H. Watanabe, T. Takewaki, Water vapor adsorbent FAM-Z02 and its applicability to adsorption heat pump, Kagaku Kogaku Ronbunshu, 31 (2005) 273-277.

[5]   S. Shimooka, K. Oshima, H. Hidaka, T. Takewaki, H. Kakiuchi, A. Kodama, M. Kubota, H. Matsuda, The evaluation of direct cooling and heating desiccant device coated with FAM, Journal of Chemical Engineering of Japan, 40 (2007) 1330-1334.

[6]   MITSUBISHI PLASTICS, Zeolitic water vapor adsorbent: AQSOA. http://www.aaasaveenergy.com/products/001/pdf/AQSOA_1210E.pdf (accessed 17-01-2015).

[7]   G. Liu, P. Tian, Y. Zhang, J. Li, L. Xu, S. Meng, Z. Liu, Synthesis of SAPO-34 templated by diethylamine: Crystallization process and Si distribution in the crystals, Microporous and Mesoporous Materials, 114 (2008) 416-423.

[8]   Y. Xu, P.J. Maddox, J.W. Couves, The synthesis of SAPO-34 and CoSAPO-34 from a triethylamine-hydrofluoric acid-water system, Journal of the Chemical Society, Faraday Transactions, 86 (1990) 425-429.

[9]   A.M. Prakash, S. Unnikrishnan, Synthesis of SAPO-34: High silicon incorporation in the presence of morpholine as template, Journal of the Chemical Society, Faraday Transactions, 90 (1994) 2291-2296.

[10]   R.D. Gougeon, E.B. Brouwer, P.R. Bodart, L. Delmotte, C. Marichal, J.-M. Chézeau, R.K. Harris, Solid-state NMR studies of the as-synthesized $ALPO_4$-5/TPAF microporous aluminophosphate, The Journal of Physical Chemistry B, 105 (2001) 12249-12256.

[11]   F. Jiang, Z. Tang, J. Zhai, J. Ye, J. Han, Synthesis of $ALPO_4$-5 crystals using TBAOH as template, Microporous and Mesoporous Materials, 92 (2006) 129-133.

[12]   Y. Wan, C.D. Williams, C.V. Duke, J.J. Cox, Systematic studies on the effect of water content on the synthesis, crystallisation, conversion and morphology of $ALPO_4$-5 molecular sieve, Journal of Materials Chemistry, 10 (2000) 2857-2862.

[13]   D. Fröhlich, S.K. Henninger, C. Janiak, Multicycle water vapour stability of microporous breathing MOF aluminium isophthalate CAU-10-H, Dalton Transactions, (2014).

[14]   T.A. Nijhuis, A.E. Beers, T. Vergunst, I. Hoek, F. Kapteijn, J.A. Moulijn, Preparation of monolithic catalysts, Catalysis Reviews, 43 (2001) 345-380.

[15]   M. De Lange, C. Ottevanger, M. Wiegman, T. Vlugt, J. Gascon, F. Kapteijn, Crystals for sustainability-structuring Al-based MOFs for the allocation of heat and cold, CrystEngComm, 17 (2015) 281-285.

[16]   T. Ahnfeldt, N. Stock, Synthesis of isoreticular CAU-1 compounds: Effects of linker and heating methods on the kinetics of the synthesis, CrystEngComm, 14 (2012) 505-511.

[17]   S.-N. Kim, J. Kim, H.-Y. Kim, H.-Y. Cho, W.-S. Ahn, Adsorption/catalytic properties of MIL-125 and NH_2-MIL-125, Catalysis Today, 204 (2013) 85-93.

[18]   N.A. Khan, I.J. Kang, H.Y. Seok, S.H. Jhung, Facile synthesis of nano-sized Metal-Organic Frameworks, chromium-benzenedicarboxylate, MIL-101, Chemical Engineering Journal, 166 (2011) 1152-1157.

[19]   Y. Hu, X. Dong, J. Nan, W. Jin, X. Ren, N. Xu, Y.M. Lee, Metal-Organic Framework membranes fabricated via reactive seeding, Chemical Communications, 47 (2010) 737-739.

[20]   V.V. Guerrero, Y. Yoo, M.C. McCarthy, H.-K. Jeong, HKUST-1 membranes on porous supports using secondary growth, Journal of Materials Chemistry, 20 (2010) 3938-3943.

[21]   M. Arnold, P. Kortunov, D.J. Jones, Y. Nedellec, J. Kärger, J. Caro, Oriented crystallisation on supports and anisotropic mass transport of the Metal-Organic Framework manganese formate, European Journal of Inorganic Chemistry, 2007 (2007) 60-64.

[22]   H. Bux, A. Feldhoff, J. Cravillon, M. Wiebcke, Y.-S. Li, J. Caro, Oriented Zeolitic Imidazolate Framework-8 membrane with sharp H_2/C_3H_8 molecular sieve separation, Chemistry of Materials, 23 (2011) 2262-2269.

[23]   M.A. Neumann, X-cell: A novel indexing algorithm for routine tasks and difficult cases, Journal of Applied Crystallography, 36 (2003) 356-365.

[24]   Materials studio v4.4, accelrys software inc. (c), San Diego, ca, 2009.

[25]   A.L. Spek, Structure validation in chemical crystallography, Acta Crystallographica Section D: Biological Crystallography, 65 (2009) 148-155.

[26]   F. Rouquerol, J. Rouquerol, K. Sing, Adsorption by powders & porous solids, Academic Press, London, 1999.

[27]   F. Schüth, K.S.W. Sing, J. Weitkamp, Handbook of porous solids, Wiley-VCH, 2002.

[28]   A. García Márquez, A. Demessence, A.E. Platero-Prats, D. Heurtaux, P. Horcajada, C. Serre, J.-S. Chang, G. Férey, V.A. de la Peña-O'Shea, C. Boissière, D. Grosso, C. Sanchez, Green microwave synthesis of MIL-100(Al, Cr, Fe) nanoparticles for thin-film elaboration, European Journal of Inorganic Chemistry, 2012 (2012) 5165-5174.

[29]   H.-Y. Cho, D.-A. Yang, J. Kim, S.-Y. Jeong, W.-S. Ahn, CO_2 adsorption and catalytic application of Co-MOF-74 synthesized by microwave heating, Catalysis Today, 185 (2012) 35-40.

[30]   H. Furukawa, F. Gándara, Y.-B. Zhang, J. Jiang, W.L. Queen, M.R. Hudson, O.M. Yaghi, Water adsorption in porous Metal-Organic Frameworks and related materials, Journal of the American Chemical Society, 136 (2014) 4369-4381.

[31]   P. Serra-Crespo, R. Berger, W. Yang, J. Gascon, F. Kapteijn, Separation of CO_2/CH_4 mixtures over NH_2-MIL-53 - an experimental and modelling study, Chemical Engineering Science 124 (2015) 96-108.

[32]   M.F. De Lange, J.-J. Gutierrez-Sevillano, S. Hamad, T.J.H. Vlugt, S. Calero, J. Gascon, F. Kapteijn, Understanding adsorption of highly polar vapors on mesoporous MIL-100(Cr) and MIL-101(Cr): Experiments and molecular simulations, The Journal of Physical Chemistry C, 117 (2013) 7613-7622.

[33]   G. Job, F. Herrmann, Chemical potential - a quantity in search of recognition, European journal of physics, 27 (2006) 353.

[34]   J. Reboul, S. Furukawa, N. Horike, M. Tsotsalas, K. Hirai, H. Uehara, M. Kondo, N. Louvain, O. Sakata, S. Kitagawa, Mesoscopic architectures of porous coordination polymers fabricated by pseudomorphic replication, Nature materials, 11 (2012) 717-723.

[35]   T. Campbell, R.K. Kalia, A. Nakano, P. Vashishta, S. Ogata, S. Rodgers, Dynamics of oxidation of aluminum nanoclusters using variable charge molecular-dynamics simulations on parallel computers, Physical Review Letters, 82 (1999) 4866-4869.

[36]   P.P. Mardilovich, A.N. Govyadinov, N.I. Mukhurov, A.M. Rzhevskii, R. Paterson, New and modified anodic alumina membranes part I. Thermotreatment of anodic alumina membranes, Journal of Membrane Science, 98 (1995) 131-142.

[37]   W. Stumm, R. Wollast, Coordination chemistry of weathering: Kinetics of the surface-controlled dissolution of oxide minerals, Reviews of Geophysics, 28 (1990) 53-69.

315

[38]   M.J. Katz, Z.J. Brown, Y.J. Colón, P.W. Siu, K.A. Scheidt, R.Q. Snurr, J.T. Hupp, O.K. Farha, A facile synthesis of UiO-66, UiO-67 and their derivatives, Chemical Communications, 49 (2013) 9449-9451.

[39]   M.G. Goesten, P.C. Magusin, E.A. Pidko, B. Mezari, E.J. Hensen, F. Kapteijn, J. Gascon, Molecular promoting of aluminum Metal-Organic Framework topology MIL-101 by n, n-dimethylformamide, Inorganic Chemistry, 53 (2014) 882-887.

[40]   E. Stavitski, M. Goesten, J. Juan-Alcañiz, A. Martinez-Joaristi, P. Serra-Crespo, A.V. Petukhov, J. Gascon, F. Kapteijn, Kinetic control of Metal-Organic Framework crystallization investigated by time-resolved in situ X-ray scattering, Angewandte Chemie International Edition, 50 (2011) 9624-9628.

[41]   E. Biemmi, S. Christian, N. Stock, T. Bein, High-throughput screening of synthesis parameters in the formation of the Metal-Organic Frameworks MOF-5 and HKUST-1, Microporous and Mesoporous Materials, 117 (2009) 111-117.

[42]   H. Reinsch, N. Stock, High-throughput studies of highly porous Al-based MOFs, Microporous and Mesoporous Materials, 171 (2013) 156-165.

[43]   Y.-B. Dong, Y.-Y. Jiang, J. Li, J.-P. Ma, F.-L. Liu, B. Tang, R.-Q. Huang, S.R. Batten, Temperature-dependent synthesis of Metal-Organic Frameworks based on a flexible tetradentate ligand with bidirectional coordination donors, Journal of the American Chemical Society, 129 (2007) 4520-4521.

[44]   Y.-X. Sun, W.-Y. Sun, Influence of temperature on Metal-Organic Frameworks, Chinese Chemical Letters, 25 (2014) 823-828.

[45]   J.W. Muller, Crystallization, 4, Revised ed., Butterworth-Heinemann Ltd, Oxford, 2001.

[46]   H. Guo, G. Zhu, I.J. Hewitt, S. Qiu, "Twin copper source" growth of Metal-Organic Framework membrane: $Cu_3(BTC)_2$ with high permeability and selectivity for recycling H_2, Journal of the American Chemical Society, 131 (2009) 1646-1647.

[47]   R. Makiura, S. Motoyama, Y. Umemura, H. Yamanaka, O. Sakata, H. Kitagawa, Surface nano-architecture of a Metal-Organic Framework, Nature materials, 9 (2010) 565-571.

[48]   K. Yusenko, M. Meilikhov, D. Zacher, F. Wieland, C. Sternemann, X. Stammer, T. Ladnorg, C. Wöll, R.A. Fischer, Step-by-step growth of highly oriented and continuous seeding layers of $[Cu_2(NDC)_2(DABCO)]$ on bare oxide and nitride substrates, CrystEngComm, 12 (2010) 2086-2090.

[49]   F. Jeremias, D. Frohlich, C. Janiak, S.K. Henninger, Advancement of sorption-based heat transformation by a metal coating of highly-stable, hydrophilic aluminium fumarate MOF, RSC Advances, 4 (2014) 24073-24082.

[50]   S. Hermes, D. Zacher, A. Baunemann, C. Wöll, R.A. Fischer, Selective growth and MOCVD loading of small single crystals of MOF-5 at alumina and silica surfaces modified with organic self-assembled monolayers, Chemistry of Materials, 19 (2007) 2168-2173.

[51]   I. Bezverkhyy, G. Ortiz, G. Chaplais, C. Marichal, G. Weber, J.-P. Bellat, MIL-53(Al) under reflux in water: Formation of γ-ALO(OH) shell and H_2BDC molecules intercalated into the pores, Microporous and Mesoporous Materials, 183 (2014) 156-161.

[52]   K.L. Nagy, A.C. Lasaga, Dissolution and precipitation kinetics of Gibbsite at 80 °C and pH 3: The dependence on solution saturation state, Geochimica et Cosmochimica Acta, 56 (1992) 3093-3111.

[53]   J.Y. Bottero, J.M. Cases, F. Fiessinger, J.E. Poirier, Studies of hydrolyzed aluminum chloride solutions. 1. Nature of aluminum species and composition of aqueous solutions, The Journal of Physical Chemistry, 84 (1980) 2933-2939.

[54]   A. Boumaza, L. Favaro, J. Lédion, G. Sattonnay, J.B. Brubach, P. Berthet, A.M. Huntz, P. Roy, R. Tétot, Transition alumina phases induced by heat treatment of Boehmite: An X-ray diffraction and infrared spectroscopy study, Journal of Solid State Chemistry, 182 (2009) 1171-1176.

[55]   G. Dorsey, The characterization of anodic aluminas i. Composition of films from acidic anodizing electrolytes, Journal of the Electrochemical Society, 113 (1966) 169-172.
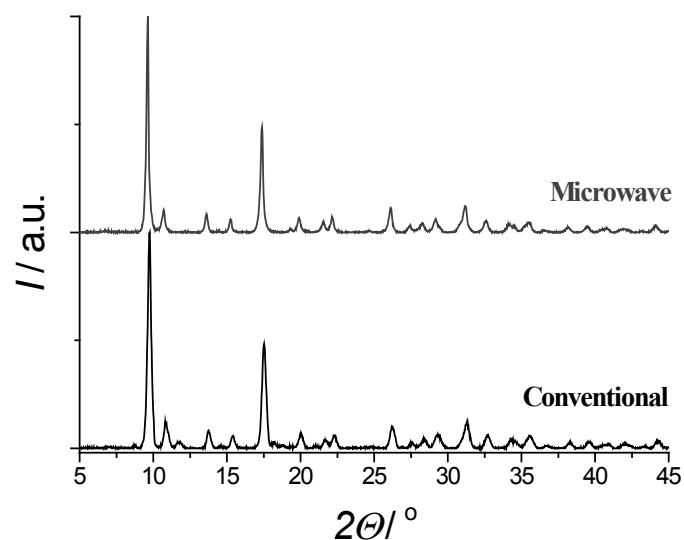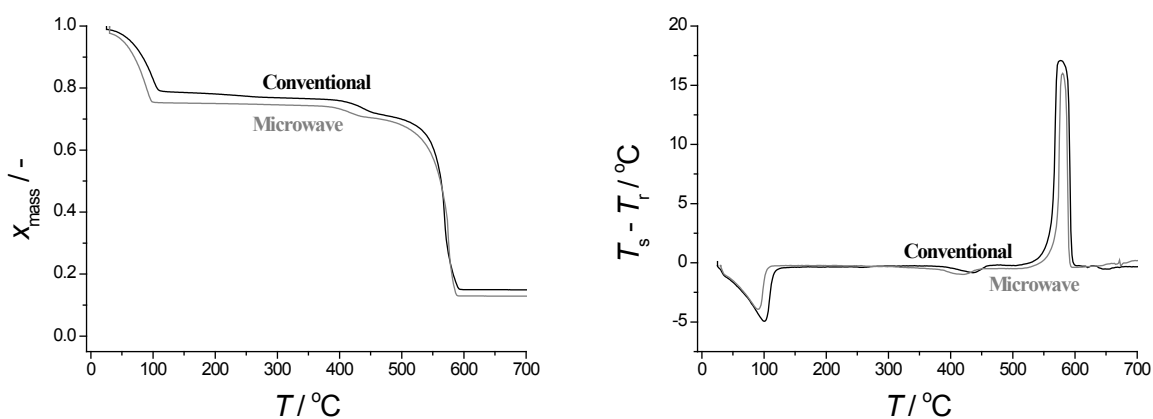
APPENDIX E

MANUFACTURE OF DENSE CAU-10-H
COATINGS ON ALUMINIUM SUPPORTS:
OPTIMIZATION AND CHARACTERIZATION

Figure E.1: XRD patterns for hydrated CAU-10-H powder synthesized using conventional and microwave heating.


Figure E.2: TGA (*left*) and SDTA (*right*) profiles of CAU-10-H powder synthesized by conventional and microwave synthesis. Measured using a flow of air (100 ml/min) and a heating rate of 5 °C/min.

E.1. POWDER SYNTHESIS

CAU-10-H has been synthesized employing either conventional or microwave heating. For comparison, XRD patterns (Fig. E.1), TGA and SDTA profiles (Fig E.2) and adsorption isotherms of water and nitrogen (Fig. E.3) are depicted. SEM images of both powders are depicted in Fig. E.4.
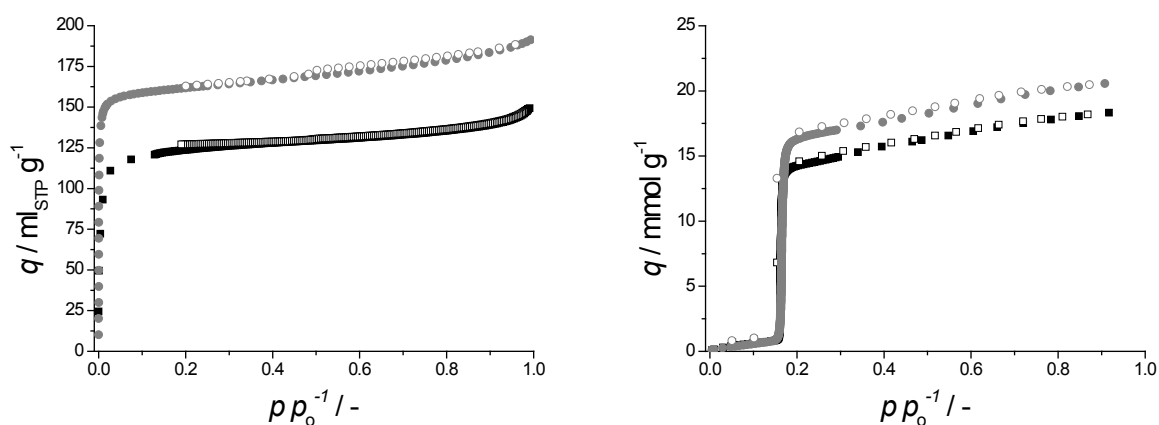
Figure E.3: Nitrogen adsorption (*left*, 77 K) and water adsorption (*right*, 298 K) isotherms of CAU-10-H synthesized by conventional heating (■) and by microwave heating (●). Closed symbols depict adsorption, open desorption. STP refers to standard pressure and temperature (0 °C, 1 bar) and p_o to the saturated vapor pressure at measurement temperature.
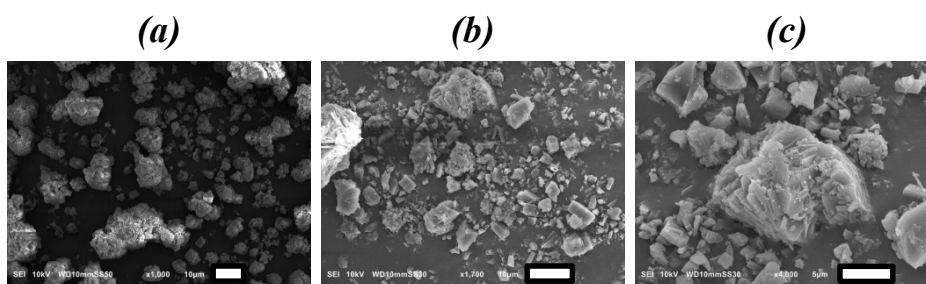
Figure E.4: SEM images of CAU-10-H synthesized with microwave synthesis (*a*, scale bar represents 10 μm) and with conventional synthesis (*b*, scale bar represents 10 μm, *c*, scale bar represents 5 μm).

The hydrated structure of CAU-10-H is refined using the XRD pattern of the sample synthesized by microwave heating. The details of the refinement are given in Fig. E.5 and Table E.1.
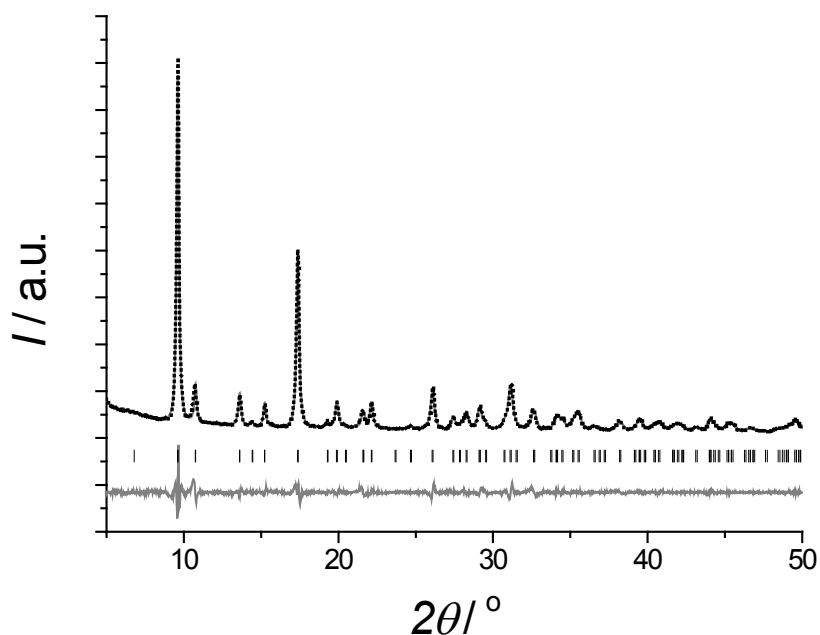
Figure E.5: Rietveld refinement of CAU-10-H in hydrated form. Experimental XRD pattern indicated by black dots, simulated by a grey line. Observed inflections are depicted by vertical dashes and the difference in reflection between simulation and experiment is indicated by the grey line at the bottom.

Table E.1: Rietveld refinement details for the hydrated form of CAU-10-H.

Molecular formula	$C_{16}H_9Al_2O_{10}$, $4H_2O$
Formula weight / g·mol^{-1}	486.2
Wavelength / Å	Co-$K\alpha$ / 1.78897
T **/ K**	293
Crystal system	tetragonal
Space group	$I4_1$ (№ 80)
a **/ Å**	21.3021(10)
c **/ Å**	10.709(3)
β **/ °**	90
V **/ Å^3**	4859.5(14)
Z	8
ρ_{calc} **/ g·cm^{-3}**	1.327
2θ **/ °**	5 – 50
R_p	5.96
R_{wp}	7.91

ENTROPY OF ADSORPTION

From the isosteric enthalpy of adsorption (Fig. 6.1) one would like to obtain an estimation for the entropy of adsorption. For adsorption one can write:

$$\Delta_{ads}G = \Delta_{ads}H - T\Delta_{ads}S \leq 0 \qquad (E.1)$$

Here G, H and S are the molar Gibbs free energy, enthalpy and entropy, respectively and T is the temperature. One can thus write:

$$\frac{\Delta_{ads}H - \Delta_{ads}G}{T} = \Delta_{ads}S \qquad (E.2)$$

Indeed, the entropy of adsorption is negative, as expected (this does not mean that the total entropy of the entire system decreases). From the isosteric enthalpy and Gibbs free energy follows:

$$\Delta_{ads}S_q = \frac{\Delta_{ads}H_q - \Delta_{ads}G}{T} = \frac{R}{T}\left(\frac{\partial \ln p}{\partial \left(\frac{1}{T}\right)}\right)_q - R\ln\left(\frac{p}{p_o}\right) \qquad (E.3)$$

Here q represents the amount adsorbed and p the pressure. The entropy of adsorption, at the start of the step in water adsorption (~1 mmol g^{-1}, Fig. 6.1), is roughly ~ 175 J mol^{-1} K^{-1}. For water in different phases (298 K, 1 bar), the entropy is tabulated in Table E.2. The vapor phase is at 1 bar. As, the step commences roughly at 0.15 p_o (0.0047 bar), this has to be adjusted in the entropy (lower relative pressure means higher entropy). By assuming an ideal gas (internal energy change is zero) and isothermal compression, this could be done by using:

$$\Delta_{compr}S = \int_{p_1}^{p_2}\frac{pdV}{T} = R\ln\left(\frac{p_1}{p_2}\right) \qquad (E.4)$$

Filling in (p_1 = 1 bar, p_2 = 0.0047 bar) results in the fact that the (molar) entropy of water vapor at 0.15 relative pressure, at 298K is ~ 233 J mol^{-1} K^{-1}. By adding to this the aforementioned entropy of adsorption, the entropy of the adsorbed phase is roughly ~58 J mol^{-1} K^{-1}. By assuming that both liquid and solid water are incompressible (no work) and that the process of depressurizing (from 1 bar to 0.0047) is isothermal, the entropies of both the liquid and the solid do not change upon pressure changes.

321

Table E.2: Entropy of different phases of water (298 K, 1 bar) [1].

| Phase:	$S / \text{J mol}^{-1} \text{ K}^{-1}$
Gas/vapor	188.7
Liquid	69.9
Solid	44.8
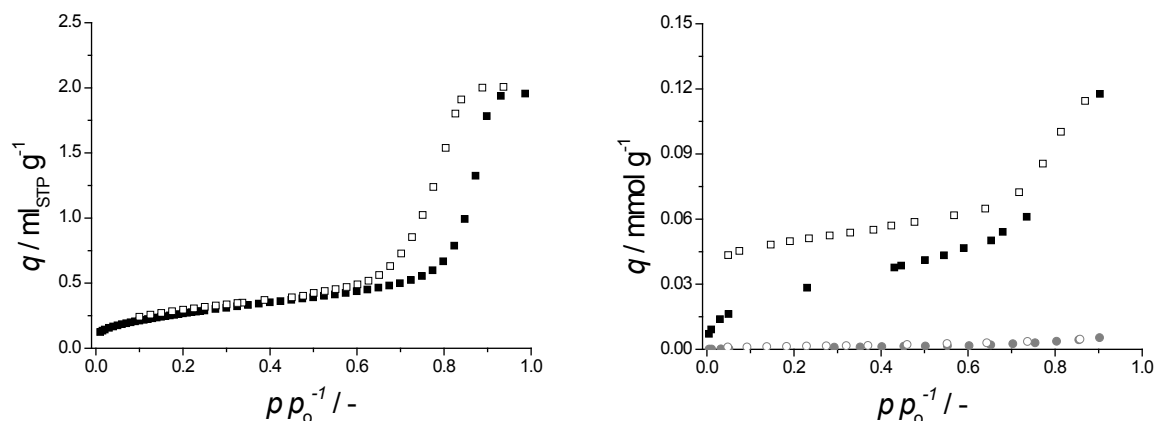
Figure E.6: Nitrogen adsorption (*left*, 77 K) and water adsorption (*right*, 298 K) isotherms of *a-Al* (■) and *m-Al* (●, only H_2O). Closed symbols depict adsorption, open desorption.

E.2. DIRECT SYNTHESIS

Nitrogen and water isotherms have been measured on pristine *m-Al* and *a-Al* substrates (Fig. E.6). For *a-Al*, nitrogen adsorption reveals mesoporosity, not surprisingly as the anodization layer is supposed to be porous. Interestingly, even though the amount adsorbed is not that high, based on the amount of mass of the whole substrate, the desorption hysteresis closes completely. The adsorbed amount is low, because compared to the weight of the non-porous, non-adsorbing bulk aluminium layer, the weight of anodized oxidic layer is significantly smaller. The adsorption hysteresis that is displayed by *a-Al* substrates when water is adsorbed does not fully close. This might well because of the stronger interactions of water with the support.

ADDITION OF ALUMINIUM SULFATE

Syntheses of CAU-10-H on *m-Al* (without pretreatment) with various amounts of added aluminium sulfate are performed. XRD patterns of both the coated substrates and filtration residues are depicted in Fig. E.7.
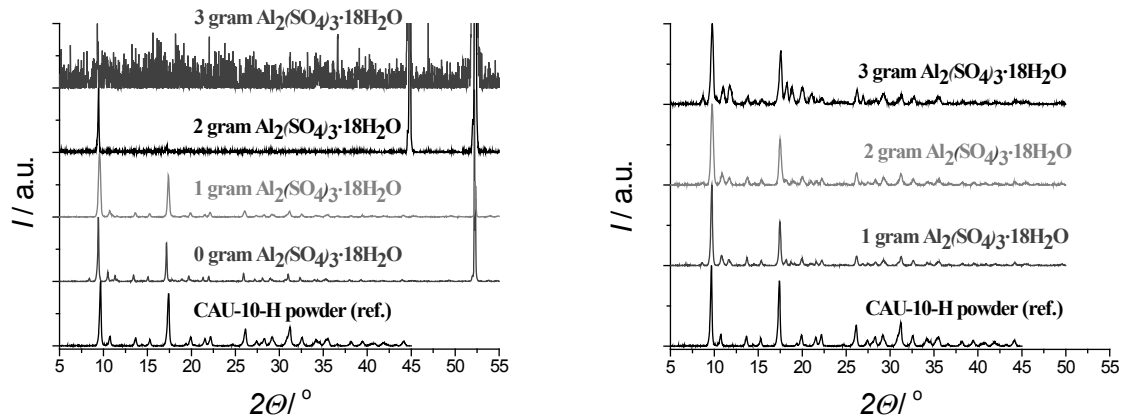
Figure E.7: XRD patterns for CAU-10-H synthesis directly on *m-Al* substrates (without pretreatment) with varying amounts of $Al_2(SO_4)_3$·$18H_2O$, both for obtained substrates (*left*) and filtration residues (*right*), when possible. No added salt represents results obtained for the standard synthesis protocol (SSP).


Figure E.8: Photographs of CAU-10-H synthesized directly on *m-Al* (without pretreatment) using standard conditions (SSP) (*left*) and with addition of 2 g $Al_2(SO_4)_3$·$18H_2O$ (*right*).

The more Al-ions are added, the less CAU-10-H can be found on the surface of the support as the inflections of CAU-10-H diminish with respect to those of the support. In fact, already at 2 grams of aluminium sulfate, the visible layer already detaches from the support during post-processing (Fig. E.8). This apparent layer consists of crystals formed in solution that agglomerated on the surface and are not attached to the support.

INFLUENCE OF HYDROCHLORIC ACID

In Fig. E.9 the XRD patterns of syntheses on both *m-Al* and *a-Al* with different concentrations of HCl are depicted. When *m-Al* is considered, the formation of secondary phase(s) is significantly more evident when the amount of HCl is doubled (200%), compared to the standard synthesis protocol (SSP).
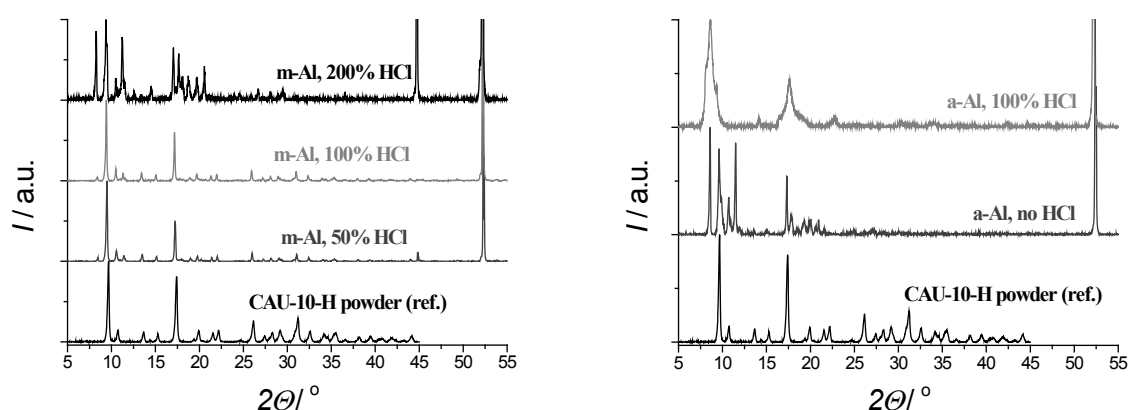
Figure E.9: XRD patterns for CAU-10-H synthesized directly on *m-Al* (left) and *a-Al* (*right*), both without pretreatment, varying the amount of HCl solution (37% in aq. solution, in all cases) added to the synthesis mixture, compared to standard synthesis conditions (denoted as 100% HCl).
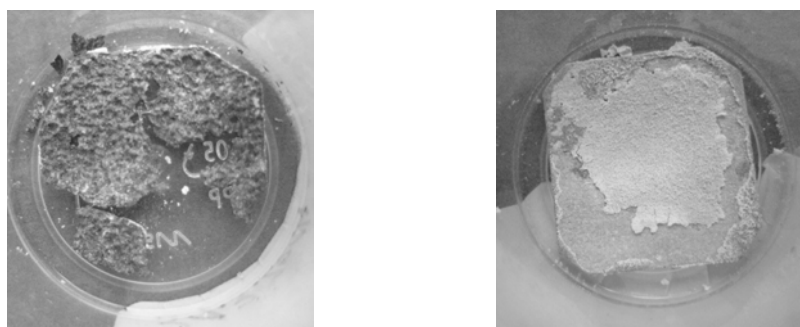
Figure E.10: Photographs of CAU-10-H directly synthesized on *a-Al* (without pretreatment) at standard conditions. First (*left*) and second (*right*) attempt.

For standard (100%) and halved (50%) amounts of HCl, the presence of byproducts is less prevalent. For *a-Al*, even without HCl, significant byproduct formation is observed. When HCl is used, a poorly crystalline product is observed.

Unexpectedly, the first trial applying standard reaction conditions (SSP) to *a-Al* substrates led to the deterioration of the substrate (Fig. E.10). Upon replication of this initial trial, the substrate could be recovered, indicating the poor reproducibility under acidic conditions for untreated *a-Al*, but still did not give satisfactory results (Figs. E.9-11). Clearly, the porous anodized layer is significantly more reactive than the surface of metallic aluminium. In Fig. E.11 the SEM images of CAU-10-H synthesized on *a-Al* are depicted, both with and without added hydrochloric acid.
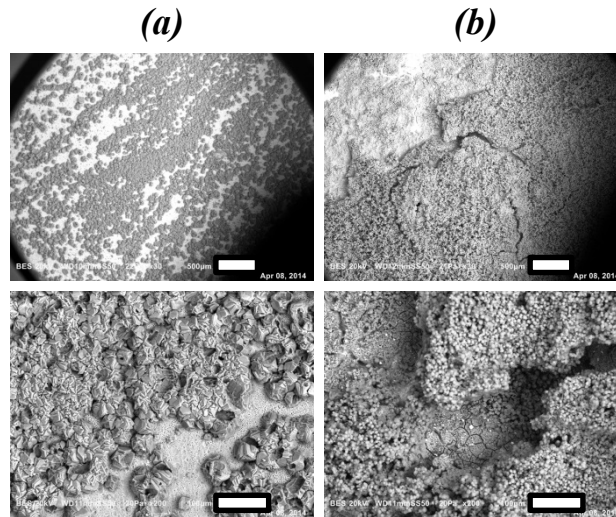
Figure E.11: SEM images of directly synthesized CAU-10-H on *a-Al* (without pretreatment) using no HCl (*a*) and 100% HCl (*b*, second attempt) (*top*, scale bar represents 500 μm, *bottom*, scale bar represents 100 μm).

DMF CONCENTRATION

SEM images of experiments with reduced amounts of DMF, employing *m-Al* are presented in Fig. E.12. In Fig. E.13 XRD patterns are displayed for the samples of these experiments for both *m-Al* and *a-Al*. TGA and SDTA profiles are depicted in Fig. E.14 for *m-Al*. for *a-Al*, SEM images are depicted in Fig. E.15.
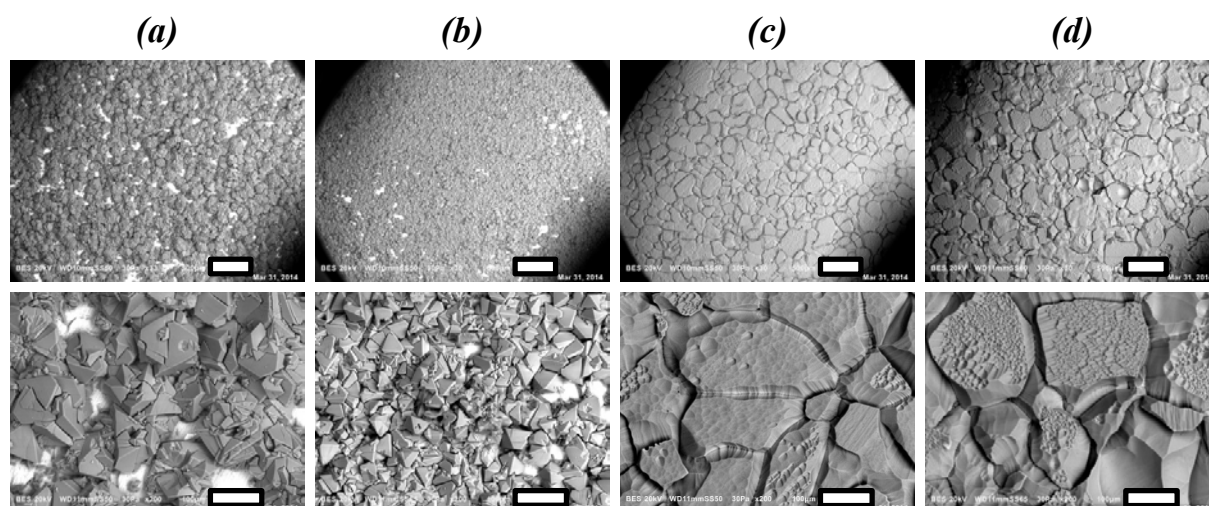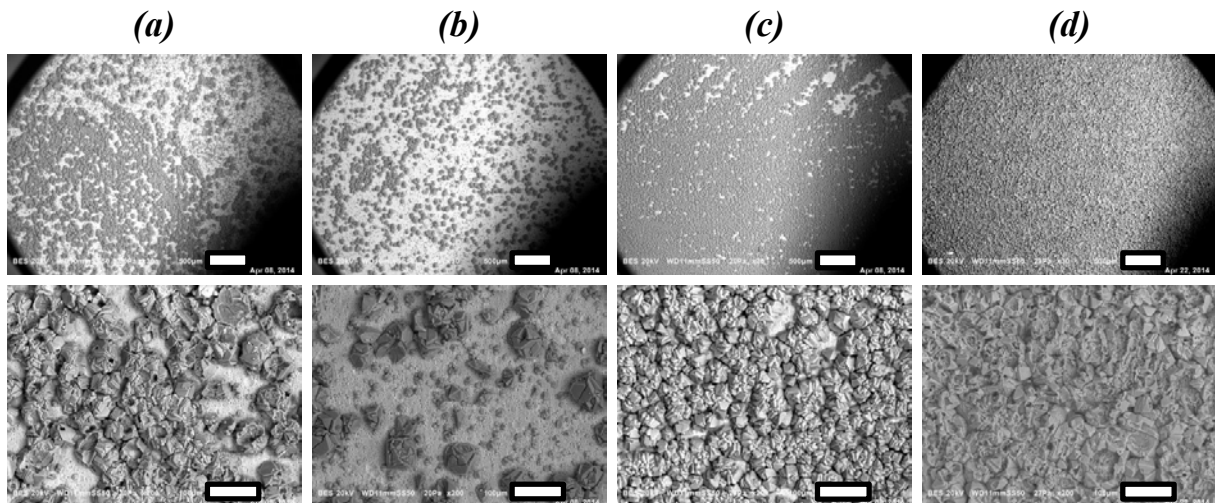
Figure E.12: SEM images for CAU-10-H synthesized directly on *m-Al* (without pretreatment), employing 75% (*a*), 50% (*b*), 25% (*c*) or 0% (*d*) of DMF **(***top*, scale bar represents 500 μm, *bottom*, scale bar represents 100 μm).
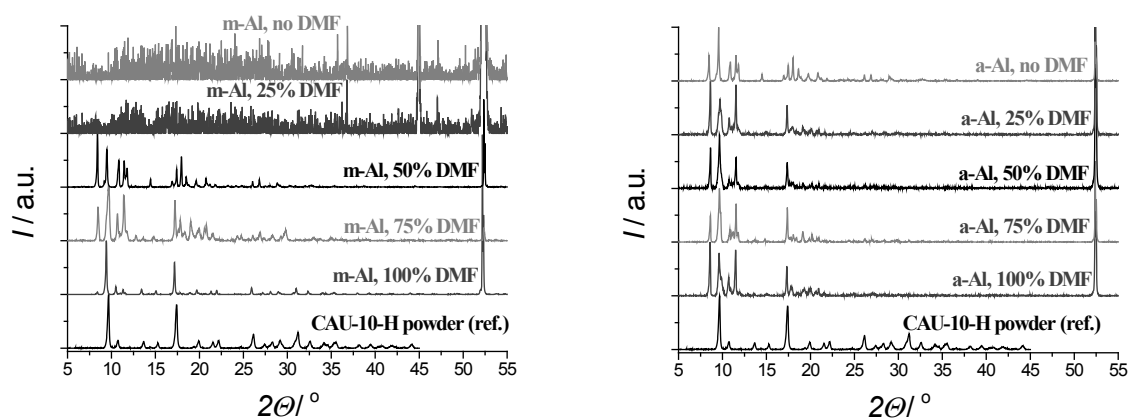
Figure E.13: XRD patterns for CAU-10-H synthesized directly on *m-Al* (*left*) and *a-Al* (*right*), both without pretreatment, varying the amount of DMF in the synthesis mixture, compared to standard synthesis conditions (≡100% DMF).
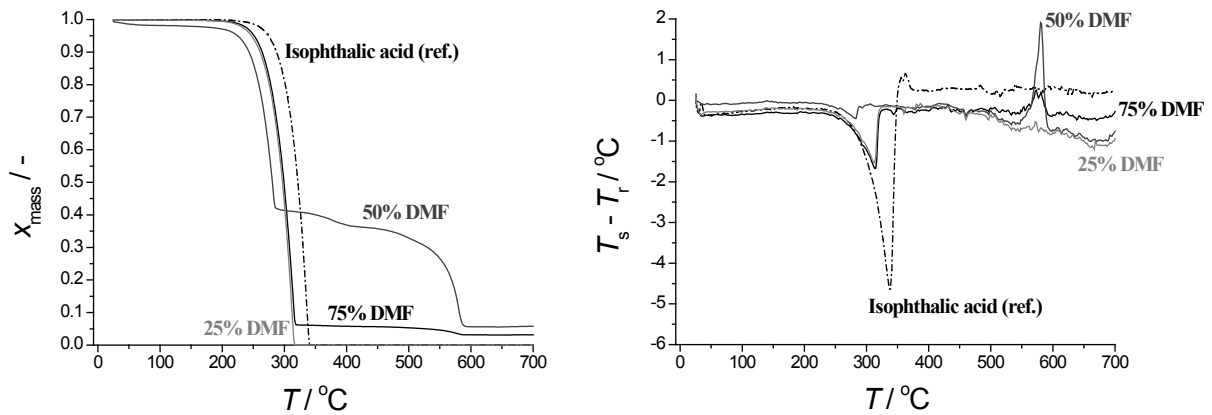
Figure E.14: TGA (*left*) and SDTA (*right*) profiles for filtration residues for the direct synthesis of CAU-10-H on *m-Al* (without pretreatment) for 75, 50 and 25 % DMF (*solid lines*). For comparison, the TGA-profiles of isophthalic acid (*dot-dashed lines*) are included. Measured using a flow of air (100 ml/min) and a heating rate of 5 °C/min.
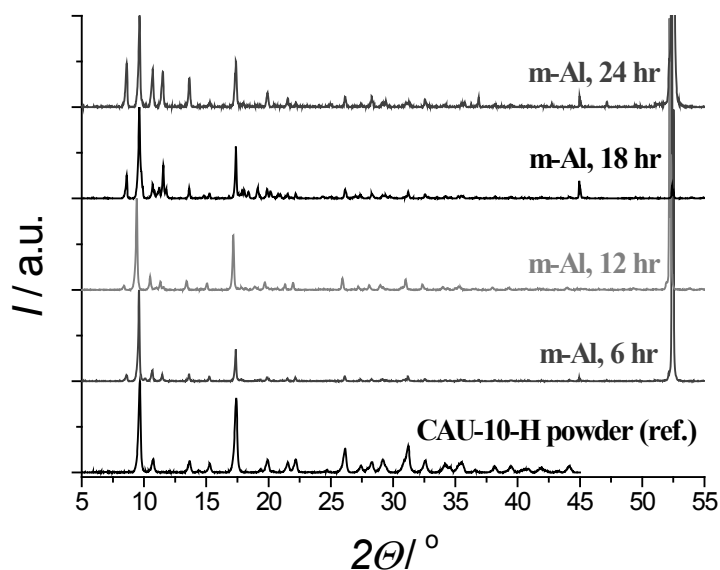

Figure E.15: SEM images for CAU-10-H synthesized directly on *a-Al* (without pretreatment), employing 75% (*a*), 50% (*b*), 25% (*c*) or 0% (*d*) of DMF (*top*, scale bar represents 500 μm, *bottom*, scale bar represents 100 μm).

INFLUENCE OF TEMPERATURE

In Fig. E.16, the XRD pattern and a SEM image of CAU-10-H synthesized on *m-Al* at 115 °C are depicted.
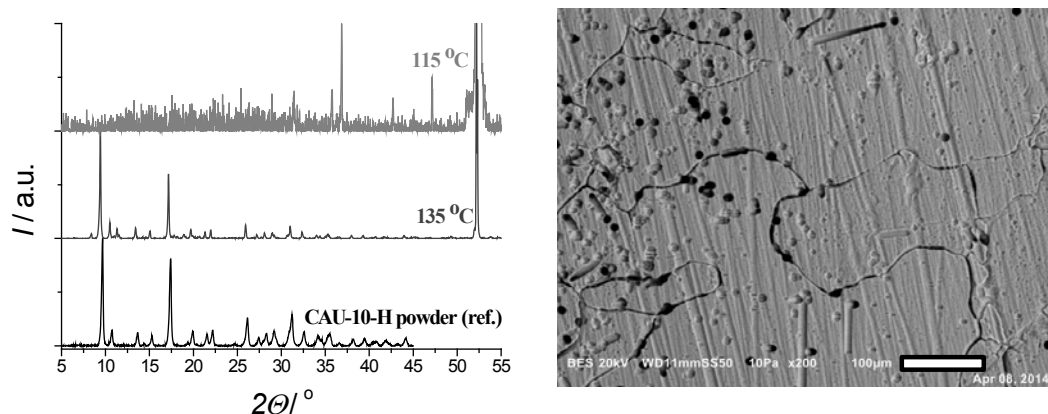
Figure E.16: XRD patterns for CAU-10-H on 115 ^{o}C and 135 ^{o}C (SSP) on *m-Al*, without pretreatment (*left*) and SEM image after synthesis at 115 ^{o}C (*top*, scale bar represents 500 μm, *bottom*, scale bar represents 100 μm).
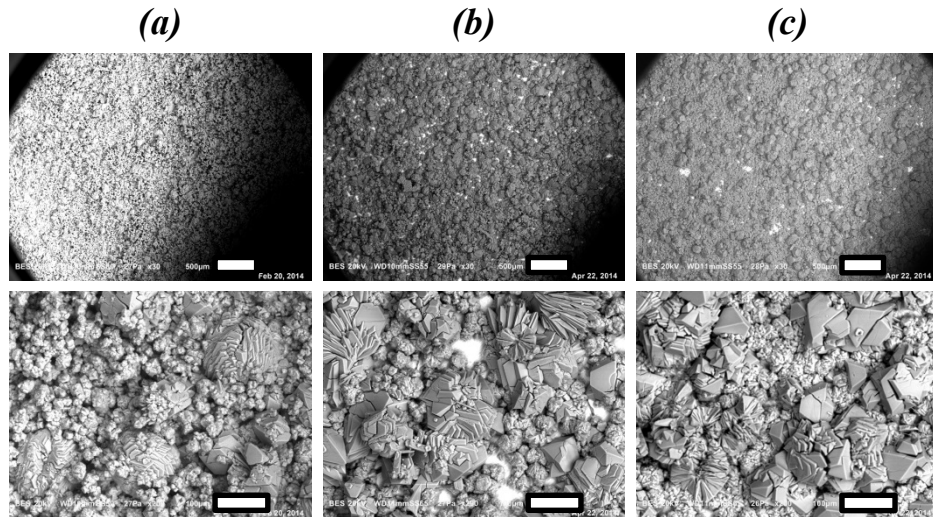

Figure E.17: XRD patterns for CAU-10-H synthesized directly on *m-Al* without pretreatment, for 6, 12 (SSP), 18 and 24 h of reaction time.

REACTION TIME (UNTREATED)

In Fig. E.17 XRD patterns of CAU-10-H on *m-Al* substrates without pretreatment are presented to show the effect of synthesis reaction time.

Figure E.18: SEM images for CAU-10-H synthesized directly on *m-Al*, depicting the effect of pretreatment. Results for untreated (*a*), method A (*b*) and method B (*c*) (*top*, scale bar represents 500 μm, *bottom*, scale bar represents 100 μm).

PRETREATMENT

In Fig. E.18 SEM images show the effect of pretreatment by method A or B (Section 6.3.2) on the synthesis of CAU-10-H on *m-Al* substrates.

REPRODUCIBILITY

SEM images of three individual experiments under identical conditions are shown for the synthesis of CAU-10-H on untreated *m-Al* (Fig. E.19), pretreated *m-Al* (method A, Fig. E.20), untreated *a-Al* (Fig. E.21) and pretreated *a-Al* (method B, Fig. E.22).
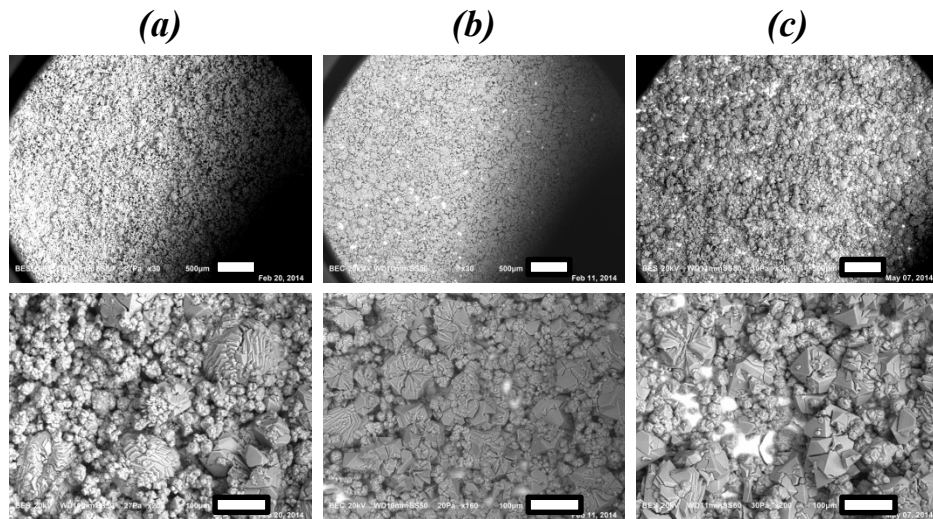
Figure E.19: SEM images for trial 1 (*a*), 2 (*b*), and 3 (*c*) for the direct synthesis of CAU-10-H on *m-Al* without pretreatment (*top*, scale bar represents 500 μm, *bottom*, scale bar represents 100 μm).
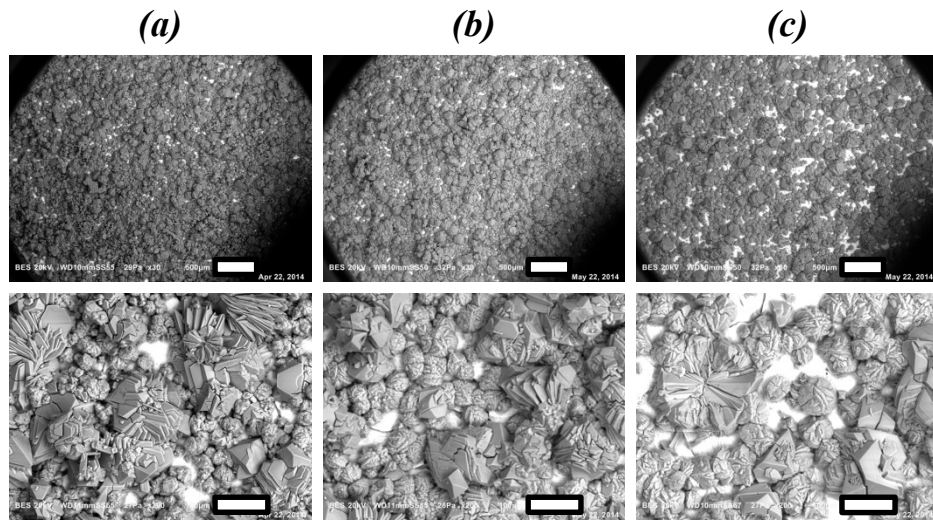
Figure E.20: SEM images for trial 1 (*a*), 2 (*b*), and 3 (*c*) for the direct synthesis of CAU-10-H on *m-Al* employing pretreatment method A (*top*, scale bar represents 500 μm, *bottom*, scale bar represents 100 μm).
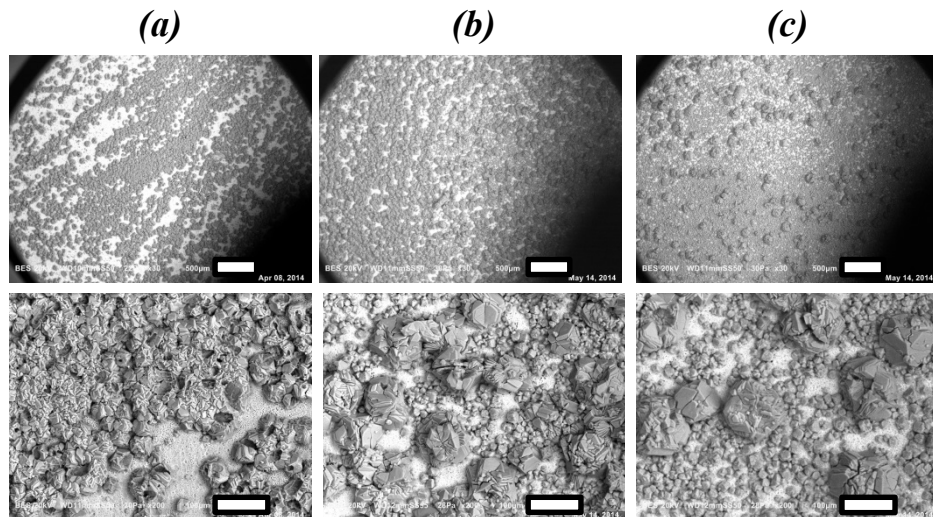
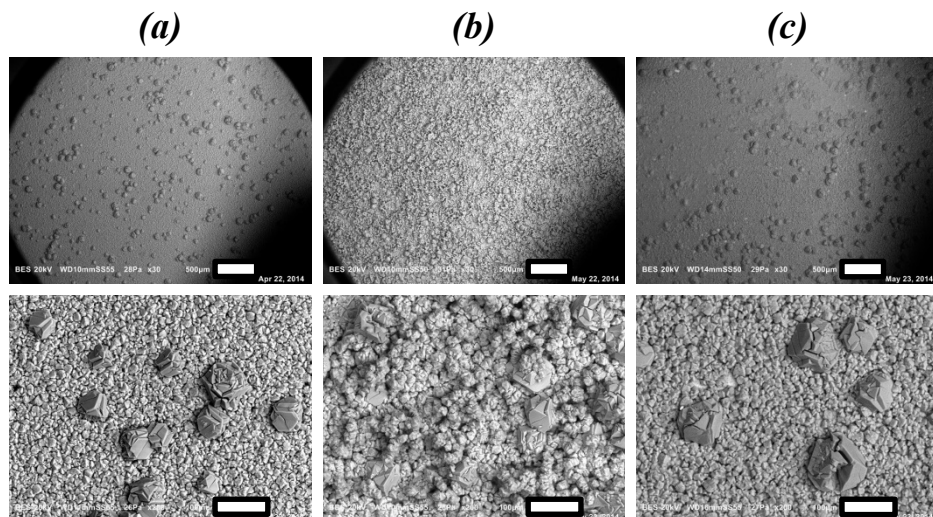**Figure E.21:** SEM images for trial 1 (*a*), 2 (*b*), and 3 (*c*) for the direct synthesis of CAU-10-H on *a-Al* without pretreatment (*top,* scale bar represents 500 μm, *bottom,* scale bar represents 100 μm).
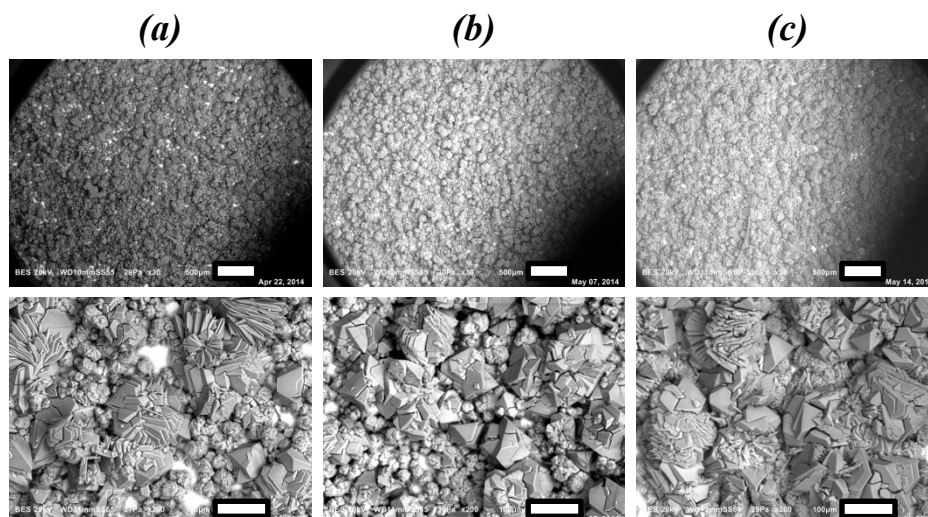

Figure E.22: SEM images for trial 1 (*a*), 2 (*b*), and 3 (*c*) for the direct synthesis of CAU-10-H on *a-Al* employing pretreatment method B (*top*, scale bar represents 500 μm, *bottom*, scale bar represents 100 μm).

Figure E.23: SEM images for CAU-10-H synthesized directly on *m-Al*, employing pretreatment method A, for 12 (SSP), 14 and 16 h of reaction time (*top*, scale bar represents 500 μm, *bottom*, scale bar represents 100 μm).

INFLUENCE OF REACTION TIME (AFTER PRETREATMENT)

For untreated *m-Al* supports it was found that extending the reaction time by 18 h or longer results in severe Ostwald ripening and formation of unwanted byproducts (Figs. 6.6, E.17). SEM images for *m-Al* pretreated with method A (Fig. E.23) or B (Fig. E.24) and *a-Al*, pretreated with method A (Fig. E.25) or B (Fig. E.26) for 12, 14 and 16 h reaction time, as well as the accompanying XRD patterns (Fig. E.27) indicate that the observed trends do not change when the support is changed or pretreatment is applied.

(a) *(b)* *(c)*
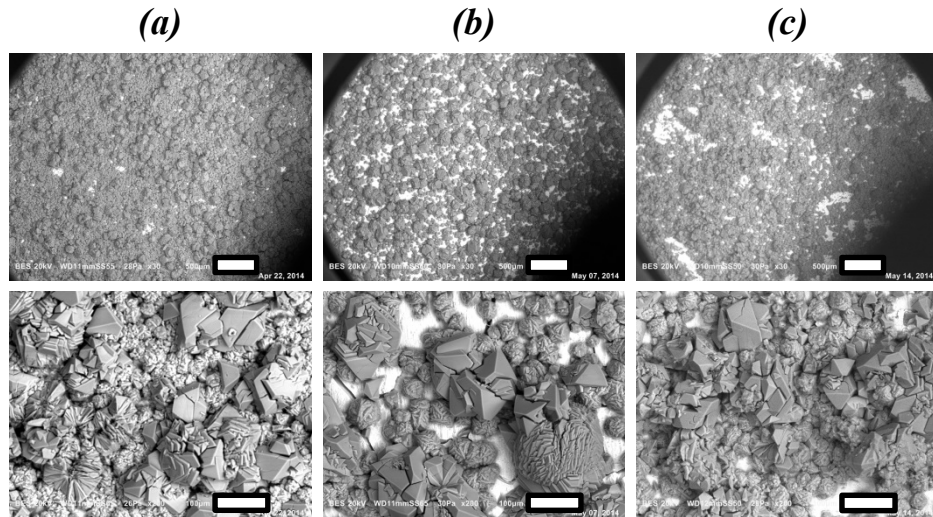
Figure E.24: SEM images for CAU-10-H synthesized directly on *m-Al*, employing pretreatment method B, for 12 (SSP), 14 and 16 h of reaction time (*top*, scale bar represents 500 μm, *bottom*, scale bar represents 100 μm).

(a) *(b)* *(c)*

Figure E.25: SEM images for CAU-10-H synthesized directly on *a-Al*, employing pretreatment method A, for 12 (SSPa), 14 and 16 h of reaction time (*top*, scale bar represents 500 μm, *bottom*, scale bar represents 100 μm).
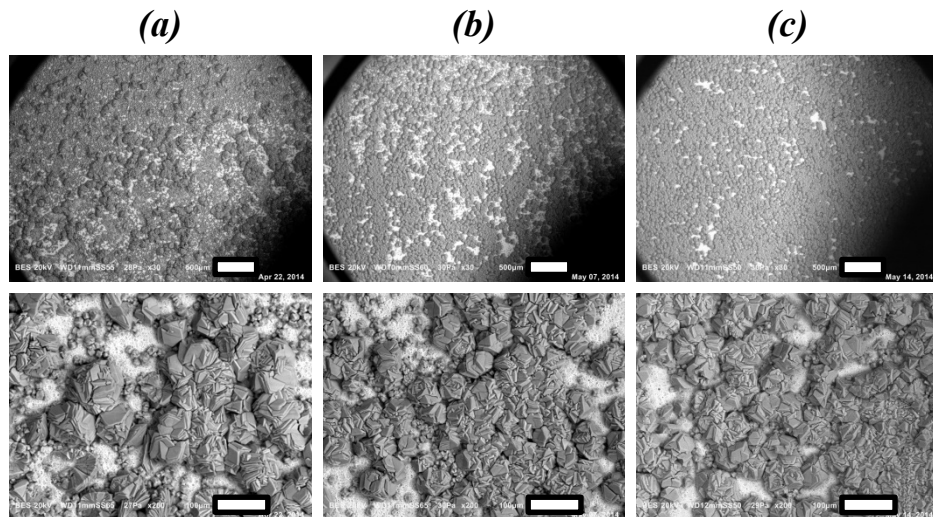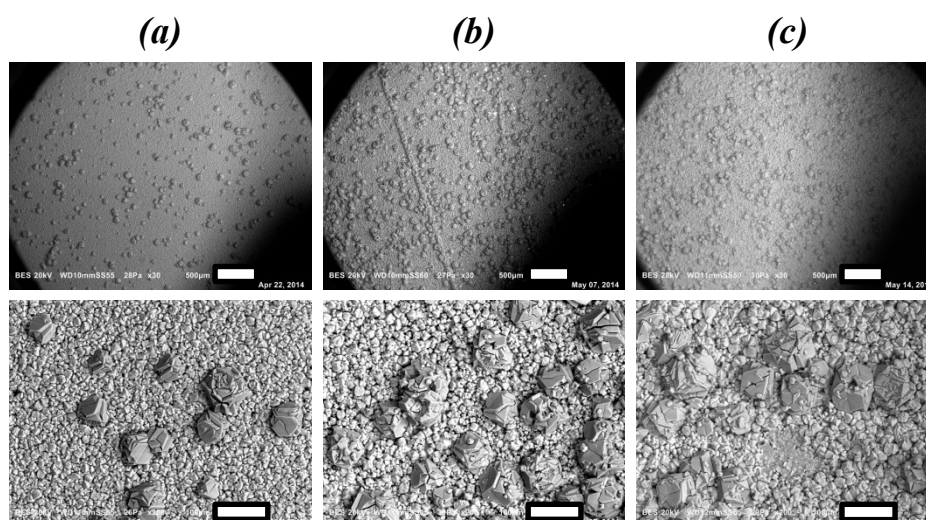
Figure E.26: SEM images for CAU-10-H synthesized directly on *a-Al*, employing pretreatment method B, for 12 (SSPa), 14 and 16 h of reaction time (*top*, scale bar represents 500 μm, *bottom*, scale bar represents 100 μm).
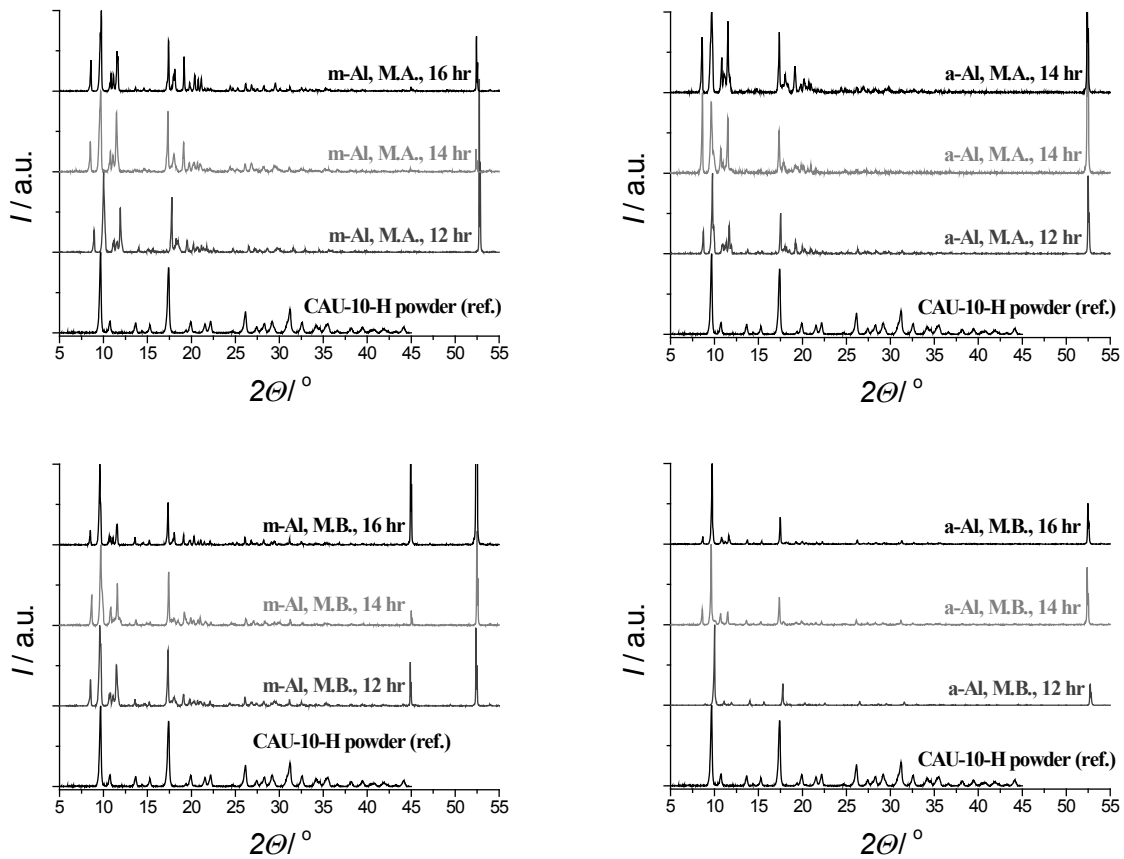
Figure E.27: XRD patterns for CAU-10-H synthesized directly on *m-Al* (*left*) and *a-Al* (*right*), employing pretreatment method A (M.A.*, top*) and method B (M.B.*, bottom*), for 12, 14 and 16 h of reaction time.

E.3. REACTIVE SEEDING

The SEM images of pretreated *m-Al* (method A) and *a-Al* (method B) after reactive seeding for either 1 or 2 h are given in Fig. E.28. SEM images after secondary growth on substrates after reactive seeding of either 3 or 4 h, employing a reactant dilution factor of 2 are depicted in Fig. E.29. Accompanying XRD patterns of both the substrates and filtration residue obtained after secondary growth are shown in Fig. E.30.
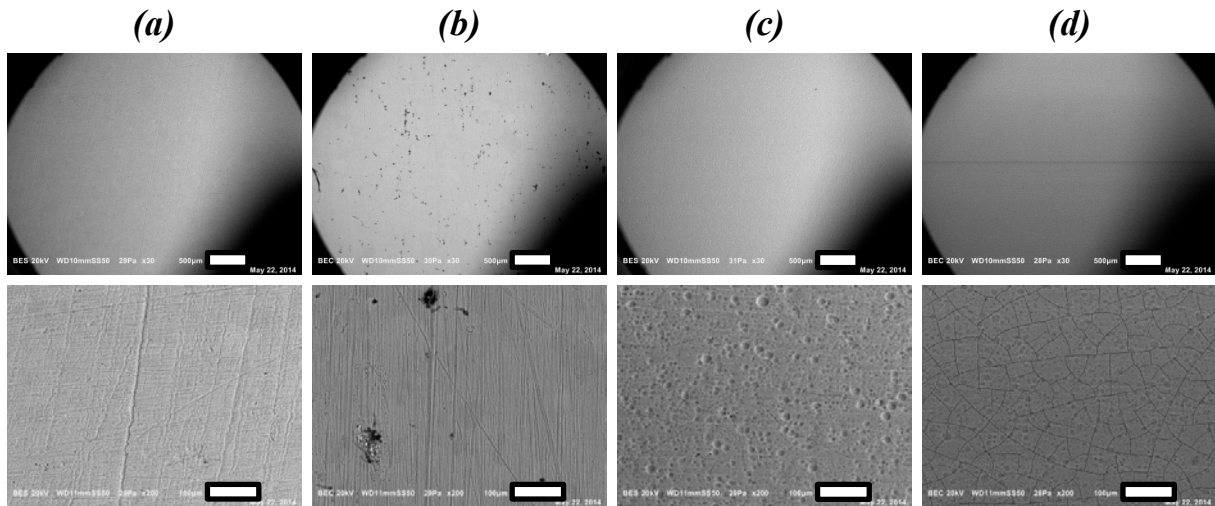
Figure E.28: SEM images after reactive seeding of CAU-10-H on pretreated *m-Al* (method A) for 1 h (*a*) and 2 h (*b*) reaction time and on pretreated *a-Al* (method B) for 1 h (*c*) and 2 h (*d*) reaction time (*top*, scale bar represents 500 μm, *bottom*, scale bar represents 100 μm).
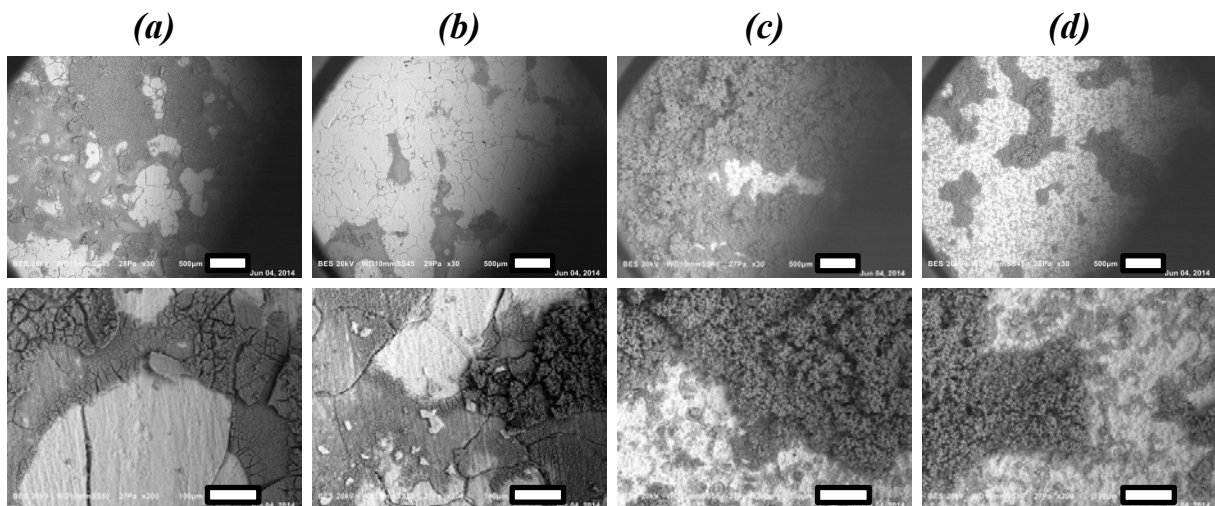
Figure E.29: SEM images of CAU-10-H synthesized by reactive seeding and secondary growth with precursor solution diluted by a factor 2, for pretreated *m-Al* (method A) employing a reaction time for the seeding step of 3 (*a*) and 4 (*b*) h and for pretreated *a-Al* (method B), employing a reaction time for the seeding step of 3 (*c*) and 4 (*d*) h (*top,* scale bar represents 500 μm, *bottom*, scale bar represents 100 μm).
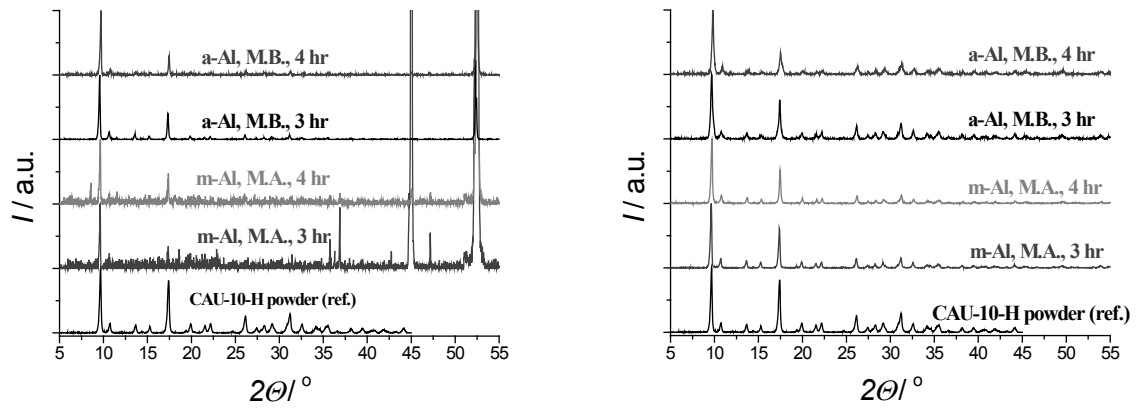
Figure E.30: XRD patterns of substrates (*left*) and filtration residue (*right*) after reactive seeding and secondary growth with a precursor solution diluted by a factor of 2, for pretreated *m-Al* (method A) and pretreated *a-Al* (method B), employing a reactive seeding time of 3 or 4 h.

(a)   *(b)*
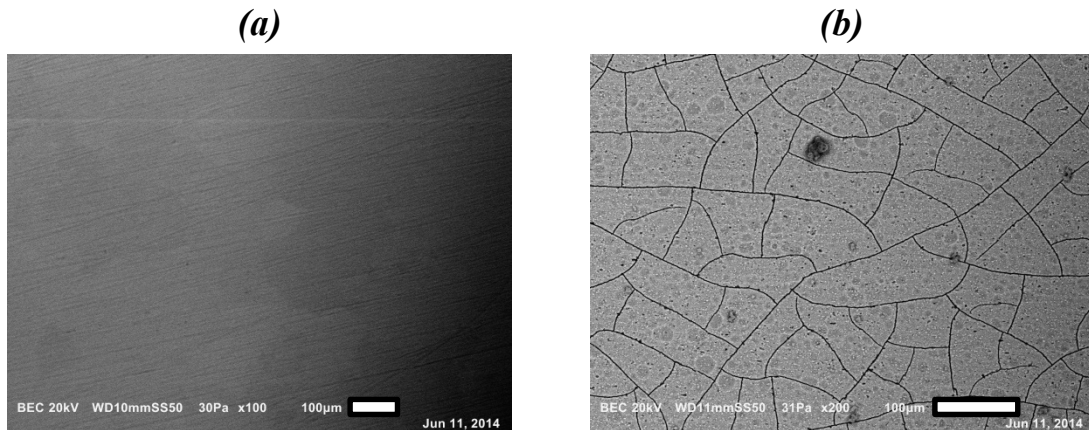
Figure E.31: SEM images after thermal seeding with solution 1, for pretreated *m-Al* (method A) (*a*) and pretreated *a-Al* (method B) (*b*).

E.4. THERMAL SEEDING

In Fig. E.31, SEM images after thermal seeding with solution 1 on both pretreated *m-Al* (method A) and *a-Al* (method B) are presented.

E.5. COMPARISON

In Fig. E.32 the XRD pattern of CAU-10-H synthesized directly on untreated *a-Al*, conditions under which significant amount of byproduct(s) are formed, is compared to possible $Al(OH)_3$ phases, γ-AlO(OH) and synthesis reactants isophthalic acid and aluminium sulfate. Clearly, none of the patterns match with any of the observed byproduct reflections. In Fig. E.32 nitrogen physisorption isotherms are depicted for selected samples.

In contrast to adsorption on bare *a-Al* (Fig. E.6), isotherms in Fig. E.33 indicate diffusional limitations, as no nitrogen seems to desorb upon pressure decrease, resulting in a hysteresis loop that clearly does not close. This is likely due to the micropores of CAU-10-H, as limitations were also observed for powder obtained from conventional synthesis (Fig. E.3) For the samples containing only a small amount of porous material the apparent amount adsorbed becomes negative, and during pressure decrease an apparent increase in adsorbed amount is observed, because of the wrongly assessed dead volume in these measurements. This effect is strongly enlarged compared to powder measurements (Chapter 2).
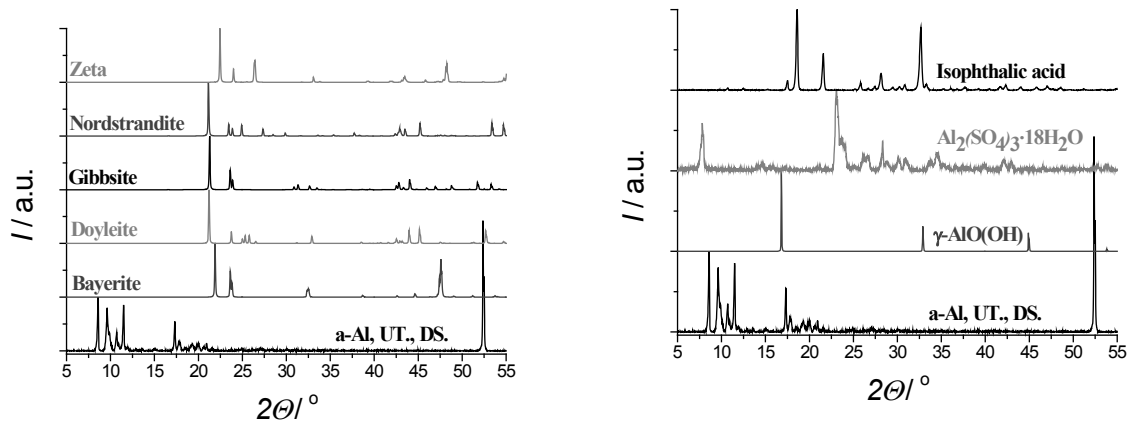
Figure E.32: XRD patterns of CAU-10-H obtained from direct synthesis (DS.) on untreated (UT.) *a-Al*, compared to selected Al(OH)$_3$ phases (*left*) and to boehmite (γ-AlO(OH)) and synthesis reactants (*right*).
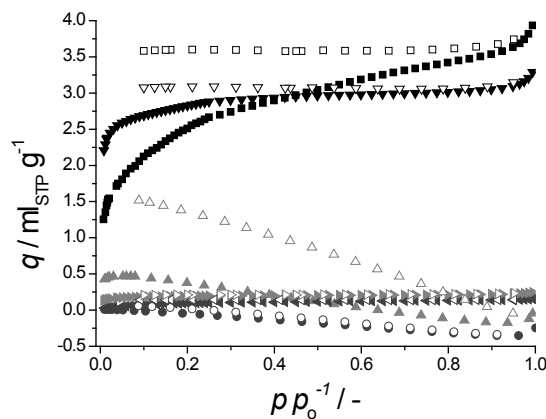
Figure E.33: N$_2$ adsorption isotherms (77 K) for direct synthesis on untreated *m-Al* (■) and *a-Al* (●) and on pretreated *m-Al* (method A) (▲) and *a-Al* (method B) (▼) and for reactive seeded on pretreated *m-Al* (method A) (◄) and *a-Al* (method B) (►). Open symbols represent the desorption branch.

E.6. REFERENCES

[1]   G. Job, F. Herrmann, Chemical potential - a quantity in search of recognition, European journal of physics, 27 (2006) 353.

SUMMARY

Global energy consumption shows a continuous rise, despite the increased tangibility of (anthropogenic) global climate change. Large contributors are households and buildings. The energy demands for heating, and especially cooling, are forecasted to increase significantly in the coming years, for these contributors (Chapter 1). Significantly reducing the energy expenditures for heating and cooling will have a large impact on the total energy consumption. To this end, thermally driven heat pumps can be employed, sustainably utilizing the available energy (*e.g.* solar or waste heat). Central in this work is the adsorption driven heat pump, which has the advantages that low driving or regeneration temperatures ($< 100 \, ^{\circ}\text{C}$) and environmentally benign working fluids (*e.g.* water) can be used. There are commercial adsorption driven heat pumps and chillers available employing silica gel or zeolite based adsorbents in conjunction with water as working fluid, of which the FAM (Functional Adsorbent Material Zeolite) Z-series, commercialized by Mitsubishi plastics as the AQSOA[tm] series show most suitable adsorption characteristics. The market for such devices is expected to grow as performance improves (Chapter 1). One way of achieving this is the development of new adsorbents, central theme in this thesis. Here a relatively novel class of materials, *i.e.* Metal-Organic Frameworks (MOFs) investigated for this purpose. MOFs, comprising inorganic clusters connected by organic ligands in 1, 2 or 3 dimensions, display a rich variety of topologies (Chapter 1). Furthermore, MOFs can be further tuned by functionalization pre- or post-synthesis and thus it is highly likely that a MOF material can be designed that has superior properties than commercially applied adsorbents.

Characterization is vital for proper assessment of (synthesized) MOFs and porous adsorbents in general. An important role herein is reserved for adsorptive characterization, for which nitrogen is the most common probe molecule (at 77 K). In Chapter 2 the uncertainties and possible inconsistencies in measurements and derived characteristic properties (pore volume, BET surface area, BJH pore size distribution) are investigated in great detail. Uncertainty in *adsorption measurements* can be decreased not only by increasing measuring accuracy or sample mass, but also by optimizing the ratio of manifold and cell volume (optimum at V_{man}/V_{cell} is 2 - 3). Further, a large sample cell volume and/or small sample mass can artificially and erroneously enlarge or even introduce artificially apparent hysteresis between ad- and desorption. To reduce the relative uncertainty in the *determination of pore volume* for

microporous materials it is beneficial to determine the pore volume at relative pressures lower than 0.9. When it comes to the *determination of BET area*, obtained surface areas and confidence intervals are strongly dependent on applied fitting strategy. To obtain a small uncertainty in BET surface area, one should at least use three degrees of freedom (at least 5 data points) and apply the direct (nonlinear) fitting method. The contrived two-point BET method is a useful tool to determine *a priori* the upper relative pressure boundary of the BET window. No method was obtained to *a priori* exclude data for the low relative pressure range where surface heterogeneity may interfere strongly, but it is suggested to use Studentized residuals for to help locate this boundary. The magnitude of the 95% confidence limits for *BJH-pore size distributions* severely impedes drawing quantitative conclusions. The artificially increased desorption hysteresis by unfit experimentation has a detrimental effect on the desorption branch-based BJH pore size analysis. For pore volumes and especially BET surface areas reported in literature, often the relative pressure (window) used and determination strategy are not reported or plainly wrong as exemplified by *the case of MIL-101(Cr)*. Using the guidelines posed in this work for the determination of both parameters, a significantly better correlation between both was obtained than was the case for the original values reported in literature.

The adsorption mechanism of polar vapors on mesoporous MOFs MIL-100(Cr) and MIL-101(Cr) has been studied by a combination of experimental and simulation techniques in Chapter 3. Results undoubtedly demonstrate that both adsorbate-adsorbent and adsorbate-adsorbate interactions rule the adsorption process. At low loadings, before all coordinatively unsaturated chromium sites are occupied, the structure determines the shape of the isotherm and the water model is less important. A clear difference is found between fully fluorinated and hydroxylated MIL-101 structures for both methanol and water, demonstrating that Cr partial charges drive the initial shape of the isotherm. At higher loadings, adsorbate- adsorbate interactions become much more important and the choice of water model determines the agreement between experimental and simulated results. In this sense, the simplest SPC/E model reproduces experimental results with the best accuracy in contrast to more advanced methods like TIP5Pew, attributed to the slightly higher Coulombic interactions predicted by the former. A composite type IV isotherm for methanol and a composite type V isotherm for water, according to the IUPAC classification have been found. This effect has, to the best of our knowledge, not been observed in adsorption in microporous materials and highlights the complexity behind molecular simulations in periodic meso-structured materials.

The potential of MOFs as adsorbents in adsorption driven allocation of heat and cold has been thoroughly assessed in Chapter 4. The *adsorption mechanism* of water on MOFs is known. Water initially adsorbs at specific hydrophilic sites (uncoordinated metal sites, OH-groups on inorganic clusters or functional groups on the organic ligand). Subsequently, additional water cluster around these initially adsorbed water molecules, after which the pores are filled via volume filling (d_p (pore diameter) $< D_c$ (critical diameter)) or capillary condensation ($d_p > D_c$). The *in silico* prediction of water adsorption in MOFs is deemed not yet mature enough for accurate selection of MOF structures. For alcohols the adsorption mechanism is somewhat similar, although the adsorption behavior is often devoid of steep steps in uptake. In this case, *In silico* prediction seems to work better, as the behavior of methanol is well described by classical force fields. *Stability* of MOFs with respect to water has been researched in a plethora of communications. Various factors that (co-)determine the structural stability have been posed, of which the most important are the metal species, its valence, coordination number and degree of filling of the coordination sphere, and the metal-ligand bond strength. Additionally, structural defects can play an important role on stability. Further, degradation reactions do not always occur in the bulk of the material. In some cases only an exterior shell is degraded, forming an impervious layer, preserving the bulk of the material. Surface tension of water might also have adverse effects on stability for MOFs with elongated ligands. Lastly, MOFs that have been claimed to be stable towards water vapor, have been shown to degrade under repeated ad- and desorption cycles. The preceding highlights the complexity of influences on water stability. Nonetheless, there are MOFs that exhibit the level of hydrothermal stability required for application in AHP/ADCs (adsorption driven heat pumps and chillers). Of these structures, some show the desired stepwise *water uptake behavior* for this target application. These are CAU-10(Al)-H, MIL-100(Fe), MIL-101(Cr), MOF-801(Zr), MOF-841(Zr) and Al-fumarate. Especially CAU-10(Al)-H stands out with respect to stability, as no degradation was observed for over 700 adsorption cycles. For methanol stability is seemingly less of an issue. However, the list of structures for which methanol adsorption has been investigated (at more than one temperature) is too limited for a proper evaluation. Only the performance of MIL-53(Cr) and Zn(BDC)(DABCO)$_{0.5}$ could be assessed. These structures exhibit the desired stepwise uptake of methanol, although this is caused by the structural flexibility of the frameworks, making that an undesired hysteresis-loop is observed. Lastly, for ammonia, because of stability issues and subsequent limited adsorption data, no suitable candidate could be identified. A thermodynamic model of the ideal adsorption heat

pump cycle has been adopted, with the aim to assess the performance of MOFs for adsorption driven allocation of heat and cold on an accurate and objective manner. Per unit volume, MOFs can in total store more energy, and release more energy per cycle when water is the working fluid of choice. Also, especially for cooling applications, MOFs clearly have been shown to display improved capacity and thermodynamic efficiency. Over a wide range of required temperature lifts for application, MOFs display higher capacity and efficiency than benchmark materials. The specific material that has optimal performance depends on the desired temperature lift. For low temperature lifts, $\Delta T_{lift} \leq 12$ K, MIL-101(Cr) has the highest energy capacity per unit volume MOF (~ 500 kWh m^{-3}). For larger required temperature lifts, $12 \leq \Delta T_{lift} \leq 20$ K, MOF-841(Zr) is the adsorbent of choice (~ 350 kWh m^{-3}). For even higher temperature lifts, CAU-10(Al)-H ($20 \leq \Delta T_{lift} \leq 26$ K) or MOF-801(Zr) can be efficiently utilized (~ 250 and ~ 280 kWh m^{-3}, respectively). The required desorption temperature increases, for the investigated adsorbent-water pairs, in the order: MIL-101(Cr) < MOF-841(Zr) < CAU-10(Al)-H < AQSOA-Z02 < MOF-801(Zr). Lastly, thermodynamic efficiency (COP$_c$) follows the same trend: MIL-101(Cr, COP$_c \sim 0.89$) > MOF-841(Zr, COP$_c \sim 0.79$) > CAU-10(Al)-H (COP$_c \sim 0.72$) > AQSOA-Z02(COP$_c \sim 0.69$) > MOF-801(Zr, COP$_c \sim 0.68$). These trends can be directly related to the material's pore size. A larger pore size means that pores are generally filled at higher relative pressure, making that the maximum temperature lift is reduced, but the material is efficiently regenerated at lower desorption temperature as well. A larger pore volume leads to an increased volumetric adsorption capacity. Because of a larger pore volume, the average adsorption enthalpy is lower (closer to the evaporation enthalpy of water) resulting in a higher thermodynamic efficiency. Lastly, MOFs have great potential for the efficient direct dehumidification of air for air-conditioning purposes. For energy storage applications, focus should be especially on low desorption temperature applications, as MOF-water pairs are likely to be more competitive in this range. In this work, however, no better performance with respect to commonly used inorganic salts have been identified in terms of energy storage capacity.

As mentioned CAU-10-H has a suitable adsorption uptake behavior and possesses an outstanding structural stability towards the reversible ad- and desorption of water. Furthermore it is based on aluminium and isophthalic acid, both of which are industrially available on a large scale (Chapter 4). For actual application however, one desires to have fast heat and mass transfer as well. An elegant way of pursuing this goal is by coating the MOF on thermally conductive interfaces (e.g. aluminium), which is the aim of Chapter 5. Growth of

CAU-10-H crystals directly on γ-alumina supports was achieved by using aluminium ions from the substrate as metal source for the MOF. Addition of acids improves the growth of these crystals. Especially hydrochloric acid has a beneficial effect on surface coverage and homogeneity of the formed crystal size and shape. The same approach has been successfully applied to coat CAU-10-H directly on metallic aluminium, which is highly desired for the target application. Again HCl has a beneficial effect on crystal growth. The adsorptive properties of CAU-10-H are similar to that of the bulk material and the coating showed to be stable in at least 5 water adsorption-desorption cycles. These adsorption measurements further indicate that, with a coating as created in this chapter, up to 38 kJ of heat can be withdrawn in the evaporator of an AHP/ADC per square meter of coated aluminium surface.

Unfortunately, broad crystal size distributions, inhomogeneous surface coverage and undesired crystalline formation of byproducts were observed. Laborious efforts to improve these coatings have been documented in Chapter 6. When it comes to the manufacture of CAU-10-H coatings on aluminium substrates, syntheses on metallic aluminium (*m-Al*) with varying manufacture conditions did not result in a notable increase in coating quality. In fact, any deviation from the defined standard synthesis protocol (*SSP,* conditions as in Chapter 5) leads to worse coatings. The porous amorphous aluminium oxide layer of anodized aluminium (*a-Al*) is more reactive and thus crystallization on the surface is easier. Substrate pretreatment improves both reproducibility and coating quality of CAU-10-H on both *m-Al* and *a-Al* substrates. For *m-Al* substrates cleaning with acetone (method A) yields optimal results. For *a-Al*, additionally the substrate should be contacted with a diluted HCl solution (6% in water) (method B) for optimal results. Despite the improvement achieved, obtained coatings are still suboptimal in coverage, homogeneity of crystal sizes and purity. In many cases an unwanted, unknown byproduct, which has neither been identified nor isolated, is formed next to CAU-10-H. Separation of crystal nucleation and growth yields significantly improved quality, showcased by the high purity and homogeneous crystal size distribution obtained by both thermal and reactive seeding on pretreated substrates. Especially reactive seeding in conjunction with pretreated *a-Al* (method B) yields full coverage of the substrate surface, a homogeneous layer thickness, narrow crystal size distribution, and high purity of the crystalline phase. This method leads to the highest water adsorption capacity observed of all coated substrates. As up to 48 kJ of heat can be withdrawn in the evaporator of an AHP/ADC per square meter of coated anodized aluminium surface (for metallic aluminium this is only 38 kJ (Chapter 5)). Furthermore, the coating created with this method does not

344

lose capacity upon repeated water adsorption-desorption cycles (at least 10) and responds much faster to temperature changes than bulk CAU-10-H powder. Additionally, based on XRD patterns of both the anhydrous and hydrated state and subsequent structural refinement, it was found that CAU-10-H does not exhibit structural changes upon water adsorption, in contrast to earlier literature. Refinement indicates that water preferentially adsorbs close to the OH-groups on the structure's helical Al-OH chains. The step-wise water uptake at a specific relative pressure reads like a phase change, resulting in a regularly ordered adsorbed water phase in between liquid and solid water.

OUTLOOK

Future endeavors to further exploit the promise that MOFs hold for application in adsorption driven heat pumps and chillers depend strongly on the desired working fluid and are thus best discussed separately, as is done below.

AMMONIA

Very few MOFs, if any, have been convincingly demonstrated to reversibly adsorb significant amounts of ammonia with structural retention. The cause of instability with respect to ammonia has received little attention. It is therefore not clear whether there exists a justifiable expectation for ammonia-stable MOFs. If any desire exists to employ MOF-ammonia working pairs in heat pumps, focus should be on resolving instability of MOFs towards ammonia.

ALCOHOLS

Interesting adsorption properties have been reported for several MOFs with respect to methanol and ethanol, though for the majority little to no information on either desorption or enthalpy of adsorption is known, making practical assessment impossible. In this thesis, the energy capacity turned out to be lower for assessed MOF-alcohol pairs than for water-MOF pairs. Because of the higher vapor pressure of alcohols, dynamics might be faster than for water, so a lower energetic capacity does not necessarily exclude a viable application. However, for most conditions the methanol-MOF pairs exhibited lower coefficients of performance (COP) than methanol-activated carbon pairs. Regarding the to be avoided adsorption-desorption hysteresis, alcohols allow for larger pore diameters than water (3.5 nm for methanol, 4.3 nm for ethanol, 2 nm for water). Focus should be on exploring adsorption

on additional MOF structures, especially comprising larger pore sizes to obtain more efficient alcohol-based working pairs.

WATER

In Chapter 4 it has been demonstrated convincingly that water-MOF working pairs exist with higher capacity and thermodynamic efficiency than benchmark sorbents. These demonstrations revolve mostly around ('static') thermodynamic studies. For actual application, mass and especially heat transfer are important as well. As transfer rates are strongly dependent on the chosen MOF morphology (coatings, packed beds *etc.*), shaping of these materials should be focused on, in conjunction with measurements on heat and mass transfer dynamics. Note that, when eligible MOF-alcohol or ammonia working pairs are developed, this would also be a logical next step in the further development of those pairs. For packed bed systems, heat transport to and in the bed is often limiting, making coatings an optimal configuration. Most work regarding MOF coatings has focused on the creation of thin films, of which the thickness is generally on the submicron-scale, orders of magnitude off for the targeted application. However, there are studies focusing on creating thick MOF films (>100 micron), suited for application. These are based direct crystallization on the surface, without the need for a physical binder material, highlighting the potential of direct growth of MOFs on various structured supports. Alternatively, binder-based coatings, granules or pellets can be utilized. For benchmark materials the adsorption dynamics of water have been determined already and thus serve as a good basis for comparison.

MOF SYNTHESIS

Current accounts of large scale synthesis of MOFs are scarce and predominantly (sub-)gram scale protocols are being used. For any MOF that shows, regardless of elected working fluid, improvements over conventional sorbents when both dynamics and thermodynamics are considered, the MOF should be synthesized on a significantly larger scale for application than is required for the assessment of their potential for application. Scaling up is thus a must. Fortunately, MOFs potentially offer advantages compared to most zeolite-based materials, as environmentally benign, room temperature, template-free and even solvent-free synthesis protocols have been developed for certain structures already. In contrast, zeolite and zeotype synthesis often requires relatively expensive sacrificial organic templates, as is the case for the synthesis of the competing alternatives SAPO-34 (AQSOA-Z02) and AlPO-5(AQSOA-Z01/Z05) discussed in this thesis.

SAMENVATTING

Ondanks de toenemende tastbaarheid van (antropogene) klimaatverandering vertoont de wereldwijde energieconsumptie een continue stijging. Een groot deel van deze energie wordt verbruikt voor verwarming en koeling in huishoudens en gebouwen. De verwachting is dat dit energieverbruik de komende jaren sterk zal toenemen (Hoofdstuk 1). Een significante reductie in het energieverbruik voor verwarming en koeling zal dus een groot effect hebben op de totale energieconsumptie. Om deze reductie te realiseren kunnen thermisch-gedreven warmtepompen worden ingezet die beschikbare duurzame zonne-energie of laagwaardige restwarmte gebruiken om te koelen of te verwarmen.

In dit onderzoeksproject staan adsorptie-gedreven warmtepompen centraal. Deze hebben als voordeel dat lage werk- of regeneratietemperaturen (< 100 ^{o}C) en milieuvriendelijke vloeistoffen (bijv. water) gebruikt kunnen worden. Commercieel beschikbare adsorptie-gedreven warmtepompen en koelsystemen maken gebruik van silica gel of zeolitische adsorbentia, met water als werkvloeistof. Van deze laatste adsorbentia vertoont de FAM (Functioneel Adsorbent Materiaal Zeoliet) Z-serie, op de markt gebracht door Mitsubishi plastics als de AQSOA^{tm} serie, het meest wenselijke adsorptiegedrag. De markt voor dit soort apparaten zal naar verwachting groeien zodra de prestaties van de warmtepomp verbetert (Hoofdstuk 1). Eén manier om dit te bewerkstelligen is het ontwikkelen van betere adsorbentia. Het vinden van nieuwe adsorbentia met betere eigenschappen staat centraal in dit proefschrift. Een relatief nieuwe klasse poreuze materialen is hiervoor onderzocht, de zogenaamde 'Metal Organic Frameworks' (MOFs). MOFs zijn opgebouwd uit anorganische clusters verbonden door organische liganden in 1, 2, of 3 dimensies en bieden een rijke variëteit aan verschillende topologieën (Hoofdstuk 1). Bovendien kunnen MOFs verder aangepast worden door functionalisering, dan wel vóór dan wel ná synthese. Het uitgangspunt in dit onderzoek was dat het zeer aannemelijk is dat een MOF materiaal ontworpen kan worden dat superieure eigenschappen heeft in vergelijking tot commercieel toegepaste adsorbentia.

Karakterisering van (gesynthetiseerde) MOFs en poreuze adsorbentia is essentieel voor mogelijke toepassingen. Adsorptie speelt hierin een belangrijke rol. Stikstof is het meest voorkomende testmolecuul (bij 77 K) voor bepaling van de textuureigenschappen van poreuze materialen. In Hoofdstuk 2 is deze techniek uitgebreid geanalyseerd. Hierbij zijn de onzekerheden en mogelijke inconsistenties in metingen en afgeleide karakteristieke

eigenschappen (porievolume, BET oppervlak, en BJH porievolume verdeling) tot in detail onderzocht. De onzekerheid in *adsorptiemetingen* kan niet alleen worden verkleind door het vergroten van de meetnauwkeurigheid of de monstermassa, maar ook door het optimaliseren van de volumeverhouding van het verdeelstuk en de monstercel (optimum bij $V_{\text{verd}}/V_{\text{cel}}$ is 2-3). Door het gebruik van een (te) groot monstercelvolume en/of een (te) kleine monsterhoeveelheid kan bovendien een foutieve vergroting van de adsorptie-desorptie hysterese ontstaan of zelfs kunstmatig een hysterese gecreëerd worden. De nauwkeurigheid van *het porievolume* van microporeuze materialen wordt vergroot door deze te bepalen bij een relatieve druk lager dan 0.9. De gebruikte strategie voor de *bepaling van het BET oppervlak* is van grote invloed op de verkregen waarde en bijhorende betrouwbaarheidsinterval. Minimaal drie vrijheidsgraden (ofwel 5 datapunten) moeten gebruikt worden om een goede nauwkeurigheid te bereiken. Verder is het aanbevolen om hierbij de directe (niet-lineaire) parameterschattingsmethode te gebruiken. De BET methode is slechts toepasbaar over een beperkt relatieve drukinterval. De bovengrens van dit relatieve drukinterval kan van te voren bepaald worden met de in dit werk afgeleide 'tweepunts-BET methode'. Voor de bepaling van de ondergrens van dit relatieve drukinterval, om de invloed van oppervlakte-heterogeniteit uit te sluiten, kon geen algemene methode gevonden worden. Echter, voor mesoporeuze materialen kan een 'Studentized' residuen analyse gebruikt worden als hulp bij het lokaliseren van deze ondergrens. De BJH theorie voor de bepaling van de *porievolumeverdeling* is ongeschikt als kwantitatieve methode vanwege de grote 95% betrouwbaarheidsintervallen. Dit verergert nog door het eerder aangehaalde onbekwaam experimenteren dat de desorptie hysterese kunstmatig vergroot. Een correcte beoordeling van gepubliceerde textuureigenschappen is vaak niet mogelijk omdat de gebruikte relatieve druk(ken) en de bepalingsstrategie niet worden vermeld of zelfs fout zijn. Dit wordt geïllustreerd aan de hand van *het voorbeeld van MIL-101(Cr),* een veelgebruikte MOF. De correlatie tussen het porievolume en BET oppervlak is significant beter wanneer de opgestelde richtlijnen voor de bepaling van deze eigenschappen gevolgd worden.

Het adsorptiemechanisme van polaire dampen in mesoporeuze MOFs MIL-100(Cr) en MIL-101(Cr) is onderzocht aan de hand van experimenten en simulaties (Hoofdstuk 3). Zowel adsorbaat-adsorbent als adsorbaat-adsorbaat interacties bepalen het adsorptieproces. Bij lage beladingen, voordat alle coördinatief onverzadigde chroom locaties bezet zijn, wordt de vorm van de isotherm bepaald door de structuur van het adsorbent en is het gekozen model voor de beschrijving van water minder belangrijk. Bij deze lage beladingen maakt het voor zowel

water als methanol veel uit of the MIL-101 structuur volledig gefluoreerd of gehydroxyleerd is. De initiële vorm van de isotherm wordt daarom bepaald door de partiële lading op de chroom-atomen. Bij hogere beladingen worden de adsorbaat-adsorbaat interacties veel belangrijker. De keuze van het water model bepaalt dan de overeenkomst tussen experimentele en gesimuleerde isotherm. Het eenvoudige SPC/E model reproduceert de experimentele resultaten met grotere nauwkeurigheid dan het meer gecompliceerde TIP5Pew model voor water. Dit is toegeschreven aan de iets sterkere Coulombische interacties in het SPC/E model. Voor zowel MIL-100(Cr) als MIL-101(Cr) kan de adsorptie van methanol beschreven worden met een samengestelde type IV isotherm in de IUPAC classificatie. Voor water is een samengestelde type V isotherm gevonden voor beide structuren. Deze bevindingen zijn, zover onze kennis strekt, niet eerder waargenomen voor microporeuze materialen en laten tevens zien hoe complex moleculaire simulaties zijn in periodieke meso-gestructureerde materialen.

De potentie van MOFs als adsorbentia in adsorptie-gedreven warmtepompen is grondig geëvalueerd in Hoofdstuk 4. Als eerste is het *adsorptiemechanisme* van water in MOFs beschreven, zoals bekend uit de wetenschappelijke literatuur. Water adsorbeert eerst op specifieke hydrofiele locaties (coördinatief onverzadigde metaal-ionen, OH-groepen op anorganische clusters of functionele groepen van de organische liganden). Vervolgens adsorberen hieraan additionele watermoleculen, en worden de poriën in toenemende mate gevuld via volumevulling (d_p (porie diameter) < D_c (kritische diameter)) of capillaire condensatie (d_p > D_c). Het *in silico* voorspellen van wateradsorptie in MOFs is nog niet rijp genoeg voor een voorselectie van geschikte MOF structuren. Het adsorptiemechanisme van alcoholen is vergelijkbaar met dat van water, maar een steile opnamestap zoals bij water is meestal afwezig. In dit geval lijken *in silico* voorspellingen nauwkeuriger omdat het adsorptiegedrag van methanol zich beter laat beschrijven door klassieke '*force fields*'. Veel literatuur behandelt de *stabiliteit* van MOFs ten opzichte van water. Veel factoren spelen hierbij een rol. De belangrijkste factoren zijn het metaal en oxidatietoestand, de metaal coördinatie en de vullingsgraad van de coördinatiesfeer, en de metaal-ligand bindingssterkte. Verder kunnen ook defecten in de structuur de stabiliteit in belangrijke mate beïnvloeden. Bovendien vindt degradatie van MOFs niet altijd plaats in de bulk van het materiaal. Soms degradeert alleen een uitwendige schil van een kristal of deeltje, waardoor een ondoordringbare laag wordt gevormd terwijl de kern intact blijft. Capillaire krachten ten gevolge van de oppervlaktespanning van water kunnen de stabiliteit van MOFs met lange

organische liganden ook negatief beïnvloeden. Ofschoon van sommige MOFs de stabiliteit ten opzichte van water was vastgesteld, bleken deze toch te degraderen na blootstelling aan herhaalde ad- en desorptie cycli. Het voorafgaande laat zien hoe complex de invloed van water op de stabiliteit van MOFs is. Desalniettemin bestaan er MOFs die voldoende stabiel zijn voor toepassing in AHP/ADCs (adsorptie-gedreven warmtepompen en koelsystemen, Engelse afkorting). Sommige van deze MOF structuren vertonen het gewenste stapsgewijze *opnamegedrag van water* voor de beoogde toepassing. Dit zijn CAU-10(Al)-H, MIL-100(Fe), MIL-101(Cr), MOF-801(Zr), MOF-841(Zr) en Al-fumaraat. CAU-10(Al)-H blinkt in het bijzonder uit in stabiliteit omdat deze structuur geen enkele degradatie vertoont na meer dan 700 adsorptie-desorptie cycli. Stabiliteit van MOFs ten aanzien van methanol lijkt minder problematisch. Helaas is het aantal structuren waarvoor methanoladsorptie onderzocht is (bij meer dan één temperatuur) te beperkt voor een goede evaluatie. Alleen de prestaties van MIL-53(Cr) en Zn(BDC)(DABCO)$_{0.5}$ konden worden bepaald. Deze structuren vertonen het gewenste stapsgewijze opnamegedrag van methanol. Dit gedrag vindt echter zijn oorsprong in de flexibele structuur van deze MOFs wat een ongewenste hysterese oplevert. Tenslotte is er weinig bekend over het adsorptiegedrag van ammoniak in MOFs. Er zijn geen geschikte stabiele kandidaten gevonden voor het gebruik van ammoniak als werkvloeistof.

Om de prestaties van MOFs in adsorptie-gedreven allocatie van warmte en koude op een nauwkeurige en objectieve manier te kunnen vaststellen is een thermodynamisch model van een ideale adsorptie-warmtepomp gebruikt. MOFs kunnen de meeste energie opslaan en afgeven per volume-eenheid in een cyclus met water als werkvloeistof. In vergelijking met bestaande sorbentia hebben MOFs met water als werkvloeistof duidelijke voordelen, in het bijzonder voor koelapplicaties. MOFs hebben een hogere werkcapaciteit en efficiëntie over een breed bereik van temperatuurliften. De temperatuurlift is het verschil in temperatuur tussen de condensor en verdamper. De benodigde temperatuurlift bepaalt in feite het materiaal dat het meest geschikt is. Voor een lage temperatuurlift, $\Delta T_{\text{lift}} \leq 12$ K, heeft MIL-101(Cr) de hoogste energiecapaciteit per MOF volume-eenheid (~ 500 kWh m^{-3}). Voor een hogere temperatuurlift, $12 \leq \Delta T_{\text{lift}} \leq 20$ K, levert MOF-841(Zr) de beste prestaties (~ 350 kWh m^{-3}). Voor een nog hogere temperatuurlift ($20 \leq \Delta T_{\text{lift}} \leq 26$ K), kan efficiënt gebruik gemaakt worden van CAU-10(Al)-H of MOF-801(Zr) (~ 250 en 280 kWh m^{-3}, respectievelijk). Voor de onderzochte adsorbent-water paren neemt de benodigde desorptietemperatuur toe in de volgorde: MIL-101(Cr) < MOF-841(Zr) < CAU-10(Al)-H < AQSOA-Z02 < MOF-801(Zr). De thermodynamische efficiëntie, uitgedrukt in de 'coefficient of performance' voor koeling,

350

COP$_c$, volgt dezelfde trend: MIL-101(Cr, COP$_c$ ~ 0.89) > MOF-841(Zr, COP$_c$ ~ 0.79) > CAU-10(Al)-H (COP$_c$ ~ 0.72) > AQSOA-Z02(COP$_c$ ~ 0.69) > MOF-801(Zr, COP$_c$ ~ 0.68). Deze trends kunnen direct gerelateerd worden aan de poriegroottes van deze materialen. Een grotere porie betekent in het algemeen dat de poriën gevuld worden bij een hogere relatieve druk. Dit resulteert erin dat de maximale temperatuurlift gereduceerd wordt. Echter, het materiaal kan dan ook bij een lagere desorptietemperatuur geregenereerd worden. Een grotere porie leidt verder tot een grotere adsorptiecapaciteit per volume eenheid. Door een groter porievolume gaat de (absolute) gemiddelde adsorptieënthalpie omlaag (benadert de enthalpie van verdamping van water), met als resultaat een grotere thermodynamische efficiëntie. Ook andere toepassingen van MOFs zijn bekeken. MOFs kunnen efficiënt gebruikt worden voor het drogen van lucht voor airconditioning. Voor energieopslag kunnen MOFs in principe ook gebruikt worden, maar hebben een lagere energieopslagcapaciteit dan de normaal gebruikte anorganische zouten. Daarom zijn MOFs het meest geschikt voor warmteopslag toepassingen met een lage desorptietemperatuur, omdat voor anorganische zouten vaker een hogere temperatuur nodig is.

Zoals eerder genoemd, vertoont CAU-10-H het gewenste adsorptiegedrag en heeft een uitstekende water stabiliteit. Bovendien is deze MOF opgebouwd uit aluminium((hydr)oxide) en isoftaalzuur, die beide op industriële schaal beschikbaar zijn (Hoofdstuk 4). Dit zijn alle positieve aspecten, maar voor een effectieve toepassing van deze MOF is echter ook snel warmte- als massatransport belangrijk. Een elegante manier om dit te bereiken is door het coaten van de MOF op thermisch geleidende oppervlakken (bijv. aluminium). Dit is het doel in Hoofdstuk 5. Voor de groei van CAU-10-H kristallen direct op γ-alumina worden aluminium ionen van het substraat gebruikt als metaalbron. Toevoeging van zuren bevordert de groei van deze kristallen. In het bijzonder heeft zoutzuur een positief effect op zowel de dekking van het oppervlak als de homogeniteit van de grootte en vorm van deze kristallen. Dezelfde aanpak is ook succesvol bij het realiseren van CAU-10-H coatings direct op metallisch aluminium, zeer aantrekkelijk voor de beoogde toepassing. Wederom heeft zoutzuur een positief effect op kristalgroei. Het adsorptiegedrag van de CAU-10-H coating is hetzelfde als dat van het bulkmateriaal en de coating is stabiel voor tenminste 5 opeenvolgende adsorptie-desorptie cycli. Met deze coating kan 38 kJ warmte per vierkante meter gecoat aluminium oppervlak onttrokken kan worden in de verdamper van een AHP/ADC.

Helaas werden een brede kristalgrootteverdeling, inhomogene dekking van het oppervlak en ongewenste vorming van bijproducten waargenomen. Inspanningen om de coating te verbeteren zijn beschreven in Hoofdstuk 6. Deze CAU-10-H coatings op metallisch aluminium (*m-Al*) konden niet verbeterd worden door de synthesecondities aan te passen. Elke afwijking van het gedefinieerde standaard synthese protocol (*SSP*) uit Hoofdstuk 5 leidde tot inferieure coatings. Gebruik van geanodiseerd aluminium (*a-Al*) leverde betere resultaten. De poreuze amorfe aluminiumoxide laag is reactiever en daardoor is kristallisatie op het oppervlak eenvoudiger. Voorbehandeling van beide substraten leidt tot zowel verbeterde reproduceerbaarheid als kwaliteit van de CAU-10-H coatings. Ondanks de bereikte verbeteringen zijn deze coatings nog steeds suboptimaal qua dekking, homogeniteit van kristallen en zuiverheid. In veel gevallen wordt een ongewenst, onbekend bijproduct gevormd naast CAU-10-H. Dit bijproduct kon echter niet geïdentificeerd noch geïsoleerd worden.

Door de kristalnucleatie- en kristalgroeistap te scheiden wordt een significante verbetering verkregen. Deze scheiding werd bewerkstelligd door gebruik te maken van thermische en reactieve "zaai-methoden" (seeding methods) op voorbehandelde substraten. Vooral het reactief "zaaien" in combinatie met voorbehandeld *a-Al* leverde een volledige dekking van het substraatoppervlak, een homogene laagdikte, een smalle kristalgrootteverdeling en hoge zuiverheid van de kristallijne fase op. Deze methode leidt tot de hoogste water adsorptiecapaciteit van alle gecoate substraten. Tot 48 kJ warmte kan onttrokken worden per vierkante meter gecoat geanodiseerd aluminium oppervlak uit de verdamper van een AHP/ADC (voor de methode uit Hoofdstuk 5 is dit slechts 38 kJ/m^2). Deze coating behoudt capaciteit gedurende tenminste 10 water adsorptie-desorptie cycli. Bovendien reageert deze significant sneller op veranderingen in temperatuur dan bulk CAU-10-H poeder.

Een detail van de adsorptie van water aan CAU-10-H is nader onderzocht. In de literatuur wordt beweerd dat CAU-10-H een structuurverandering ondergaat als water opgenomen wordt. Een structuuranalyse op basis van röntgendiffractiepatronen vòòr en ná wateradsorptie toont aan dat er van een structuurverandering geen sprake is. Deze analyse laat wel zien dat watermoleculen preferentieel adsorberen vlakbij de OH-groepen op de helische Al-OH ketens van deze MOF op een zeer geordende wijze. De opnamestap van water resulteert in levert een fase op ergens tussen vloeibaar en vast water.

VOORUITZICHTEN

Wat is er nu nodig om de belofte die MOFs hebben voor toepassing in adsorptie-gedreven warmtepompen en koelsystemen verder in te lossen? Omdat dit nauw samenhangt met de keuze van de werkvloeistof worden de benodigde inspanningen hieronder per werkvloeistof apart besproken.

AMMONIAK

Van weinig tot geen MOFs is overtuigend aangetoond dat zij stabiel zijn in contact met ammoniak én significante hoeveelheden ammoniak reversibel kunnen adsorberen. De oorzaak van de instabiliteit ten opzichte van ammonia is nauwelijks onderzocht. Het kan daarom niet voorspeld worden of er stabiele ammoniak-MOFs werkparen gevonden zullen worden. Mocht er een behoefte zijn ammoniak toe te passen in warmtepompen, bijvoorbeeld voor het maken van ijs, moet de focus dus liggen op de (in)stabiliteit van MOFs ten opzichte van ammoniak.

ALCOHOLEN

Voor methanol en ethanol zijn interessante adsorptie-eigenschappen gerapporteerd voor verscheidene MOFs. Voor de meeste is er echter weinig tot geen informatie beschikbaar over het desorptiegedrag en/of de adsorptieënthalpie. Dit maakt een goede evaluatie praktisch onmogelijk. In dit proefschrift bleek de energiecapaciteit voor MOF-alcohol werkparen lager te zijn dan voor water-MOF paren. Door de hogere dampdruk van alcoholen zou het massatransport sneller kunnen zijn dan voor water. Een lagere energiecapaciteit sluit een eventuele toepassing dus niet noodzakelijkerwijs uit. Echter, voor de meeste condities hebben MOF-methanol paren een lagere prestatiecoëfficiënt (COP) dan de huidige methanol-actieve kool paren. Een mogelijk voordeel van alcoholen is dat een grotere poriediameter gebruikt kan worden zonder een ongewenste adsorptie-desorptie hysterese te introduceren (3.5 nm voor methanol en 4.3 nm voor ethanol, tegenover 2 nm voor water). De nadruk zou hier dus moeten liggen op het onderzoeken van alcohol adsorptie aan een breder scala aan MOF structuren, in het bijzonder die met grotere porieafmetingen, teneinde efficiëntere alcohol-MOF werkparen te ontdekken.

In Hoofdstuk 4 is overtuigend aangetoond dat er water-MOF werkparen bestaan met hogere capaciteit en thermodynamische efficiëntie dan vergelijkbare materialen. Deze vergelijking is voornamelijk gebaseerd op een ('statische') thermodynamische analyse. Voor daadwerkelijke toepassing zijn massa- en in het bijzonder warmtetransport echter ook belangrijk. Omdat transportsnelheden sterk afhankelijk zijn van de gekozen MOF morfologie (coatings, gepakt bed *etc.*), moet de nadruk voor verder onderzoek en ontwikkeling liggen op de vormgeving van deze materialen in combinatie met het bepalen van de warmte- en massatransport dynamica. Dit is uiteraard ook een logische stap voor de verdere ontwikkeling van gevonden geschikte MOF-alcohol of MOF-ammoniak paren. Voor gepakt bed-systemen is het warmtetransport van en naar het bed vaak limiterend, waardoor coatings een optimale configuratie zijn. In de meeste studies naar MOF coatings ligt de nadruk op de fabricatie van dunne filmlagen. De dikte van deze films is in het algemeen minder is dan een micrometer, grootte ordes verwijderd van toepassing in warmtepompen. Er zijn echter ook studies gericht op het fabriceren van dikke MOF lagen (> 100 micrometer), geschikter voor deze toepassing. Deze zijn gebaseerd op kristallisatie van de MOF direct op het oppervlak, zonder een bindmiddel te gebruiken. Dit laat de mogelijkheid zien om MOFs direct te laten groeien op warmtewisselingsoppervlakken. Als alternatief kunnen bindmiddelen gebruikt worden om coatings, korrels of andervormige deeltjes te produceren. Het dynamische gedrag van wateradsorptie aan bestaande sorbentia is bekend wat als een goede basis voor vergelijking met deze nieuwe MOF systemen kan dienen.

MOF SYNTHESE

Er is maar weinig gepubliceerd over de synthese van MOFs op grote schaal en er worden dus hoofdzakelijk de (sub-)gram protocollen van laboratoria gebruikt. Iedere MOF die betere transport- en thermodynamica eigenschappen laat zien dan conventionele sorbentia moet voor verder ontwikkelingswerk op een significant grotere schaal geproduceerd worden. Opschaling is dus een must. Gelukkig zijn er een aantal voordelen te noemen voor MOFs ten opzichte van de bestaande materialen die vooral zijn gebaseerd op zeolieten. Sommige MOFs kunnen milieuvriendelijke gesynthetiseerd worden bij kamertemperatuur en zonder gebruik van 'templates', en soms zelfs zonder oplosmiddelen. Dit in tegenstelling tot de synthese van zeolieten waarvoor vaak relatief dure 'sacrificial' templaatmoleculen nodig zijn. Dit is ook het geval voor de synthese van de vergelijkingsmaterialen SAPO-34 (AQSOA-Z02) en AlPO-5

(AQSOA-Z01/Z02), die uitvoerig besproken zijn in dit proefschrift. Deze templaatvrije synthese zou wel eens een belangrijk voordeel van MOFs kunnen zijn voor gebruik in warmte pompen.

ACKNOWLEDGEMENTS

As *No man is an island, entire of itself*[1], this work would not be without the invaluable aid of others. First and foremost, I wish to thank Thijs Vlugt, Jorge Gascon and Freek Kapteijn for their continued confidence and support. It has been a privilege working in your employ. I am truly grateful for all the opportunities you have provided to improve and develop myself in many aspects. I sincerely hope we'll stay in touch. Thijs, the knowledge you possess of all computational techniques and thermodynamic principles is impressive and has benefited me greatly. Jorge, I have learned a lot from your pragmatic and result-driven approach and vast knowledge of the field of MOFs in general. The great advancements you have met in the past few years are as inspiring as impressive. Freek, your meticulous eye for even the smallest of details, combined with your ability to create a clear and convincing structure out of verbal chaos, has truly significantly improved this manuscript. This work would not have been as it exists now without your expert guidance and knowledge of engineering principles, statistics and mathematics.

The much appreciated help of the technicians of the *Catalysis Engineering* section, Bart van der Linden, Harrie Jansma, Kevin Mouthaan and Willy Rook, has been of vital importance, as without these people, presented experiments and analyses would have been impossible. A special thanks to Willy, as your assistance and vast practical knowledge of adsorption has proven an invaluable asset to this thesis and Chapter 2 in particular. Also, I am grateful for the help of technicians outside of the group, in particular Ben Norder, Piet Droppert, Duco Bosma and Ruben Abellón for their assistance with various experimental techniques. Alla Dikhtiarenko is gratefully acknowledged for the refinement, as presented in Chapter 6. Further, I wish to express my gratitude for Els Arkesteijn, who tirelessly helped with all arrangements regarding visa applications, all sorts of required forms and all sorts of other necessities. Thanks to all group members of both *Catalysis Engineering* and *Engineering Thermodynamics*, for making my stay in both groups as pleasant as it has been. In particular, I wish to acknowledge Mahinder, Maarten, Emanuel, Abrar, Canan and Maxim. The chats and discussions we've had not only regarding science and research but also regarding life, the universe and everything I have thoroughly enjoyed. It has been a great pleasure meeting all of you, and I hope we'll stay in touch.

---

[1] John Donne, *Meditation XVII,* (**1623**).

Further, I would like to thank Sofia Calero, Roger Gläser and Weidong Zhu and their groups for making my stays in Sevilla, Leipzig and Jinhua truly enjoyable. I would like to thank Juan-José Gutierrez-Sevillano and Said Hamad for their invaluable help with the computations in Chapter 3 and Andreas Möller and Marcus Lange for sharing their wisdom and experience of gravimetric adsorption. Weidong and staff, I am ever so grateful for your care and for making my trip to China a truly great cultural experience. I look back in joy to the activities I've attended, the legacy of Chinese whiskey and (most of) the exotic cuisine.

I have been blessed with a group of skillful, talented and kind M.Sc. and B.Sc. students, of which the daily supervision I have thoroughly enjoyed. Lisette, you experienced that research not always yields the progress one desired. Nonetheless, this did not affect in any way your drive and enthusiasm. I've got to know you as a very open and friendly person. Ben, you've shown during your stay you're a true and pragmatic chemical engineer with impressive "common sense". What I remember most is the friendship we shared during your project. You are, without a doubt, the most mentally resilient person I know. I hope we'll stay in touch in the future. Mariëlle, I have truly enjoyed your stay in our group. Your thesis is one of the best I've read. No wonder it got rewarded at last year's NPS meeting ('best B.Sc. thesis 2014'), congratulations once again. Coen, working with you was a true pleasure. Not only did you have the group's record in the successful synthesis of different structures, you made an important first step in coming from powder materials to actual coatings. Karlijn, you have shown great flexibility during your stay. The great change in the scope of the project, due to unforeseen circumstances, did not knock you of your feet. Even though you mentioned that computational work was not really your cup of tea at the start, you have shown that you can quickly adapt. Thomas, your stay has been memorable. The fact that you combined an M.Sc. degree with a full-time job and starting a family is as impressive as inspiring. You've generated an unparalleled amount of results, whilst retaining the highest possible level of meticulousness, and structured this perfectly in an outstanding thesis, a textbook example of German "Gründlichkeit". I wish you and your family all the best in the future.

I want to explicitly thank my family for their interest, support and encouragement, even though I suppose a PhD project and this particular topic must have sounded pretty vague and abstract mostly. In retrospect, the explanations from my part might not have been particularly insightful either. The moments shared have been a great and much needed distraction, especially in the final hours. Without those, I would surely have lost at least some of my marbles. I hope you will forgive me my preoccupation while writing this thesis and the

physical and mental absentness that went along with it. Thessa, thank you for showing me that achievements are their own rewards. You have worked vigorously to graduate and had to make sacrifices to get as far as you did. I am very proud of you. We'll be sure to visit you soon in Zürich, I am sure your stay there will be a success. Hans, Elly, Marit and Christa, I couldn't be happier with having you as parents and sisters (in law). You truly are family, thank you for absorbing me in it. Thank you for your support, guidance and interest. I have enjoyed all get-togethers and outings. I hope there will be plenty more of those. Jan, Lies, nothing of this would have been possible without your everlasting love, guidance and support. Thank you for enabling me to embark on this scientific journey. Mom, thank you for teaching me the true meaning of respect and care. Dad, thank you for showing me the true power of reason and perseverance. Without both of you, I wouldn't be where I stand today. For this I am eternally grateful. Marloes, you more than anyone have seen my trials and tribulations. Without you, all of this would have been devoid of meaning, devoid of sense. Thank you for not only accepting and understanding my hermitage, my whims and mental absentness, but also for your unconditional love, care and support. Thank you for soothing my grief after setbacks and disappointments. Thank you for being there for me in the hour of need. You have been my rock. I look forward to our life together.

LIST OF PUBLICATIONS

PEER-REVIEWED JOURNAL ARTICLES

De Lange, M. F.; Ottevanger, C. P.; Wiegman, M.; Vlugt, T. J. H.; Gascon, J.; Kapteijn, F., Crystals for sustainability - structuring Al-based MOFs for the allocation of heat and cold. *CrystEngComm*, **2015**, 17, 281-285

De Lange, M. F.; Vlugt, T. J. H.; Gascon, J.; Kapteijn, F., Adsorptive characterization of porous solids: Error analysis guides the way. *Microporous and Mesoporous Materials*, **2014**, 200, 199-215.

De Lange, M. F.; Gutierrez-Sevillano, J.-J.; Hamad, S.; Vlugt, T. J. H.; Calero, S.; Gascon, J.; Kapteijn, F., Understanding Adsorption of Highly Polar Vapors on Mesoporous MIL-100(Cr) and MIL-101(Cr): Experiments and Molecular Simulations. *The Journal of Physical Chemistry C*, **2013**, 117 (15), 7613-7622.

Ferrando-Soria, J.; Serra-Crespo, P.; de Lange, M.; Gascon, J.; Kapteijn, F.; Julve, M.; Cano, J.; Lloret, F.; Pasán, J.; Ruiz-Pérez, C.; Journaux, Y.; Pardo, E., Selective Gas and Vapor Sorption and Magnetic Sensing by an Isoreticular Mixed-Metal–Organic Framework. *Journal of the American Chemical Society*, **2012**, 134 (37), 15301-15304.

De Lange, M.F.; Verouden, K.J.F.M.; Vlugt, T.J.H.; Gascon, J.; Kapteijn, F.; Adsorption driven heat pumps - The potential of Metal-Organic Frameworks (review), *Chemical Reviews*, *submitted 2015*

De Lange, M.F.; Zeng, T.; Vlugt, T.J.H.; Gascon, J.; Kapteijn, F.; Structuring CAU-10-H for adsorptive allocation of heat and cold, *in preparation*

Gücüyener, C.; De Lange, M.F.; Kosinov, N.; Hensen, E.J.M.; Gascon, J.; Kapteijn, F.; High silica SSZ-13 membranes for H_2/CH_4 separation with extremely high H_2 Fluxes, *in preparation*

Goesten, M.G.; Szécsényi, A.; De Lange, M.F.; Sai Sankar Gupta, B.; Kapteijn, F.; Gascon, J.; Sulfonated Porous Aromatic Frameworks as solid acid catalysts, *Journal of Catalysis, under revision*

Goesten, M.G.; De Lange, M.F.; Olivos Suarez, A. I.; Bavykina, A.V.; Serra-Crespo, P.; C. Krywka, C.; Bickelhaupt, F.M.; Kapteijn, F.; Gascon, J.; The oscillatory growth of Zirconium and Hafnium based UiO-66: a solid-state clock reaction, *Chemical Science*, *submitted*

CONFERENCES AND MEETINGS

De Lange, M.F., Vlugt, T.J.H., Gascon, J., Kapteijn, F., Adsorptive Characterization of Porous Solids: Error Analysis Guides the Way, *AIChE Annual Meeting 14*, Atlanta, United States, 16-21 November, **2014** (***oral***)

De Lange, M.F., Vlugt, T.J.H., Gascon, J., Kapteijn, F., MOFs in heat pumps – from fundamentals to application, *Netherlands Process Technology Symposium (NPS 14)*, Utrecht, Netherlands, 3-5 November, **2014** (***oral***)

De Lange, M.F., MOFs in heat pumps – from fundamentals to application, *ChemE Faculty Colloquium*, Delft, Netherlands, 27 October, **2014** (***oral***)

De Lange, M.F., Vlugt, T.J.H., Gascon, J., Kapteijn, F., MOFs in heat pumps – from fundamentals to application, *4th International Conference on Metal-Organic Frameworks and Open Framework Compounds (MOF 14)*, Kobe, Japan, 28 Sept.-1 Oct., **2014** (***poster***)

De Lange, M.F, Vlugt, T.J.H., Gascon, J., Kapteijn, F., MOFs in heat pumps – from fundamentals to application, *6th FEZA conference*, Leipzig, Germany, 8-11 September, **2014** (***oral***)

De Lange, M. F., Vlugt, T. J. H., Gascon, J., Kapteijn, F., Adsorptive characterization of porous solids: Error analysis guides the way, faculty colloquium, Zhejiang Normal University, Jinhua, China, 8 April, **2014 (oral)**

De Lange, M.F., Vlugt, T.J.H., Gascon, J., Kapteijn, F., MOFs in heat pumps – from fundamentals to application *ADEM conference*, Ermelo, Netherlands, 3-4 April, **2014** (***poster***)

De Lange, M.F., Gutierrez-Sevillano, J.J., Hamad, S., Gascon, J., Vlugt, T.J.H., Calero, S., Kapteijn, F., Adsorption of highly polar vapors on mesoporous MIL-100 and -101: Experiments and molecular simulations, *17th International Zeolite Conference*, Moscow, Russia, 7-12 July, **2013** (***poster***)

De Lange, M.F., Gutierrez-Sevillano, J.J., Hamad, S., Gascon, J., Vlugt, T.J.H., Calero, S., Kapteijn, F., Understanding adsorption of highly polar vapors on mesoporous MOFs, *16th*

and final Workshop of the International Research Training Group "Diffusion in Porous Materials", Delft, Netherlands, 2-4 April, **2013** (*oral*)

De Lange, M.F., Gutierrez-Sevillano, J.J., Hamad, S., Gascon, J., Vlugt, T.J.H., Calero, S., Kapteijn, F., Adsorption of polar vapors on mesoporous MOFs: Combination of experiments and simulations, *3rd International Conference on Metal-Organic Frameworks and Open Framework Compounds"(MOF 12)*, Edinburgh, Great Britain, 16-19 September, **2012** (***poster***)

De Lange, M.F., Gutierrez-Sevillano, J.J., Hamad, S., Gascon, J., Vlugt, T.J.H., Calero, S., Kapteijn, F., Adsorption of polar vapors on mesoporous MOFs: Combination of experiments and simulations, *The XXXVII Iberian Adsorption Meeting (Reunión Ibérica de Adsorción, RIA)*, Seville, Spain, 12-14 September, **2012** (***oral***)

De Lange, M.F., Gascon, J., Vlugt, T.J.H., Kapteijn, F., Metal-organic Frameworks in heat pump applications, *NCCC (Netherlands' Catalysis and Chemistry Conference) XIII*, Noordwijkerhout, Netherlands, 5-7 March, **2012** (***poster***)

De Lange, M.F., Gascon, J., Vlugt, T.J.H., Kapteijn, F., Metal-organic Frameworks in heat pump applications, *Netherlands Process Technology Symposium (NPS 11)*, Papendal, Netherlands, 24-26 October, **2011** (***poster***)

De Lange, M.F., Gascon, J., Vlugt, T.J.H., Kapteijn, F., Metal-organic Frameworks in heat transfer applications, *ADEM conference*, 26-27 May, **2011** (***oral***)

ABOUT THE AUTHOR

Martijn (pronunciation[2]: mɑrˈtɛin) Ferdinand de Lange was born in Rotterdam on the 7th of October 1986 and grew up carefree in Oostvoorne, a coastal village just south of the river Maas. His constellation being *libra*, one might mention that his love for equilibrium – what is adsorption else than equilibrium – was already written in the stars. He would however merely laugh at such remarks. He started his education at Jenaplanschool 'De Driehoek' (primary school), where he struggled with his left-handedness. *E.g.* he was puzzled by every-day traffic and his first articles were written in mirror-image. Later he obtained his VWO-diploma (high school) from the Maerlant College in Brielle in 2005, after which he started his higher education at the Delft University of Technology. He received his M.Sc. degree Chemical Engineering from the same institution in 2011 (*Cum Laude*), explaining perhaps the excessive amount of equations present in this thesis. Luckily though, the majority is hidden from sight in appendices. Directly after he started his PhD at the same university under the caring supervision of Thijs, Freek and Jorge, of which this is the ultimate document. The topic being the assessment of Metal-Organic Frameworks in adsorption driven heat pumps, as a clever observer might have already noticed. Martijn especially enjoyed the multi-faceted approach and he has thoroughly enjoyed getting to grip with all the different tools and theorems employed in each of these facets. He wishes to continue following a path in research and development. During his PhD he has been visiting scientist at the Universität Leipzig (Germany), Universidad Pablo Olavide (Sevilla, Spain) and Zhejiang Normal University (Jinhua, China). In total he had the opportunity to visit eight countries divided over three continents, for which he is truly grateful. Martijn currently resides in Rotterdam, where he happily shares his life with his love and best friend, Marloes.

---

[2] According to the International Phonetic Alphabet (IPA).